The Design of Ruthenium and Iridium Triplet Photosensitisers

Lukas Jakob Hallen B.A. (Mod.)

Trinity College Dublin
Coláiste na Tríonóide, Baile Átha Cliath
The University of Dublin

A thesis submitted to the University of Dublin for the degree of Doctor of Philosophy

2023

September 2022

Declaration

I declare that this thesis has not been submitted as an exercise for a degree at this or any other university and it is entirely my own work

I agree to deposit this thesis in the University's open access institutional repository or allow the Library to do so on my behalf, subject to Irish Copyright Legislation and Trinity College Library conditions of use and acknowledgement.

I consent to the examiner retaining a copy of the thesis beyond the examining period, should they so wish.

X

Lukas Jakob Hallen B.A. (Mod.)

Summary

Chapter 1

This chapter contains a general introduction to photon-induced transitions between electronic energy. Applications that involve such transitions include but are not limited to photodynamic therapy, bioimaging and photocatalysis. Further introductions to triplet photosensitiser behaviour and design then leads to a discussion on how to influence the properties of these compounds by modifying their structure. Particular emphasis is placed on the effects of substituting 2,2'-bipyridine ligands at the 4,4'-position for use as ligands for ruthenium and iridium transition metal complexes.

The chapter then details the synthesis and characterisation of three bipyridine ligands, three ruthenium and three iridium complexes bearing 4-phenylacetylene, 4-acetyletrifluorotoluene and 4-ethynylanisole functional groups. Structural characterisation was completed using multinuclear and 2D NMR spectroscopy along with mass spectrometry. Several crystal samples of the compounds were found suitable for single crystal x-ray diffraction studies.

A wide range of analytical techniques were used to probe the properties of the prepared compounds, including UV-Vis absorption spectroscopy, emission under both air and argon atmospheres, low temperature emission studies, quantum yields of luminescence and emission lifetimes. The results of this analysis demonstrated that substitution at the 4-position of bipyridine ligands exerted significant influence on the properties of the transition metal excited state.

Chapter 2

This chapter follows on from the results of Chapter 1, introducing both triphenylamine and pyrene moieties as chromophores for triplet photosensitisers. The unique spectroscopic properties of pyrene are discussed, with particular emphasis on the extended emission lifetime of the pyrene ^{3}IL excited state. Additionally, the high efficiency of an acetyl-triphenylamine bipyridine as a ligand for transition metal complexes is highlighted.

Synthesis and characterisation of the complexes was attempted via the synthetic routes established in Chapter 1, but required extensive modification of these procedures to generate the ligands and related ruthenium and iridium complexes. Extensive single crystal x-ray diffraction studies were obtained for the structures generated for this chapter.

The spectroscopic analysis of the triphenylamine ligand and complexes revealed significantly more complicated excited state behaviour than the compounds investigated in chapter 1. The iridium complex showed solvent-dependent emission, with measurements performed in MeCN resulting in high-energy emission while similar measurements in CH_2Cl_2 showing low-energy emission. Through extensive investigation including solvatochromic low-temperature emission studies, it was determined that different excited states were accessed in different solvents. While this had recently been reported in triphenylamine-containing rhenium complexes, this was the first time this behaviour has been found in iridium complexes.

The spectroscopic properties of the pyrene iridium complex showed a ^{3}LC excited state, with a significantly enhanced emission lifetime and high sensitivity to the presence of oxygen. Samples of this compound have

been sent to collaborators in Spain to investigate its cytotoxic properties and potential as a photodynamic therapy agent

Chapter 3

Chapter 3 introduces unsymmetric bipyridine ligands, ruthenium, and iridium triplet photosensitisers. Special emphasis is placed on the difficult synthesis of such compounds, as unsymmetric systems require sequential reactions and twice or more the synthetic effort of symmetric ones. The unpredictable photophysical properties of the few reported unsymmetric transition metal triplet photosensitisers are discussed. New work by Dr. Eoghan McGarrigle's research group in UCD allows for facile and modular access to unsymmetric bipyridine systems.

Dr. Alexandra Horan of UCD generated the unsymmetric bipyridine ligands discussed in this chapter. The ruthenium and iridium complexes that incorporate them are synthesised using the methods established in chapters 1 and 2. The structural characterisation of these complexes is significantly more difficult compared to the symmetric complexes of previous chapters due to the loss of equivalency of the protons forming the complexes. Nonetheless, the complexes are fully characterised using a combination of 2D and multinuclear NMR spectroscopy, in conjunction with mass spectrometry and single crystal x-ray diffraction techniques.

The spectroscopic analysis of the ligand systems shows them to be high-performing light harvesting chromophores, with long absorption wavelengths and high quantum yields of emission. Interestingly, the structural variation between them leads to differences in the electronic energy levels but also causes varying degrees of sensitivity to solvent, with isomers showing different solvatochromic emission shifts.

The analysis of the complexes reveals the same behaviour as the triphenylamine iridium complex in chapter 2, with different excited states accessed in different solvents. The MeCN excited state is determined to have a greater degree of metal character, with high-energy emission and low emission lifetimes. Meanwhile, the CH_2Cl_2 excited state has greater ligand character, showing longer emission wavelengths and emission lifetime.

Chapter 4

This chapter introduces 2-photon absorption and its biological and manufacturing applications, including lithography and photodynamic therapy. The factors influencing the ability of a compound to undergo two-photon absorption are examined, along with the two main methods by which the two-photon absorption cross section is measured. The design of ruthenium complexes with large two-photon absorption cross-section is studied, particularly the work done by Gasser and co-workers in recent years. Finally, a set of ligands and ruthenium complexes are proposed as synthetic targets for this chapter that are predicted to have large two-photon absorption cross sections.

Discussion then turns to the synthesis of this family of ligands and complexes, along with structural characterisation via familiar NMR techniques. The spectroscopic properties of the compounds are subsequently investigated, including via acid titration studies. The low emission intensities of the ruthenium and iridium complexes prevent in-depth investigation into their excited state behaviour, but a surprising oxygen response for one of the all-carbon ligands was detected. Thanks to computational studies performed

by Eli Zysmann-Coleman and co-workers, it was determined that this response manifested due to thermally accessed delayed fluorescence (TADF) behaviour. Using computational studies as a guide, more efficient TADF molecules were designed based on the ligand skeleton as future synthetic targets.

Chapter 5

Chapter 5 introduces picolinate compounds as ligands for iridium complexes, particularly as use as triplet exciton harvesters in organic light emitting diodes (OLEDs). A discussion on the advantages of OLEDs over regular LEDs follows, including references to specific iridium complexes such as FIrpic that have long been the subject of intense interest for commercial applications. Further discussions concentrate on how the substitution of picolinate ligands, while not widely explored, offers significant potential for the tuning of excited states. In particular, small changes to the geometry of iridium picolinate complexes can lead to the population of excited states with much higher degrees of ligand-centred character than seen in polypyridyl systems.

Synthesis of a family of picolinate ligands and the iridium complexes forms the next part of the discussion. Incorporation of alkyne linkers into the picolinate ligands is achieved off-complex despite reports that this is not a viable synthetic route. Single crystal x-ray studies of the picolinate complexes show that substitution of the picolinate can significantly influence the bond lengths between the ligand and the iridium metal centre. This weakening of the bond is supported by mass spectrometry results, which show separation of the picolinate ligand from the rest of the iridium complex.

The spectroscopic analysis of the picolinate ligands and iridium complexes show largely charge-transfer excited states, with little to no LC character. The excited state is significantly moderated by modification of the picolinate pyridine ring. These results are promising indicators for the future of substituted picolinate iridium complexes.

Chapter 6

Chapter 6 contains all the synthetic procedures and experimental data for the newly prepared compounds presented in this thesis.

Acknowledgements

I would like to thank my supervisor Professor Sylvia M. Draper for giving me the opportunity to pursue and complete this PhD. While it was not always an easy road, the range and depth of skills that I acquired over the last four years will serve me well for a lifetime. As I move forward in my professional career, I can be confident that I have the tools to overcome any obstacle in my way.

I also extend my thanks to all the technical staff at the TCD School of Chemistry. Without Dr John O'Brien and his vast expertise in NMR spectroscopy, this thesis would not have been possible. His patience for my Friday afternoon sample submissions cannot be overstated or underestimated. Similarly, I lost track of the number of times that I asked Dr. Manuel Reuther for help fixing a problem with one of the fluorimeters in the school. Special thanks also to Dr. Brendan Twamley, who somehow managed to coax incredible x-ray crystal data out of nearly every sample that I brought him (no matter how much toluene was floating around in it). Dr. Gary Hessman and Mark Keegan also helped make this thesis possible. On The administrative side I must thank Dr. Noelle Scully, Dr. Sinead Boyce and AnneMarie Farrell.

I thank all Draper group members past and present who helped guide my path over the last four years – Marta, Nidhi, Xiaoneng, Justo, Colin and Eugene. Special shoutout to Claire for sticking it out with me for the last year (we did it!), I would not have made it without you.

Dr. Robert Conway-Kenny deserves his own paragraph. I cannot thank you enough for the endless advice, guidance and cappuccinos over the last four years. I treasure every robust discussion (read shouting match) over unusual spectroscopic results that I had, they were incredibly fun, and I miss them every day. Even after you moved on the greener pastures you were always there with encouragement and support from the side-lines, I would not be where I am without you. One could not ask for a better leb ded.

Thanks to my brother Tobi, who put up with four straight years of 'look at this cool colour I made' without throwing me out a window (I promise I won't do it again). The Covid-19 pandemic was challenging in many aspects, but the walls of 61 Collins Square held strong against it.

No acknowledgement is complete without thanking mom and dad – There is not enough ink in existence to list all the ways in which you contributed to this work. Thank you for encouraging my curiosity, my love of science and all my weird habits that allowed me to make this journey. There are no better parents in the world.

Finally, my thanks to Maeve. You are an incredibly gifted scientist and have contributed to this thesis in so many ways despite our fields of study being so different. Thank you for every moment that we spend together, every second that you make my life better by just standing next to me, the unspoken support that is the rock on which I build my life. You were there through every failed experiment, every moment of frustration, every feeling of doubt that I would ever make it this far. You shared in every Eureka!, every moment of success and feeling of triumph. Words cannot do justice what you mean to me, I would not have become who I am today without you.

Table of Contents

List of Figures

List of Tables

List of Schemes

Abbreviations

1D	one-dimensional
2D	two-dimensional
a.u.	arbitrary units
bpy	2,2'-bipyridine
Bu	Butyl
C	Celsius
cm	Centimetre
COSY	correlation spectroscopy
d	Doublet
dd	double doublet
DEPT	distortionless enhancement by polarisation transfer
DFT	density functional theory
DMF	dimethylformamide
DMSO	dimethylsulfoxide
e	Electron
em	Emission
g	Gram
HMBC	heteronuclear multiple-bond correlation
HSQC	Heteronuclear multiple-quantum correlation

HOMO	Highest occupied molecular orbital
hr	Hour
Hz	Hertz
J	coupling constant
K	Kelvin
kJ	Kilojoule
L	Ligand
LUMO	lowest unoccupied molecular orbital
m	Multiplet
min	Minute
mol	Mole
m/z	mass to charge ratio
MALDI-TOF MS	matrix-assisted laser desorption/ionisation – time of flight
max	Maximum
mg	Milligram
MHz	Megahertz
mL	Millilitre
mmol	Millimole
MS	mass spectrometry
nm	Nanometre
NMR	nuclear magnetic resonance
ns	Nanosecond
OLED	organic light emitting diode
Ph	phenyl
r.t.	room temperature
s	Singlet
t	Triplet

THF	Tetrahydrofuran
TOCSY	total correlation spectroscopy
UV/Vis	ultraviolet-visible
°	Degrees
δ	chemical shift
ε	molar absorption coefficient
λ	Wavelength
μs	Microsecond
%	Percentage
dppz	Dipyridophenazine
dbpz	dibenzophenazines

1: 4,4-bipyridines bearing donor/acceptor moieties

1.1 Introduction

1.1.1 Harnessing Light

The use of light by humankind as a source for change and growth dates back to the earliest days of our transition from small bands of hunter/gatherers to settled agricultural societies. Not coincidentally, the cradles of ancient civilizations (Mesopotamia, Egypt, China, India and Mesoamaerica) were all located at latitudes where the days are long and winters short.[1] The sun provides earth with a functionally infinite supply of energy, its annual delivery of 173,000 terawatts totalling more than 10,000 times the world's entire energy use.[2] Learning how to effectively harness and control this energy has been at the forefront of modern science since the invention of the first solar cell by Charles Fritts in 1883.[3] Solar energy harvested by photovoltaic cells to produce electricity is now considered one of the major tools in humanity's struggle to gain independence from fossil fuels and avert the catastrophic consequences of unchecked climate change.[4]
However, photons are useful to humanity beyond the raw power they contain. Light interacts with matter via a multitude of different mechanisms and harnessing them has allowed humanity to solve a myriad of challenges . Examples of its applications include photodynamic therapy, bioimaging and photocatalysis, among others. [5–9]

1.1.1.1 Photodynamic Therapy

Clearly surpassing the total number of fatalities even from the current Covid-19 pandemic, in 2018 alone, cancer claimed 9.6 million lives, making it the second leading cause of death in the world amongst diseases.[10] The number of cancer patients is expected to reach 22.2 million by the year 2030.[11] As a result, understanding cancer and developing anticancer treatments is and will remain a field of intense study.[12] Cancer develops when cells undergo mutation and begin to multiply uncontrollably, often fatally impairing vital body functions and resulting in organ failure. The treatment of many cancers is challenging, since the malignant cells do not usually result directly from any external pathogens, and often vary only slightly from healthy cells.[13] This makes designing capable of distinguishing between healthy and cancerous cells very difficult.[13] It had been assumed for a long time that cancer cells multiply more rapidly than healthy cells, so that drugs primarily effective during a cell's reproductive cycle or targeting DNA such as cisplatin were of great interest (**Figure 1**).[14]

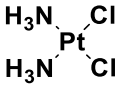

Figure 1. Cisplatin - a widely used anticancer drug.[14]

However, chemotherapy agents typically show very poor selectivity between healthy and cancerous tissue, severe side effects including alopecia, gastrointestinal toxicity, and reduced red and white cell count caused by bone marrow toxicity are common.[14] Despite their efficacy, other non-discriminatory treatment methods such as radiotherapy carry numerous damaging side effects as well, due to their equally poor selectivity.[11] To address this, the design of therapies specifically targeting cancer cells has been an area of active research over the last few decades, with numerous different strategies proposed and investigated.[15–17]

In recent years, the use of Photodynamic Therapy (PDT) in cancer treatment has evolved as an area of particular interest.[18–20] PDT involves the use of a non-toxic compound that, when excited using light of a specific wavelength, produces singlet oxygen or other reactive oxygen species (ROS), which damage the irradiated cells and lead to cell death.[21] This allows specific areas of tissue to be targeted using a beam of light, with non-irradiated tissue remaining undamaged.

An ideal PDT agent will show low dark toxicity, possess a high singlet oxygen quantum yield, good bio- and photo-stability, and undergoes rapid excretion from the body following treatment.[22] Another important feature for a potential PDT agent is its photoactive window, *i.e.*, the range of wavelengths in which it absorbs light. The wavelength of light required to excite a compound greatly influences its effectiveness as a PDT agent, as tissue, blood, and other biological molecules have their own specific absorption windows.[23] These contribute to a low penetration of certain wavelengths deep into tissue, typically wavelengths below 500 nm, as a large number of biological structures absorb in the blue and near-UV range.[24] **Figure 2**, adapted from work by Heinemann *et al*., shows the effective penetration depth of different wavelengths through biological tissue.[24]

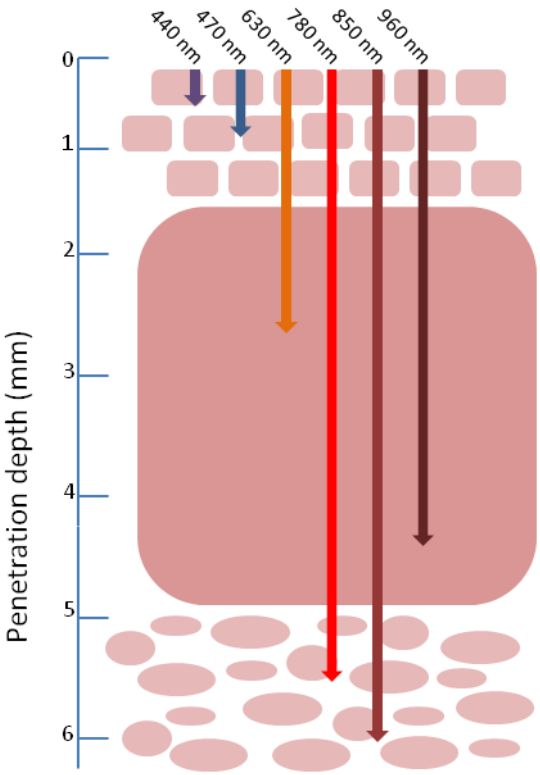

Figure 2. Approximate tissue penetration depth of different wavelengths.[24]

It remains true that there are fewer types of far-red and near-IR absorbing compounds compared to those which actively absorb in the blue and UV; this undoubtedly presents a challenge to the design of novel PDT agents.[25] UV active PDT agents such as Psoralen (**Figure 3**) are therefore limited to topical use, for the treatment of skin conditions such as psoriasis.[26]

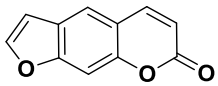

Figure 3. The PDT agent Psoralen (also known as psoralene).[26]

Therefore, the design of PDT agents with strong absorptions in the biological window that allow greater tissue penetration is an area of great research interest.

1.1.1.2 Bioimaging

The use of light-activated compounds is not limited to therapeutic biological applications, but includes diagnostic uses too. In the mid-20th century, the mechanism of enzyme binding was probed by Gregorio Weber using the fluorescent properties of molecules.[27] This discovery marked the start of a huge interest in the use of fluorescent molecules to study biological systems.[8] While there are some fluorescent biomolecules naturally present in human cells already, by far the more common approach to these investigations has been the addition of foreign, strongly fluorescent molecules to biological systems.[28] By exploiting the inherently different chemical affinities of these dyes for different parts of the cell, they helped paint the picture of biochemistry emerging over the latter part of the 20th century, on which work continues to this day.

One of the most well-known forms of bioimaging is the almost ubiquitous use of green-fluorescent protein (GFP).[29] First discovered in jellyfish, the DNA that coded for this protein was later spliced into E. Coli bacteria, allowing them to fluoresce green.[30] Modifications to the structure of the protein have generated an extensive library of derivatives fluorescing in distinct colours, each suitable for different applications.[29] Using gene insertion techniques such as CRISPR it is now also possible to induce the expression of green-fluorescent protein in more complex organisms such as mice or fish (**Figure 4**).

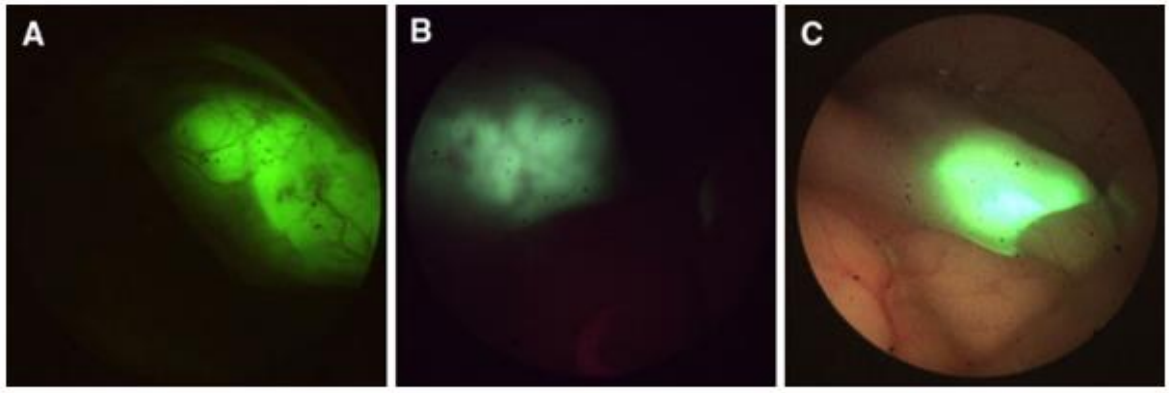

Figure 4. Fluorescence observed from a GFP-Expressing protein with differing emission filters. Images adapted from work by Tran Cao *et al*.[30]

One application of dyes such as green-fluorescent protein combines the imaging and therapeutic benefits of light-active compounds in fluorescence-guided surgery for cancers.[31] When operating to remove cancerous tissue, the full removal of the affected cells is paramount to the success of the procedure and the long-term health of the patient. However, distinguishing between cancerous and non-cancerous tissue during the operation was previously dependent on the visual and tactile senses of the surgeon, which increased the risk of trace amounts of tumour remaining after completion of the surgery. Using dye-expressing pancreatic tumours in mice, Tran Cao *et al*. have shown that it is possible to highlight cancerous cells against non-fluorescent healthy tissue, significantly increasing the ease and reliability with which the two different tissue types can be distinguished.[30]

Although not without its challenges, including enhancing fluorescence to be easily visible by naked eye, significant progress has been made in overcoming them. These include using excitation sources compatible with the rest of the surgical procedure and ensuring the delivery of dye to the cancerous tissue. Once perfected, this approach promises to revolutionise the way in which cancer surgeries are performed.[31]

1.1.1.3 Photocatalysis

Another way in which light can be harnessed for human benefit is photocatalysis.[32] Photocatalysis describes the use of light to promote chemical reactions that, in the absence of light, would either not occur or occur much more slowly.[33] While research in photocatalysis has increased significantly over the last two decades, its first principles were observed at the start of the 20th century. The initial discoveries were limited to the bleaching of organic dyes by active oxygen species, which themselves were produced following the absorption of ultraviolet light by TiO_2.[34] However, during the 1960-70s the use of photocatalysis in the

reduction/oxidation of simple organic molecules was discovered, leading to a remarkable growth of interest in the field.[32] This interest was rewarded by the discovery of the photoelectrochemical splitting of H_2O into H_2 and O_2 using platinum and TiO_2 by Akira Fujishima and Kenichi-Honda.[35]

While the potential for photocatalytic water splitting is great, significant challenges remain– including increasing the solar-to-energy efficiency and overall system lifetime, which would allow it to economically compete with the steam reforming of natural gas and other hydrocarbons.[36]

Applications of photocatalysis include the 'fixing' of CO_2 into hydrocarbons, which has potential for both reducing greenhouse gas atmospheric concentration and fuel production. In 2006 Tran *et al.* reported the production of methane gas when CO_2 and water vapour were passed over TiO_2 pellets in the presence of UV light.[33] TiO_2 has remained attractive photocatalytic material due to its high chemical stability, availability, low cost and environmental impact and negligible toxicity. The introduction of modified TiO_2 surfaces with intentionally induced defects has increased the efficiency of CO_2 fixing due to an increased number of reaction sites.[9] Additions of noble metals such as gold, palladium and silver have been shown to increase reaction rates using a similar mechanism of adding reaction sites to the TiO_2 surface. Finally, modern materials chemistry has generated novel materials such as graphic carbon-nitride that show higher baseline efficiency than more traditional photocatalysts such as TiO_2.[36]

1.1.2 Photophysical Processes

1.1.2.1 Electronic Transitions

The applications for photoactive materials are widespread and of importance to the future development in several sectors including energy and healthcare. Before continuing to discuss the relevance of this work to the overall body of photoactive materials, it is important to lay a foundation of knowledge and establish a common nomenclature for discussing the interactions of light with materials, as these can often vary between and occasionally even within publications.

When discussing the interaction of light with materials we most often refer to the part of the electromagnetic spectrum between 200-1100 nm, containing what is commonly referred to as visible light. Visible light is the section of the electromagnetic spectrum that humans have evolved to detect, between high-energy blue light (~450 nm) to low-energy red light (~740 nm). Ultra-violet (UV) light describes the region of the spectrum at higher energies and lower wavelengths than blue light, while infrared (IR) light describes the region of the spectrum at lower energies and higher wavelengths than red light.

1.1.2.2 Excited State Formation

Light in the visible and UV spectrum possesses the correct energy to induce electronic excitation in molecules, where electrons absorb the energy of the incident photons to transition from the lower energy ground state (GS) to higher-energy excited states (ES). Beyond IR light there is insufficient energy in a single photon to induce such excitation, while electromagnetic radiation with a wavelength shorter than UV light is too high in energy to cause electronic transitions.

The mechanisms which govern the absorption of the photon (and population of the ES) followed by the subsequent relaxation of the system back down to the ground state have been the subject of intensive

research since the first discovery of fluorescence.[37] Due to the enormous efforts that researchers have committed to this subject; a set of governing principles have been established. The excitation of electrons leads to an occupation of quantised atomic or molecular orbitals. A number of factors can influence the exact energy of the orbital. These include the presence and strength of bond, the elements involved in bonding and even the local environment of the molecule.

Of great importance to the process of electromagnetic absorption is the matching of energies of the incident photon and the gap between the occupied ground state and empty excited state. In order to induce excitation from the former into the latter, an incident photon must possess an energy to match the energy gap between the two states.

Once excited, the electron will occupy a previously empty and higher energy state, often one that has non-bonding or antibonding character. The excited state is inherently unstable, and the system will attempt to revert into the lower energy, more stable ground state. This can occur via a range of decay pathways, all leading to the relaxation of the excited system back into the ground state.

Molecular and atomic orbitals are classed as bonding, non-bonding or antibonding. Bonding orbitals form when two atoms share electron density, transitioning from two non-bonding orbitals into one lower energy bonding and one higher energy non-bonding orbital. The relative position of these orbitals, combined with the degree of population by electrons, control the photophysical processes that can occur in the molecule. Transitions typically occur from occupied bonding or non-bonding orbitals into antibonding orbitals. The nomenclature used to describe these transitions depends on the orbitals involved.

Most orbitals in simple hydrocarbon-based compounds arise due to the formation of σ- and π-bonds, in turn establishing σ- and π-bonding and σ*- and π*-antibonding orbitals. Non-bonding orbitals can be found in some hydrocarbon molecules that contain heteroatoms such as oxygen, nitrogen or phosphorous. These orbitals are shorthanded as n-orbitals.[37]

Thus, a transition from a bonding π-orbital into a non-bonding π-orbital is a π-π* transition (**Figure 5**). A transition from a non-bonding n-orbital into an antibonding π* orbital is a n-π* transition. This terminology has been in use since Kasha first proposed his rules governing electronic relaxation and is still utilised today.[37]

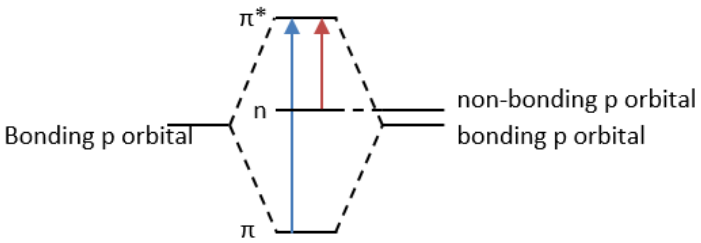

Figure 5. Simplified diagram showing two bonding p-orbitals forming a π bond, with a low-level bonding π and a high level antibonding π^*orbital.

The above transition types commonly show large energy gaps between the ground and the excited state, requiring light of short wavelength to induce excitation. Both transition types occur in the UV and blue light regions of the electromagnetic spectrum. A few notable exceptions include heavily fused nanographenes or n-doped superbenzenes, where the high degree of conjugation results in high energy ground state π-orbitals and low energy π* excited state orbitals.[38] This lowers the energy gap between the ground and the excited state, allowing light of longer wavelength and lower energy to induce transitions.

For the most part, the aforementioned transitions describe the photophysical behaviour of simple aromatic hydrocarbons such as benzene, naphthalene and those with heteroatoms such as furans or pyridines. Even the larger aromatic compounds mentioned in the paragraph above are at their core similar to benzene, with largely symmetrical structures and electron distribution.

More complex photophysical behaviour is possible when compounds have large dipole moments, areas of high and low electron density. In these molecules, electronic excitation can result in the transition of electrons from the area of high density (the ground state) to the area of low density (the excited state). These transitions, termed charge-transfer (CT) transitions, can occur at much longer wavelengths and lower energies than π-π* and n-π* transitions, and are commonly found in dyes such as nile red, rhodamine or azo dyes.[39,40]

There are established rules governing the transition probability of an electron from a ground state orbital into an excited state orbital beyond requiring a photon with the correct energies. One of these rules, the Laporte Rule, prohibits the transitions between orbitals with the same symmetry (gerade or ungerade) in centrosymmetric molecules. Additionally, the spin selection rule states that the transition must maintain the spin of the electron – transitions where the spin of the electron changes are disallowed.

These rules can be broken, notably due to coupling with vibronic transitions that disrupt structural symmetry, but they will strongly influence the probability of a photon absorption and subsequent excitation.

1.1.2.3 Excited State Behaviour

The discussion so far has revolved around the excitation of an electron occupying a low-energy ground state orbital to a high-energy excited state orbital after absorption of a photon. Of potentially greater importance is

the subsequent nature of the excited state. Being inherently unstable, the excited states presents opportunities for chemistry that are not viable in the ground state. The instability of the excited state is what makes photoactive compounds particularly useful, as it is possible to influence the behaviour of the excited state to promote desired processes.

In all but the simplest molecules, more than one absorption process may be possible. In this instance, Kasha's rule states that upon excitation into a higher-level excited state S^{n+1} the species will relax to the lowest-energy excited state excited state S^1 within an extremely short timeframe (femtosecond-picosecond).[37] This prohibits a great number of interactions that are theoretically possible with S^{n+1}. However, it is important to note that Kasha's rule was established on the basis of simple aromatic molecules, and as the complexity of the excited system increases the intricacies of excited state behaviour can be expected to increase as well.[37]

One common consequence of excitation into an ES is immediate relaxation of the molecule into the ground state via vibrational and rotational decay. This translates the electronic energy of the excited state into kinetic energy via bond vibration and rotation of the molecule, a process termed internal conversion.[41] It is a non-radiative decay pathway, meaning that the relaxation of the excited state into the ground state is not accompanied by the release of a photon.

The converse situation is radiative emission, where the electron in the excited state relaxes back to the ground state accompanied by emission of a photon. This photon has lower energy than the one that was initially absorbed, with the energy gap termed the Stokes shift. The magnitude of a Stokes shift depends on the nature of the excited state and can range from less than 10 to over 100 nm.[42]

Due to the spin selection rule, excitation of a singlet ground state will result in population of a singlet excited state. Emission from this excited singlet state to the singlet ground state is termed fluorescence. In larger photoactive materials, specifically those containing heavy atoms such as halogens or metals, it is possible for the excited system to undergo intersystem crossing (ISC). The process of ISC leads to a change in the spin of the excited electron from singlet to triplet. The process of ISC is dependent on the degree of spin-orbit coupling, i.e., the degree to which the orbital angular momentum and the spin of the electron are correlated. These interactions increase in magnitude with higher atomic numbers, a phenomenon known generally as the 'heavy atom effect'.[5]

The heavy atom effect describes the propensity of photoactive molecules containing atoms of higher atomic number to have a greater rates of ISC. For heavier transition metals such as ruthenium, iridium and osmium the heavy atom effect is so significant that the rate of ISC is unity, i.e., every excited state electron will undergo ISC.[43]

Triplet excited states have lower energy than their singlet excited state equivalents, as the electronic repulsion of the separate spin states reduces. Once the triplet excited state the same types of relaxation pathways (internal conversion, radiative decay etc.) are available as in the singlet state. The radiative decay of the triplet excited state to the singlet ground state is called phosphorescence.

In addition to relaxation pathways, another major process that excited state molecules can undergo is reactions with secondary molecules. The nature of these interactions can vary, from energy transfer (both

Foerster and Dexter) to exciplex/excimer formation and redox reactions.[44,45] Many potential applications for light-active molecules are derived from these processes. In essence, they enable the transformation of systems not usually sensitive or reactive to light by using additive light-harvesting compounds. These compounds are classified as photosensitisers.

1.1.2.4 Triplet Photosensitisers

A photosensitiser is defined as a molecule with the ability to absorb light and, once in the excited state, transfer its energy to another molecule in order to promote chemical change.[21] This transfer results in the relaxation of the photosensitiser to its ground state, leaving it chemically unchanged. Photosensitisers play a pivotal role across many fields of chemistry.[6,21]

One of the most common compounds to react with excited state photosensitisers (to be **sensitised** by them) is oxygen. Molecular oxygen is unusual since it has a triplet ground state spin, but a singlet excited state.[25] Due to the laws of spin preservation, this means that any sensitiser aimed at sensitising oxygen must be designed to have a triplet excited state. Singlet oxygen, and other related reactive oxygen species, are highly unstable and react with a wide range of substrates, notably biomolecules and many photoinitiators.[46] Consequently, a high level of interest exists for designing triplet photosensitisers that can efficiently sensitise oxygen.

This efficiency is measured by the ratio of photons absorbed to molecules of singlet oxygen produced, called the singlet oxygen quantum yield. Other important parameters commonly used to evaluate the performance of triplet photosensitisers are the excited state lifetime, i.e., how long the electron stays in the excited state before radiative decay occurs; the range of wavelengths at which the sensitiser absorbs; the intensity of absorption, usually measured at the lowest energy absorption band; and the quantum yield of luminescence - how many photons are emitted per photon absorbed.[25,40,47]

Triplet photosensitisers can occur in a wide range of chemical forms, from tetrapyrroles and BODIPY derivatives to quantum dots.[48] The common feature of all of these disparate compounds is their ability to sensitise triplet oxygen to singlet oxygen.

The wide range of reported triplet photosensitisers shows that there is no 'one size fits all' approach to their design – the desired properties of a photosensitiser are dependent on the specific application it is being designed for.[5] The specific electronic properties of a photosensitiser are highly dependent on the structure of the molecule, also called the structure-property relationship. Addition or removal of one or two atoms, such as transition metals, can have dramatic effects on the performance of a photosensitiser.[49]

The nuances of structure-property relationship for triplet photosensitisers are not only quite difficult to predict from the outset. It is equally challenging to determine which alteration on the structure actually led to the change observed in the photophysical properties.[40,50] Consequently, a systematic approach to triplet photosensitiser design is necessary to allow for a more controlled investigation of structure-property relationships..

The above approach is an important feature of photosensitiser design and reflected in this thesis, as many of the generated compounds show large degrees of similarity with one another. That being the case, it will be

important to highlight seemingly minor structural differences having significant effects on photophysical properties.

1.1.2.6 Organometallic Triplet Photosensitisers

One other large class of triplet photosensitiser are organometallic systems based on a transition metal centre bonded to organic, carbon-based ligands. Such systems provide an attractive platform for a diverse range of triplet photosensitisers, as the transition metal centre provides the large spin-orbit coupling constant required for efficient ISC, while the ligand framework presents almost unlimited scope for structural modification.

Some of the most widely explored organometallic triplet photosensitiser frameworks include pyridyl ligands such as 1,10-phenanthroline (**phen**), 2,2'-bipyridine (**bpy**) and 2-phenylpyridine (H**ppy** as a free ligand, **ppy** as a metal ligand).[51,52] Combined with second and third row transition metal centres such as ruthenium, rhenium, iridium and osmium these ligands produce triplet photosensitiser systems with good stability, high absorption in the visual range, long excited state lifetimes and high singlet oxygen quantum yields.[50,53,54] Of these, ruthenium and iridium are the most widely explored.

1.1.3 Ruthenium and Iridium Triplet Photosensitisers

1.1.3.1 Photophysical Properties

Ruthenium and iridium are both transition metals commonly employed as centres in organometallic triplet photosensitisers.[50,53,55] They are stable in a number of oxidation states, but ruthenium is most commonly found as Ru(II) and iridium as Ir(III), leaving them both as d^6 transition metals, forming low-spin octahedral complexes with all of their electrons occupying d-orbitals.[43,56] This results in their reasonably high stability to both chemical and environmental challenges and enhanced usefulness as triplet photosensitisers.

The photophysical properties of ruthenium and iridium triplet photosensitisers can differ depending on the ligand framework and oxidation state. However, there are some general processes and a nomenclature worth discussing and defining at this point.

The metal itself will play a key role in many of the photophysical processes the complex undergoes. The electrons populating the d-orbitals can be readily excited into higher-lying orbitals, but the nature of the lowest excited state will depend on the structure of the complex. One of the most common transitions in ruthenium and iridium triplet photosensitisers are metal-to-ligand charge transfer (MLCT) transitions.

In MLCT transitions, the metal d-electrons are excited into the ligand antibonding π* orbitals. This means that the highest occupied molecular orbital (HOMO) in these complexes is commonly centred around the metal, while the lowest unoccupied molecular orbital (LUMO) is centred around the ligand. The extent of conjugation within the ligand will strongly influence the energy of the π* LUMO orbital, which in turn affects the energy gap between it and the HOMO. This is one of the methods by which the absorption wavelength of transition metal complexes can be tuned. A higher degree of conjugation will result in lower lying π* orbitals, a smaller energy gap between the HOMO and LUMO and longer absorption wavelengths. As a benchmark, the MLCT absorption band of tris-(2,2'-bipyridine)ruthenium(II) $[Ru(bpy)_3]^{2+}$ lies at ~450 nm, while the MLCT absorption band of tris (2-(pyridin-2-yl)phenyl)iridium(III) $[Ir(ppy)_3]$ lies at 370 nm.[57,58]

The higher energy gap in the iridium complex is due to lower lying d-orbitals. In some rare cases, the high spin-orbit coupling constant of iridium is so high (3909 cm^{-1}) that direct absorption from the singlet ground state into the triplet excited state is observable, albeit at very low intensity.[43,59] This is noted as ^{3}MLCT absorption to specify the spin state of the excited state populated by the absorption.

Other important absorption transition types in ruthenium and iridium triplet photosensitisers include metal-centred (MC) transitions occurring between metal states, e.g., between t_2g and e_g orbitals. Formally contrary to the Laporte rule, small distortions in octahedral geometry break the centrosymmetry of the molecule and enable the transitions. They occur at higher energies than MLCT and do not usually play important roles in the absorption spectra of ruthenium and iridium complexes. For ruthenium polypyridyl complexes these transitions occur between 320 and 370 nm, while for similar iridium complexes the energies are in the UV range.

In addition to the above metal transitions, the ligand-based transitions also contribute to absorption spectra. $\pi - \pi^*$ and $n - \pi^*$ transitions are common, overlapping with higher-energy MLCT and MC transitions. Once the ligand is bonded to the metal, these transition types are combined under the ligand-centred (LC) term. Charge-transfer transitions are of particular interest for transition metal triplet photosensitisers and will be discussed in depth later in this thesis. An important distinction to make here is that once the ligand is formally bonded to the metal centre, a charge transfer transition (CT) is renamed an intra-ligand charge-transfer (ILCT) transition, typically shifted to longer absorption wavelengths.[60]

While other transition types are occasionally found in organometallic triplet photosensitisers, including ligand-ligand charge transfer (LLCT) and ligand-to-metal charge transfer (LMCT) they do not commonly feature in ruthenium and iridium photochemistry.

The first excited state of ruthenium is typically ^{1}MLCT in nature, but this rapidly undergoes ISC to populate the ^{3}MLCT state. For some ruthenium complexes, the ^{3}MC state can be thermally populated once ISC has been completed.[56] The process leads to non-radiative decay of the excited state back into the ground state on very short timescales. As a result, this phenomenon can shorten the overall excited state lifetimes of ruthenium complexes significantly, leading to decreased photosensitiser performance.

A summary of the above photophysical processes is presented in a simplified Jablonski diagram (**Figure 6**).

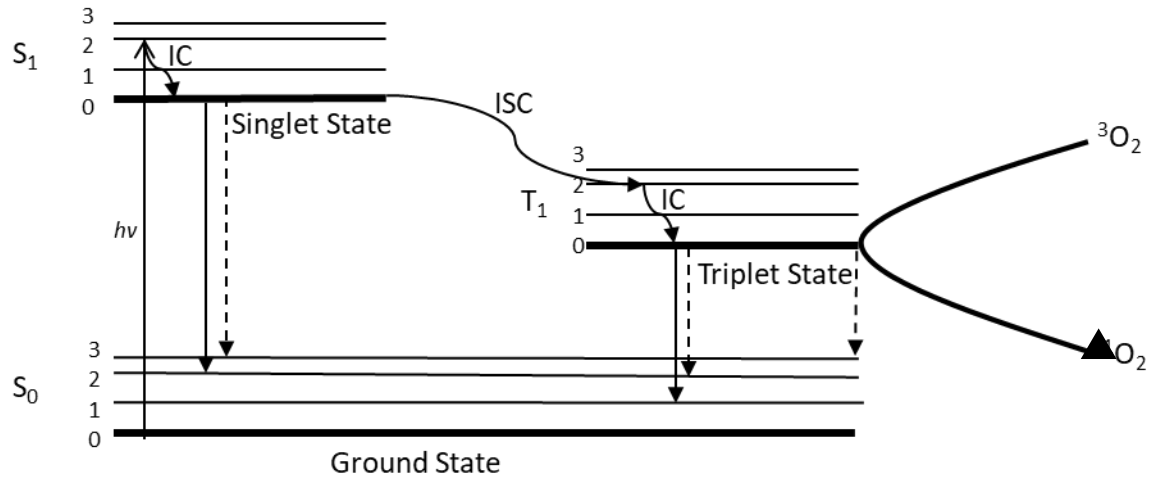

Figure 6. Simplified Jablonski diagram showing absorption, radiative emission (solid line), non-radiative emission (dashed line), intersystem crossing (ISC), internal conversion (IC), and triplet-triplet annihilation processes.

While isomerisation of ruthenium and iridium metal complexes is prevalent throughout the literature, they will not be discussed in this work.[61, 152] Purification of the metal complexes presented in this thesis was extremely challenging, and further resolving the varying isomers was beyond the scope of this work.

"Given their tuneable photophysical properties, scope for structural modification and general stability it is unsurprising that ruthenium and iridium triplet photosensitisers have been widely explored for numerous applications.[21,50,61]

1.1.3.2 Ruthenium Complexes as Photodynamic Therapy Agents

In 1993, porfimer sodium, also known as Photofrin was approved as the first PDT drug with an absorption window between 405 and 630 nm, allowing it to function as a PDT agent in subcutaneous tissues.[21] Photofrin consists of a mixture of porphyrin oligomers up to 8 units long. Since its introduction, 13 other PDT agents approved for clinical use have been macrocyclic organic molecules.[62] Many share similar problems, including a difficult total synthesis, purification issues, as well as poor solubility in aqueous media.[63] Consequently, there is still a need for soluble and nontoxic, rapidly excreted PDT agents, ideally synthesised using common pharmaceutical preparation and purification techniques. In recent years, systems derived from the archetypical ruthenium polypyridyl complex, $[Ru(bpy)_3]^{II}$, have shown promise in addressing these criteria.[24]

Ruthenium polypyridyl complexes are coordination complexes consisting of a Ru(II) centre coordinated to three bipyridine-containing ligands, including 1,10-phenanthroline or 2,2'-bipyridine. $[Ru(bpy)_3]^{II}$ is shown in **Figure 7**.

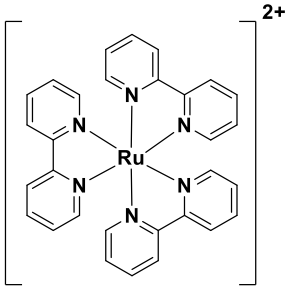

Figure 7. $[Ru(bpy)_3]^{2+}$ - a typical ruthenium polypyridyl complex.

Ruthenium polypyridyl complexes usually show MLCT transitions between 400 and 600 nm, facilitating excitation at a greater tissue depth than other topical PDT agents such as Psoralen.[24] Upon excitation from the ground state (S_0) to the first singlet excited state (S_1), the second row Ru(II) centre facilitates efficient intersystem crossing (ISC) to the first triplet excited state (T_1) at unity (100 % conversion), due to the strong spin-orbit coupling.

While oxygen can become sensitised by singlet electronic states, the rate of sensitisation will be highest for spin-allowed transitions.[64] Using triplet photosensitisers, generating singlet oxygen from the triplet state of the metal will result in a net zero spin change, making this a formally allowed energy transfer process.[64] Additionally, the use of triplet photosensitisers has the added benefit of extended triplet state lifetimes, allowing for a greater number of intermolecular interactions to take place before decay to the photosensitiser ground state.[64]

The lifetime of $^1O_2$ within biological tissue is approximately 40 ns, allowing it to react with biological tissue within a 20 nm radius.[46] The reactions of $^1O_2$ with biological tissue led to cell damage and death in a process known as Type II photodynamic therapy and are considered the primary mechanisms of action for most ruthenium photodynamic therapy agents.[21,48]

However, additional challenges remain and need to be overcome before ruthenium polypyridyl complexes can be offered as widespread therapy options. Despite their ability to be photoexcited beyond those of topical-restricted compounds, wavelengths between 400 and 650 nm are still not ideal for treating deep subcutaneous tumours, and complexes absorbing significantly further into the red region are notably rarer.[40,48] Another drawback of current PDT treatments is the problem of the coherence of the light beam, as it is currently not possible to target an area of tissue in 3D space. If a directed light beam (or laser) is applied to a targeted area, penetration along its path will proceed uniformly through the tissue, potentially damaging healthy cells *via* the generation of $^1O_2$, or other ROS. One proposed solution to this problem is the use of two-photon absorption (TPA).[67] TPA describes the process by which the simultaneous absorption of two photons by a molecule results in an electronic ES; a process which can be restricted to a much smaller region

in space through control of a lasers focal point, as the absorption process is proportional to the square of the laser intensity.[68] This topic will be elaborated on in later chapters.

1.1.3.3 Iridium Complexes as Bioimaging Dyes

In previous decades, dyes used for bioimaging were predominantly organic in nature, rarely containing any organometallic components.[69,70] In recent years, there has been a growing interest in the use of iridium complexes as bioimaging agents.[8,28] The iridium metal centre is largely inert, rarely interacting chemically with biomolecules. When the iridium is surrounded by cyclometallated or datively bonding polypyridyl and phenylpyridyl ligand scaffolds, as the Ir-C and Ir-N bonds remain robust in the cellular environments.

The use of iridium complexes as bioimaging agents has several distinct advantages over conventional and previously used bioimaging dyes. The first is that their excitation wavelength is on average at lower energies than those of comparable organic dyes, which has two benefits for bioimaging; natively fluorescent biomolecules, such as those containing tryptophan moieties, can themselves be inherently fluorescent when excited at the correct wavelength.[28] The result is a phenomenon called autofluorescence, in which the emission of light by biomolecules reduces the signal-to-noise ratio and reduces sensitivity.[30] Using longer wavelengths of light reduces the excitation of biomolecules and increases the signal-to-noise ratio is. Additionally, the lack of competitive absorption of light by biomolecules means that the penetration depth of that light through the cellular media is increased, allowing deeper tissues and cell structures to be identified.[8]

Furthermore, iridium complexes are reported to have long emission lifetimes, ranging from tens of nanoseconds to milliseconds.[50,71] This allows time-gated emission detection to be used, further reducing the signal-to-noise ratio and minimising the impact of autofluorescence. As an example of how significant this phenomenon is, Murphy *et al.* showed that the luminescence of an iridium complex could be distinguished from the luminescence of Hoechst 33343, an organic dye, simply by gating the emission detection at 10 ns.[72]

Another advantage of using iridium complexes for bioimaging is the degree to which their properties can be influenced by modifying their chemical structure. This not only facilitates a significant degree of control over their photophysical properties, such as emission wavelength, lifetime and quantum yield, but also over their interactions with cellular media.[52,73,74] Recent years have seen a significant rise in the number of organelle-targeting iridium complexes.[28] These either take advantage of cellular mechanisms to accumulate within discrete areas of the overall cell or exhibit switch-on luminescence in localised cellular media, giving a signal response within a specific environment. Both processes enable researchers to probe the function and workings of those structures. These probes include localisations in cellular membranes that have not traditionally been accessible for bioimaging, including the nucleus. Previous switch-on organometallic complexes emitted in the nucleus, such as ruthenium dipyridophenazine derivatives, intercalated between DNA base-pairs, markedly enhancing their cytotoxicity.[24,75] On the other hand, iridium complexes have been reported to exhibit switch-on behaviour by reacting with histidine containing proteins, not DNA strands or base pairs, which significantly reduces their toxicity.[76]

It is also possible to append structures to the spectator ligands of iridium complexes that promote localisation within specific regions of the cell without significantly affecting photophysical properties. This allows the researchers to tailor bioimaging compounds for specific tasks, seriously increasing potential research output.

This has allowed the development of iridium complexes targeting the nucleus, the Golgi apparatus and the cytoplasm among others.[77]

While iridium is considered largely non-toxic to humans, certain iridium complexes can exhibit high toxicity within cells, measured by their IC_{50} concentrations.[28] The toxicity of iridium complexes is proportional to the uptake rate of the complex into the cell, which in turn depends on the lipophilicity of the complex. The greater the lipophilicity, the higher the uptake, the lower the IC_{50} and the more toxic the compound is to cells. This problem can be readily alleviated by appending polyethylene glycol (PEG) chains to the spectator ligands. The steric bulk of these chains reduces the potential interactions of the iridium complexes with biomolecules, reducing the chance of cellular damage and death.[28]

1.1.4 Ruthenium and Iridium Complexes Bearing 4,4' substituted 2,2'-bipyridine ligands

This is not an exhaustive description of the multitude of applications for which ruthenium and iridium complexes are suited. However, it does provide an insight into why these compounds qualify for such a wide variety of uses. The inherent stability of their metal centres, the ability to modify the photophysical properties and a large body of extant literature from which to draw guidance are all contributing factors.

There is however always more to learn. In recent years it has been suggested that the description of triplet photosensitiser behaviour has been oversimplified.[78–80] Observations including dual emission from a number of ruthenium complexes and solvent-dependent excited state switching in rhenium bipyridyl systems suggests that the photophysical properties of triplet photosensitisers are far more specific to the individual complex, and therefore ill-suited to generalisations.

As a result, this work intends to provide insight into how small changes in the overall chemical structure of single ligands can exert significant influence on the overall properties and behaviour of iridium and ruthenium triplet photosensitisers. These compounds, while designed with applications in photocatalysis, photodynamic therapy and bioimaging in mind, are not necessarily tailored specifically to these tasks. Rather, they were created to enhance and further the understanding of structure-property relationships, as well as promoting new synthetic pathways and approaches to the design of triplet photosensitisers.

The foundation of this work will initially rest on 4,4-substituted 2,2'-bipyridine ligands. The reasons for choosing the 4,4'-position are twofold. The first is that 4,4'-dibromo-2,2'-bipyridine is readily commercially available, which avoids tedious bromination procedures previously developed in the Draper group.[40,71,81] While these bromination reactions were successful, the low yields prohibit the synthesis of a wide range of photosensitisers for comparative purposes, as the starting material is scarce and expensive.[50] The second reason why the 4,4' position was chosen is the interesting photophysical behaviour of complexes bearing its substitution pattern , as reported on over the last few decades.

Wang *et al.* laid the groundwork in 2001 by comparing the spectroscopic properties of two ruthenium complexes, both bearing 2,2'-bipyridine ligands substituted at the 4,4' and 5,5' positions with diethylbenzamides, bonded to the pyridine rings via acetylene linkers (**Figure 8**).[82]

The paper discusses the photophysical properties of the free ligands. The authors show the change in position of substitution on the ligand having significant effects on the UV-Vis absorption spectrum of the ruthenium complexes. At higher energies, **1.02** manifests a significant absorption band at 380 nm lacking in **1.01,** while the latter shows a shoulder at a higher energy peak around 320 nm absent in the former. These changes likely relate to the different absorption of their free ligands.

Of equal interest are the changes observed at lower energies. Both compounds show low absorption maxima at ~495 nm, but the intensity of the transitions is significantly different, with the molar absorption coefficient of **1.01** more than doubling **1.02's** at 495 nm. The authors assign these peaks as ^{1}MLCT transitions from the metal d-orbitals into the empty ligand π* orbitals.

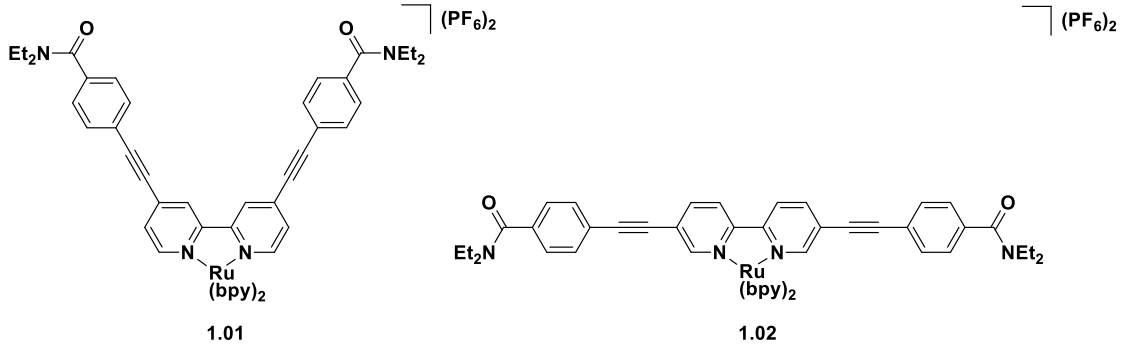

Figure 8. Structure of two ruthenium complexes bearing a modified bipyridine ligand substituted at the 4,4' and 5,5' position.[82]

The excited state properties of the two complexes differ even more significantly. **1.01** emits at 670 nm while **1.02** does so at 695 nm, suggesting a lower energy excited state in **1.02**. The quantum yield of **1.01** is 4.5 times greater than that of **1.02**, and the lifetime is three times as long. Using single-vibrational mode Franck-Condon band shape expressions, it was determined that the MLCT excited state is more delocalised in **1.01** than in **1.02**, accounting for the extended emission lifetime. Radiative decay constant k_r was enhanced for **1.01** beyond expectations based on the band gap law. The authors then contend that despite the higher degree of conjugation in **1.02** (resulting in a lower lying π* orbital for MLCT absorption), the interaction between the metal d-orbitals and the empty ligand π* orbitals is enhanced in **1.01**. This is due to larger orbital coefficients on the pyridine nitrogen atoms (which is dependent on the substitution pattern on the pyridine ring), resulting in a higher degree of delocalisation in the MLCT excited state.

The work demonstrates the remarkable difference of varying positional substitutions on the electronic properties of ruthenium bipyridyl systems. Furthermore, the results suggest that modifying the 4-position of the pyridyl ring affords more intense absorption, longer excited state lifetime and greater quantum yields of luminescence than the 5-position.

Zhao *et al.* reported 4,4'-substituted bipyridine complexes and their copper complexes, as shown in **Figure 9**.[60]

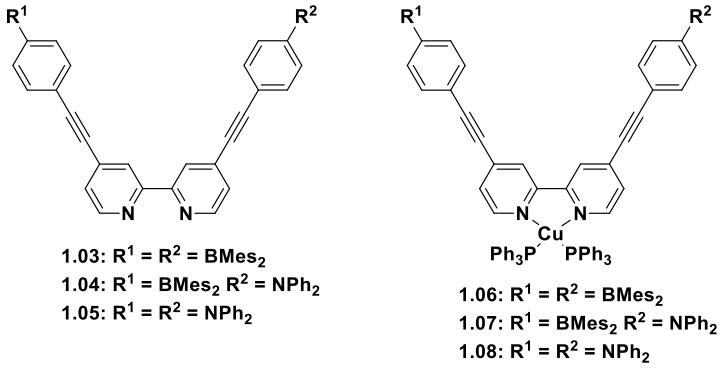

Figure 9. 4,4'-substituted bipyridines and their copper complexes reported by Zhao *et al*.[60]

All three ligands **1.03-1.05** display strong absorption between 230 and 340 nm, indicative of π – π* and n – π* transitions. In addition, **1.05** manifests a broad absorption band at 380 nm, most likely caused by a charge-transfer transition from the triphenylamine donors to the bipyridine core. **1.04** exhibits a shoulder absorption band at the same wavelength but reduced in intensity due to the replacement of one of the triphenylamine moieties with a boron group.

The absorption of **1.06** is notably different from those of **1.07** and **1.08**. The former shows a high intensity absorption peak at 330 nm, but low absorption beyond 400 nm. **1.07** and **1.08** meanwhile show a reduced absorption intensity in the UV, but a significantly enhanced one at 430 nm, with **1.08** manifesting the higher molar absorption coefficient. The absorption behaviour of the copper complexes mirrors the pattern of the free ligands, with the absorption maxima shifted by 60 nm into the red. This is indicative of charge-transfer behaviour, as complexation to a metal centre lowers the LUMO of the bipyridine core, reducing the energy gap and bathochromically shifting the absorption. Judging by these data, the $BMes_2$ groups appear to display a lower degree of charge-transfer character, as the maximum absorption band of **1.03** and **1.06** manifest at approximately the same wavelength. The higher wavelength transitions in **1.06** likely arise due to MLCT transitions from the copper centre into the ligands.[60]

Charge-transfer (CT) behaviour is confirmed by solvatochromic emission studies performed on the free ligands, which show emission wavelength and widening of the emission band with increasing solvent polarity. Charge-transfer transitions result in a redistribution of electron density in the excited state. This allows for a stabilisation of the induced dipole of the excited state by solvent molecule rearrangement, lowering the HOMO-LUMO gap and redshifting emission wavelength. **1.04** and **1.05** show significant solvatochromic effects on their emission bands, from 400 nm in hexane to 560 nm in DMF. The solvatochromic emission behaviour is reduced in **1.03** compared to **1.04** and **1.05**, validating the assumption that the former manifests less extensive CT behaviour.

The quantum yields of luminescence of the prepared compounds vary significantly. The luminescence quantum yield of the copper complexes in degassed CH_2Cl_2 is below 3 % at 298 K. For the free ligands, **1.03** and **1.04** show quantum yields of 18 % and 26 % at room temperature, while **1.05** shows a quantum yield of 100 %. This means that for every photon absorbed a photon is emitted, marking **1.05** as an extremely efficient photon harvester with very low rates of non-radiative excited state decay.[60]

In summary, this paper indicates that the inclusion of triphenylamine moieties linked by acetylenes to a bipyridine acceptor results in an extremely efficient harvesting of photons. If this efficiency were to be maintained when transitioning from free ligand to metal complex, it could result in an extremely efficient triplet photosensitiser. Unfortunately, the use of a copper metal centre reduces the quantum yield of luminescence significantly, even under an atmosphere free of oxygen (which if present competes with radiative emission by quenching the excited state).

Tor and co-workers reported the synthesis of a family of ruthenium complexes bearing phenanthroline ligands, including those shown in **Figure 10**.

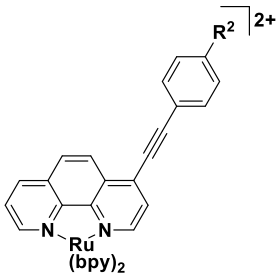

1.09: R = H
1.10: R = OMe
1.11: R = CF_3

Figure 10. Ruthenium complexes prepared by Glazer *et al.*[84]

Modifying the substitution patterns on the phenanthroline systems, allowed the authors to investigate the resulting changes in the photophysical properties of the complexes. As with Zhao *et al.*, the work showed substitution at the para-position resulted in enhanced absorption intensities for the MLCT band compared to other substitution positions.[82]

In particular, Tor and co-workers discovered that substitution at the para-nitrogen induced dual emission in ruthenium complexes. This phenomenon is forbidden according to Kasha's rule, and dual emission is in fact considered a classic sign of a contaminated sample. However, after rigorous purification and analysis of the prepared compounds, the authors were able to verify that the emissive behaviour originated from a single compound. They proposed that the dual emission, one at higher energies with a shorter lifetime and the other at higher energies with longer lifetimes, originate from two separate MLCT transitions. These transitions are localised on the bipyridine and phenanthroline ligands, respectively. Crucially, this behaviour was not observed for ruthenium complexes substituted at different positions on the phenanthroline ligand. This echoes the work by Zhao *et al.*, who showed that substitution at the para-position significantly enhanced the delocalisation of the excited state. This delocalisation could potentially result in a spatially and electronically isolated excited state on the phenanthroline and extended alkyne linker that is not accessible when the complex is excited into the MLCT of the bipyridine ligand. The importance of the substitution position is highlighted by the fact that the nature of the substituent affects only the emission wavelengths and not the observation of dual emission.

The presence of two distinct but accessible excited states was also observed for rhenium ligands bearing 4-substituted bipyridyl ligands.[54] Sutton *et al.* reported the synthesis of two rhenium complexes shown in **Figure 11.**

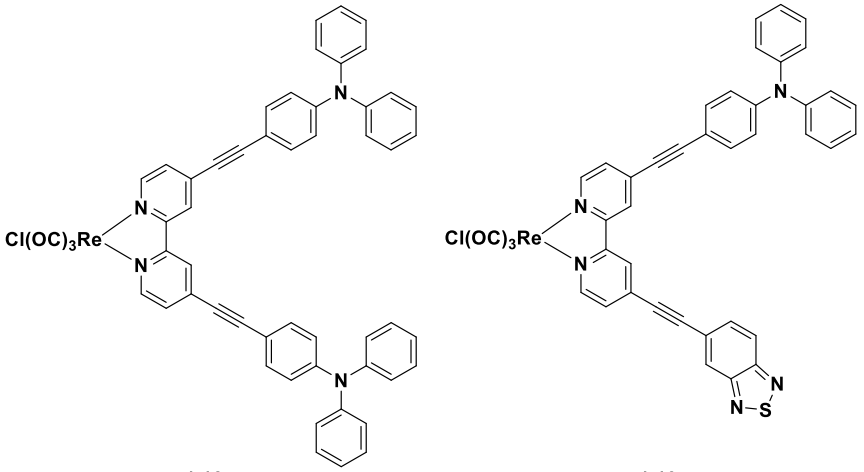

1.12 **1.13**

Figure 11. Rhenium complexes bearing 4,4-substituted bipyridyls prepared by Sutton *et al.*[54]

The free ligand **1.12** displays the same charge-transfer absorption band at 380 nm seen by Zhao and co-workers, while the free ligand of **1.13** shows a higher-energy absorption band at 365 nm.[60] The rhenium complexes show longer wavelength absorption maxima, with both **1.12** and **1.13** absorbing beyond 450 nm. Interestingly, the absorption manifests solvatochromic behaviour, suggesting that the ground state is sensitive to the solvent environment. The absorption maxima in CH_2Cl_2 is notably redshifted compared to the maxima in MeCN, and the molar absorption coefficient is increased in the former solvent as well. This is unusual – it is the transition to the excited state which generates the solvent-stabilised dipole resulting in solvatochromic behaviour. The process of absorption itself should therefore not be significantly influenced by solvent, as the dipole has not yet been formed.

The second point of interest is that CH_2Cl_2 results in redshifted absorption compared to MeCN even though the former is less polar than the latter. This is a reversal of standard solvatochromic trends, and casts doubts on whether the observed solvatochromic response is due to the presence of a dipole. Any dipole present in the ground state should be more stabilised in MeCN than in CH_2Cl_2. Additionally, it is important to note that both of the complexes **1.12** and **1.13** show this behaviour, although the exact values of peak absorption and the extent of solvent-dependent shifts differ slightly.

The emissive behaviour of the complexes in different solvents is equally intriguing. **1.12** in MeCN shows intense high-energy emission at 460 nm with a long tail. **1.13** manifests a similar high-intensity, high-energy band at **440** nm but also a distinct secondary peak at 680 nm. In CH_2Cl_2, the high energy emission peak of **1.12** is significantly quenched, and a new absorption band at **680** nm dominates the emission spectrum. The spectrum for **1.13** is similar, with the previously weaker emission at longer wavelengths rising sharply in intensity while the high-energy peak is reduced. The authors also investigate a range of different solvents, with Toluene and $CHCl_3$ mirroring the pattern of CH_2Cl_2 while acetone and DMF mimic the MeCN emission pattern. This notable change of emission peak intensity cannot be explained by stabilisation of an excited

state by solvent rearrangement – there is no clear trend in the solvent properties that would account for all variations. Additionally, significant changes in emission lifetime were recorded. In CH_2Cl_2 the complexes showed sub 10 ns emission lifetimes at high energy, while the emission lifetimes at low energies is 200 ns for **1.12** and 100 ns for **1.13**. In MeCN only the high-energy emission lifetime was recorded, also showing sub 10 ns lifetimes. The authors suggest that the high energy peak is singlet in nature, while the low energy state is triplet.

Using extensive time-resolved IR and transient absorption and emission spectroscopy in conjunction with computational modelling the authors proposed a mechanism for the observed behaviour. They suggest that the choice of solvent influences which triplet state is lowest in energy, resulting in population of a non-radiative ^{3}ILCT 'dark state' in MeCN and a radiative ^{3}MLCT state in CH_2Cl_2. This swapping of orbital energies requires that the two excited states are almost isoenergetic, allowing for subtle changes in the electronic environment to influence their relative energies. However, the potential for these complexes to act as triplet photosensitisers is limited by their lifetimes, which are too short for use in applications such as photodynamic therapy.

Taking all these publications into consideration, it is clear that transition metal complexes bearing polypyridyl ligands substituted at the position para to the coordinating nitrogen show unique and interesting photophysical properties. However, many of the above works discuss small numbers of prepared compounds, which limits the ability to predict trends and behaviour in photophysical attributes.

1.15 The Sonogashira Coupling Reaction

Before discussing the aims of the project, brief mention of the synthetic approach must be made. Most of the compounds discussed in the preceding introduction are produced using palladium-catalysed coupling reactions to append different donor/acceptor moieties to halogenated polypyridyl precursors.

The Sonogashira coupling reaction specifically is widely used, as it allows facile introduction of acetylene linkers, which are often applied as 'molecular wires' to enhance electronic conjugation along a ligand framework.[50,85] Standard Sonogashira conditions utilise two concurrent cycles, one involving copper (cycle B) and the other palladium (cycle A) as a catalyst.[86] These cycles are shown in **Scheme 1**.

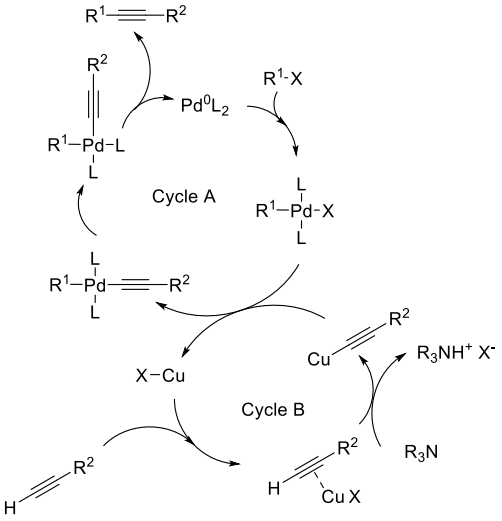

Scheme 1. Sonogashira catalytic cycle.[86]

However, the use of copper in Sonogashira reactions using bipyridine as one of the reagents can lead to significant yield loss and purification issues, as the copper can coordinate to the nitrogen atoms of the bipyridine rings.[60] However, an alternative, copper-free Sonogashira reaction is also possible using the proposed mechanism displayed in **Scheme 2**.

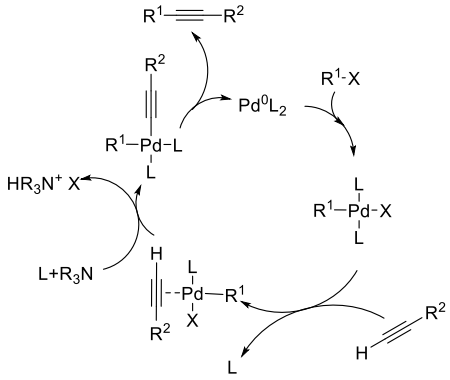

Scheme 2. Copper-free Sonogashira catalytic cycle.

As this project will make extensive use of bipyridyl systems, the copper-free Sonogashira reaction will be used.

1.2 Aims

To prepare a set of transition metal complexes bearing bipyridine ligands substituted at the 4,4'-position by acetylene-linked donor/acceptor moieties to determine photophysical trends, as shown in **Figure 12**.

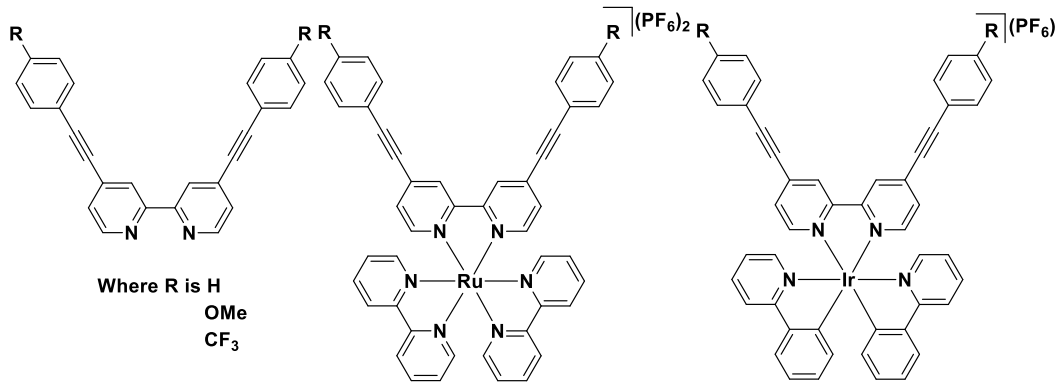

Figure 12. Structures of the target ligands and their ruthenium and iridium complexes.

1.3 Synthesis and Characterisation

1.3.1 Synthesis and Characterisation of PhL, CF_3L, OMeL

The synthetic approach to substituted bipyridine ligand systems often involves carbon-carbon bond forming palladium catalysed coupling reactions.[50,87] Such reactions are used due to their high functional group tolerance, low toxicity and good efficiency. While their yields can vary dramatically, it is unusual for them to outright fail. Additionally, there is a wide scope for increase by using different catalysts or solvent systems, as these can have significant effects on the product yield of the reaction.

For this project, the Sonogashira coupling reaction will be used to access the target ligands from commercially available 4,4-dibromo-2,2-bipyridine. Following purification of the ligand, the ruthenium and iridium complexes will be produced via reactions with [Ru(bipyridine)$_2$Cl$_2$] and [(Ir(phenylpyridine)Cl)$_2$] respectively.

Several different variations of the Sonogashira reaction were used to access the target bipyridine ligands. The unsubstituted phenyl ligand (**PhL**) was generated according to **Scheme 3** shown below. These ligands have previously been prepared by James *et al.* among others, but the corresponding ruthenium and iridium complexes have not been reported.[87]

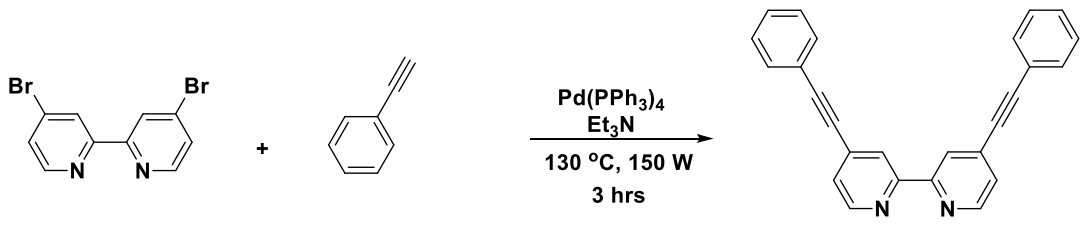

Scheme 3. Synthesis of **PhL.**

Many Sonogashira reactions employ copper as a co-catalyst to prepare the acetylene for transmetallation onto the active palladium catalyst.[50,81] However, the use of copper in the synthesis of substituted bipyridines is problematic due to the ability of the bipyridine complexing to them, forming copper bipyridine complexes that are well represented in literature.[60] The presence of these trace copper complexes in the crude reaction mixture significantly complicates purification via column chromatography, reducing reaction yield. A copper-free Sonogashira mechanism using two separate palladium catalytic cycles is therefore preferred, and is applied consistently throughout the work presented in this thesis.

Sonogashira coupling reactions also require moderately elevated temperatures in order to activate the palladium catalyst, and the chosen temperature can play a large role in the efficiency of the reaction. The Draper group has previous experience performing palladium catalysed coupling reactions as well as metal complexations in a microwave oven.

The purification of the target ligand **PhL** was attained using silica column chromatography. Strong interactions between the pyridyl nitrogen atoms and the stationary silica phase mean that common non-polar mobile phase mixtures such as hexane, petroleum ethers and ethyl acetate will not move the product off the baseline. Highly polar mixtures composed of dichloromethane, chloroform and methanol are instead required to achieve good fraction mobility and separation. For **PhL**, the column was initially flushed with 400 mL neat chloroform to remove trace impurities resulting from catalyst degradation, leftover starting material and side products before a methanol gradient was introduced to elute the target fraction rising from 0.05 % to 2 % MeOH per volume. While the identity of the side product fractions was not identified, typical impurities include the mono-coupled intermediate. The final product **PhL** was recovered from the column as a colourless band and precipitated with diethyl ether from dichloromethane, with the solid then isolated by filtration and washed with hexane.

The ligand was characterised by NMR spectroscopy, and the ^{1}H spectrum of **PhL** is displayed in **Figure 13**

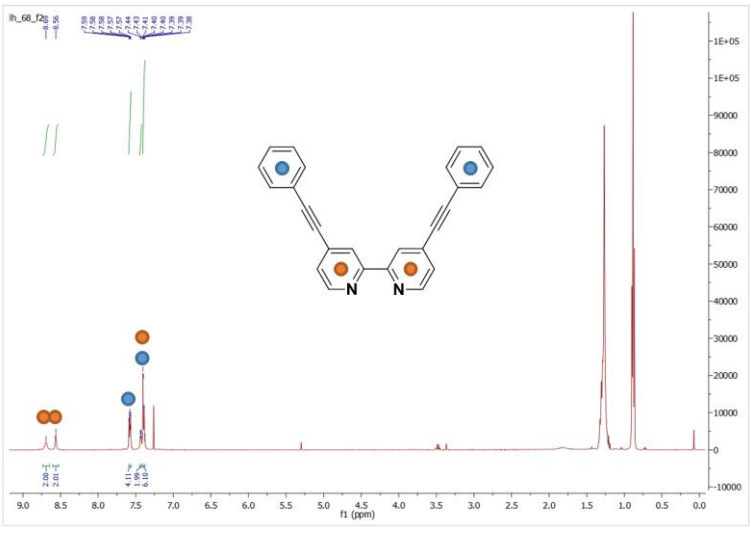

Figure 13. ^{1}H NMR spectrum of **PhL** showing the assigned spin systems of the compound. ($CDCl_3$, 400 MHz, 298 K).

The signals are all found in the aromatic region, where the induced ring current in the conjugated ring systems has a deshielding effect. The high degree of symmetry in the ligand results in a low number of individual signals all integrating to more than one proton. The protons on the pyridine are shifted further downfield to those on the phenylacetylene, due to the electron-withdrawing effect of the nitrogen reducing the extent to which the protons are shielded from the magnetic field of the NMR experiments.

The multiplicity of the pyridine signals is difficult to interpret, as they are very broad and featureless. There should be two doublets and one singlet, but between the broadening and the overlap of the pyridine and phenylacetylene signals these cannot be readily distinguished. Solvent signals from the hexanes used to wash the solid ligand precipitate can be found upfield, but they do not interfere with the ligand signals and are consequently of no great importance.

The ^{13}C spectrum of PhL is shown in **Figure 14**, with the ligand signals appearing between 85 and 150 ppm. The intensity of the carbon signals differs significantly, with the signals of the phenyl ring having greater intensity than those of the bipyridine ring. This may relate to the broadening of signals in the ^{1}H spectrum, and could be indicative of in-solution processes such as stacking or restricted rotation. The signals of the alkyne bridge linker are visible between 80 and 100 ppm, as they are less deshielded by the ring current than the carbons forming the full ring.

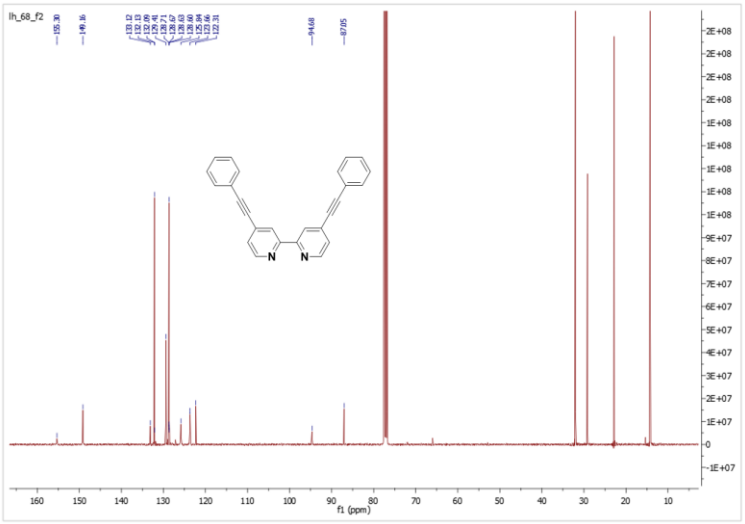

Figure 14. ^{13}C spectrum of **PhL** ($CDCl_3$, 101 MHz, 298 K).

The syntheses of the methoxyphenyl and trifluorotoluene ligands were performed using similar reaction profiles, as shown in **Scheme 4**. As product yield for **PhL** was low, different parameters were investigated to increase ligand yield. For **OMeL**, toluene was added to the microwave vessel to ensure full solution of starting material and catalyst, while **CF_3L** was synthesised using more traditional round-bottom flask chemistry. Neither approach significantly increased the yield, but in all 3 ligand syntheses sufficient material was recovered to proceed with metal complexation, so no further optimisation attempts were needed. The purification procedure for the compounds remained largely the same as for **PhL**, with **OMeL** appearing as a yellow band on the silica column while **CF_3L** was white. OMeL has previously been reported in literature.[87]

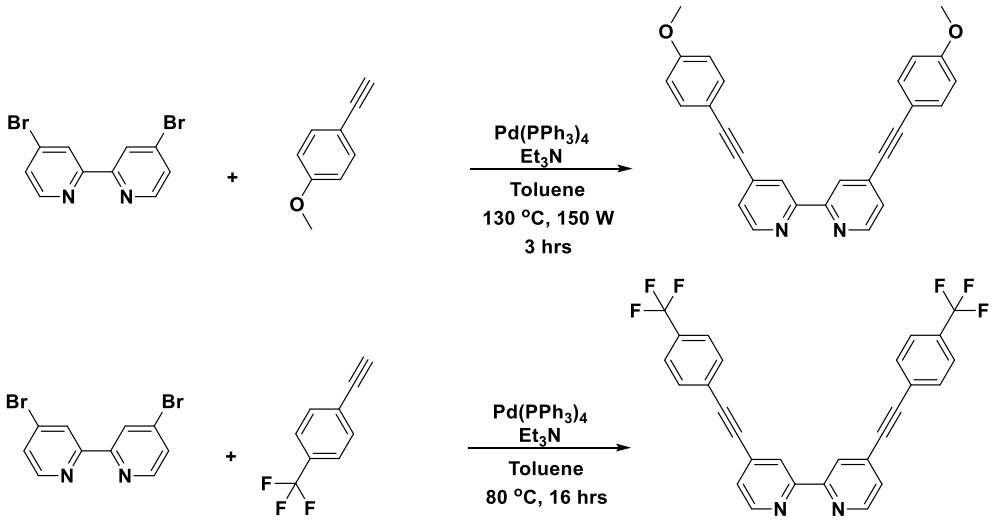

Scheme 4. Synthesis of **OMeL** (top) and **CF₃L** (bottom).

The ^{1}H NMR spectra of **OMeL** (A) and **CF₃L** (B) with the assigned spin systems are shown below in **Figure 15.**

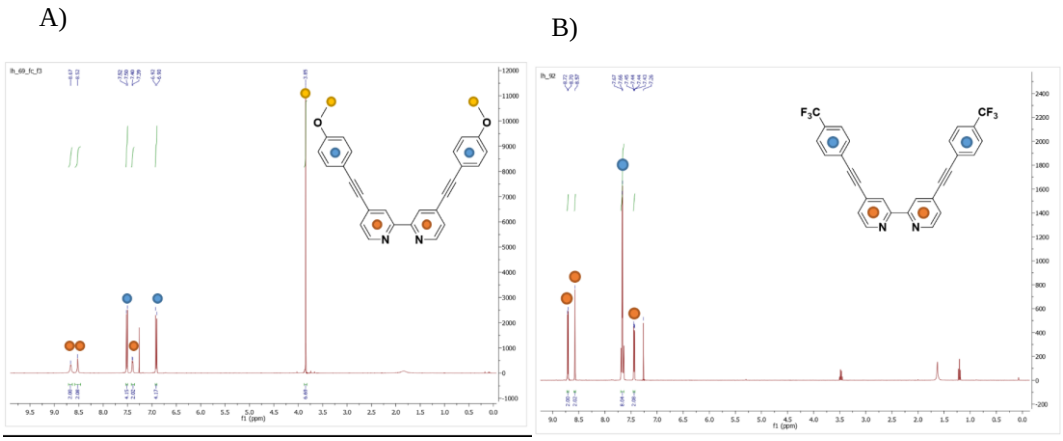

Figure 15. ^{1}H NMR spectra of **OMeL (A)** and **CF₃L (B)** with the assigned spin systems ($CDCl_3$, 400 MHz, 298 K).

The ^{1}H NMR spectra of the two ligands resembles that of **PhL**, with the proton signals appearing in the aromatic region (aside from the methoxy proton signals of **OMeL** at 4 ppm). Interestingly, one significant difference is that the resolution of the pyridine signals in the CF_3L spectrum is notably improved compared to those of **OMeL** and **PhL**. This allows the visualisation of the two doublet one singlet pattern expected of pyridine rings with the substitution pattern of the ligand system. In general terms, the shift of the phenyl protons is greater in **CF₃L** than in the other two ligand systems due to the electron-withdrawing effect of the **CF₃** moiety. This results in an almost complete overlap of the phenyl signals, while in **OMeL** and **PhL** a gap appears between them.

The ^{13}C spectrum of **OMeL** is shown in **Figure 16** and is similar to that of **PhL**. The signal intensity is significantly lower, but this is due to a dilute sample or a lower number of scans more than any inherent property of the compound. The second alkyne signal is barely visible at 95 ppm, while the methoxy carbon signal can be found at 56 ppm.

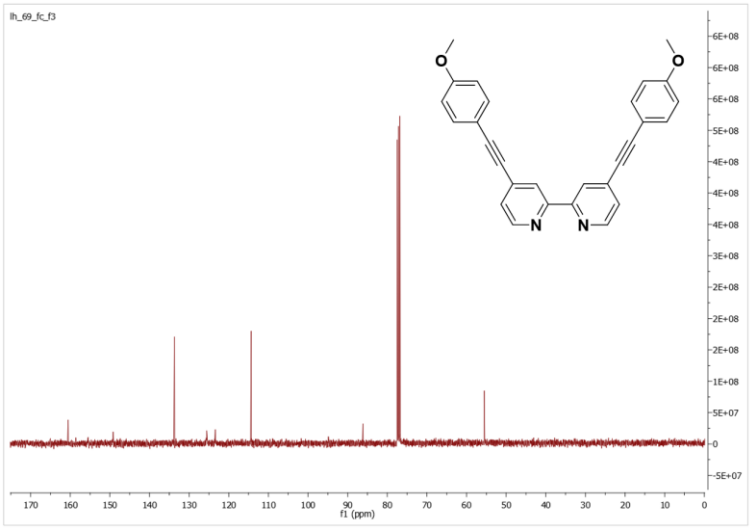

Figure 16. ^{13}C NMR spectrum of **OMeL** ($CDCl_3$, 101 MHz, 298 K).

The ^{13}C spectrum of **CF_3L** is of much greater interest, as ^{19}F is a spin-active nucleus. Carbon signals are typically decoupled from protons bonded to them for visual clarity, which combined with the low natural abundance of ^{13}C results in a spectrum comprised of singlets. However, since ^{19}F has a functional abundance of 1, coupling between ^{13}C and ^{19}F atoms results in multiplicity in the carbon spectrum. This is shown in **Figure 17**, at 132 ppm – the carbon signal is split into a quartet by the presence of the fluorine atoms. It is important to note that this is the alpha carbon and as such still part of the phenyl ring – the carbon bonded directly to all 3 fluorine atoms experiences such a large degree of splitting that it commonly vanishes into the baseline. Trace remnants can be seen at around 120 ppm.

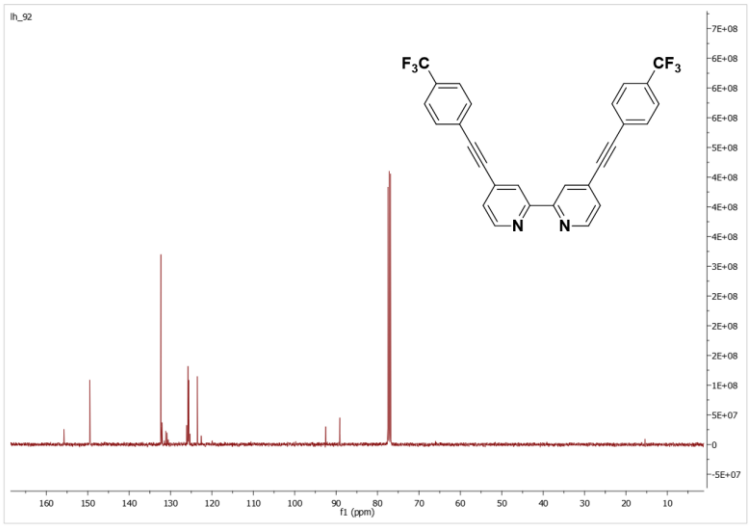

Figure 17. ^{13}C spectrum of **CF_3L** showing ^{19}F coupling ($CDCl_3$, 101 MHz, 298 K).

The synthesis of all 3 ligands was also confirmed by mass spectrometry (see experimental section).

1.3.2 Synthesis and Characterisation of PhRu, CF_3Ru, OMeRu

Complexation of the ligand onto the metal was performed by simply heating the two reagents in a suitable solvent overnight under an argon atmosphere. The ruthenium coupling was performed in a microwave reactor and the conditions are shown in **Scheme 5**.

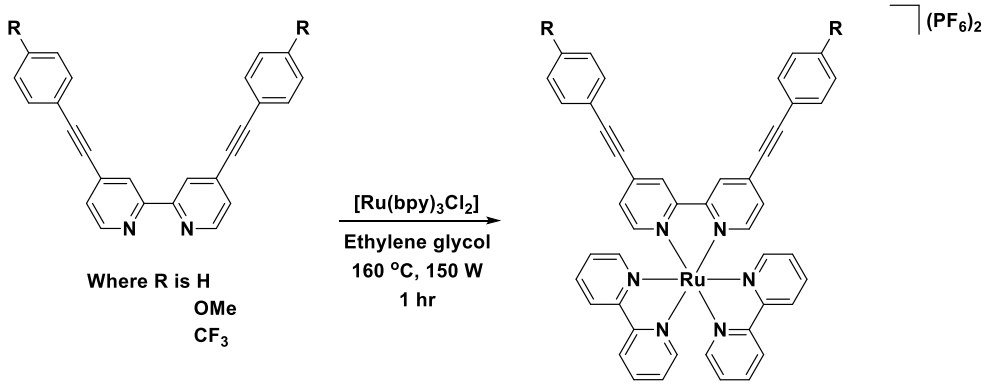

Scheme 5. Synthesis of the ruthenium complexes **PhRu**, **OMeRu** and **CF_3Ru.**

The progress of the reaction could be monitored by the colour change in the reaction vessel. $[Ru(bpy)_2Cl_2]$ is a granular black solid, and the ligands were all yellow or white solids. Over time, the reaction would develop from a suspension of black and white solids to a deep, dark red solution as the complexation proceeded. Following cooling to room temperature, anion exchange was used to precipitate the product from the ethylene glycol solvent, allowing for filtration of the solid product. This was a key part of the procedure as the ethylene glycol is a very high boiling point solvent, and removal in a rotary evaporator would have been difficult, resulting in significantly more complicated complexation.

The solid was washed with diethyl ether to remove any residual ethylene glycol, the solid was dissolved in a 90:9:1 mixture of $MeCN:H_2O:KNO_3$ (sat. aq.) and loaded onto a silica column with a mobile phase of the same composition. The product would elute as a dark red band, and after it was concentrated on a rotary evaporator, the product was again precipitated via anion exchange using saturated aqueous KPF_6.

The ^1H NMR spectrum of **PhRu** is shown below in **Figure 18**. It displays significantly more signals due to the presence of the spectator bipyridine ligands.

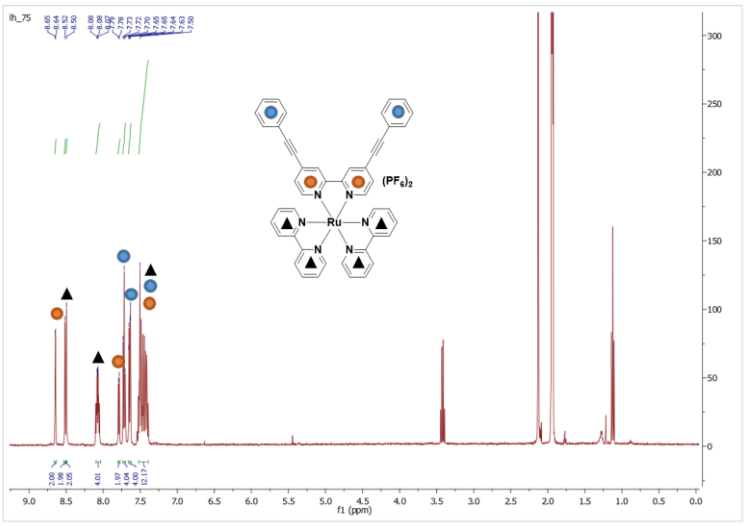

Figure 18. ^{1}H NMR Spectrum of **PhRu** with spin systems assigned (400 MHz, MeCN-d_3, 298 K).

The spectator bipyridine ligands are not involved with the photophysics in any meaningful way, and consequently they will be assigned using the same symbol to avoid cluttering the spectrum. The large number of signals present in this spectrum requires more advanced NMR techniques to fully assign the spin systems.

Figure 19 shows the TOCSY NMR spectrum for **PhRu**, visualising which proton signals are interacting with each other. The diagonal running from the top right of the spectrum to the bottom left can be thought of as the regular 1D NMR spectrum. The peaks on either side of the diagonal, termed 'cross peaks', arise due to through-bond interactions between different protons. These interactions only have a limited range of 3-4 bond lengths. This, combined with the structure of the complex, means that the interactions recorded on the TOCSY spectrum only occur between protons of the same spin system.

As the number of proton signals and the value of their integrals differ across the spin systems of the complex, the above technique allows us to immediately identify the relevant systems. The phenyl system, shown in blue, has three members and integrates to 10 protons. The pyridine ring systems of the substituted bipyridine are shown in orange, have three members and integrate to 6. The spectator ring systems make up the remaining signals which integrate to 14 protons.

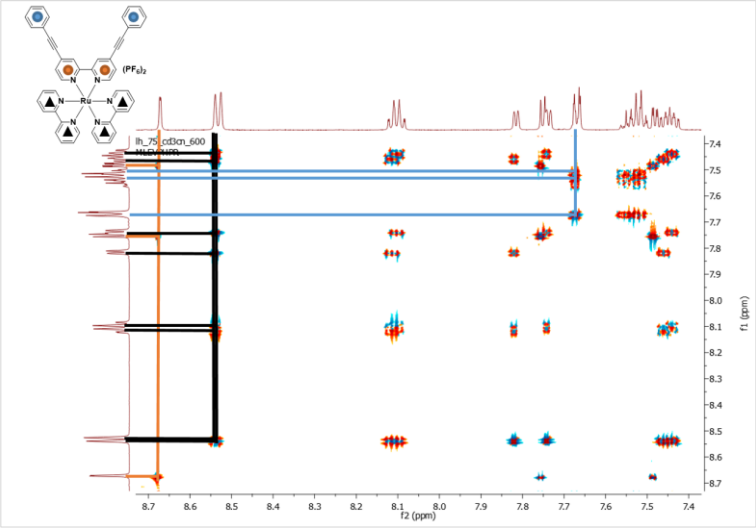

Figure 19. [1]TOCSY NMR spectrum of **PhRu** with spin systems assigned (600 MHz, MeCN-d_3 298 K).

The splitting of the spectator bipyridine signals discussed in the earlier paragraph is clearly evident on this spectrum. While the signals are very close together, it is possible to distinguish between the individual rings.

The phenyl ring system remains at the same shifts shown in **PhL**, but the bipyridine rings of the same ligand have changed significantly. Although not directly involved in conjugation, the donation of the electron lone by the pyridyl nitrogen draws electron density away from the ring system, shifting the proton signals further downfield. The most upfield signal cluster arises due to the overlap of spectator ligand, pyridine ring and phenyl ring signals. Full assignment of the protons was completed using further 2D NMR techniques, including HMBC and HSQC and is listed in the experimental section of this thesis. The ^{13}C spectrum of **PhRu** is shown in **Figure 20**.

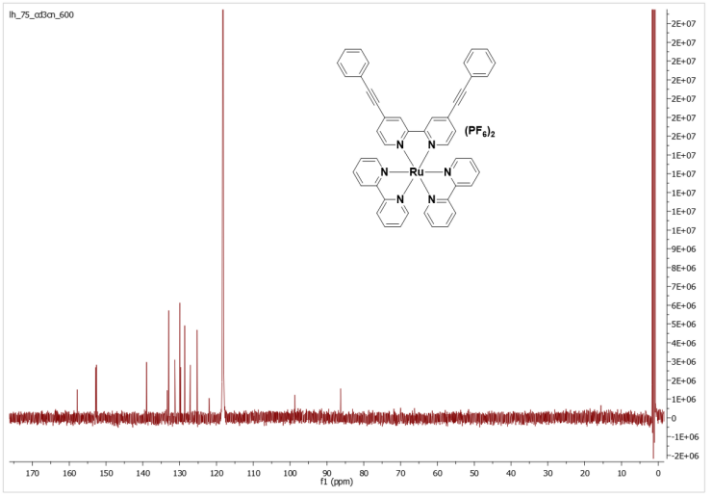

Figure 20. ^{13}C spectrum of **PhRu** (MeCN-d_3, 125 MHz, 298 K).

This spectrum manifests a largely expected behaviour, with the difference in signal intensity arising due to a differing number of equivalent carbon atoms throughout the complex structure. The alkyne signals can again be found between 80-100 ppm, while the carbon atoms in the coordinating pyridine rings display the greatest downfield shift.

The ^{1}H NMR spectrum of **OMeRu** is shown in **Figure 21**, and is largely similar to that of PhRu.

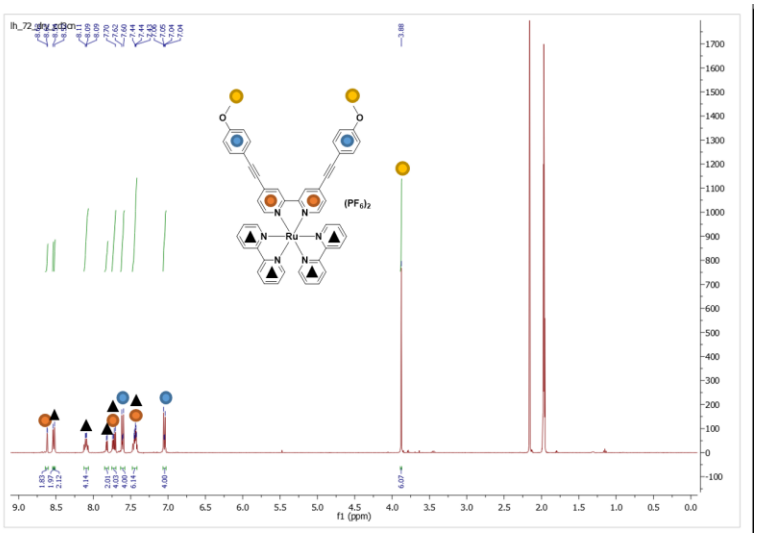

Figure 21. ^{1}H NMR spectrum of **OMeRu** with spin systems assigned (MeCN-d_3, 400 MHz, 298 K).

The greatest difference lies in the presence of the methoxy proton peak at 3.8 ppm, which is the only signal of the complex appearing under 7 ppm. The TOCSY spectrum of **OMeRu** (**Figure 22**) also resembles that of **PhRu**, with the exception of one set of phenyl ring signals resulting in a less overlapped spectrum.

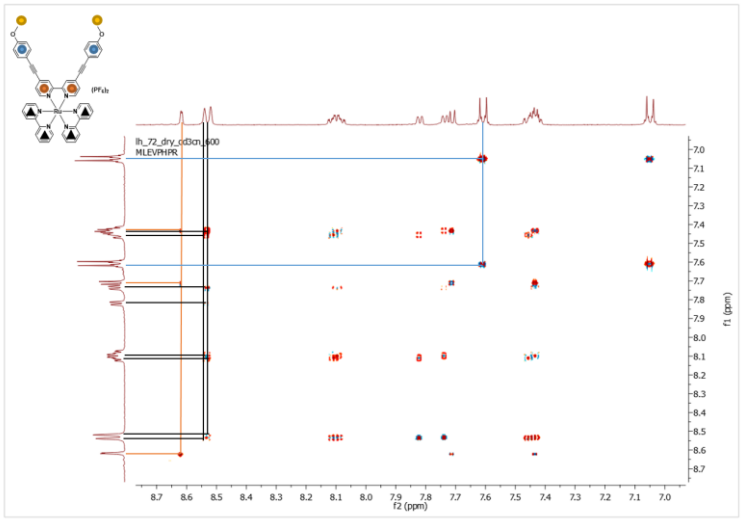

Figure 22. TOCSY NMR spectrum of **OMeRu** (MeCN-d_3, 600 MHz, 298 K).

The ^{13}C NMR spectrum of **OMeRu** is shown in **Figure 23** and differs from that of **PhRu** by having slightly lower shifts and by the presence of the alkyl methoxy signal at 55 ppm.

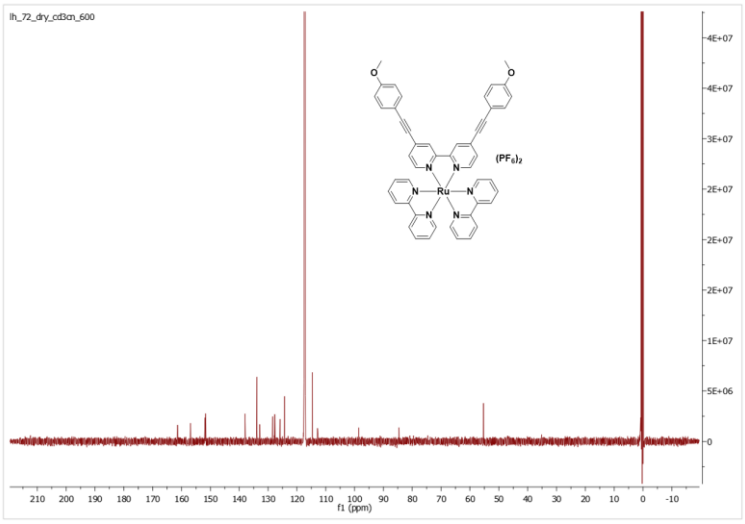

Figure 23. ^{13}C NMR spectrum of **OMeRu** (MeCN-d_3, MeCN, 298 K).

Finally, the ^{1}H NMR spectrum of **CF_3Ru** is displayed in **Figure 24 A**, again showing large degrees of similarity with the previous two complexes. The shifts of the two signals originating from the phenyl ring are nearly identical, resulting in significant overlap. Using the TOCSY spectrum (**Figure 24 B**) it is possible to assign all remaining signals to their spin systems. The ^{13}C spectrum of **CF_3Ru** shows the same carbon signal splitting observed in **CF_3L** due to the presence of fluorine atoms, with the alpha carbon appearing as a quartet at **131** pm and the CF_3 carbon as a very low intensity, high coupling quartet centred at **124** ppm.

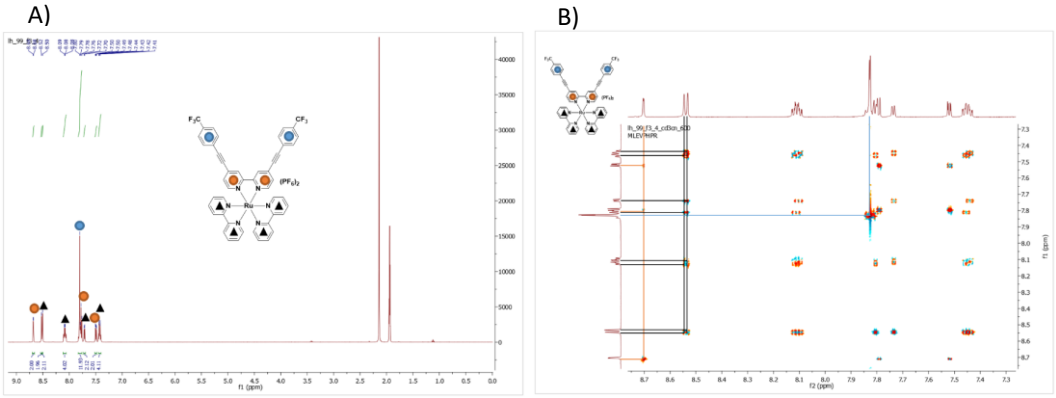

Figure 24. A) ^{1}H NMR spectrum of **CF_3Ru** (600 MHz, MeCN-d_3, 298 K) B) TOCSY NMR spectrum of **CF_3Ru** (600 MHz, MeCN-d_3, 298 K).

The ^{13}C spectrum of **CF_3Ru** (**Figure 25**) shows the same carbon signal splitting observed in **CF_3L** due to the presence of fluorine atoms, with the alpha carbon appearing as a quartet at 126 pm and the CF_3 carbon as a very low intensity, high coupling quartet centred at 131 ppm.

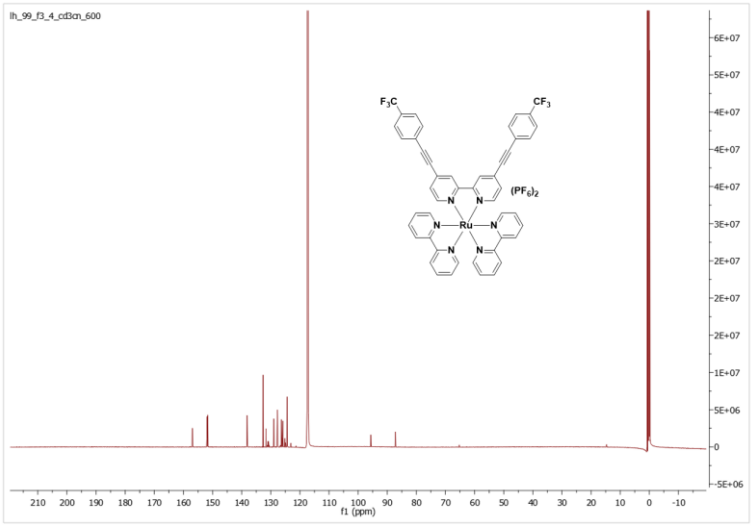

Figure 25. ^{13}C NMR spectrum of **CF_3Ru** (MeCN-d_3, 600 MHz, 298 K).

1.3.3 Synthesis and Characterisation of PhIr, CF_3Ir, OMeIr

The synthesis of the iridium complexes **PhIr**, **OMeIr** and **CF_3Ir** was completed by refluxing the iridium dimer [$(Ir(ppy)_2Cl)_2$] in $CHCl_3$ together with the corresponding ligand, as shown in **Scheme 6**.

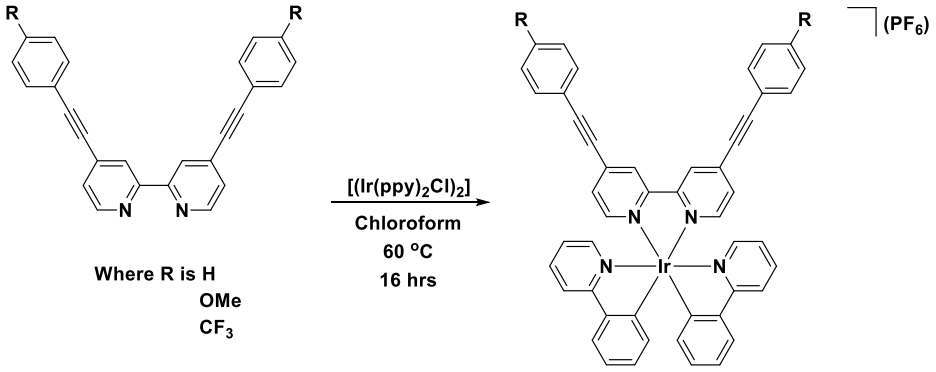

Scheme 6. Synthesis of the iridium complexes **PhIr**, **OMeIr** and **CF_3Ir**

The complexation occurs at lower temperatures than the equivalent ruthenium reactions. Unlike ruthenium, iridium(III) spectator ligands comprise one datively bonded pyridine ring and one covalently bonded phenyl ring. This results in a series of potential isomers depending on the relative orientation of the spectator ring systems. The most stable version is the one shown in the scheme above and forms due to the trans-effect of the Ir-C bond, which causes the atoms trans to the carbon to become more labile.[43] Over time, this leads to the adoption of the isomer shown above, as it is the most thermodynamically stable isomer available to the complex.

The purification of this complex was again performed using flash silica column chromatography with a CH_2Cl_2:MeOH mobile phase. The reduced charge of the overall complex results in less complicated behaviour on the silica than the equivalent ruthenium complex, and consequently the purification of the iridium complexes overall is significantly easier than of the ruthenium complexes.

The asymmetry of the iridium spectator phenylpyridine ligands gives rise to a larger number of signals in the ^{1}H NMR spectrum, as can be seen in **Figure 26**.

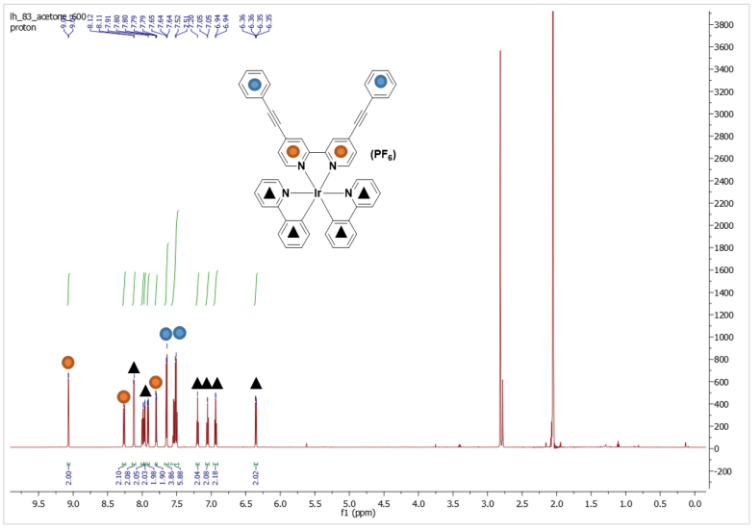

Figure 26. ^{1}H NMR spectrum of **PhIr** (600 MHz, MeCN-d_3, 298 K).

As with ruthenium complexes and the free ligand systems most peaks in the NMR spectrum can be found in the aromatic region between 7 and 10 ppm. For iridium, the high electron density of the iridium metal centre results in a greater shielding effect on some of the protons in the coordinating ring systems. Additionally, the phenyl ring of the spectator ligands has higher electron density than an equivalent pyridine ring. This is reflected in the ^{1}H NMR spectrum by a distinct upfield shift in one of the spectator ring systems (**Figure 27**) where three of the four ring signals are further upfield than the most upfield signal of the other ring. In general, the resolution of the complex structure is good, with clearly visible multiplicities and little signal overlap aside from the phenylacetylene ring systems.

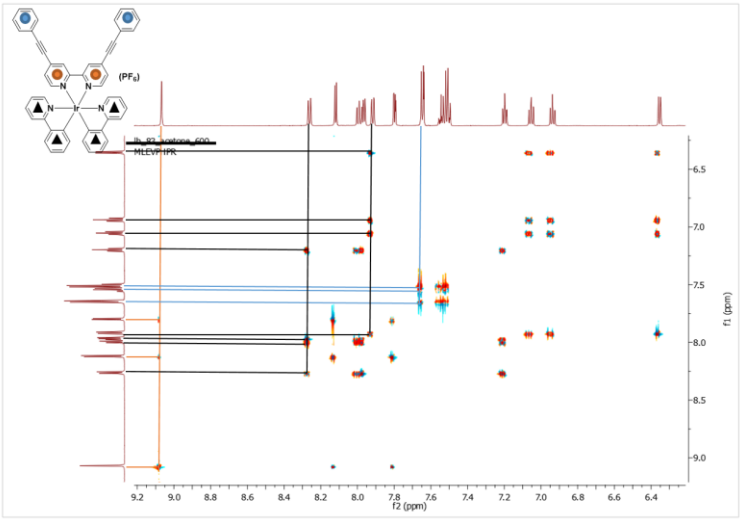

Figure 27. TOCSY NMR spectrum of **PhIr** (600 MHz, MeCN-d_3, 298 K).

The ^{13}C NMR spectrum of **PhIr** is shown in **Figure 28**, and resembles the ^{13}C spectra of the ruthenium complexes quite closely, with the highest downfield signal at 170 ppm and the two alkyne signals between 80-100 ppm

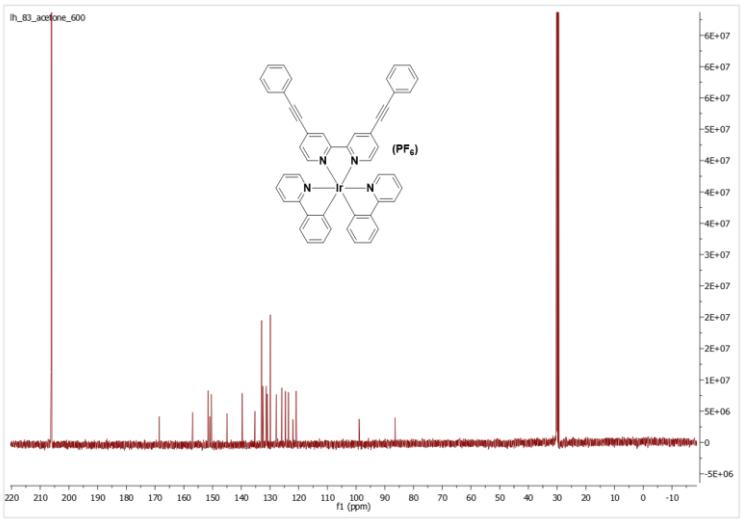

Figure 28. ^{13}C NMR spectrum of **PhIr** (151 MHz, acetone-d_6, 298 K).

The ^{1}H NMR spectrum of **OMeIr** is shown in **Figure 28**, with trace toluene signals in the spectrum represented by a star. The solvent was used to wash away organic impurities following filtration of the iridium sample, and some of it remained in the sample submitted for NMR analysis. The spectrum shows the expected features, including a high degree of signal splitting in the spectator ligands and the appearance of the singlet methoxy peak at 3.8 ppm.

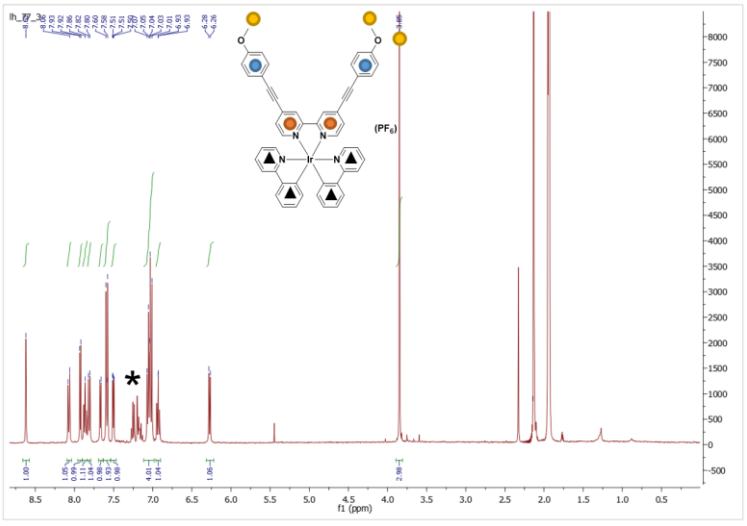

Figure 29. ^{1}H NMR spectrum of **OMeIr**, residual toluene marked with a star (400 MHz, MeCN-d_3, 298 K).

The TOCSY and ^{13}C NMR spectra of **OMeIr** are displayed in **Figure 30 A** and **B** respectively. The ^{13}C spectra shows two peaks in the aliphatic region, but using HMBC 2D NMR spectroscopy it was possible to assign the more upfield signal as the methoxy carbon (see experimental for full assignment).

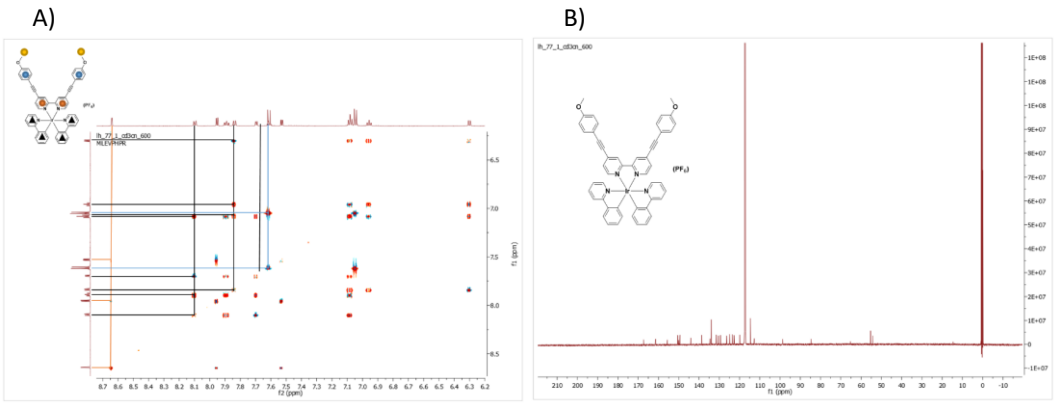

Figure 30. A) TOCSY NMR of **OMeIr** (600 MHz, MeCN-d_3, 298K) B) ^{13}C NMR of **OMeIr** (151 MHz, MeCN-d_3, 298 K).

Finally, the NMR of **CF_3Ir** is shown below in **Figure 31**, displaying the expected narrowing of the gap between the phenylacetylene signals. It also manifests an overall downfield shift for this ring system due to the electron-withdrawing effect of the CF_3 moieties.

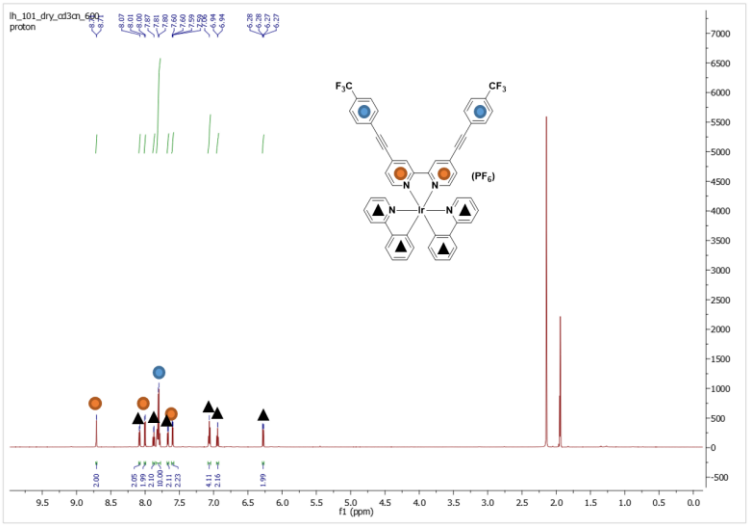

Figure 31. ^{1}H NMR of **CF_3Ir** (600 MHz, MeCN-d_3, 298 K).

The TOCSY NMR spectra for CF_3Ir is shown in **Figure 32 A**.The ^{13}C spectrum of **CF_3Ir** (**Figure 32 B**) shows the now familiar splitting pattern in the carbon signals induced by the fluorine atom.

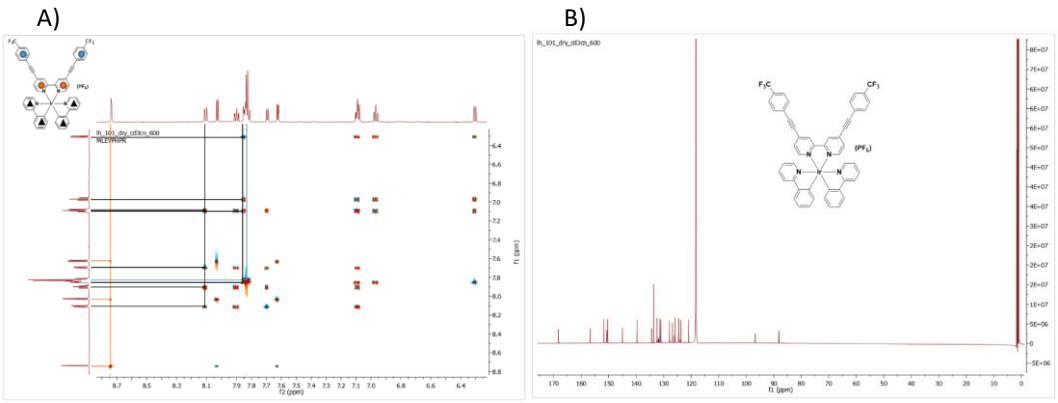

Figure 32. A) TOCSY NMR spectra of **CF_3Ir** (600 MHz, MeCN-d_3, 298 K) B) ^{13}C NMR spectra of **CF_3Ir** showing the expected signal splitting due to fluorine atoms in the **CF_3** group (151 MHz, MeCN-d3, 298 K).

1.3.4 Crystallographic Analysis

1.3.4.1 PhIr

A crystal of **PhIr** suitable for x-ray diffraction studies was grown from the slow evaporation of chloroform. Dr. Brendan Twamley of Trinity College Dublin conducted data collection and refinement. A specimen of $C_{51.85}H_{35.85}Cl_{11.55}F_6IrN_4P$, approximate dimensions 0.039 mm x 0.082 mm x 0.269 mm, was used for the X-ray crystallographic analysis. The X-ray intensity data were measured (λ = 1.54178 Å) on a Bruker Apex Kappa Duo with an Oxford Cobra Cryosystem low temperature device using a MiTeGen micromount. Using the OLEX2 Software Package, the structure was solved with the SHELXT structure solution program using Intrinsic Phasing and refined with the SHELXL refinement package with Least Squares minimisation, using the space group $P2_1/n$, with Z = 4 for the formula unit, $C_{51.85}H_{35.85}Cl_{11.55}F_6IrN_4P$. The final anisotropic full-matrix least-squares refinement on F^2 with 934 variables converged at R1 = 6.57%, for the observed data and wR2 = 18.56% for all data. The goodness-of-fit was 1.051.

The crystal structure of PhIr is shown in **Figure 33**, with hydrogen atoms omitted for clarity. The complex has adopted an octahedral geometry, with the coordinating nitrogen atoms evenly spaced around the metal centre. The nitrogen atoms of the spectator phenylpyridine ligands have adopted the expected *trans* -configuration, which is the most thermodynamically stable isomer that this type of iridium complex can adopt.[43]

The bipyridine ligand bearing the phenylacetylene units shows low degrees of distortion, with the phenyl units slightly out of plane with the pyridine rings. The acetylene linkers show no twist or flex, remaining at 180 °. The PF_6^- counterion is situated between the acetylene linkers.

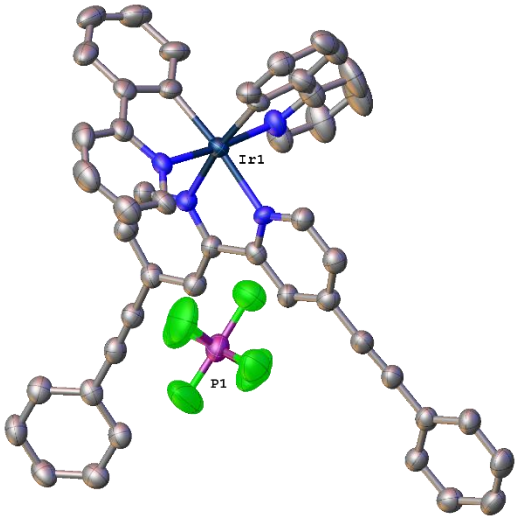

Figure 33. Molecular structure of **PhIr** with displacement shown at 50% probability. Hydrogen atoms omitted and only selected atoms labelled for clarity.

The crystal lattice of PhIr is shown in **Figure 34**, displaying the arrangement of the molecules of the complex in 3D space.

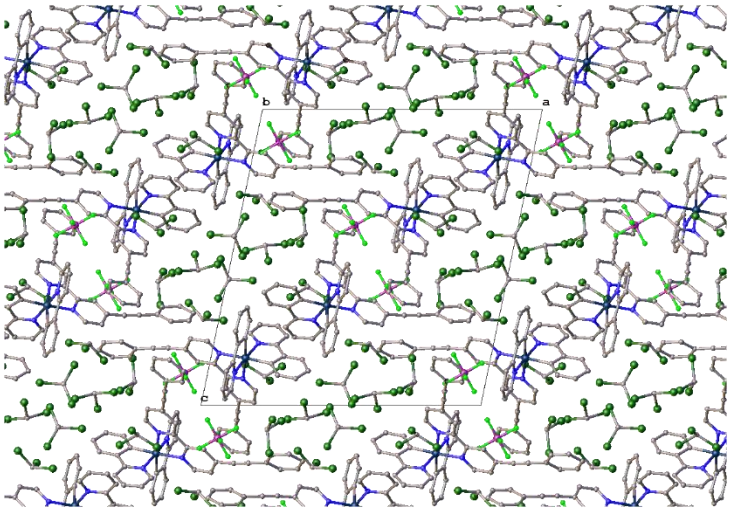

Figure 34. Schematic packing diagram of the majority occupied moiety in the PhIr crystal viewed normal to the b-axis.

The lattice shows few interactions between the individual complex molecules, with the metal centres remaining spatially isolated from each another. The acetylene linkers do reside closer to those of other molecules, but no obvious H-bonding or other intermolecular interactions are observed.

1.3.4.2 OMeIr

Two crystals of **OMeIr** were grown that were suitable for x-ray diffraction studies. Dr. Brendan Twamley of Trinity College Dublin conducted data collection and refinement. The first crystal was grown via the slow evaporation of MeCN-d_3 in an NMR sample tube, and no trace of solvent remains in the structure. A specimen of **OMeIr**, approximate dimensions 0.060 mm x 0.150 mm x 0.160 mm, was used for the X-ray

crystallographic analysis. The X-ray intensity data were measured (λ = 1.54178 Å) on a Bruker Apex Kappa Duo with an Oxford Cobra Cryosystem low temperature device using a MiTeGen micromount. Using the OLEX2 Software Package, the structure was solved with the SHELXT structure solution program using Intrinsic Phasing and refined with the SHELXL refinement package with Least Squares minimisation, using the space group $P2_1/n$, with Z = 8 for the formula unit, $C_{50}H_{36}F_6IrN_4O_2P$. The final anisotropic full-matrix least-squares refinement on F^2 with 1157 variables converged at R1 = 10.45%, for the observed data and wR2 = 28.50% for all data. The goodness-of-fit was 1.015.

The structure of this first crystal is shown in **Figure 35**. Several points of interest can be found in the structure of this crystal. The first is the side-by-side arrangement of two ethynylanisole fragments from separate complexes, with the phenyl ring slotting next to the acetylene of the opposing complex. This allows for a very tightly-packed arrangement, with the methoxy unit situated next to and pointing away from the coordinating bipyridine ring. Additionally, the PF_6 counterions can be found in this region of the unit cell, quite far removed from the metal centre.

The other ethynylanisole moiety is also of significant interest, as the acetylene bond (which is usually straight) shows significant torsion and flex away from the other parts of the metal complex. Finally, we can observe the expected *trans* arrangement of pyridine rings of the spectator phenylpyridine rings.

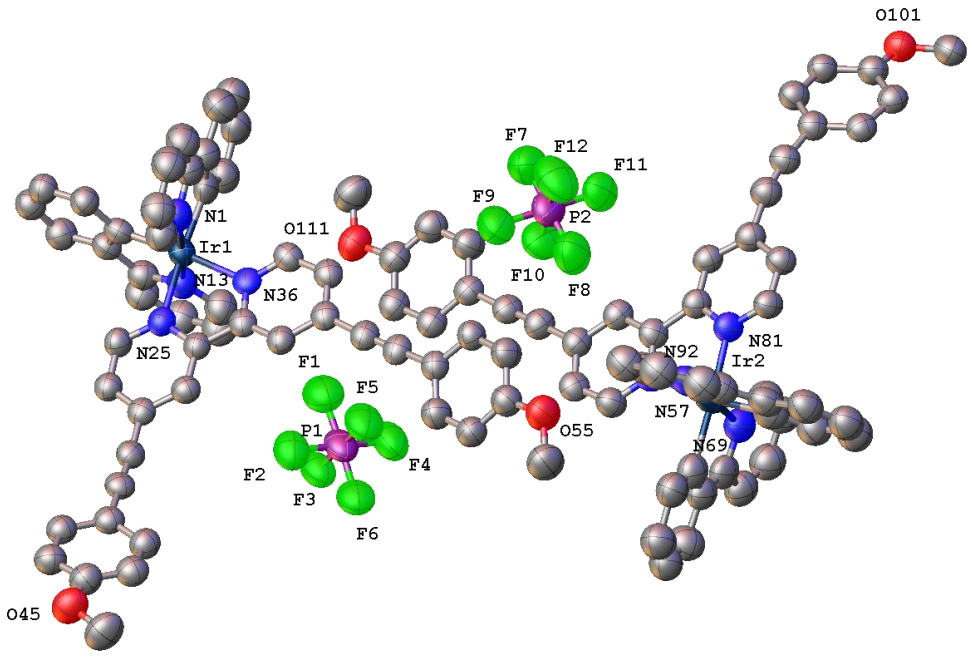

Figure 35. Molecular structure of crystal sample TCD 1852, showing the two independent salts in the asymmetric unit. Atomic displacement shown at 50% probability, hydrogen atoms omitted for clarity and heteroatoms labelled only.

The packing structure of TCD 1852 can be viewed in **Figure 36 A**. It shows that the individual complexes arrange themselves in an offset zig-zag pattern, with significant channels left between the individual metal

complexes. Further investigation of the torsion observed in one of the ethynylanisole moieties (**Figure 36 B**) shows that they flex towards the methoxy unit of a neighbouring complex, potentially indicating hydrogen bonding or other through-space interactions.

A)

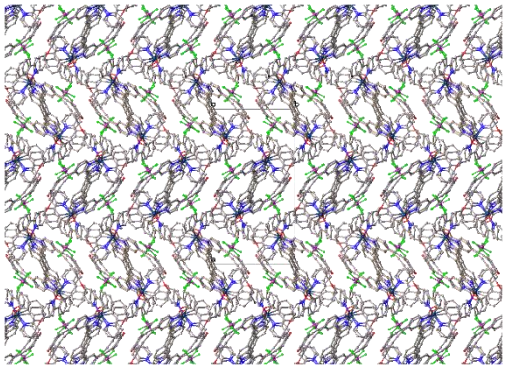

B)

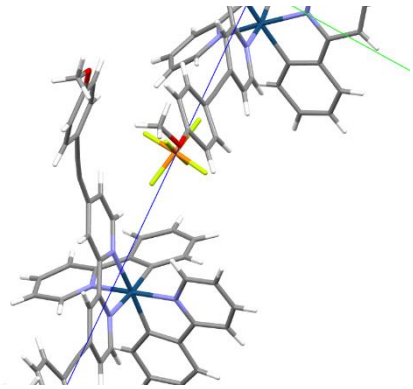

Figure 36. A) Schematic packing diagram of TCD1852 viewed normal to the c-axis with hydrogen atoms omitted **B)** Enhanced view of the bend in the acetylene linker in one complex towards the methoxy unit of an adjacent complex.

The second crystal (TCD1829) was grown from the slow diffusion of CH_2Cl_2 into toluene, and residual toluene solvent can still be found in its structure. A clear yellow blade-like specimen of TCD1829, approximate dimensions 0.030 mm x 0.110 mm x 0.260 mm, was used for the X-ray crystallographic analysis. The X-ray intensity data were measured (λ = 1.54178 Å) on a Bruker Apex Kappa Duo with an Oxford Cobra Cryosystem low temperature device using a MiTeGen micromount. Using the OLEX2 Software Package, the structure was solved with the SHELXT structure solution program using Intrinsic Phasing and refined with the SHELXL refinement package with Least Squares minimisation, using the space group $P2_1/c$, with Z = 4 for the formula unit, $C_{57}H_{44}F_6IrN_4O_2P$. The final anisotropic full-matrix least-squares refinement on F^2 with 678 variables converged at R1 = 6.75%, for the observed data and wR2 = 17.36% for all data. The goodness-of-fit was 1.145. The structure of TCD1829 is shown in **Figure 37**, and even a cursory examination shows significant differences to the structure of TCD1852. The significant bend of the acetylene bond observed in TCD1852 is not present in this molecule, and the PF_6 counterion is now more closely associated with a pyridine ring of the spectator ligands.

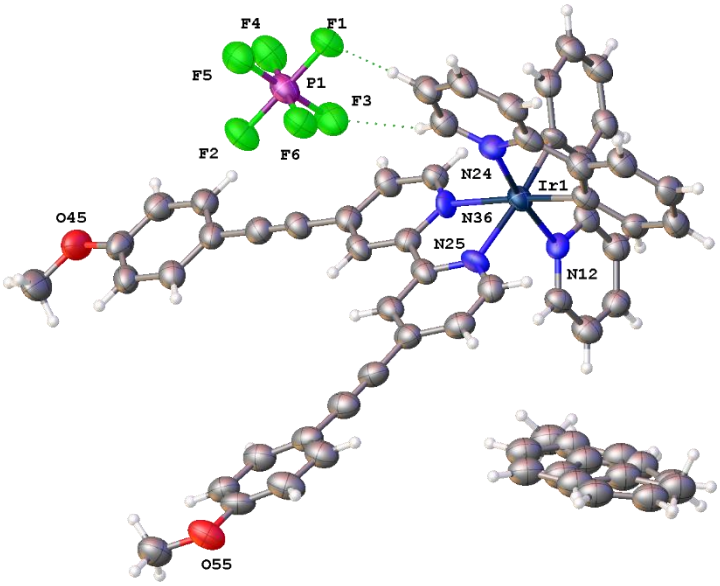

Figure 37. Molecular structure of TCD1829, showing the ion pair and disordered toluene. Atomic displacement shown at 50% probability and heteroatoms labelled only.

The packing structure of sample 2 is also significantly different than that in sample 1, as shown in **Figure 38**.

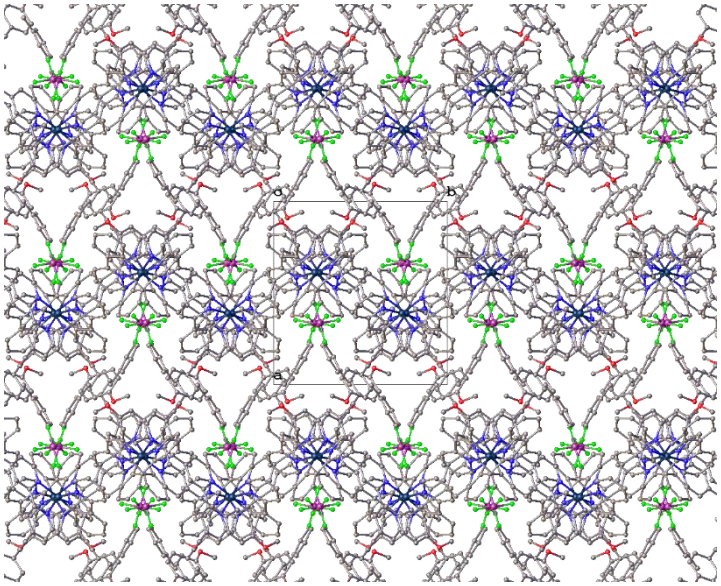

Figure 38 Schematic packing diagram of the majority occupied moiety in TCD1829 viewed normal to the c-axis with hydrogen atoms omitted.

The difference in packing structure could be an indication that in the solid state the lowest energy conformation of the complex is dependent on the electronic environment. This in turn could be reflected by solvent-dependent photophysical properties such as emission solvatochromism, if this behaviour is maintained in fluid solution.

1.3.4.3 CF_3Ru

A crystal of **CF_3Ru** suitable for x-ray diffraction studies was grown. Dr. Brendan Twamley of Trinity College Dublin conducted data collection and refinement. A specimen of $C_{96.50}H_{64}F_{36}N_{12}O_{1.50}P_4Ru_2$, approximate dimensions 0.030 mm x 0.087 mm x 0.148 mm, was used for the X-ray crystallographic analysis. The X-ray intensity data were measured (λ = 1.54178 Å) on a Bruker Apex Kappa Duo with an Oxford Cobra Cryosystem low temperature device using a MiTeGen micromount. Using the OLEX2 Software Package, the structure was solved with the SHELXT structure solution program using Intrinsic Phasing and refined with the SHELXL refinement package with Least Squares minimisation, using the space group $P\bar{1}$, with Z = 2 for the formula unit, $C_{96.50}H_{64}F_{36}N_{12}O_{1.50}P_4Ru_2$. The final anisotropic full-matrix least-squares refinement on F^2 with 1382 variables converged at R1 = 9.90%, for the observed data and wR2 = 29.17% for all data. The goodness-of-fit was 1.050.

The unit cell of **CF_3Ru** is shown in **Figure 39**, showing that there are two distinct conformations adopted by CF_3Ru molecules in the crystal lattice. Both show significant distortions in the alkyne bond, similarly to those observed in the first **OMeIr** sample.

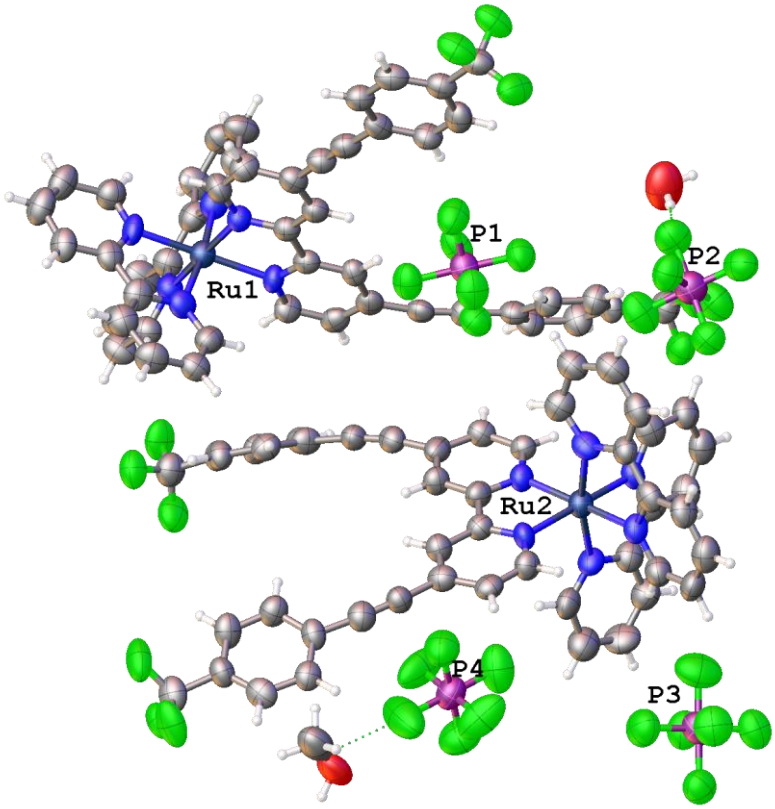

Figure 39. Asymmetric unit in **CF_3Ru**, showing the two unique molecules, four PF_6 counterions and water and half occupied MeOH solvates. Atomic displacement shown at 50% probability and selected heteroatoms labelled only.

An overly fit of the two different conformations adopted by the ruthenium complex is shown in **Figure 40**. It is clear from this comparison that one of the conformations experiences significantly more twist in the

acetylene bonds than the other, but the arrangement of the ligands around the metal centre also show subtle differences.

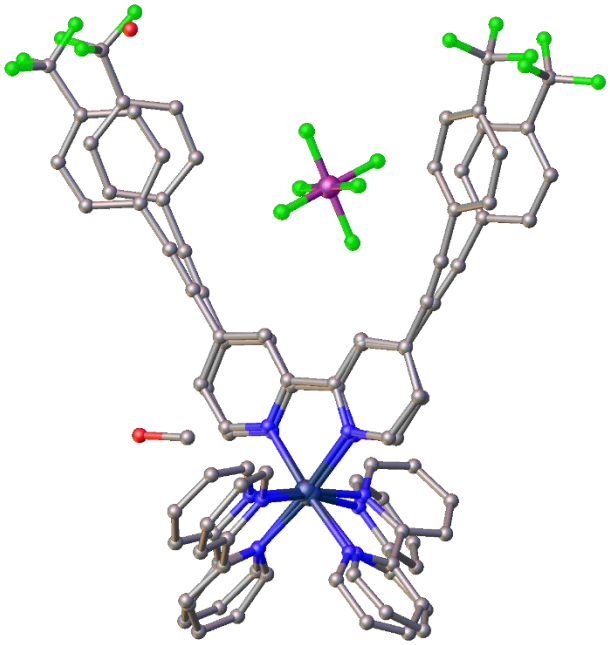

Figure 40. Overlay fit of both complexes in **CF_3Ru.**

The packing structure of CF_3Ru is shown in **Figure 41**. The two different conformations form pairs in the unit cell, with the cells packed in slanting vertical columns. The residual solvent molecules and PF_6^- counterions fill the voids between the complex pairs.

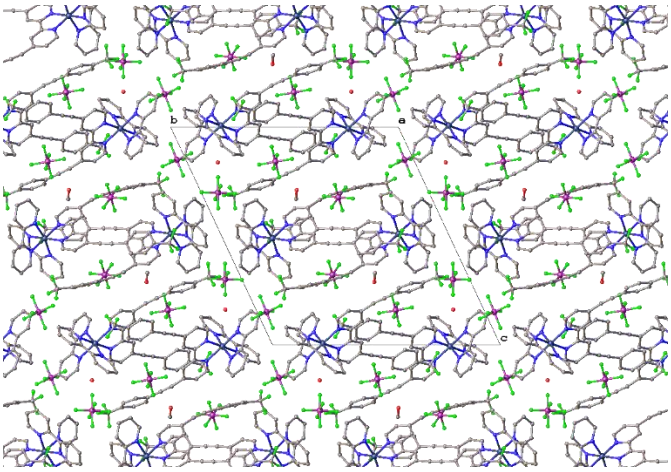

Figure 41. Schematic packing diagram of **CF_3Ru** viewed normal to the a-axis with hydrogen atoms omitted**.**

1.3.4.4 CF_3Ir

A crystal of **CF_3Ir** suitable for x-ray diffraction studies was grown. Dr. Brendan Twamley of Trinity College Dublin conducted data collection and refinement. A specimen of $C_{50}H_{30}F_{12}IrN_4P$, approximate dimensions 0.028 mm x 0.077 mm x 0.109 mm, was used for the X-ray crystallographic analysis. The X-ray intensity data were measured (λ = 1.54178 Å) on a Bruker Apex Kappa Duo with an Oxford Cobra Cryosystem low

temperature device using a MiTeGen micromount. Using the OLEX2 Software Package, the structure was solved with the SHELXT structure solution program using Intrinsic Phasing and refined with the SHELXL refinement package with Least Squares minimisation, using the space group P2/n, with Z = 4 for the formula unit, $C_{50}H_{30}F_{12}IrN_4P$. The final anisotropic full-matrix least-squares refinement on F^2 with 601 variables converged at R1 = 13.87%, for the observed data and wR2 = 37.91% for all data. The goodness-of-fit was 1.083.

The crystal structure of **CF_3Ir** is shown in **Figure 42**. Unlike **CF_3Ru**, **CF_3Ir** adopts a single conformation throughout the crystal structure. It also does not show the same degree of twist and bend in the alkyne subunits. The PF_6 counterion slots between the alkyne bonds, and the nitrogen atoms on the spectator ligand rings show the expected *trans* conformation.

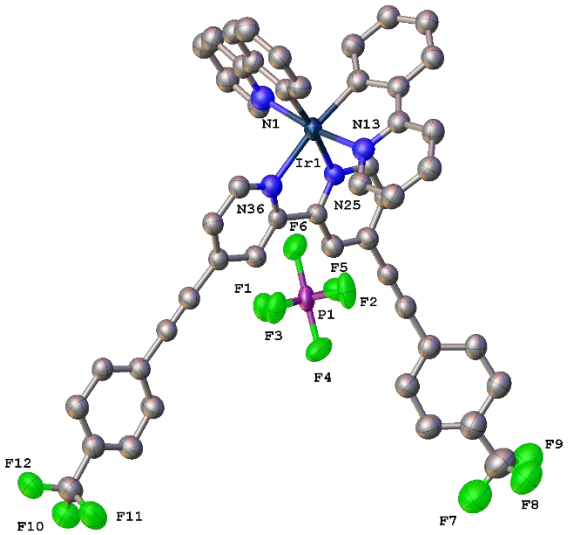

Figure 42. Molecular structure of **CF_3Ir**, with PF_6 counterion. Atomic displacement shown at 50% probability and heteroatoms labelled only.

The packing structure of **CF_3Ir** (**Figure 43**) shows that despite the single adopted conformation the complexes still form pairs, with the alkyne bonds of two separate molecules aligning alongside each another. However, unlike CF_3Ru, the remaining alkyne chain of each complex is also subtly interacting with the spectator ligands of a third complex, suggesting a greater degree of intermolecular interactions.

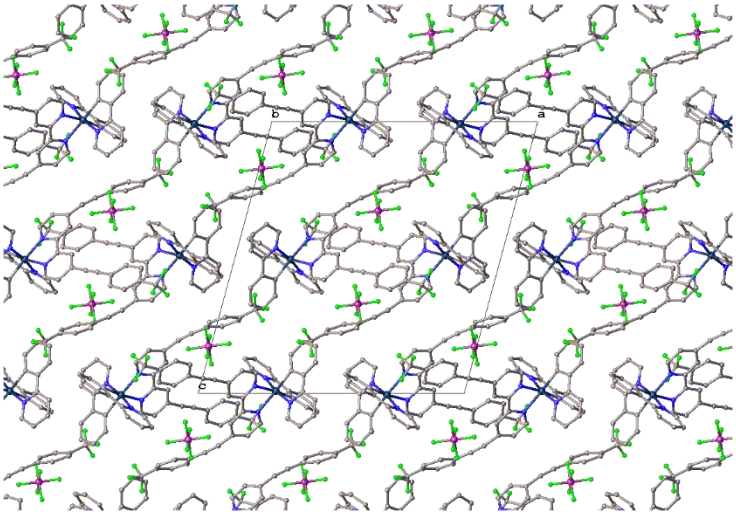

Figure 43. Schematic packing diagram of **CF_3Ir** viewed normal to the b-axis with hydrogen atoms omitted.

The crystal structure of the complexes shows that despite the similarity in chemical composition, the complexes adopt distinctly different solid state packing structures. This suggests that this family of complexes may have significant sensitivity to the local electronic environment (such as solvent), which will be investigated further in the next section.

1.4 Photophysical Analysis

1.4.1 Spectroscopic Analysis of PhL, OMeL and CF_3L

1.4.1.1 Solvatochromic Absorption and Emission of PhL, CF_3L and OMeL

The photophysical properties of the prepared compounds were probed using UV-Vis spectroscopy and fluorometry. The initial analysis will focus on the behaviour of the ligand, followed by an investigation of the ruthenium and iridium complexes.

The behaviour of **PhL** and **CF_3L** is expected to be basic, with π-π* and n-π* transitions dominating the electronic behaviour. **OMeL** has the potential for charge-transfer (CT) behaviour, with the electron-rich methoxy moieties shifting charge into the electron-poor pyridine rings.

The normalised absorption and emission spectra of **PhL** are shown in **Figure 44**. The absorption bands are at high energies above 350 nm, typical of π-π* and n-π* transitions.[56] The latter are more likely to be at lower energy than the former, due to the relative position of the non-bonding n orbital compared to the bonding π orbital. There are no changes in the absorption profiles in different solvents, suggesting that the ground state is unaffected by solvent polarity.

The normalised emission spectrum in CH_2Cl_2 is shown on the same graph as a dashed line. It displays a number of different peaks, with the highest intensity band closest in energy to the absorption bands. The intensity of the emission was extremely weak, which combined with the vibrational fine structure is indicative of π*-π emission. This indication is supported by the small gap between the absorption and

emission peaks (30 nm), a difference termed the Stokes shift. This type of transition is not expected to show solvatochromism and is of limited interest to this project, so the quantum yield of fluorescence was not established.

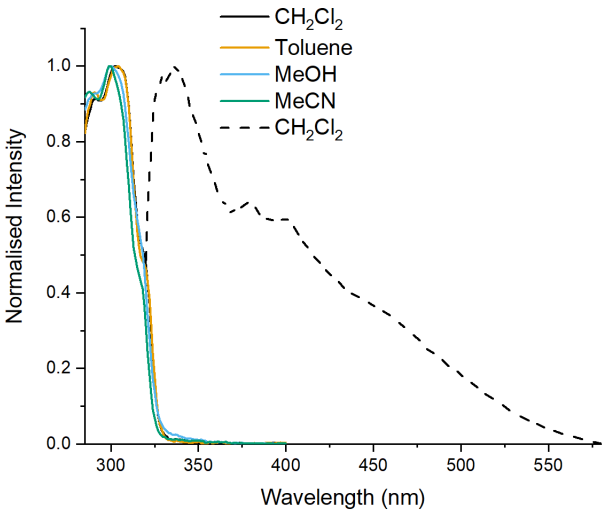

Figure 44. Normalised absorption and emission spectra of **PhL**; UV-vis spectra shown with solid lines and emission spectra shown with dotted lines (λ_{ex} = 290 nm), [10^{-5} M], 298 K.

The absorption and emission spectra for **CF_3L** is displayed in **Figure 45**, and shows much the same behaviour as **PhL**. High energy absorption bands combined with low emission intensity, a small stokes shift and structured emission spectra are all represented again. A small shoulder absorption peak at lower energies is the main change from the previously examined **PhL** spectrum. The degree of fine structure is reduced in comparison to **PhL**, but these transitions are still likely π/n-π* in nature.

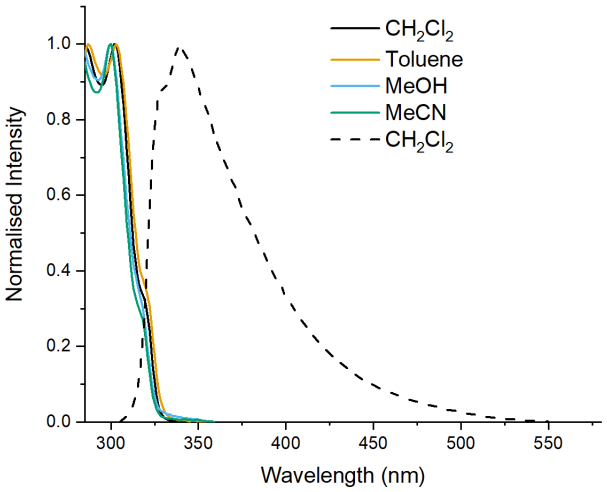

Figure 45. Normalised absorption and emission spectra of **CF_3L**; UV-vis spectra shown with solid lines and emission spectra shown with dotted lines (λ_{ex} = 290 nm), [10^{-5} M], 298 K.

It is with **OMeL** that we encounter the first distinct differences in absorption and emission behaviour. The spectrum, displayed in **Figure 46**, still shows similar absorption behaviour at slightly lower energies. However, the emission spectrum in CH_2Cl_2 (dashed black line) is broad and featureless, with a significant Stokes shift of 60 nm, doubling that of the other ligand systems.

Further emission studies in a range of solvents with differing polarities (remaining dashed lines) showed solvent-dependent emissive behaviour. In more polar solvents such as MeCN and MeOH, the emission wavelength increased and the emission profile broadened, while in less polar solvents such as toluene the emission is shifted to higher energies and the emission band profile is narrowed. This behaviour is typical of CT transitions, as the induced dipole of the excited state is stabilised by solvent rearrangement. The more polar the solvent, the stronger the stabilisation and the longer wavelength/lower energy the resulting emission band becomes. The broadening of the emission spectra is due to the enhanced interactions between the solvent and the excited state, increasing the degree of the vibrational and rotational coupling.

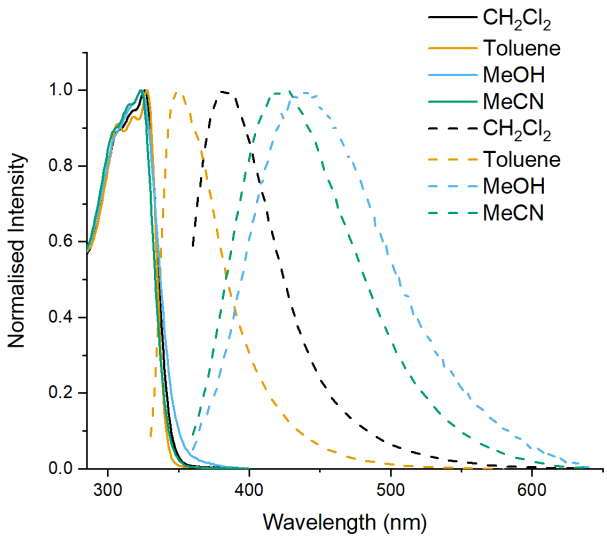

Figure 46. Normalised absorption and emission spectra of **OMeL** in a range of solvents; UV-vis spectra shown with solid lines and emission spectra shown with dotted lines (λ_{ex} = 320 nm), [10^{-5} M], 298 K.

The molar extinction coefficients for the three ligands are shown in **Table 1**. The data reinforces the impact that substituting the phenylacetylene has on the spectroscopic properties of the ligand series. **OMeL** and **CF$_3$L** both show significantly enhanced absorption compared to **PhL.**

Table 1. Molar extinction coefficients for **PhL**, **OMeL** and **CF$_3$L** (CH_2Cl_2, 10^{-5} M, 298 K).

Compound	Wavelength (nm)	ε (L mol^{-1} cm^{-1})
PhL	300	23422
OMeL	325	56393
CF$_3$L	305	63936

1.4.1.2 Emission Lifetime of OMeL

The emission lifetime of **OMeL** in CH_2Cl_2 was 4.5 ns, which is indicative of a ^{1}CT excited state. If the ^{3}CT of the excited state were to be accessible via intersystem crossing (ISC) facilitated by the heavy atom effect of transition metal ions, it could prove a promising triplet photosensitiser ligand candidate.

1.4.2 Spectroscopic Analysis of PhRu, RuCF$_3$ and OMeRu

1.4.2.1 Solvatochromic Absorption and Emission of PhRu, CF$_3$Ru and OMeRu

The absorption spectrum of **PhRu** is shown below in **Figure 47**. As expected, there are a greater number of absorption bands than for the **PhL**. This is due to the greater number of photoactive components forming the overall transition metal complex. The π- π* and n- π* transitions found in the **PhL** are also represented in the spectator ligands of the ruthenium complex, with all 6 pyridine and both phenyl rings contributing to the intensity of the high energy absorption bands. At lower energies, around 350-400 nm, ^{1}MC transitions between ruthenium d-orbitals can be observed.[56]

Finally, between 450 and 500 nm, we observe the ^{1}MLCT absorptions between the ruthenium d-orbitals and empty metal π* orbitals ubiquitous in ruthenium complexes.[56] These are of lower intensity than the π- π* and n- π* transitions, and show some degree of sensitivity to solvent.

The emission spectra, shown by the dashed lines, are all centred past 650 nm, with a Stokes shift of almost 200 nm. The emission wavelength is sensitive to solvents, with CH_2Cl_2 manifesting the highest energy emission wavelength and MeCN the lowest. The emission profile is largely broad and featureless, although there are suggestions of a secondary emission peak at 700 nm due to a pronounced shoulder in the main emission band.

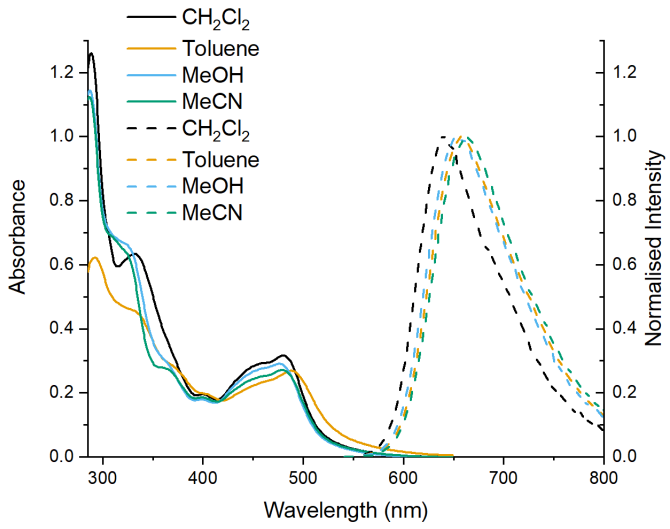

Figure 47. Absorption and normalised emission spectra of **PhRu** in a range of solvents; UV-vis spectra shown with solid lines and emission spectra shown with dotted lines (λ_{ex} = 480 nm), [10^{-5} M], 298 K.

The absorption and emission spectrum of **CF_3Ru** is shown in **Figure 48**, and closely resembles that of **PhRu**. Again, at high energies we observe the typical π- π* and n- π* transitions, while the MLCT occurs between 400 and 500 nm with the MC bracketed by these aforementioned transition types.

The intensity of the transitions, specifically the π- π* and n- π*, is lower than in **PhRu.** This could be due to the presence of the CF_3 groups quenching transitions in the phenyl rings they are appended to, but is difficult to determine. Differences in solution concentration are an additional potential source, but unlikely due to the similar absorbance of the MLCT bands. The absorption wavelength of the MLCT band is redshifted by 10 nm in **CF_3Ru** compared to **PhRu**. This can be explained by the lowering of the ligand LUMO orbitals due to the presence of the electron withdrawing CF_3 groups. The emission wavelengths and band profile are again very similar to **PhRu,** suggesting a shared excited state.

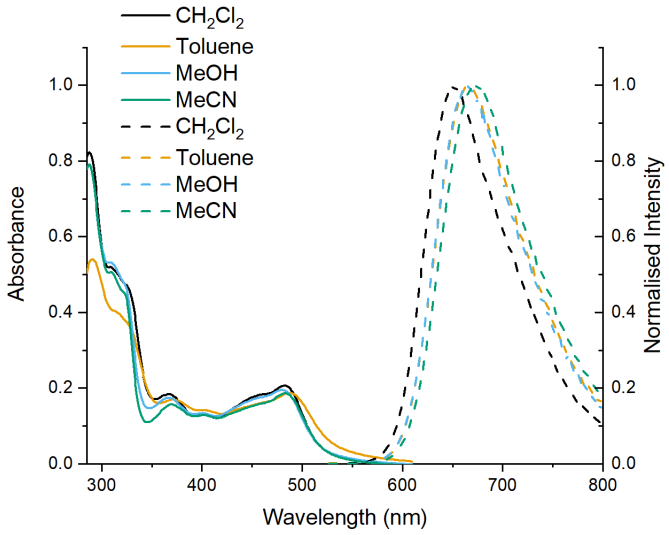

Figure 48. Absorption and normalised emission spectra of **CF_3Ru** in a range of solvents; UV-vis spectra shown with solid lines and emission spectra shown with dotted lines (λ_{ex} = 490 nm), [10^{-5} M], 298 K.

The spectrum for **OMeRu** is displayed in **Figure 49**, and shows a distinct difference in the absorption spectrum compared to the other two ruthenium complexes. A new broad absorption band appears between 350 and 400 nm, indicative of the CT process from the methoxy groups into the bipyridine ligand core. This absorption process is the same as the one observed in the free ligand, with the increased absorption wavelength arising due to coordination of the pyridine nitrogen with the metal centre.[88]

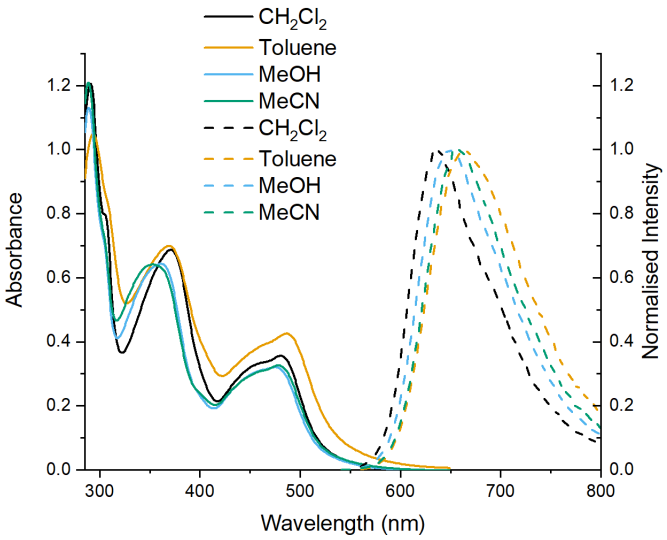

Figure 49. Absorption and normalised emission spectra of **OMeRu** in a range of solvents; UV-vis spectra shown with solid lines and emission spectra shown with dotted lines (λ_{ex} = 490 nm), [10^{-5} M], 298 K.

Additionally, **OMeRu** shows significant variations in the absorbance of the MLCT band in toluene. This could be an indication that the solvent-dependent arrangement observed for this complex in the solid state is mirrored in solution, although direct comparisons between solid and solution behaviour are difficult to make. The emissive behaviour is again similar to that of **PhRu** and **CF_3Ru**, with changing solvents shifting the emission wavelength by up to 20 nm.

1.4.2.2 Comparison of the Absorption and Emission Properties of **PhRu**, **CF_3Ru** and **OMeRu**

Figure 50 shows the normalised absorption and emission spectra for the three ruthenium complexes in MeCN. From this graph the differences in behaviour are readily identifiable –the absorption spectrum of **PhRu** and **CF_3Ru** are similar, with the latter having an MLCT absorption redshifted by 10 nm due to the electron-withdrawing effect of the trifluorotoluene moieties.

OMeRu and **PhRu** share similar MLCT absorption properties, but the former shows the previously discussed CT absorption at 370 nm. The high degree of similarity seen for the MLCT absorption suggests that the ground state is not significantly perturbed by the presence of the methoxy moieties.

The emission profiles of the three ruthenium complexes are similar, suggesting that all three complexes share the same general excited state that is subtly changed depending on the structure of the complexes in question. **CF_3Ru** has the lowest energy emission, with **OMeRu** showing the highest energy and **PhRu** acting as an average baseline between the two. While the numerical difference in wavelengths is small, this trend does indicate that electron-withdrawing units will lower the energy of the HOMO-LUMO gap, while electron-donating effects will increase it, leading to higher-energy emission.

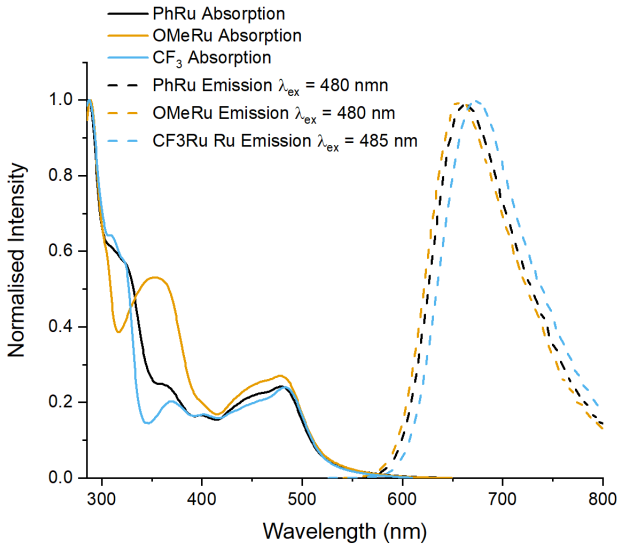

Figure 50. Absorption and normalised emission spectra of **PhRu**, **CF_3Ru** and **OMeRu** in MeCN; UV-vis spectra shown with solid lines and emission spectra shown with dotted lines (λ_{ex} = 480 nm for **PhRu** and **OMeRu**, 490 nm for **CF_3Ru**), [10^{-5} M], 298 K.

The molar extinction coefficients for the MLCT absorption band of the ruthenium complexes are shown in **Table 2**. The data shows that the intensity of the MLCT absorption band is strongly influenced by the presence of substituents on the phenylacetylene ring. The electron-donating effect of the OMe group increases the molar extinction coefficient, while the presence of the CF_3 group reduces it.

Table 2. Molar extinction coefficients for **PhRu**, **OMeRu** and **CF_3Ru** (MeCN, 10^{-5} M, 298 K).

Compound	Wavelength (nm)	ε (L mol^{-1} cm^{-1})
PhRu	480	27100
OMeRu	480	32500
CF_3Ru	485	18600

1.4.2.3 Excitation Studies of PhRu, CF_3Ru and OMeRu

Excitation studies were performed to confirm that the observed emission originates from the prepared complexes. Unlike emission spectra, where the excitation wavelength is held constant and the emission wavelength scanned, excitation spectra are carried out by holding the emission wavelength constant and scanning the excitation wavelength. This results in a spectrum displaying which excitation wavelengths lead to the observed emission. When compared to the UV absorption spectrum of a complex, the corresponding excitation spectrum should match the peak positions. Complications arise when multiple absorption transitions lead to emission, as the efficiency of the absorption-emission process varies between them. This can result in absorption and excitation spectra having different band intensities – but as long as the peak wavelengths match, it can be confidently assumed that any observed emission is originating from the absorbing species (in this case the three ruthenium complexes). **Figure 51** shows the excitation studies for the three complexes.

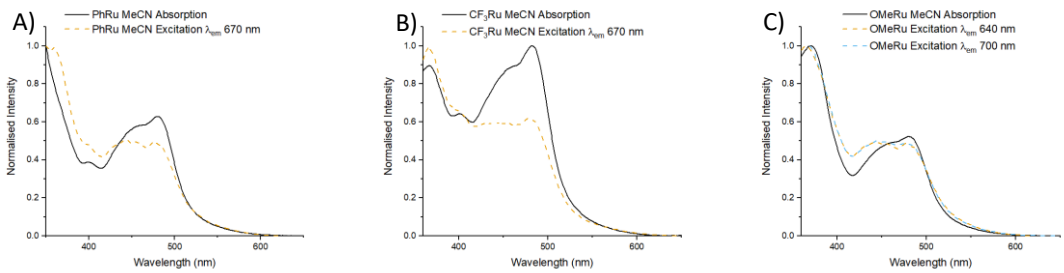

Figure 51. Normalised excitation studies of **PhRu** (A), **CF$_3$Ru** (B) and **OMeRu** (C) in MeCN (dashed lines), compared to normalised absorption profiles of **PhRu** (A), **CF$_3$Ru** (B) and **OMeRu** (C) in MeCN (solid lines) [10-5 M], 298 K.

These graphs show that the observed emission arises from the absorption bands of the complexes. While the intensity of the excitation/absorption bands differs in all three complexes, the peak positions of the excitation and absorption spectra match each other closely for every complex. For **OMeRu**, excitation spectra were taken at 640 and 700 nm to confirm that the observed shoulder forms part of the emission profile of the overall complex, and the two resulting excitation spectra overlap perfectly.

Although the changes in the MLCT absorption and emission properties of the three complexes are very similar, further analysis of the excited state properties are in order to understand the structure/property relationships of this family of compounds more comprehensively.

1.4.2.4 Degassing Studies of PhRu, CF$_3$Ru and OMeRu

The first step to an in-depth analysis is a comparison of the emission of the complexes in air vs. argon. If a triplet excited state is present (a prerequisite for any triplet photosensitiser), the presence of oxygen in the air will quench the intensity of the emission. This occurs via energy transfer from the complex triplet excited state to the oxygen triplet ground state, resulting in a complex singlet ground state and an oxygen singlet excited state. Although transitions from singlet to triplet electronic states is formally forbidden, the net spin change of this process is zero, allowing it to proceed with reasonable efficiencies. **Figure 52** shows the normalised emission intensity of the three complexes under argon (yellow line) and air (black line) atmospheres.

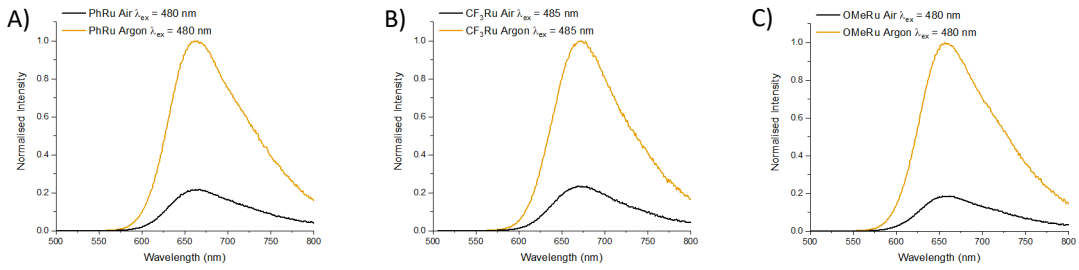

Figure 52. Emission spectra of **PhRu** (A), **CF$_3$Ru** (B) and **OMeRu** (C) in MeCN under either air (black line) or argon (yellow line) atmospheres [10^{-5} M], 298 K.

The emission intensity increases significantly under argon compared to air for all three complexes, suggesting that the excited state is indeed triplet in nature. The emission intensity in air is quenched by 79 %,

73 % and 82 % compared to argon for **PhRu**, **CF_3Ru** and **OMeRu** respectively. This indicates that **OMeRu** is the most effective complex in the series for sensitising oxygen, as its emission is quenched in air by the highest degree. There are no significant changes in band shape or width when the samples are degassed.

1.4.2.5 Low Temperature Emission Studies of PhRu, CF_3Ru and OMeRu

The second set of measurements probed to further investigate the excited state properties of the three complexes were low-temperature emission measurements. In this investigation, a 4:1 Ethanol:Methanol solution of the complexes was frozen at 77 K using liquid nitrogen. At this temperature the solvent mixture will form a glass matrix, suspending the complexes in a solid suspension. This prevents any solvent-based stabilisation of the excited state as well as leading to resolution of any fine structure that may usually be obscured by vibrational and rotational coupling. These low temperature spectra are then compared to the room temperature spectra.

For CT based emission bands, low temperature emission studies often show a shift to higher energies in the matrix emission compared to the fluid emission. This is because in a matrix, rearrangement of solvent molecules to allow for stabilisation of the excited state is not possible. Consequently, the excited state is not stabilised, and the emission shifts to higher energies. The low temperature emission studies for the three complexes are shown in **Figure 53**.

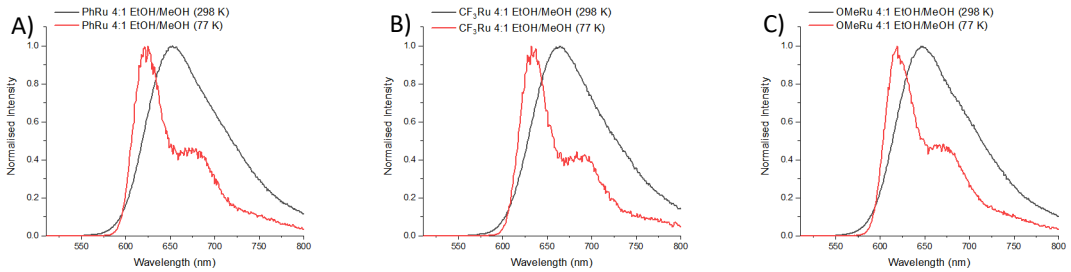

Figure 53. Low temperature emission studies of **PhRu** (A), **CF_3Ru** (B) and **OMeRu** (C), recorded in a MeOH/EtOH 4:1 solution at 298 K (black line) and in a frozen glass at 77 K (red line), (λ_{ex} = 480 nm for PhRu and OMeRu 490 nm for CF_3Ru), [10^{-5} M].

All three complexes show a shift to higher emission wavelengths at low temperatures, supporting the designation of the excited state as CT in nature. Additionally, the single peak at room temperature resolves into two distinct peaks at 77 K, one at higher energies with greater intensity and one at longer wavelengths with lower intensity. The magnitude of the emission wavelength shift at low temperatures was similar, with shifts of 31, 33 and 26 nm recorded for **PhRu**, **CF_3Ru** and **OMeRu** respectively.

Comparing the low temperature emission spectra of all three ruthenium complexes (**Figure 54**), the same trends can be observed as for the spectra at 298 K. **OMeRu** has the highest energy emission wavelength, followed by **PhRu** and **CF_3Ru**. The overall emission profile does not change regardless of the substituent used, with **CF_3Ru** showing a slightly less intense shoulder peak than the other two complexes. In summary, the low temperature emission spectra confirm that the excited state is CT in nature, and suggest that there are two electronic states with very similar energies contributing to the overall emission profile at 298 K.

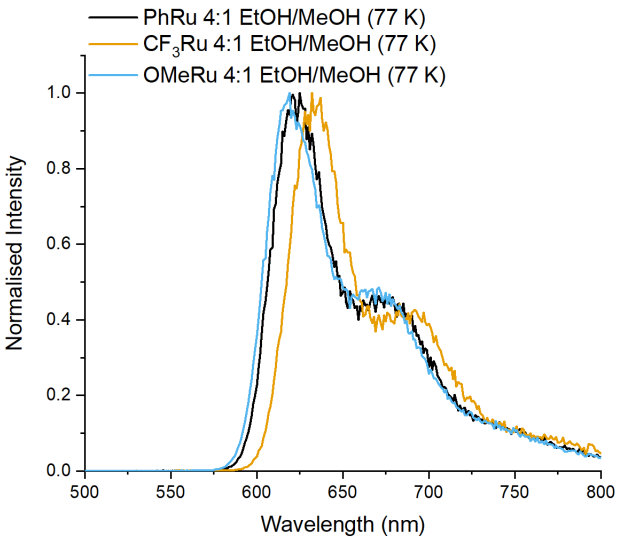

Figure 54. Low temperature emission studies of PhRu (black line), CF_3Ru (yellow line) and OMeRu (blue line), recorded in a MeOH/EtOH 4:1 frozen glass at 77 K (λ_{ex} = 480 nm for PhRu and OMeRu 490 nm for CF_3Ru), [10^{-5} M].

1.4.2.6 Quantum Yield of Phosphorescence and Emission Lifetime of PhRu, CF_3Ru and OMeRu

Of key interest in the development of efficient triplet photosensitisers are the emission and excited state lifetimes of the complexes. The former describes the rate of radiative decay from the excited state to the ground state, while the latter takes both the radiative and non-radiative decay rates into account. For this thesis, only the emission lifetime could be measured. The measurement was performed in MeCN and under an argon atmosphere. The emission lifetime for the three complexes is reported below in **Table 3** and compared to that of [$Ru(bpy)_3(PF_6)$].

Table 3. Emission lifetime of **PhRu**, **CF_3Ru** and **OMeRu** in MeCN under an argon atmosphere, 10^{-5} M, 298 K.

Complex	Lifetime (μs)
PhRu	1.43
CF_3Ru	1.01
OMeRu	1.49
[$Ru(bpy)_3(PF_6)$].[89]	0.89

The emission lifetime of all three complexes is longer than that of [$Ru(bpy)_3(PF_6)$], with **OMeRu** having the longest at 1.49 μs, marking it as a triplet photosensitiser with good potential for applications. An interesting side note is that the range of lifetimes matches the trends in quenching by oxygen, with **OMeRu** having the longest lifetime and being the most susceptible to quenching by oxygen. This shows the relationship between

these two properties, as complexes with longer emission excited states are more likely to collide and interact with ground state triplet oxygen.

Finally, quantum yield of phosphorescence measurements were performed on the three ruthenium complexes using $[Ru(bpy)_3(PF_6)]$ as a standard, with the latter having a quantum yield of phosphorescence of 9.7 %.[40] As with the emission lifetime, the quantum yield of phosphorescence was recorded in MeCN under an argon atmosphere (**Table 4**).

Table 4. Quantum yields of phosphorescence for **PhRu**, **CF_3Ru** and **OMeRu** in MeCN under an argon atmosphere, measured using $[Ru(bpy)_3(PF_6)_2]$ in MeCN as a standard.[40]

Complex	Quantum Yield (%)
PhRu	15.95
CF_3Ru	13.40
OMeRu	17.37
$[Ru(bpy)_3(PF_6)]$[40]	9.7

The quantum yields of the three prepared complexes are higher than those of $[Ru(bpy)_3(PF_6)]$, suggesting that they do not have access to as many non-radiative decay pathways, improving their efficiency as potential triplet photosensitisers. Of the three complexes, **OMeRu** has the highest quantum yield of phosphorescence, once again highlighting its potential amongst the three presented complexes.

While the excited state as ^{3}CT in nature can now be generally confirmed thanks to the degassing and low temperature emission experiments, the exact nature of the emission is still undetermined. Of specific interest is the distinction between ^{3}MLCT and ^{3}ILCT excited states, as the latter are reported to have significantly longer emission lifetimes than the former, increasing their efficiency as triplet photosensitisers in a wide range of applications.[41,84,90] For these complexes, assignment of the excited states of all three complexes as ^{3}MLCT seems appropriate. This is due to the large degree of similarity between the spectroscopic properties of the three ruthenium complexes investigated thus far. Since neither **PhRu** nor **CF_3Ru** have the prerequisite structural features to undergo ILCT, their excited states are a process of elimination ^{3}MLCT. And since **OMeRu** is spectroscopically so similar to its two cousins, its excited state is likely ^{3}MLCT in nature as well.

1.4.3 Spectroscopic Analysis of PhIr, CF_3Ir, OMeIr

1.4.3.1 Solvatochromic Absorption and Emission of **PhIr**, **CF_3Ir**, **OMeIr**

The absorption and emission properties of the three iridium complexes were measured in the same fashion as those of the ruthenium complexes. The solvatochromic absorption and emission behaviour of **PhIr** is shown in **Figure 55**. The greatest immediate and apparent difference to **PhRu** is the lack of significant absorption bands past 450 nm. This is due to the lower-lying iridium d-orbitals resulting in higher energy MLCT transitions, usually centred around 370 nm.[43] However, due to the higher spin-orbit coupling coefficient of iridium compared to ruthenium (3909 cm^{-1} and 1042 cm^{-1} respectively), iridium complexes can show ^{3}MLCT

absorption.[43,57] As this is a spin-forbidden process, the intensity of these transitions remains low, but still clearly discernible for **PhIr** at ~500 nm.

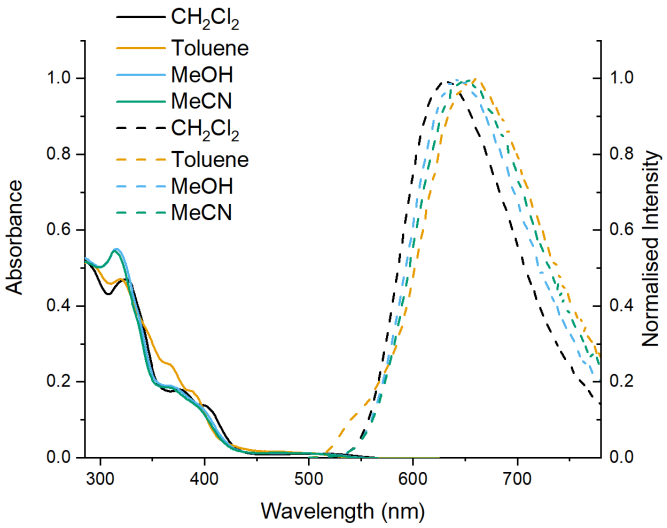

Figure 55. Absorption and normalised emission spectra of **PhIr** in a range of solvents; UV-vis spectra shown with solid lines and emission spectra shown with dotted lines (λ_{ex} = 400 nm), [10^{-5} M], 298 K.

Interestingly, despite the higher absorption energies, the emission wavelength of **PhIr** is roughly comparable to that of **PhRu** (650 nm vs 660 nm respectively). This is the result of the very large Stokes shift for **PhIr** of 250 nm, taken from the ^{1}MLCT absorption as opposed to the ^{3}MLCT absorption. The solvent effect on the absorption and emission wavelengths of **PhIr** are similar to the behaviour observed for **PhRu**. The absorption wavelengths are not greatly affected, although CH_2Cl_2 and toluene do induce a very slight redshift in **^{1}MLCT** absorption wavelength compared to **MeCN** and **MeOH**.

The emission wavelength also shifts depending on solvent polarity, indicating an induced dipole in the excited state characteristic feature of CT emission.

The absorption and emission spectra of **CF_3Ir** and **OMeIr** are displayed below in **Figure 56**, and are very similar to those of **PhIr**. The greatest difference between **PhIr** and **CF_3Ir** is a slight red-shift in the absorption spectra due to the electron-withdrawing effect of the CF_3 moieties. **OMeIr** has more pronounced differences to the other two complexes, with strong absorption around 400 nm, likely due to the CT processes from the methoxy units into the bipyridine ligand core. The CT absorption band shifts to lower energies in toluene and CH_2Cl_2. All three complexes show ^{3}MLCT absorption past 500 nm. The emission of **CF_3Ir** and **OMeIr** are sensitive to solvent, with **OMeIr** also showing variations in the absorption spectra depending on the solvent used.

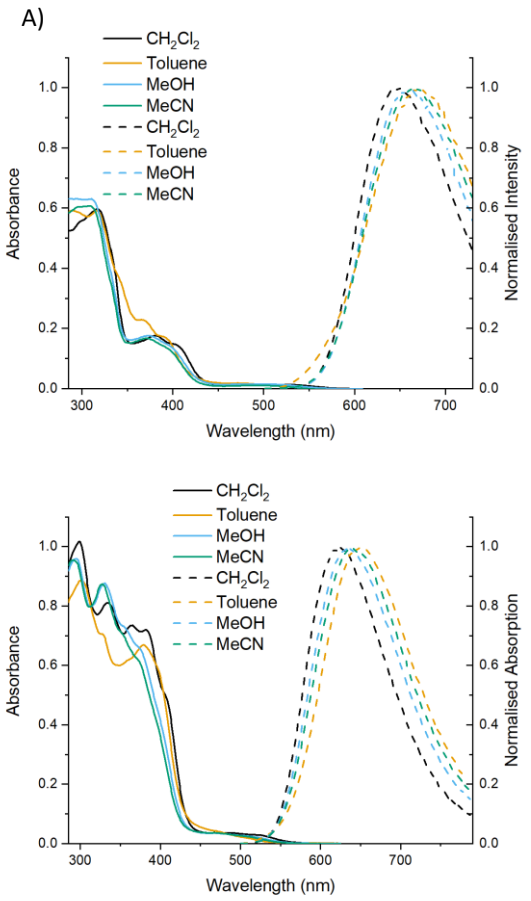

Figure 56. Absorption and normalised emission spectra of **CF_3Ir** (A) and **OMeIr** (B) in a range of solvents; UV-vis spectra shown with solid lines and emission spectra shown with dotted lines (λ_{ex} = 400 nm), [10^{-5} M], 298 K.

1.4.3.2 Comparison of the Absorption and Emission Wavelengths of **PhIr**, **CF_3Ir**, **OMeIr**

A comparison of absorption and emission spectra for all three iridium complexes in MeCN is shown in **Figure 57**.

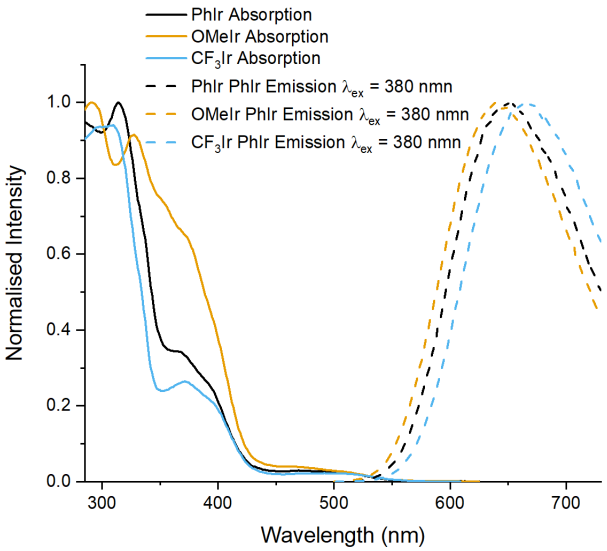

Figure 57. Normalised Absorption and emission spectra of **PhIr**, **CF₃Ir** and **OMeIr** in MeCN; UV-vis spectra shown with solid lines and emission spectra shown with dotted lines (λ_{ex} = 380), [10^{-5} M], 298 K.

From this graph the differences in absorption around 350-400 nm between the three complexes become evident. **OMeIr** shows far more intense absorption in this region than the other two iridium complexes, suggesting that the CT band observed in the **OMeL** and **OMeRu** is present in the iridium complex as well. There is no observable difference in the ^{3}MLCT absorption between the three iridium complexes, suggesting that the transition is unaffected by modification of the phenylacetylene ring. The emission wavelengths of the three iridium complexes follow the same pattern as those of the ruthenium complexes. **OMeIr** emits at the highest energy, **CF₃Ir** at the lowest and **PhIr** between the two. The magnitude of difference between the three emission peaks is more pronounced for the iridium complexes than for the ruthenium, with a 30 nm difference between **OMeIr** and **CF₃Ir** and a 15 nm difference between **OMeRu** and **CF₃Ru**. This suggests that the excited state of the iridium complexes is more strongly affected by modification of the phenylacetylene ring than the excited state of the ruthenium complexes.

The molar extinction coefficients for the three iridium complexes are shown in **Table 5**. While both PhIr and CF_3Ir show low molar extinction coefficients, the values for OMeIr are significantly increased. This is due to the presence of the ILCT transition from the electron-donating methoxy groups into the bipyridine core, a process which is not possible in the other two complexes.

Table 5. Molar extinction coefficients for **PhIr**, **OMeIr** and **CF₃Ir** (MeCN, 10^{-5} M, 298 K).

Compound	Wavelength (nm)	ε (L mol^{-1} cm^{-1})
PhIr	390	14400
OMeIr	370, 390	62579, 46010
CF₃Ir	390	16130

1.4.3.3 Excitation Studies of **PhIr**, **CF_3Ir**, **OMeIr**

Excitation spectra for the three iridium complexes were performed in similar fashion to those conducted for the ruthenium species (**Figure 58**). They show that the emission of all three complexes is generated by absorption from the weak ^{3}MLCT band as well as the higher energy ^{1}MLCT (and in the case of **OMeIr** ^{1}ILCT) bands.

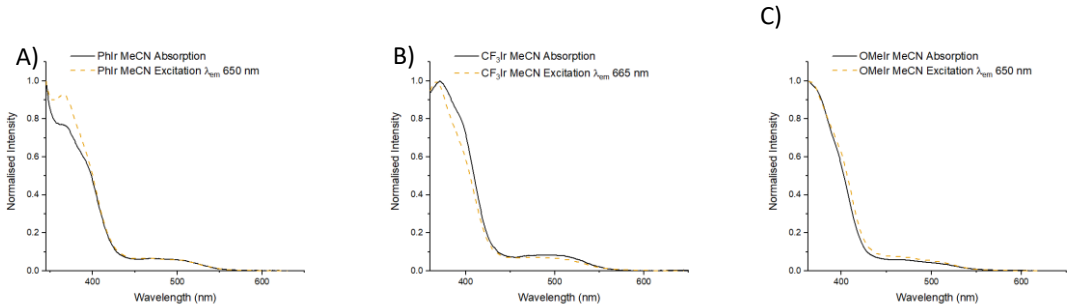

Figure 58. Normalised excitation studies of **PhIr** (A), **CF_3Ir** (B) and **OMeIr** (C) in MeCN (dashed lines), compared to normalised absorption profiles of **PhIr** (A), **CF_3Ir** (B) and **OMeIr** (C) in MeCN (solid lines) [10-5 M], 298 K.

1.4.3.4 Degassing Studies of **PhIr**, **CF_3Ir**, **OMeIr**

While the contribution of a triplet absorption band to the emission strongly suggests that the latter also has triplet character, the emission of the complexes was measured under argon and compared to the emission in air in **Figure 59**. As expected, the emission appears significantly more intense under argon than in air, indicating the presence of a triplet state quenched by singlet oxygen. Interestingly, the magnitude of the quenching is lower than that measured in the ruthenium complexes, with a maximum quenching of 60% observed in **OMeIr** compared to 82% in **OMeRu**. Even so, the trend within the iridium complex series remains the same as within the ruthenium complexes. The addition of electron-donating methoxy units enhances the ability of the complex to sensitise molecular oxygen, as demonstrated by a 60% quenching efficiency in OMeIr compared to 50% in PhIr. The addition of electron-withdrawing CF_3 moieties on the other hand reduces the ability to sensitise molecular oxygen, with the emission of CF_3Ir being quenched by 38% in air.

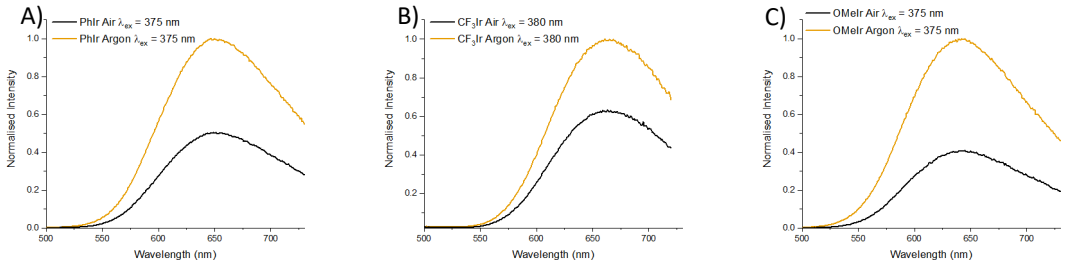

Figure 59. Emission spectra of **PhIr** (A), **CF_3Ir** (B) and **OMeIr** (C) in MeCN under either air (black line) or argon (yellow line) atmospheres [10^{-5} M], 298 K.

As with the ruthenium complexes, no change in band shape or emission wavelength was detected upon removal of oxygen and introduction of argon to the solution.

1.4.3.5 Low Temperature Emission Studies of **PhIr**, **CF_3Ir**, **OMeIr**

The low-temperature emission spectra of the iridium complexes displayed below in **Figure 60**. They manifest the same shift to higher energy emission at low temperatures as the ruthenium complexes, indicating the presence of a charge-transfer excited state that cannot be stabilised by solvent rearrangement in a frozen glass matrix. There is also a resolution of some fine structure, with the appearance of a low energy shoulder at 600 nm.

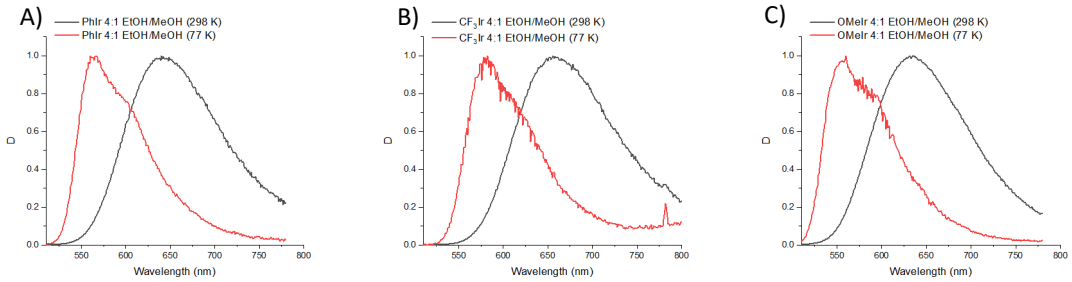

Figure 60. Low temperature emission studies of **PhIr** (A), **CF_3Ir** (B) and **OMeIr** (C), recorded in a MeOH/EtOH 4:1 solution at 298 K (black line) and in a frozen glass at 77 K (red line). (λ_{ex} = 400 nm), [10^{-5} M].

This suggests that the single broad emission peak observed at room temperature is in fact an amalgamation of two distinct electronic energy levels, which broaden at room temperature (via vibrotational coupling and solvent stabilisation) to appear as a single broad emission peak.

A comparison of the low temperature emission spectra of the three iridium complexes (***Figure 61***) reveals the same trend in emission wavelength as the room-temperature spectra, with OMeIr emitting at the highest and CF_3Ir at the lowest energies. The low resolution of these spectra is due to imperfections in the glass matrix, which can result in photon scattering, as well as the use of silicon glass in the walls of the tubes used to perform the measurements.

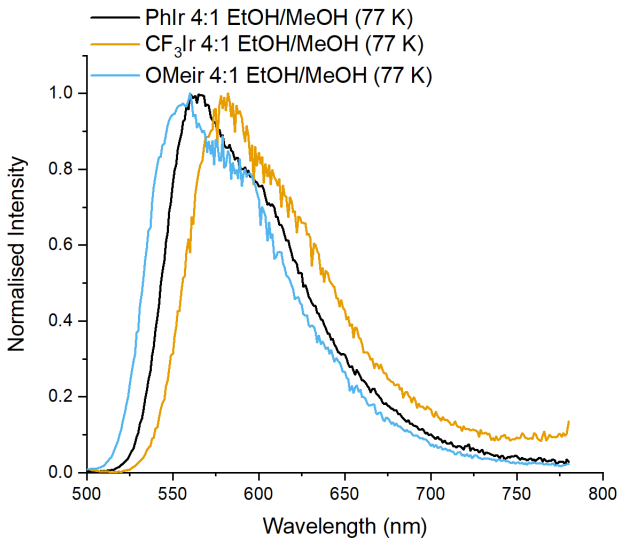

Figure 61. Low temperature emission studies of **PhIr** (black line), **CF$_3$Ir** (yellow line) and **OMeIr** (blue line), recorded in a MeOH/EtOH 4:1 frozen glass at 77 K (λ_{ex} = 400 nm), [10^{-5} M].

1.4.3.6 Quantum Yield of Phosphorescence and Emission Lifetime of **PhIr**, **CF$_3$Ir**, **OMeIr**

As with the ruthenium complexes, the lifetime of the iridium complexes is of particularly high interest for their intended purpose as triplet photosensitisers. The lifetime of iridium complexes in general is shorter than that of equivalent ruthenium complex, accounting for the lower degree of oxygen sensitivity shown by the iridium complex emission in this thesis.[43,56] The shorter lifetime results in less possibility for interactions with triplet oxygen and other photosensitiser compounds. The lifetimes of the three prepared iridium complexes, shown in **Table 6**, are noticeably shorter than those of the ruthenium complexes, with all but **OMeIr** under 200 ns. Once again the trends in the ruthenium complexes are reflected in the iridium series, showing the consistent influence that the ligand systems have on the excited state of the complexes.

Table 6. Emission lifetime of PhIr, CF$_3$Ir and OMeIr in MeCN under an argon atmosphere, 10^{-5} M, 298 K.

Complex	Lifetime (µs)
PhIr	0.17
CF$_3$Ir	0.13
OMeIr	0.21
[Ru(bpy)$_3$(PF$_6$)].[89]	0.89

The lifetime for CF$_3$Ir was collected using both a 372 nm laser diode and a 458 nm laser diode to determine whether the excitation wavelength and corresponding absorption band (^{1}MLCT and ^{3}MLCT) had an influence on the emission lifetime. This was not the case, with the two values falling within the margin of each other's error. . This demonstrates the principle of ultrafast intersystem crossing present in heavy

transition metal complexes, where the singlet excited state is almost instantly converted to the triplet upon excitation.

Finally, the quantum yields of phosphorescence of the three iridium complexes were determined using [Ru(bpy)$_3$(PF$_6$)] in MeCN as a standard. It is best practice to attempt matching the excitation and emission wavelength of any analytes with quantum yield standards, however due to the large Stokes shift of the iridium complexes this was not possible. Consequently, it was decided to use [Ru(bpy)$_3$(PF$_6$)] in an effort to match emission wavelength and to ensure continuity with the quantum yield values obtained for the ruthenium complexes in this thesis. The results of these measurements are shown in **Table 7**.

Table 7. Quantum yields of phosphorescence for **PhIr**, **CF$_3$Ir** and **OMeIr** in MeCN under an argon atmosphere, measured using [Ru(bpy)$_3$(PF$_6$)$_2$] in MeCN as a standard.[40]

Complex	Quantum Yield (%)
PhIr	6.4
CF$_3$Ir	4.87
OMeIr	10.44
[Ru(bpy)$_3$(PF$_6$)][40]	9.7

Yet again, the trends observed match those of the ruthenium complexes, even if the absolute value for all iridium complexes is lower than for their ruthenium equivalents.

1.4.4 Comparison of Ruthenium and Iridium Triplet Photosensitisers

Figure 62 compares the ruthenium and iridium complexes bearing the same ligand systems. From this comparison it is possible to garner some new insights into the structure/property relationships of 4,4-substituted bipyridyl ligand systems appended to ruthenium and iridium metal centres.

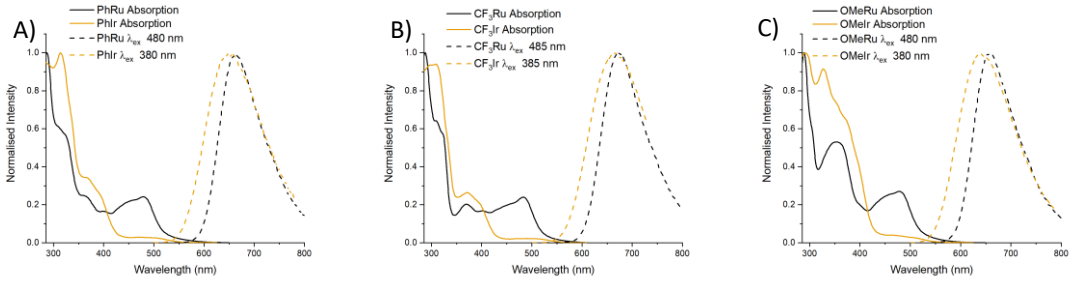

Figure 62. Normalised absorption and emission spectra of ruthenium and iridium complexes with **Ph** (A), **CF$_3$** (B) and **OMe** (C) ligands in MeCN 10^{-5}M, 298 K.

The largest difference can be seen in the absorption wavelength of the ^{1}MLCT transitions. All ruthenium complexes absorb strongly between 450 and 500 nm, whereas the corresponding iridium complexes show much weaker absorption in this window. Lower energy absorption processes are of interest in a variety of applications for triplet photosensitisers, particularly in photodynamic therapy due to the biological window.[24] The emission wavelength of the ruthenium and iridium complexes is similar, with the iridium complexes at

slightly higher energies than their ruthenium counterparts. This suggests that the energy gap between the emissive excited state and ground state is similar for the two transition metal centre types, which is surprising given the difference in ^{1}MLCT absorption. This suggests that there may be a significant contribution of the ligand involvement to the final emissive excited state, as this is a commonality between all the different substitution types (Ph, CF_3 and OMe).

The ligand participation hypothesis is also supported by the observation that the trends in emission wavelength, lifetime and phosphorescence quantum yield are the same across the ruthenium and iridium series. Although the metal centre plays a role in the absolute value of the obtained measurements, the ligands have a clear and sustained influence on the properties of the complex's electronic energy levels.

Analysing these trends, it rapidly becomes clear that the OMe framework offers the highest performance as a potential triplet photosensitiser, boasting both the longest lifetime, greatest oxygen sensitivity and highest phosphorescence quantum yield in both the ruthenium and iridium series. The CF_3 moiety performs poorly in all of those categories, with its only notable contribution being a redshift in the ^{1}MLCT absorption in the ruthenium series.

However, there remains significant room for improvement. While the OMe moiety performed best in the prepared ligand series, the ^{1}CT transition observed for the free ligand remained at high energies for **OMeIr** and **OMeRu**, limiting its contribution to the performance of the complexes. Ligand designs encouraging lower energy CT transitions with 'stronger' electron donors may result in the generation of triplet photosensitisers where the intra-ligand charge transfer (ILCT) process occurs at lower energies than the MLCT transitions, shifting the absorption of the complexes further into the biological window.

More formal electron-withdrawing groups could potentially have the same effect by shifting the MLCT absorption further into the red, but may suffer from adverse performance in other aspects of triplet photosensitiser design. It is important to remember that even though the CF_3 group did induce the lowest energy absorption transition of the six prepared complexes, absorption wavelength is not the only consideration when evaluating the performance and efficiency of triplet photosensitisers. Emission lifetime, ability to sensitise triplet oxygen and the quantum yield of luminescence are all equally important parameters that must improve alongside absorption wavelength, not sacrificed for it.

As a result, the introduction of more formal electron-withdrawing functional groups may be counterproductive. An alternative design pathway could be developed using MLCT transitions but focussing on the delocalisation of the resulting excited state in addition to the absorption wavelength. Lu *et al.* showed that pyrene bearing polypyridyl triplet photosensitiser systems populate ^{3}IL excited states completely delocalised from the metal centre, resulting in emission lifetimes orders of magnitude greater than any recorded in this body of work.[50] While the cumbersome synthetic approach to these systems limit their potential for widespread applications, the insights gleaned into the excited state properties of pyrene-bearing triplet photosensitisers will contribute to future design considerations.

2: 4,4-bipyridines Bearing Highly Conjugated Chromophores

2.1 Introduction

While the complexes generated in Chapter 1 showed promising triplet photosensitiser behaviour, significant issues in their performance remain. In particular, extending the emission lifetime and pushing the absorption wavelengths further into the biological window are imperative if they are to function as suitable PDT agents. In this chapter, further modifications of the 4,4'-positions of bipyridyl ruthenium and iridium triplet photosensitisers will be presented.

2.1.1 Integrating Lessons Learned from Chapter 1

There are several conclusions to be drawn from the last chapter on how to improve the design and synthesis of efficient iridium and ruthenium triplet photosensitisers bearing 4,4-substituted bipyridine ligands. For instance, the addition of electron-donating/withdrawing groups impacts the absorption and emission wavelengths of the complexes, indicating an influence on both the highest occupied molecular orbital (HOMO) and the lowest unoccupied molecular orbital (LUMO) of the molecules.

Specifically, the addition of electron-donating groups to the bipyridine ligands allows incorporation of intra-ligand charge-transfer (ILCT) transitions into the photophysical behaviour of the complex. Furthermore, electron-donating groups increase the quantum yields of phosphorescence, the sensitivity of the excited state to ground-state molecular oxygen as well as the emission lifetime. However, the methoxy units used as electron donating groups in the previous chapter lead to relatively high-energy charge-transfer transitions, and the excited state of the molecule was still predominantly MLCT in nature. Additionally, inclusion of electron-donating units leads to a decrease in MLCT emission wavelength, suggesting a destabilisation of the LUMO. Consequently, further efforts should focus on introducing lower energy charge-transfer transitions which absorb at energies comparable to or lower than the MLCT transition, which should also lead to the emissive excited state adopting more ILCT character.

The inclusion of electron-withdrawing units did result in a redshift in MLCT absorption wavelength, but also negatively influenced the other parameters influencing triplet photosensitiser efficiency. Phosphorescence quantum yield, emission lifetime and sensitivity to molecular oxygen were all decreased in the CF_3 complexes compared to the OMe or Ph families. As the excited state properties of all three complex types

were largely similar, this suggests that the CF_3 group was negatively influencing the photophysical properties of the MLCT excited state. A potential solution to this issue may lie in the introduction of electron-withdrawing units which lower the energy of MLCT transitions, while also facilitating the population of ligand-based excited states distinct and decoupled from metal-based MLCT excited states.

2.1.2 Photophysical Properties of Pyrene

One functional group that is well-known to induce this type of behaviour is pyrene.[50,71,91,92] Pyrene is a widely studied polyaromatic molecule composed of 4 conjugated six-membered rings (**Figure 63**). Unmodified pyrene is a chromophore that absorbs in the UV region through $\pi - \pi^*$ transitions, with a reduced HOMO-LUMO gap compared to benzene due to the greater conjugation. Pyrene emission is unusual as it displays fine structure, uncommon to other highly conjugated polyaromatic molecules.[44] At low concentrations, pyrene emits between 370 and 420 nm, showing distinct vibronic structure.[44] At higher concentrations, pyrene can form excimers, which are pairings of two pyrene molecules formed when an excited state pyrene interacts with a ground state pyrene molecule.[44] This interaction results in a redshift in emission wavelength and a broadening of the emission band.

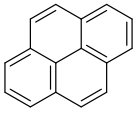

Figure 63. The chemical structure of pyrene.

2.1.3 Triplet Photosensitisers bearing pyrene chromophores

The low-energy $\pi - \pi^*$ excited state of pyrene makes it an attractive candidate for integration into triplet photosensitiser design. Standard π - π^* excited states are too high in energy to play a significant role in the steady-state photophysical behaviour of transition metal complexes. However, it is possible to design complexes with the pyrene $\pi - \pi^*$ excited state as the lowest energy level, allowing it to participate in room-temperature photophysical processes. This was demonstrated by Castellano and co-workers in 2002 when they described the properties of a platinum complex bearing pyrenes linked to the metal centre by acetylenes (**Figure 64**).[93]

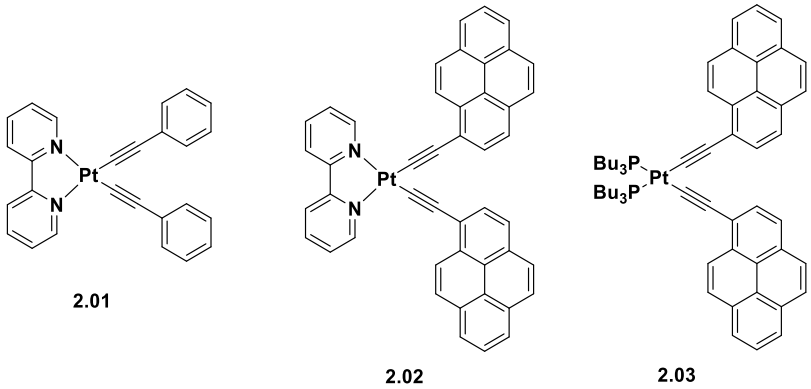

Figure 64. Structure of platinum complexes investigated by Pomestchenko *et al.*[93]

2.01 and **2.03** were prepared as model compounds for **2.02**, with the former possessing an MLCT transition to the bipyridine ligand like **2.02** while **2.03** did not, allowing the absorption and emission properties of the complexes to be defined via process of elimination. The absorption spectra of **2.01** shows a series of sharp transitions between 350 and 400 nm, with a weaker shoulder at higher energies. The former can be attributed to a series of π - π^* within the pyrene moieties, the latter to metal-based MLCT transitions. **2.01**, which does not bear any pyrene moieties, only manifests a weak absorption band between 350-450 nm assigned to MLCT transitions. The emission spectra of the two compounds follows similar trends to the absorption, **2.01** displaying a broad and featureless emission band at 480 nm, while **2.02** shows a highly structured emission band shifted to lower wavelengths by 100 nm. Additionally, the spectra of **2.01** were collected in air, while oxygen had to be removed from the atmosphere to obtain an emission spectrum for **2.02**. This indicates that **2.02** has a triplet excited state very sensitive to the presence of triplet oxygen, more so than the excited state of **2.01**. **2.02** also shows a significantly longer emission lifetime of 48.5 μs compared to 1.25 μs for **2.01**. While the absorption and emission data for **2.03** were not reported, the lifetime was measured at 68 μs, suggesting that pyrene is responsible for **2.02**'s extended lifetime.

Low-temperature emission studies showed small temperature-dependent Stokes shifts for **2.02** and **2.03**, indicating that the emission is not a result of charge-transfer excited state. **2.01**, meanwhile, manifests the low-temperature hypsochromic shift characteristic of MLCT excited states. This, combined with the fact that there was no significant change in band shape or fine structure, is strongly suggestive of an intra-ligand ^{3}IL excited state in **2.02** and **2.03**.

The above work by Castellano and co-workers shows that coupling a transition metal to a pyrene via an acetylene allows population of the ^{3}IL excited state of the pyrene through enhanced spin-orbit coupling due to the heavy atom effect.

Two publications by Draper and co-workers in 2016 indicate that this behaviour is not limited to early-row transition metals like platinum.[50,71] **Figure 65** shows the structures of a set of iridium triplet photosensitisers for triplet-triplet annihilation upconversion bearing pyrenes linked to phenanthroline ligands via acetylene bonds.[71]

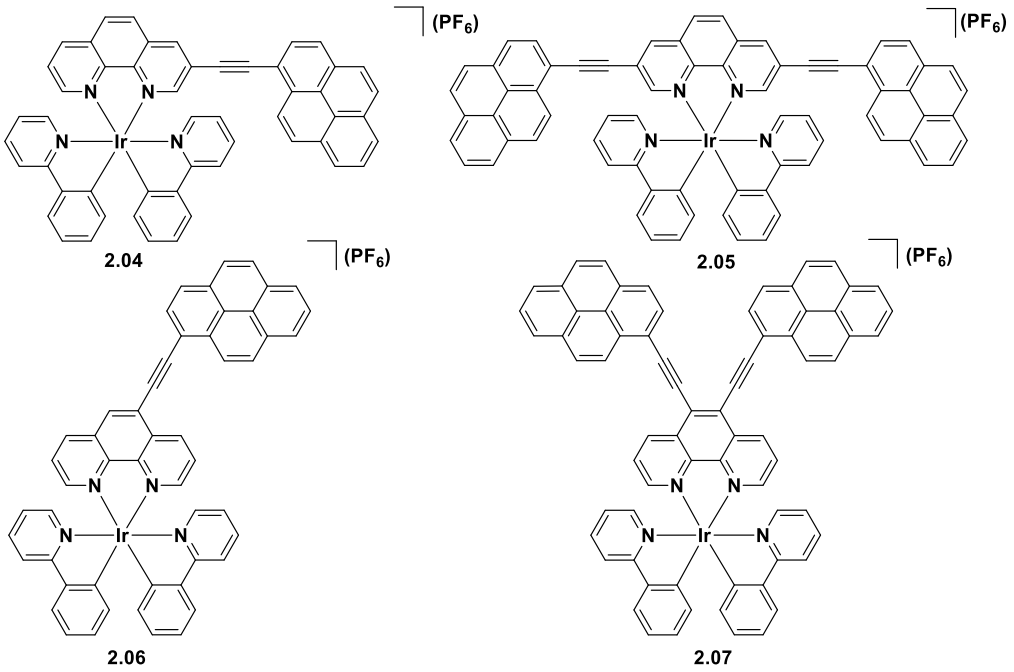

Figure 65. Pyrene-containing iridium photosensitisers prepared by Lu *et al.*[71]

These complexes display strong absorption in the visible region, unlike the iridium complexes described in Chapter 1. **2.05** and **2.07** show strong absorption peaks past 480 nm, which is comparable to ruthenium MLCT transition energies. All complexes bar **2.07** manifest sharp emission profiles with defined peaks and lifetimes ranging from 73 to 213 μs. Interestingly, **2.07** shows a higher degree of MLCT emission behaviour, with broad featureless emission bands and a biexponential lifetime consisting of one 90.8 and one 1.3 μs component. This suggests that the substitution position of the acetylpyrene on the ligand rings has significant influence over the degree of metal orbital involvement in the excited state. **2.04-2.07** show high upconversion quantum yields, reflecting their high efficiency as triplet photosensitisers.[71]

Draper and co-workers also prepared a set of iridium triplet photosensitisers bearing asymmetric phenanthroline ligands, as shown in **Figure 66**.[50] These are interesting structures as they potentially allow for the absorption to be influenced by the electron-rich triphenylamine moieties while the emission is dominated by the electron-accepting pyrene groups. All three complexes display strong visible absorption, with a broad featureless peak at 480 nm likely due to CT transitions from the triphenylamine donor along the acetylene bonds into the ligand scaffold.

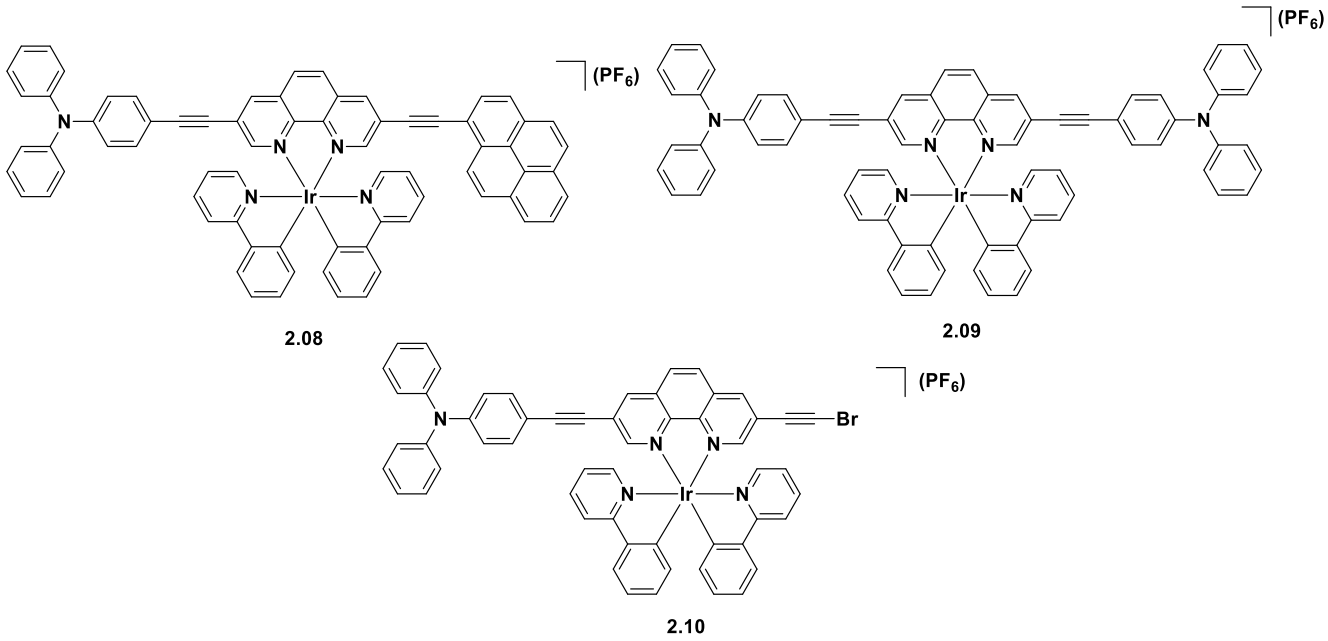

Figure 66. Iridium triplet photosensitisers bearing asymmetric phenanthroline ligands prepared by Lu *et al.*[50]

The absorption of **2.10** is half the intensity of **2.08** and **2.09**, suggesting that the bromine is not as efficient at harvesting photons as either the pyrene or the triphenylamine units. Interestingly, the small difference in absorption profiles between **2.08** and **2.09** suggests that the pyrene and triphenylamine units have comparable influence on the absorption of the iridium photosensitisers.

When investigating the emission however, significant divergences in behaviour become apparent. **2.09** and **2.10** show broad featureless bands centred at 700 nm, typical of MLCT excited states. **2.08** however, manifests the narrow bands and multiple peaks typical of pyrene-dominated excited states. This is confirmed by contrasting the emission lifetime of the complexes, with **2.09** and **2.10** showing sub 3 μs lifetime, while **2.08** is reported as having an emission lifetime of over 45 μs. It not only demonstrates the ability of pyrene to significantly extent the emission lifetime of triplet photosensitisers, but also the possibility to modulate the absorption and emission properties of triplet photosensitiser separately by introducing unsymmetric ligand systems.

The behaviour of pyrene-containing triplet photosensitisers is not always predictable. The work of Purkayastha and co-workers, for example, describes the synthesis and behaviour of a novel quinoxaline iridium complex containing a pyrene appendage, as shown in **Figure 67**.[92]

The complex is compared to a set of previously published iridium and rhenium pyrene-containing ones, and at first glance does not distinguish itself by any novel photophysical properties. The absorption and emission profiles of **2.11** match those of the reference compounds, with a broad and featureless emission band around 600 nm characteristic of MLCT excited states suggesting minimal involvement of the pyrene in the excited state. However, despite low sensitivity of the emission intensity to the presence of molecular oxygen, the singlet oxygen quantum yield (measured using singlet oxygen scavengers) was determined to be 72 %, a significant increase over the nearest reference compound at just under 60 %. Using density functional theory

in conjunction with cyclic voltammetry experiments the authors were able to identify a non-emissive 'dark' ^{3}ILCT/^{3}IL excited state contributing to the high singlet oxygen quantum yield.

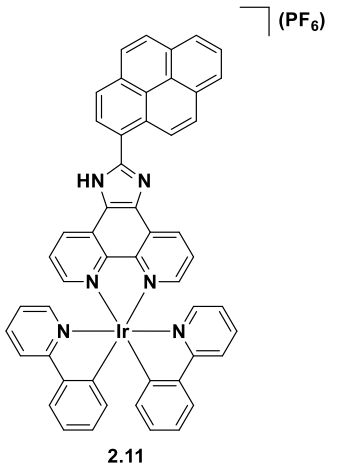

2.11

Figure 67. Iridium quinoxaline complex with a pyrene appendage.[92]

This excited state was populated by internal conversion from the emissive and shorter-lived ^{3}MLCT state of the complex, explaining the low luminescence and charge-transfer behaviour of the emission profile. Dark states have since been discovered in a wider range of transition metal complexes, but they typically involve larger and more heteroatom-containing chromophores.[40] The presence of such a dark state in a molecule with as basic a structure as pyrene is indicative of its complex photophysical behaviour.

While the properties of pyrene-containing transition metal triplet photosensitisers are impressive, appending pyrene to any photosensitiser design will not necessarily improve its excited state properties. This was demonstrated by Liu and co-workers, who designed two iridium complexes bearing pyrene-substituted quinoxaline ligands for applications in organic light-emitting diodes (OLEDs).[94] The structure of these complexes (**Figure 68**) directly relates to their photophysical properties.

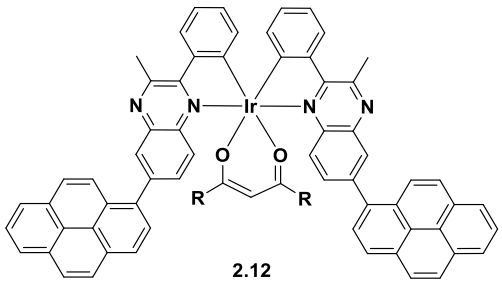

2.12

Where R is ^{t}Bu

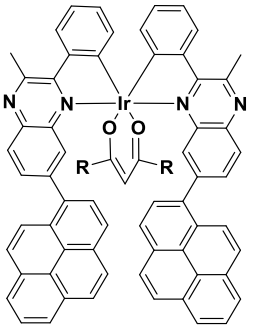

2.13

Figure 68. Iridium complexes bearing pyrene-substituted quinoxaline ligands.[94]

Photophysical analysis of the prepared complexes showed ^{3}MLCT absorption from the iridium d-orbitals to empty ligand π^* orbitals, and broad featureless emission between 660 and 675 nm. The quantum yield of the complexes' phosphorescence lies between 12 and 19%, with emission lifetimes of around 1.2 μs in room

temperature solutions. These properties indicate a CT-based excited state, either within the quinoxaline ligands or involving around iridium metal orbitals. Crystallographic analysis of the three complexes shows large dihedral angles between the pyrene moieties and the rest of the ligand structure.

The authors propose that this high degree of twisting prevents effective electronic communication between the pyrene units and the rest of the molecule, preventing the former from significantly influencing the electronic states of the latter. Their work demonstrates the importance of establishing effective communication between the pyrene and the rest of the molecule to ensure the performance enhancements observed in the previously discussed publications.[94]

This design principle is not limited to pyrene-containing iridium complexes. Vonlanthen *et al.* generated a series of trisbypiridine ruthenium complexes bearing pyrene dendrimers, shown in **Figure 69**.[95] The ligands show complex photophysical properties, with the absorption spectrum dominated by pyrene $\pi - \pi^*$ transitions, characterised by sharp bands and highly resolved fine structure. The emission band exhibits a broad peak between 450 and 500 nm, likely arising from excimer formation.[44] These features remain consistent when the ligands are complexes to the ruthenium metal centre. This suggests that there is no electronic communication along the alkane chains linking the separate parts of the molecules, leading to spatial and electronic isolation. The component parts of the complexes do not interact to form a combined excited state, but instead behave independently.

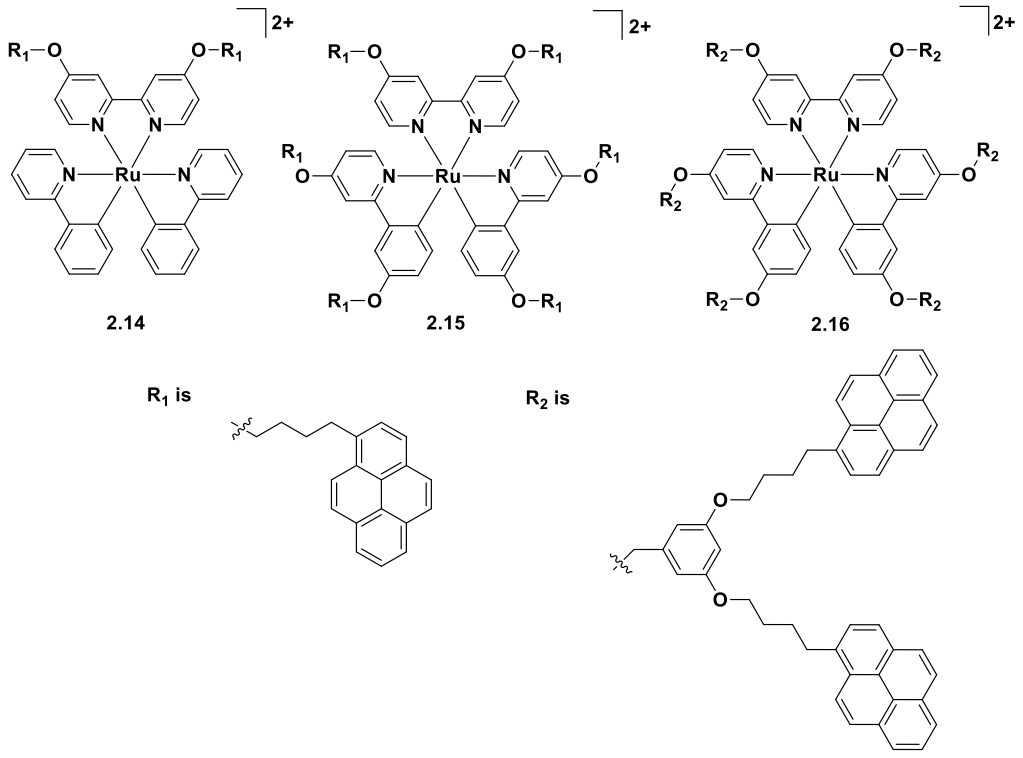

Figure 69. Trisbipyridine ruthenium complexes bearing pyrene dendrimers.[95]

While the authors do indicate that a FRET process transfers energy from the pyrene units to the ruthenium core, this does not result in enhanced emission from ruthenium excited states. Population of higher-energy, metal-centred (MC) states may be leading to rapid and nonradiative decay. The pyrene moieties are too spatially separated to affect the properties of the emissive ruthenium excited states. Like the work of Liu and

co-workers, this publication highlights how crucial communication between the pyrene and metal fractions are when trying to modify the spectroscopic behaviour of a complex.

Ruthenium complexes incorporating pyrene have already been investigated for biological applications, as shown by Mukhopadhyay and co-workers.[96] In their publication, they describe the interactions of a set of pyrene-bearing ruthenium arene complexes (**Figure 70**) with cellular media. These interactions include DNA and protein binding, two photon cell imaging and cytotoxicity.[96]

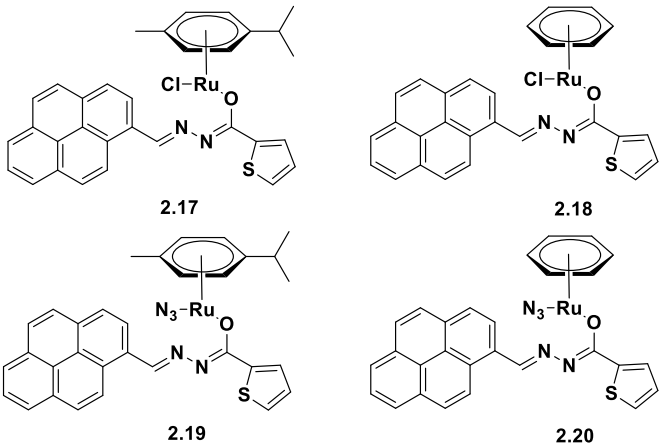

Figure 70. Ruthenium arene complexes bearing pyrene moieties for biological applications.[96]

While the spectroscopic properties of the complexes were not reported, their publication does show the wide range of biological applications which pyrene-containing transition metal complexes are suited for.

2.1.4 Triplet Photosensitisers Bearing Triphenylamine Chromophores

However, it is important to remember that unique spectroscopic properties are not the sole remit of pyrene-containing triplet photosensitisers. Triphenylamine donor fragments have been used in the design of highly efficient photosensitisers.[50,54,60] The work of Zhao *et al.* demonstrates the high efficiency of bis-triphenylamine bipyridyl ligands as photon harvesters, boasting a luminescence quantum yield of 100% and long absorption wavelengths.[60] If these properties were able to be maintained (or even enhanced) following complexation to a ruthenium or iridium metal centre, population of the ^{3}ILCT state could result in a set of highly efficient triplet photosensitisers.

Additionally, Sutton *et al.* provided evidence for triphenylamine rhenium systems with multiple isoenergetic excited states.[54] The difference between these excited states was so small that different solvent systems lead to the population of different states. The solvent interactions stabilised some excited states more than others, resulting in radically different solvent-dependent photophysical properties. This discovery carries significant implications for triplet photosensitiser design as the impact of the local electronic environment on the properties of the triplet photosensitiser must now be more carefully considered when evaluating its performance.

2.2 Aims

Incorporating lessons learned from the work presented in the previous chapter, with the aim going forward to generate triplet photosensitisers including pyrene and triphenylamine groups into their overall structures (**Figure 71**).

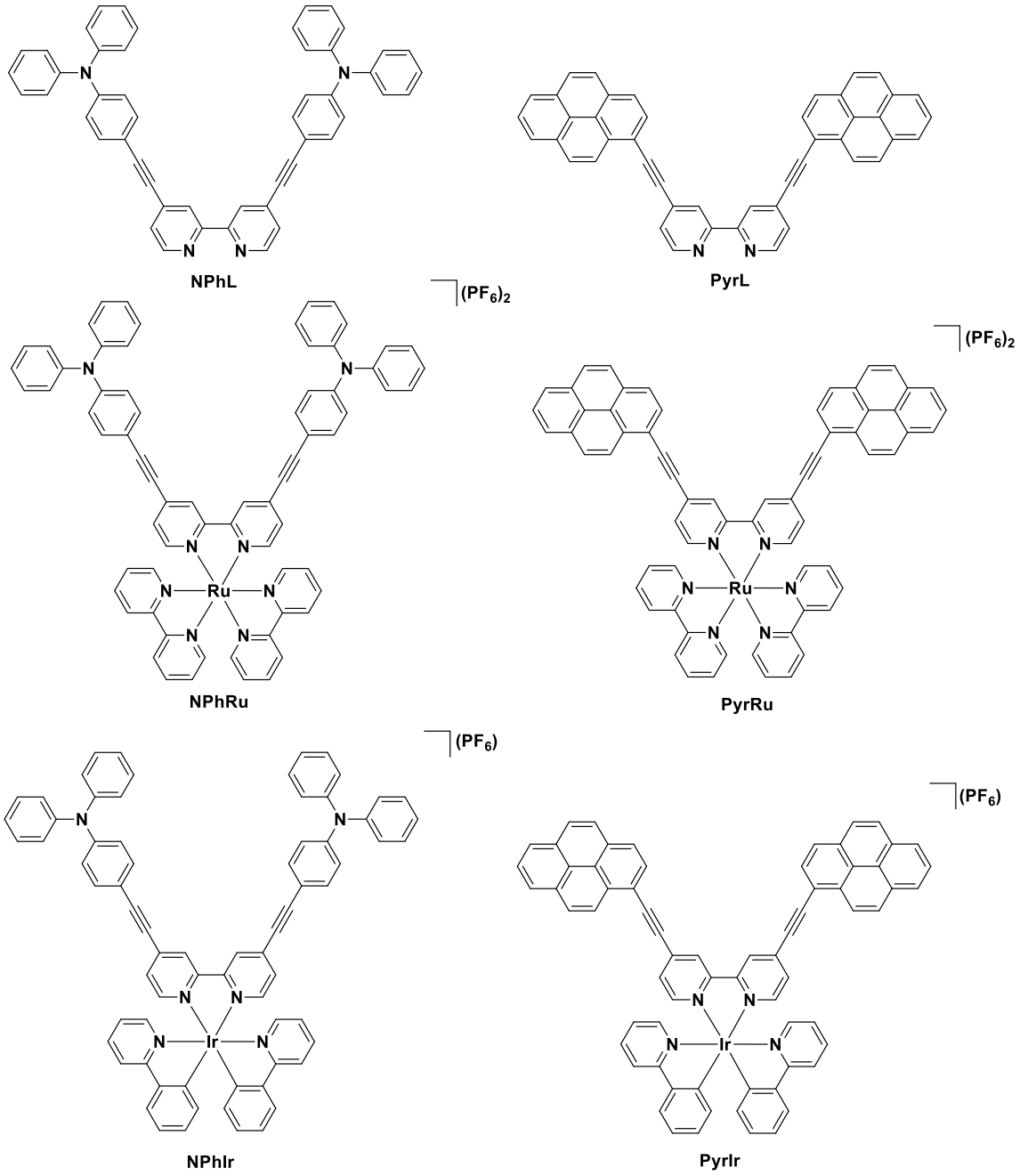

Figure 71. Target Compounds for Chapter 2.

2.3 Synthesis and Characterisation

2.3.1 Synthesis and Characterisation of NPhL, NPhIr and NPhRu

Synthesis and characterisation of the ligand systems **NPhL** and **PyrL** were undertaken using the protocols developed for **OMeL**, **PhL** and **CF_3L** described in the previous chapter. The use of Sonogashira coupling reactions to link acetyltriphenylamine and acetylpyrene groups with 4,4'-dibro-2,2'-bipyridine provided the most efficient pathway to the desired target products. The two acetylene units were either commercially available in the case of the pyrene or had well established methods of preparation in the case of the triphenylamine.[97] The synthetic route used by Wang and co-workers to generate the 4,4'-bis(triphenylamine)-2,2'-bipyridine initially linked acetylene to the bipyridine core and then appended the triphenylamine via Sonogashira coupling.[98] In this work, the acetylene will be appended to the triphenylamine initially and then coupled to the dibrominated bipyridine. This is due to the high cost of the dibrominated bipyridine – it was more economical to use the bipyridine as sparingly as possible.

2.3.1.1 Synthesis and Characterisation of **NPhL**

The synthesis of the **NPhL** is shown below in **Scheme 7** and was performed in a microwave reactor.

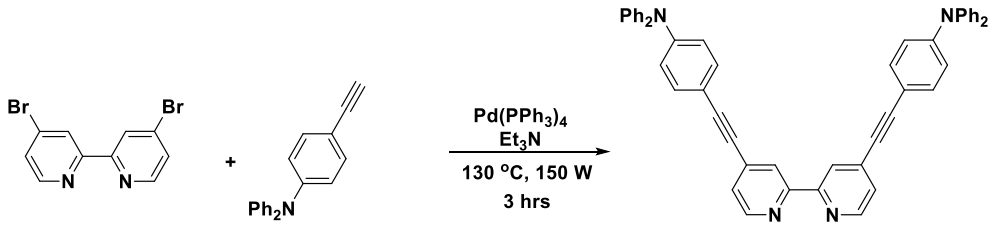

Scheme 7. Synthesis of **NPhL.**

Purification of **NPhL** proved challenging, as there were several highly luminescent impurities with R_f values very similar to those of the product contained in the reaction mixture. This reduced the effectiveness of the chromatographic solvent systems used to purify previous ligands. Consequently, a new methodology using an ethyl acetate/petroleum ether mobile phase was developed, with a gradually increasing ethyl acetate gradient. This allowed isolation of **NPhL** with a yield of 45 %, which proved sufficient for subsequent complexation to ruthenium and iridium metal centres.

NPhL was characterised using ^{1}H, ^{13}C and multinuclear NMR spectroscopy. The ^{1}H NMR spectrum of **NPhL** is shown in **Figure 72** with signals assigned to spin systems using coloured dots.

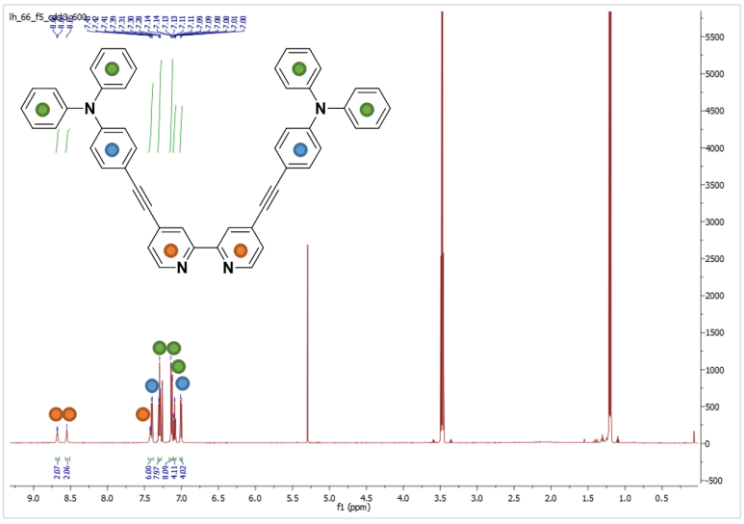

Figure 72. ^{1}H NMR spectrum of **NPhL** showing the signals assigned to the spin systems in the compound. ($CDCl_3$, 400 MHz, 298 K).

All signals are found in the aromatic region of the spectrum due to the induced ring current of the conjugated ring systems. The most downfield spin systems are on the pyridyl ring, as the nitrogen atom induces an electron-withdrawing effect. The signals of the electron-rich triphenylamine group are further upfield, clustered close together due to the high degree of similarity in their electronic environments. The signals in the spectrum integrate to 34, accounting for all of the protons in the structure. The TOCSY spectrum of **NPhL** is shown below in **Figure 73**.

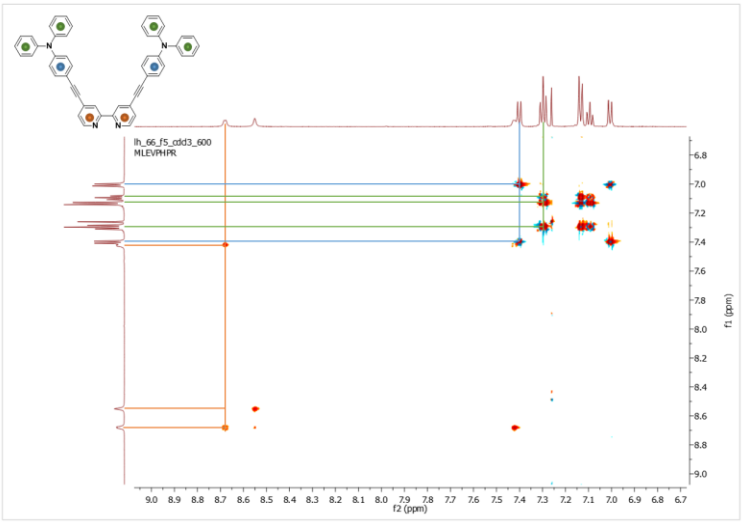

Figure 73. TOCSY NMR spectrum of **NPhL** with spin systems assigned (600 MHz, $CDCl_3$ 298 K).

This spectrum shows the correlation between the protons in the different spin systems forming the overall structure of the molecule. There are three distinct ring systems clearly identifiable on the spectrum, the first being the pyridine ring system, the second the proximal phenyl ring between the pyridine and the acetylene and the third the distal rings bonded to the nitrogen. In the two first systems two symmetrical ring systems

contribute to the signals, while the distal ring system is comprised of four electronically equivalent ring systems. No interactions are seen between the spin systems, indicating a state of electronic isolation.

The ^{13}C NMR spectrum of **NPhL** is shown below in **Figure 74**. There are four solvent peaks at 77, 54, 66 and 15 Hz, with the majority of the remaining signals located in the aromatic region of the spectrum. The exceptions are the two acetylene signals, which usually appear between 80 and 100 ppm. Interestingly, one of the acetylene signals is shifted significantly downfield, potentially due to the strong deshielding effect of the triphenylamine moiety. The intensity of the signals also varies widely, with four medium and two high intensity signals.

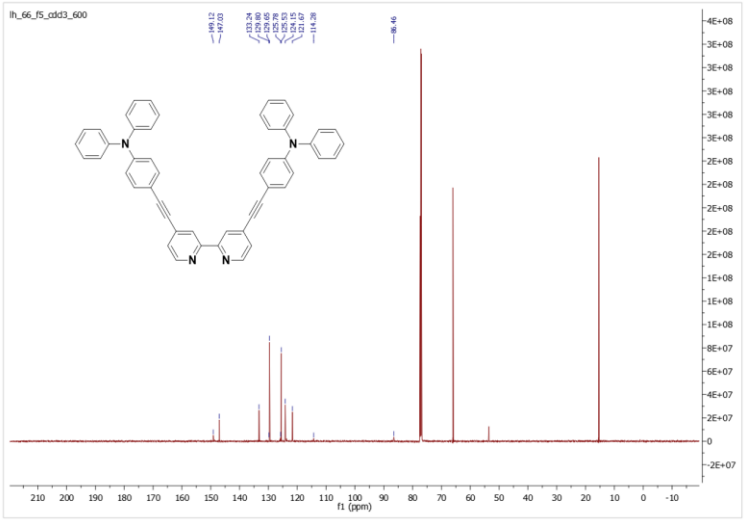

Figure 74. ^{13}C spectrum of **NPhL** ($CDCl_3$, 101 MHz, 298 K).

The number of signals visible in the aromatic spectrum does not correlate with the number of carbons in the molecular structure. This was investigated using multinuclear NMR spectroscopy, as the presence of the desired target compound was already confirmed using ^{1}H and TOCSY NMR spectroscopy. **Figure 75** shows the HSQC NMR spectrum of **NPhL**, demonstrating the correlation between carbon and proton signals in the compound. Judging by this spectrum, the pyridine protons appear to be correlated to very weak carbon signals, of such low intensity that they almost vanish into the baseline unless magnified.

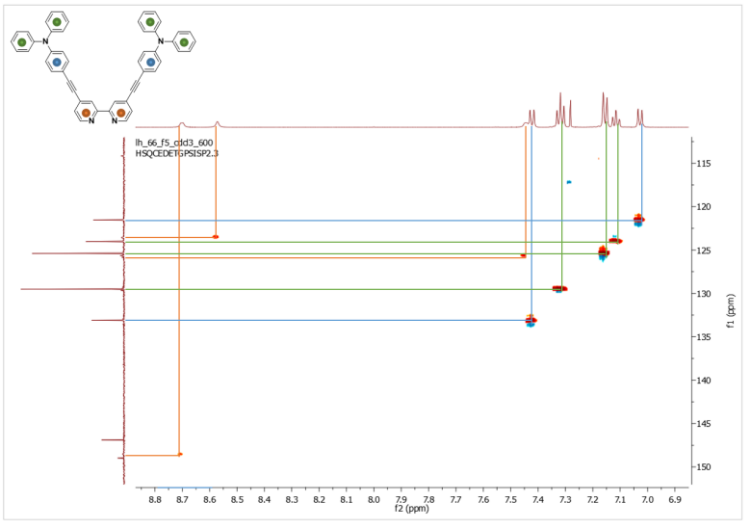

Figure 75. HSQC NMR spectrum of **NPhL** showing the correlation of carbon atoms and protons (600 MHz, CDCl3 298 K).

This spectrum also allows us to assign the high-intensity carbon signals as those forming part of the distal triphenylamine phenyl rings.

2.3.1.2 Synthesis and Characterisation of **NPhIr**

Synthesis of **NPhIr** was undertaken in the same way as in the previous chapter, via reflux of **NPhL** with $[Ir(ppy)_2Cl]_2$ in chloroform for 16 hours (**Scheme 8**).

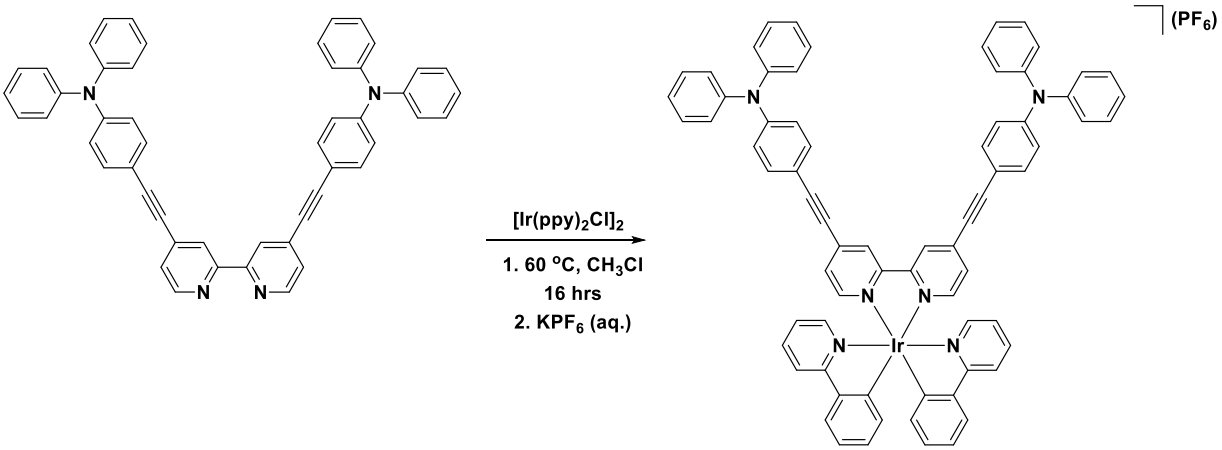

Scheme 8. Synthesis of **NPhIr.**

Purification of **NPhIr** was achieved by using silica column chromatography with a CH_2Cl_2:MeOH gradient resulting in the elution of an orange band. Following removal of the solvent and precipitation using a concentrated aqueous KPF_6 solution, the orange solid was isolated by filtration and washed with hexanes and toluene. The ^1H NMR spectrum of **NPhIr,** signals assigned to individual spin systems, is shown below in **Figure 76**, while residual traces of toluene solvent are marked with an *.

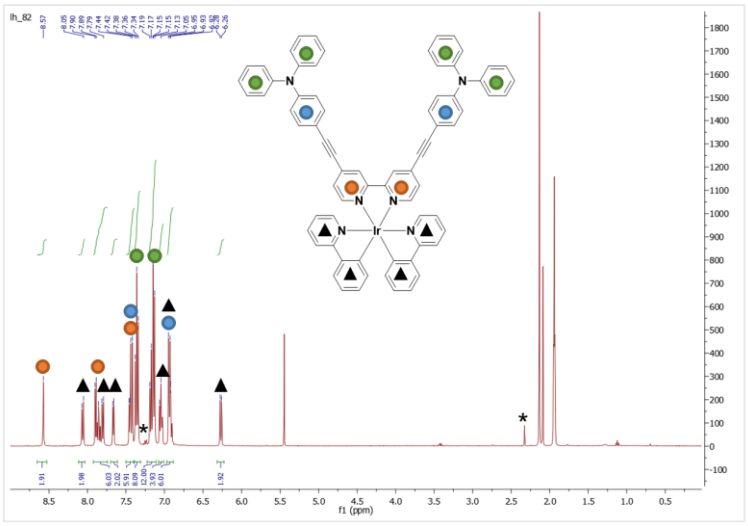

Figure 76. ^{1}H NMR spectrum of **NPhIr** showing the signals assigned to the spin systems in the compound. (MeCN-d_3, 600 MHz, 298 K).

The aromatic nature of the complex structure results in the appearance of signals between 6.25 and 9 ppm, in the aromatic region of the spectrum. The signals are clustered, with the substituted bipyridine ligand ring signals appearing the furthest downfield. The triphenylamine signals are clustered between 7 and 7.5 ppm and have the highest intensity of all signals owing to the large number of protons they represent. The integration of all signals sums to 50 protons, their varying degrees of equivalence depending on the specific ring and spin systems.

The TOCSY NMR spectrum is shown below in **Figure 77**, with the individual spin systems marked by coloured bars. It shows heavy clustering of the triphenylamine signals between 7 and 7.5 ppm, with two signals overlapping significantly at 7.2 ppm. The proton signals of the phenylpyridine ring systems are split, due to the differing electronic environment of the coordinating phenyl and pyridine rings.

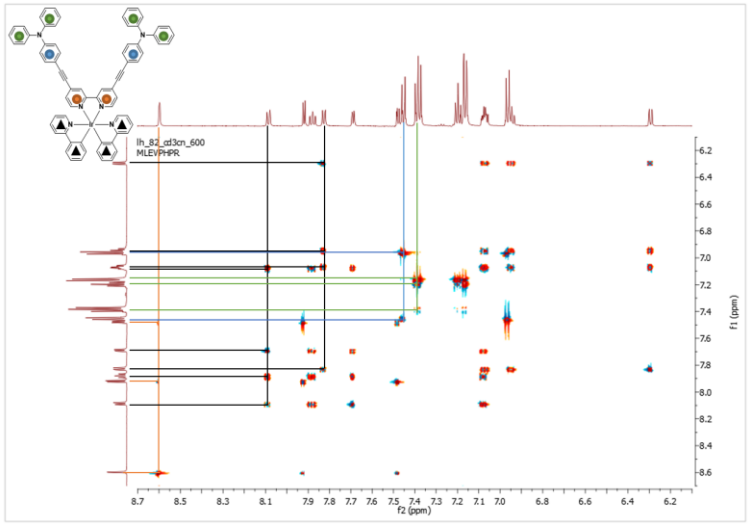

Figure 77. TOCSY NMR spectrum of **NPhIr** with spin systems assigned (600 MHz, $CDCl_3$ 298 K).

The ^{13}C spectrum for **NPhIr** is displayed in **Figure 78**, showing a high number of peaks in the aromatic region beyond 100 ppm. The intensity of the signals varies, likely due to the higher degrees of symmetry for some segments of the complex resulting in higher numbers of equivalent carbon atoms. Although the appearance of the two acetylene carbon atoms below 100 ppm is expected, one additional peak in this region is observed.

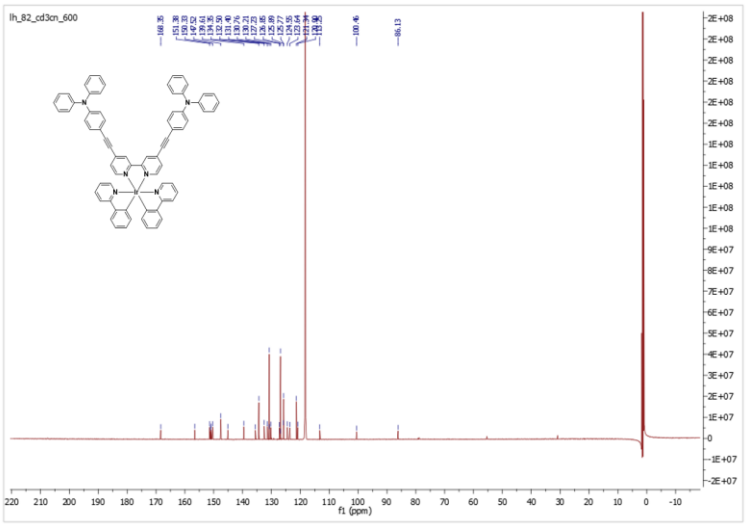

Figure 78. ^{13}C spectrum of **NPhIr** (MeCN-d_3, 101 MHz, 298 K).

Using HMBC and HSQC NMR experiments, it is possible to observe the correlations between these carbon atoms and adjacent proton signals. The HSQC spectrum, **Figure 79 A**, indicates the correlation of carbon atoms with any protons directly bonded to it. This spectrum highlights that none of the three peaks observed below 100 ppm are directly bonded to any protons, marking them as quaternary carbons.

The HMBC spectrum, shown in **Figure 79 B**, reveals the correlation of carbon atoms with protons over 3 or 4 bonds, allowing longer-range interactions to be observed. This spectrum shows that all three peaks below 100 ppm interacting with protons signals through multiple bonds. The most downfield signal interacts strongly with signals on the bipyridine ring, suggesting that it represents the acetylene carbon immediately adjacent to the bipyridine ring. The other two signals meanwhile interact with signals arising from the proximal triphenylamine ring, suggesting that one signal forms part of the remaining acetylene carbon while the other signal represents the quaternary carbon bonded directly to the triphenylamine nitrogen. The electron-donating effect of the nitrogen lone pair would account for the difference in shift between this carbon and the other quaternaries in the complex, as the added electron density shields the atom from the induced magnetic field of the NMR experiment.

A) B)

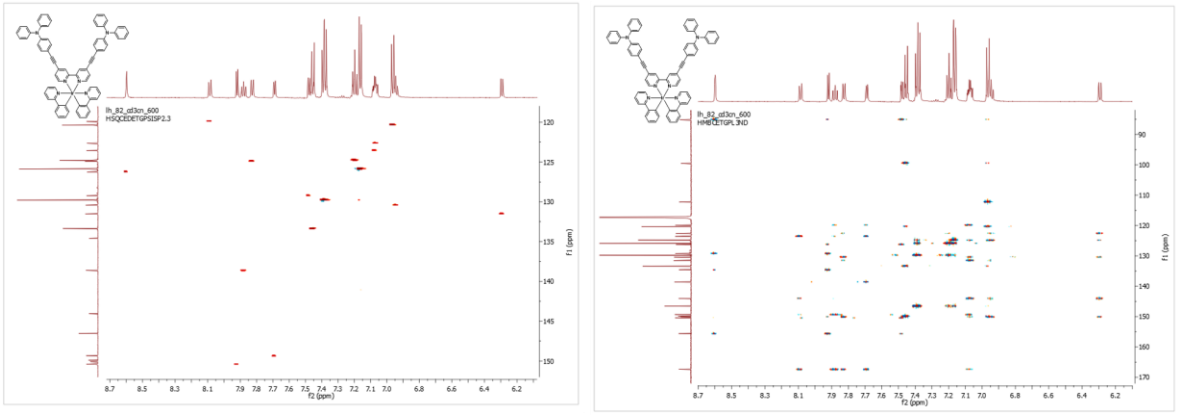

Figure 79. HSQC (A) and HMBC (B) NMR spectra of **NPhIr** showing the correlation of carbon atoms with adjacent protons (MeCN-d_3, 101 MHz, 298 K).

2.3.1.3 Synthesis and Characterisation of **NPhRu**

The synthesis of **NPhRu** proceeded according to the protocols developed in the previous chapter. **NPhL** and $[Ru(bpy)_3(PF_6)_2]$ were combined in ethylene glycol and heated to 150 °C in a 150 W microwave reactor for 90 minutes (**Scheme 9**).

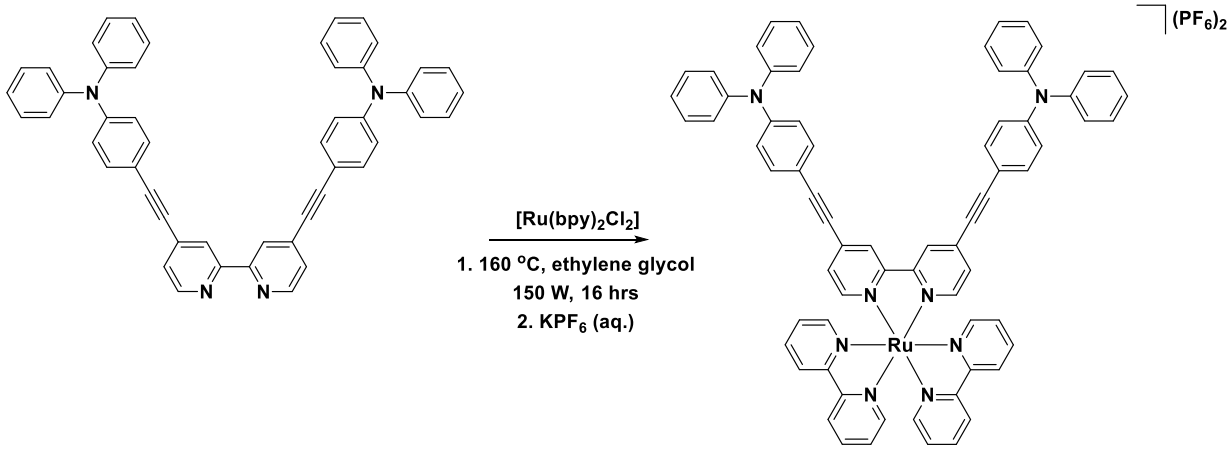

Scheme 9. Synthesis of **NPhRu.**

The reaction mixture was added dropwise to a stirring solution of saturated aqueous KPF_6, resulting in the precipitation of a red solid. Filtration of the mixture allowed for isolation and drying of the precipitate, which was washed with water and dissolved in MeCN. Purification was completed via silica column chromatography using an MeCN:H_2O:KNO_3 (aq.) (90:9:1) mobile phase to give a red solid. The ^{1}H NMR spectrum for **NPhRu** is shown below in **Figure 80**. Similarly, to **NPhIr**, all of the complex signals appear in the aromatic region of the spectrum between 7 and 9 ppm. The number of signals is lower than in **NPhIr**, due to the higher degree of symmetry of the spectator ligands (bipyridine vs. phenylpyridine).

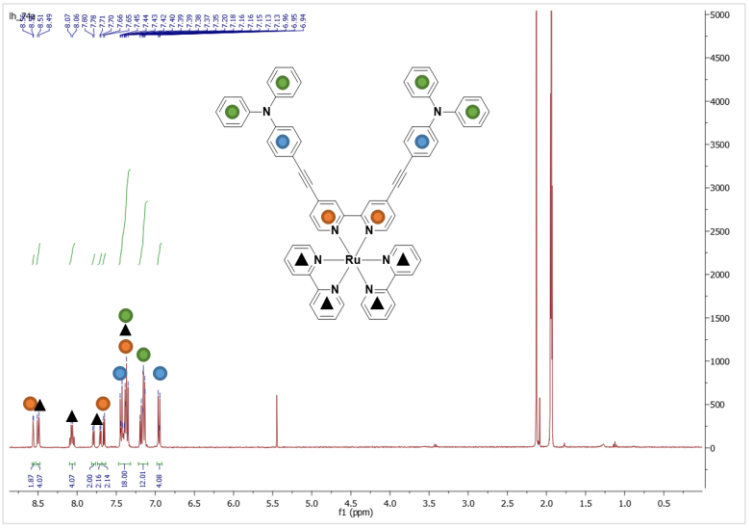

Figure 80. ^{1}H NMR spectrum of **NPhRu** showing the signals assigned to the spin systems in the compound. (MeCN-d_3, 600 MHz, 298 K).

The spectrum integrates to 50 protons, with the three triphenylamine signals integrating for the greatest number of protons.

The TOCSY spectrum for **NPhRu** showing the signal correlations within the distinct spin systems is displayed in **Figure 81**.

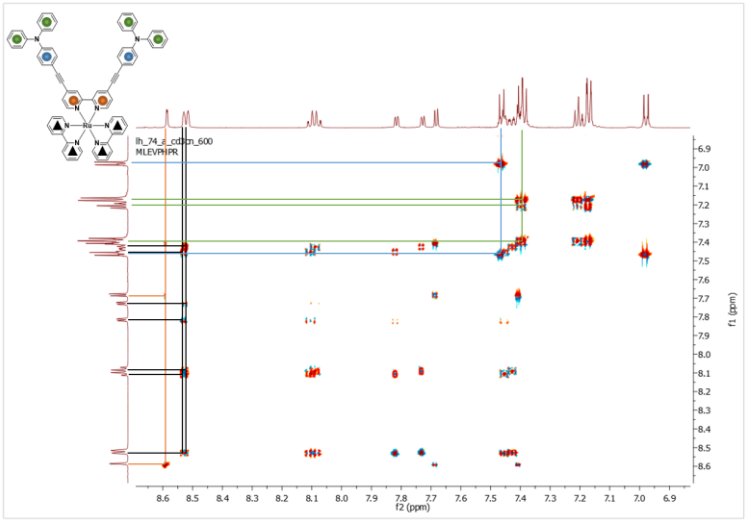

Figure 81. TOCSY NMR spectrum of **NPhRu** with spin systems assigned (600 MHz, $CDCl_3$ 298 K).

The ^{13}C NMR spectrum for **NPhRu** (**Figure 82**) shows large degrees of similarity with the ^{13}C spectrum of **NPhIr**. The majority of the signals appear between 120 and 180 ppm, with **NPhRu** showing a reduced number of signals compared to the iridium complex due to the higher degree of symmetry in the spectator ligands.

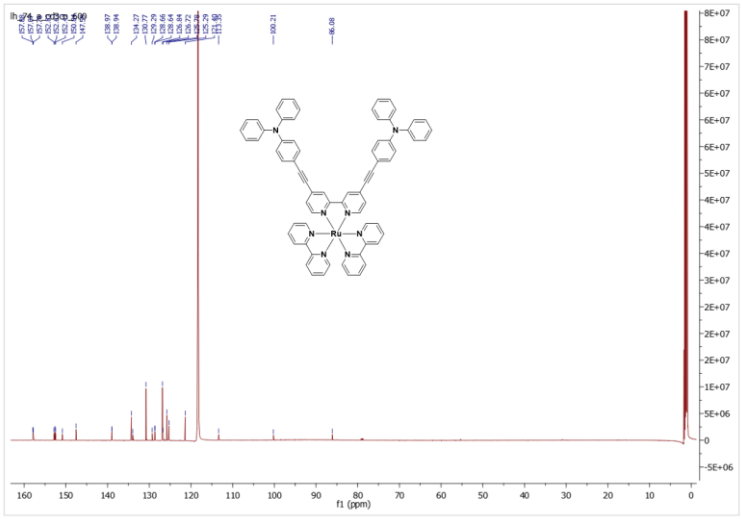

Figure 82. ^{13}C spectrum of **NPhRu** (MeCN-d_3, 101 MHz, 298 K).

NPhRu also shows the presence of the three upfield peaks separate from the rest of the carbon signals, between 80 and 110 ppm. Due to reduced resolution of the HMBC and HSQC spectra, (**Figure 83**), the same number of interactions between proton and carbon atoms cannot be observed. While this prevents definitive assigning of the carbon atoms, they likely originate from the two acetylene carbon atoms as well as the quaternary carbon directly bonded to the nitrogen of the proximal triphenylamine ring.

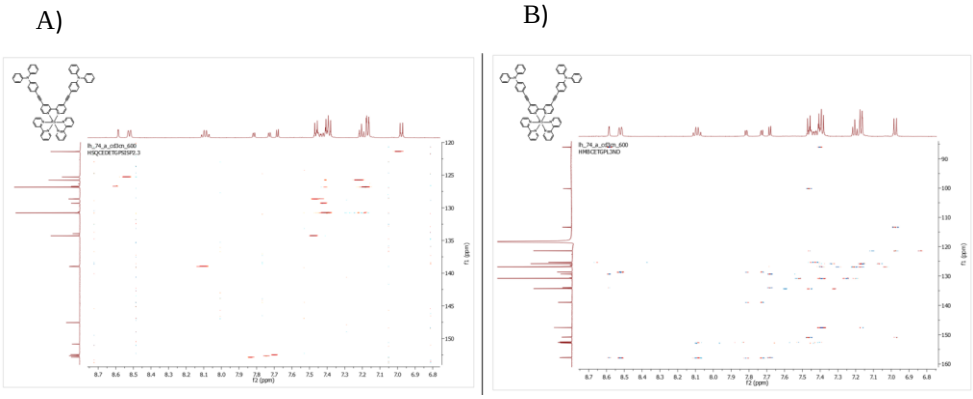

Figure 83. HSQC (A) and HMBC (B) NMR spectra of **NPhRu** showing the correlation of carbon atoms with adjacent protons (MeCN-d_3, 101 MHz, 298 K).

2.3.2 Synthesis and Characterisation of PyrL, PyrIr, and PyrRu

2.3.2.1 Synthesis and Characterisation of **PyrL**

Similar efforts were made to generate **PyrL**, as shown in **Scheme 10**. However, the synthesis of this ligand turned out to be far more complex than previously prepared systems, in particular **NPhL**. **PyrL** proved insoluble in a vast majority of solvents, including CH_2Cl_2, CH_3Cl and acetone. This made the purification significantly more challenging, as loading the crude reaction mixture onto silica columns for purification was impossible. Even when partial dissolution was achieved with heating and sonication, the volume of solvent used resulted in very long bands on the chromatography column. The issue was compounded by a significant

portion of the material crashing out of solution and precipitating as a solid onto the silica particles. This resulted in streaking as portions of the solid material then re-dissolved over time.

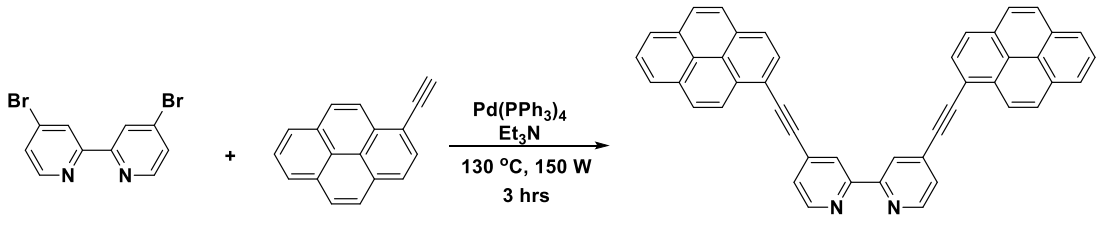

Scheme 10. Synthesis of **PyrL.**

Consequently, it was not possible to fully purify **PyrL** via the previously established methodology (**Figure 84**). While the main fraction is the product, significant contamination of the baseline makes photophysical analysis of this sample impossible. Additionally, the repeated purification attempts resulted in drastically reduced yields, often leaving barely enough product to run an NMR experiment.

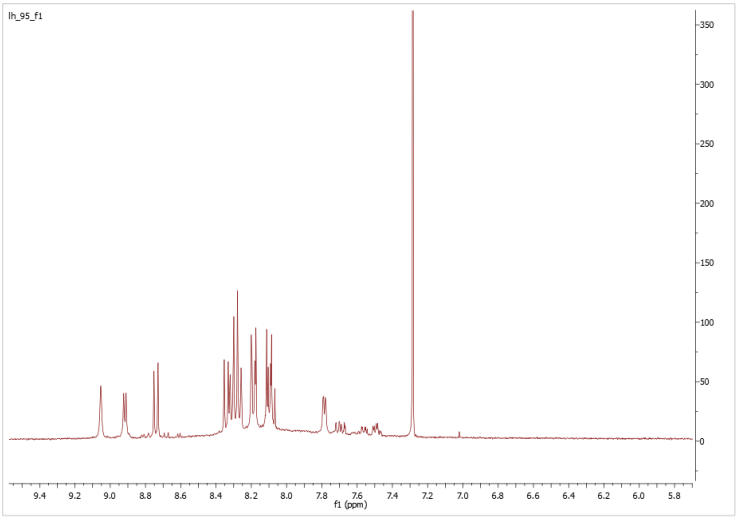

Figure 84. ^{1}H NMR spectrum of **PyrL** showing impurities in the aromatic region. ($CDCl_3$, 400 MHz, 298 K).

More standard Sonogashira coupling conditions were used (**Scheme 11**) to try and minimise the amount of side product generated over the course of the reaction.

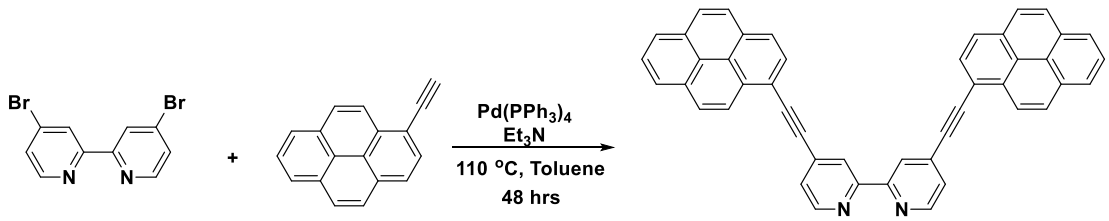

Scheme 11. Alternative synthesis of **PyrL**

The longer reaction times were intended to ensure its completion, as the mono-substituted intermediate product was likely the greatest source of contamination. The effort was unsuccessful, however, since the

same purification issues were encountered. Consequently, an attempt was made to induce complexation of the pyrene ligand onto $Fe(Cl)_3$ and generate a homoleptic iron complex. It was hoped that this complex would be more soluble in MeCN than the ligand, allowing for purification.

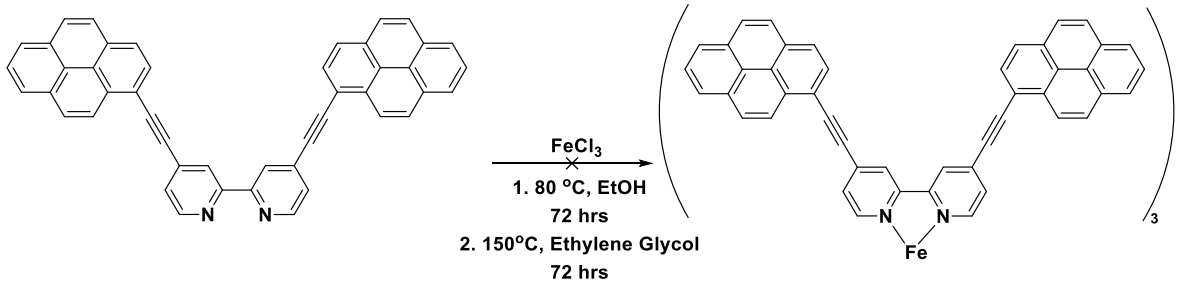

Scheme 12. Attempted complexation of **PyrL** with $FeCl_3$.

Initially, this complexation was attempted in EtOH at 80 °C, but after several hours no visible change in the reaction mixture was observed, with crude **PyrL** remaining suspended as a granular yellow solid. A second attempt was then undertaken using ethylene glycol at significantly higher temperatures to force the ligand into solution, but even after three days of reflux no change in the reaction could be observed via thin-layer chromatography (TLC).

As a result, it was decided to test the complexation of the crude **PyrL** reaction mixture with iridium. Admittedly, iridium is more expensive than iron, but known to form complexes with polypyridyl ligands bearing pyrene moieties, and the reaction was considered more likely to succeed.[50,71] The reaction is shown below in **Scheme 13**.

2.3.2.2 Synthesis and Characterisation of **PyrIr**

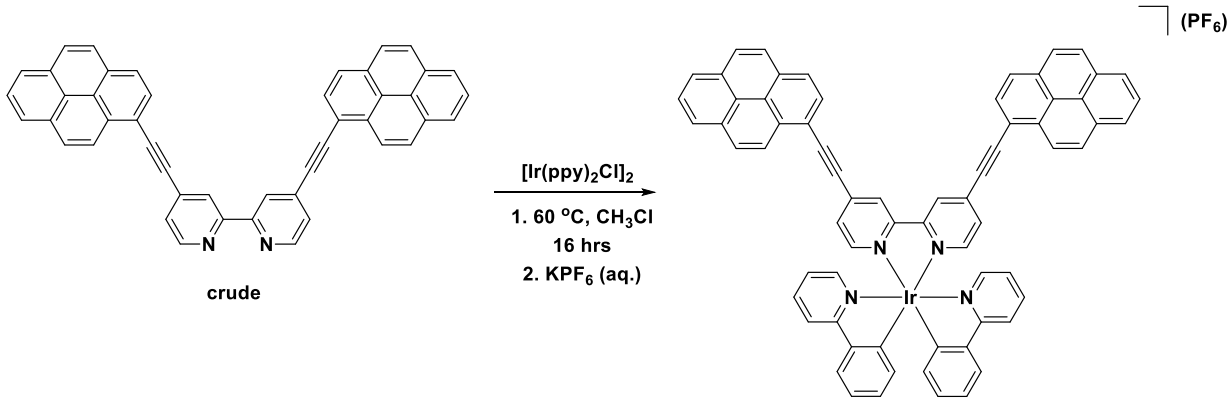

Scheme 13. Synthesis of **PyrIr.**

The initial yellow suspension went into solution, accompanied by a decrease in the luminescence associated with the crude **PyrL** mixture. Reaction progress was monitored via TLC, which showed the formation of new non-luminescent product material with an R_f similar to previously prepared iridium complexes. It was isolated using CH_2Cl_2:MeOH mobile phase gradient chromatography, leaving unreacted ligand and side products at the start of the column. In this way, the insolubility of the starting material aided in the

purification of the final target complex. The solid was isolated by precipitation and washed with large quantities of toluene to remove any trace organic impurities.

The ^{1}H NMR spectrum for **PyrIr** is shown in **Figure 85**

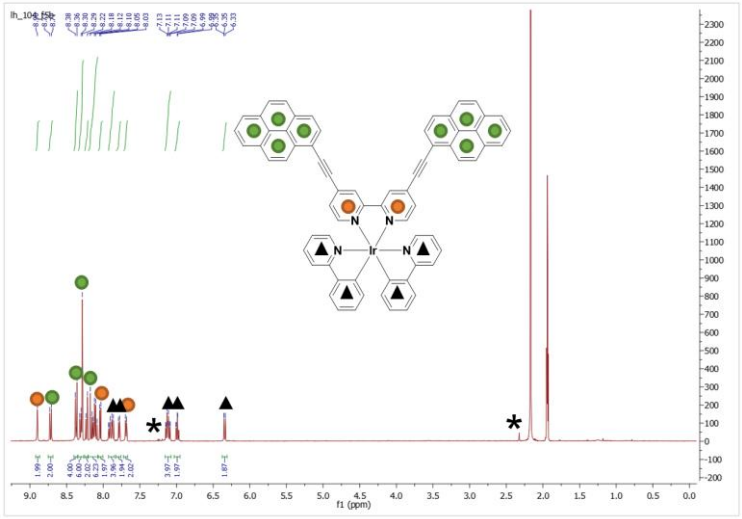

Figure 85. ^{1}H NMR spectrum of **PyrIr** with the individual signals assigned to the spin systems of the complex. ($CDCl_3$, 400 MHz, 298 K).

The ^{1}H NMR spectrum shows trace residues of toluene from the purification process (marked with an *). The rest of the spectrum mirrors that of previously prepared iridium complexes quite closely, with addition of numerous signals in the aromatic region originating from pyrene protons. These can be assigned using HH COSY multinuclear NMR, as shown in **Figure 86**.

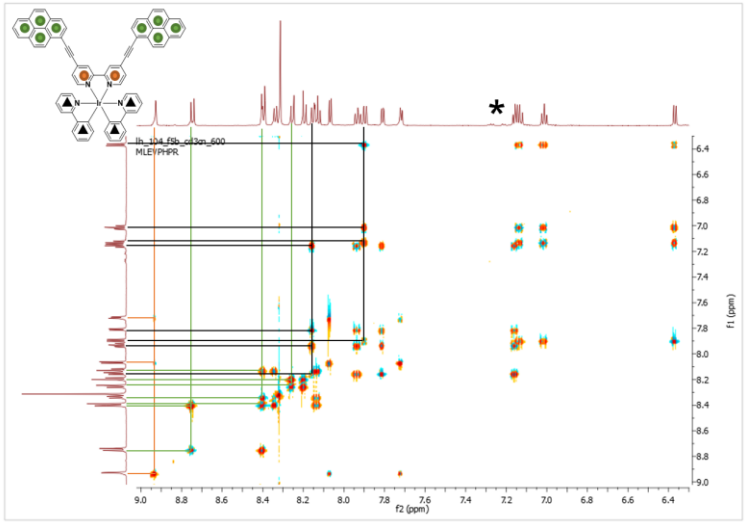

Figure 86. ^{1}HH COSY NMR spectrum of **PyrIr** with spin systems assigned (600 MHz, $CDCl_3$ 298 K).

The spectrum integrates to 40, matching the number of total protons in the complex. The ^{13}C spectrum of the complex shows a large number of clustered carbon peaks, as the electronic environment of the atoms in the pyrene molecule is similar.

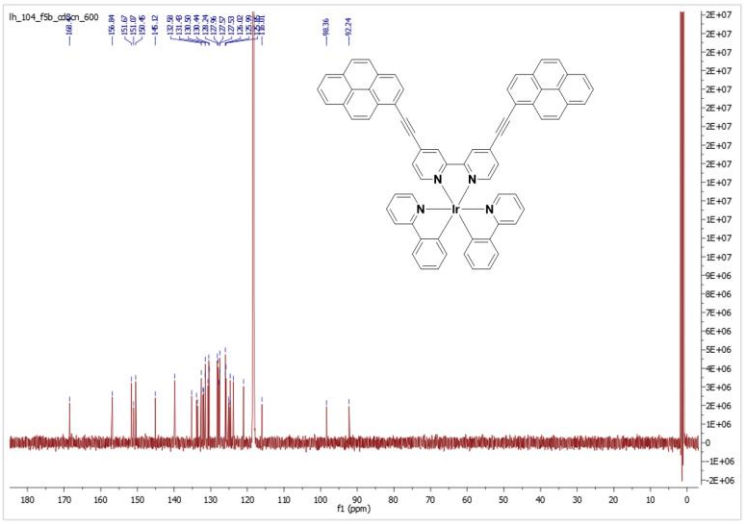

Figure 87. ^{13}C spectrum of **PyrIr** ($CDCl_3$, 101 MHz, 298 K).

Again, the acetylene signals are observed at lower shifts than the remaining signals, between 90 and 100 ppm.

2.3.2.3 Synthesis and Characterisation of **PyrRu** and **BrRu**

Similar attempts to synthesis **PyrRu** were carried out, using ethylene glycol as solvent and increasing the temperature to 150 ºC.

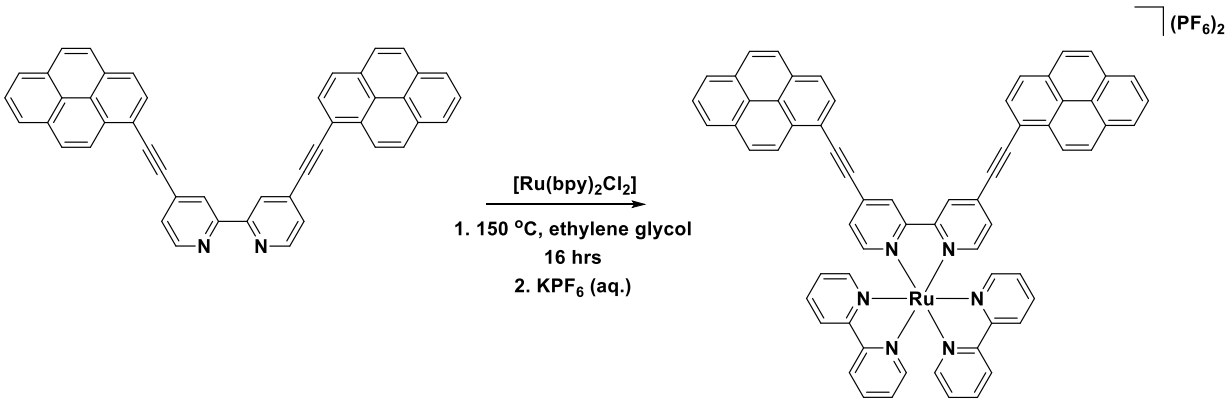

Scheme 14. Attempted Synthesis of **PyrRu.**

The attempt initially progressed similarly to the iridium complexation, where high temperatures solubilised **PyrL** and allowed for reaction with the ruthenium precursor. The colour of the solution transitioned from a mixed black/yellow precipitate to a deep red solution, indicative of the formation of a tris(bipyridyl)ruthenium complex. The resulting crude mixture was purified following the same protocol as the other ruthenium complexes presented in this work. However, unlike with **PyrIr**, it was not possible to remove all impurities from the **PyrRu** sample.

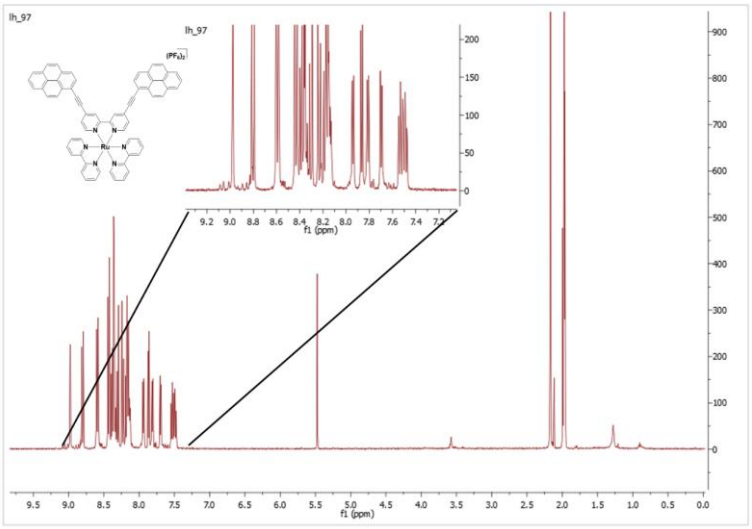

Figure 88. ^{1}H NMR spectrum of **PyrRu** with inset of the aromatic region highlighting remaining impurities. ($CDCl_3$, 400 MHz, 298 K).

Despite repeated efforts, it was not possible to remove these impurities. The reaction itself was undertaken several times, with the result remaining consistent. Due to the highly sensitive nature of photophysical measurements, small impurities can result in large errors in the obtained data. This made the **PyrRu** samples obtained via complexation of crude **PyrL** unsuitable for further work.

Consequently, an alternative synthetic pathway to access **PyrRu** had to be discovered. The search for it was based on previously published work by the Draper group pioneering 'on the complex' synthesis and is shown in **Scheme 15**.[71]

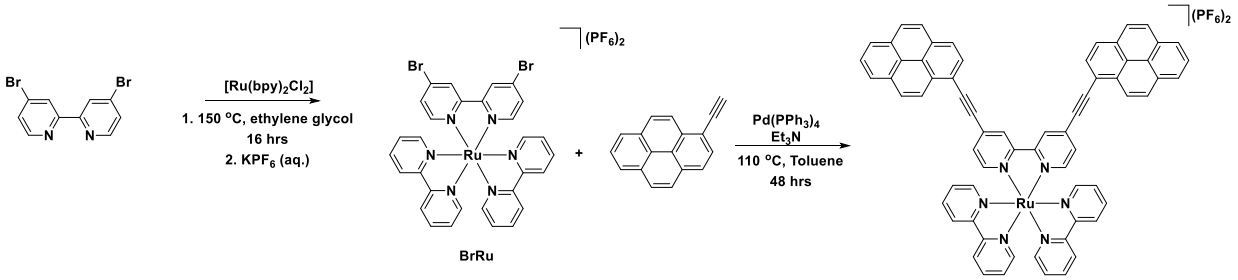

Scheme 15. On the complex synthesis of **PyrRu.**

This led to the synthesis of the intermediate product **BrRu**, whose ^{1}H NMR spectrum is shown below in **Figure 89**. While it is not designed to be an efficient photosensitiser, enough was recovered to allow for photophysical analysis, as a full description of its photophysical properties was not found in literature. While it may not perform as well as some of the other, rationally designed triplet photosensitisers it can serve as a good benchmark against which to measure performance.

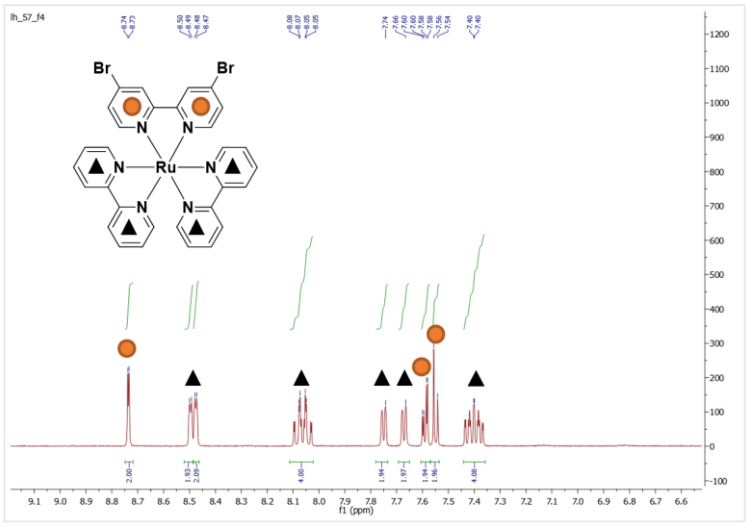

Figure 89. ^{1}H NMR spectrum of **BrRu** with signals assigned to the spin systems of the complex. (MeCN-d_3, 400 MHz, 298 K).

While **BrRu** was synthesised in high yields, the ensuing complexation with ethynylpyrene to generate **PyrRu** was less successful. The consumption of the starting materials was observed by TLC, but it was accompanied by the formation of a complex mix of products. Separation of these products proved impossible, as many of them behaved as ruthenium complexes during the purification process. This led to the results shown in **Figure 90**, where the NMR shows many incoherent peaks in the aromatic region, indicating a complex mix of compounds present in the sample.

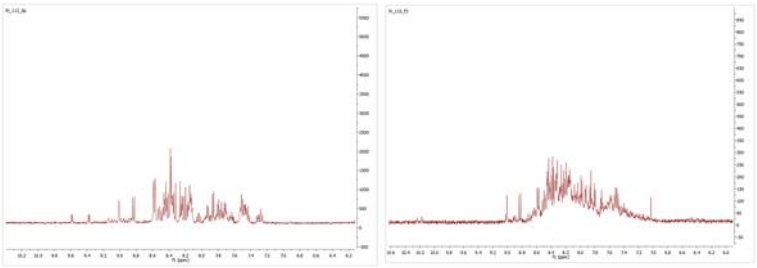

Figure 90. ^{1}H NMR spectrum of crude **PyrRu** reaction mixtures ($CDCl_3$, 400 MHz, 298 K).

The mixture of peaks is so complex that it is not possible to determine whether the target product was generated. In summary, **PyrRu** could not be isolated. While it should undoubtedly be possible to purify from complexation of crude **PyrL**, external factors (including but not limited to time pressure and expenses) compelled attention to be focused on other alternative projects.

2.3.3 Crystallographic Analysis

2.3.3.1 **NPhL**

Crystals of **NPhL** suitable for x-ray diffraction studies were obtained from the slow diffusion of CH_2Cl_2 into hexane. Data collection and refinement was conducted by Dr. Brendan Twamley in Trinity College Dublin

A specimen of $C_{25}H_{17}N_2$, approximate dimensions 0.226 mm x 0.246 mm x 0.354 mm, was used for the X-ray crystallographic analysis. The structure was solved with the SHELXT structure solution program using Intrinsic Phasing and refined with the SHELXL refinement package using Least Squares minimisation with Olex2, using the space group $P2_1/n$, with Z = 4 for the formula unit, $C_{25}H_{17}N_2$. The final anisotropic full-matrix least-squares refinement on F^2 with 244 variables converged at R1 = 4.95%, for the observed data and wR2 = 13.05% for all data. The goodness-of-fit was 1.055. Figure 91 shows the orientation of a single molecule of **NPhL** in the crystal lattice.

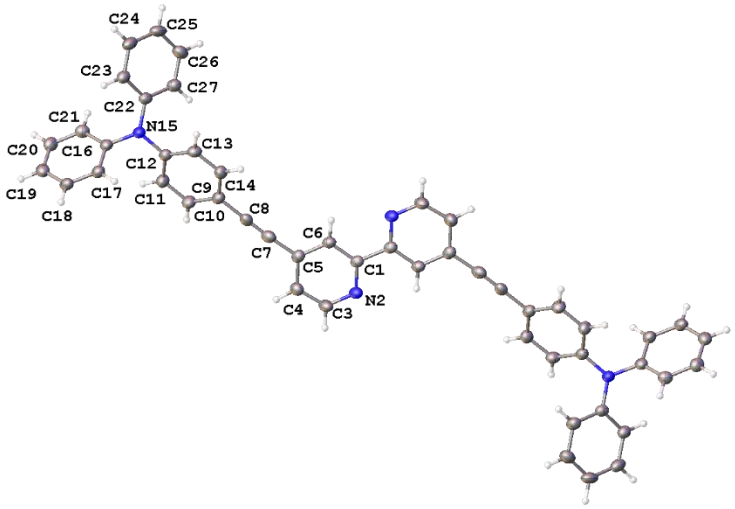

Figure 91. Symmetry generated molecular structure of **NPhL** (symmetry generation = 2-X, 1-Y, 1-Z) with atomic displacement shown at 50% probability. Symmetry unique atoms labelled only.

The nitrogen atoms of the bipyridine core are in a trans configuration, leading to the acetylene bonds and triphenylamine moieties on opposite sides of the molecule. This reduces the steric interactions between the large triphenylamine donor groups.

The phenyl units of the donor groups also twist relative to each other, allowing them to pack more closely together with phenyl groups of other ligand molecules as shown in **Figure 92**.

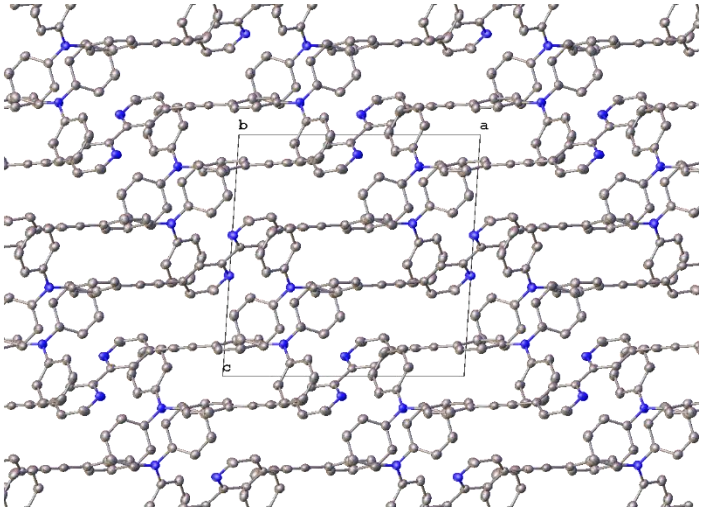

Figure 92. Packing diagram of **NPhL** viewed normal to the b-axis, with atomic displacement shown at 50% occupancy and hydrogen atoms omitted (there are no significant hydrogen bonding interactions).

2.3.3.2 **BrRu**

Crystals of **BrRu** suitable for single crystal x-ray diffraction were grown from the slow evaporation of acetonitrile. The moisture in the air resulted in the incorporation of water into the crystal structure, resulting in a complex hydrogen-bonding framework between the metal complexes, the NO_3^- counterions and water molecules.

A specimen of $C_{30}H_{30}Br_2N_8O_{10}Ru$, approximate dimensions 0.060 mm x 0.090 mm x 0.130 mm, was used for the X-ray crystallographic analysis. The structure was solved with the SHELXT structure solution program using Intrinsic Phasing and refined with the SHELXL refinement package using Least Squares minimisation with Olex2, using the space group $P2_1/n$, with Z = 4 for the formula unit, $C_{30}H_{30}Br_2N_8O_{10}Ru$. The final anisotropic full-matrix least-squares refinement on F^2 with 461 variables converged at R1 = 10.65%, for the observed data and wR2 = 30.84% for all data. The goodness-of-fit was 1.155. The molecular structure of **BrRu** is shown in **Figure 93**.

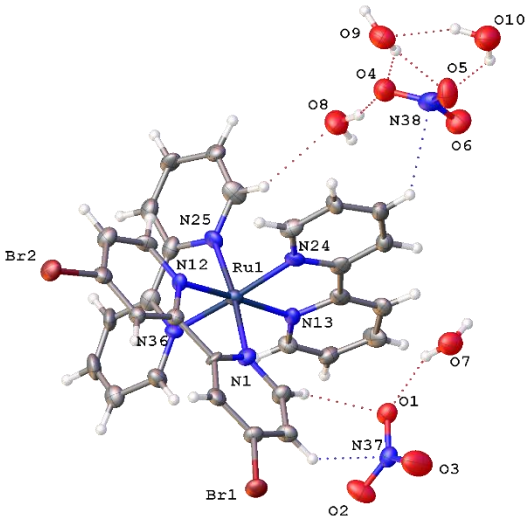

Figure 93. Molecular structure of **BrRu** with heteroatom labelling. Dotted lines represent hydrogen bonding interactions. Atomic displacement shown at 50% probability.

The overall structure of the molecule is a classical octahedral ruthenium trisbipyridine complex. The hydrogen bonding interactions occur between the protons on the pyridine rings and water/NO_3^- molecules filling the space between metal complexes. This is well demonstrated in the packing diagram for the crystal, shown in **Figure 94**. The packing shows strong interactions between the NO_3^- counterions, water molecules and individual metal complexes. No interactions between individual metal ions are observed.

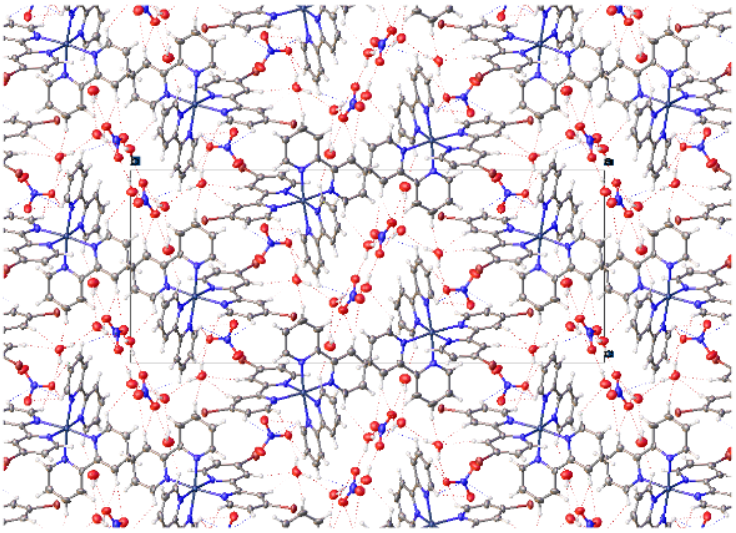

Figure 94. Packing diagram of **BrRu** viewed normal to the a-axis showing the hydrogen bonding network.

2.3.3.3 **NPhIr**

Crystal samples of **NPhIr** suitable for single crystal x-ray diffraction studies were obtained by the slow evaporation of acetone, of which traces remain in the crystal lattice. A specimen of $C_{75}H_{56}F_6IrN_6OP$, approximate dimensions 0.025 mm x 0.094 mm x 0.376 mm, was used for the X-ray crystallographic analysis. Using the OLEX2 Software Package, the structure was solved with the SHELXT structure solution

program using Intrinsic Phasing and refined with the SHELXL refinement package with Least Squares minimisation, using the space group Cc, with Z = 4 for the formula unit, $C_{75}H_{56}F_6IrN_6OP$. The final anisotropic full-matrix least-squares refinement on F^2 with 814 variables converged at R1 = 3.48%, for the observed data and wR2 = 8.72% for all data. The goodness-of-fit was 1.055. **Figure 95** shows the structure of a single molecule in the crystal lattice.

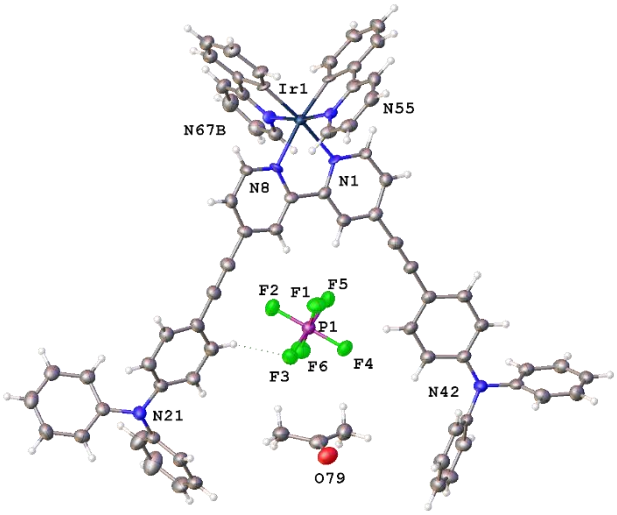

Figure 95. Disordered molecular structure of **NPhIr**, showing the acetone solved salt. Atomic displacement shown at 50% probability and heteroatoms labelled only.

The metal centre has adopted a distorted octahedral structure, with angles of 172° running from the substituted ligand through the metal centre to the trans coordinating nitrogen. Unlike the free ligand **NPhL**, the nitrogen atoms of the substituted ligand adopt a *cis* configuration in order to coordinate to the iridium atom. The triphenylamine phenyl rings are twisted relative to one another. The PF_6 counterion is situated between the proximal phenyl rings, with some weak H-F bonding to one of the rings. The residual acetone solvent is placed between two distal triphenylamine phenyl rings. **Figure 96** shows the crystal packing structure of **NPhIr**, with significant twists manifesting in the triphenylamine and acetylene portions of the complex in order to accommodate a stable structure.

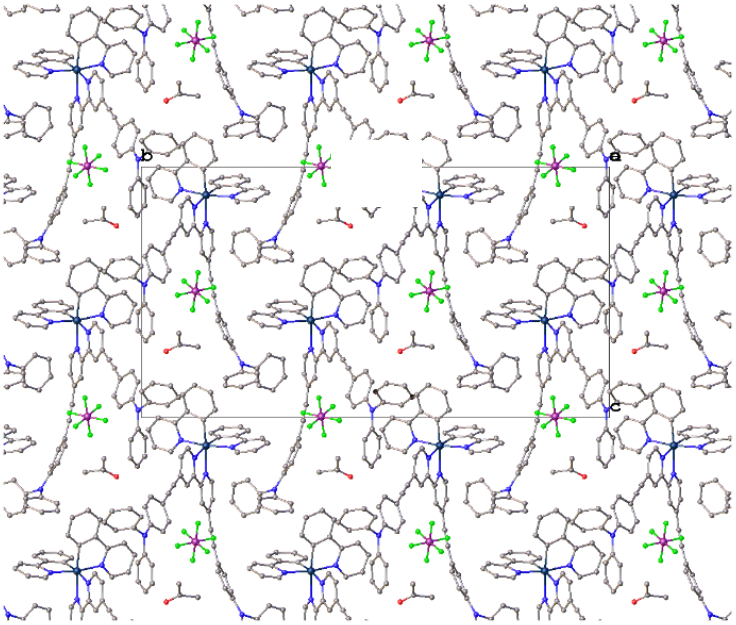

Figure 96. Schematic packing diagram of **NPhIr** viewed normal to the a-axis with hydrogen atoms omitted.

2.3.3.4 **PyrIr**

Finally, a crystal of **PyrIr** suitable for analysis by single crystal x-ray diffraction studies was obtained via the slow diffusion of CH_2Cl_2 into toluene. A specimen of $C_{68}H_{40}F_6IrN_4P$, approximate dimensions 0.075 mm x 0.162 mm x 0.234 mm, was used for the X-ray crystallographic analysis. Using the OLEX2 Software Package, the structure was solved with the SHELXT structure solution program using Intrinsic Phasing and refined with the SHELXL refinement package with Least Squares minimisation, using the space group $P2_1/c$, with Z = 4 for the formula unit, $C_{68}H_{40}F_6IrN_4P$. The final anisotropic full-matrix least-squares refinement on F^2 with 887 variables converged at R1 = 5.61%, for the observed data and wR2 = 15.89% for all data. The goodness-of-fit was 1.084. Pyrene moieties disordered and modelled each in two locations with C39:C39b 62:38% and C57:C57b 61:39% occupied. Modelled with a combination of geometric (SADI) and displacement (RIGU, ISOR, SIMU) restraints using rigid groups. The anion PF6 was also modelled using a rigid group over two locations with 52:48% occupancy and displacement restraints (ISOR). The large residual density is located near the heavy Ir atom, ca. 1.12 Å, and the intensity (3.44 eA^{-3}) is smaller than the 0.1*Z eA^{-3} (Z = 77 for Ir). This originates from absorption or is a Fourier truncation error.

The conformation of **PyrIr** shown in **Figure 97**, displays a typical distorted octahedral geometry. The crystal structure shows the two pyrene moieties adopting different orientations, with one aligning itself horizontally and the other vertically.

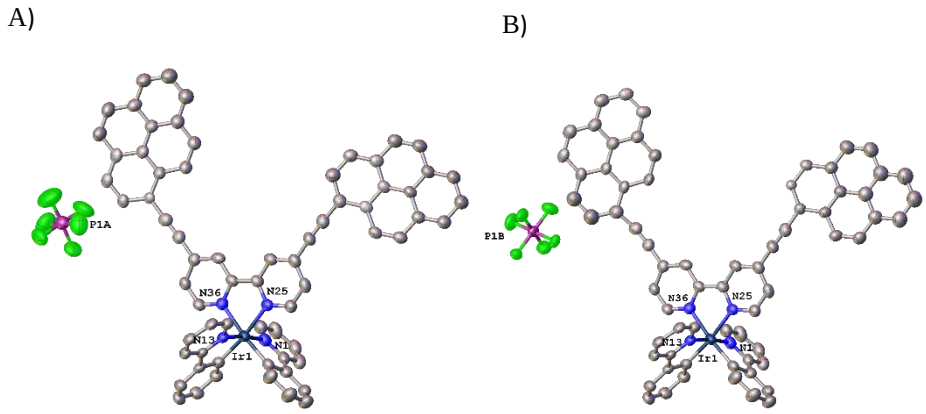

Figure 97. Each disordered moiety in **PyrIr** with (A) majority occupied pyrene units at 62 and 61% occupancy with the anion PF_6 at 52% occupancy and (B) minority occupied pyrene moieties at 38 and 39% occupancy with the PF_6 anion at 48% occupancy. Atomic displacement shown at 50% probability and selected heteroatoms labelled only. Hydrogen atoms omitted for clarity.

As shown in **Figure 98**, this change in orientation allows the pyrene moieties of different **PyrIr** molecules to adopt a 'face-to-face' configuration in which significant segments of their structure overlap, resulting in a highly ordered and structured crystal formation.

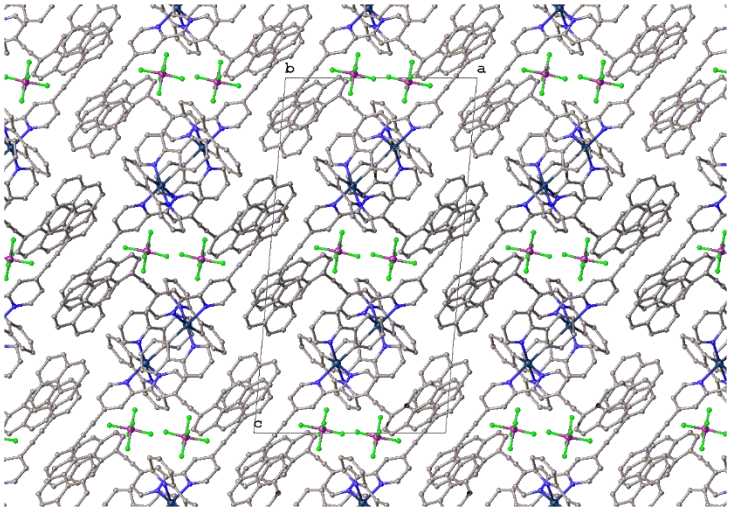

Figure 98. Schematic packing diagram of the majority occupied disordered moieties in **PyrIr** viewed normal to the b-axis with hydrogen atoms omitted for clarity.

2.4 Photophysical Analysis

2.4.1 Spectroscopic Analysis of NPhL

2.4.1.1 Solvatochromic Absorption and Emission of **NPhL**

The absorption and emission properties of **NPhL** were investigated in a range of solvents, as shown in **Figure 99**.

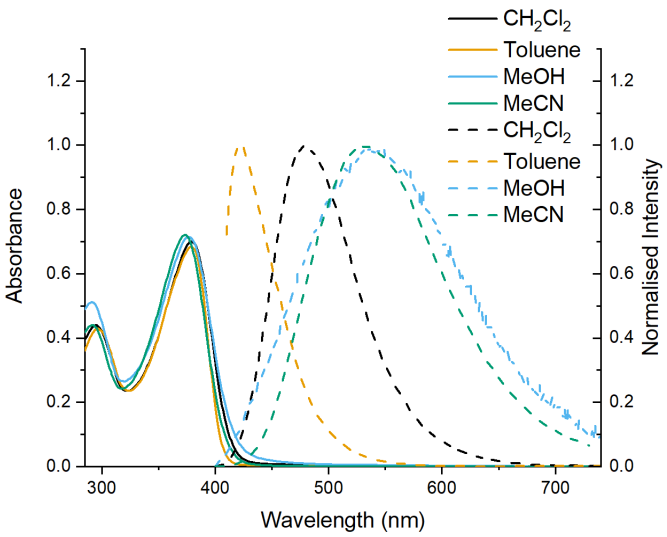

Figure 99. Absorption and normalised emission spectra of **NPhL** in a range of solvents; UV-vis spectra shown with solid lines and emission spectra shown with dotted lines (λ_{ex} = 380 nm), [10^{-5} M], 298 K.

The ligand shows strong absorption in the UV spectrum with one band around 290 nm and another, more intense absorption at 380 nm. **NPhL** absorbs at significantly longer wavelengths than the absorption spectra for **OMeL** and **CF_3L**. The absorption spectrum does not change in different solvents, suggesting that the ground state is not sensitive to solvent.

As reported above, the emission of the ligand is very intense.[60] The emission wavelength is sensitive to solvent polarity, with toluene and CH_2Cl_2 resulting in higher energy emission and MeCN and MeOH in longer wavelengths and lower energies. Additionally, the emission band broadens significantly in more polar solvents, with toluene showing the narrowest emission profile and MeOH the widest. This behaviour suggests a charge-transfer excited state, where stabilisation of the induced dipole of the excited state by solvent molecule rearrangement lowers the energy of the HOMO-LUMO gap. The extent of this solvatochromism is significant, ranging from an emission wavelength of 420 nm in toluene to 540 nm in MeOH and MeCN. The emission intensity of the ligand is significantly reduced in MeOH, accounting for the higher levels of noise in the emission band.

The molar extinction coefficient for **NPhL** at 375 nm in CH_2Cl_2 was calculated to be 69640 L mol^{-1} cm^{-1}, indicating a strong absorption process.

2.4.1.2 Excitation Studies of **NPhL**

The excitation profile of **NPhL** is displayed in **Figure 100**. It shows a match between the absorption bands at 290 nm and 380 nm and the excitation response, indicating that the observed emission is occurring due to the absorption of photons by the ligand.

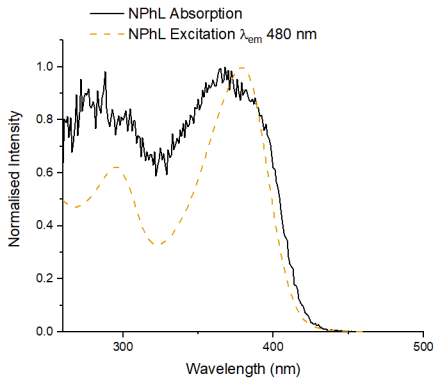

Figure 100. Normalised excitation study of **NPhL** in CH_2Cl_2 (dashed line), compared to normalised absorption profiles of **NPhL** in CH_2Cl_2 (solid line) [10^{-5} M], 298 K.

Low temperature emission spectra, emission lifetime and quantum yield of luminescence of **NPhL** were reported by Wang and co-workers.[60] The results show that the excited state has singlet charge-transfer character, as expected of organic molecules lacking a heavy atom.

In summary, **NPhL** manifests redshifted absorption and emission wavelengths compared to previously prepared ligand systems, coupled with a high quantum yield of luminescence.[60] If these properties could be maintained when the ligand is complexed to a metal centre, the resulting complex should prove to be a highly efficient triplet photosensitiser.

2.4.2 Spectroscopic Analysis of NPhRu

2.4.2.1 Solvatochromic Absorption and Emission of **NPhRu**

The absorption and emission spectra of **NPhRu** in a range of solvents are shown in **Figure 101**.

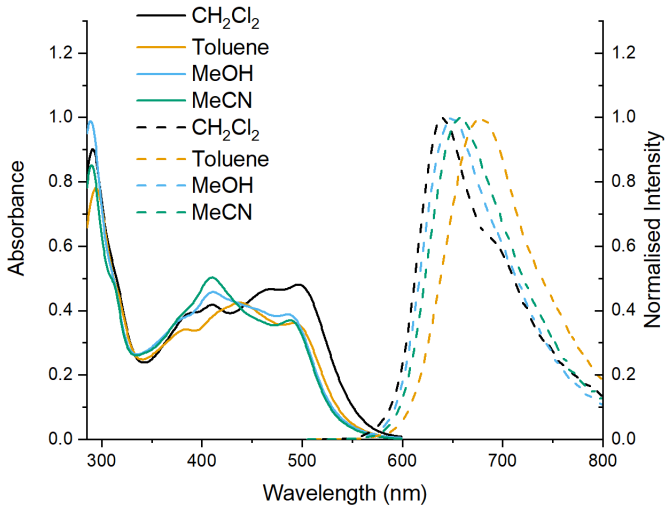

Figure 101. Absorption and normalised emission spectra of **NPhRu** in a range of solvents; UV-vis spectra shown with solid lines and emission spectra shown with dotted lines (λ_{ex} = 490 nm), [10^{-5} M], 298 K.

The absorption spectrum of **NPhRu** shows many different transitions, as is typical of ruthenium metal complexes. At higher energies below 400 nm the absorptions are largely based on π – π*, n – π* and metal-centred (MC) transitions and are not particularly strongly affected by solvents. They remain at similar intensities and wavelengths regardless of their environment.

The transitions beyond 400 nm are much more complex, varying greatly in intensity between the different solvents. While this makes an assignment of transition types to individual absorption bands difficult, it is possible to predict the transition types most likely to appear in this region based on the structure of **NPhRu**. The main transition types expected beyond 400 nm are MLCT from the ruthenium metal d-electrons into empty ligand π* orbitals and intra-ligand charge-transfer (ILCT) transitions from the triphenylamine donor units into the bipyridine core. While charge-transfer absorption occurred at 380 nm in the free ligand, ligand absorption bands are known to red-shift upon complexation to a metal centre. [50,60] The high degree of variation between the absorption bands depending on which solvents the measurements were performed in suggests that the ground state is highly sensitive to the local electronic environment.

This is unusual, as neither the free ligand nor typical ruthenium model complexes such as Ru(bipyridine)$_3$ commonly behave in this way. The difference is most significant between MeCN and CH_2Cl_2, with the former showing the highest-intensity absorption at 400 nm and the latter showing high-intensity absorption at 510 nm. According to Beer's law, absorbance is dependent on path length, the concentration of the solution and the molar extinction coefficient of the sample at a given wavelength. As the concentration of the solutions and the path length were both held constant during solvatochromic experiments, the molar extinction coefficient must be the cause of the changing absorbance values.

The emission properties of **NPhRu** are equally unusual. In MeCN, the emission from the complex is a single broad band centred at 660 nm, typical of ruthenium ^{3}MLCT transitions. The properties are similar in MeOH, with a slight increase in emission wavelength. In CH_2Cl_2, the emission wavelength is 640 nm, in line with the expected solvatochromic stabilisation of the excited state by more polar solvents. However, unlike in MeCN and MeOH, there is a clear shoulder visible at 700 nm in the CH_2Cl_2 emission spectrum that is absent in the profiles in MeCN and MeOH. Furthermore, the toluene emission spectrum is actually at the longest wavelength of 680 nm, which runs contrary to solvatochromic stabilisation principles.

Taking both the absorption and emission trends of **NPhRu** in different solvents into account, the electronic nature of **NPhRu** seems far more complex than in other triplet photosensitisers investigated so far.

The molar extinction coefficient of **NPhRu** was calculated at the MLCT absorption maxima in both CH_2Cl_2 and MeCN. In CH_2Cl_2, the molar extinction coefficient was 47881 L mol^{-1} cm^{-1} at 500 nm. In MeCN, the obtained value at 490 nm was 37000 L mol^{-1} cm^{-1}. This difference shows the significant influence that the solvent has on the absorption processes of **NPhRu**.

2.4.2.2 Excitation of **NPhRu**

The excitation spectrum of **NPhRu**, shown in **Figure 102**, indicates that the observed emission arises from absorption by the same processes detected in the absorption spectrum.

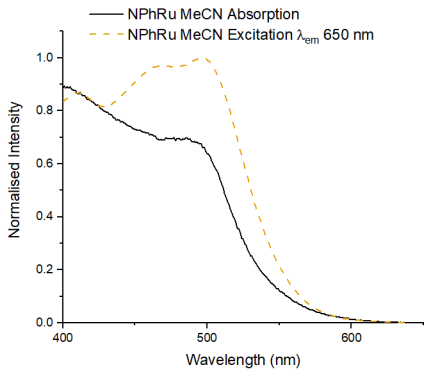

Figure 102. Normalised excitation study of **NPhL** in CH_2Cl_2 (dashed line), compared to normalised absorption profiles of **NPhL** in CH_2Cl_2 (solid line) [10^{-5} M], 298 K.

2.4.2.3 Degassing Studies of **NPhRu**

Degassing studies in MeCN shown in **Figure 103** were performed to determine whether the excited state was triplet in character. A clear increase in emission intensity is observed when oxygen is removed from the atmosphere prior to excitation, suggesting that the excited state responsible for the observed emission is triplet in nature. The sensitivity of the emission is moderate, with a 53 % decrease observed in air relative to argon. The profile of the emission remains constant in both environments.

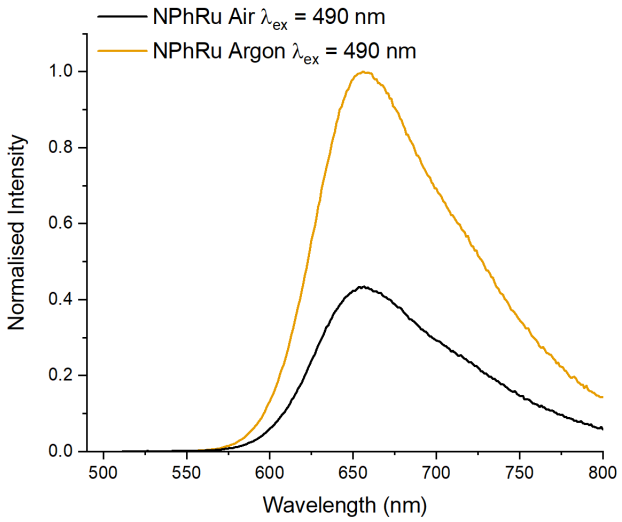

Figure 103. Emission spectra of N**PhRu** in MeCN under either air (black line) or argon (yellow line) atmospheres [10^{-5} M], 298 K.

2.4.2.4 Low Temperature Emission Studies of **NPhRu**

Low temperature emission studies (**Figure 104**) show similar results to those from the previous chapter. The shift of the emission peak to higher energies suggests a charge-transfer excited state, while higher resolution of the emission band reveals a secondary shoulder peak at higher wavelengths.

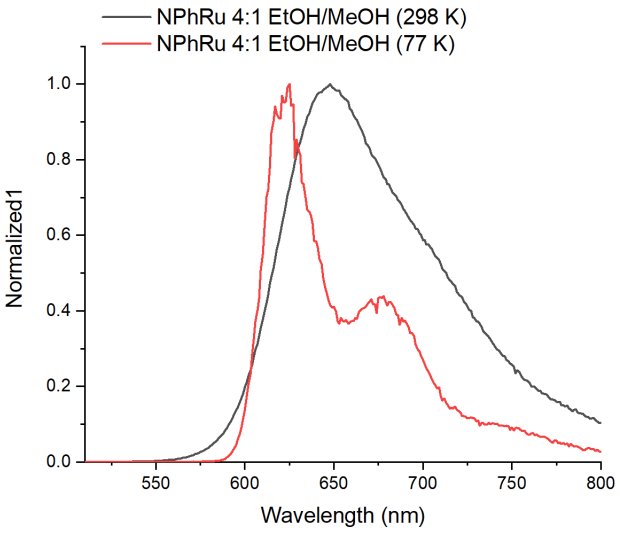

Figure 104. Low temperature emission studies of **NPhRu** recorded in a MeOH/EtOH 4:1 solution at 298 K (black line) and in a frozen glass at 77 K (red line). (λ_{ex} = 490 nm), [10^{-5} M].

The appearance of the secondary shoulder presents a potential explanation for the behaviour observed in the room-temperature solvatochromic absorption and emission studies. Given the variations in intensity of different absorption bands depending on solvent, it is possible that similar behaviour is observed for the emission. CH_2Cl_2 and toluene could be enhancing the emission intensity of the secondary shoulder peak, leading to an overall redshift of the emission wavelength relative to MeCN and MeOH. If verified, this would indicate factors beyond solvent polarity exerting influence over the electronic states of **NPhRu**.

2.4.2.5 Quantum Yield of Phosphorescence and Emission Lifetime of **NPhRu**

The emission lifetime of **NPhRu** was recorded at 400 ns using time-correlated single photon counting with a 460 nm pulsed laser excitation source. This is a remarkably short lifetime, only half that of [$Ru(bpy)_3(PF_6)_2$]. It suggests that the excited state rapidly decays back to the ground state.

The quantum yield of phosphorescence of **NPhRu** was recorded at 5.54% via the relative method using [$Ru(bpy)_3(PF_6)_2$] as a standard.[40] Combined with the short emission lifetime, the low quantum yield of phosphorescence suggests that nonradiative decay pathways are readily accessible in **NPhRu**, leading to poor triplet photosensitiser performance. The complicated behaviour of the complex in different solvents demonstrates that it is more sensitive to the local environment than the other triplet photosensitisers presented previously in this work.

2.4.3 Spectroscopic Analysis of NPhIr

2.4.3.1 Solvatochromic Absorption and Emission of **NPhIr**

The absorption and emission spectra of **NPhIr** in a variety of solvents are shown in **Figure 105**. They resemble those of **NPhRu**, with the higher energy transitions dominated by $\pi - \pi^*$ and $n - \pi^*$ transitions. The spectra show a broad peak between 400 and 500 nm which shifts depending on the solvent. As iridium MLCT transitions occur at higher energies, typically 370 nm, this is likely the ILCT transition of the bis-

triphenylaminebipyridine. Unlike **NPhRu**, the changes in absorption are not limited to intensity – the peak position of the absorption band changes, from a maximum of 450 nm in CH_2Cl_2 to a minimum of 425 nm in MeCN. Additionally, some shifts in absorption wavelength can be seen around 350 nm. This is unusual, as none of the other higher energy by $\pi - \pi^*$ and $n - \pi^*$ transition bands show the same behaviour. Low solubility leading to the formation of aggregates or particles could be a potential explanation for the observed behaviour, but in that scenario, one would expect all transitions to be affected, including those at higher energies. As this is not the case, the individual excited state energies are being affected by the solvent.

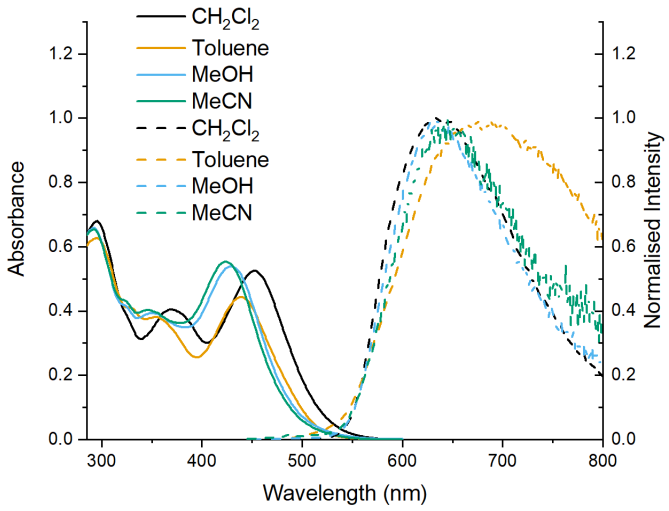

Figure 105. Absorption and normalised emission spectra of **NPhIr** in a range of solvents; UV-vis spectra shown with solid lines and emission spectra shown with dotted lines (excitation at the low energy peak depending on solvent), [10^{-5} M], 298 K.

The emission profiles of **NPhIr** in the different solvents are as remarkable as the absorption bands. The lowest energy emission is observed in toluene, with a very broad emission band centred at 690 nm. The emission wavelengths of CH_2Cl_2, MeCN and MeOH are all very similar in energy at 635 nm. The complex shows very weak emission in MeCN, as evidenced by the low resolution of the emission band. The similarity between the emission wavelengths in the three more polar solvents suggests that the emissive excited state is not greatly stabilised by solvent rearrangement.

The molar extinction coefficient of **NPhIr** was calculated at the ILCT absorption maxima in both CH_2Cl_2 and MeCN. In CH_2Cl_2, the molar extinction coefficient was 52500 L mol^{-1} cm^{-1} at 450 nm. In MeCN, the obtained value at 425 nm was 55400 L mol^{-1} cm^{-1}. Unlike NPhRu, the absorption is stronger in MeCN than in CH_2Cl_2, indicating that the metal centre has an effect on the interactions of the complex with the local solvent environment.

2.4.3.2 Solvent and Excitation Wavelength Dependent Emission Profile of **NPhIr**

Excitation at different wavelengths in the same solvent is a routine part of photophysical experimental procedure. Typically, changes in excitation wavelength do not result in any changes to the emission spectrum, as Kasha's rule is followed. However, in the case of **NPhIr** dissolved in MeCN, significant

changes were observed in emission depending on excitation wavelength. As shown in **Figure 106**, excitation at lower wavelengths resulted in the formation of a weak secondary emission peak at 530 nm.

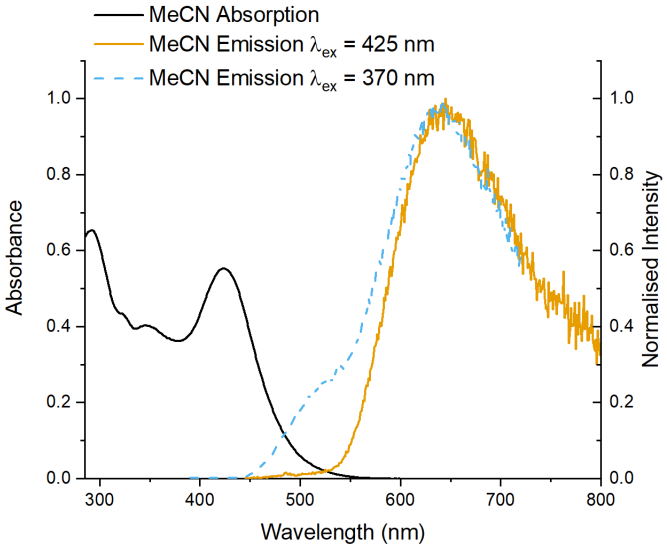

Figure 106. Absorption and emission profiles of **NPhIr** in MeCN with changing excitation wavelengths [10^{-5} M], 298 K.

2.4.3.3 Excitation Studies of **NPhIr**

Excitation studies were performed to rule out the presence of any trace impurity which could have caused the observed shoulder (**Figure 107**). These studies show that both the emission shoulder at 530 nm and the main emission band at 630 nm arise due to the contribution from a transition at 370 nm. The lower energy ILCT absorption band does contribute to the emission observed at 630 nm, but not to the high energy emission shoulder.

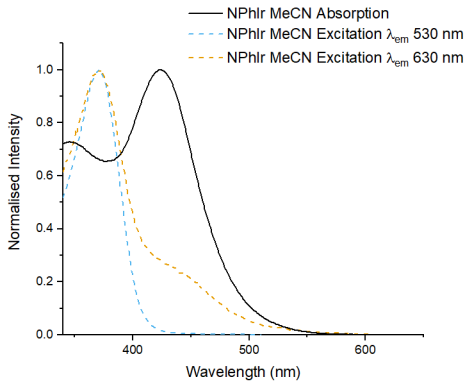

Figure 107. Normalised excitation studies of **NPhIr** in MeCN (dashed lines), compared to normalised absorption profiles of **NPhIr** in MeCN (solid line) [10^{-5} M], 298 K.

2.4.3.4 Degassing Studies of **NPhIr**

Degassing studies in MeCN were performed, and are shown in **Figure 108** A and B.

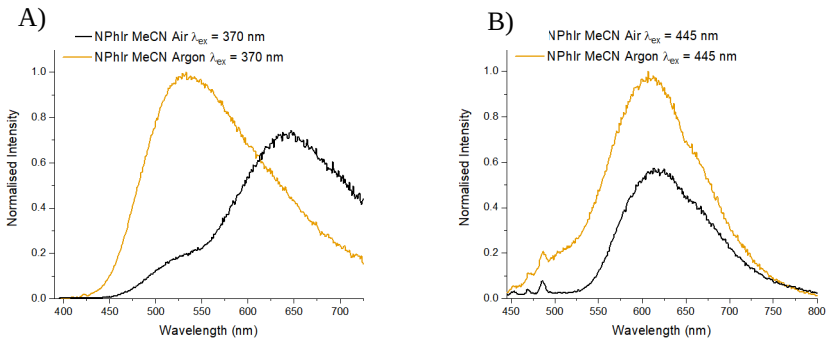

Figure 108. Emission spectra of **NPhIr** in MeCN under either air (black line) or argon (yellow line) atmospheres with excitation at 370 nm (A) or 445 nm (B) [10^{-5} M], 298 K.

In **Figure 108A**, the removal of oxygen from the atmosphere results in a change in the emission profile as well as an increase in emission intensity. The emission under an argon atmosphere manifests as a single broad peak at 530 nm. The removal of oxygen causes a greater increase in intensity of the 530 nm emission than the 630 emission, resulting in the former dominating the emission spectrum. Meanwhile, B shows the emission generated by excitation at 445 nm leads to an increase in emission intensity, indicating a triplet excited state is responsible for both emissions.

In order to determine whether this behaviour was solvent-specific, CH_2Cl_2 solutions of **NPhIr** were degassed and are shown in **Figure 109.**

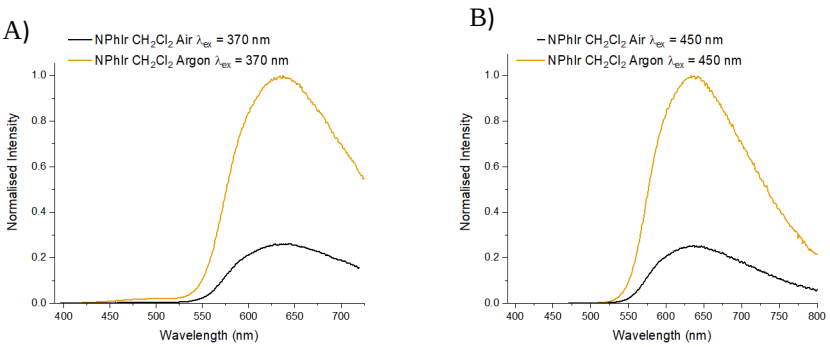

Figure 109. Emission spectra of **NPhIr** in CH_2Cl_2 under either air (black line) or argon (yellow line) atmospheres with excitation at 370 nm (A) or 445 nm (B) [10^{-5} M], 298 K.

These spectra show that in CH_2Cl_2, the emission remains at 630 nm regardless of excitation wavelength. Combined with those from the excitation studies, these findings suggest a very low probability of the observed emission at 530 nm in MeCN resulting from an impurity. In order for an impurity to be the cause, an impurity would have to have efficient access to a triplet excited state following absorption at 380 nm in MeCN but remain undetectable in CH_2Cl_2.

The excitation studies performed on the CH_2Cl_2 samples further preclude the presence of an impurity, as shown in **Figure 110**. The obtained results reveal both absorption peaks at 420 and 370 nm contributing to emission from the 640 peak. The occurrence of the 370 nm absorption peak in the MeCN excitation spectra is therefore not due to an impurity, but rather part of the **NPhIr** absorption profile.

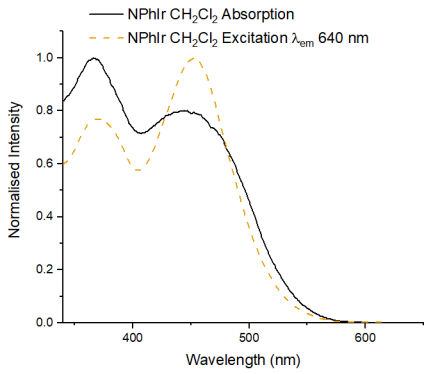

Figure 110. Normalised excitation studies of **NPhIr** in CH_2Cl_2 (dashed lines), compared to normalised absorption profiles of **NPhIr** in CH_2Cl_2 (solid line) [10^{-5} M], 298 K.

2.4.3.5 Low Temperature Emission studies of **NPhIr**

Low-temperature emission studies were performed (**Figure 111**) to determine whether this unique behaviour could be observed at 77 K.

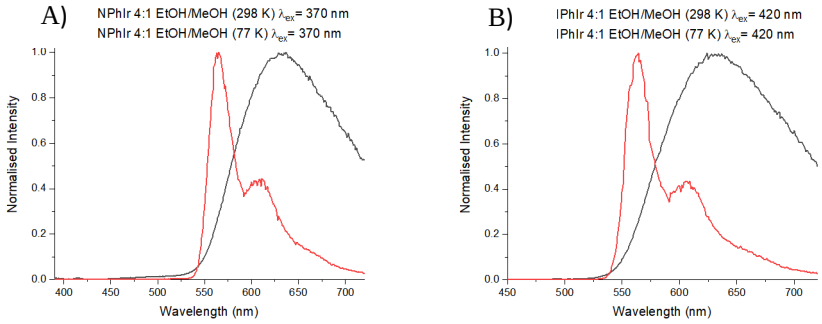

Figure 111. Low temperature emission studies of **NPHIr** recorded in a EtOH/MeOH 4:1 solution at 298 K (black line) and in a frozen glass at 77 K (red line). (λ_{ex} = 370 nm (A) and 420 nm (B)), [10^{-5} M].

The low temperature emission studies show the same behaviour as previously investigated iridium metal complexes, with a shift of emission wavelengths to higher energies and resolution of the single broad band into two distinct peaks. Unfortunately, the MeOH:EtOH mixture does not result in the same photophysical behaviour observed in MeCN, with the emission at room temperature registering as a single broad peak at 640 nm. In order to obtain low-temperature emission spectra, a solvent must form a glass instead of ice; MeCN forms the latter. However, methyltetrahydrofuran (mTHF) is an alternative low-temperature solvent with behaviour and properties different from MeOH:EtOH, so it was decided to examine the low-temperature spectra in this solvent.

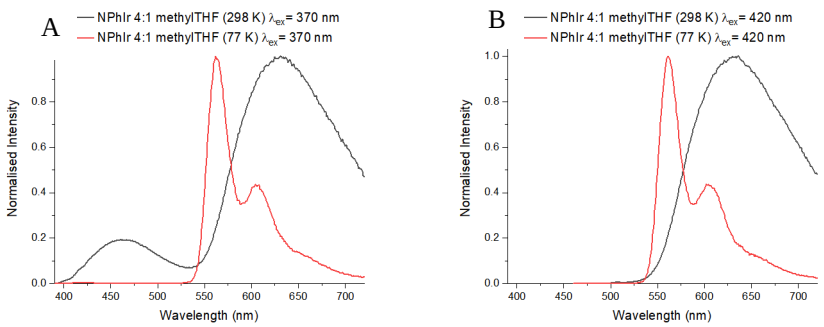

Figure 112. Low temperature emission studies of **NPhIr** recorded in methyltetrahydrofuran at 298 K (black line) and in a frozen glass at 77 K (red line). (λ_{ex} = 370 nm (A) and 420 nm (B)), [10^{-5} M].

Fortuitously, the room-temperature emission spectrum of **NPhIr** in mTHF manifests the same high-energy peak as MeCN when excited at 370 nm. This indicates that the secondary peak is not generated by an interaction unique to MeCN and **NPhIr**. At 420 nm, the room-temperature emission spectrum shows a single broad peak at 640 nm. At low temperatures, both emission spectra are identical, with no trace of a high-energy peak observed. This suggests that population of the higher-energy state requires thermal energy.

2.4.3.6 Quantum yield of Phosphorescence and Emission Lifetime of **NPhIr**

The lifetime and quantum yields of luminescence of **NPhIr** were determined under a variety of different conditions, as shown in **Table 8**. The lifetimes indicate a complex, multi-emission behaviour in MeCN while CH_2Cl_2 shows consistent lifetimes regardless of excitation wavelength.

Table 8. Emission lifetime and quantum yield of luminescence of **NPhIr** under a range of different conditions [10^{-5} M], 298 K [a] fitted using biexponential decay curves [b] recorded using $[Ru(bpy)_3(PF_6)_2]$ in MeCN as a standard. [40]

Solvent	**CH_2Cl_2**		**MeCN**	
Excitation Wavelength (nm)	370	450	370	420
Lifetime (ns)	880	870	3.7 & 27[a] (93 % to 7 %)	22 & 267[a] (75% to 25 %)
Quantum Yield (%)[b]	12.26	19.67	1.67	0.345

The quantum yields of luminescence exhibit large differences depending on solvents, with CH_2Cl_2 showing yields of over 10 % regardless of excitation wavelength, while in MeCN the yield is reduced under 2 %. This correlates with the shorter emission lifetimes in MeCN suggesting the presence of multiple nonradiative decay pathways.

In summary, these findings suggest that different excited states are populated depending on the solvent. This has not been reported for iridium complexes, but it does match the results obtained by Sutton *et al.* for rhenium complexes bearing similar ligands.[49] They coined the phrase 'solvent-dependent excited state switching' and postulated that a change of solvents results in alternate population pathways for MLCT and ILCT excited states. A combination of time resolved spectroscopy and density functional theory was used to support their theory. Such methods are unavailable for this current project, but the similarity of the reported

properties of the rhenium complexes and those observed for **NPhIr** strongly suggest that the same phenomenon is occurring.

2.4.4 Spectroscopic Analysis of BrRu

2.4.4.1 Solvatochromic Absorption and Emission of **BrRu**

The absorption and emission spectra for **BrRu** are shown below in **Figure 113**.

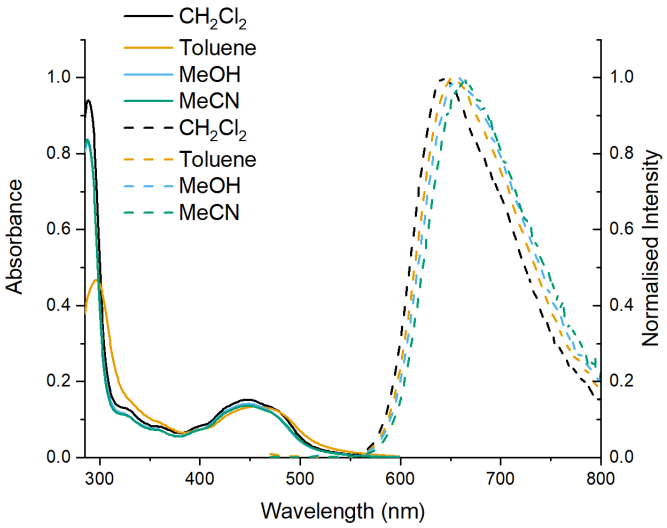

Figure 113. Absorption and normalised emission spectra of **BrRu** in a range of solvents; UV-vis spectra shown with solid lines and emission spectra shown with dotted lines (λ_{ex} = 450 nm), [10^{-5} M], 298 K.

The absorption spectra displays a smaller number of absorption bands than those of **NPhRu** and **NPhIr** due to the lack of photon-harvesting groups on the bipyridine ligands. The absorption is composed of π – π*, n – π* and MC transitions at higher energies, and MLCT transitions at lower energies between 450 and 500 nm. The emission bands appear as single broad peaks beyond 650 nm, with the emission wavelength showing some weak solvent sensitivity, indicating the presence of a dipole in the excited state.

The molar extinction coefficient of **BrRu** was calculated at the MLCT absorption maxima in MeCN. The obtained value at 450 nm was 15100 L mol^{-1} cm^{-1}. The lack of photon-harvesting chromophores reduces the intensity of absorption bands at low energies in **BrRu** compared to the **NPhIr** and **NPhRu**.

2.4.4.2 Excitation Studies of **BrRu**

The excitation spectra for **BrRu** are shown in **Figure 114**. They reveal that the emission at 670 nm is primarily generated by absorption into the bands at 450 nm.

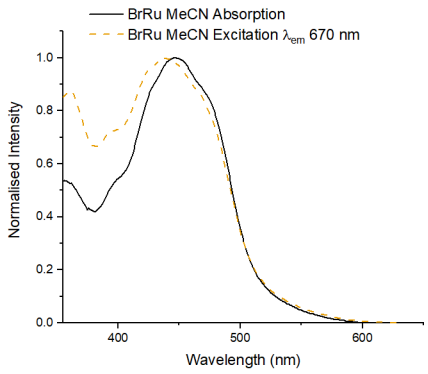

Figure 114. Normalised excitation studies of **BrRu** in MeCN (dashed lines), compared to normalised absorption profiles of **NPhIr** in MeCN (solid line) [10^{-5} M], 298 K.

2.4.4.3 Degassing Studies of **BrRu**

Degassing studies were performed on **BrRu** in MeCN, and the results are shown in **Figure 115**.

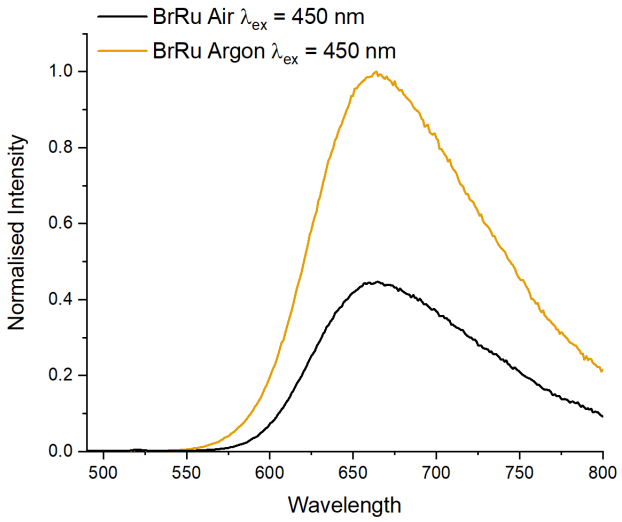

Figure 115. Emission spectra of **BrRu** in MeCN under either air (black line) or argon (yellow line) atmospheres [10^{-5} M], 298 K.

They exhibit an increase in emission intensity under argon atmosphere, indicating that the emission excited state is triplet in character. The emission is quenched by 55 % in air, indicating moderate sensitivity and ability to generate singlet oxygen.

2.4.4.4 Low Temperature Emission of **BrRu**

Finally, low temperature spectra of **BrRu** displayed in **Figure 116** manifest the typical behaviour of ruthenium complexes, with emission wavelengths shifted to higher energies at low temperatures and the single broad emission band resolved into two distinct peaks.

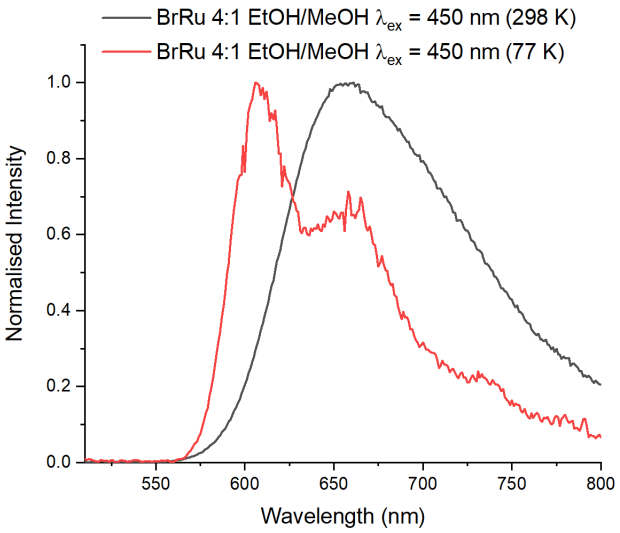

Figure 116. Low temperature emission studies of **BrRu** recorded in a MeOH/EtOH 4:1 solution at 298 K (black line) and in a frozen glass at 77 K (red line).

2.4.4.5 Quantum Yield of Phosphorescence and Emission Lifetime of **BrRu**

The quantum yield of phosphorescence for **BrRu** was determined to be 3.964 % via the relative point method using $[Ru(bpy)_3(PF_6)_2]$ in MeCN as the reference compound.[40] The lifetime of the complex was determined at 442 ns, half that of $[Ru(bpy)_3(PF_6)_2]$.

The low quantum yields of luminescence and short emission lifetime suggest rapid deactivation of the emissive excited state, which may be facilitated by the presence of the bromine atoms enhancing spin-orbit coupling due to the heavy atom effect.

2.4.5 Spectroscopic Analysis of PyrIr

2.4.5.1 Solvatochromic Absorption and Emission of **PyrIr**

The absorption and emission spectra of **PyrIr** in a range of solvents are displayed in **Figure 117**. The absorption spectra show the typical high energy π – π* and n – π* transitions, with the iridium MLCT bands appearing at 370 nm. Beyond 350 nm, a large number of distinct peaks can be observed, which are typical of pyrene-based π – π* IL transitions.[44] Due to the highly conjugated nature of pyrene, the HOMO-LUMO gap is significantly decreased, pushing typically high-energy π – π* transitions into the visible spectrum. A weak shoulder absorption band past 500 nm can be assigned to iridium ^{3}MLCT absorption. The absorption bands are moderately sensitive to solvent, particularly those at lower energies. As they are dominated by the pyrene moiety, the arrangement of solvent molecules around that group could exert significant influence on the absorption wavelength.

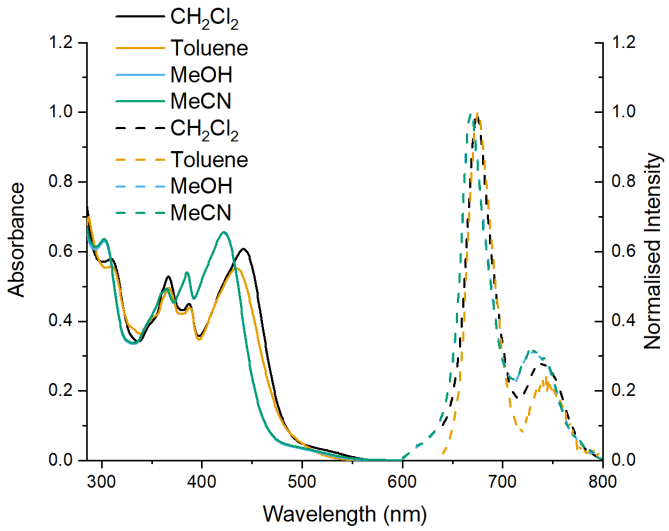

Figure 117. Absorption and normalised emission spectra of **PyrIr** in a range of solvents; UV-vis spectra shown with solid lines and emission spectra shown with dotted lines (excitation at the low energy peak depending on solvent), [10^{-5} M], 298 K.

The emission bands of **PyrIr** are different from those of other triplet photosensitisers presented in this thesis. Instead of one broad emission band, we see distinct peaks, namely one narrow, intense emission band at 670 nm and one weaker, broad emission band at 750 nm. The emission wavelength of the high energy band is not sensitive to solvent, while the lower energy peak fluctuates slightly in both intensity and exact peak position depending on the solvent.

The molar extinction coefficient of **PyrIr** was calculated at the π – π* absorption maxima in both CH_2Cl_2 and MeCN. In CH_2Cl_2, the molar extinction coefficient was 60700 L mol^{-1} cm^{-1} at 440 nm. In MeCN, the obtained value at 420 nm was 65500 L mol^{-1} cm^{-1}.

2.4.5.2 Excitation Studies of **PyrIr**

Excitation studies performed on **PyrIr**, as shown in **Figure 118**, demonstrate that the emission at 650 nm arises from absorption into all of the lower energy transitions, including the pyrene π – π* and iridium ^{3}MLCT transitions.

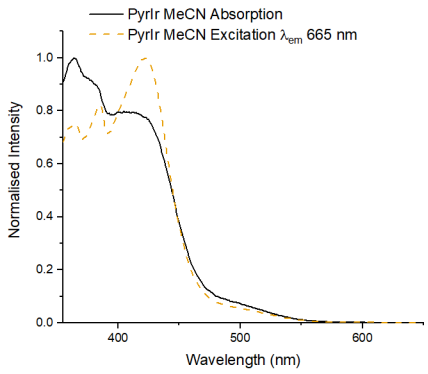

Figure 118. Normalised excitation studies of **PyrIr** in MeCN (dashed lines), compared to normalised absorption profiles of **PyrIr** in MeCN (solid line) [10^{-5} M], 298 K.

2.4.5.3 Degassing Studies of **PyrIr**

Degassing studies were performed at various excitation wavelengths to determine the presence of different emissive states, comparable to those found in **NPhIr**. The results of these studies, shown in **Figure 119 A** and **B**, show that the emission remains constant regardless of excitation wavelength.

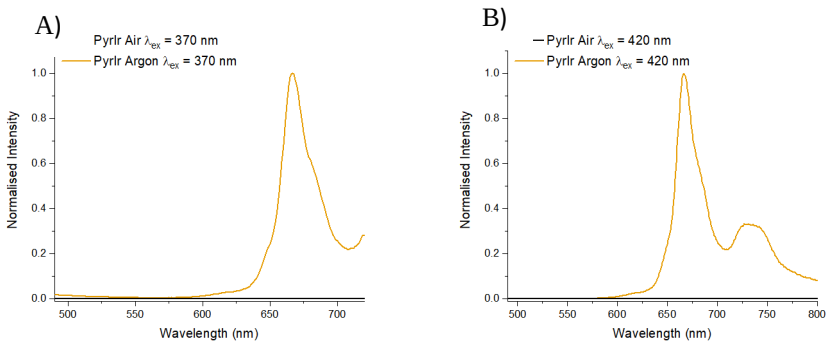

Figure 119. Emission spectra of **PyrIr** in MeCN under either air (black line) or argon (yellow line) atmospheres with excitation at 370 nm (A) or 445 nm (B) [10^{-5} M], 298 K.

Additionally, the degassing studies show that the emission is incredibly sensitive to oxygen, with the in-air emission becoming nearly indistinguishable from the baseline. This on-off emission behaviour is indicative of an excited state capable of sensitising molecular oxygen with high levels of efficiency.

2.4.5.4 Low Temperature Emission Studies of **PyrIr**

To determine the nature of the excited state, low-temperature studies were performed on **PyrIr**, shown in **Figure 120**.

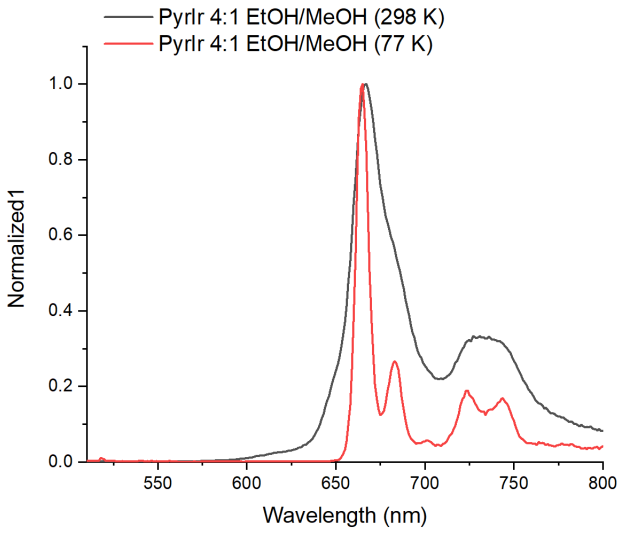

Figure 120. Low temperature emission studies of **PyrIr** recorded in a MeOH/EtOH 4:1 solution at 298 K (black line) and in a frozen glass at 77 K (red line).

The low temperature emission spectrum of **PyrIr** does not shift to higher energies than the room temperature emission, unlike previously investigated triplet photosensitisers. It resolves from two distinct bands at room temperature to five at low temperatures, indicating the presence of a multitude of excited states with very similar energies.

2.4.5.5 Quantum Yield of Phosphorescence and Emission Lifetime of **PyrIr**

The emission lifetime for **PyrIr** was recorded at one μs following excitation at 460 nm. The quantum yield of phosphorescence for **PyrIr** was recorded at 2.85% following excitation at the sample wavelength.

Given the long emission lifetime, insensitivity to solvent, and lack of shift in low temperature emission spectra, it is likely that the excited state for PyrIr is ^{3}IL in nature, centred on the pyrene molecule.

2.4.6 Summary

In summary, three novel triplet photosensitisers (**NPhRu**, **NPhIr** and **PyrIr**) were developed and their photophysical properties investigated. The NPh series of complexes displayed unusual interactions between their photophysical behaviour and the solvents the measurements were conducted in. While these interactions had been previously observed in rhenium complexes, these are the first instances where such behaviour has been observed in iridium.[54] It would have significant implications for triplet photosensitiser design, if the local environment that the complex is excited in turned out to determine which excited state is populated. This would require the testing of a photosensitiser in conditions to match those of its final application as closely as possible, since behaviour recorded under research conditions may not conclusively reflect on its eventual performance.

PyrIr shows high potential as a triplet photosensitiser due to its long absorption wavelengths, high emission lifetime and significant sensitivity to singlet oxygen. Of all the 4,4-bipyridine complexes generated over the course of this project, it shows the most promise, so will therefore be investigated further by means of

transient spectroscopy, so that its suitability for photodynamic therapy may be assessed. In the meantime, samples of **PyrIr** have been sent to collaborators in Spain to establish it's cytotoxicity in the dark and under illumination.

Some of the unusual photophysical behaviour observed in the complexes (specifically NPhRu and BrRu) could not be examined due to time constraints. The emission behaviour in toluene for both systems is anti-solvatochromic, suggesting that the presence of two excited states is not limited to NPhIr. Future work will be done to probe the behaviour of these complexes more closely in a wider range of solvents.

3.: Accessing Unsymmetric Triplet Photosensitisers

3.1 Introduction

3.1.1 Unsymmetric Ruthenium Complexes

3.1.1.1 Improving Optical Performance

Until now, the work presented in this thesis has concentrated on the synthesis and analysis of symmetrically substituted bipyridine systems. There is, however, a growing field of work investigating the synthesis and properties of unsymmetrical polypyridyl structures.[83,99–101] Facile access to unsymmetric bipyridine systems would allow for more tailored synthetic approaches, leading to finer control over the properties of triplet photosensitisers. However, synthesis of these systems has thus far been very restricted, demanding significantly more synthetic effort than corresponding symmetric systems.[50] Consequently, most 'unsymmetric' bipyridine-based transition metal complexes are substituted at a single position, significantly easing the added synthetic burden. However, this approach limits the design scope for unsymmetric triplet photosensitisers, with few reports of bipyridine ligands bearing two substituents of significantly different chemical and photophysical character.[49,50]

Nonetheless, it is still valuable to investigate the synthetic approach to and spectroscopic behaviour of mono-substituted unsymmetric bipyridine

Reports of unsymmetric bipyridyl ruthenium complexes date back decades, with Song *et al.* describing the synthesis of a ruthenium complex bearing a mono-substituted bipyridyl ligand in 2003 (**Figure 121**).[90]

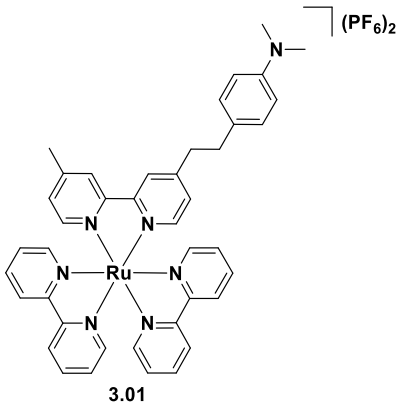

3.01

Figure 121. Ruthenium complexes bearing an unsymmetrical bipyridyl ligand that displays simultaneous ^{3}ILCT and ^{3}MLCT emission.[90]

Complex **3.01** was generated in response to recent (at the time) discoveries of simultaneous ^{3}MLCT and ^{3}ILCT emission bands at low temperature.[102] This dual emission was not observed at room temperature, as complexes usually rapidly relax to a single emissive exited state, as proscribed by Kasha's Rule.[37] Zhang and co-workers attempted to induce ILCT transitions in the bipyridine ligand, like work presented earlier in this thesis. Unlike previous work, this complex does show simultaneous dual emission at room temperature from a ^{3}MLCT state and a much less intense but longer lasting ^{3}ILCT state. Dual emission has since been recorded in several other unsymmetric ruthenium complexes, suggesting that this specific structural feature is linked with observation to the complex emission behaviour.[49,78,80,83]

One attractive feature of unsymmetric bipyridines is the ability to independently tune separate properties of the system. A demonstration of this principle can be found in the work of Chandrasekharam *et al.* via the generation of the structures exhibited below in **Figure 122**.[103]

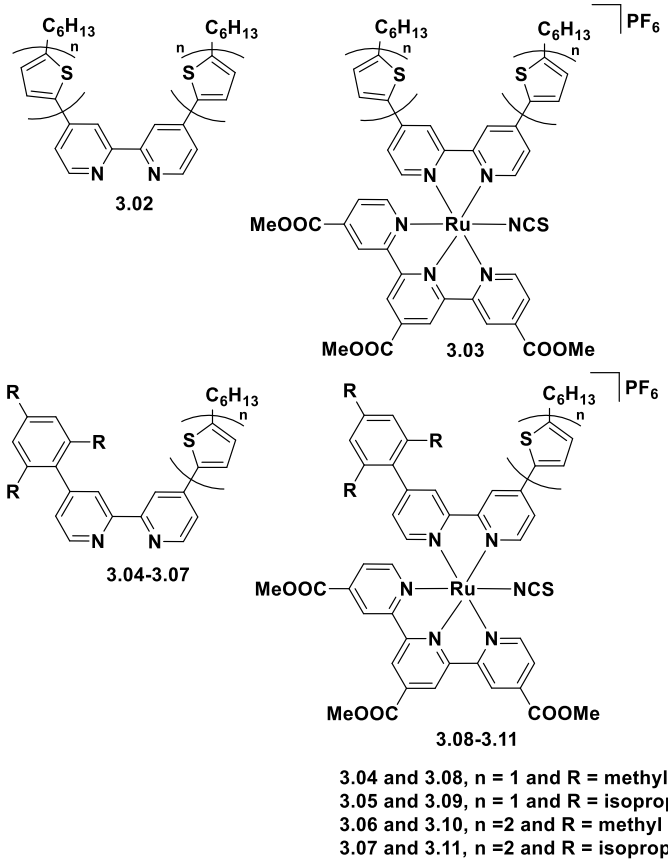

Figure 122 Literature examples of ruthenium complexes with unsymmetric bipyridines functionalised with thiophenes and alkyl benzenes.[103]

These complexes were designed as components of nanocrystalline TiO_2 dye solar cells, with the substituted bipyridines acting as photon harvesters and the terpyridine acting as an anchoring ligand for the TiO_2. The authors realised that by unsymmetrically substituting the bipyridines it would be possible to simultaneously tune several different properties relevant for cell dye performance, including molar absorption, electron donation capacity and ligand bulk. It is important to note that the photophysical properties of the generated

complexes, which are of the greatest interest to this thesis, do not vary significantly between the symmetric and unsymmetric complexes depicted in **Figure 2**.

The molar extinction coefficients of the low-energy MLCT transitions for complexes **3.10** and **3.11** are higher than for **3.03**, **3.08** and **3.09** due to the presence of two linked thiophene moieties in the former. The maximum absorption wavelength varies by only five nm between the ruthenium complexes, due to the thiophene moiety governing the absorption process, a consistent structural feature across this family of complexes. The emission wavelengths of the complexes display larger variations, with **3.11** manifesting an emission peak at 760 nm while **3.09** manifests an emission peak at 719 nm. This suggests that unsymmetric substitution can affect absorption and emission properties of complexes to varying degrees.[103]

The aim of Han *et al.* was not to solely modify the excited state properties of the complexes, but also their bulk physical behaviour and hole-transport capabilities.[103] Despite the similarities in the photophysical properties of the complexes, significant differences in behaviour were found when the oxidation potential, LUMO energies and current densities were measured. As a result, when deposited on TiO_2 films, the unsymmetric bipyridine complexes (**3.08 - 3.11)** show generally increased light-to-electrical conversion efficiency as solar cell dyes compared to the symmetrically substituted reference compound **3.03**.[103]

3.1.1.2 Synthetic Approach

The work by Han and co-workers is an excellent introduction to the potential of unsymmetric bipyridine, including a demonstration of the advantages that unsymmetrically substituted bipyridines offer for improving the overall performance of ruthenium complexes. However, it also exposes some of the drawbacks inherent in current design approaches.

The synthetic path for the precursor ligand is a two-step Suzuki coupling reaction, with the thiophene boronic acids being coupled first and the alkyl benzene boronic acids last. A generic example of a synthetic pathway to unsymmetric bipyridine compounds is displayed in **Scheme 16.**[50,103]

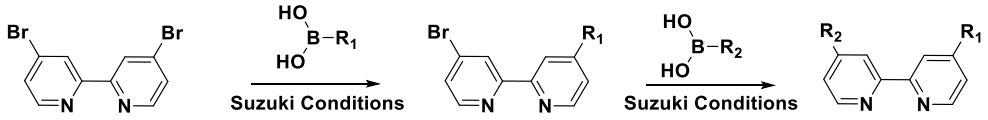

Scheme 16. Generalised synthetic approach to unsymmetric bipyridines using sequential Suzuki coupling reactions.

Given the difficulties commonly encountered in synthesising and purifying polypyridyl ligands, introducing an entire second coupling reaction represents a substantial additional synthetic effort. Furthermore, the second coupling reaction introduces significant extra cost due to the increased use of palladium catalysts.

3.1.1.3 Influencing Electronic Properties

Publications by Benson *et al.* demonstrate how unsymmetric bipyridyl ligands may be used to influence the electronic properties of ruthenium complexes.[101] The authors generated a series of ruthenium complexes with unsymmetric hydroxyl- and methoxy-substituted bipyridine ligands and their related complexes, exhibited in **Figure 123.**[101]

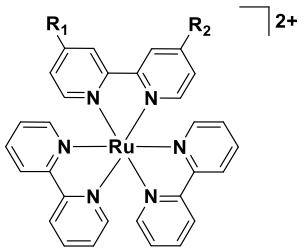

3.12, R_1 = OH, R_2 = H
3.13, R_1 = OCH_3, R_2 = H
3.14, R_1 = OH, R_2 = OCH_3

Figure 123. Literature examples of ruthenium complexes with unsymmetrical bipyridines functionalised with hydroxy and methoxy units.[101]

The authors investigated whether ruthenium complexes could be used as models to study photoinduced photon coupled electron transfer (PCET) reactions. PCET reactions are of significant interests in the fields of artificial photosynthesis and photocatalysis, and hydroxyl-substituted bipyridyl ruthenium complexes were chosen to explore how protonation of metal complexes would affect the parameters governing PCET. To prevent the complication of having to resolve several different protonation sites, as would have been necessary for symmetric dihydroxy bipyridines, three unsymmetric ruthenium complexes were generated. Complex **3.12** has a single hydroxyl moiety at the 4-position of bipyridine, while **3.13** bears a single methoxy substitute at the same position. Complex **3.14** meanwhile bears both a hydroxy and a methoxy substituent at the 4,4'-positions of the bipyridine rings. Their electrochemical analysis indicates that deprotonation of the single hydroxyl group significantly increases the negative charge held by the ligand, resulting in easier oxidation of the metal centre.

Reducing the complexity of model complexes is a powerful tool for probing the mechanisms of electronic behaviour in transition metal reactions.

The discussions so far have described the effect and potential of unsymmetrical bipyridyl ligands and their possible role in fine-tuning electrochemical and physical properties, but breaking symmetry can also exert significant influence on the photophysical properties of bipyridyl system.

This was clearly demonstrated by the work done by Sarma *et al.* who, over three separate publications, reported the syntheses of unsymmetrical bipyridine ligands, compared them to their symmetric counterparts and used them to produce a series of ruthenium arene complexes.[99,100,104] In the first two publications, they describe the changes observed when transitioning from symmetric Donor-Acceptor-Donor (DAD) 2,2'-bipyridine dyads to unsymmetric donor-acceptor (DA) derivatives. The library of compounds assembled during this work is so extensive that only a small section can be examined in detail. The structures of these compounds are displayed in **Figure 124.**

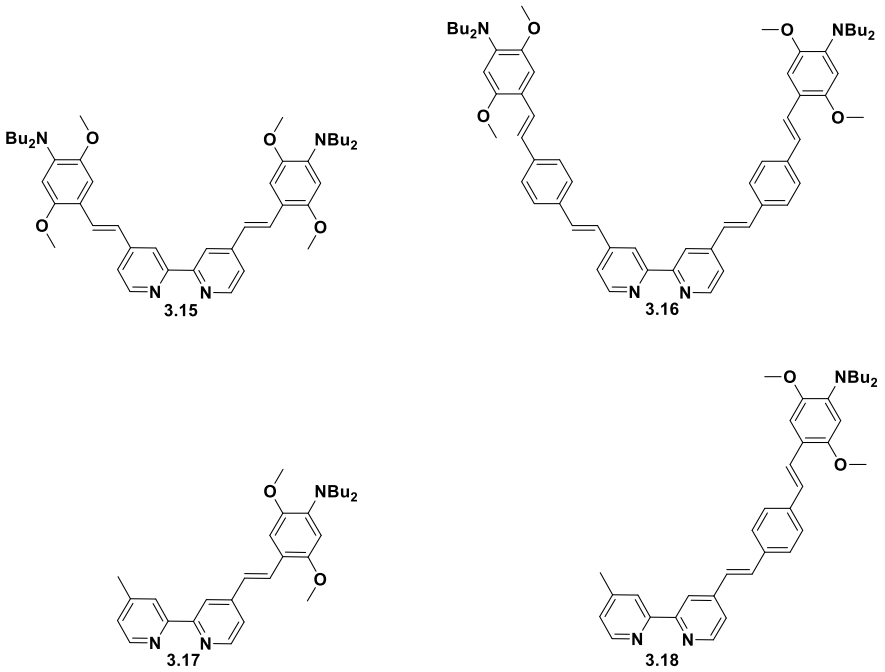

Figure 124. Symmetric and unsymmetrical donor-acceptor bipyridines.[99,104]

During this investigation, several key discoveries were made; For the **3.15**/**3.17** pair, the absorption and emission is redshifted in **3.15**, but only by 4 and 11 nm respectively. This small change suggests that the extended conjugation in **3.15** has a negligible effect. The quantum yield of fluorescence is increased in **3.17** relative to **3.15**, potentially due to a larger number of accessible rotational and vibrational states in the secondary donor arm of **3.15** allowing for enhanced nonradiative decay processes. In the **3.16** and **3.18** pair, the changes in absorption and emission follow the same trend, although the shifts are greater, and the maximum absorption and emission wavelengths are redshifted relative to **3.15** and **3.17** due to increased conjugation. Interestingly, the trend in quantum yield of fluorescence reverses – **3.18** demonstrates lower efficiency than **3.16**. This indicates that the effects of unsymmetric substitution cannot be consistently predicted, and that the trends in photophysical properties when transitioning from symmetric to unsymmetric substitution patterns depends on the overall structure of the molecules in question.[99,104]

In their most recent work, Das *et al.* attached their unsymmetric ligands to ruthenium(p-cymene)Cl_2 and investigated the spectroscopic behaviour of the resulting complexes. The structure of the complexes is shown in **Figure 125.**[100]

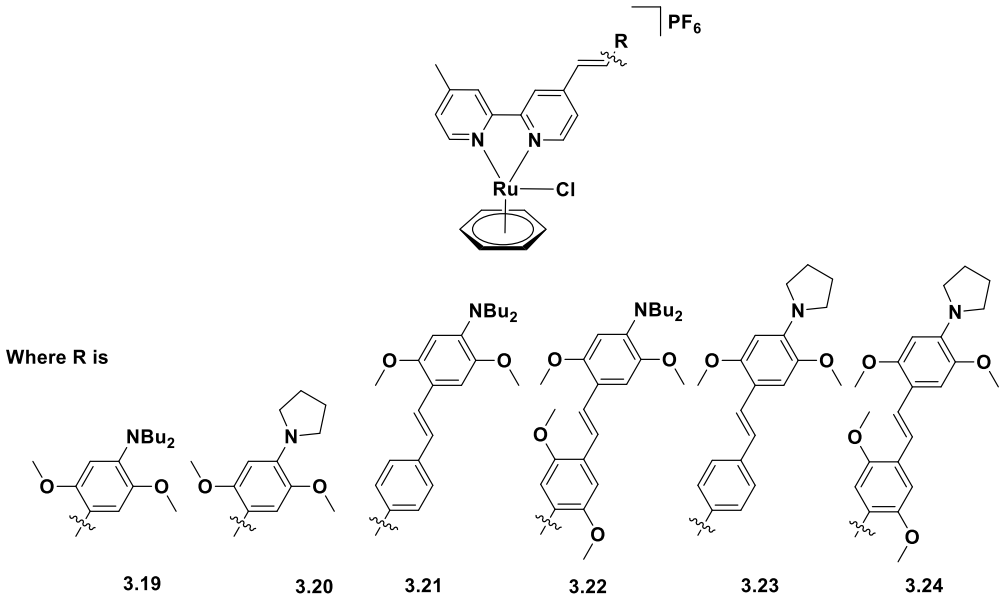

Figure 125. Unsymmetric bipyridyl ruthenium complexes.[100]

While it is not possible to compare the unsymmetric to the symmetric ruthenium complexes, as they had not been published at the date of submission, some interesting aspects to the photophysical properties of these compounds already appear worth discussing. They all exhibit intense absorption bands past 500 nm, with broad emission spectra characteristic of charge transfer (CT) excited states. The emission lifetime is remarkably short, under one ns, but it is unclear whether these measurements were taken in deaerated or aerated solutions. Due to this uncertainty, it is also not possible to determine whether the excited states are triplet in nature.

The authors present DFT studies showing the charge-transfer excited state to be ligand-to-metal charge transfer (LMCT) in nature, with electron density from the electron-rich ligand orbitals filling empty metal orbitals. The filling of these would likely lead to rapid decay of the excited state via population of nonradiative metal-centred (MC) states in ruthenium polypyridyl complexes.[105] The nonradiative decay pathways would result in short emission lifetimes. Luminescence quantum yields range from 15 to 21 %, relatively high compared to other ruthenium complexes such as $[Ru(bpy)_3PF_6]$, which has a quantum yield of 9.6 % in MeCN.[40]

Of particular interest are the solvatochromic studies completed on the various ruthenium complexes. As we have already seen, solvents with increased polarity are able to stabilise the induced dipole of the excited state, leading to a bathochromic shift in emission wavelength, as the HOMO-LUMO gap is lowered. For this family of complexes however, emission wavelength in CH_2Cl_2 is longer than the emission wavelength in DMF, despite the latter having a relative polarity of 0.386 compared to the former's 0.309. An equivalent trend is seen in the absorption wavelength, where the λ_{max} in CH_2Cl_2 is bathochromically shifted compared to the λ_{max} DMF. This is similar to the behaviour to that observed by Gordon *et al.* as well as to the work presented in Chapter 2 of this thesis, and could be indicative of Excited State Switching (ESS).[54]

The properties of complexes bearing two different unsymmetric bipyridyl ligands were investigated by Martin *et al.*[78] A bichromophoric ruthenium complex with one singlet and one triplet excited state was generated, emitting simultaneously at comparable intensities. Keyes and co-workers utilised a ruthenium metal centre complexed to two bipyridine ligands mono-substituted with carboxylic acid groups and one phenanthroline ligand mono-substituted with a brominated BODIPY chromophore (**Figure 126**).

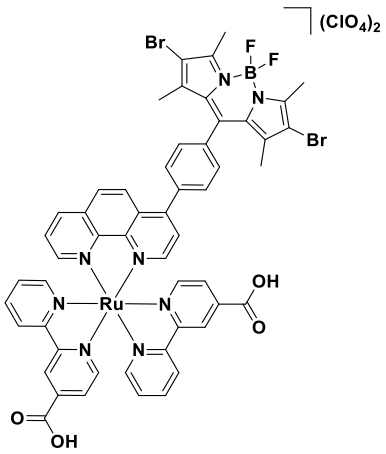

3.25

Figure 126. Dual emissive ruthenium complex with two unsymmetric polypyridyl ligands.[78]

Complex **3.25** manifests one high-energy emission and one low-energy emission band. The band at higher energies (originating from the BODIPY chromophore) is not sensitive to oxygen while the low-energy band is. Interestingly, when the measurements were repeated in aqueous solvents, the BODIPY emission band is quenched and the ruthenium emission band redshifted. The authors were not able to account for the mechanism of this process, but suggested solvent promoted inter-system crossing or energy/electron transfer as possible explanations. This phenomenon is another example of the influence the local environment can exert on the properties of triplet photosensitisers.

3.1.2 Unsymmetric Iridium Complexes

While the discussion so far has dealt with ruthenium complexes bearing mono-substituted polypyridyl ligands, the series of iridium triplet photosensitisers previously designed by the Draper group warrant revisiting. They represent one of the few examples of unsymmetric transition metal complexes bearing two different substituents on the same polypyridyl ligand.[50]

The publication by Lu *et al.* describes the synthesis of iridium triplet photosensitisers with 3,8-substituted phenanthroline ligands (**Figure 127.**) for triplet-triplet annihilation upconversion (TTA-UC).[50]

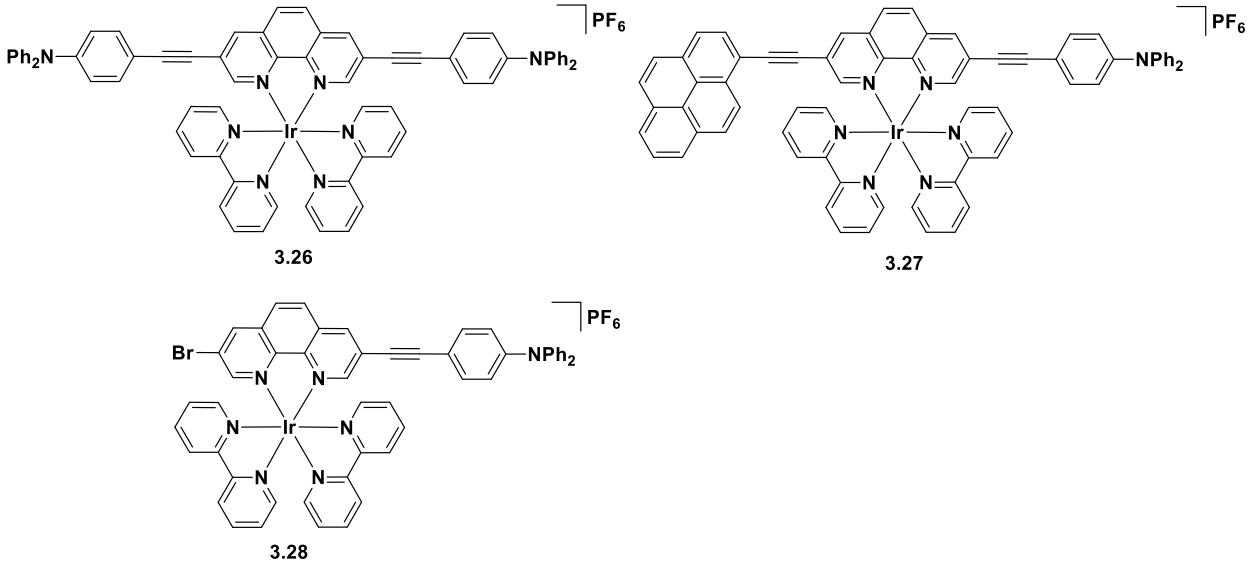

Figure 127. Iridium triplet photosensitisers for TTA-UC bearing unsymmetrical phenanthroline ligands.[50]

These systems present an excellent opportunity to compare the effects of symmetric and unsymmetric substitution on the same ligand. The absorption spectra of all three compounds are similar, with the exception of the molar extinction coefficient for **3.28** being halved compared to those of the other two iridium complexes. This is due to the lack of a second photon-harvesting moiety in complex **3.28**.

The emission spectra of the compounds indicate significant differences in behaviour between complexes **3.27** and **3.26**. The emission band for **3.26** is broad and featureless, typical of iridium ^{3}MLCT excited states; meanwhile, the emission spectrum for **3.27** is significantly sharper and manifests more structures, suggesting a ligand-centred (LC) emissive state with low charge-transfer character. The emission lifetimes of the complexes also differ significantly, with the unsymmetric complex having a lifetime 40 times longer than the symmetric complex (40 μs vs 1 μs). This longer lifetime results in a significantly enhanced performance for **3.27** as a triplet-triplet upconverter, at the time recording the highest reported upconversion quantum yield at 28.1 %.

However, despite this improved performance of complex **3.27** over **3.26**, their work also highlights the significant drawbacks researchers currently face when investigating unsymmetric transition metal complexes. The synthetic approach to the complexes is arduous – the authors were unsuccessful in synthesising the free ligand in quantities large enough to carry out complexation. Instead, they were forced to resort to 'on the complex' synthesis, were the dibrominated phenanthroline is complexed to the metal centre prior to the Sonogashira coupling reaction with the respective alkyne units. In fact, the unsymmetric complex resulted from the incidental purification of the mono-substituted complex. It was not initially a synthetic target.

Consequently, while this publication serves as an excellent proof-of-concept for the potential of unsymmetrically substituted polypyridyl complexes, significant challenges remain before unsymmetric complexes become can more mainstream. A universal synthetic approach that is versatile, tolerant of a high

number of functional groups and allows for simpler purification methods is required to fully explore the properties of unsymmetrical triplet photosensitisers.

3.1.3 Improving Synthetic Access

The approach pioneered by McGarrigle and co-workers outlines a novel avenue to unsymmetric bipyridines via pyridylsulfonium salts (**Scheme 17**).[106,107] It offers significant functional group tolerance, allowing for the synthesis of a large variety of unsymmetric ligands. In their publication the McGarrigle group does not itself investigate the photophysical properties of these compounds, nor complex them to transition metal centres, they do acknowledge the potential of this synthesis for such an application.

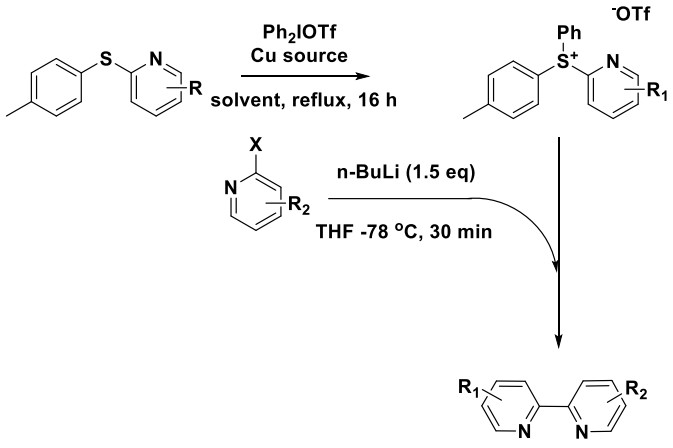

Scheme 17. Synthesis of unsymmetric bipyridines via pyridylsulfonium salts.[107]

It is important to note that the addition of the R_1 and R_2 functional groups does involve the use of palladium-catalysed coupling reactions, but it crucially occurs before the formation of the bipyridine core, significantly simplifying synthesis.

While a wide range of mono-substituted triplet photosensitisers based on ruthenium and iridium metal centres has been reported in literature, few examples of Donor-Polypyridyl-Acceptor complexes exist.[50] Those that are reported manifest interesting and non-typical optical properties, but suffer from cumbersome, low-yielding and expensive synthetic pathways. Clearly, significant opportunities remain to develop methods for creating a family of readily accessible ruthenium complexes bearing unsymmetrical bipyridine ligands. Furthermore, it has not yet been established whether the structure-property relationships of symmetric triplet photosensitisers mirror those of unsymmetric triplet photosensitisers. For example, while the effects of increased conjugation of symmetric ruthenium complexes is well-documented to result in increased absorption and emission wavelengths, no such studies are reported for unsymmetric structures. In general, the properties of unsymmetric complexes are only compared to their symmetric counterparts, rather than to other unsymmetric photosensitisers.[103]

3.2 Aims

Research will be aimed at generating a family of ruthenium complexes bearing unsymmetric bipyridine ligands and investigate their photophysical properties. The synthetic route will be designed with ease of use and versatility in mind, with ligands generated off-complex and their photophysical properties examined prior to complexation. It should then be possible to determine the effects of unsymmetric increases in conjugation on the photophysical properties.

3.3 Synthesis and Characterisation

3.3.1 Ligand Synthesis

This project aims to synthesise a series of novel transition metal complexes bearing unsymmetrically substituted bipyridine ligands and to investigate their photophysical properties. The ligands have varying degrees of conjugation between the donor, bipyridyl core and acceptor unit, which should affect photophysical properties such as absorption and emission wavelength, emission lifetime and quantum yields (both of luminescence and singlet oxygen). The ligands are designed to undergo charge-transfer transitions, with the electron-rich triphenylamine donating electron density into the electron-poor trifluorotoluene ring. When complexed to a metal centre, this configuration should result in a ^{3}ILCT excited state, with low energy absorption and emission wavelengths, long emission lifetime and high singlet oxygen quantum yields.

The project was completed in collaboration with Dr. Alexandra Horan and Prof. Eoghan McGarrigle of University College Dublin. The Ligands **L1**, **L2** and **L3** (**Scheme 18**) were synthesised by Dr. Horan at UCD using the synthetic approach pioneered in their 2020 publication.[107] All characterisation, including NMR, Mass spectrometry and elemental analysis of the ligands was also completed at UCD and will not be discussed in this chapter. Full synthesis and characterisation of the compounds is detailed in the experimental section.

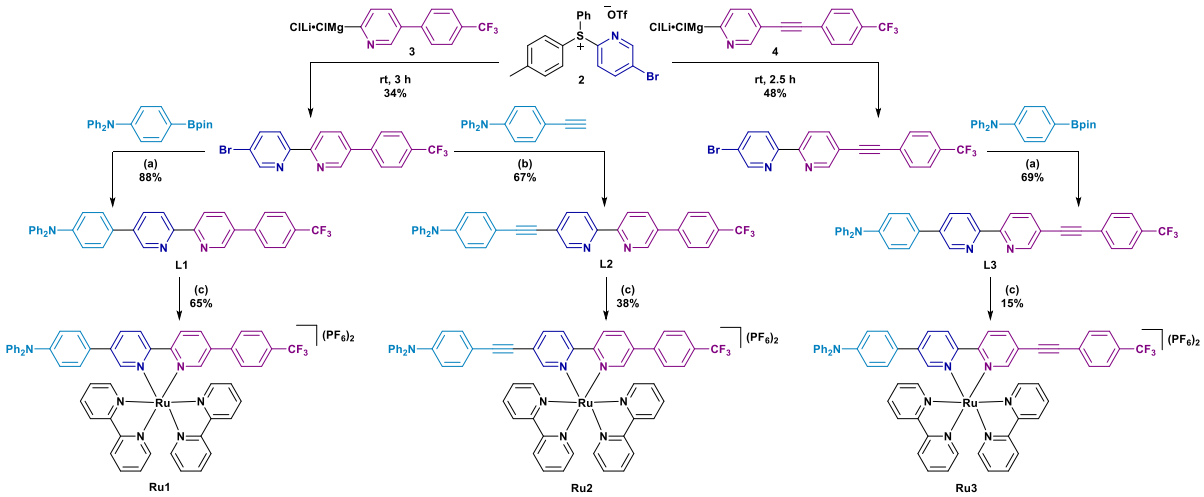

Scheme 18. Synthetic pathway to ligands **L1-3** and complexes **Ru1-3** [a: Amine (1.2 equiv.), $Pd(PPh_3)_4$ (3 mol%), K_2CO_3 (3.0 equiv.) THF:H_2O (2:1), 80 °C, 22 h], [b: Amine (1.2 equiv.) $Pd(PPh_3)_4$ (3 mol%) CuI (3 mol%) Et_3N:toluene (3:1), 80 °C, 5 h], [c: $Ru(bpy)_2Cl_2$ (0.9 equiv.), ethylene glycol, 140 °C, 16 h].

3.3.2 Synthesis of Ru1, Ru2, Ru3 and Ir1

The synthesis of the ruthenium complexes **R1**, **R2** and **R3** (**Figure 128**) was completed under the standard conditions detailed in previous chapters.[40]

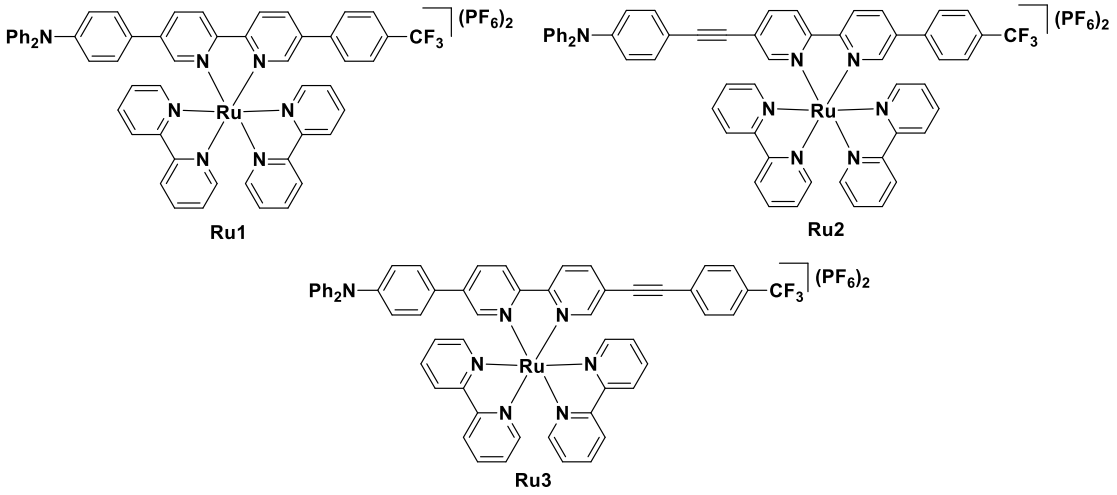

Figure 128. Structure of **Ru1**, **Ru2** and **Ru3.**

The ligands were refluxed with $[Ru(bpy)_2Cl_2(PF_6)_2]$ in ethylene glycol under an argon atmosphere for 16 hours. The complex was then precipitated using saturated aqueous KPF_6 and isolated by filtration, before being purified by flash column chromatography using silica as the stationary phase and a 90:9:1 mixture of MeCN, H_2O and sat. aq. KNO_3.

The yields of the reactions different significantly, with the synthesis of complex **R1** resulting in a yield of 56 %, while those of **R2** and **R3** were reduced. This is noteworthy given the structural similarities between the

three complexes. A potential explanation lies in the alkyne linkers of **Ru2** and **Ru3** resulting in a larger ionic radius, which in turn could influence the interactions of each complex with the silica stationary phase. Sufficient material was recovered from all three complexation reactions to proceed to photophysical analysis.

Additionally, significant amounts of **L1** remained following successful synthesis of **Ru1**, which was used to synthesise **Ir1** by reflux with $[Ir(ppy)_2Cl]_2$ in $CHCl_3$ overnight (**Scheme 19**). The obtained quantities of **L2** and **L3** were fully consumed by the preparation of their respective ruthenium complexes, so direct comparisons between iridium complexes were not possible. However, it is still worth investigating how significantly the change of metal centre will affect observed photophysical properties. The results can then be compared to those in Chapters 1 and 2, where symmetric bipyridine units were complexed to ruthenium and iridium.

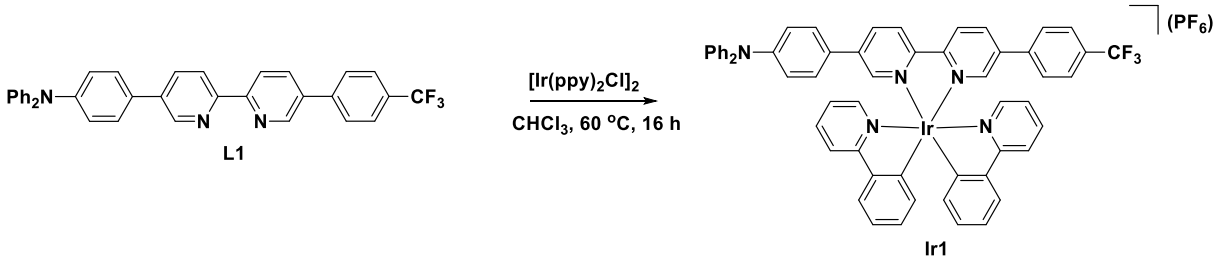

Scheme 19. Synthesis of **Ir1** from **L1.**

3.3.3 Structural Characterisation of Ru1, Ru2, Ru3 and Ir1

The synthesis of the four metal complexes was confirmed by mass spectrometry and the characterisation completed using multinuclear and 2D NMR spectroscopy. The unsymmetrical nature of the bipyridine ligand resulted in a reduction of the equivalency seen in previously analysed ruthenium complexes.

The ^{1}H NMR spectrum of **Ru1** is displayed below in **Figure 129.**

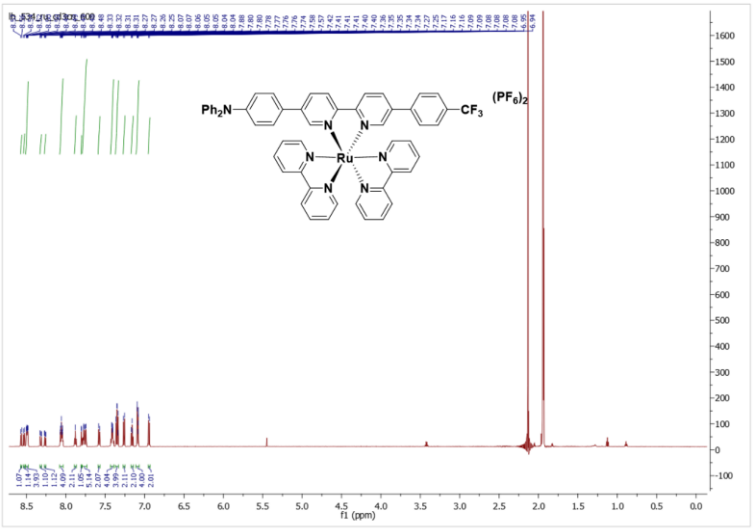

Figure 129. ^{1}H NMR Spectrum of **Ru1** (MeCN-d_3, 600 MHz, 298 K).

Despite the low symmetry of the complex structure, the NMR spectrum contains clearly resolved peaks between 6.8 and 8.6 ppm. Using 2D HH COSY NMR spectra it is possible to identify the separate spin systems in the overall complex. This is particularly useful since the spin systems present in the complex are very isolated, allowing for the assignment of a proton signal to a specific ring system. A TOCSY spectrum of **Ru1** is found in **Figure 130,** with coloured dots identifying the individual spin systems.

The spectator pyridine ring systems can be easily assigned (black), as they have the largest number of individual signals in the system and all integrate to one proton. They are not equivalent due to through-space effects originating from the trifluorotoluene and triphenylamine signals. This means the number of spectator ligand signals is increased compared to other ruthenium complexes presented in this thesis.

The spin systems of the distal triphenylamine rings are also easy to assign by integration and multiplicity (red). They can be seen in a classical two triplet and one doublet, with one triplet integrating to 2 and the other two signals integrating to 4. The remaining spin systems are the trifluorotoluene ring signal, the proximal triphenylamine signal and the pyridine rings of the substituted ligand. The latter rings manifest three signals each, integrating to one, shown in blue. The two remaining phenyl rings display two signals each, integrating to two, shown in yellow.

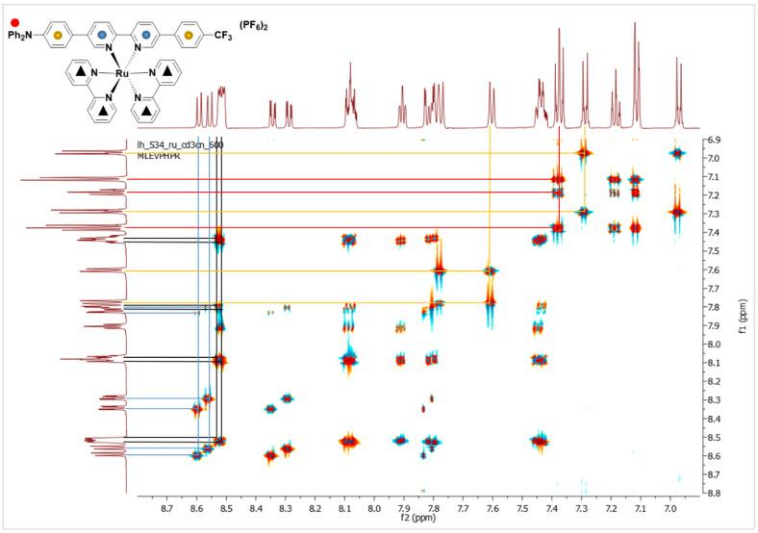

Figure 130. HH COSY NMR Spectrum of **Ru1** with assigned spin systems (MeCN-d_3, 600 MHz, 298 K).

It is currently not possible to fully assign the remaining spin systems solely relying on the TOCSY, as they are identical in terms of the number of signals, their multiplicity and their integration.

The ^{13}C NMR for **Ru1**, displayed in **Figure 131**, contains many peaks, with significant variation in the intensity of the signals. The peaks cluster very closely together, indicating that some carbon atoms are in very similar electronic environments, differing only by the effects of the trifluorotoluene and triphenylamine moieties. As ^{19}F is an NMR-active nucleus with a spin of ½, we observe splitting of the adjacent carbon signals into quartets. The carbon directly bonded to the fluorine atoms displays such low intensity that it is difficult to distinguish from the baseline, faintly visible as a series of peaks between 122 and 126 ppm. The α-carbon is still low in intensity but can be clearly seen as a quartet centred around 130 ppm. The β-carbon is more readily visible as a quartet at 126 ppm.

A)

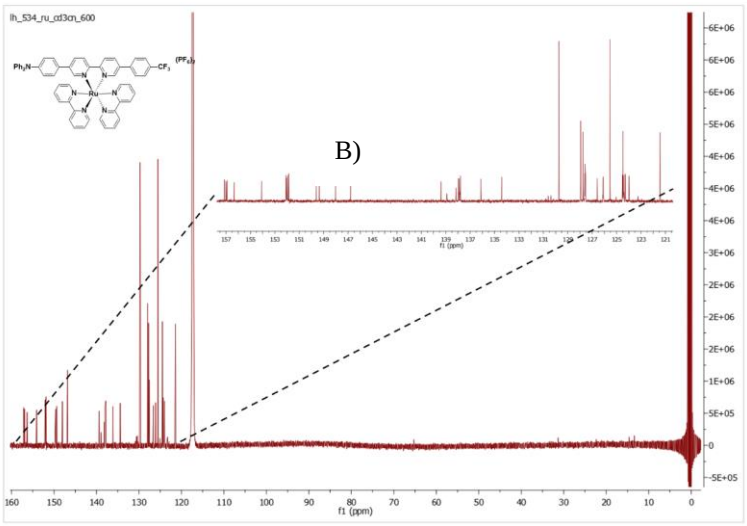

Figure 131. ^{13}C NMR Spectrum of **Ru1** with inset highlighting 125-157 ppm (MeCN-d_3, 150 MHz, 298 K).

Applying HSQC and HMBC 2D NMR experiments (**Figure 132 (A)** and **(B)** respectively) it is now possible to distinguish the proton signals on the trifluorotoluene ring. The β-carbon is directly bonded to a proton, which is easily identified using HMBC as the β-proton; the HSQC indicates interactions between the α-carbon and the γ-proton signal, while very weak interactions can be observed between the α-proton and the carbon bonded directly to the fluorine atoms.

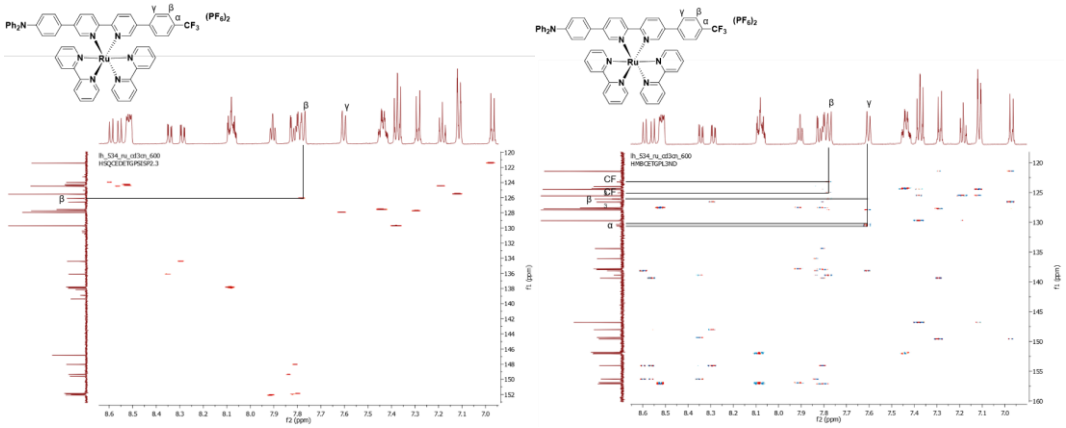

Figure 132. (A) HSQC NMR spectrum of **Ru1**, showing the correlation between the β-carbon and the β-proton. γ-proton signal subsequently assigned using the TOCSY (MeCN-d_3, 150 MHz, 298 K). (B) HMBC NMR spectrum of **Ru1**, displaying through-bond interactions of the α, β and γ proton and carbon signals. (MeCN-d_3, 150 MHz, 298 K).

Using further 2D NMR spectroscopy it was then possible to assign the ring signals on the substituted bipyridine, as shown in **Figure 133**.

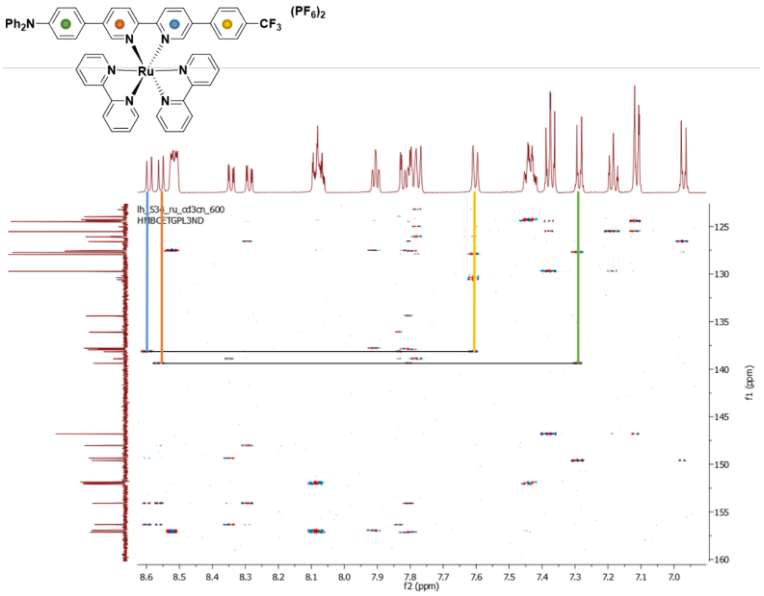

Figure 133. HMBC NMR Spectrum of **Ru1**, revealing through-bond interactions between carbons and protons across spin systems (MeCN-d_3, 150 MHz, 298 K).

This finally allows for the complete assignment of the spin systems in the **Ru1** NMR spectrum, shown in **Figure 134.**

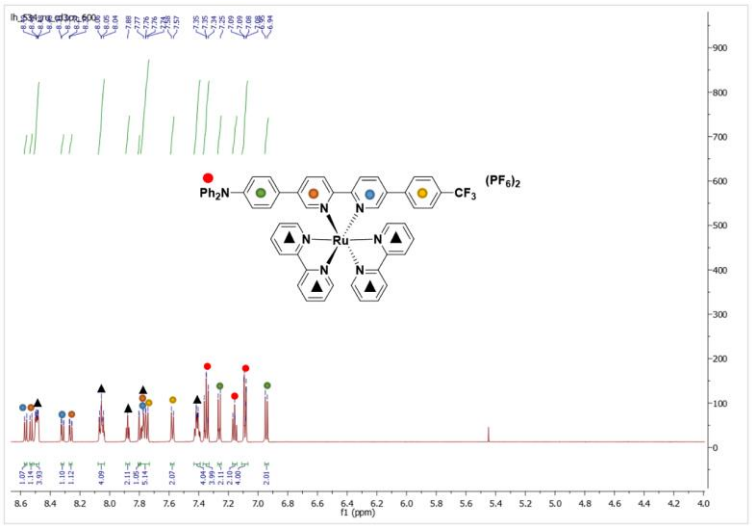

Figure 134. ^{1}H spectrum NMR of **Ru1** with spin systems assigned (MeCN-d_3, 150 MHz, 298 K).

The NMR spectra of complexes **Ru2** and **Ru3** are functionally identical to the spectrum of **Ru1**, as there is no change in the number or multiplicities of any proton signals. However, the presence of the acetylene linker either on the donor- or acceptor side of the bipyridine rings does affect the shift of nearby proton signals.

For **Ru2**, the assignment of the spin systems was completed in a manner identical to **Ru1**, and the results can be seen in **Figure 135.**

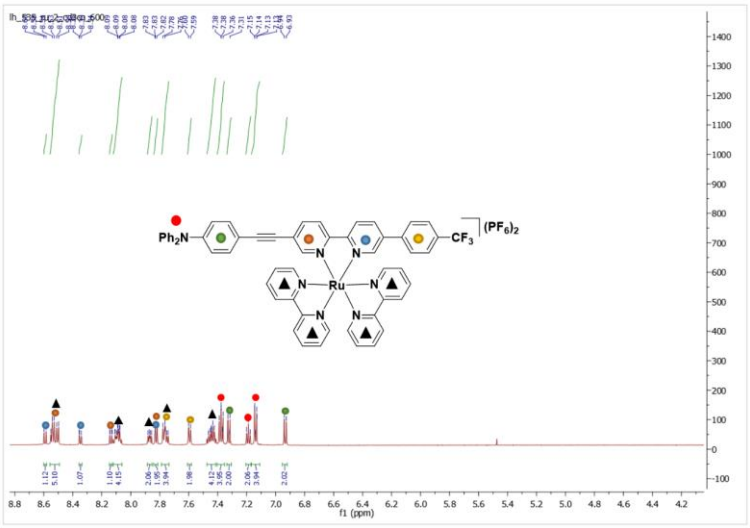

Figure 135. ^{1}H NMR spectrum of **Ru2** between 4 and 9 ppm, with spin systems assigned (MeCN-d_3, 600 MHz, 298 K).

Overlaying the NMR spectra of complex **Ru1** with **Ru2** (**Figure 136**) makes it possible to determine the effects of increased conjugation on the shift of individual proton signals. The greatest shift is observed in those spin systems closest to the acetylene moiety, notably the pyridine ring and the proximal triphenylamine ring. Interestingly, one of the signals on the pyridine ring is much more strongly affected than the others, indicating that the acetylene linker does not affect all the protons in the ring systems to the same degree.

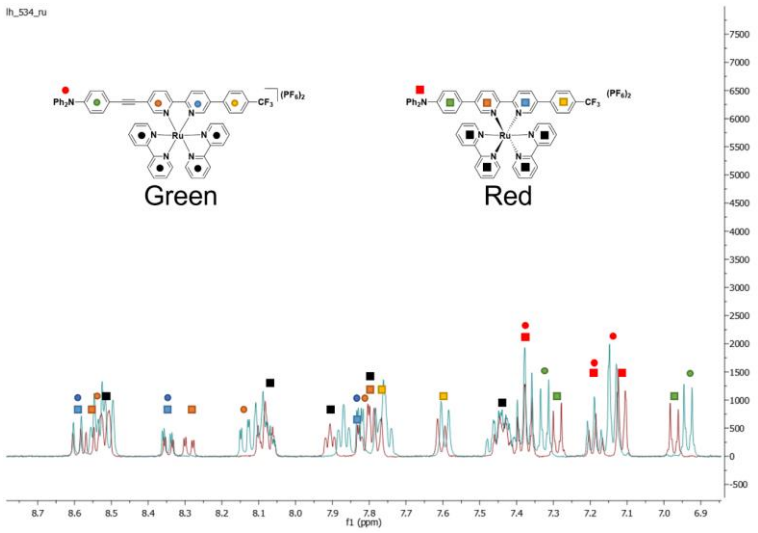

Figure 136. Overlay of the ^{1}H NMR spectra of **Ru1** (Red) and **Ru2** (Green) between 7 and 9 ppm (MeCN-d_3, 400 MHz, 298 K).

The same analysis was performed for complex **Ru3**, with its ^{1}H NMR spectrum displayed in **Figure 137.**

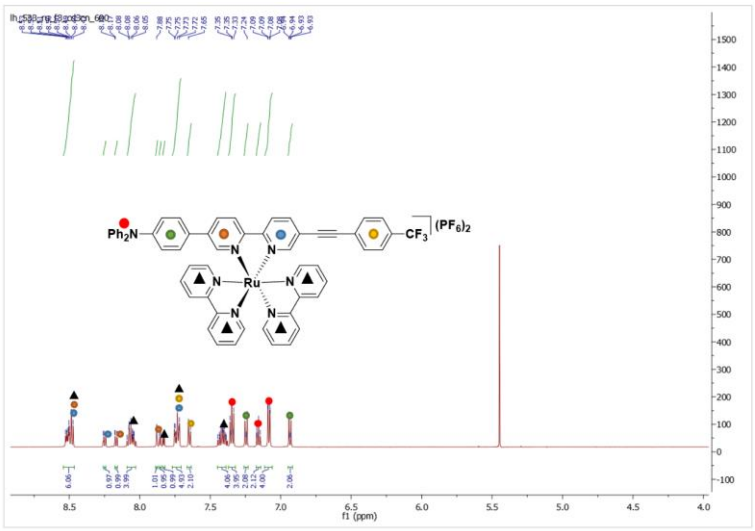

Figure 137. ^{1}H NMR spectrum of **Ru3** between 4 and 9 ppm with spin systems assigned (MeCN-d_3, 600 MHz, 298 K).

Again, no significant changes are immediately observed when comparing the **Ru3** spectrum with that of complex **Ru1**, except for increased signal overlap in the former. This can make an immediate identification of the signals difficult but using TOCSY experiments it remains relatively facile to track the spin systems through the overlap. Interestingly, the increased conjugation of the trifluorotoluene via the acetylene does not lead to a general deshielding of the complex. Additionally, a reversal in the trend of pyridine signals is found – for complexes **Ru1** and **Ru2**, the proton signals of the pyridine ring proximal to the trifluorotoluene are more deshielded than on the other pyridine ring. In the case of **Ru3**, this trend is reversed for the most upfield pyridyl proton signal. The overlayed proton spectra can be seen in **Figure 138.**

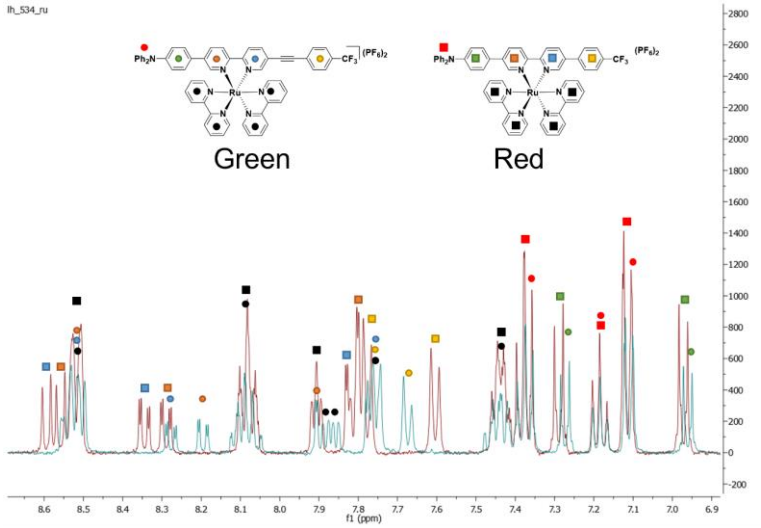

Figure 138. Overlay of the ^{1}H NMR spectra of **Ru1** (Red) and **Ru3** (Green) between 7 and 9 ppm (MeCN-d_3, 400 MHz, 298 K).

Besides the appearance of the acetylene signal peaks at 98.67 and 84.51 ppm for **Ru2**; 95.21 and 87.14 ppm for **Ru3**, no major differences are observed in the ^{13}C NMR spectra between the three complexes.

The NMR spectrum of **Ir1** is displayed below in **Figure 139**. Due to the inherent lack of equivalency common to iridium complexes with phenylpyridine spectator ligands the number of signals is not increased compared to previously analysed iridium complexes. Solvent residues can be observed at 7.59 and 7.20 ppm ($CHCl_3$ and Toluene respectively), but do not interfere with the assignment of the signals. There is significant overlap between the phenylpyridine signals and those of the active ligand, but TOCYS and HSQC allow for resolution of all signals.

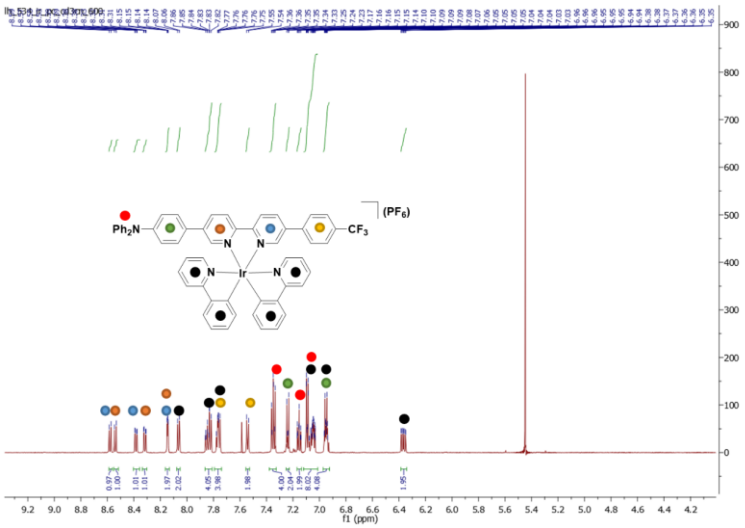

Figure 139. ^{1}H NMR spectrum of **Ir1** with spin systems assigned.

In summary, the systematic analysis of the NMR spectra of complexes **Ru1**, **Ru2**, and **Ru3** provide some insight into the electronic changes occurring due to the presence and position of the acetylene linker. Both **Ru2** and **Ru3** manifest unexpected changes in their NMR spectra which suggest that the addition of the acetylene linker influences the electron density on parts of the ligand, specifically around the pyridine rings. Further UV-Vis and emission spectroscopy may provide a deeper insight into the changes to electronic energy levels.

3.3.4 Crystallographic Analysis

3.3.4.1 Crystallographic Analysis of Ru1

Crystals of complex **Ru1** suitable for single-crystal x-ray diffraction were grown by the slow evaporation of a CH_2Cl_2/Toluene solution. Consequently, disordered toluene is present in the crystal structure. Data collection and refinement was conducted by Dr. Brendan Twamley at Trinity College Dublin.

A specimen of $C_{58.38}H_{44.50}Cl_{1.50}F_{15}N_7P_2Ru$, approximate dimensions 0.032 mm x 0.093 mm x 0.227 mm, was used for the X-ray crystallographic analysis. The X-ray intensity data were measured (λ = 1.54178 Å) on a Bruker Apex Kappa Duo with an Oxford Cobra Cryosystem low temperature device using a MiTeGen micromount. Using the OLEX2 Software Package, the structure was solved with the SHELXT structure solution program using Intrinsic Phasing and refined with the SHELXL refinement package with Least Squares minimisation, using the space group $P\bar{1}$, with Z = 4 for the formula unit, $C_{58.38}H_{44.50}Cl_{1.50}F_{15}N_7P_2Ru$.

The final anisotropic full-matrix least-squares refinement on F^2 with 1625 variables converged at R1 =

14.97%, for the observed data and wR2 = 49.95% for all data. The goodness-of-fit was 1.092. The structure of **Ru1** is shown in **Figure 140**.

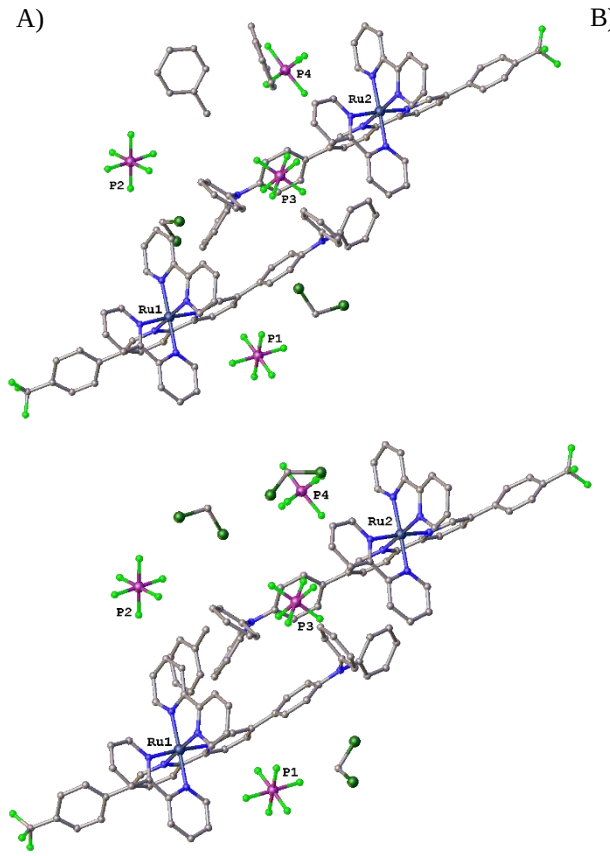

Figure 140. Individual representations of each disordered moiety in the **Ru1** crystal with (A) the majority occupied moiety (phenyl/CF_3 71 and 69%, toluene 0.25% occupied and CH_2Cl_2, 50% occupied) and (B) minor occupied moiety (phenyl/CF_3 29 and 31%, toluene 0.25% occupied and CH_2Cl_2, 25% occupied).

The high degree of disorder in the crystal makes analysis difficult, but some structural features still become quickly apparent. In both formats the complexes adopt a typical distorted octahedral structure, with the triphenylamine groups aligning themselves face-to-face. The twist between the pyridine and the trifluorotoluene ring is more pronounced than the twist between the other pyridine and the proximal NPh_3 phenyl ring.

The crystal packing of **Ru1** is displayed in **Figure 141**. The image indicates that the trifluorotoluene rings of separate molecules align themselves face-to-face, resulting in a repeating pattern with significant void space between the complexes filled by solvent and counterion molecules.

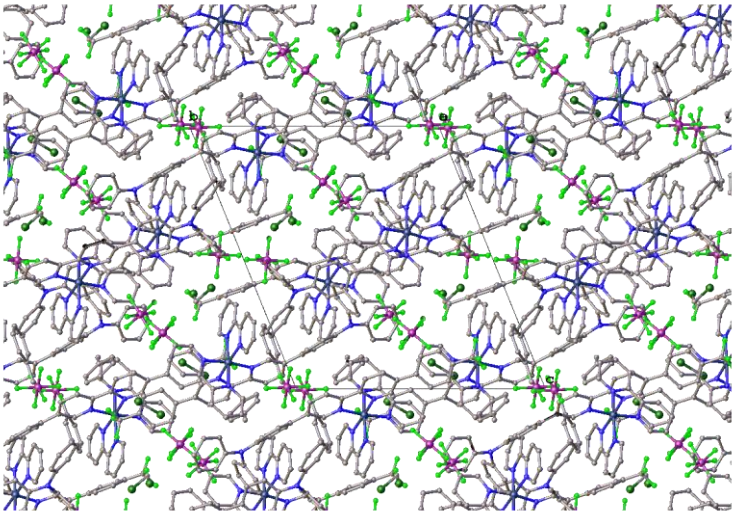

Figure 141. Schematic packing diagram of the major occupied moieties in the **Ru1** crystal sample only viewed normal to the a-axis, with hydrogen atoms omitted for clarity.

3.3.4.2 Crystallographic Analysis of Ru2

Crystals of **Ru2** suitable for single-crystal x-ray diffraction were obtained by the slow diffusion of a concentrated solution of the complex in CH_2Cl_2 into toluene. Consequently, disordered toluene was detected in the packing lattice (removed for clarity in Error! Reference source not found.). Data collection and refinement was conducted by Dr. Brendan Twamley at Trinity College Dublin.

A specimen of $C_{57}H_{40}F_{15}N_7P_2Ru$, approximate dimensions 0.031 mm x 0.034 mm x 0.219 mm, was used for the X-ray crystallographic analysis. Using the OLEX2 Software Package, the structure was solved with the SHELXT structure solution program using Intrinsic Phasing and refined with the SHELXL refinement package with Least Squares minimisation, using the space group C2/c, with Z = 8 for the formula unit, $C_{57}H_{40}F_{15}N_7P_2Ru$. The final anisotropic full-matrix least-squares refinement on F^2 with 937 variables converged at R1 = 9.01%, for the observed data and wR2 = 29.35% for all data. The goodness-of-fit was 1.036.

Figure 142A shows that the phenyl ring linked to the substituted bipyridine by the acetylene appears to be functionally coplanar with the chelated bipyridines. On the other hand, the phenyl ring of the trifluorotoluene moiety is twisted at an angle of 48.6^o w.r.t the adjacent bipyridine ring (**Figure 142B**). This represents the same behaviour observed for the **Ru1** crystal sample.

A)

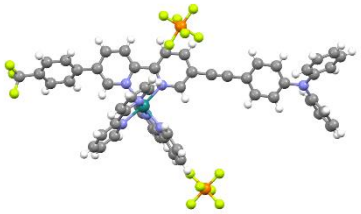

B)

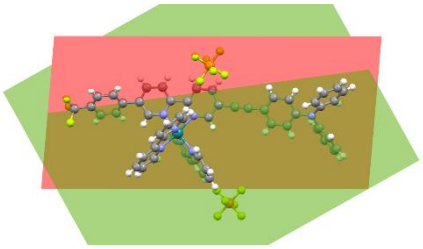

Figure 142. (A) Crystal Structure of **Ru2** (thermal ellipsoids shown at 50% probability) (B) demonstration of the ring twist of the trifluorotoluene phenyl unit w.r.t the adjacent pyridine ring.

The packing structure for **Ru2** is displayed in **Figure 143.** It shows significant differences to that of **Ru1**, indicating that the small structural changes can have significant impact on the spatial arrangement of the ruthenium complexes.

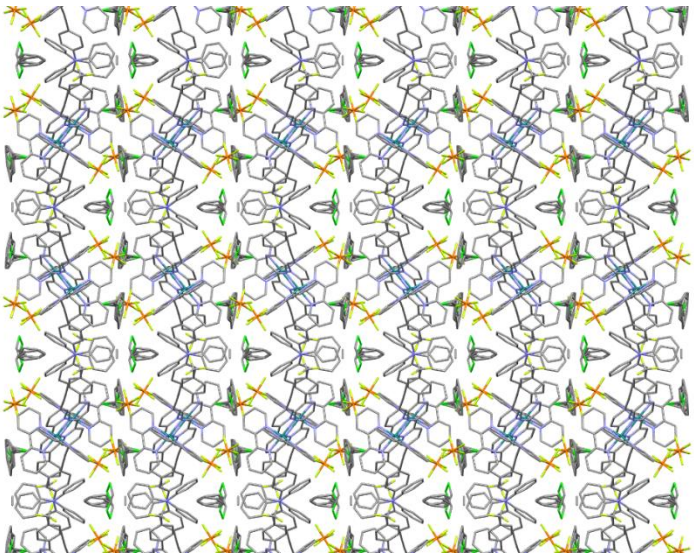

Figure 143. A 3x3x3 crystal packing structure of **Ru2** viewed along the b-axis. Capped stick representation was chosen for visual clarity. Note toluene and CH_2Cl_2 solvent molecules between the layers of **Ru2.**

3.3.4.3 Crystallographic Analysis of Ir1

Crystals of **Ir1** suitable for single-crystal x-ray diffraction were obtained from the slow evaporation of CH_2Cl_2 and hexane. Data collection and refinement was conducted by Dr. Brendan Twamley at Trinity College Dublin.

A specimen of $C_{57}H_{40}F_9IrN_5P$, approximate dimensions 0.025 mm x 0.043 mm x 0.135 mm, was used for the X-ray crystallographic analysis. The X-ray intensity data were measured (λ = 1.54178 Å) on a Bruker Apex Kappa Duo with an Oxford Cobra Cryosystem low temperature device using a MiTeGen micromount. Using the OLEX2 Software Package, the structure was solved with the SHELXT structure solution program using Intrinsic Phasing and refined with the SHELXL refinement package with Least Squares minimisation, using the space group $P2_1/c$, with Z = 4 for the formula unit, $C_{57}H_{40}F_9IrN_5P$. The final anisotropic full-matrix least-squares refinement on F^2 with 678 variables converged at R1 = 6.64%, for the observed data and wR2 = 17.96% for all data. The goodness-of-fit was 1.070.

The crystal structure of two disordered moieties within the sample are displayed in **Figure 144** A and B. The crystal shows the same distorted octahedral geometry adopted by the iridium metal centre that is observed in the ruthenium crystal samples. The arrangement of the nitrogen atoms in the spectator phenylpyridine ligands is *trans*, as this is the most thermodynamically stable isomer the complex can adopt.[43]

The crystal exhibits a less distinct difference in the twist angle between the bipyridine rings and the neighbouring phenyl/trifluorotoluene rings than is observed in the equivalent ruthenium sample.

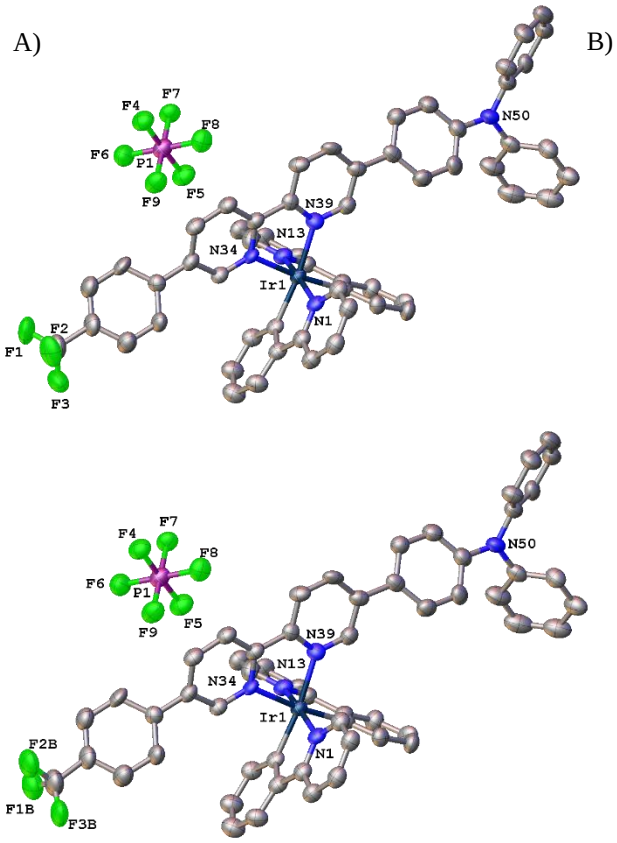

Figure 144. Individual images of each disordered moiety in the **Ir1** crystal sample with (A) 70% occupied and (B) 30% occupied. Atomic displacement shown at 50% probability and heteroatoms labelled only with hydrogen atoms omitted for clarity.

The crystal lattice structure of the **Ir1** crystal sample can be found in **Figure 145**.

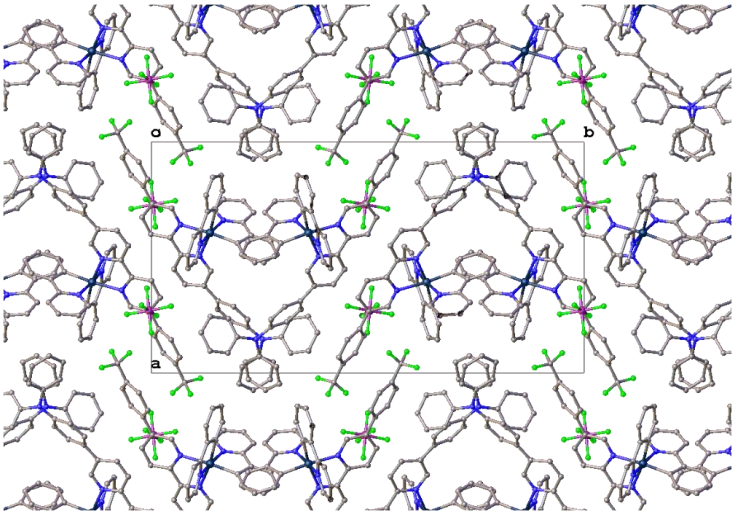

Figure 145. Schematic packing diagram of the major occupied moiety in the **Ir1** crystal sample viewed normal to the c-axis with hydrogen atoms omitted.

The crystal lattice exhibits significant differences to that of the ruthenium crystals. In the Ir1 crystal, there is significant spatial overlap between the NPh_2 groups of neighbouring metal complexes. Additional overlap between the phenyl rings of one of the spectator phenylpyridine ligands results in spatially isolated pairs of complexes. The trifluorotoluene rings of different pairs to appear to adopt a quasi-face-to-face arrangement, although there is a significant distance between the rings.

3.4 Photophysical Analysis

3.4.1 Spectroscopic Analysis of L1, L2 and L3

3.4.1.1 Solvatochromic Absorption and Emission of **L1**, **L2** and **L3**

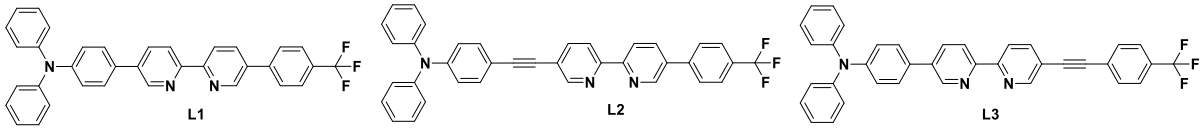

Solvatochromic absorption and emission studies were performed on **L1**, **L2** and **L3** to help probe the nature of their electronic states. The results of these studies for **L1** are displayed in **Figure 146**.

The absorption spectrum comprises two main bands, one at 380 nm and another at 300. The higher energy transitions are likely due to $\pi - \pi^*$ and $n - \pi^*$ transitions. The lower energy absorption band is typical of CT transitions involving triphenylamine groups. The solvents have no significant effects on absorption wavelength or intensity.

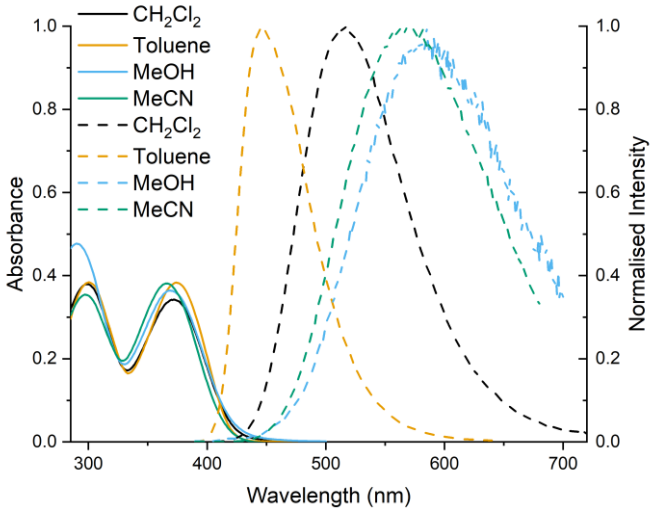

Figure 146. Solvatochromic studies of **L1** in Toluene, CH_2Cl_2, MeCN and MeOH; UV-vis spectra shown with solid lines and normalised emission spectra shown with dotted lines (λ_{ex} = 370 nm), [10^{-5} M], 298 K.

The emission spectrum displays the results expected when performing solvatochromic emission studies on charge-transfer compounds. Toluene, the least polar of the solvents, manifests the highest energy emission wavelength and the narrowest emission band, with CH_2Cl_2, MeCN and MeOH successively showing lower and lower emission wavelength and continuously broadening emission bands. The emission wavelength is 450 nm in toluene, 520 nm in CH_2Cl_2, 570 nm in MeCN and 586 nm in MeOH. The emission intensity, normalised in **Figure 146**, drops markedly with increasing solvent polarity, as evidenced by the reduced signal-to-noise ratio in MeCN and MeOH. This reflects the band gap law, by which lower HOMO-LUMO gaps have greater access to more nonradiative decay pathways, e.g., vibrotational coupling, than higher energy gaps.

In charge-transfer excited states, the shifting of electron density from the electron-rich HOMO into the electron-poor LUMO induces a significant dipole. Polar solvent molecules, possessing their own dipole moment, can stabilise the charge-transfer excited state by spatially rearranging themselves. This results in a reduction of the HOMO-LUMO gap upon excited state population, resulting in a significant Stoke's shift and a longer emission wavelength in polar solvents. As this trend is observed in **L1**, the excited state likely has a large degree of CT character.

The solvatochromic emission studies for **L2** are exhibited in **Figure 147**. They display the same trends as **L1**, but generally shifted to longer wavelengths.

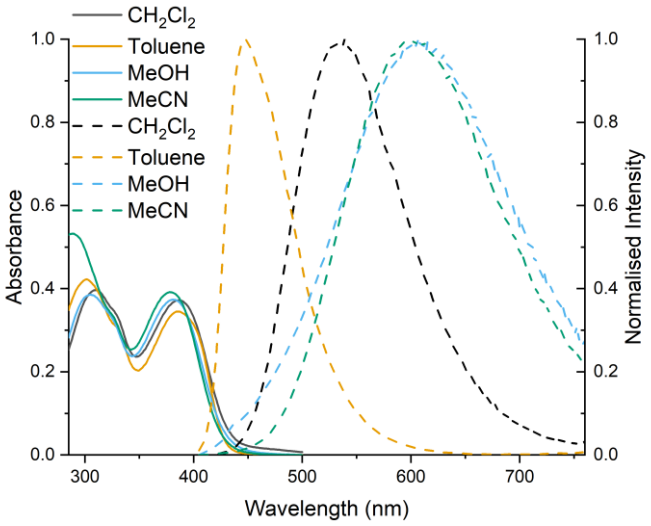

Figure 147. Solvatochromic studies of **L2** in Toluene, CH_2Cl_2, MeCN and MeOH; UV-vis spectra shown with solid lines and normalised emission spectra shown with dotted lines (λ_{ex} = 385 nm), [10^{-5} M], 298 K.

The absorption bands are shifted to higher energies due to the increased conjugation of the acetylene linker. There are indications of a slight hypsochromic shift in absorption wavelength in MeCN compared to CH_2Cl_2, suggesting that the ground state may be sensitive to solvent. The emission wavelength is 450 nm in toluene, 540 nm in CH_2Cl_2, 600 nm in MeCN and 613 nm in MeOH.

The solvatochromic absorption and emission spectrum of **L3** is displayed in **Figure 148.**

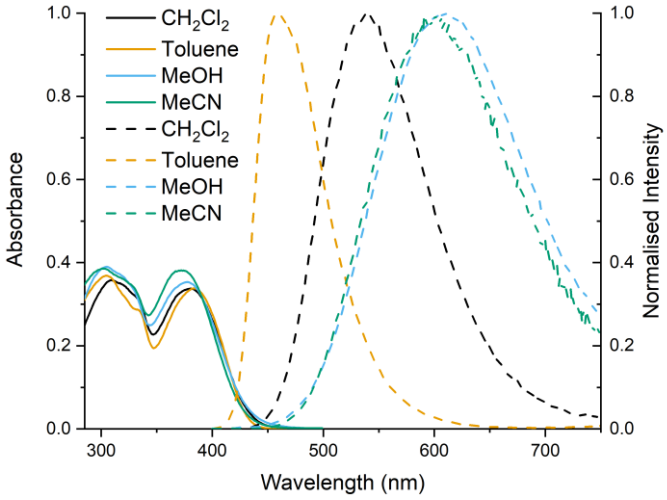

Figure 148. Solvatochromic studies of **L3** in Toluene, CH_2Cl_2, MeCN and MeOH; UV-vis spectra shown with solid lines and normalised emission spectra shown with dotted lines (λ_{ex} = 380 nm), [10^{-5} M], 298 K.

The results of the solvatochromic studies on **L3** are almost identical to those of **L2**, with the shift between the CH_2Cl_2 and MeCN absorption more pronounced in **L3** than **L2**. A direct comparison of the shifts between **L2** and **L3** is shown in **Figure 149**. While the more polar solvents have the same emission wavelength, the emission of **L2** in Toluene is 450 nm compared to 460 nm in **L3**.

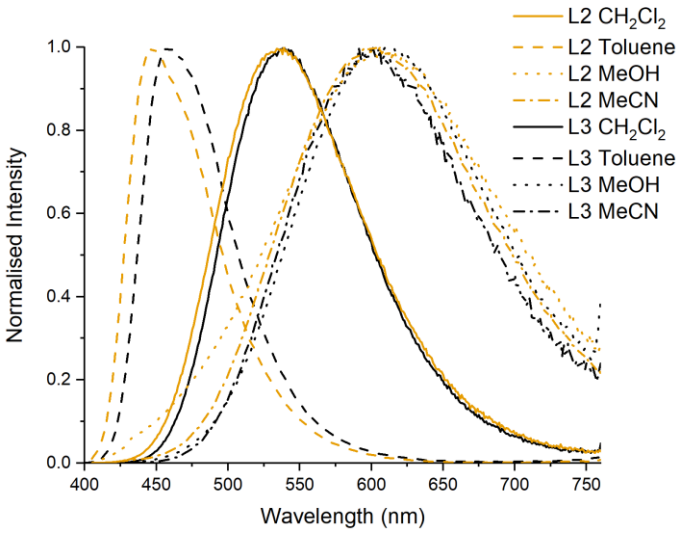

Figure 149. Comparison of solvatochromic studies of **L2** and **L3** in Toluene, CH_2Cl_2, MeCN and MeOH (λ_{ex} = 385 nm for **L2**, 380 nm for **L3**), [10^{-5} M], 298 K.

While this does not present a large difference, it is the first significant divergence in the photophysical properties of **L2** and **L3**. The increased conjugation to the electron-withdrawing trifluorotoluene moiety resulted in a reduction in emission energy. It is not immediately clear why this disparity only occurs in toluene. It may be that the variations in excited state dipole between **L2** and **L3** leads to different degrees of stabilisation in the polar solvents, coincidentally yielding the same emission wavelength despite the 'original', non-stabilised energies of the excited states being different.

The molar extinction coefficients of **L1**, **L2** and **L3** are reported below in **Table 9**. They indicate that enhancing the conjugation of the donor group to the bipyridine core leads to a marginal increase in the absorption of the CT transition.

Table 9. Molar extinction coefficients for L1, L2 and L3 (CH_2Cl_2, 10^{-5} M, 298 K).

Compound	Wavelength (nm)	ε (L mol^{-1} cm^{-1})
L1	375	34100
L2	385	36800
L3	380	33700

3.4.1.2 Comparison of Absorption and Emission Properties of **L1**, **L2** and **L3**

L1, **L2** and **L3** represent a class of under-explored bipyridyl systems, in which a donor moiety on one pyridine ring is designed to push electron density to an acceptor moiety on the other ring. A comparison of

the structural differences between the three ligands in combination with changes in their photophysical properties should provide insights into the importance of conjugation, and whether the position of the acetylene plays a significant role. In **Figure 150**, basic UV-Vis and absorption data for **L1**, **L2** and **L3** in CH_2Cl_2 are displayed.

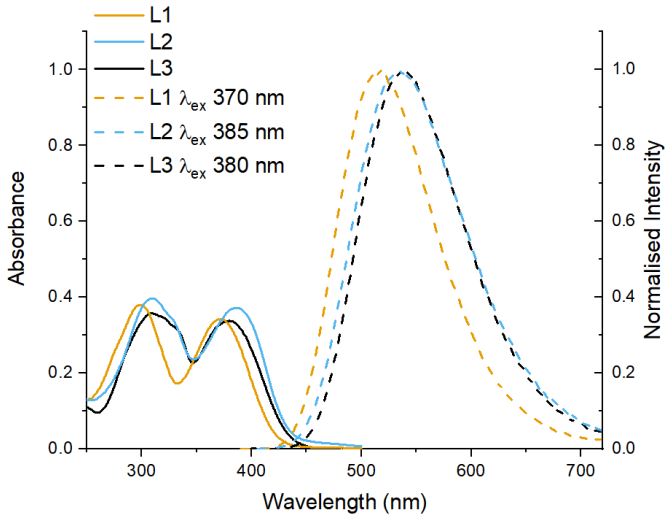

Figure 150. Absorption and emission spectra of **L1**, **L2** and **L3** in CH_2Cl_2; UV-vis spectra shown with solid lines and normalised emission spectra shown with dotted lines (λ_{ex} = 370 nm, 385 nm and 380 nm for **L1**, **L2** and **L3** respectively), [10^{-5} M], 298 K.

The UV absorption spectra of the three ligands are largely similar, with all three displaying two main absorption bands with similar molar extinction coefficients. The first, centred around 300 nm, likely manifests due to high-energy π- π* transitions in the phenyl and pyridine rings, with **L2** and **L3** exhibiting a shoulder at around 320 nm typical of acetylene bond absorption. The lower-energy absorption of all three ligands peaks at around 380 nm, with slight differences in the specific absorption wavelength providing some insight into the electronic properties of the individual ligands. **L1** shows the highest energy transitions of the series, based largely on a lower extent of conjugation across its entire structure. The lack of an acetylene bond leads to an increase in the energy difference between its ground and excited states relative to **L2** and **L3**.

The absorption spectra of **L2** and **L3** appear at higher energies than that of **L1**, peaking at 385 and 380 nm respectively. The difference is indicative of the importance that the placement of the acetylene linker has on the photophysical properties of the ligand. Increasing conjugation to the electron donating moiety leads to a smaller HOMO-LUMO gap as the energy of the HOMO increases. Although increasing conjugation to the electron-withdrawing species should decrease the energy of the LUMO, it seems as though this effect has a marginally lower impact on the CT absorption band.

The emission spectra of the three ligands follow largely the same trends as the absorption spectra. The emission bands are broad and featureless, with stokes shifts of around 120 nm observed for all three ligands. These two factors strongly suggest that the emissive state is charge-transfer in nature, a theory to be

confirmed via low-temperature emission studies. **L1** emission peaks at 520 nm, the highest energy emission of the three ligands. **L2** and **L3** emit at the same wavelength, 540 nm, with nearly identical emission spectra. One would expect that the increased conjugation to the electron-withdrawing trifluorotoluene group in **L3** would lead to a lower-lying LUMO, resulting in lower emission wavelength. As we have seen, this trend occurs in toluene, suggesting that solvents play an important role in the photophysical properties of the ligands.

3.4.1.3 Low Temperature Ligand Studies of **L1**, **L2** and **L3**

Although the broad emission band, high stokes shift and sensitivity of emission wavelength to solvent suggest a charge-transfer excited state, low-temperature studies were performed in a 4:1 MeOH/EtOH glass at 77 K to confirm the nature of the excited states. At low temperatures, solvent rearrangements around the induced dipole of the excited states are not possible, preventing stabilisation and thus hypsochromically shifting the emission wavelength. If no shift is observed, then the dipole does not possess an excited state stabilised by solvent rearrangement. The low temperature measurements were taken in glass NMR tubes, so the signal-to-noise ratios of the emission spectra are lower than those obtained when using a quartz cuvette. The low temperature emission spectra for **L1**-**L3** are shown in **Figure 151.**

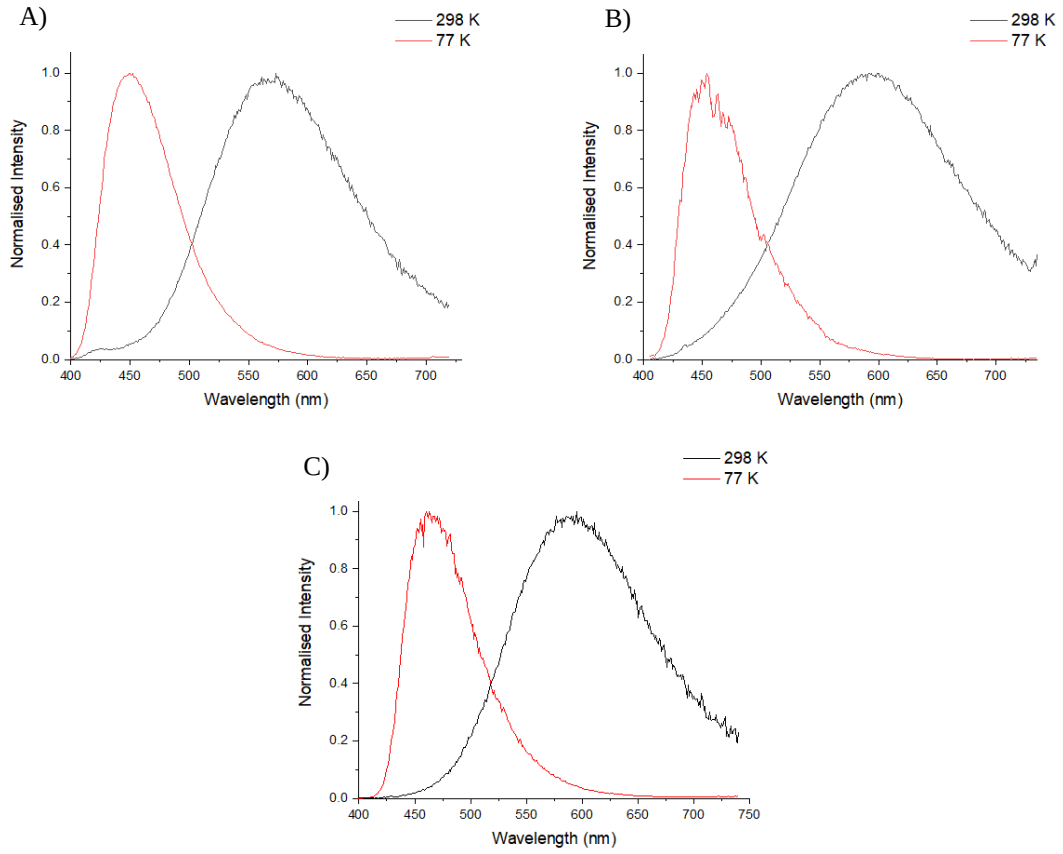

Figure 151. Low temperature emission studies of **L1** (A), **L2** (B) and **L3** (C). Recorded in a MeOH/EtOH 4:1 solution at 298 K and in a frozen glass at 77 K. (λ_{ex} = 370 nm for **L1**, 385 nm for **L2**, 380 nm for **L3**), [10^{-5} M].

All three compounds exhibit the intense hypsochromic shift at lower temperature characteristic of charge-transfer excited states, confirming the results of the emission studies. The intensity of the emission, though normalised in **Figure 151**, also increased significantly at lower temperatures. This is the result of blocking nonradiative rotational and vibrational decay pathways when the compound is suspended in a frozen glass matrix. Comparing the low-temperature emission bands (**Figure 152**) offers some additional insight into the nature of the excited states of the three compounds prior to solvent interaction and stabilisation.

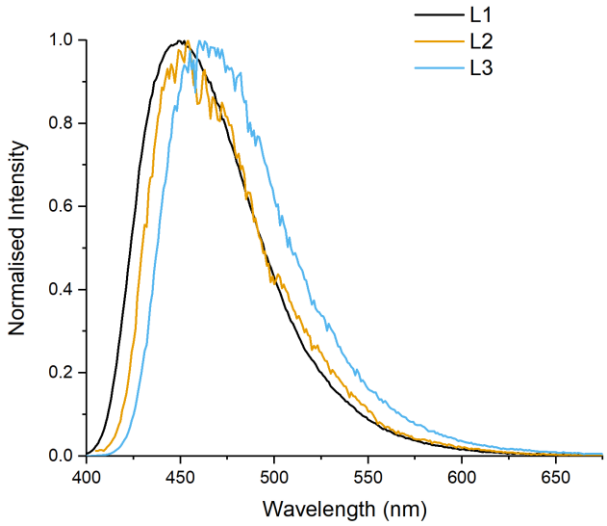

Figure 152. Low temperature emission studies of **L1**, **L2**, and **L3**. Recorded in a MeOH/EtOH 4:1 solution at 298 K and in a frozen glass at 77 K. (λ_{ex} = 370 nm for **L1**, 385 nm for **L2**, 380 nm for **L3**), [10^{-5} M].

There are two important pieces of information to be drawn from this comparison. Firstly, the energies of the excited states in **L1** and **L2** are similar, suggesting that the acetylene linker to the triphenylamine does not have a significant effect on the absolute emission energy. However, it does result in a greater degree of stabilisation when dissolved in polar solvents, leading to **L2** showing redshifted emission at room temperature. Secondly, the emission of **L3** is lower in energy than those of **L1** and **L2**, which was the original expectation when these ligands were designed.

While the position of the acetylene linker was expected to influence emission wavelength, it was not anticipated to influence the degree of solvent interactions. These two factors resulted in **L2** and **L3** having the same emission wavelength in polar solvents at room temperature. However, at lower polarity or lower temperatures, where the factor of solvent stabilisation is reduced in importance, the difference in emission energy is detectable.

3.4.1.4 Quantum Yields of Fluorescence and Emission Lifetime of **L1**, **L2** and **L3**

The emission lifetimes and quantum yields of fluorescence of all three ligands were measured in CH_2Cl_2 using fluorescein in 0.1 M aqueous NaOH as a quantum yield standard.[108] The results of the measurements are shown in

Table 10.

Table 10. [a] Fluorescence quantum yield with Fluorescein as a standard (Φ_f = 79 % in 0.1 M aq. NaOH).[108] [b] Emission lifetime in CH_2Cl_2, fitted monoexponentially.

	Φ_{em} [%][a]	τ_{em} [ns][b]
L1	86.9	3.21
L2	95.4	3.47
L3	86.8	3.02

The emission lifetimes all manifest between 3-3.5 ns, which is in line with other ^{1}CT active ligands.[40] The quantum yields of emission (Φ_{em}) for the three complexes range from 86.8/9 % for **L3** and **L1** to 95.4 % for **L2**. These are high quantum yields, with more than eight of every ten photons absorbed by the molecule re-emitted at longer wavelengths. The high level of efficiency is comparable to that reported by Wang *et al.* on their bis-triphenylamine bipyridine species with a quantum yield of 100 %.[60] It is a promising indicator for the suitability of these compounds as ligands for triplet photosensitisers, as high quantum yield efficiency is a highly desired property in a wide range of applications. Once complexed to the metal center, the ^{1}CT excited state should be able to access its triplet state, which would allow the resulting excited state to sensitise singlet oxygen for PDT or act as a TTA-UC sensitiser.

In summary, the photophysical properties of **L1** behaved as expected compared to **L2** and **L3**. The enhanced conjugation of the latter two, irrespective of the actual placement of the acetylene linker, resulted in lower energy absorption and emission wavelengths, due to a lowering of the HOMO-LUMO gap. The quantum yield and lifetime of **L1** was not significantly altered compared to the other two ligands, suggesting that if higher variance in properties is desired more radical modification of the donor/acceptor species may be required.

Comparing **L2** with **L3** is more challenging, as they behave very similarly at room temperature in polar solvents. It is required to expose them to either less polar solvents or lower temperatures to observe significant divergences in their behavior. The longer absorption wavelength of **L2** is rationalized by the enhanced conjugation of the triphenylamine donor, resulting in a higher energy HOMO, reducing the HOMO-LUMO gap in the ground state relative to **L3**. In the latter, the increased conjugation to the trifluorotoluene acceptor leads to a lower energy emission, which can be observed in either nonpolar solvents or at low temperatures, both regimes limiting the stabilization of the excited state by solvent rearrangement. When rearrangement is allowed, the emission spectra of **L2** and **L3** behave very similarly. This leads us to the conclusion that the extent of excited state stabilization is affected by the position of the acetylene linker, something which to the best of my knowledge, has not been previously observed or reported. Other photophysical parameters such as emission lifetime and fluorescence quantum yield are only minorly affected by the position of the acetylene linker although a 10% increase in quantum yield is observed for **L2**, highlighting the importance of conjugation to the donor moiety for that specific photophysical parameter.

3.4.2 Spectroscopic Analysis of Ru1, Ru2 and Ru3

3.4.2.1 Solvatochromic Absorption and Emission of **Ru1**, **Ru2** and **Ru3**

The absorption and emission of the three complexes were recorded in the same solvents as the ligands, and the spectrum of **Ru1** is shown in **Figure 153.**

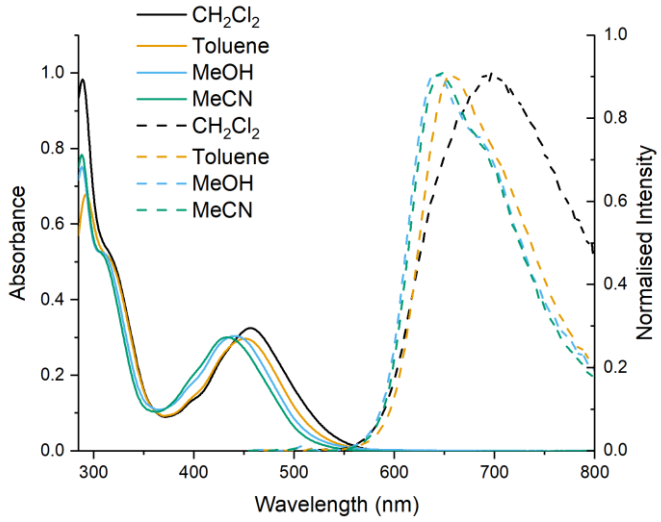

Figure 153. Solvatochromic studies of **Ru1** in CH_2Cl_2, MeCN, Toluene and MeOH; UV-vis spectra shown with solid lines and normalised emission spectra shown with dotted lines (λ_{ex} was absorption max), [10^{-5} M], 298 K.

The absorption for the complex is broadly in line with similar compounds both reported in literature and discussed earlier in this thesis. High energy absorptions under 300 nm can be assigned to ligand-based π - π* and π – n* transitions, while the broad peak centred around 450 nm (depending on solvent) likely arises due to ^{1}MLCT transitions from metal d-orbitals into empty ligand π* orbitals.

It is also likely that the ^{1}CT absorption observed in the ligands has been redshifted and is at least partially contributing to this peak, accounting for its very broad nature. The shifting of ligand CT bands to lower energies following complexation occurs due to donation of electron density from the pyridine ligand to the ruthenium metal centre via dative bonds. This loss of electron density reduces the energy of the ligand orbitals involved in the original CT transition, resulting in an overall lower transition energy.

The choice of solvent has a significant effect on the peak absorption wavelength of the low-energy band, with a 25 nm difference between MeCN and CH_2Cl_2. This is unusual, as the absorption wavelengths of ruthenium MLCT transitions are not usually influenced by solvent. The difference in absorption wavelength could arise due to different extents of solubility, although less soluble complexes reported by the Draper group in earlier work have not displayed this level of solvent sensitivity.[50,71] However, the fact that this solvent-dependent absorption does not affect the higher-energy absorption bands of **Ru1** suggests that it is the CT transition specifically which is being affected.

The emission spectra display large, broad emission peaks with shoulders appearing in polar solvents. Interestingly, the solvatochromic effect is different in the complex than in **L1**. Unlike **L1**, the complex **Ru1** manifests its lowest energy emission band in CH_2Cl_2 and toluene, with MeCN and MeOH displaying the highest energy emission. At first glance, this is a startling observation – solvent stabilisation should increase with solvent polarity, but in this case the most polar solvents (MeOH and MeCN) manifest the highest energy emission. Additionally, the behaviour is not simply a pure reversal of the expected trend. When

taking only the toluene and CH_2Cl_2 emission into account, the expected solvatochromism trend holds true; the toluene peak is at higher energy than the CH_2Cl_2.

The behaviour of **Ru2** is similar, as can be seen in **Figure 154.**

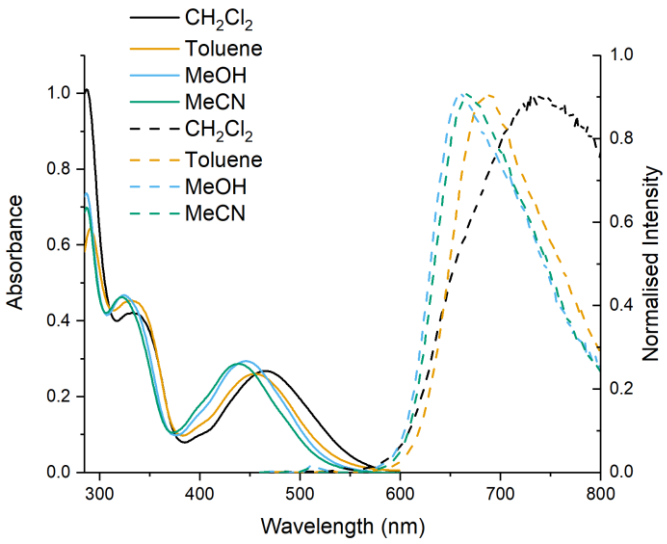

Figure 154. Solvatochromic studies of **Ru2** in CH_2Cl_2, MeCN, Toluene and MeOH; UV-vis spectra shown with solid lines and normalised emission spectra shown with dotted lines (λ_{ex} was absorption max in given solvent), [10^{-5} M], 298 K.

Very similar trends in the absorption spectrum are observed in complex **Ru2** compared to **Ru1**, except for a distinct shoulder at 330 nm arising due to the presence of the alkyne triple bond. Aside from this, the same solvent-dependent changes in the broad absorption band manifest at 450 nm. The band position in each solvent does not shift significantly between **Ru1** and **Ru2**.

The emission spectra again follow similar trends to those of **Ru1**, but here the peak emission wavelength is redshifted in MeCN by 25 nm (from 645 nm in **Ru1** to 670 in **Ru2**). The shift in emission wavelength in CH_2Cl_2 is more pronounced at 45 nm, (from 700 nm in **Ru1** to 720 nm in **Ru2**).

The absorption and emission properties of **Ru3** are displayed in **Figure 155**.

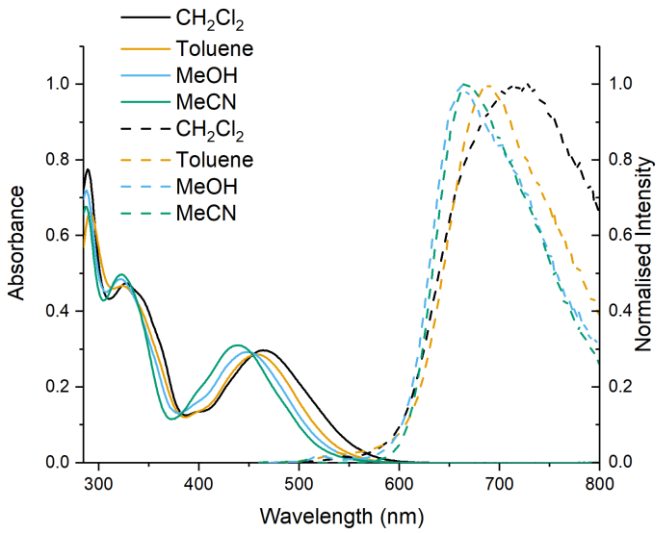

Figure 155. Solvatochromic studies of **Ru3** in CH_2Cl_2, MeCN, Toluene and MeOH; UV-vis spectra shown with solid lines and normalised emission spectra shown with dotted lines (λ_{ex} was absorption max in given solvent), [10^{-5} M], 298 K.

The absorption spectrum is almost identical to that of complex **Ru2**, with the same acetylene absorption manifesting at 325 nm and the by now familiar solvent-dependent changes in the low-energy absorption bands. In MeCN, the emission of **Ru3** occurs at the same wavelength as the one of **Ru2**, namely at 670 nm, while in CH_2Cl_2 the emission manifests at 720 nm, between the emission bands of **Ru1** and **Ru2**.

Table 11 was created to visualise the changes in absorption and emission energies in CH_2Cl_2 and MeCN more easily.

Table 11. [a] In MeCN [10^{-5} M], 298 K. [b] Molar extinction coefficient at the absorption maxima past 400 nm. [c] Emission maximum in MeCN, excited at the corresponding λ_{abs} value. [d] CH_2Cl_2 [10^{-5} M], 298 K.[40] [e] Molar extinction coefficient at the absorption maxima past 400 nm. [f] Emission maximum in CH_2Cl_2, excited at the corresponding λ_{abs} value.

Solvent	**MeCN**			**CH_2Cl_2**		
	λ_{abs} [nm][a]	**ε (x 10^4) [$M^{-1}cm^{-1}$][b]**	**λ_{em} [nm][c]**	**λ_{abs} [nm][d]**	**ε (x 10^4) [$M^{-1}cm^{-1}$][e]**	**λ_{em} [nm][f]**
Ru1	435	3.00	645	455	3.25	700
Ru2	440	2.87	670	465	2.87	745
Ru3	440	3.11	670	465	2.96	720

Several noteworthy observations arise from this data. In both solvents, the low energy absorption wavelengths of the three complexes change depending on the presence of the acetylene linker, but not on its position. Interestingly, the emission spectra of the three complexes does follow the trends set by the ligands in MeCN. In MeCN, there is a redshift of 25 nm in the emission wavelength when the acetylene linker is present, although its position does not have an effect. In CH_2Cl_2, the trends in absorption wavelengths

remains largely similar although larger differences in emission wavelength are observed between **Ru1** and **Ru2**/**3** in this solvent than in MeCN. The emission spectra now also display a new phenomenon, in which the position of the acetylene does in fact influence the emission wavelength.

3.4.2.2 Excitation Studies of **Ru1**, **Ru2** and **Ru3**

In order to confirm that the observed results were not caused by to luminescent impurities, excitation studies were performed on the three ruthenium complexes, shown in **Figure 156**.

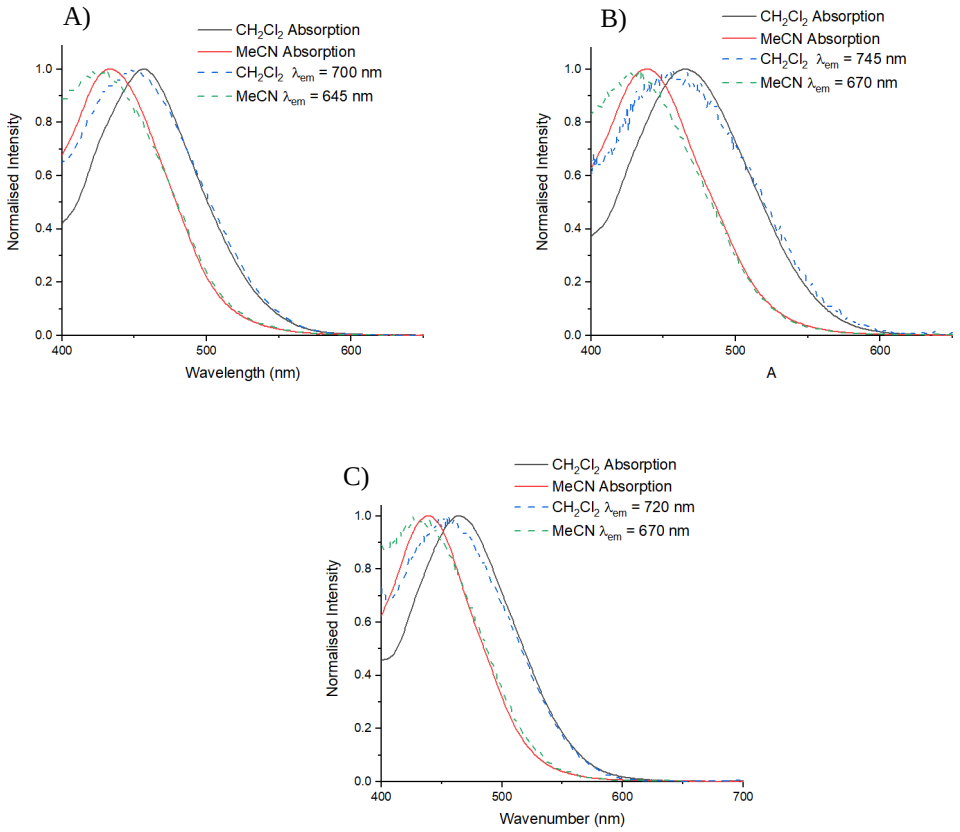

Figure 156. Excitation studies of **Ru1** (A), **Ru2** (B) and **Ru3** (C) in MeCN and CH_2Cl_2 (dashed lines), compared to absorption profiles of **Ru1** (A), **Ru2** (B) and **Ru3** (C) in MeCN and CH_2Cl_2 (solid lines) [10^{-5} M], 298 K.

The excitation profile overlaps with the respective absorption band and manifest the same solvent-dependent behaviour. There is a difference in the exact peak wavelength for each absorption/excitation spectrum pair. It is likely due to several absorption processes occurring within the absorption band; these processes all have their individual emission efficiencies, meaning that some may contribute more to emission than others. Consequently, the peak of the excitation profile will shift as the contribution to the emission of these different transitions will be different to their molar absorption coefficient. The broad agreement between the absorption and excitation profiles, combined with the fact that the latter also show solvent-dependent shifts, strongly suggests that the observed phenomena are not caused by impurities but rather due to the inherent

properties of the complexes. Additionally, this reduces the likelihood that excimer formation is responsible for the change in emission wavelength, as the absorption wavelength would not be affected by this process.

3.4.23 Degassing Studies of **Ru1**, **Ru2** and **Ru3**

To investigate whether the emissive excited state of these complexes was triplet or singlet in nature, degassed emission studies were performed. Due to the different behaviour in MeCN and CH_2Cl_2, the studies were conducted in both solvents. The results of these studies for **Ru1** can be seen in **Figure 157.**

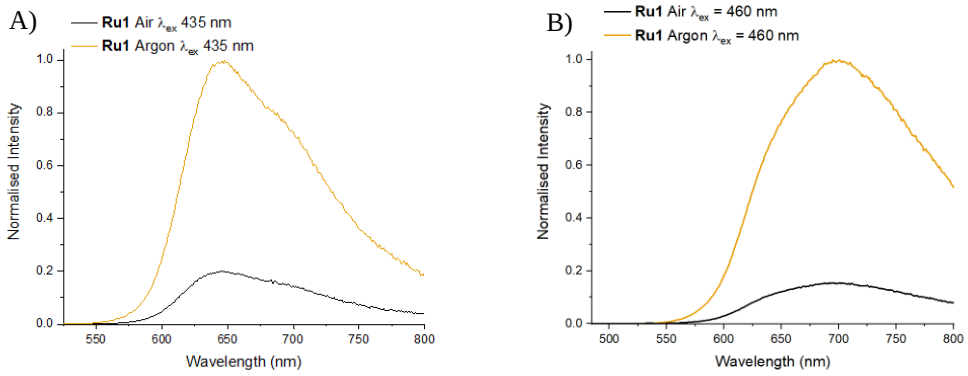

Figure 157. Emission spectra of **Ru1** in MeCN (A) and CH_2Cl_2 (B) under either air (black line) or argon (yellow line) atmospheres [10^{-5} M], 298 K.

In both solvents, the emission intensity is significantly increased under an argon atmosphere, indicative of a triplet excited state which is capable of sensitising molecular oxygen. When oxygen is present, emission intensity is reduced due to this nonradiative decay pathway. Removal of oxygen, such as in an argon atmosphere, will result in an increase in emission intensity. The profile of the emission does not change depending on atmosphere, although it is evident that the structure of the emission band is different in CH_2Cl_2 compared to MeCN. The extent to which the emission is quenched in air does not differ significantly depending on solvent used, with an intensity reduction of 85% recorded in CH_2Cl_2 and 81% recorded in MeCN.

Figure 158 shows the results of the same experiment for **Ru2**.

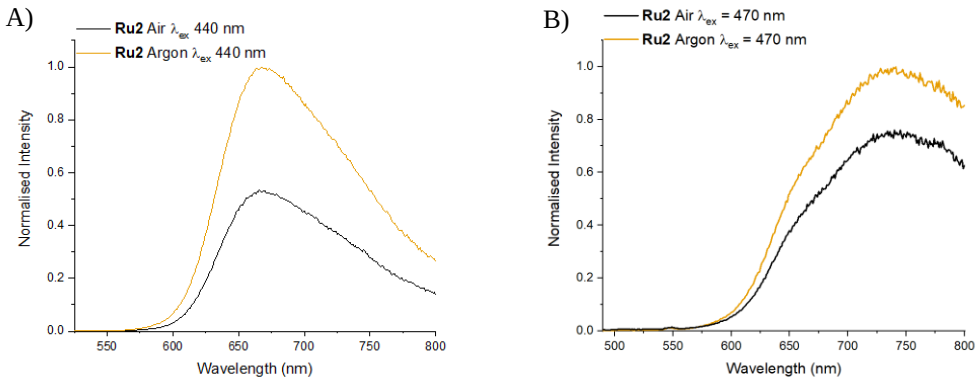

Figure 158. Emission spectra of **Ru2** in MeCN (A) and CH_2Cl_2 (B) under either air (black line) or argon (yellow line) atmospheres [10^{-5} M], 298 K.

Similarly to **Ru1**, complex **Ru2**'s emission is quenched in air, indicating a triplet excited state. The emission band shape again changes significantly, but unlike **Ru1** the extent of emission quenching changes based on the solvent. In MeCN, the emission is quenched by 48 %, while in CH_2Cl_2 it is quenched by 25 %. The reason for this is not immediately clear, as there are a number of factors that can influence the singlet oxygen quantum yield of an excited state, such as excited state lifetime. Regardless of the underlying mechanism, significant changes in the ability to sensitise oxygen are apparent when swapping from MeCN to CH_2Cl_2.

The results for **Ru3** are shown in **Figure 159.**

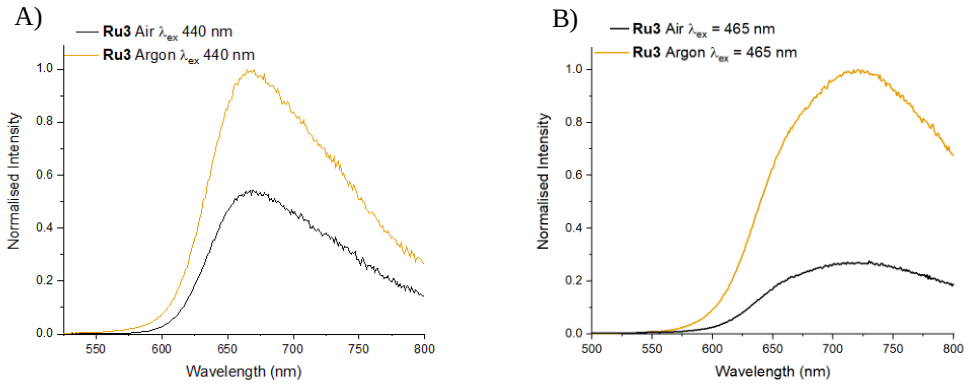

Figure 159. Emission spectra of **Ru3** in MeCN (A) and CH_2Cl_2 (B) under either air (black line) or argon (yellow line) atmospheres [10^{-5} M], 298 K.

As with the other two complexes the emission intensity of **Ru3** is enhanced under an argon atmosphere, indicating a triplet excited state. Similarly, to **Ru2**, the degree of quenching is dependent on the solvent the measurement is performed in. For MeCN, the emission intensity is quenched by 47%, while in CH_2Cl_2 it is reduced by 83%. This suggests that the presence of the acetylene linker is affecting the excited state properties which govern the ability of the complex to sensitise singlet oxygen, and that these properties change depending on the surrounding solvent environment. Unlike **Ru2**, complex **Ru3** exhibits enhanced quenching in CH_2Cl_2 compared to MeCN. This is an indication that the position of the acetylene linker affects the singlet oxygen quantum yield. The exact mechanisms by which this occurs are not readily apparent from the measurements reported so far, but investigation of the emission lifetime could provide important insights into the excited state of the complexes. Longer emission and excited state lifetimes are associated with greater ability to sensitise oxygen, as the excited state persists for longer and therefore has a greater chance of encountering and reacting with ground-state triplet oxygen.

3.4.2.4 Low Temperature Emission Studies of **Ru1**, **Ru2** and **Ru3**

The low-temperature emission spectra of complexes **Ru1**-**Ru3** were recorded in a 4:1 EtOH:MeOH glass at 77 K and are shown in **Figure 160.**

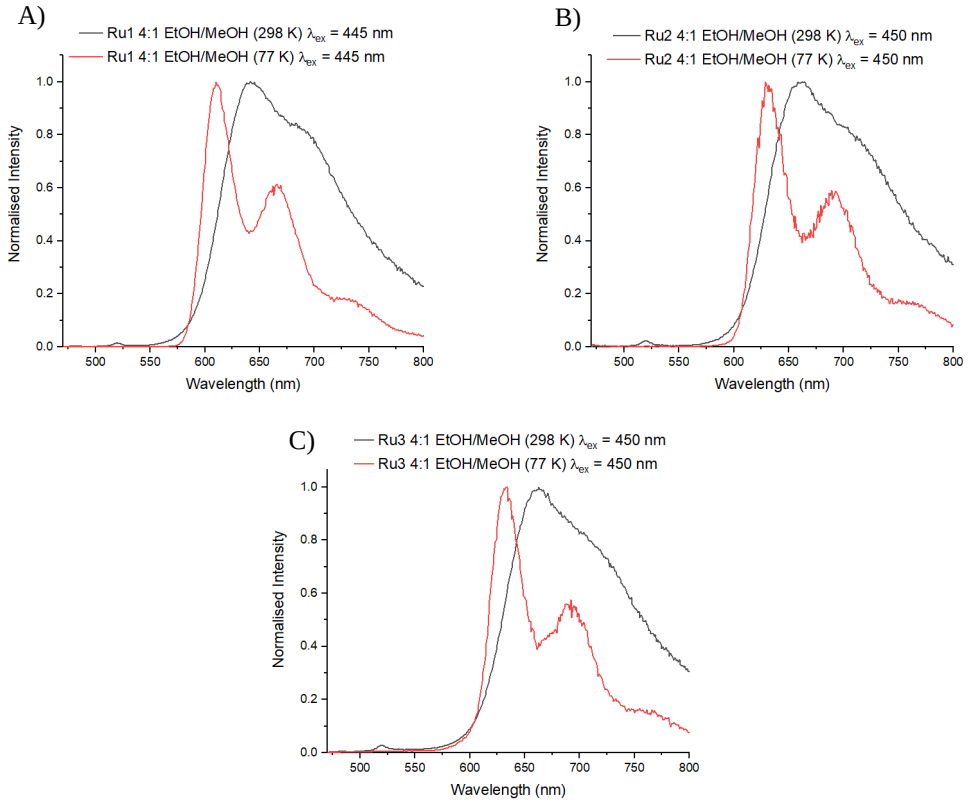

Figure 160. Low temperature emission studies of **Ru1** (A), **Ru2** (B) and **Ru3** (C). Recorded in a MeOH/EtOH 4:1 solution at 298 K (black line) and in a frozen glass at 77 K (red line). (λ_{ex} = 445 nm for **Ru1**, 450 nm for **Ru2**, 450 nm for **Ru3**), [10^{-5} M].

Reduction of temperature results in a blueshift of the average emission wavelength and a resolution of the broad bands observed at room temperature into three more distinct bands at low temperature. The presence of multiple emission bands at low temperatures is not unusual for ruthenium bipyridine complexes, and they are likely to stem from a mix of ^{3}ILCT and ^{3}MLCT excited states. The profiles of the three complexes are similar, indicating that the structural changes do not lead to the population of different excited states. **Figure 161** compares the low temperature emission of all three complexes**.**

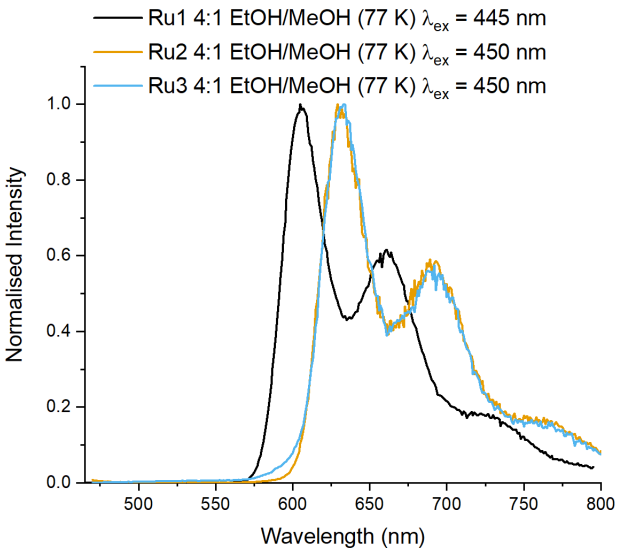

Figure 161. Low temperature emission studies of **Ru1**, **Ru2**, and **Ru3**. Recorded in a MeOH/EtOH 4:1 solution at 298 K and in a frozen glass at 77 K. (λ_{ex} = 445 nm for **Ru1**, 450 nm for **Ru2**, 450 nm for **Ru3**), [10^{-5} M].

The presence of the acetylene linker leads to a pronounced redshift in low-temperature emission for **Ru2** and **Ru3** compared to **Ru1**. The position of the acetylene linker does not affect the energy levels of the complexes, as the low temperature emission spectra for **Ru2** and **Ru3** are very similar. This presents a change compared to the free ligand, as **L2** and **L3** manifested different emission wavelengths at low temperatures. It suggests that the metal dominates the excited state of the ligand, reducing the influence of the position of the acetylene linker.

Given the stark disparity in emission character under different solvent conditions, solvatochromic low-temperature emission studies of the complexes could provide insight into the origin of the observed changes. Unfortunately, only a limited number of solvents are suitable for low-temperature emission studies due to the necessity of forming a glass at 77 K as opposed to an ice. 2-methyltetrahydrofuran (2-mTHF) was chosen as a non-polar solvent to contrast with the more polar EtOH/MeOH solution used for the previously discussed experiments. The low temperature and room temperature emission spectra of **Ru3** in an EtOH/MeOH and 2-mTHF glass are reported in **Figure 162**.

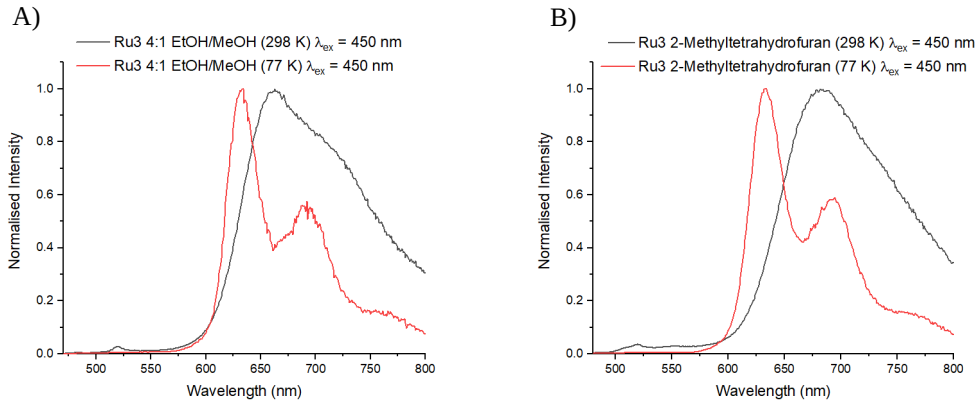

Figure 162. Low temperature emission studies of **Ru3** recorded in a MeOH/EtOH 4:1 (A) or 2-methyltetrahydrofuran (B) solution at 298 K and in a frozen glass at 77 K. (λ_{ex} = 450 nm), [10^{-5} M].

At room temperature, the emission of **Ru3** in 2-mTHF is at lower energies than in EtOH/MeOH, matching the pattern observed by previous solvatochromic experiments (e.g., CH_2Cl_2 vs MeCN) where the less polar solvent leads to a redshift in emission energies, shown in **Figure 163A**. At 77 K however, the emission spectra of **Ru3** in the two solvent systems are identical (**Figure 163B)**.

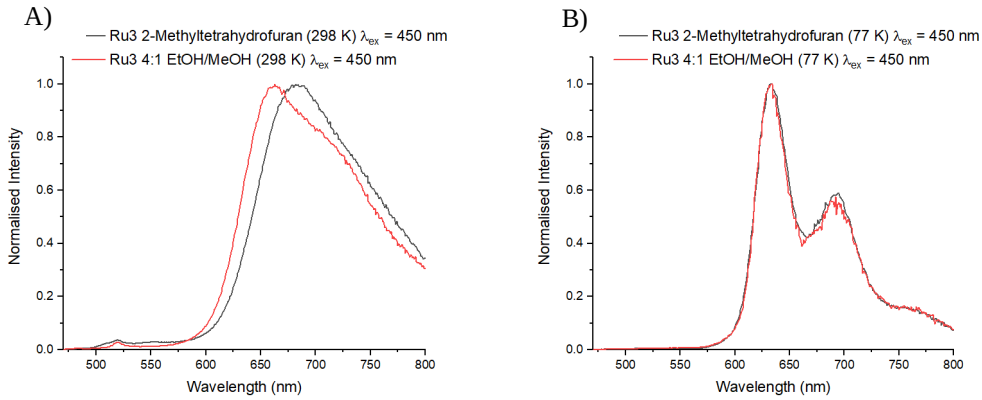

Figure 163. Low temperature emission studies of **Ru3** recorded in a MeOH/EtOH 4:1 or 2-methyltetrahydrofuran solution at 298 K (A) and in a frozen glass at 77 K (B). (λ_{ex} = 450 nm), [10^{-5} M].

This is a key finding, as it demonstrates that the observed trends are due to dynamic interactions between the solvent molecules and the ruthenium complexes. The solvent molecules must be free to arrange themselves around the metal complexes in solution to produce the observed properties.

3.4.2.5 Quantum Yields of Phosphorescence and Emission Lifetimes of **Ru1**, **Ru2** and **Ru3**

The emission lifetimes for complexes **Ru1**-**Ru3** were measured in deaerated MeCN and CH_2Cl_2, with the results reported in **Table 12**.

Table 12.[a] Emission lifetime in deaerated MeCN, fitted monoexponentially.[b] Emission lifetime in deaerated CH_2Cl_2, fitted monoexponentially.

	τ_{em} [µs][a]	τ_{em} [µs][b]

	MeCN	CH_2Cl_2
Ru1	1.04[f]	2.85[f]
Ru2	0.213[f]	0.42[f]
Ru3	0.231[f]	1.42 [f]

The emission lifetimes of the complexes under an argon atmosphere vary significantly based on solvent. $[Ru(bpy)_3(PF_6)_2]^{2+}$, commonly used as a benchmark against which to compare other ruthenium complexes, has an emission lifetime of 0.89 μs in MeCN.[40] In MeCN, **Ru1** has a lifetime of 1.04 μs, suggesting that as in $[Ru(bpy)_3]^{2+}$ the excited state is ^{3}MLCT in nature, since ^{3}ILCT excited states tend to have significantly longer lifetimes.[50] **Ru2** and **Ru3** have lifetimes of 0.213 and 0.231 μs respectively, which present some of the shortest ruthenium triplet excited states found by this author in literature. They are significantly shorter than the lifetimes observed for **Ru1**, suggesting that the presence of the acetylene results in much shorter emission lifetimes. This could potentially arise from new nonradiative decay pathways accessible by virtue of the acetylene linker, allowing for relaxation from the excited state to the ground state without emission of a photon. Additionally, the lower energies of the **Ru2** and **Ru3** excited states lead to a greater nonradiative rate constant according to the band gap law.

In CH_2Cl_2, the lifetime of complex **Ru1** increases to 2.85 μs, while the lifetimes of **Ru2** and **Ru3** rise to 0.42 and 1.42 μs respectively. While it is not uncommon for emission lifetime to vary depending on the solvent, the magnitude of the change is unusual. The lifetime of **Ru2** is almost doubled, and the increase recorded for **Ru1** and **Ru3** are even more significant. The change in emission lifetime for **Ru2** and **Ru3** also account for the difference observed in the degassing studies. Short emission lifetimes reduce the chance of singlet oxygen sensitisation, explaining the low reduction in emission intensity observed for **Ru2** in deaerated vs aerated CH_2Cl_2. Meanwhile, **Ru3** has significantly longer emission lifetimes than **Ru2** in CH_2Cl_2, which helps explain why its emission intensity is much more sensitive to the presence of oxygen in CH_2Cl_2.

The quantum yields of emission for the three ruthenium complexes were measured in CH_2Cl_2 and MeCN using $[Ru(bpy)_3(PF_6)_2]$ as a standard, and the results of these measurements are reported in **Table 13**.[58]

Table 13. Phosphorescent quantum yield in deaerated MeCN with $[Ru(bpy)_3](PF_6)_2$ as a standard (Φ_p = 9.5 % in MeCN).[58]

	Φ_{em} [%][a] MeCN	Φ_{em} [%][a] CH_2Cl_2
Ru1	2.79	3.40
Ru2	0.78	1.02
Ru3	1.12	2.38

In MeCN, the quantum yields of emission (Φ_{em}) for complexes **Ru1**, **Ru2** and **Ru2** are 2.79 %, 0.78 % and 1.12 % respectively. This is lower than the Φ_{em} of $[Ru(bpy)_3(PF_6)_2]$, (9.5 % in MeCN).[40] The reduction can be explained at least partially by the band gap law, which states that the lower energy an excited state is the greater the nonradiative rate constant becomes due to enhanced vibrational and rotational coupling of

electronic excited states.[105] This results in a shortening of the emission lifetime and a reduction in the quantum yield of emission for complexes emitting at long wavelengths. Given that the emission wavelength for $[Ru(bpy)_3(PF_6)_2]$ is 615 nm in MeCN, and that the emission wavelength of all three reported complexes is significantly longer, the band gap law predicts the observed reduction in the emission quantum yields for **Ru1**-**Ru3**.

In CH_2Cl_2 the emission quantum yields for complexes **Ru1**-**Ru3** are 3.40 %, 1.02 % and 2.38 %, indicating an increase in the emission quantum yield when changing from MeCN to CH_2Cl_2 solvent systems. This is in contravention to the band gap law, as the emission wavelength for all three complexes is significantly longer in CH_2Cl_2 than it is in MeCN. The lower energy should result in a greater number of accessible nonradiative decay pathways, lowering the quantum yield of emission.

Contrasting the quantum yields of emission of the three complexes against one another, **Ru1** has the greatest quantum yield in both solvents, while **Ru2** has the smallest. This is reminiscent of their emission lifetimes in CH_2Cl_2, and the two combined results allow some greater insight into the excited state properties of the complexes in CH_2Cl_2. Short emission lifetimes can be associated with high quantum yields for emission, as is the case in the ligand systems reported earlier in this chapter. In this scenario, the radiative transition from $T^* \rightarrow T^0$ is efficient, with rapid relaxation from the excited state T* to the ground state T^0 accompanied by emission from a photon leading to short emission lifetimes. Alternatively, if the radiative transition is inefficient, nonradiative decay from T* to T^0 results in low quantum yields of emission. Emission lifetime is still short because these nonradiative decay pathways are accessible. For ruthenium complexes, a common nonradiative decay pathway is via metal-centred (MC) transitions.[105] So, since **Ru2** has both low quantum yields of emission and short emission lifetimes, it may be because it is able to access nonradiative MC decay pathways.

Complexes **Ru1** and **Ru3** on the other hand show significantly longer lifetimes in CH_2Cl_2 and higher quantum yields of emission, suggesting that they do not have access to these nonradiative decay pathways. Table **14** compares all the photophysical properties discussed so far for the ruthenium complexes in MeCN and CH_2Cl_2

Table 14.[a] In MeCN [10^{-5} M], 298 K. [b] Molar extinction coefficient at λ_{abs}. [c] Emission maximum in MeCN, excited at the corresponding λ_{abs} value. [d] Phosphorescent quantum yield in deaerated MeCN with $[Ru(bpy)_3](PF_6)_2$ as a standard (Φ_p = 9.5 % in MeCN).[40] [e] Emission lifetime in deaerated MeCN. [f] Fitted monoexponentially. [h] In CH_2Cl_2 [10^{-5} M], 298 K. [i] Molar extinction coefficient at the absorption maxima past 400 nm. [j] Emission maximum in CH_2Cl_2, excited at the corresponding λ_{abs} value. [k] Phosphorescent quantum yield in deaerated CH_2Cl_2 with $[Ru(bpy)_3](PF_6)_2$ in MeCN as a standard (Φ_p = 9.5 % in MeCN).[40] [l] Emission lifetime in deaerated CH_2Cl_2. [m] Fitted monoexponentially.

	MeCN					**CH_2Cl_2**				
	λ_{abs} [nm][a]	ε (x 10^4) [$M^{-1}cm^{-1}$][b]	λ_{em} [nm][c]	Φ_{em} [%][d]	τ_{em} [ns][e]	λ_{abs} [nm][h]	ε (x 10^4) [$M^{-1}cm^{-1}$][i]	λ_{em} [nm][j]	Φ_{em} [%][k]	τ_{em} [μs][l]
Ru1	435	3.00	645	2.79	1044.9[f]	455	3.25	700	3.40	2.85[m]
Ru2	440	2.87	670	0.78	213.32[f]	465	2.87	745	1.02	0.42[m]
Ru3	440	3.11	670	1.12	231.82[f]	465	2.96	720	2.38	1.42 [m]

The table indicates significant differences in all measured photophysical properties when changing from MeCN to CH_2Cl_2 solvent systems. These changes run contrary to many established photophysical trends (solvatochromic excited state stabilisation, band gap law etc.).

The only possible explanation to account for all these changes is that there are two different excited states present, with one being accessible in MeCN and MeOH, while the other is accessible in CH_2Cl_2 and toluene. While not definitively proven yet, such behaviour has in recent years been reported in the literature.[54,80,83,100] The novel conclusion from this series of complexes lies in the realisation that the structural changes within the series influence the photophysical properties of the two excited states independently.

In the high-energy excited state, accessed in MeCN, the position of the acetylene only has moderate influence on the photophysical properties, with the emission wavelength, lifetime and quantum yields of emission not changing substantially from **Ru2** to **Ru3**.

In CH_2Cl_2 on the other hand, the position of the acetylene linker does have significant impact on these photophysical properties – complex **Ru2** has a longer emission wavelength compared to **Ru3** but a shorter emission lifetime, lower oxygen sensitivity and reduced quantum yields of emission.

This could be explained by according a greater metal character to the high-energy excited state than to the low-energy excited state. A higher degree of metal orbital involvement could be responsible for the reduction in emission lifetimes and quantum yields. In CH_2Cl_2 contrastingly, a more ligand-based, ^{3}ILCT-type excited state is dominant, with a lower HOMO-LUMO gap and a longer emission lifetime. This idea is represented in the simplified Jablonski diagram below (**Figure 164)**.

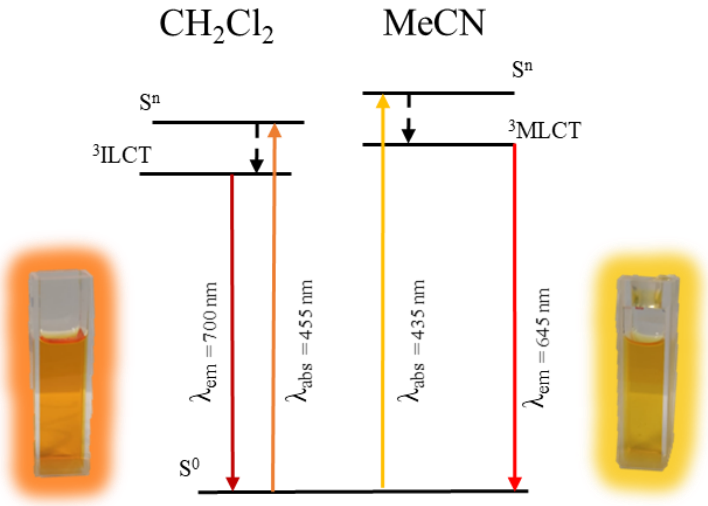

Figure 164. Simplified Jablonski diagram indicating the effect that CH_2Cl_2 and MeCN have on the relative position of the excited states in **Ru1**, **Ru2** and **Ru3.**

More data is necessary to definitively prove this hypothesis, including solvent-dependent density functional theory (DFT) and transient absorption and emission spectroscopy. However, if the theory were confirmed,

this work would demonstrate the possibility of independently tuning the photophysical properties of two accessible excited states using unsymmetric bipyridine ligands. Further exploration of this field could then lead to carefully designed triplet photosensitisers with individually tailored properties that vary depending on the surrounding environment.

3.4.3 Spectroscopic Analysis of Ir1

3.4.3.1 Solvatochromic Absorption and Emission of Ir1

While the aim of this collaboration was to generate novel ruthenium species bearing unsymmetric ligands, sufficient material of **L1** was generated to attempt complexation with $[Ir(ppy)_2Cl]_2$. This would allow for an investigation into the effects of different metal centres have on the photophysical properties of unsymmetric bipyridyl ligands.

The UV-Vis absorption and in-air emission spectra of **Ir1** in a range of solvents are shown in **Figure 165.**

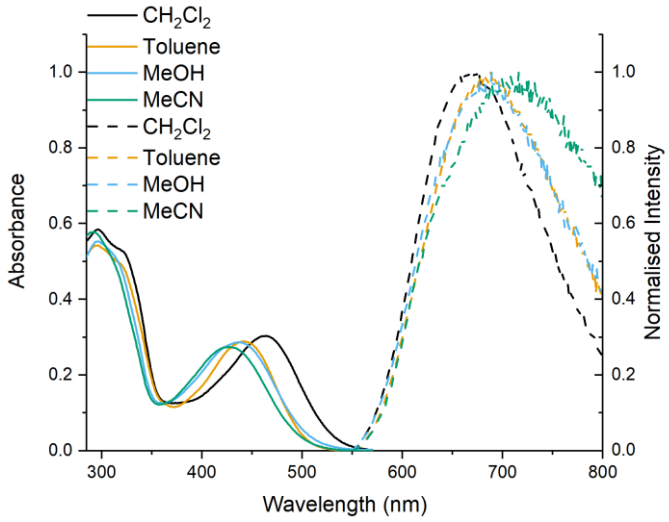

Figure 165. Solvatochromic studies of **Ir1** in CH_2Cl_2, MeCN, Toluene and MeOH; UV-vis spectra shown with solid lines and normalised emission spectra shown with dotted lines (λ_{ex} was absorption max in a given solvent), [10-5 M], 298 K.

The absorption spectrum of complex **Ir1** is comprised of a broad, solvent-sensitive peak between 400 and 500 nm, with the remaining transitions at higher energies under 350 nm. While superficially similar to **Ru1**, an important distinction must be made regarding the relative energies of ruthenium and iridium MLCT. The latter tend to occur at much higher energies, around 370 nm for $[Ir(ppy)_3]^{3+}$.[43] This means that the broad absorption band is probably due to ILCT transitions within the unsymmetric bipyridine exclusively, with little or no contribution from MLCT transitions. The effect of solvent on the peak position of this band is significant, with a maximum of 425 nm in MeCN and 465 nm in CH_2Cl_2. This presents a greater solvatochromic shift than those observed in the ruthenium complexes, caused by the lack of other transitions contributing to the absorption.

MLCT transitions are not typically solvent sensitive, so an overlap of ruthenium MLCT and ILCT transitions will appear to be less solvent sensitive than a purely ILCT peak, even though the sensitivity of the actual ILCT transition may be identical. Consequently, it is difficult to draw a direct comparison between the degree of solvent sensitivity of the iridium and ruthenium absorption spectra. The emission of **Ir1** manifests as a single broad peak past 600 nm. Interestingly, it conforms more to general solvatochromic behaviour, with CH_2Cl_2 emission at higher energies than MeCN. Excitation spectra of **Ir1** in different solvents showed the same solvatochromic shift pattern as the absorption spectra.

3.4.3.2 Excitation Studies of Ir1

Excitation studies of **Ir1** in CH_2Cl_2 and MeCN are shown in **Figure 166**.

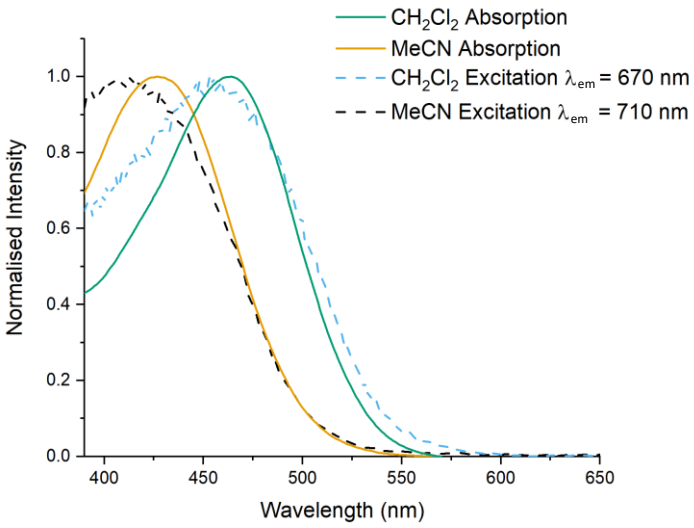

Figure 166. Excitation studies of **Ir1** in MeCN and CH_2Cl_2 (dashed lines), compared to absorption profiles of **Ir1** in MeCN and CH_2Cl_2 (solid lines) [10^{-5} M], 298 K.

This mirrors the behaviour of the ruthenium complexes, with the shift in excitation spectra echoing the change in absorption spectra depending on solvent polarity.

3.4.3.3 Degassing Studies of Ir1

The oxygen sensitivity of **Ir1** in CH_2Cl_2 and MeCN was investigated and the results are displayed in **Figure 167**.

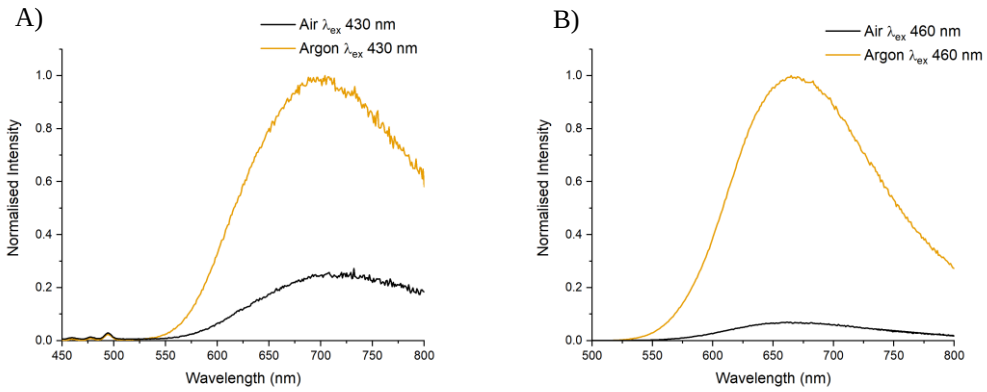

Figure 167. Emission spectra of **Ir1** in MeCN (A) and CH_2Cl_2 (B) under either air (black line) or argon (yellow line) atmospheres [10^{-5} M], 298 K.

The emission is sensitive to oxygen in both solvents, but significantly more so in CH_2Cl_2 than in MeCN (93 % to 75 % quenching respectively). This constituted a notable contrast to complex **Ru1**, where the difference in sensitivity was a mere 4 %.

3.4.3.4 Low Temperature Emission Studies of Ir1

The low temperature emission studies of **Ir1** are reported below in **Figure 168**.

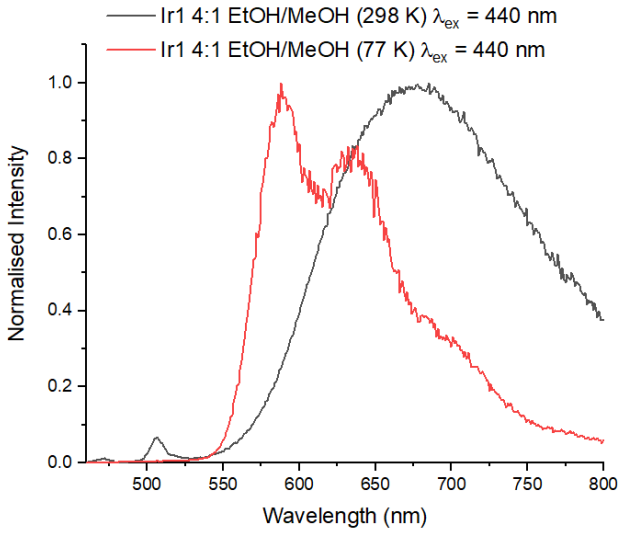

Figure 168. Low temperature emission studies of **Ir1** recorded in a MeOH/EtOH 4:1 solution at 298 K (black line) and in a frozen glass at 77 K (red line). (λ_{ex} = 440) [10^{-5} M].

The low temperature emission displays a shift to higher energies compared to the room temperature spectra. Additionally, the single broad emission peak resolves into two distinct separate peaks with a shoulder at 700 nm. This is similar to the results obtained from the ruthenium low temperature emission spectra, although the emission peak of complex **Ir1** at 77 K is shifted to higher energies by 20 nm (610 nm to 590 nm) compared to **Ru1** at the same temperature.

This indicates that the change of the metal centre has influenced the energy levels of the emissive excited states.

3.4.3.5 Quantum Yield of Phosphorescence and Emission Lifetime of Ir1

The quantum yield of emission for **Ir1** also changes significantly based on solvent. Using $[Ru(bpy)_3(PF_6)_2]$ in MeCN as a standard, the quantum yield of **Ir1** was calculated to be 4.41 % in CH_2Cl_2 while in MeCN it measured 0.35%.[58] Finally, the recorded emission lifetimes of **Ir1** were remarkably short, with a value of 30 ns in CH_2Cl_2 and 10 ns in MeCN. These properties all differ substantially from those of **Ru1**, suggesting that the choice of transition metal centre has a significant impact on the photophysical properties of the resulting complex. A potential explanation for this may lie in the importance of matching the energies of the ligand excited states with those of the metal. If these energies are not matched, then the complicated switching observed in the ruthenium complexes may not be possible.

3.5 Future Work

There is substantial scope for future work to be derived from this project. The highest priority is to further probe the properties of the excited states of **Ru1-3** and **Ir1** with transient spectroscopy and density functional theory (DFT) calculations. The work reported by Sutton *et al.* provides an excellent framework for these investigations – their use of transient Raman and IR spectroscopy enabled them to differentiate the changes in bond vibrations that occurred in the different excited states, allowing them to confirm the excited-state switching behaviour.[54] Use of DFT will establish the presence and energy levels of ligand- and metal-based excited states.

An additional method to investigate the complex excited state behaviour of the reported complexes is via Electric Field-Induced Second Harmonic Generation (E-FISH) experiments. E-FISH allows the degree of polarisation in the excited state to be quantified and gives information on the 'direction' of polarisation.[109] Given the significant expected differences in the makeup of MLCT and ILCT excited states, these techniques could be used to verify the solvent-dependent excited state switching mechanism.

Further research into the macroscopic behaviour is also required – of particular interest is the behaviour of these complexes in aqueous media, as it would determine their suitability for biological applications such as photodynamic therapy. The cytotoxicity (both in the presence and absence of electronic excitation) is another important property to be investigated.

Once these experiments have been analysed, the lessons they impart can be incorporated into the design of the next generation of unsymmetric bipyridine ligands. It is important to remember that this work represents a proof-of-concept; it was intended to determine whether unsymmetric substitution could be used to enhance the ability of chemists to tailor the properties of triplet photosensitisers. In this it succeeded, showing that small changes to the symmetry of the ligand systems can exert significant measurable influence on the photophysical properties of the overall transition metal complex. The use of stronger electron-accepting groups, such as pyrene or anthracene, could promote further redshifting of the emission and extend excited state lifetime (**Figure 169**)

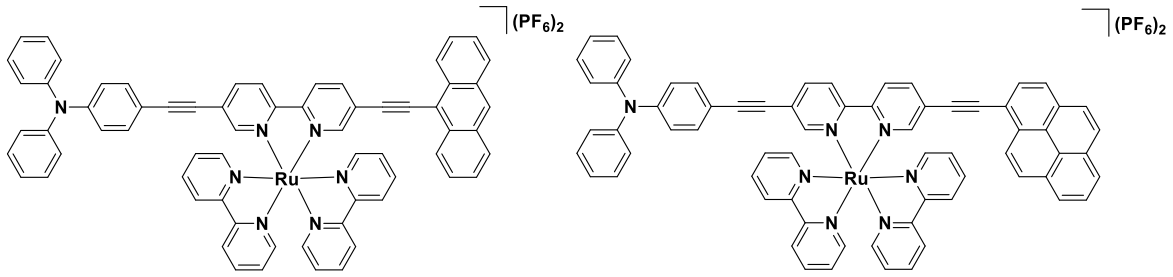

Figure 169. Structures of proposed ruthenium triplet photosensitisers bearing highly conjugated electron-accepting groups.

Additionally, the convergent synthetic approach may facilitate the generation of larger photosensitiser structures bearing multiple self-contained chromophores with discrete photophysical processes. Such chromophores utilised previously by the Draper group include BODIPY, Naphthylamide and Nile Red; choosing appropriate pairings to prevent overlap of absorption wavelengths leads to the structures proposed in **Figure 170**.[40,50]

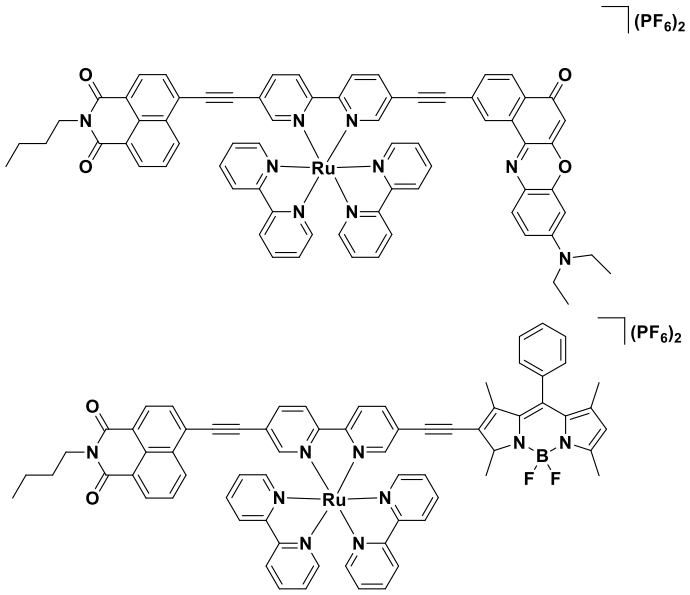

Figure 170. Proposed ruthenium complexes bearing dual self-contained chromophores.

Additionally, recent work has demonstrated that appending sugars to ruthenium and iridium complexes enables them to target multiresistant gram-positive bacteria.[110] The synthetic approach pioneered in this work could allow for a singly bipyridine ligand to bear both a biochemical targeting moiety and a therapeutic group capable of inducing cell-death once transported to the target bacterium.

Finally, this work demonstrates the importance of measuring the properties of triplet photosensitisers in varying environments – the behaviour of the unsymmetric metal complexes show drastic changes depending on the solvent the measurements are performed in. This has significant implications for triplet photosensitiser design, as the properties measured in one environment may not be indicative of performance in another. Given the wide range of complex, multi-component environments triplet photosensitisers are designed to operate in, the properties observed in neat HPLC solvents lose relevance. Instead, it is vital to measure the

performance and efficiency of a triplet photosensitiser in an environment that mirrors that of its intended application as closely as possible, and preferably test it for the application itself.

Using PDT as an example, high singlet oxygen quantum yields, long emission lifetimes and low energy absorption in MeCN may not translate into cellular media. When evaluating the potential of a PDT agent it is preferable to investigate its properties while it is in an actual cell. This has become the focus of recent review articles in an attempt to establish a baseline ability to compare the PDT efficiency of different ruthenium complexes.[111] Given the significant environment-dependent changes in behaviour detected during this work, efforts to codify efficacy tests become more and more crucial.

There remains significant additional scope for investigations into the photophysical properties of ruthenium and iridium complexes. In particular, the solvent-complex interactions appear to determine significant portions of the photophysical properties displayed by transition metal photosensitisers.

It appears as though reports on solvatochromic emission behaviour, while not widely represented in literature, are critical to understanding the nature and properties of triplet photosensitisers.

Further synthetic work to explore these relationships will require close collaboration with computational chemists in order to understand the exact nature of the excited states being affected, as they are very difficult to assign confidently using solely spectroscopic techniques.

4.: Dipyridophenazine Triplet Photosensitisers for Two-Photon Absorption

4.1 Introduction

4.1.1 Two-Photon Absorption

Two-photon absorption (TPA) was first predicted by Maria Goeppert Mayer in 1931, and describes the simultaneous absorption of two photons to excite an electron from a lower energy ground state into a higher energy excited state.[68] Not until the invention and development of lasers would the theory be proven experimentally by Kaiser *et al.* in 1961, using a ruby laser to excite europium-doped CaF_2 crystals.[112] This delay between the theoretical prediction and the experimental observation can be accounted for by the conditions required for a measurable TPA process to occur in a sample. Interaction of the fluorophore with a single photon with an energy less than that of the HOMO-LUMO gap leads to the population of a virtual excited state, similar to Raman spectroscopy.[112a] The impact of a second photon within the lifetime of this virtual excited state (on the order of femtoseconds) with an energy matching the gap between the virtual excited state and the LUMO can lead to population of the formal excited state.[112a] Since the excitation of the electron is reliant upon two photons interacting almost simultaneously with the molecule, TPA is nonlinearly proportional to photon density. Specifically, TPA is proportional square of the excitation beam intensity used, as an higher beam intensity affects both the rate of population of the virtual excited state as well as the rate of population of the formal excited state .[113] Observing TPA in measurable quantities was therefore not possible before the invention of lasers, and even remained difficult until the introduction of the Ti:sapphire laser, which has since become the chosen excitation source for TPA studies.[109,114] While a complete review of two-photon absorption, and its use in photodynamic therapy is outside the scope of this work, a comprehensive introduction follows here.

Two-photon absorption occurs when a single low energy photon excites an electron of that molecule into a virtual excited state.[68] If, during this extremely short-lived excited state, the molecule then interacts with a second photon with a wavelength equal in energy to the difference between the virtual excited state and the first electronic excited state, promotion of the electron from the virtual excited state to the first excited state is possible.[113,115] It is therefore a requirement for the energy of the first (and subsequent) photon to be lower in energy to that of the Highest Occupied Molecular Orbital (HOMO), and the Lowest Unoccupied Molecular Orbital (LUMO). This process is reliant upon the spatial and temporal proximity of a secondary

photon almost immediately following absorption of the first photon. If the two photons are of equal energy, each equal to half of the HOMO-LUMO gap, the process is referred to as degenerate TPA **(Figure 171).**

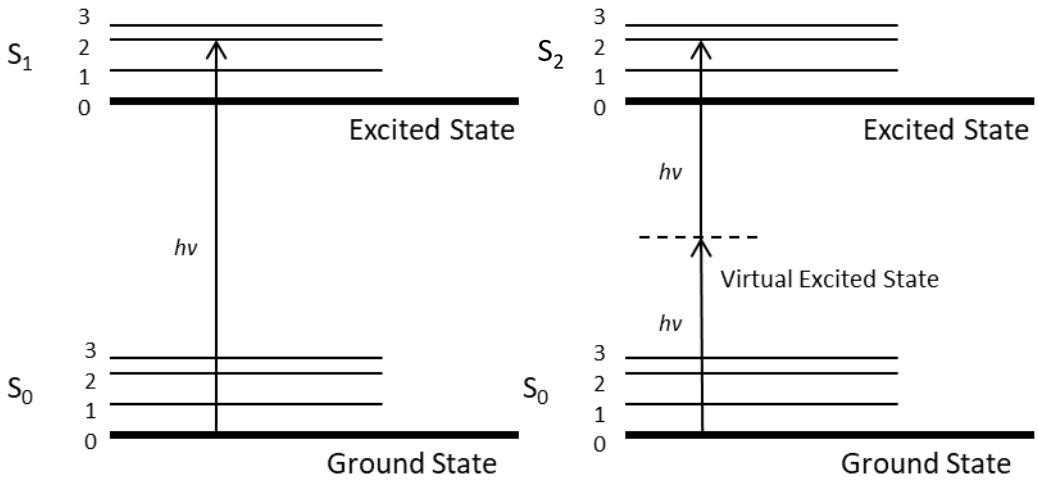

Figure 171. Simplified Jablonski diagram showing one-photon absorption (left) and degenerate two-photon absorption (right).

If the two photons differ in energy but their sum still provides the energy required for promotion from the ground to the first electronic excited state, the event is designated as non-degenerate TPA.[113]

Two-photon absorption increases by the square of the intensity of incident light. This can be proven using a variety of mathematical methods, including second-order perturbation theory. However, for the scope of this work, it is sufficient to rely upon rate laws to show the dependence of TPA on the square of incident light as described by Fisher *et al*.[109] Regarding the photochemical reaction:

$$S_0 + 2h\nu \rightarrow S_1$$

S_0 is the electronic ground state, S_1 is the first electronic excited state, and $2h\nu$ represents two photons. In this process, the absorption of $2h\nu$ results in the excitation from S_0 to S_1. This depicts a simplified scenario in which the two photons are absorbed at the exact same moment in time This is unlikely to occur even at high incident light intensity. However, for this example, the extremely short-lived duration of the virtual excited state allows for the approximation of a single-step reaction to be acceptable. Using rate laws, the change in concentration or population of the first excited state S_1 can be expressed as a function of the concentration of the reactants S_0 and $h\nu$, multiplied by the two-photon absorption cross section δ, which is correlated to the probability of TPA occurring and unique to every compound.

$$\frac{dS_1}{dt} = \delta[S_0][h\nu]^2$$

The above formula illustrates the dependence of TPA on the square of the concentration (or intensity) of the incident photon.

Broader availability of increasingly powerful laser systems has made it easier to investigate the TPA properties of compounds, leading in turn to a sharp rise in interest in the design and synthesis of TPA compounds over the last few decades.[113,115,116] From the resulting body of research, it has been established that TPA obeys selection rules different from one-photon absorption (OPA), and are inversed in a

centrosymmetric molecule. An exhaustive theoretical treatment of TPA selection rules for both degenerate and non-degenerate processes can be found in the work of Bonin *et al.*[117]

For this project, the structural features resulting in a high TPA ability are of greater relevance when designing TPA-active compounds. These features (a so-called design language) have been thoroughly researched in recent years, and a review by Anderson *et al.* collates the most pertinent ones.[113] Of particular interest are molecules with high intrinsic symmetry, long conjugated π-systems, and a high degree of planarity.[115]

Before proceeding it is important to appraise the manner in which the ability of a given TPA-active compound can be measured. The first method relies on the calculation of the two-photon absorption cross section. This value is determined using a Z-scan method, which measures the attenuation of a laser beam as a function of the position of the sample, while it is moved along the z-axis of the detector.[113] However, since this technique measures all non-linear optical processes occurring in a sample, it can suffer from an overestimation of the cross-section, because additional factors may lead to beam attenuation aside from TPA.

The second and more accurate technique is called Two-Photon Excited Fluorescence (TPEF), which measures the light emitted by a sample following its irradiation at a suitable TPA wavelength.[113] The resulting signal can then be compared to the TPEF spectrum of a reference compound with a known cross-section, allowing facile calculation of the cross-section of the sample. A large number of two-photon reference compounds are available, and the technique has been constantly optimised in recent years due to its advantages over the z-scan technique.[113,118] The TPA cross section is usually quoted in units of Goeppert-Mayer, where 1 GM is 10^{-50} cm^4 s $photon^{-1}$.[114] It is important to note that the cross-section is dependent on the excitation wavelength, and thus this value must accompany any reported two-photon cross section value. The GM unit of measurement, it is now possible to objectively compare the TPA ability of different molecules. One of the most widely studied groups of TPA compounds have been stilbene, and stilbene derivatives, particularly those with donor groups such as amines.[115] Albota *et al.* describes the TPA ability of three stilbene compounds in **Figure 172**.

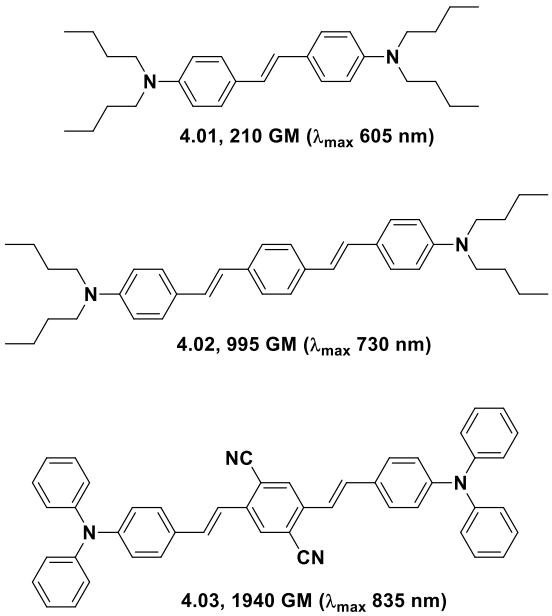

Figure 172. TPA ability of strengths of stilbene derivatives, expressed in GM.[115]

As highlighted by these examples, the TPA ability of compounds increases according to three parameters for basic Donor-Acceptor-Donor structures.

1. The increasing size of the conjugated π-system
2. The strength of the donor groups
3. The presence of electron withdrawing groups on the acceptor core

The effects other structural features exert on the TPA ability of a compound are still being investigated.[113] Even using the guidelines developed above, it remains very difficult to predict the ability of a compound to undergo TPA, and further research is required to allow a deeper understanding of how these and other factors individually and in conjunction, affect TPA. It is therefore an exciting time to develop novel structures and probe their TPA ability.

4.1.2 Two-Photon Absorption in Photodynamic Therapy

The potential application of TPA for use in PDT has been proposed for decades, but the recent development of advanced laser systems has led to a surge of interest in the field.[24,67,109] The differences between one-photon absorption (OPA) *versus* TPA suggest that the latter is ideal for improving issues in conventional photodynamic therapy. The long wavelengths typical of TPA could demonstrate high skin and tissue penetration, and the dependence on the square intensity of the laser beam for significant TPA to occur should allow for improved spatial control.[109] Controlling where the beam of the laser is focussed in 3D space would then make it possible to isolate very small regions selectively for excitation, reducing the excitation bleed compared to OPA. This is illustrated in **Figure 173**, and highlights the increased spatial selectivity of TPA compared to OPA.[119]

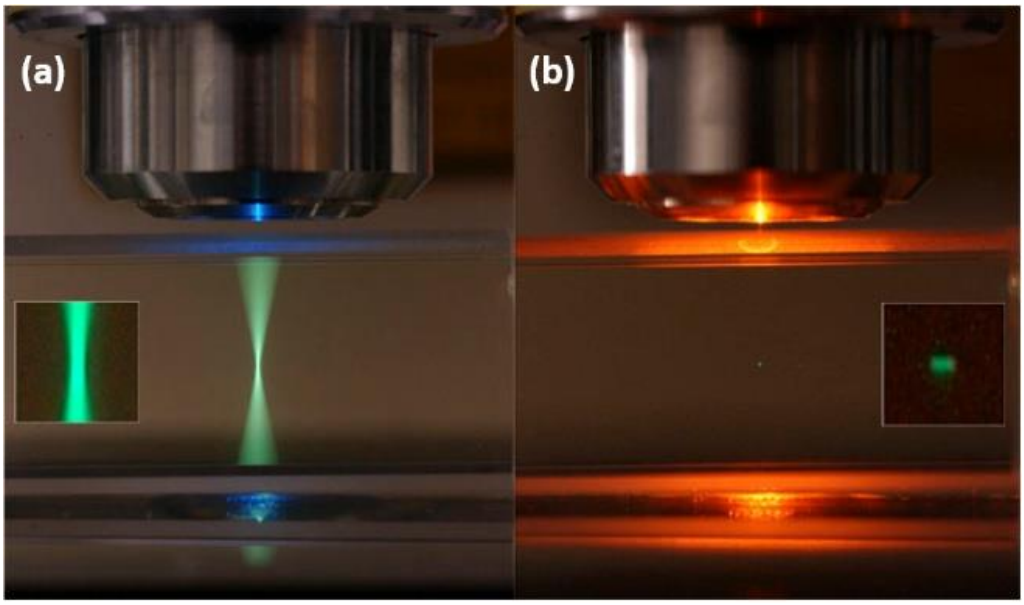

Figure 173. (a) One-photon absorption, performed at lower wavelengths and (b) two-photon absorption.[119]

One potential problem for TPA is the required higher intensity of the laser for significant excitation. While this does allow for greatly increased spatial control, it has the potential to cause photodamage to healthy tissue. Wachter *et al.* investigated this possibility and found that while older laser sources did carry the risk for photodamage, more modern Ti:sapphire lasers resulted in a much reduced tissue damage compared to previous Q-switched lasers due to their lower pulse energy.[109] The Ti:sapphire lasers also have the advantage of very short pulse times, thereby preventing excited state absorption which could potentially compete with TPA and lead to undesirable competitive deactivation pathways.[109]

To summarise, there are obviously clear advantages in using TPA dyes in PDT *versus* their OPA counterparts, and the development of such dyes is worth exploring. While the relationship between the ability of a compound to absorb two photons and its structure is still being investigated, studies of TPA dyes should ideally include a family of similar compounds to further scientific understanding in the field. PDT active ruthenium polypyridyl complexes with large TPA cross-sections has remained a relatively unexplored field of research until recently.[19,53]

4.1.3 The Two-Photon Absorption Properties of Polypyridyl Ruthenium Complexes

Ruthenium polypyridyl complexes are a widely investigated class of compounds.[19,24,51,67] Applications for these complexes range from photodynamic therapy to water splitting, their promising properties continuously fuelling research into novel derivatives and areas.[24,51,67] In a significant proportion of these efforts, new advances rely on functionalised 2,2'-bipyridines (bpy), or extended 1,10-phenanthroline derivatives.[71,120]

There is currently a lack of TPA-active PDT agents, with one of the most widely used PDT agents Photofrin, a porphyrin polymer, having a GM value of only 10 in EtOH.[24] Work using substituted 1,10-phenanthroline for TPA was carried out by Lemercier *et al.* over the last decade.[121,122] These compounds rely on adding fluorenyl and oligofluorenyl groups at the 5-position of 1,10-phenanthroline. The addition of alkyl bonds

linking the oligofluorenes increases the TPA values from 40 to 225 GM. However, those values are still several hundred GM below those investigated by Albota *et al.*[115]

Heinemann *et al.* together with the Chao research group investigated the suitability of a number of Ru-polypyridyl TPA compounds for PDT, exhibited in **Figure 174**.[24]

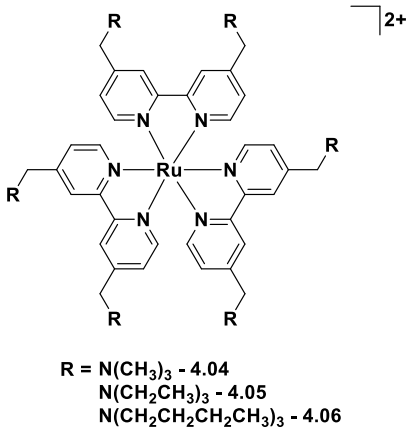

R = $N(CH_3)_3$ - 4.04
$N(CH_2CH_3)_3$ - 4.05
$N(CH_2CH_2CH_2CH_3)_3$ - 4.06

Figure 174. Ru-polypyridyl TPA-active PDT agents **4.04-4.06**.[19,24]

The compounds manifest GM values of up to 250 GM when excited at 800 nm using substituted bipyridine ligands, representing significant improvements in TPA cross section values compared to currently clinically approved PDT agents. Additionally, at 800 nm, the penetration depth of light through skin and tissue is quite significant and may allow for subcutaneous excitation of the PDT agents in cancerous tissue. The overall formal positive charge of the compound induced lysosome-targeting, which resulted in a high percentage of cell death.[19,24,63]

Later efforts to generate ruthenium complexes with high TPA cross-sections have led Gasser *et al.* to develop a series of styryl-4,4-bipyridyl ligands as two-photon chromophores, as shown in **Figure 175**.[123,124] In addition to the homoleptic *tris*-complex displayed in the Figure, the authors also report the properties of the heteroleptic *mono*- and *bis*-analogues.

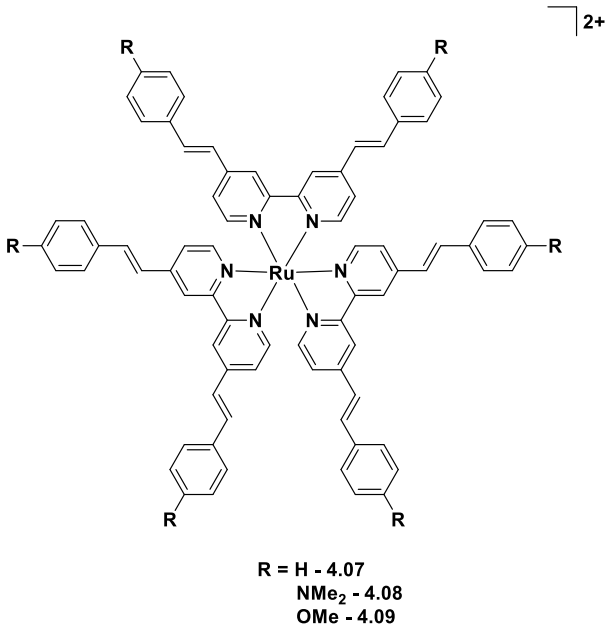

Figure 175. TPA-active ruthenium complexes with styryl 4,4'-bipyridyl photon harvesting ligands.[123]

This set of complexes shows remarkably high two-photon absorption cross sections, with GM values up to 2175 recorded for **4.08**. The cross sections of the homoleptic complexes were all increased relative to their heteroleptic sister compounds. These cross sections are almost a full order of magnitude greater than those of previously discussed ruthenium complexes, indicative of the large effect increased conjugation can have on the TPA cross section of a compound. Further investigation of the photophysical properties of the complexes showed that they can access the triplet state, with singlet oxygen quantum yields ranging from 16-77 % in MeCN and 1-11% in aqueous solution. The relatively low singlet oxygen quantum yield in the latter solvent system could be explained by the excited state lifetime recorded for the complexes in degassed solutions (222-543 ns). These lifetimes are shorter than the 900 ns of [ruthenium(bipyridine)$_3$(PF_6)$_2$], a typically used benchmark for polypyridyl ruthenium complexes. It is also significantly shorter than other rationally designed triplet photosensitisers, as long excited state lifetimes are considered an important property of efficient triplet photosensitisers.[40,50] The biological activities of the compounds were probed, all of them proving to be non-toxic in the dark but toxic when irradiated with 500 nm or 800 nm light, with IC_{50} values in the micromolar range. Interestingly, it is the *mono*-methoxy complex that demonstrates the best performance in cell studies, with the *tris*-complexes showing some of the lowest tumour growth inhibition by this series of complexes. The contrast between two-photon absorption cross section and *in-vivo* biological performance highlights the importance of balancing the varying photophysical properties of the complexes when designing efficient triplet photosensitisers and/or PDT agents. While the cross section is an important parameter, the contribution of excited state lifetime and singlet oxygen quantum yield to the overall efficiency of the PDT agent should not be underestimated.

Durand *et al.* demonstrated that increasing the number of TPA chromophores on a complex has a non-linear effect on the cross-section of the generated $[RuL_{3-n}(bpy)_n]^{2+}$ set of complexes, of which the homoleptic (n=3) set are shown in **Figure 176**.[124] As the number of light-harvesting moieties increases, in this specific

case when moving from *mono*- to *bis*- and *tris*-complexes, the cross-section of the latter complexes is greater than would be expected if the cross-section were linearly dependent on the extent of conjugation.

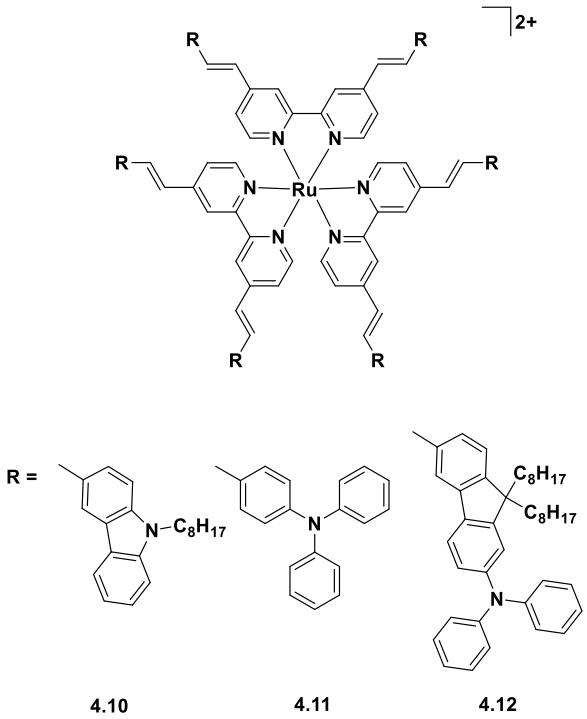

Figure 176. Homoleptic TPA-active ruthenium complexes with styryl 4,4'-bipyridyl photon harvesting ligands.[124]

For example, the *mono*-triphenylamine complex has a cross section of 311 GM, while the *tris*-triphenylamine complex has a cross section of 1465 GM, much higher than the approximately 930 GM anticipated if the relationship between cross section and extent of conjugation were linear. The above publication shows that while conjugation is an important parameter, its exact contribution to the size of the TPA cross section is not yet fully understood. The authors subsequently published a series of DFT studies investigating the electronic structure of the generated species, and implied that the reason for this non-linear enhancement is due to the mixed charge-transfer nature of the excited states. While the excited states of all the complexes are a mix of LLCT, MLCT and ILCT transitions, increasing the number of photon-harvesting ligands (n) results in a greater proportion of ILCT contribution. In complexes where the ILCT is aligned with the MLCT and LLCT, contribution of the metal orbitals to the excited states results in enhanced conjugation across the central metal atom, elevating TPA response beyond the purely additive.[125]

As the cross-section seems to be dependent on the size of the conjugated π-system, it is worth exploring larger polypyridyl systems to investigate whether their TPA values are higher than those of 2,2'-bipyridine and 1,10-phenanthroline.

While less widely explored than the two previously mentioned polypyridyl ligands, dipyridophenazine (**dppz**; **Figure 177**) derivatives and complexes have also been studied for their photophysical properties.[24,126,127] The extended π-system of the fused ring system, and inclusion of the iminic nitrogen-

containing pyrazine ring results in a redshift in both the absorption and emission spectra when compared to 1,10-phenanthroline and 2'2-bipyridine systems.[24,126,128]

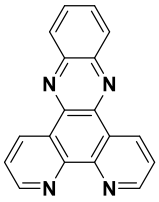

Figure 177. Dipyridophenazine (dppz).

The standard synthetic preparation for **dppz** includes oxidation of 1,10-phenanthroline, followed by condensation with a phenyldiamine (**Scheme 20**).[126] However, functionalisation of the **dppz** core following the secondary condensation step has reportedly been very difficult due to low reactivity.[120] Consequently, standard practice aims at functionalising the diamine with various electron donors first, followed by the construction of the Donor-Acceptor-Donor (DAD) systems using the extended π-system of the **dppz** as an acceptor.[126,129] This has led to the widespread application of functionalised 2,1,3-benzothiadiazole as a building block for the desired **dppz** compounds, often functionalised utilising palladium catalysed cross-coupling reactions.[126]

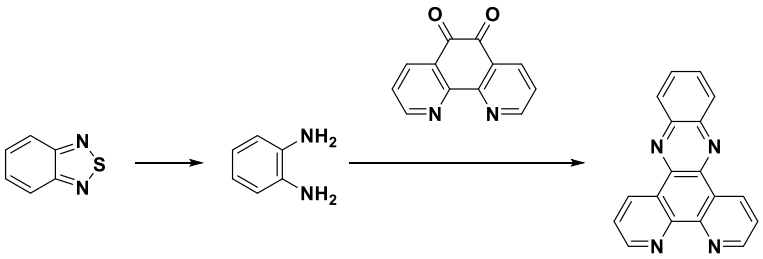

Scheme 20. Common synthetic pathway to **dppz**.[75]

This methodology often results in ligands with pronounced absorption bands past 500 nm, further red-shifted than similar phenanthroline or bipyridine complexes.[126] An interesting property of dppz compounds is the quenching of their emission in protic media such as H_2O, while showing moderate to strong emission in less protic solvents like CH_2Cl_2 or MeCN.[75] This has been postulated to be due to protonation of the iminic nitrogen atoms of the pyrazine ring in the excited state, providing a non-radiative decay pathway in protic media. However, when introduced to cellular media, luminescence is once again observed. This light-switch effect is caused by the intercalation of dppz into the DNA helix, which sterically blocks the non-radiative pathway by preventing protonation of the imines.[75]

Since its discovery, the reaction has been exploited by other groups to generate a number of PDT agents that specifically target DNA.[24,67] Heinemann *et al.* published a review about the use of Ru(II) polypyridyl complexes in PDT applying both OPA and TPA.[24] This review included a number of dppz compounds complexed to a Ru(II) centre, with either bipyridine or phenanthroline as spectator ligands. Two of the complexes (**Figure 178**) showed good cellular uptake and excellent cytotoxicity when irradiated at 420 nm.

However, as previously mentioned, penetration of high energy wavelengths through the skin is very low, restricting PDT use to topical applications.

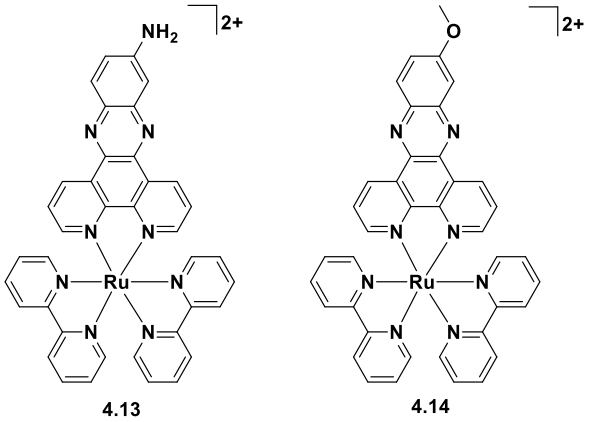

Figure 178. Ru(II)-bearing dipyridophenazine (**dppz**) PDT agents **4.13** and **4.14**.[24]

Additionally, Heinemann et al. investigated the TPA properties of two **dppz** derivatives, shown in **Figure 179**.

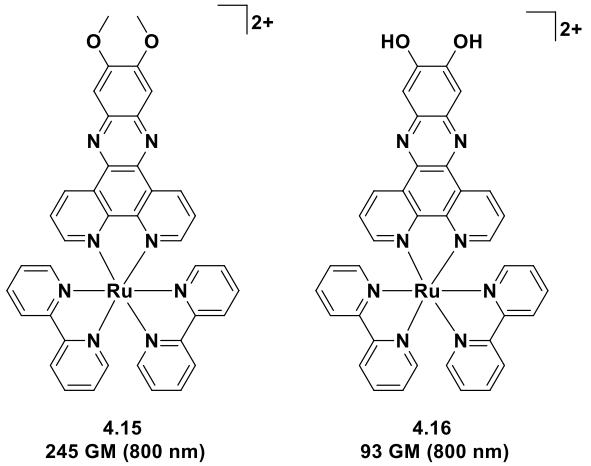

Figure 179. Ru-bearing dppz TPA PDT complexes **4.15** and **4.16**.[24]

The large difference in TPA cross section values between both compounds, due to the simple substitution of methoxy for hydroxyl moieties, demonstrates the large effect which small changes in structure can have on the TPA cross sections of very similar compounds.

Hua *et al.* recently published a paper investigating the TPA properties of a family of dibenzophenazines (dbpz) substituted with triphenylamine derivatives, two of which are shown in **Figure 180**.[129] The structures show interesting luminescent properties and TPA values up to 800 GM.

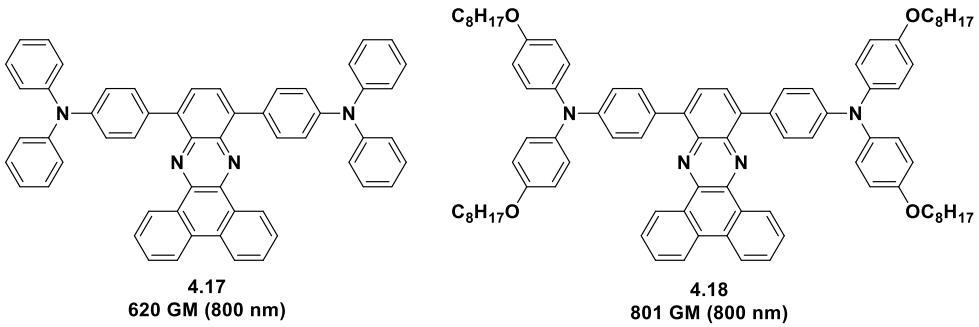

Figure 180. dbpz TPA-active derivatives **4.17** and **4.18**.[129]

The lack of a bidentate bis-pyridine ring system prevents complexation to metal centres, limiting the ability of these compounds to act as PDT agents, since a heavy metal atom is required for access to the triplet state necessary to generate $^1O_2$. The pyridyl, and Ru-dppz complex analogues of these systems have been synthesised by Geng *et al.* already (**Figure 181**), but neither their TPA nor their PDT properties have been investigated.[126]

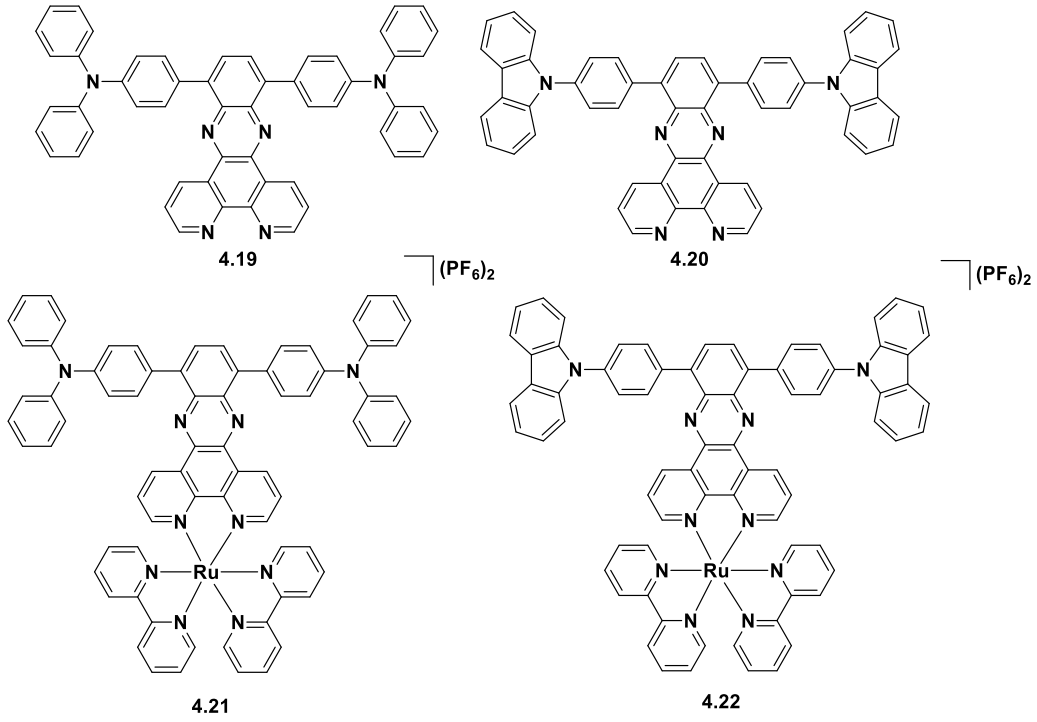

Figure 181. dppz compounds, and their Ru(II)()(bpy)$_2$ complexes **4.19-4.22** synthesised by Geng *et al.*[126]

4.1.4 The Suzuki-Miyaura Coupling Reaction

Due to the extensive use of Suzuki-Miyaura couplings, commonly referred to as Suzuki couplings, the functionalisation of dppz and 2,1,3-benzothiadiazole derivatives is worth describing with regard to this coupling type. The use of palladium catalysts in cross-coupling reactions to form carbon-carbon and carbon-heteroatom bonds has been one of the most successful innovations in the last few decades of synthetic chemistry.[130–132] One of the most common of these reactions is the Suzuki cross-coupling reaction, in which a boronic acid is coupled to an aryl halide. The reaction is both reliable and scalable, the increasing availability of commercial sources for boronic acids resulting in a widespread industrial use of this versatile

reaction.[133,134] It follows a catalytic cycle similar to other coupling types, including Heck and Sonogashira couplings (**Figure 182**).

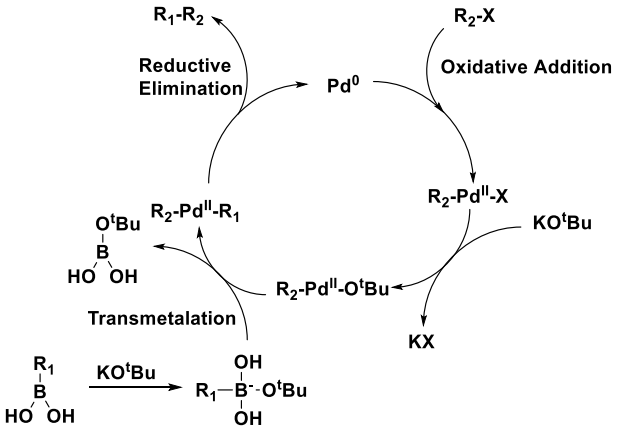

Figure 182. Suzuki cross-coupling reaction mechanism cycle.

The application of Suzuki reactions in academic research has also become increasingly viable due to the commercial availability of boronic acids. Of particular relevance to the development of a TPA active compound is the 4-diphenylaminophenylboronic acid, which can be used to add a triphenylamine moiety to an aryl halide at very low cost. Triphenylamine represents a common building block in TPA-active dyes as it is a strong formal electron donor (the nitrogen atom) which typically results in large cross-section values.[129]

4.2 Aims

The aim of this work is to develop novel two-photon active PDT agents combining the low dark toxicity, high stimulated cytotoxicity and good metabolic clearance of PDT agents with the long absorption wavelength and spatial selectivity of two-photon absorbers. To this end, it is important to study how well the design principles for high two-photon absorption, originally developed for organic chromophores, translate to metal-ligand complexes. In order to investigate this question, a family of compounds has been selected including an organic chromophore with a high two-photon cross section (**NPhC**). The project primarily seeks to track the changes in the two-photon absorption properties of this family of compounds from organic two-photon absorber to free ligand to metal complex, as well as research the effects of different amine donors on the two-photon absorption cross sections. Following completion of the initial project, the influence of different transition metal centres (Ruthenium and Iridium) on the properties of these compounds will also be investigated.

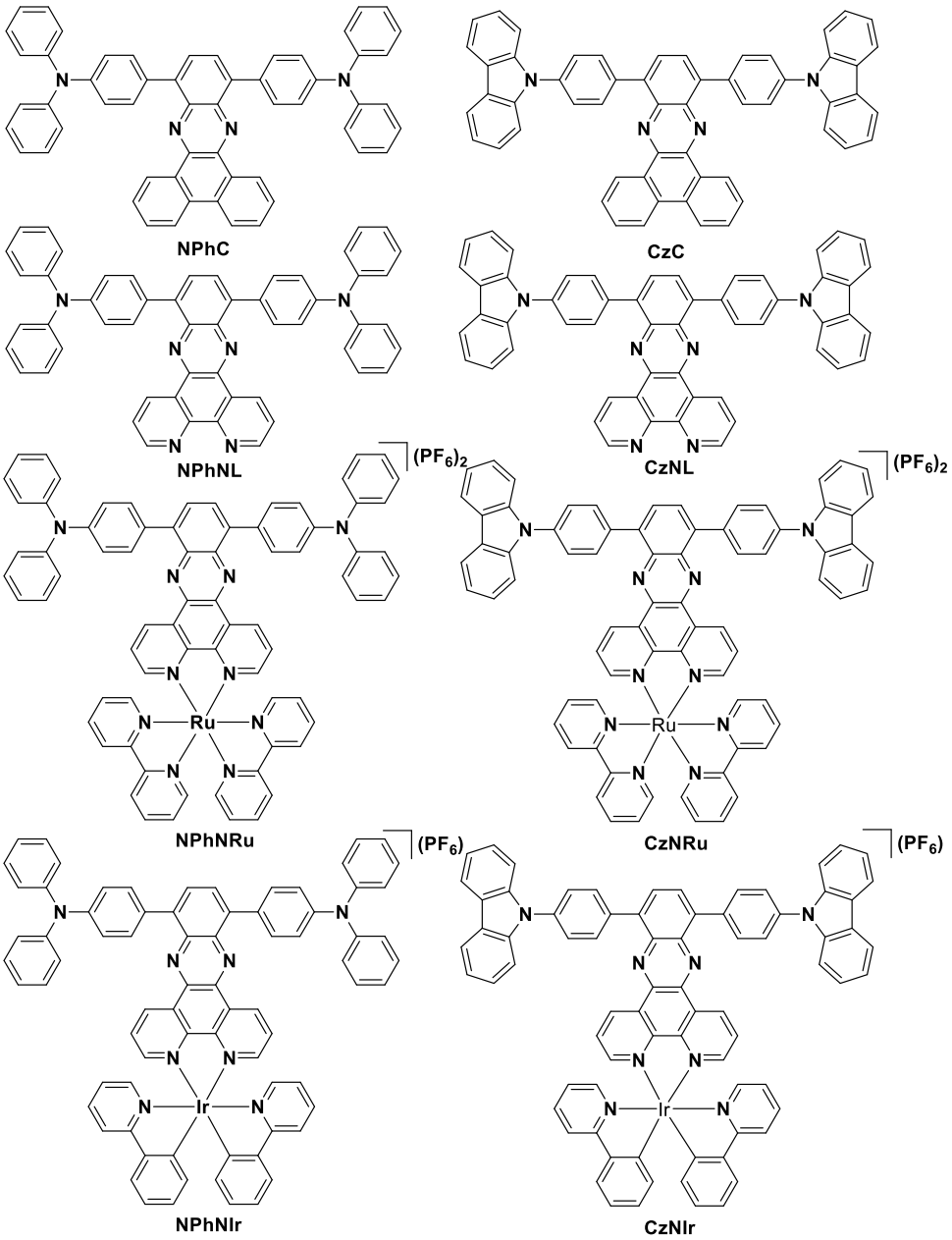

Figure 183. Target compounds **NPhC**, **CzC**, **NPhNL**, **CzNL**, **NPhNRu**, **CzNRu**, **NPhNIr** and **CzNIr**.

Once the two-photon absorption trends have been established, further two-photon active PDT agents will be designed building on lessons learned from the initial family of compounds. Ideally this will facilitate the modification of existing two-photon active compounds in order to make them suitable ligands for metal complexes with high PDT efficiency.

4.3 Synthesis and Characterisation

4.3.1 Synthesis and Characterisation of Intermediate 1-3

For previously published syntheses of dppz derivatives, the desired functional groups were introduced before the final condensation.[24,128,135] This is due to the reportedly low activity of the dppz extended ring system in

most reactions - specifically around the single benzene ring at the "top" of the molecule.[136] Common synthetic preparations used widely across dppz syntheses employs 2,1,3-benzothiadiazole (**Scheme 21**) as a diamine precursor. 2,1,3-benzothiadiazole is readily commercially available, air- and light-stable, and has been extensively modified through numerous reactions.[126,137] Particularly relevant to this project is the ability to selectively brominate the 4- and 7-positions on the benzene ring, facilitating further functionalisation by using palladium catalysed cross-coupling reactions, specifically the Suzuki coupling. Applying this methodology, a number of donor-substituted dppz derivatives have been synthesised.[126,128,135] However, there are some problems with this early functionalisation method. The use of expensive palladium catalysts early in the synthetic process results in lower efficiency than comparative late-stage functionalisation. Additionally, while the reduction of benzothiadiazole proceeds under mild conditions, it has been reported that sterically constrained systems show significantly lower reaction yields than sterically unencumbered systems, which limits the potential functionalisation of dppz.[137] Consequently, it was decided to synthesize the dibrominated dppz and dibenzophenazine (dbpz) displayed in **Scheme 21** as precursors for the target compound.

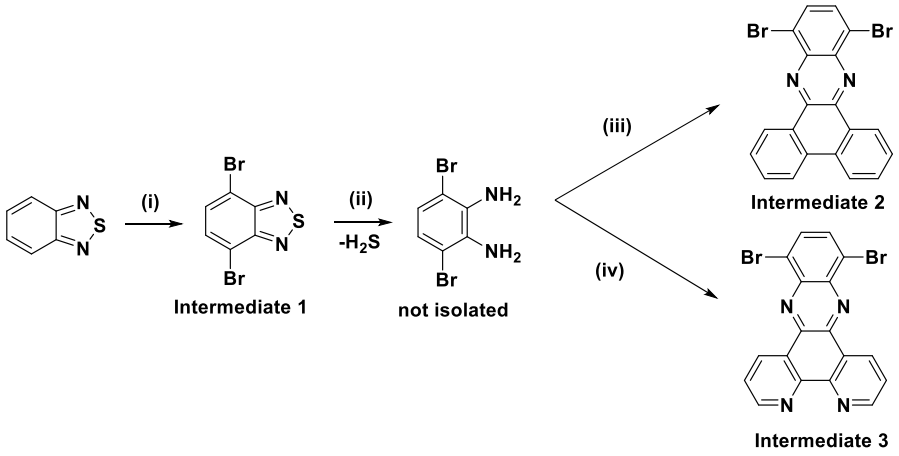

Scheme 21. Synthesis of 4,7-dibromo-2,1,3-benzothiadiazole from 2,1,3-benzothiadiazole**,** 3,6-dibromobenze-1,2-diamine from 4,7-dibromo-2,1,3-benzothiadiazole and synthesis of **Intermediate 2** and **Intermediate 3** from the condensation of 3,6-dibromobenze-1,2-diamine and the appropriate dione. (i) HBr/Br_2, 140 ^oC, 6 h. (67 %) (ii) $NaBH_4$, EtOH, 80 ^oC, 30 h. [137] (iii) 9,10-phenanthrenequinone, HCl, EtOH, 80 ^oC, 12 h. (50.3 %) (iv) 1,10-phenanthroline-5,6-dione (**L3**), HCl, EtOH, 80 ^oC, 12 h. (82 %).

As shown, from 4,7-dibromo-2,1,3-benzothiadiazole (**Intermediate 1**) was used to synthesize **Intermediates 2** and **3**, which would then be followed by coupling reactions, increasing both the efficiency of the overall synthesis due to late-stage functionalisation, and allowing for the creation of increasingly sterically constrained dppz and dbpz systems. Each precursor for the **Intermediate 2** and **3** systems, as well as both compounds themselves, have been reported in literature, and were synthesised according to reported literature procedures.[39,126,129,135,137] 3,6-dibromobenze-1,2-diamine was never isolated as it is unstable in air, with the two reactions (i) and (ii) taking place in one pot.[137] 1,10-phenanthrenequinone was bought commercially.

4.3.2 Synthesis and Characterisation of NPhC and NPhNL

Intermediate 2 and **3** and were then reacted using Suzuki coupling reaction conditions previously developed in the Draper group to form **NPhC** and **NPhNL**, shown in **Scheme 22**.

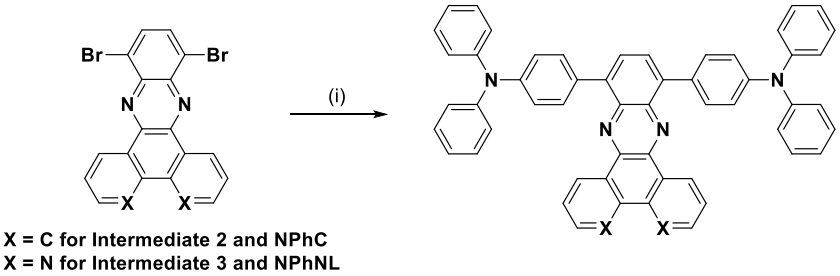

Scheme 22. Synthesis of **NPhC and NPhNL**. (i) 4(diphenylamino)-phenylboronic acid, $Pd(PPh_3)_4$, Na_2CO_2, EtOH/Toluene, 110 °C, 36 h (**NPhC** – 43%, **NPhNL** – 46 %).

The reactions were successful, although yields were never greater than 50 %. The products were analysed by NMR spectroscopy, with the ^{1}H NMR spectrum for **NPhC** shown in **Figure 184** with spin systems assigned.

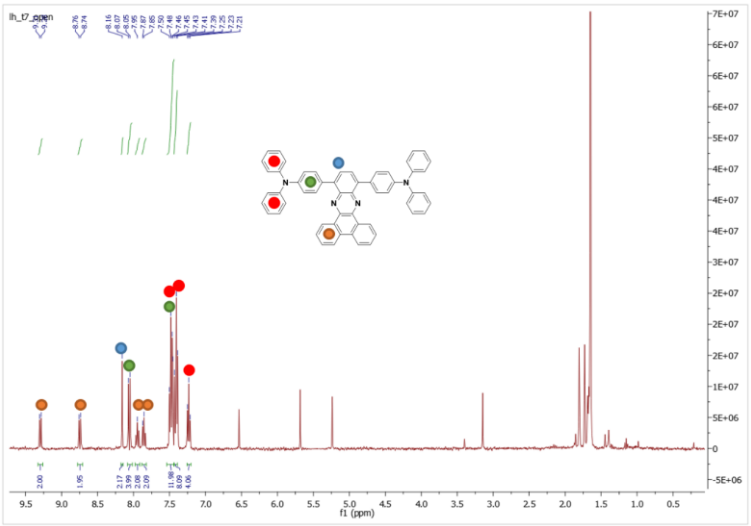

Figure 184. ^{1}H NMR spectrum of **NPhC** with spin systems assigned (400 MHz, CH_2Cl_2, 298 K).

Due to the highly insoluble nature of **NPhC**, the NMR experiments were performed in non-deuterated CH_2Cl_2. This necessitated the removal of CH_2Cl_2 solvent peak at 5.5 ppm, with satellite peaks remaining behind.

The signals resulting from **NPhC** protons are all found in the aromatic region of the spectrum between 7 and 9.5 ppm. The downfield shift results from the ring current that the external magnetic field of the NMR magnet induces in the conjugated hydrocarbon rings. This ring current generates its own magnetic field, which aligns with the external magnetic field on the outside of the ring systems where the protons are located. This enhances the deshielding effect experienced by these protons, resulting in their signals appearing at higher ppm. There are 10 signals in the spectrum, with each signal corresponding to at least two protons due to the high degree of symmetry in **NPhC**. The multiplicity of the signals in the system is complicated, as subtle difference in the electronic environment of some protons results in small J coupling differences, resulting in very fine double doublets or doublet of triplets.

The ^{13}C spectrum for **NPhC** is shown in **Figure 185**, with all signals appearing beyond 100 ppm due to the ring current effect induced by the conjugated ring systems. HSQC NMR experiments were used to assign the carbons as CH (bonded to a proton) or C_q (bonded to zero protons), with the list appearing in the experimental section. As all of the carbons in the system are conjugated, no carbon bonds more than one proton.

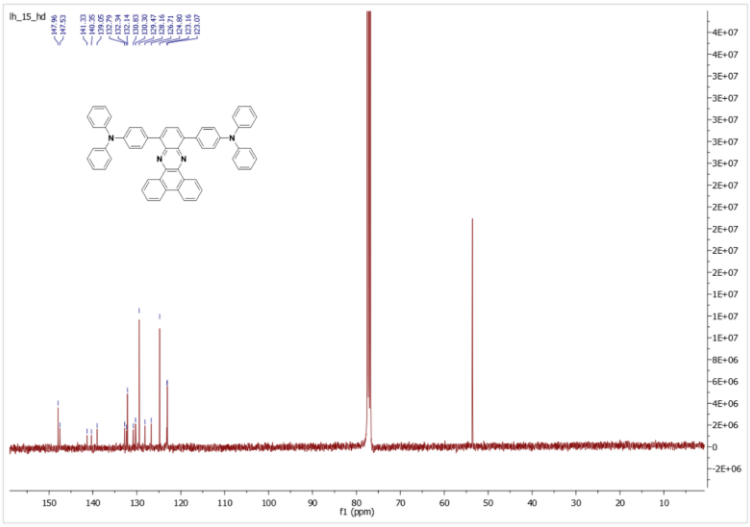

Figure 185. ^{13}C NMR spectrum of **NPhC** (151 MHz, $CDCl_3$, 298 K).

The ^{1}H NMR spectrum of **NPhNL** is displayed in **Figure 186**, with the signals of the orange ring broadened significantly and lower resolution than any other signals in the spectrum. This behaviour could indicate some partial in-solution stacking, where the pyridine rings of two molecules interact with one another, leading to a wide range of slightly different electronic environments for the protons on those rings, leading to signal broadening.

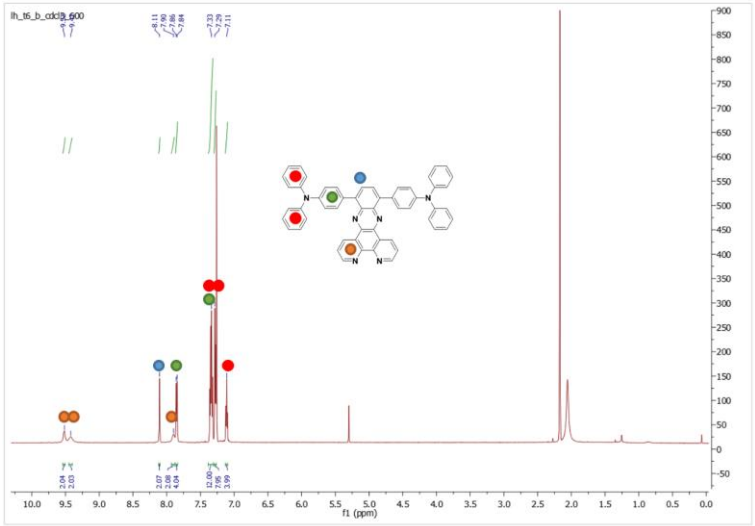

Figure 186. ^{1}H NMR spectrum of **NPhNL** with spin systems assigned (400 MHz, $CDCl_3$, 298 K).

The TOCSY spectrum of **NPhNL** (**Figure 187**) shows that the interactions of the orange protons are significantly weaker than those of the other protons in the compound. This may reflect weaker coupling but

could also result from the same phenomenon that leads to the broadening of the proton signals in the ^{1}H NMR spectrum.

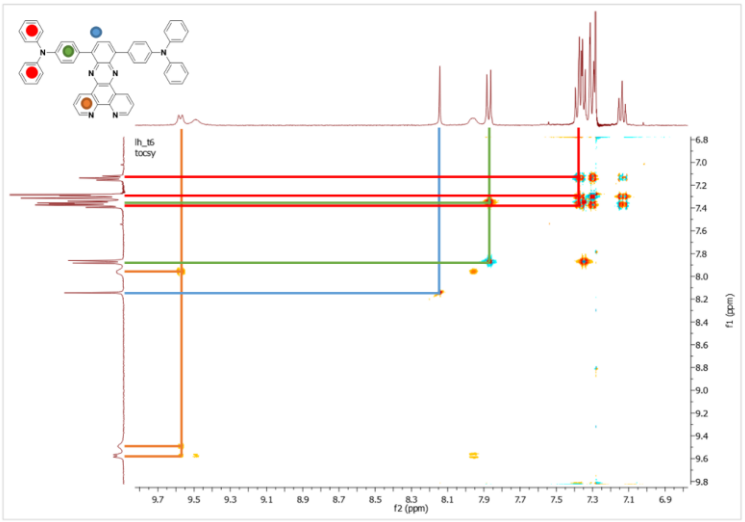

Figure 187. TOCSY NMR spectrum of **NPhNL** showing the interactions of the protons in the discrete spin systems (400 MHz, $CDCL_3$, 298 K).

The ^{13}C NMR spectrum for **NPhNL** is displayed in **Figure 188** below.

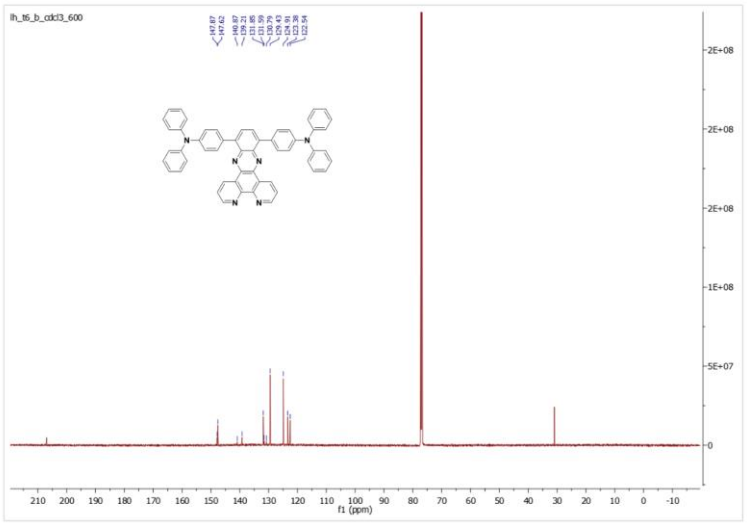

Figure 188. ^{13}C NMR spectrum of **NPhNL** (151 MHz, $CDCl_3$, 298 K).

4.3.3 Synthesis and Characterisation of CzC and CzNL

CzC and **CzNL** were synthesised in an identical way to **NPhC** and **NPhNL** except using 4(9H-carbazol)phenylboronic acid as a Suzuki coupling agent (**Scheme 23**).

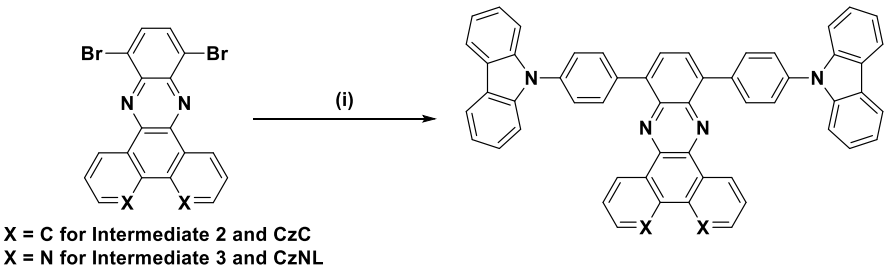

Scheme 23. Synthesis of **CzC** and **CzNL** (i) 4(9H-carbazol)phenylboronic acid, $Pd(PPh_3)_4$, Na_2CO_2, EtOH/Toluene, 110 ºC, 36 h (**CzC** – 56 %, **CzNL** – 50.3 %).

The ^{1}H NMR spectrum of **CzC** is shown in **Figure 189**, and closely resembles that of **NPhC**. The largest difference is a greater number of signals arising from the carbazole compared to the triphenylamine due to the loss of symmetry, resulting in a two doublet and two triplet splitting pattern.

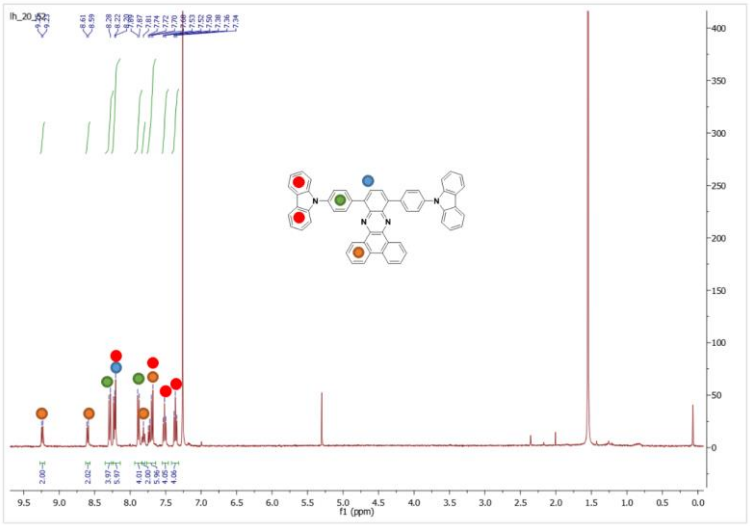

Figure 189. ^{1}H NMR spectrum of **CzC** with spin systems assigned (400 MHz, $CDCl_3$, 298 K).

The TOCSY spectrum for **CzC** is shown below in **Figure 190**, displaying the interactions of protons in the individual spin systems. It is clear from this spectrum that the interactions between protons depends on their position within the system, with some being far more strongly coupled than others, resulting in stronger TOCSY responses. The carbazole moieties form a particularly recognisable pattern as all four signals interact with one another strongly.

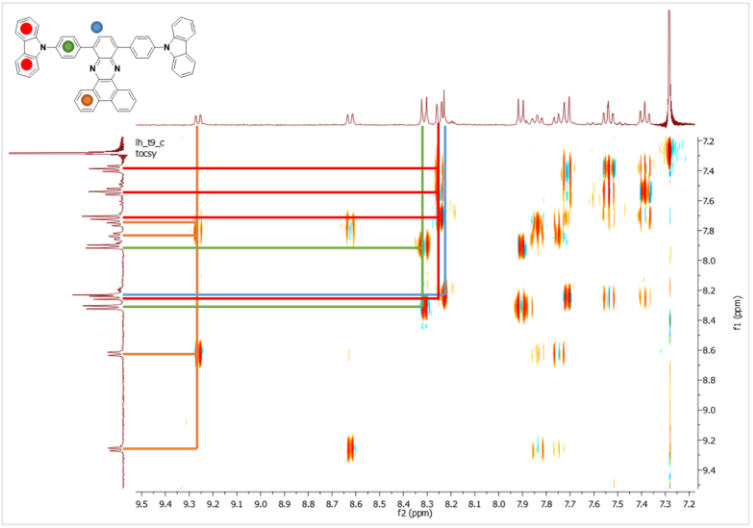

Figure 190. TOCSY NMR spectrum of **CzC** showing the interactions of the protons in the individual spin systems (400 MHz, $CDCl_3$, 298 K).

The ^{13}C NMR spectrum for **CzC** is displayed in **Figure 191** below.

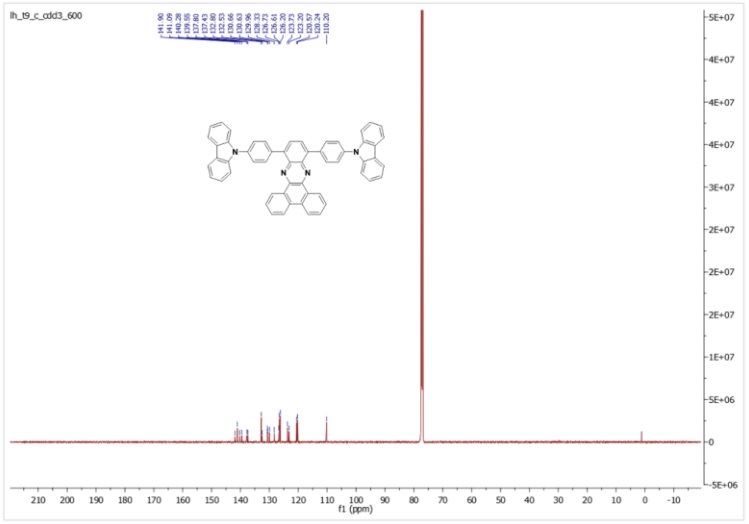

Figure 191. ^{13}C NMR spectrum of **CzC** (151 MHz, $CDCl_3$, 298 K).

The ^{1}H NMR spectrum of **CzNL** (**Figure 192**) was taken in non-deuterated CH_2Cl_2, with spin-locking removing the large solvent peak and leaving the satellite signals below 7 ppm. The signals in the spectrum mirror those of **CzC**, excepting the loss of one of the proton signals in the orange ring due to the transition from a benzene to a pyridine ring. The resolution of all signals is equal, unlike **NPhNL**, suggesting that no intermolecular in-solution stacking is occurring.

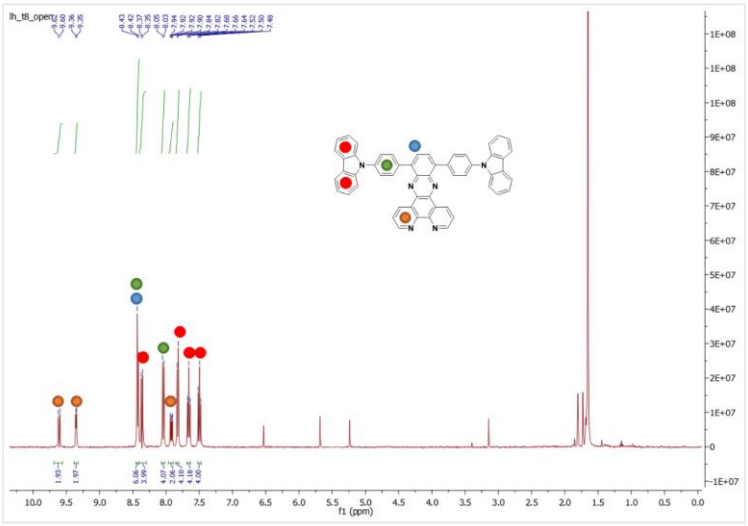

Figure 192. ^{1}H NMR spectrum of **CzNL** with spin systems assigned (400 MHz, CH_2Cl_2, 298 K).

The TOCSY spectrum for **CzNL** (**Figure 193**) shows the interactions within the discrete spin systems. There is significant overlap of signals around 8.3 ppm in the ^{1}H spectrum which would be difficult to resolve in isolation. Using the TOCSY spectrum we can see that this signal overlap is comprised of signals from the red, blue and green spin systems, exemplifying the high utility of this spectroscopic analytical technique.

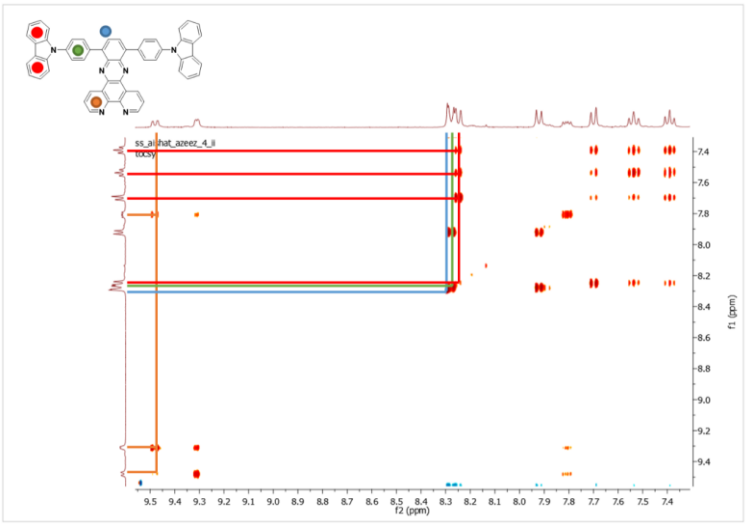

Figure 193. TOCSY NMR spectrum of **CzNL** showing the interactions of protons within the discrete spin systems (400 MHz, $CDCl_3$, 298 K).

The ^{13}C NMR spectrum for **CzNL** is displayed in **Figure 194** below.

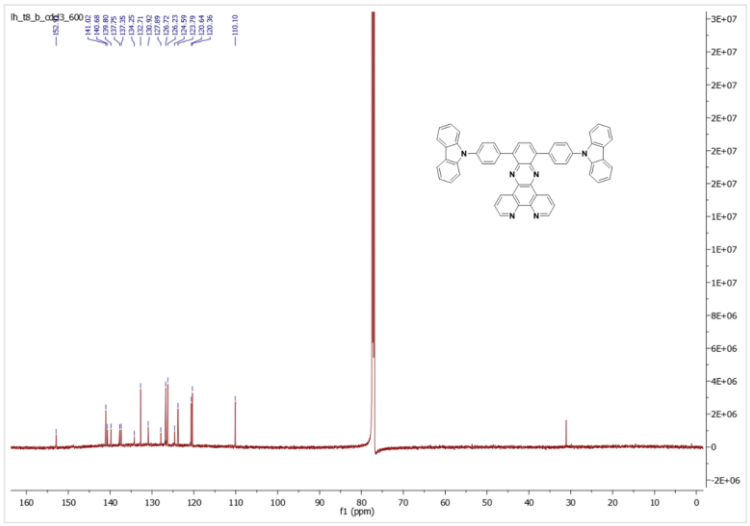

Figure 194. ^{13}C NMR spectrum of **CzNL** (151 MHz, $CDCl_3$, 298 K).

4.3.4 Synthesis of NPhNRu and CzNRu

NPhNRu and **CzNRu** were synthesized by complexation of **NPhNL** and **CzNL** with $[Ru(bpy)_2Cl_2]$ (**Scheme 24**).

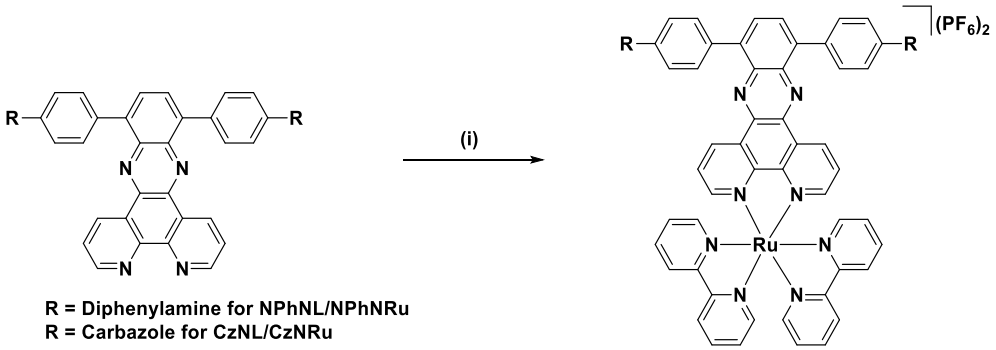

Scheme 24. Synthesis of **NPhNRu** and **CzNRu**. (i) $Ru(bpy)_2Cl_2$, ethylene glycol, 160 ºC at 150 W, 1h.

The ^1H NMR spectra of **CzNRu,** which is far more soluble, is shown in **Figure 195**, with a large number of signals visible in the aromatic region between 7 and 10 ppm.

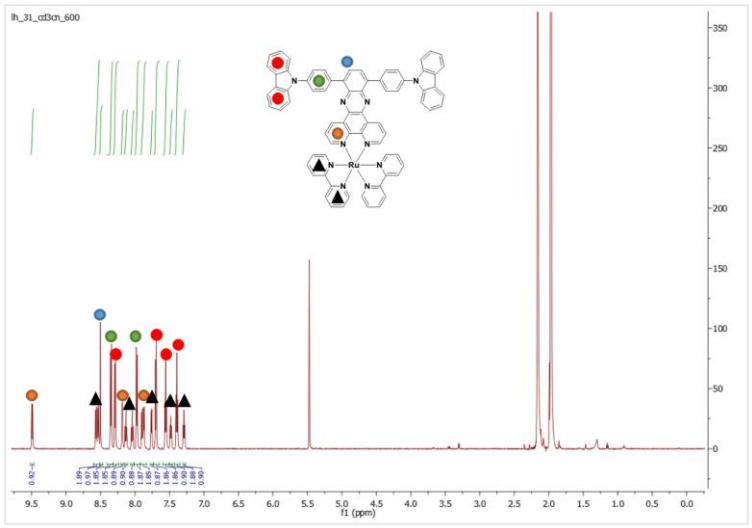

Figure 195. ^{1}NMR Spectrum of **CzNRu** in MeCN-d_3. The peak at 5.49 ppm is due to residual CH_2Cl_2.

Despite the complexity of the full ^{1}H spectrum, there are several distinct spin systems making up the total molecule that are easy to identify using the ^{1}H-^{1}H COSY techniques shown in **Figure 196**.

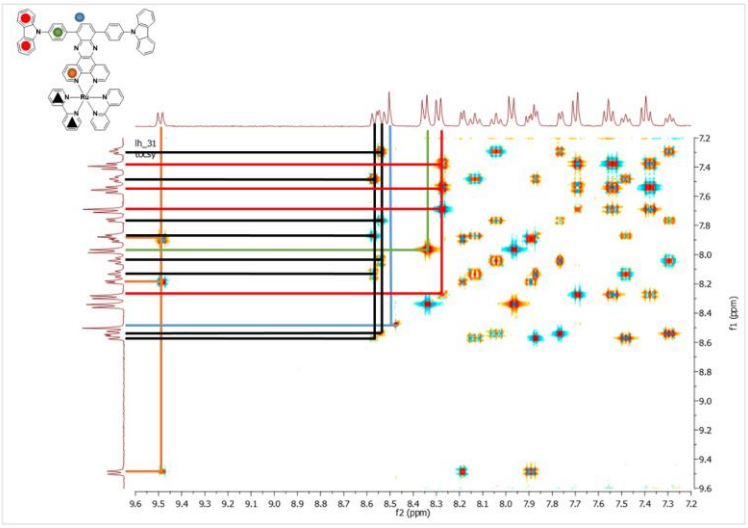

Figure 196. TOCSY of **CzNRu** showing five distinct spin systems, and one singlet at 8.51 ppm from the "top" of the dppz core.

From this spectrum, five distinct spin systems, and one singlet can be identified. The singlet can be immediately assigned to H-4 as it is the only proton signal that is not neighboured by at least one other. The spin system marked in blue, consisting of three members, is labelled as the phenanthroline ring system. The signal at 9.47 ppm is characteristic of H-3, while signals H-1 and H-2 will be further upfield due to the electron-donating effect of the ruthenium metal centre. The two four-membered spin systems highlighted in orange and black are almost overlapping and are typical of the two rings on the auxiliary 2-2'-bipyridine ligands. The two doublets and two triplets of the magenta spin system are assigned to the carbazole ring moieties.

Finally, the spin system highlighted in yellow is assigned as the phenyl spacer rings between the nitrogen atom and the dppz core. Without further NMR experiments, it is not possible to confidently assign these signals, but it is likely that the more shifted signal is H-5 due to the proximity of the extended dppz core. H-6 is assumed to be more shielded due to the through-bond donating effect of the nitrogen atom. To confirm this, NMR experiments using through-space interactions were performed. The first of these spectra, shown in **Figure 197**, shows the correlation of the peak at 8.35 ppm (H-5 or H-6) to the singlet peak at 8.51 ppm (H-4).

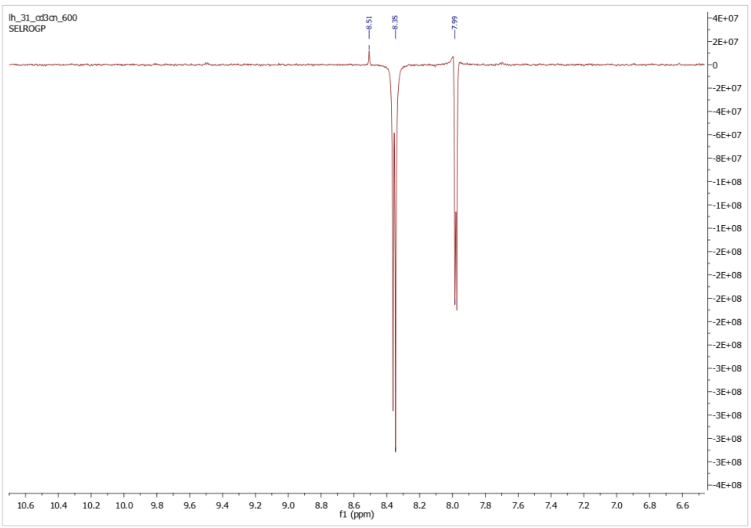

Figure 197. Selective 1D ROESY NMR of **CzNRu**, showing phase selected proton signals and strongly interacting proton signals as negative peaks, while proton signals within 5 Å show as positive signals. Targeting the peak at 8.25 ppm.

The other peak at 7.99 ppm represents the other proton on the phenyl ring. This correlation suggests the peak at 8.35 ppm to be H-5, and further experiments were done to confirm this hypothesis. The peak at 7.99 ppm (H-5/6) was also investigated using the same selective 1D ROESY experiment, exhibited in **Figure 198**.

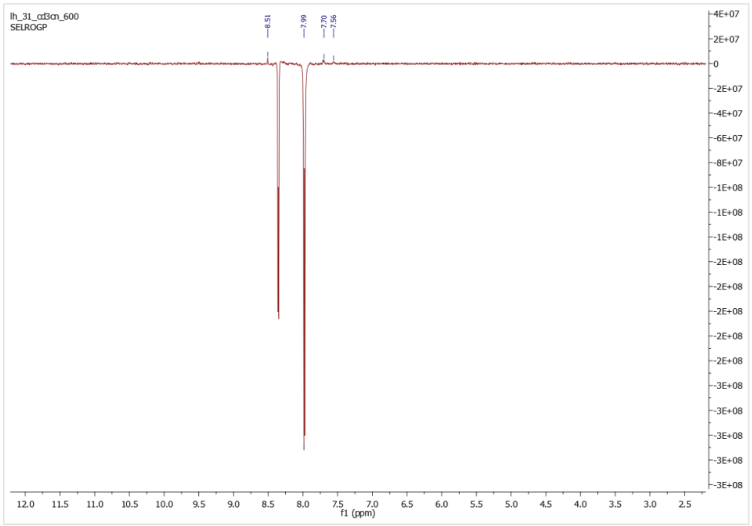

Figure 198. Selective 1D ROESY NMR of **CzNRu**, showing phase selected proton signals and strongly interacting proton signals as negative peaks, while proton signals within 5 Å show as positive signals. Targeting the doublet peak at 7.99 ppm (H-5/6).

This peak, while still exhibiting interaction with the singlet at 8.51 ppm (H-4), also shows a through-space interaction with the carbazole peaks at 7.70 and 7.56 ppm (H-7 and H-8). For final confirmation, the same experiment was run on the singlet peak at 8.51 ppm (H-4), with the result exhibited in **Figure 199**.

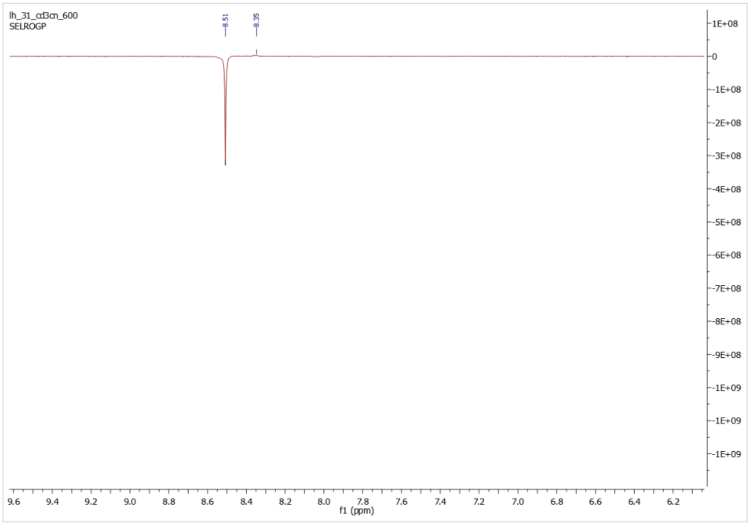

Figure 199. Selective 1D ROESY NMR of **CzNRu**, showing phase selected proton signals and strongly interacting proton signals as negative peaks, while protons within 5 Å show as positive signals. Targeting the H-5 singlet.

This spectra demonstrates the correlation of the H-4 at 8.51 with the peak at 8.35 ppm, allowing the ^{1}H NMR signals to be fully assigned to the corresponding proton signals H-5.

The ^{13}C NMR spectrum of **CzNRu** is displayed below in **Figure 200**.

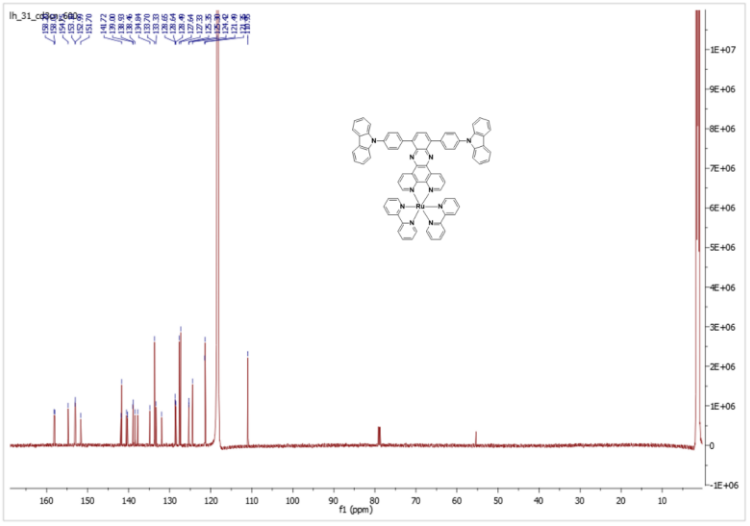

Figure 200. ^{13}C NMR spectrum of **CzNRu** (151 MHz, MeCN-d_3, 298 K).

The same NMR analysis was performed on **NPhNRu**, whose ^{1}H NMR spectrum with assigned spin systems is displayed in **Figure 201.**

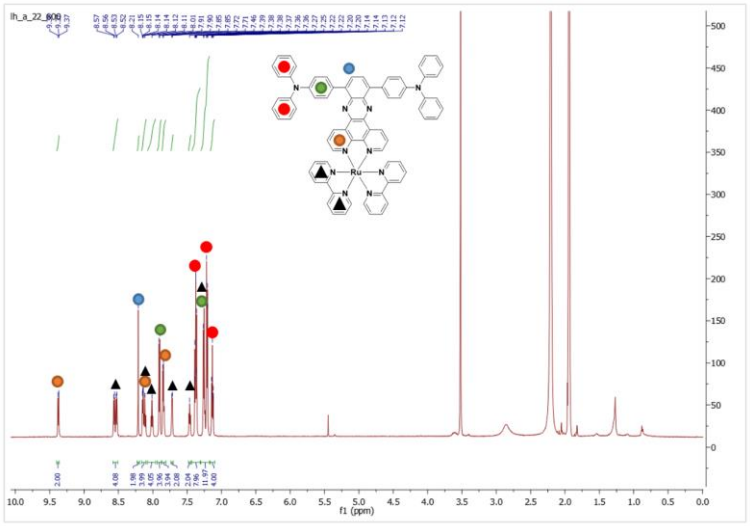

Figure 201. ^{1}H NMR spectrum of **NPhNRu** with assigned spin systems (600 MHz, MeCN-d_3, 298 K).

The TOCSY (A) and ^{13}C NMR (B) spectra of **NPhNRu** are shown below in **Figure 202**.

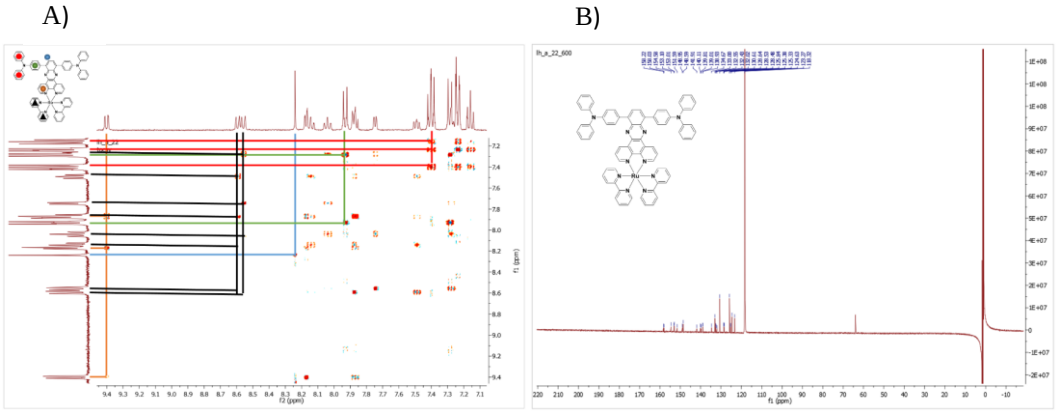

Figure 202. (A) TOCSY of **NPhNRu** showing 5 spin systems and one singlet at 8.51 ppm from the "top" of the dppz core. (B) ^{13}C NMR spectrum of **NPhNRu** (151 MHz, $CDCl_3$, 298 K).

4.3.5 Synthesis of NPhNIr and CzNIr

NPhNIr and **CzNIr** were synthesised following the synthetic methods developed for iridium complexes in earlier chapters.

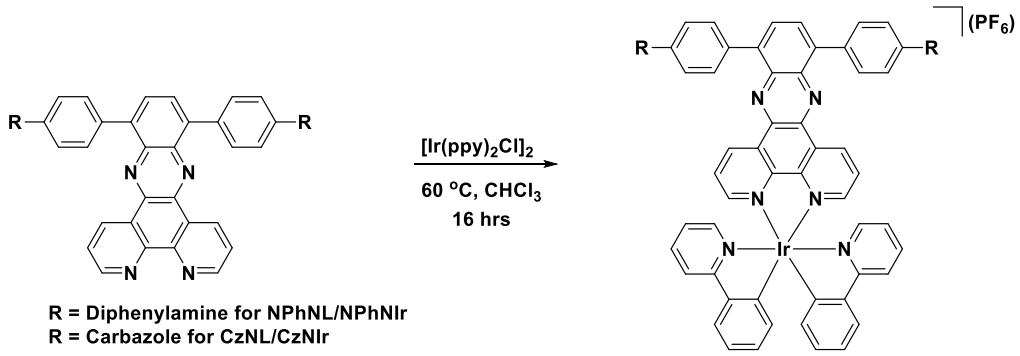

Scheme 25. Synthesis of **CzNIr** and **NPhNIr**.

The ligands were refluxed in chloroform in the presence of $[Ir(ppy)_2Cl]_2$ for 16 hours, followed by evaporation and purification via silica column chromatography using CH_2Cl_2:MeOH gradients as a mobile phase. The products eluted as dark orange bands, and after anion exchange from Cl^- to PF_6^- they were isolated by precipitation, filtered, and dried.

The ^{1}H NMR spectrum of **CzNIr** (**Figure 203**) resembles that of **CzNRu**, but with a larger number of signals due to the loss of symmetry when transitioning from bipyridine to phenylpyridine ligands. There is significant overlap of signals from protons on those rings, leading to a complex set of multiplets in the aromatic region.

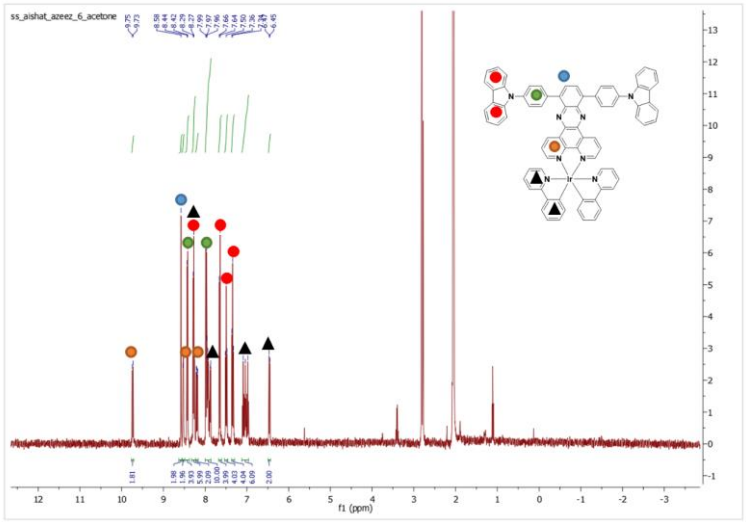

Figure 203. ^{1}H NMR spectrum of **CzNIr** showing the assigned spin systems (400 MHz, MeCN-d_3, 298 K).

Despite the apparent complexity, the individual spin systems remain easily identifiable using TOCSY NMR experiments, as shown in **Figure 204**. The carbazole and spectator ligand ring systems are both comprised of 4 signals, but can be differentiated based on integration value, with the former integrating to 4 protons per signal and the latter to 2.

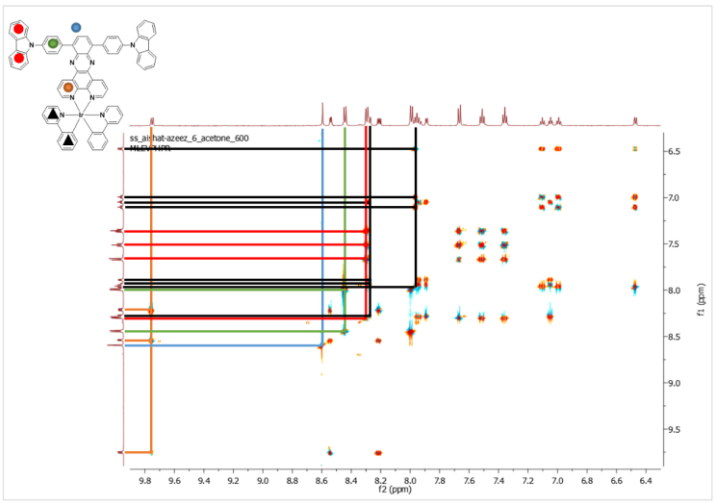

Figure 204. TOCSY NMR spectrum of **CzNIr**, showing the interactions of protons in the discrete spin systems (600 MHz, MeCN-d_3, 298 K).

The TOCSY (A) and ^{13}C NMR (B) spectra of **CzNIr** are shown below in **Figure 205**.

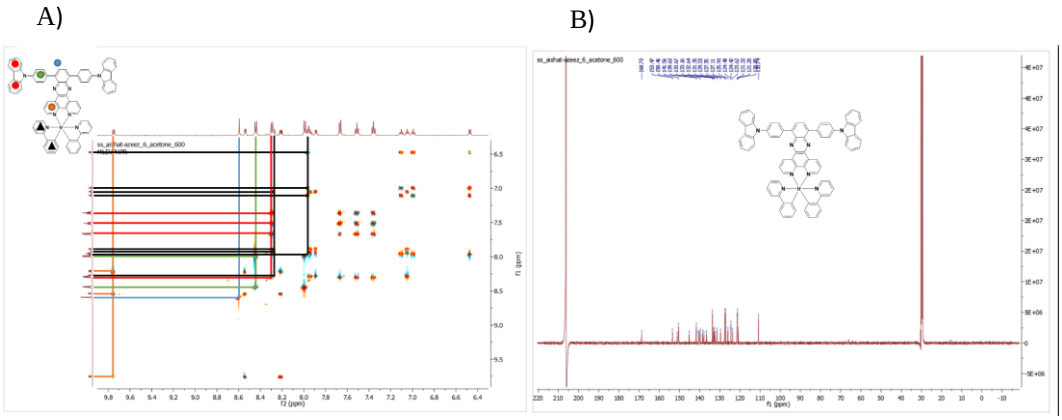

Figure 205. (A) TOCSY of **CzNIr** showing 5 spin systems and one singlet at 8.51 ppm from the "top" of the dppz core. (B) ^{13}C NMR spectrum of **CzNIr** (151 MHz, $CDCl_3$, 298 K).

The NMR spectrum for **NPhNIr** (**Figure 206**) shows the same patterns previously established in this work, and the signals were assigned in similar fashion. For the full assignment please see the experimental section.

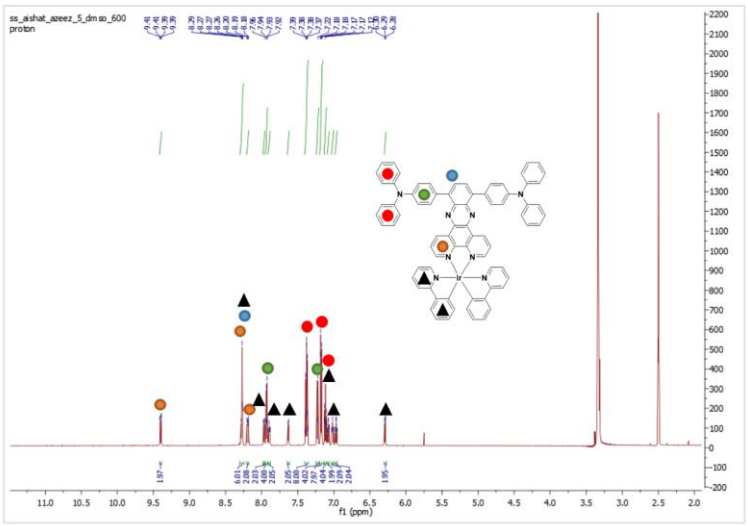

Figure 206. ^{1}H NMR spectrum of **NPhNIr** with spin systems assigned (600 MHz, DMSO-d_6, 298 K).

The TOCSY (A) and ^{13}C NMR (B) spectra of **NPhNIr** are shown below in **Figure 207**.

A) B)

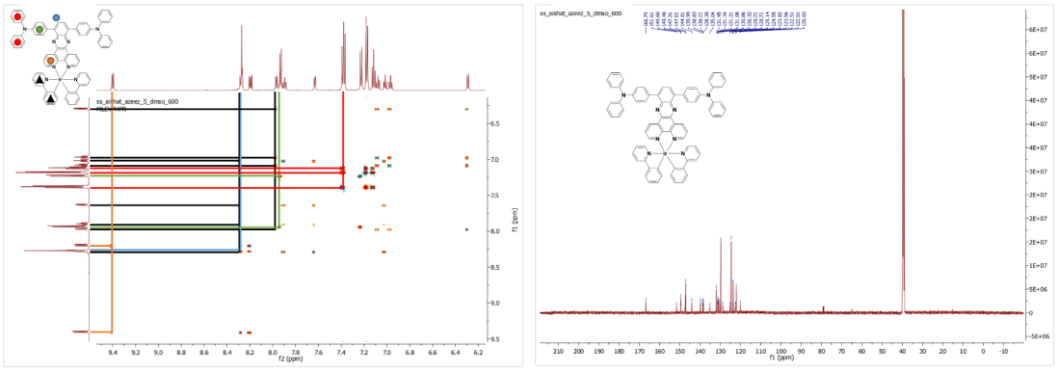

Figure 207. (A) TOCSY of **NPhNIr** showing 5 spin systems and one singlet at 8.51 ppm from the "top" of the dppz core. (B) ^{13}C NMR spectrum of **NPhNIr** (151 MHz, $CDCl_3$, 298 K).

4.3.6 Crystallographic Analysis of CzNIr

A crystal sample of **CzNIr** suitable for x-ray analysis was grown. The specimen of **CzNIr** ($C_{76}H_{48}IrN_8$) approximate dimensions 0.020 mm x 0.080 mm x 0.180 mm, was used for the X-ray crystallographic analysis. The X-ray intensity data were measured (λ = 1.54178 Å) on a Bruker Apex Kappa Duo with an Oxford Cobra Cryosystem low temperature device using a MiTeGen micromount. A total of 2125 frames were collected. The total exposure time was 40.22 hours. The integration of the data using a monoclinic unit cell yielded a total of 38065 reflections. Very weak diffraction from a poorly diffraction crystal. Diffraction limit was 0.95 Angstroms. Rigid groups were used to model the carbazole and phenazine groups. Many restraints were applied to improve the model (DFIX, SIMU, SADI, ISOR, FLAT and RIGU). This is a connectivity diagram only. All counterions, solvent etc. were removed from the structure using a solvent mask which reveals two voids, V=718 Angstroms3, electrons = 212 and V=737 Angstroms, electrons = 234.

Structure also refined as an inversion twin with a Flack = 0.49(5), Hooft = 0.7(13). A unit cell of **CzNIr** is shown in **Figure 208**.

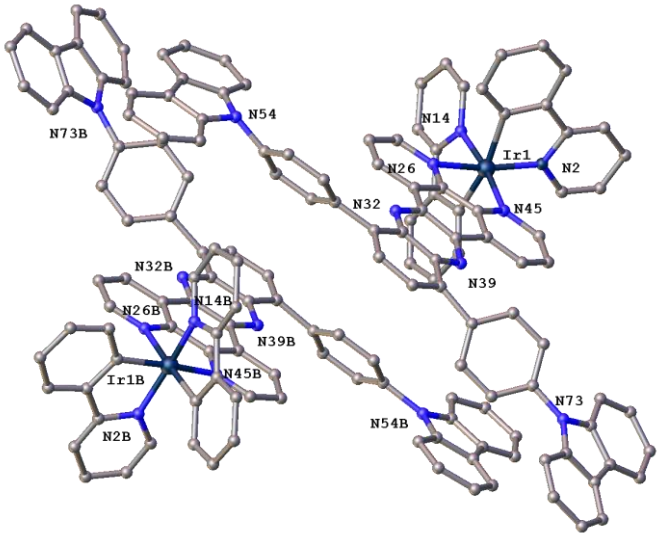

Figure 208. Unit cell of **CzNIr.**

The structure exhibits significant twists in the bonds connecting the bridging phenyl ring to the dppz core and the carbazole. The two molecules are slightly offset w.r.t the iridium metal centre, allowing for the carbazole moieties of one complex to slot into the gap between the carbazole and bridging phenyl moieties of the other.

This arrangement suggests that the substituted dppz ligand is the region of the complex that largely influences the packing structure within the crystal. This is like some of the other crystal structures discussed previously in this thesis and can be rationalised by the large size of the ligand relative to the metal centre and spectator ligands. The packing structure of the crystal is shown in **Figure 209**.

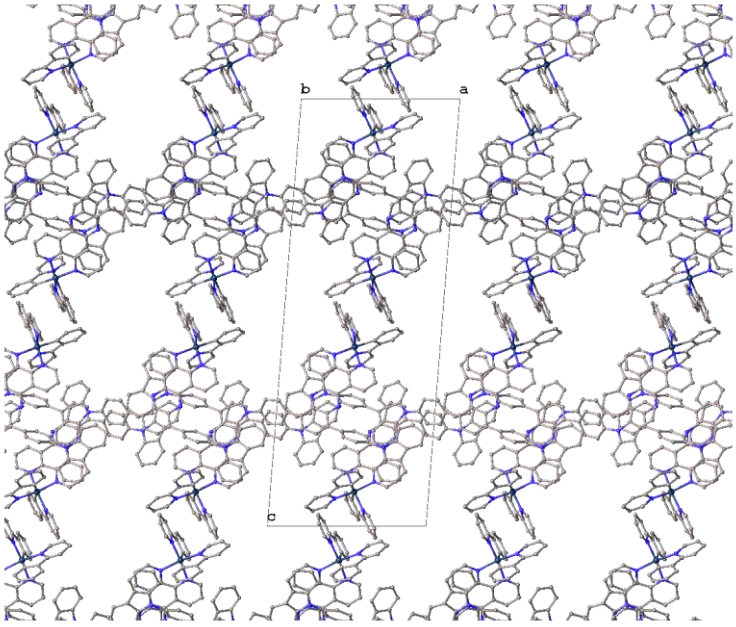

Figure 209. Packing structure of **CzNIr.**

The packing structure is shown with solvent molecules and counterions removed to improve visual clarity. There are two distinct regions within the packing lattice, one where the metal ion and spectator ligands are localised and another that is dominated by the DPPZ ligand. The DPPZ ligands of different molecules form complex arrangements, while the spectator ligands have simpler 'face-to-face' interactions. Large unoccupied voids within the packing lattice are hosts to the removed solvent and counterion molecules.

4.4 Photophysical Analysis

Unfortunately, no two-photon absorption data could be obtained in time for the submission of this work. While examining the two-photon absorption properties of the compounds are the primary motivating factor for this project, literature data for the one-photon photophysical properties of each respective compound are limited, or non-existent. As a result, the one-photon photophysical properties of each compound were explored and are reported here for the first time.

4.4.1 Spectroscopic Analysis of DPPZ and DBPZ

4.4.1.1 Solvatochromic Absorption and Emission of DPPZ and DBPZ

The large Stokes shift and broad emission band suggest a charge-transfer transition between the nitrogen donor species, and the central core acceptor.[138] To confirm this, both low-temperature and solvatochromism studies were performed in CH_2Cl_2, Toluene, and Butyronitrile as the chosen solvents of varying polarity. While use of a protic alcohol like MeOH or EtOH is often found in the literature, none of the four compounds were sufficiently soluble in either solvent to be useful for these measurements, and similar issues were found when attempting to use acetonitrile. Butyronitrile was chosen as it is a polar solvent that is also able to form a glass when frozen, allowing it to be used for low-temperature measurements. The absorption and emission profiles of the four compounds are presented in the **Figure 210**.

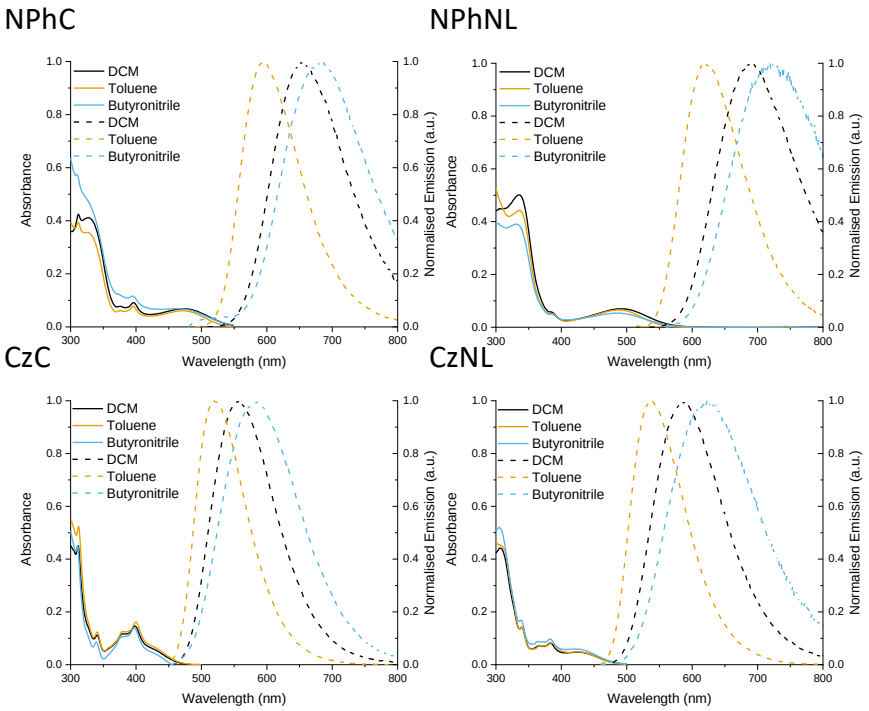

Figure 210. Solvatochromism absorption and emission of **NPhC, NPhNL, CzC and CzNL** in CH_2Cl_2, Toluene, and Butyronitrile, with excitation at the lowest energy peak for each compound (see **Table 15**).[10^{-5} M], 298 K.

The studies showed insignificant changes in the absorption spectrum, with differences in intensity likely resulting from changes in concentration due to the solubility issues. The absorption peaks remained constant for all compounds in all solvents, indicating that the ground state is not affected by solvent polarity. However, the emission maxima of each compound are greatly affected by solvent polarity. This suggests a polarised excited state, as the dipole formed by charge transfer can be stabilised by solvents which have a strong permanent dipole moment. This supports the postulation that a charge transfer transition occurs, from the nitrogen donor group of the respective donor system, to the highly conjugated and low-energy π* structure of the dppz or dbpz core, as the excited state is stabilised by solvents of greater polarity, resulting in a red-shift with increasing polarity. As a final confirmation of the CT nature of the excited state, low temperature measurements were performed.

4.4.1.2 Comparison of the Absorption and Emission properties of DPPZ and DBPZ

The emission and absorption data of the ligands **NPhC, NPhNL, CzC** and **CzNL** are shown in **Figure 211**, and agree with the data already available in the literature.[126,129]

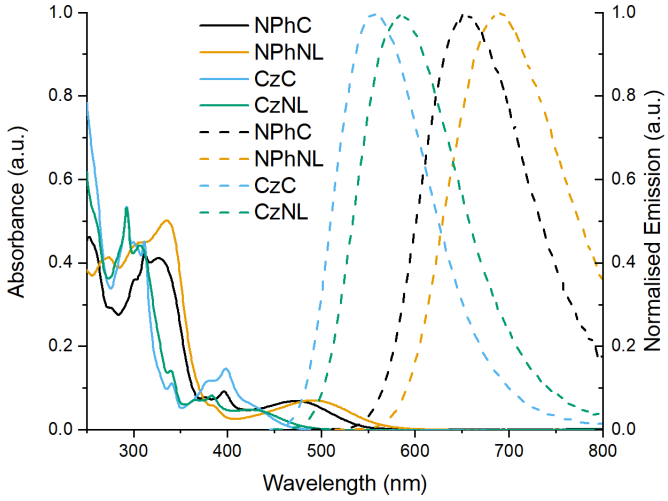

Figure 211. Absorption and normalised emission spectra of **NPhC, NPhNL, CzC and CzNL** in CH_2Cl_2, excited at the lowest energy transition for each compound (see **Table 15**). [10^{-5} M] 298 K.

Several different transition classes can manifest as absorption bands in the UV and visible spectrum. One subclass of these transitions can be described as locally-excited transitions, which usually occur within electronically discrete parts of the molecule, such as strongly conjugated ring systems. Two common examples of locally-excited transitions are π-π^* and n-π^* transitions, shown in **Figure 212**.

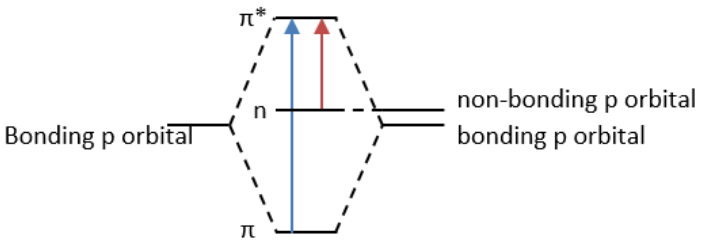

Figure 212. Simplified diagram showing two bonding p-orbitals forming a π bond, with a low-level bonding π and a high level antibonding π^*orbital.

The electronic transition between these two orbitals (blue arrow) is a high-energy π- π^* transition. The diagram also displays a non-bonding p-orbital, which is populated by electron lone pairs such as those found on nitrogen and oxygen. These electrons can also undergo transitions to the π^* orbital (red arrow), resulting in lower energy n- π^* transitions. These transitions will typically be found at high wavelengths in the UV and blue parts of the spectrum due to the high energy gaps between the ground state and excited state orbital.

Another possible transition involves the transfer of charge from electron-rich parts of the molecule to electron-poor parts of the molecule. These charge-transfer (CT) transitions typically involve the population of the overall molecular LUMO by excitation of the electrons in the HOMO. These transitions often result in broad and featureless peaks in the absorption spectrum due to the high number of vibrational and rotational states in the HOMO and LUMO leading to strong vibrational and rotational coupling.

All compounds manifest a broad absorption as their lowest energy peak, with the TPA-containing compounds **NPhNL** and **NPhC** manifesting at 495 and 470 nm respectively. The carbazole-containing compounds **CzC** and **CzNL** are more blue-shifted, with absorption peaks between 380 and 400 nm, showing long and broad shoulders until 450 nm. Higher energy transitions for all four compounds show a large number of peaks, likely arising from a combination of a number of π-π* and n-π* transitions. The large number of discrete high-energy peaks may be the result of the large number of discrete spin systems within the compounds, all of which may show their own absorption bands arising from locally-excited transitions. The transition at the longest wavelength for all compounds could arise from a CT transition from the amine donors into the acceptor core, but further investigation of the photophysical properties of the compounds would be needed to confirm this theory. The emission spectra of all four compounds are broad, featureless, and exhibit a large Stokes shift. **NPhC** and **NPhNL** are red-shifted compared to **CzC** and **CzNL**, and both dppz compounds are red-shifted compared to their respective dbpz equivalent. **Table 15** summarises the spectroscopic data for the compounds.

Table 15. Absorption and emission properties of **NPhC**, **NPhNL**, **CzC** and **CzNL** in. CH_2Cl_2 [10^{-5}M] 298 K.

From these values, it becomes clear that there are some governing factors that determine absorption and emission in the series. The first of these is the presence of either triphenylamine or carbazole donating groups, with the former resulting in lower energy (longer wavelength) transitions than the latter. This suggests a greater HOMO-LUMO gap in the carbazole compounds than in the triphenylamine compounds. This trend is supported by the emission data, which shows a significant redshift of the peak when comparing the triphenylamine compounds to the carbazole compounds. This shift would again arise from a lower HOMO-LUMO gap in the triphenylamine compounds. This suggests that the HOMO of **NPhNL** is higher in energy than the HOMO of **CzNL**, as the acceptor and associated LUMO are the same, but the emission and absorption properties are quite different. The increase in energy of the HOMO results in a lower energy HOMO-LUMO gap and more red-shifted emission and absorption maxima for **NPhNL** than **CzNL.** The same holds true for **NPhC** and **CzC.**

Compound	λ_{abs}(nm)	$\varepsilon\ 10^3$ (L mol^{-1}cm^{-1})	$\lambda_{emission}$(nm)	Stokes Shift (nm)
NPhC	470, 400, 380, 340, 310	6.83, 8.82, 7.41,36.99, 41.06	655	185
NPhNL	495, 385, 340	7.00, 5.72, 49.06	690	195
CzC	435, 400, 380, 340, 310	4.86, 14.39,11.70, 11.82, 43.73	555	120
CzNL	440, 385, 340	4.2, 8.02, 14.17	590	150

Another trend suggested by the emission data is that the dbpz cores result in a higher energy LUMO than the dppz cores. This observation can be made my comparing the properties of **NPhC**, whose emission and absorption wavelengths are blue-shifted compared to those of **NPhNL.** Since both compounds use a triphenylamine donor but a different acceptor core, it is likely the LUMO of **NPhC** is higher in energy than the LUMO of **NPhNL**. This results in a lower energy HOMO-LUMO gap and higher emission and absorption maxima for **NPhNL** than **NPhC.** The same holds true for **CzC** and **CzNL.**

To further investigate the nature of the lowest-level excited state, which is most likely to result in emission according to Kasha's rule, solvatochromic and low temperature measurements were performed and are discussed in the following sections.

4.4.1.3 Low Temperature Measurements of DPPZ and DBPZ

Further confirmation of the charge-transfer nature of each compound can be obtained from low temperature experiments, where upon freezing the solvent at 77 K, a dramatic change in solvent viscosity affects the ability of the solvent to reorganise to stabilise the excited state, resulting in a blue-shift in emission in a given solvent. Low temperature measurements were undertaken using a borosilicate glass NMR tube, in specially constructed liquid nitrogen Dewar flask. First, a room temperature measurement was taken, and

subsequently, the sample was cooled to 77 K before a second measurement was taken. Butyronitrile was chosen as the low temperature solvent, as it has the greatest stabilisation effect on the excited state due to its strong dipole moment and should therefore exhibit the greatest change upon freezing. The results of each experiment are presented in **Figure 213**.

.

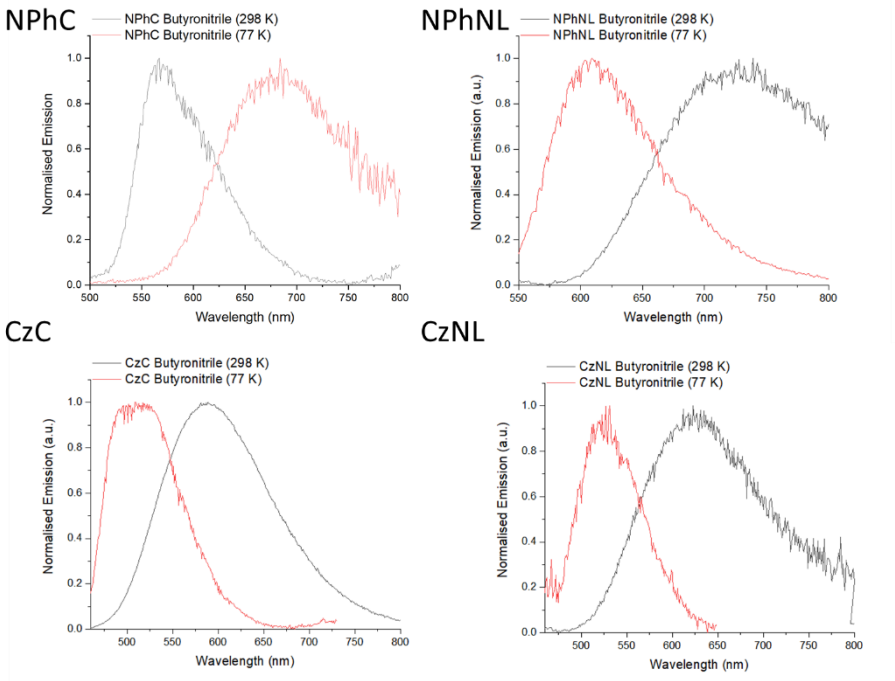

Figure 213. Room and low temperature (77 K) emission spectra of **NPhC, NPhNL, CzC and CzNL** in Butyronitrile, excited at the lowest energy transition. The low resolution is a result of the imperfections in the butyronitrile glass, and the use of a borosilicate glass NMR tube [10^{-5} M].

These measurements help confirm the charge transfer nature of the excited state. All of the compounds show blue-shifts in emission at 77 K compared to the room temperature measurements. However, these measurements do suffer from significant noise compared to standard emission spectra. This can arise due to two reasons. The first of these is the use of borosilicate NMR tubes instead of standard quartz cuvettes. The glass itself can interact with the light in the spectrometer, leading to scattering. Additionally, butyronitrile may not form a perfect glass when cooled to 77K. The presence of ice or imperfections in the glass can contribute to this scattering as well. The two combined result in spectra that are only qualitatively useful for analysis by observing the change in peak position, which is clearly observed for all compounds, confirming a CT excited state.

4.4.1.4 Trifluoroacetic Acid Titrations

Considering the high number of nitrogen atoms in each structure, and the previously reported performance of dppz derivatives in protic media, the behaviour of **NPhC, NPhNL, CzC** and **CzNL** upon sequential addition of increasing amounts of acid were investigated.[75] Both the absorption and emission spectra of the compounds were obtained following addition of 10, 20, 30, 40, 50 and 100 µl 0.1 M trifluoroacetic (TFA) solutions in CH_2Cl_2 to 2 mL solutions of the respective ligands in DCM at 10^{-5} M concentrations. The

absorption spectra are reported in **Figure 214**. These graphs show two distinct behaviour patterns for the four compounds. **NPhNL** and **CzNL** show immediate change upon addition of 10 µl of TFA, indicating a significant change in the ground state energies. Following this change, subsequent additions resulted in a slight red-shift of the charge-transfer bands, accompanied by a steady reduction in absorption intensity for all peaks.

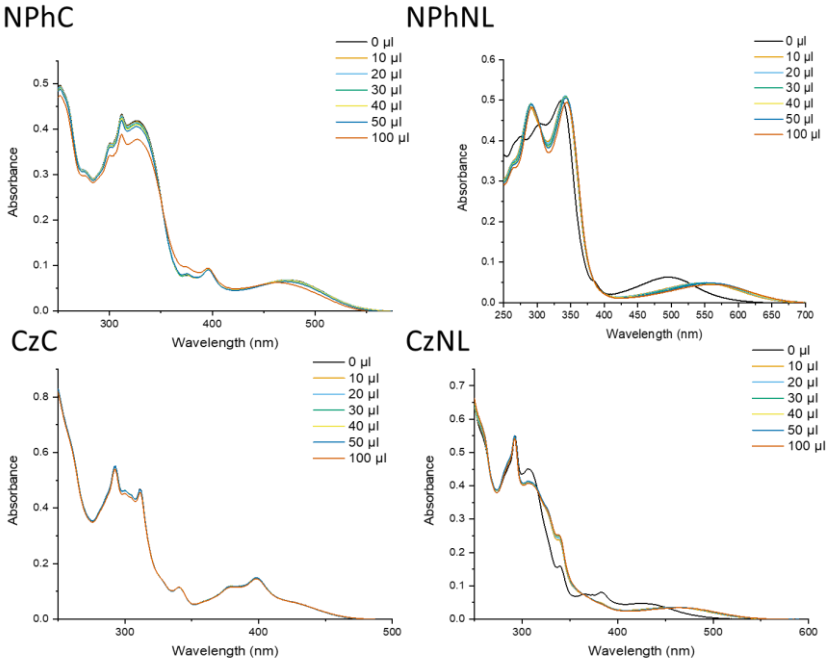

Figure 214. Observation of the effect of 0.1 M quantities of TFA to **NPhC, NPhNL, CzC** and **CzNL** in the respective UV spectra CH_2Cl_2 [10^{-5} M] 298 K.

NPhC exhibits a blue-shift, combined with a reduction in absorption intensity in the assigned charge transfer band. In the higher energy UV region, increases and decreases in absorption relates to changes in locally excited transitions. **NPhNL** shows an immediate change upon addition of the acid, suggesting a change in the ground-state molecular configuration. Additional aliquots of acid do not significantly change the absorption spectrum, aside from changes to the intensity of locally-excited transitions and a slight bathochromic shift of the charge-transfer absorption band. The absorption profile of **CzC** exhibits minimal changes. **CzNL** once again shows an immediate change upon addition of acid, followed by similar trends as those observed in **NPhNL.** Further to each measurement of the UV profile, and emission spectrum was also collected after every addition of TFA (**Figure 215**).

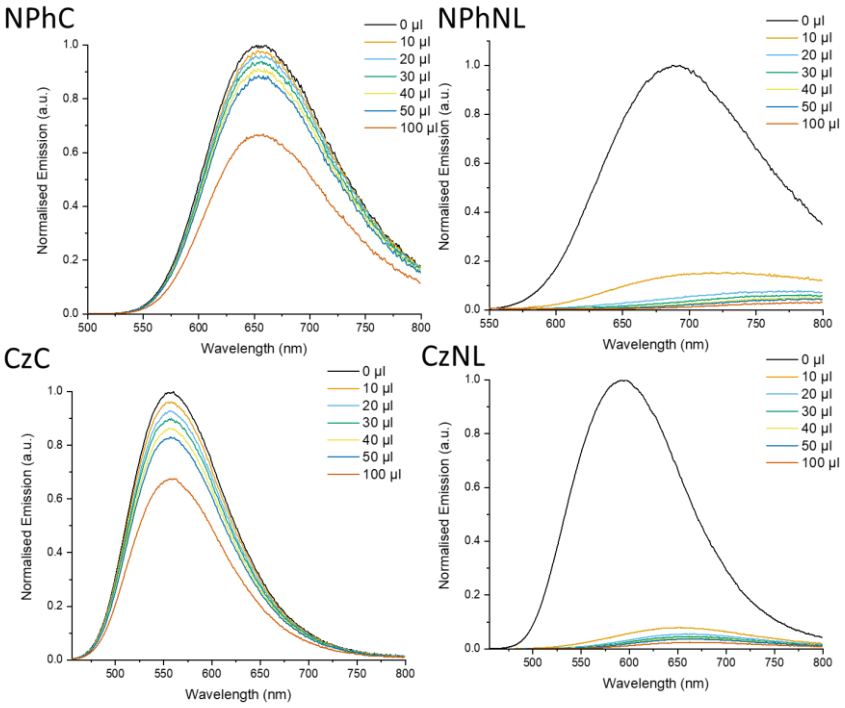

Figure 215. Observation of the effect of 0.1 M quantities of TFA to **NPhC, NPhNL, CzC and CzNL** in the respective emission spectra, excited at the lowest energy transition CH_2Cl_2 [10^{-5} M] 298 K.

Again, the behaviour of each system upon sequential addition of TFA is defined along the lines of either a dppz or dbpz core. The former shows almost complete quenching of emission along with a red-shift in emission maxima upon addition of TFA, while the quenching of the dbpz is less sensitive to TFA.

However, further acid titration studies are required to further assess the sensitivity of the compounds to acid. Specifically, equivalents of TFA should be used instead of fixed molar concentrations, as the use of the latter could lead to oversaturation of the sample solution following first addition if the concentrations used are too high. Additionally, the excitation wavelength used in the emission experiments should be fixed at the isosbestic point in the charge-transfer absorption to minimise the effect of changing molar extinction coefficients on the emission intensity.

To summarise, the compounds exhibit a pronounced charge-transfer transition absorption between 400 and 500 nm, with broad emission maxima between 500 and 700 nm. The transition type was confirmed by low temperature and solvatochromism experiments as charge transfer, while TFA titrations resulted in the quenching of dppz and dbpz emissions in acidic media. Further excitation studies confirmed that all UV transitions resulted in emission from the same low-energy charge transfer excited state.

4.4.1.5 Quantum Yield of Luminescence and Emission Lifetime of DPPZ and DBPZ

The quantum yields of **NPhC**, **NPhNL**, and **CzNL** have been reported in literature. However, the quantum yield of the novel compound **CzC** was obtained using the single-point method, along with the quantum yield of **CzNL** for comparison to literature. The result was within an acceptable margin of error of 5%, and the quantum yields of all compounds are given in **Table 16**.

Table 16. Quantum yields of **NPhC, NPhNL, CzC and CzNL**. The QY of **CzC** and **CzNL** were measured in DCM using 0.1 M quinine sulphate in H_2SO_4 as a standard.[139]

Compound	**NPhC**[129]	**NPhNL**[126]	**CzC**	**CzNL**[126]
Quantum Yield (%)	30.5	23.0	60.3	36.0

The quantum yield describes the efficiency with which absorbed photons are emitted from the excited state. To put it another way, it is the proportion of radiative decay of the excited state compared to the overall decay of the excited state back to the ground state. Alternative, non-radiative deactivation pathways back to the ground state include vibrational and rotational transitions, where the excited state energy results in a change in molecular motion. The quantum yields of the prepared compounds show two clear trends. Firstly, the dppz compounds have lower quantum yields than their dbpz equivalents, though the difference is relatively minor. Secondly, the triphenylamine-containing compounds also have lower quantum yields than their carbazole counterparts. The latter trend can be rationalised by the greater number of non-radiative decay pathways available to **NPhC** and **NPhNL,** as the free phenyl rings have a far greater potential number of rotational transitions than the planar and less labile carbazole moiety. Consequently, the excited state is quenched to a larger degree by nonradiative pathways in **NPhC** and **NPhNL**. This results in **NPhNL** having the lowest quantum yield at 23 %, while **CzC** has the highest at 60.3 %.

4.4.2 Photophysical Properties of NPhNRu and CzNRu

4.4.2.1 Degassing Studies of NPhNRu and CzNRu

The complexes **NPhNRu** and **CzNRu** (**Figure 216**) have both been reported in literature, no reports exist on the sensitivity of their emission to oxygen.[126]

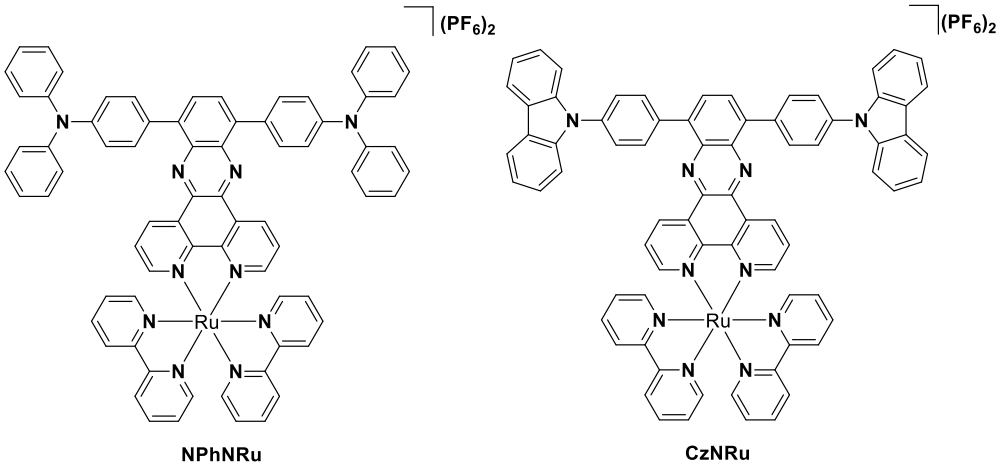

Figure 216. Chemical structures of **NPhNRu** and **CzNRu**.

Consequently, the UV and emission spectra of the two complexes were taken in MeCN, both as aerated samples, and degassed in Ar. An oxygen response between the two samples facilitates confirmation of the triplet character of the excited state. The absorption spectrum of both compounds is presented in **Figure 217**. The spectra show less fine structure than the spectra of the four compounds investigated above. This is likely due to a large number of overlapping transitions. The spectrum of **NPhNRu** manifests a broad emission at 450 nm, with a long shoulder that reaches past 600 nm. This shoulder is likely the same charge-transfer band observed in **NPhNL** but red-shifted by the lowering of the LUMO energy caused by coordination of the electropositive Ru(II) centre.

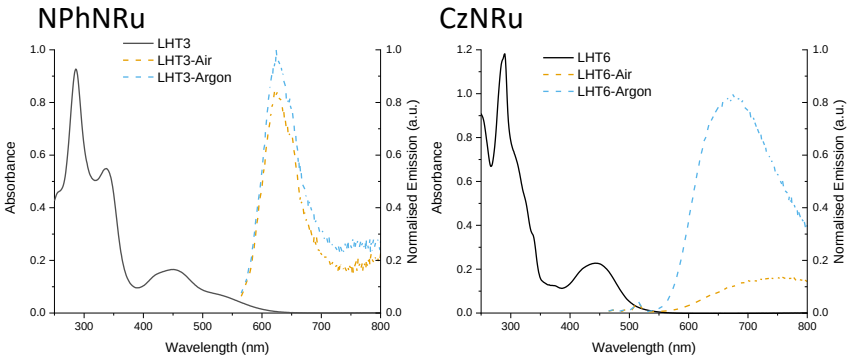

Figure 217. UV-Vis absorption and emission spectrum of **NPhNRu** and **CzNRu** in MeCN [10^{-5} M] Emission shown in air and argon.

The transitions at 450 nm are a combination of ligand transitions observed in **NPhNL**, combined with the new ^{1}MLCT absorptions from the Ru(II) centre to the auxiliary and dppz-type ligands. This is confirmed through comparison with the parent complex $[Ru(bpy)_3][(PF_6)_2]$.[45] High-energy transitions past 300 nm are likely due to π-π* transitions in all of the ligands. **CzNRu** shows a similar profile, but with a less defined shoulder tailing out at 500 nm. Similar transition bands at 450 nm are again likely originating from ^{1}MLCT transitions, with higher energy transitions once again likely being ligand-centred in nature. The molar extinction coefficients for the complexes are reported below in **Table 17**.

Table 17. Molar extinction coefficients for **NPhNRu** and **CzNRu** (MeCN, 10^{-5} M, 298 K).

Compound	Wavelength (nm)	ε (L mol^{-1} cm^{-1})
NPhNRu	450, 550	18500, 8000
CzNRu	450	21000

Both complexes are only weakly emissive in air, and **NPhNRu** exhibits a very small oxygen response compared to **CzNRu**, where emission is increased by 90 % in argon. However, even under argon, the emission of **CzNRu** is very low, and lamp artefacts can be clearly seen around 500 nm due to the large slit widths required to obtain a clean spectrum. The reduced emission of both complexes in air is due to the quenching of a triplet excited state by triplet oxygen (a process which generates $^1O_2$).

The lack of oxygen response in **NPhNRu** suggests alternative mechanisms for relaxation aside from oxygen quenching. One possible explanation put forward in this work is that a photoinduced electron transfer (PET) process is occurring, where the nitrogen atom formally donates an electron into the dppz core. PET processes are typically non-luminescent.[140–142] PET is a non-radiative decay pathway that is a competitive process with phosphorescence and other photonic processes, resulting in a lowering emission. One method to confirm the presence of PET is *via* acidification studies, where protonation of the donor nitrogen atom prevent the electron transfer. However, this is not possible for this compound due to the previously observed quenching of emission in protic media of **NPhNL**. In future work, cyclic voltammetry (CV) and computational studies will be used to confirm the PET process proposed.

4.4.3 Photophysical Properties of NPhNIr and CzNIr

4.4.3.1 Solvatochromic Absorption and Emission of **NPhNIr** and **CzNIr**

The complexes **NPhNIr** and **CzNIr** (**Figure 218**) were generated in an attempt to elucidate the effect that changing the transition metal centre would have on the two-photon cross section. Neither complex has been reported in literature, so their photophysical properties were more thoroughly investigated than those of **NPhNRu** and **CzNRu.**

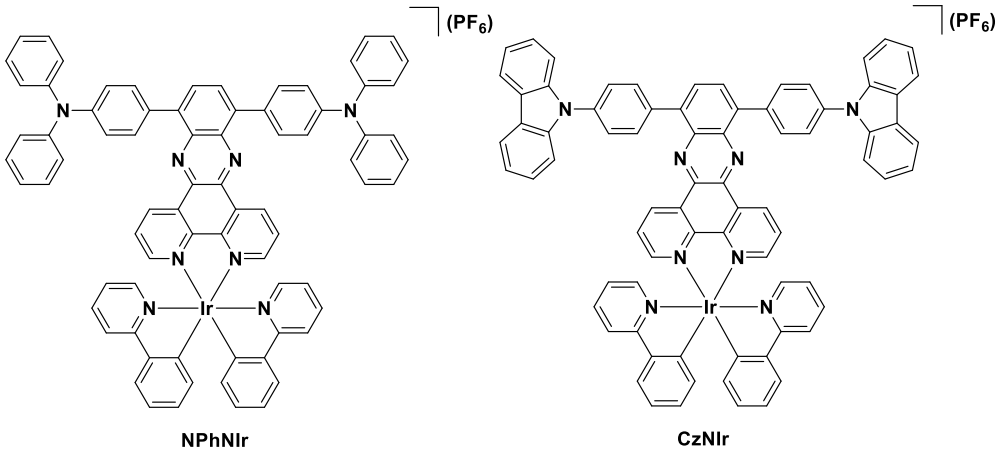

Figure 218. Chemical structure of **NPhNIr** and **CzNIr.**

The absorption and emission spectra of **NPhNIr** and **CzNIr** are shown in **Figure 219**. The absorption spectrum of **NPhNIr** shows high intensity transitions below 400 nm, which is characteristic of high energy π- π* and n- π* transitions in the ligand ring systems. Additionally, due to a combination of the high field strength of the 2-(pyridin-2-yl)phenyl-CN (ppy) spectator ligands and the increased size of the central iridium ion relative to ruthenium the energy gap between the t_2g and e_g (Δ_{oct}) is large.[143] This results in a lowering in energy of the t_2g set of orbitals, which in turn increases the energy required to populate empty ligand π* orbitals. The spectroscopic result of this behaviour is that given the same ligand structure, iridium MLCT transitions occur at higher energies than those of ruthenium. Consequently, it can be assumed that the high intensity of the transitions under 400 nm also include the ^{1}MLCT transitions from iridium d-orbitals into empty ligand π orbitals

A)

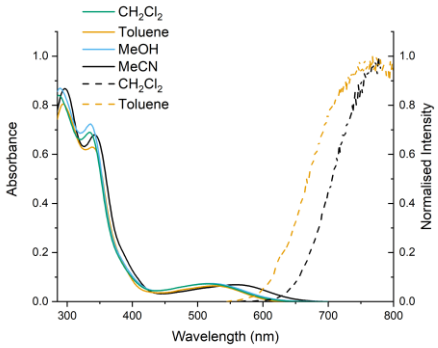

B)

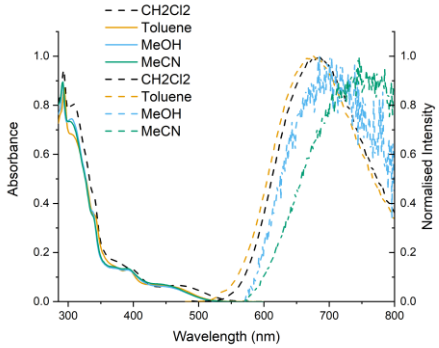

Figure 219. UV-Vis absorption and emission spectrum of **NPhNIr** (A) and **CzNIr** (B) in a range of solvents (for excitation wavelength see **Table 18**) [10^{-5} M], 298 K.

In addition to the higher-energy transitions, we can also observe lower intensity bands at 550 nm for **NPhNIr** and at 450 nm for **CzNIr**. These can be assumed to be the ILCT transitions of the dppz ligands that have previously been observed in this project. They are not substantially shifted compared to the same transitions in ruthenium, suggesting that the metal centre does not exert significant influence over the orbitals involved in those specific electronic transitions. Most of the absorption bands are not sensitive to solvent, although a redshift in the ILCT absorption band of **NPhNIr** is noted in CH_2Cl_2. The molar extinction coefficients for the two iridium complexes are shown below in **Table 18**.

Table 18. Molar extinction coefficients for **NPhNIr** and **CzNIr** (MeCN, 10^{-5} M, 298 K).

Compound	Wavelength (nm)	ε (L mol^{-1} cm^{-1})
NPhNIr	570	10500
CzNIr	470	8000

NPhNIr is not emissive in MeOH or MeCN, but a very low intensity transition is observed centred around 800 nm in CH_2Cl_2 and Toluene. The emission peak of the toluene is at higher energy than that of the CH_2Cl_2 due to the lack of solvent stabilisation of the excited state. **CzNIr** manifests an emission peak centred around 670 nm in Toluene and CH_2Cl_2 and very low-intensity bands at 700 and 750 nm in MeOH and MeCN respectively. This relative increase in intensity can be ascribed to either a reduction of nonradiative,

vibrational and rotational decay pathways available in the carbazole moiety compared to the triphenylamine as well as higher energies reducing the influence of the band-gap law.

4.4.3.2 Degassing Studies of **CzNIr**

Degassing studies in MeCN were performed for **NPhNIr** in MeCN but no emission was observed. Degassing studies of **CzNIr** were performed in MeCN and the results are reported below in **Figure 220.**

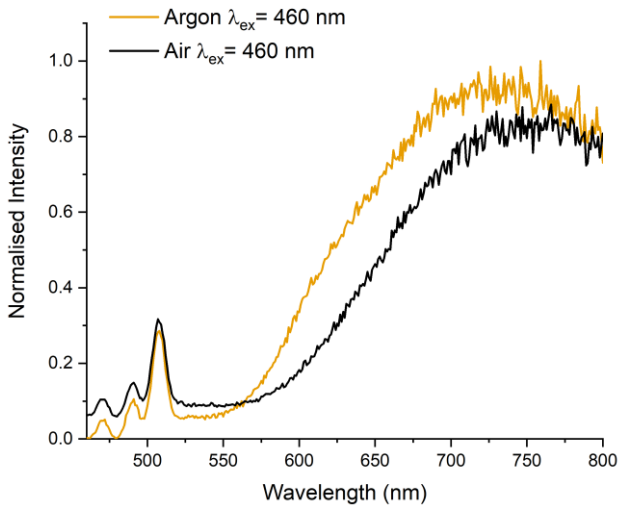

Figure 220. Emission of **CzNIr** in MeCN in air (black line) or argon (orange line) [10^{-5} M] 298 K.

The studies show a small sensitivity to oxygen, with a hypsochromic shift observed in the emission wavelength. This low sensitivity is reflected in the emission lifetime of **CzNIr**, which was measured at a mere 2 ns. The emission lifetime of iridium complex is known to be shorter than that of ruthenium, in part due to the spin-orbit coupling constant of the former being three times the size of the latter.[43] This results in a more efficient intersystem crossing process, leading to more 'allowed' and therefore more rapid T^1-S^0 radiative transitions. However, 2 ns is far shorter than the values obtained for most iridium complexes, suggesting that significant nonradiative decay is leading to quenching of the excited state.[28,50,94] In summary, the photophysical properties of the iridium dppz complexes largely mirror those of their ruthenium counterparts. While the low-energy absorption bands suggest the presence of reasonably efficient ILCT transitions, which are suggested to increase two-photon absorption cross sections, the short emission lifetime and low emission intensity of the complexes preclude their application as triplet photosensitisers.

4.4.4 CzC

4.4.4.1 Degassing Studies of CzC

CzC was also degassed with argon to determine if there was an oxygen response. Surprisingly, despite containing no heavy atoms, a small but measurable oxygen response was discovered, as shown in **Figure 221.**

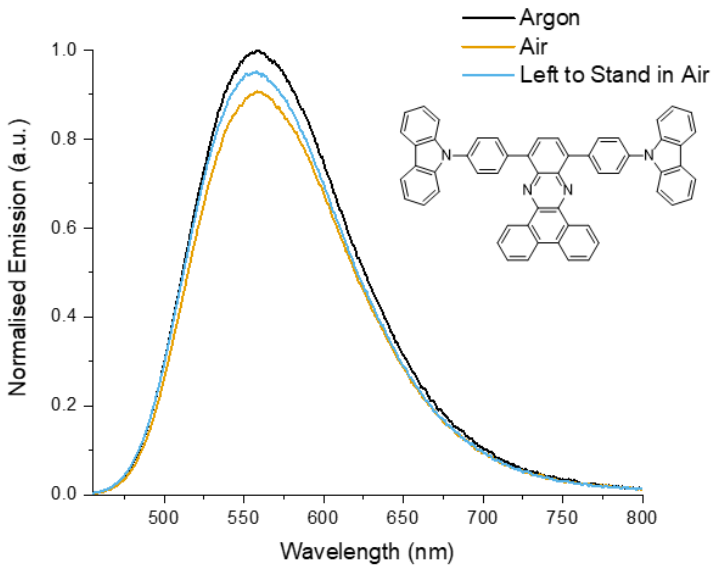

Figure 221. Emission spectra of **CzC** in air and argon [10^{-5} M].

To confirm that this was not due to a concentration change due to the freeze-pump-thaw method of degassing, three measurements were undertaken. First, the sample was measured in air, then a measurement was taken further to degassing, and lastly, the solution left to stand in air for an hour before a final measurement was taken. Despite efforts to prevent concentration, some solvent was lost to evaporation. However, it is clear in **Figure 221** that the initial oxygen response was not caused by a concentration change, as the emission intensity of the final measurement is again lower than that of the argon measurement.

Due to the lack of heavy atoms to induce and assist ISC, an alternative mechanism is proposed to allow for the oxygen quenching response. One process that could account for the oxygen response is significant S_1 and T_1 mixing, where the energy levels of the two excited states are close enough in energy to both influence the character of the final excited state. Crucially, access to the T_1 excited state is allowed, which may explain the oxygen response. This process, known in the literature as Thermally Assisted Delayed Fluorescence (TADF), is caused by spatially isolating the HOMO and LUMO energies, minimising the energy difference between S_1 and T_1. Despite access to the T_1 excited state, thermal repopulation to the S_1 energy level must occur before any emissive processes.[144]

4.4.4.2 Computational Measurements of CzC

To further explore this possibility, computational measurements of the HOMO and LUMO energies of **CzC** were performed by Prof. Eli Zysman-Coleman of the University of St. Andrew's in Scotland. These measurements are displayed in **Figure 222**.

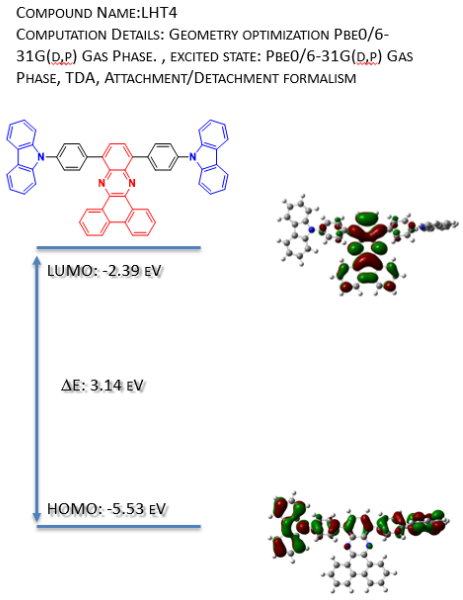

Figure 222. Computational (density functional theory, DFT) measurements of the HOMO and LUMO energies and orbitals of **CzC**. Courtesy of the Zysmann-Coleman group.

This initial calculation further supports the charge transfer nature of the excited state in **CzC**. Here, the HOMO is located almost exclusively across the carbazole donors, while the LUMO is dispersed across the dppz core. The Draper and Zysmann-Coleman groups have worked together previously, with a particular focus on the development of novel compounds that exhibit TADF behaviour. A simplified Jablonski diagram is provided in **Figure 223** which details the photophysical processes found in this photophysical phenomenon.

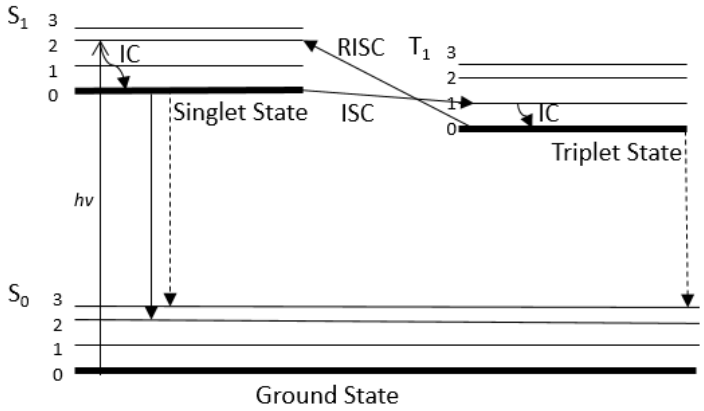

Figure 223. Simplified Jablonski diagram showing intersystem crossing (ISC) and reverse intersystem crossing (RISC) typical of TADF active compounds. Also shown are non-radiative decay pathways (dashed line), internal conversion (IC) and radiative decay pathways (solid line).

TADF active compounds are highly sought after for organic light emitting diode (OLED) technology and other electronic applications.[144] One of the simplest metrics used to determine if a compound is TADF active is the difference in energy between the S_1 and T_1 excited states (ΔE_{ST}). This calculation, performed for **CzC** (gas phase), is included in **Figure 224**.

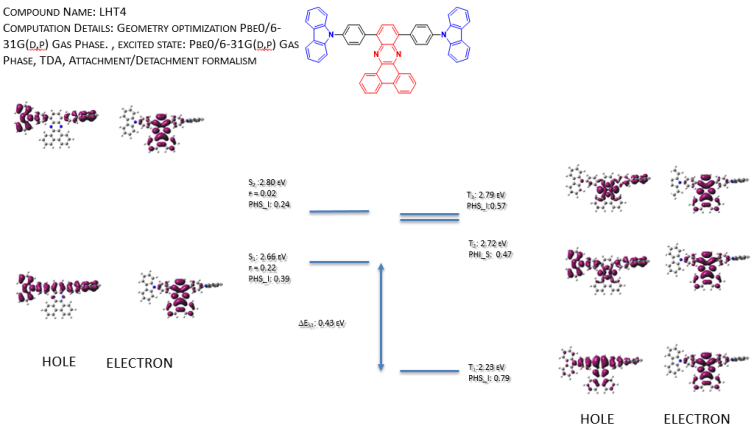

Figure 224. S_1-T_1 energy gap (ΔE_{ST}) for **CzC**. Courtesy of the Zysmann-Coleman group.

The calculation of ΔE_{ST} for **CzC** has a value of 0.43 eV; a value considered large by the standards of many modern TADF compounds found in the literature.[144] From the computational studies performed, the observed spatial overlap of S_1 and T_1 is small, likely resulting in the oxygen response presented in **Figure 221**. Additional modelling provided by the Zysman-Coleman group showed that the removal of the phenyl spacer group and choice of a different amine donor reduced spatial overlap further, lowering ΔE_{ST} by an order of magnitude to 0.0217 eV. This is shown in **Figure 225**.

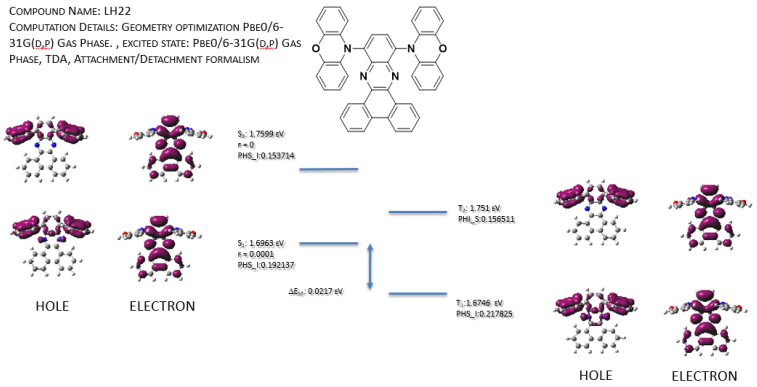

Figure 225. S1-T1 energy gap (ΔEST) for **LH22**. Courtesy of the Zysmann-Coleman group.

A proposed synthetic preparation, using the Buchwald-Hartwig reaction, is presented in **Scheme 26**.

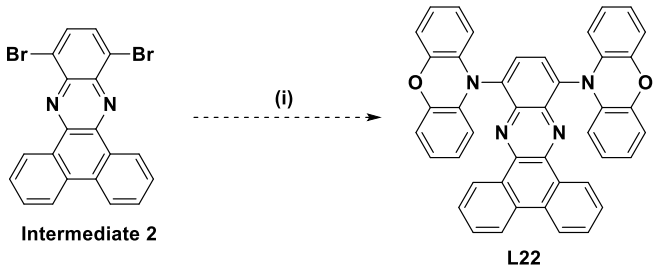

Scheme 26. Proposed Buchwald-Hartwig coupling reaction of **Intermediate 20** and phenoxazine to give **L22**. (i) Phenoxazine, NaO^{t}Bu, Pd(^{t}Bu)$_3$, Toluene, 110 ^{o}C, 36 h.

As part of this work, this reaction was attempted several times using widely used Buchwald-Hartwig conditions reported in the literature. However, no product **L22** was found in these attempts. Analysis of more recent literature reports that the amine-halide coupling reactions using **Intermediate 2** have required harsher reaction conditions, including elevated temperatures, than those attempted here.[145] This suggests that similar conditions may be required for the proposed reaction to proceed.

To investigate whether the problem may have been as a result of the increased steric strain of the final product, a Suzuki coupling reaction using **Intermediate 3** and 9-anthraceboronic acid was performed (**Scheme 27**).

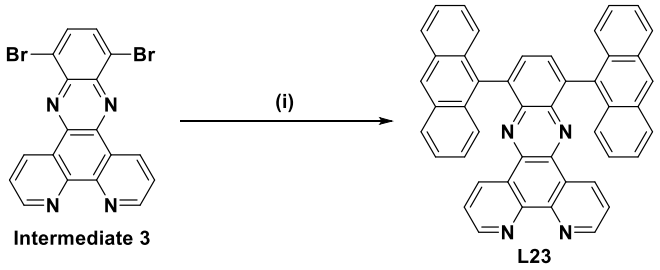

Scheme 27. Attempted Suzuki cross-coupling reaction using **Intermediate 3** to form L23 (i) (i) 9-anthraceneboronic acid, Pd(PPh$_3$)$_4$, Na$_2$CO$_2$, EtOH/Toluene, 110 ^{o}C, 36 h.

This reaction was successful, and the product (**L23**) was confirmed using high resolution mass spectrometry (APCI) and is presented in **Figure 226**. Despite this, purification proved extremely difficult. Multiple attempts using column chromatography (silica) and preparative thin layer chromatography (silica), separation from an unknown impurity could not be achieved. It is proposed that the unreacted anthracene boronic acid may be stacking with the anthracene moieties of the final product, preventing purification. However, the successful formation of **L23** demonstrates that should this purification be overcome, the enhanced steric strain around the dppz core system should not prevent compounds of this type from being synthesized.

Meas. m/z	#	Ion Formula	m/z	err [mDa]	err [ppm]	rdb	N-Rule	e⁻ Conf	mSigma
635.224198	1	C46H27N4	635.223023	1.2	1.8	35.5	ok	even	4.9

Figure 226. [APCI] HRMS spectrum of the reaction mixture shown in **Scheme 27**, demonstrating the successful synthesis of **L23**.

4.4.5 Conclusion

The synthesis of target molecules **NPhC**, **NPhNL**, **NPhNRu**, **CzC**, **CzNL** and **CzNRu** was completed successfully using novel synthetic pathways that open the door to further dppz and dbpz derivatives. Their photophysical properties were investigated, exhibiting a complex absorption behaviour including a large number of π-π* and n-π* transitions, as well as a broad and featureless charge transfer band beyond 400 nm. The emission profiles of the compounds showed a broad featureless emission with a substantial Stokes shift, suggesting a charge-transfer emissive state. This was further investigated using low-temperature and solvatochromic measurements, the results of which supported the postulated charge-transfer nature of the excited state. The two metal complexes **NPhNRu** and **CzNRu** were degassed to identify any changes in their emissive properties. **NPhNRu** showed no significant increase in emission upon degassing, while **CzNRu** did, suggesting an emissive triplet excited state. Finally, studies into the emissive behaviour of **CzC** showed a weak oxygen response, leading to the design and attempted synthesis of compounds showing TADF behaviour. Collaborations with the Zysmann-Coleman group have shown that small changes to the structure of dppz and dbpz derivatives can have a large impact on the singlet-triplet energy gap, $\Delta S_1 - T_1$, and work on this project is ongoing.

4.5 Future Work

As described extensively in the introduction to this work, the measurement of the two-photon absorption spectra of **NPhNL** to **CzNRu** still remains to be carried out. To achieve this, discussions are on-going with various international collaborators.

Furthermore, the photophysical properties of **CzNRu** must be investigated further, including the determination of the triplet state lifetime, and the singlet oxygen quantum yield. If these results indicate promising potential for its use as a two-photon PDT agent, arrangements will be made to test the compound in a cancer cell line with an existing collaborator. Additionally, considering the likely PET process occurring in **NPhNRu**, it is worth investigating alternative weaker donor groups, such as alkyl amines, to determine whether stronger luminescence could be observed.

Based on the results of these investigations, the obtained insights into the design of PDT agents with large two-photon cross sections will lead to the development of novel compounds that combine high singlet oxygen quantum yields, low dark toxicity and high biocompatibility with large two-photon cross sections and long absorption wavelengths. Some initial designs based on already obtained results from this project are revealed below in **Figure 227**.

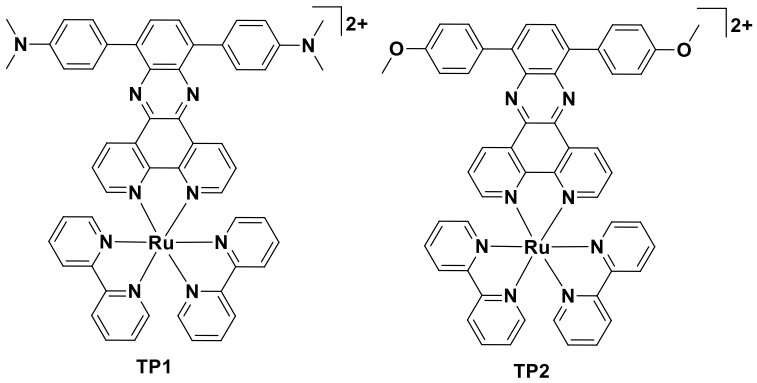

Figure 227. Proposed two-photon active ruthenium complexes **TP1** and **TP2.**

However, it may be necessary to develop new ligand systems if the two-photon absorption performances of the target compounds in this report are unsatisfactory. It has been reported that extended π-conjugated dihydrophenanthrene compounds exhibit strong two-photon absorption, shown in **Figure 228**.[146]

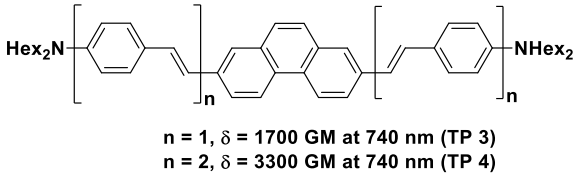

Figure 228. Two-photon absorption properties of extended phenanthrene systems.[46]

These systems could easily be adapted to metal ligands by using phenanthroline as the base of the π-system, as shown in **Figure 229**.

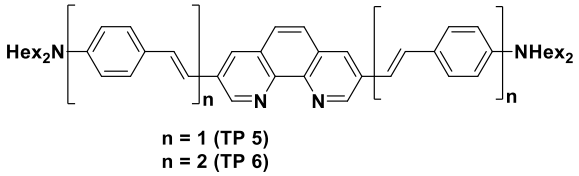

Figure 229. Proposed two-photon active ligands **TP5** and **TP6**.

Subsequently, the introduction of electron-withdrawing groups at the 5 and 6 position of the phenanthroline may result in higher two-photon absorption cross sections, with the proposed structures shown in **Figure 230**

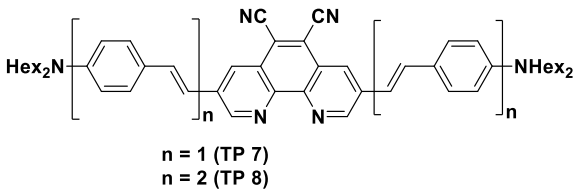

Figure 230. Proposed two-photon active ligands with electron withdrawing groups **TP7** and **TP8.**

Recent work has shown that going from heteroleptic metal complexes to homoleptic metal complexes containing 3 two-photon active ligands increases the cross section by a factor greater than 3, which opens the door to further derivatives.[124]

As work with the Zysmann-Coleman group is on-going, other compounds have been proposed in order to lower the ΔE_{ST}. Initial efforts will concentrate on the continued use of **Intermediate 1** and **2** as the starting material. Further attempts at directly coupling amine donors to the bromine atoms on the dppz/dbpz core will continue in an attempt to lower ΔE_{ST}. In addition to those efforts, additional calculations indicated that the choice of the amine donor may allow for the retention of the phenyl spacer group while minimising ΔE_{ST}, enabling use of the already utilised Suzuki coupling reaction to create high-performance TADF compounds, as shown below in **Figure 231**.

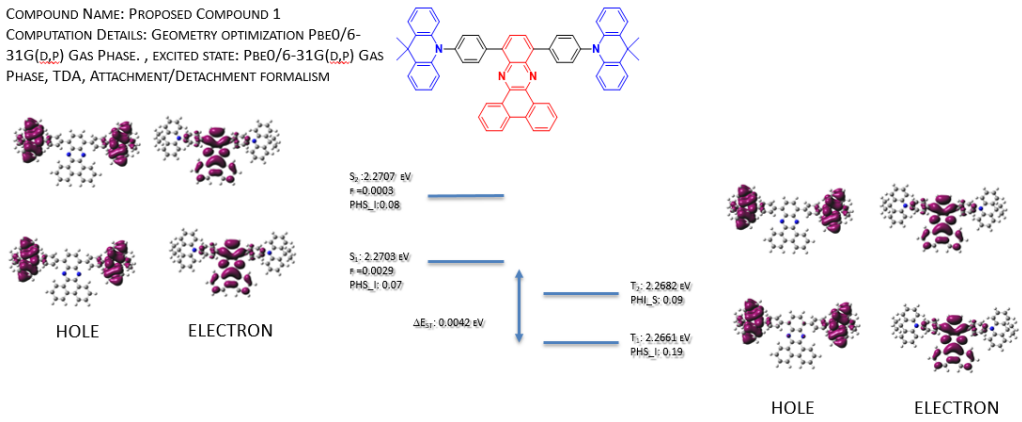

Figure 231. S1-T1 energy gap of proposed Compound 1, courtesy of the Zysmann-Coleman Group.

Dimethylacridine (DMAC), phenoxazine and phenothiazine are all common donors in TADF materials, leading to the design of the novel compounds in **Figure 232**, which can all be accessed using already developed synthetic techniques.[47,147–149]

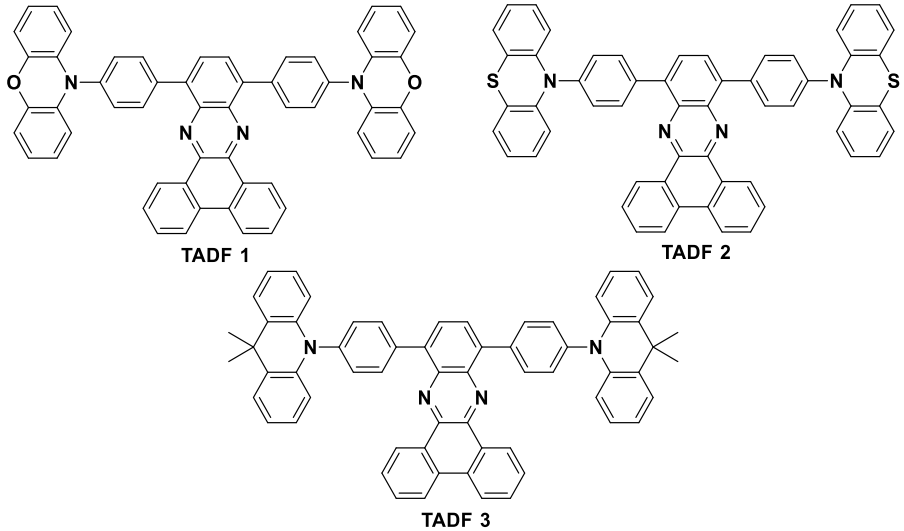

Figure 232. Three novel structures TADF 1, TADF 2 and TADF 3 using DMAC, phenoxazine and phenothiazine as donor groups.

Comparative systems lacking the phenyl spacer may also be of interest, leading to the design of the six compounds shown in **Figure 233**.

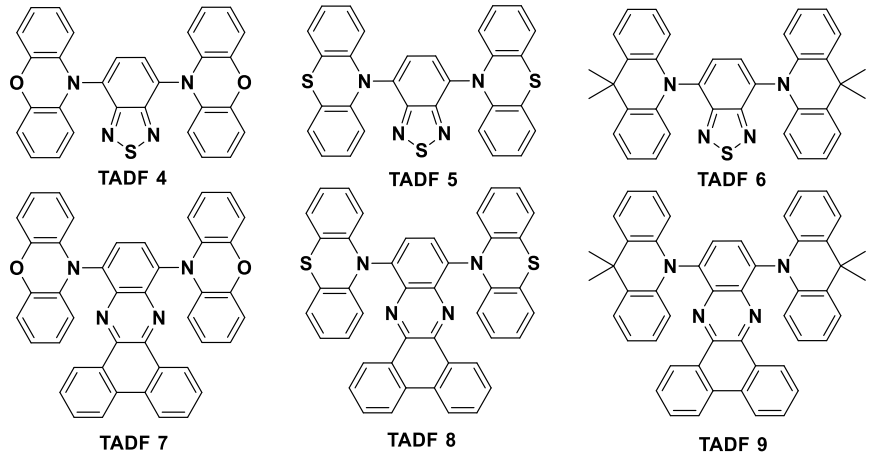

Figure 233. TADF materials lacking the phenyl spacer ring.[50]

Of these, **TADF 6** has already been synthesised by Ni *et al.*, showing a S_1-T_1 energy gap of 0.11 eV.[149] There are two potential synthetic routes to **TADF 7**, **TADF 8** and **TADF 9**, either through optimization of the direct coupling of the amine donor onto the dibenzophenazine (dbpz) core or ring opening of the **TADF4**, **TADF5** or **TADF6** precursor. The final goal of this project is the design of a family of synthetically accessible TADF molecules for use in OLEDs. This goal will be met using design principles developed in collaboration with the Zysmann-Coleman group, taking advantage in their particular expertise in the creation of solid-state films incorporating the designed TADF molecules.

5.: Iridium Picolinate Triplet Photosensitisers

5.1 Introduction

5.1.1 Picolinate

While polypyridyl ligands such as phenanthroline, bipyridine and terpyridine are perhaps the most widely studied class of ligands for iridium and ruthenium photosensitisers, they are by no means the only one.[24,150,151] Another type of chelating ligand that has garnered significant interest in recent years are picolinates (**Figure 234**).

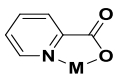

Figure 234. Picolinate binding a metal centre.

Unlike polypyridyl ligands, picolinate ligands bind the metal centre via the nitrogen atom of a singly pyridine ring as well as the α-oxygen of a carboxylic acid fragment. This results in an overall neutral charge for the complex when used in octahedral iridium (III) complexes with two phenylpyridine ligands, removing the need for counterions. Picolinate containing metal complexes have different physical and spectroscopic properties compared to polypyridyl metal complexes.[73,152,153] One field of application for which picolinate iridium complexes have been widely explored is the design of organic light emitting diodes (OLEDs).[52,61,73,148]

5.1.2 Organic Light Emitting Diodes (OLEDs)

OLEDs are devices emitting light as a response to an electric current, and a simple diagram displaying a general OLED structure is shown in **Figure 235**. Emission occurs as electron-hole pairs (termed excitons) recombine in the emissive layer, leading to the generation of a photon.[154–156]

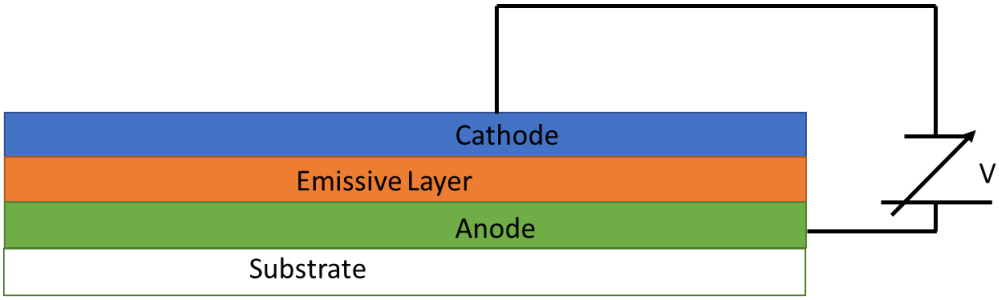

Figure 235. Simple schematic diagram of an OLED, formed of conductive cathode and anode films surrounding an emissive layer.[157]

They differ from standard light emitting diodes (LEDs) by the nature of their emitting component. In OLEDs, the light emitting component are typically organic hydrocarbon-based dyes, ranging from small molecules to transition metal complexes.[43] In LEDs, the light emitting component is formed by semiconductors such as gallium arsenides, zinc selenide and indium gallium nitride.[158]

OLEDs have significant advantages over standard LEDs. These include their ability to diffuse light evenly over a large area, to emit light even when made very thin, and bend and flex to form a variety of shapes.[157]

The wavelengths of light generated by OLEDs are determined by the photophysical properties of the emitting component or components. Thus, tuning emission wavelengths to suit the needs of OLED development is an important area of study in synthetic photochemistry.[52]

On average, 3 out of 4 excitons generated by charge recombination are triplet in nature.[155,159] Consequently, dyes exclusively emitting from a singlet excited state are only able to harvest 25 % of generated excitons, while the remaining 75 % of triplet excitons decay non-radiatively. This significantly limits the efficiency of conventional OLEDs. However, by employing emitters with high degrees of spin-orbit coupling, harvesting all the generated excitons becomes possible.[73,153] As iridium is a third-row transition metal, it has extremely high spin-orbit coupling coefficients due to the heavy atom effect.[43] Therefore, Iridium complexes are particularly attractive OLED components, as they are able to harvest all excitons generated by the application of an electric current.

5.1.3 Tuning the Photophysical Properties of Iridium Picolinate Complexes

One of the most widely studied iridium complexes for OLED applications is **FIrpic**, displayed below in **Figure 236.**

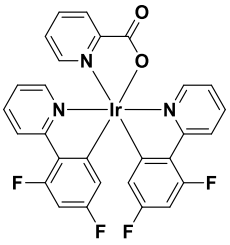

Figure 236. FIrpic.[153]

FIrpic incorporates picolinate as one of its three ligands, along with two difluorinated phenylpyridine systems. It has a number of properties making it interesting as an OLED component, including facile synthesis, high stability and suitable photophysical properties.[153]

FIrpic exhibits several different absorption processes; at wavelengths shorter than 300 nm, the absorption spectrum is dominated by π – π* and n - π* transitions. Between 300 and 420 nm the absorption spectrum shows less intense singlet charge-transfer processes from the iridium metal centre to the various ligands. A very weak absorption peak around 450 nm is assigned to ^{3}MLCT aborption.[153,160]

The emission of **FIrpic** in CH_2Cl_2 at room temperature manifests as a main emission peak at 468 nm, with hyperfine structure resulting in two shoulder peaks at 495 and 535 nm.[153,160] This emission appears at much shorter wavelengths and higher energies compared to other iridium complexes, including those discussed in this thesis. Additionally, the emission is not sensitive to solvent, and low temperature emission shows no significant shifts in emission wavelength relative to room temperature emission. This suggests that the excited state character of the emission is largely ligand-centred (LC), with no dipole forming to be stabilised by more polar solvents. Emission lifetime is recorded at around 2 μs in a variety of environments, including CH_2Cl_2 and solid-state polymers.[153]

A multitude of analytical and computational techniques have been employed over decades to further probe the nature of **FIrpic's** excited state.[153] Results have confirmed the LC nature of the excited state, localised largely on the phenylpyridine rings with little to no involvement of the picolinate fragment in the emission process. However, the investigations have also shown the performance and characteristics of devices generated using **FIrpic** as a dopant emitter differ significantly based on their composition and generation.[153] Thus, research of these properties has persisted into the present day, despite the relative simplicity of **FIrpic's** structure. Modifications to the picolinate ligand could result in changes to the photophysical properties of this type of iridium complex, allowing for a more customised tailoring to suit the needs of OLED applications.

In 2007, Bolink and co-workers described the properties of a simple iridium (III) complex bearing a picolinate ligand substituted with a dimethylamine donor group *para* to the nitrogen atom (**5.01**, **Figure 237**).

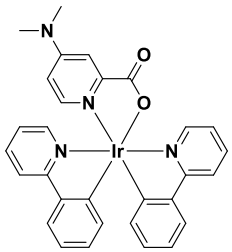

5.01

Figure 237. Iridium (III) picolinate complex prepared by Nazeeruddin and co-workers.[52]

As the picolinate ligand is substantially smaller and less conjugated than comparable polypyridyl ligands, the absorption spectrum past 350 nm is dominated by ^{1}MLCT and ^{3}MLCT transitions. At higher wavelengths, the $\pi - \pi^*$ and $n - \pi^*$ transitions of the two phenyl and three pyridyl rings appear. No mention is made in the publication of a potential charge-transfer transition originating from the dimethylamine donor group, but if one had occurred it would likely have been at high energies.[52] This is due to the lack of spatial separation between the donor dimethylamine and acceptor pyridine/carbonyl groups as well as the reduced level of conjugation in the picolinate ligand overall. No mention is made of solvatochromic absorbance.

The emission appears as a sharp band at around 510 nm with an excited state lifetime of 32 ns. Given that the ^{3}MLCT of the complex exhibits a shoulder at 480 nm, the Stokes shift of the complex in MeCN is surprisingly low at 30 nm. Degassing the complex in MeOH results in an increase in emission intensity and a longer excited state lifetime of 1.95 μs, confirming the triplet state character of the excited state. The complex showed a 70 % quantum yield of phosphorescence in solution at room temperature.[52]

The complex was used to prepare a doped film the photophysical properties of which were investigated. Interestingly, the emission wavelength was not significantly affected by the change of environment, with the film manifesting an emission peak at 506 nm and a shoulder at 535 nm, with an excited state lifetime of 2.42 μs.[52] This suggests that the local electronic environment does not have a significant effect on the properties of the excited state, indicating a low charge-transfer character. If a charge-transfer character had dominated the excited state, the local electronic environment would have influenced the resulting dipole, leading to changes in emission wavelength.

Using cyclic voltammetry, the authors showed that the LUMO is localised on the phenylpyridine, suggesting a high degree of ligand-centred (LC) excited state character. Overall, the film displayed good characteristics, including high quantum yields of luminescence and emission at a highly desirable green wavelength.[52]

Minaev and co-workers used DFT to investigate the electronic properties of **5.1** and related compound **5.2**, using $Ir(ppy)_2(pic)$ as a baseline for comparison (**Figure 238**).

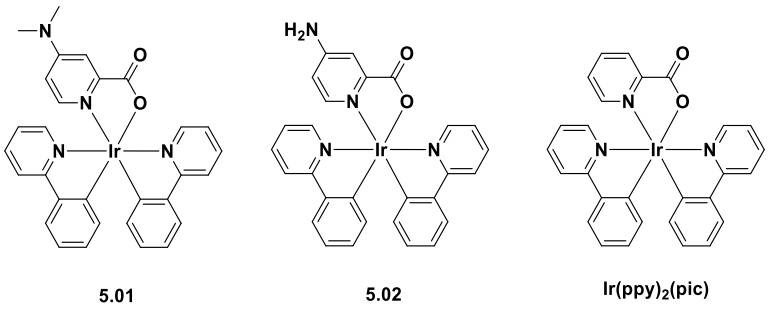

Figure 238. Iridium picolinate complexes investigated by Minaev *et al*.[159]

Their studies indicated that the introduction of the amine and dimethylamine donor groups on the picolinate ring had notable effects on the properties of the LUMO compared to $Ir(ppy)_2(pic)$.[159] In the latter, the LUMO is localised on the picolinate ligand. In compounds **5.01** and **5.02**, the electron donating effect of the amine groups leads to destabilisation of the picolinate orbital, pushing it to higher energies. As a result, a 2-(pyridin-2-yl)phenyl-CN ligand orbital becomes the new LUMO, leading to the excited state containing significant LC character. This change results in remarkable increases in the quantum yields of luminescence in **5.01** compared to $Ir(ppy)_2(pic)$, improving the efficiency of the former complex as an OLED component compared to the latter.[159]

The authors also find solvents to affect the ground state of compound **5.02**, suggesting a strong dipole moment stabilised in more polar solvents, resulting in lowering the overall HOMO energy. The authors speculate this ground state solvent stabilisation should result in a blueshift in emission wavelength with more polar solvents as the HOMO-LUMO gap is increased.[159]

In 2010, Baranoff and co-workers published additional work describing the effects the presence of different isomers has on the performance of films containing compound **5.01**.[61] Given the higher degree of inherent asymmetry in picolinate compared to polypyridyl ligands, picolinate complexes possess increased geometric complexity. Two potential isomers of **5.01** are shown below in **Figure 239**

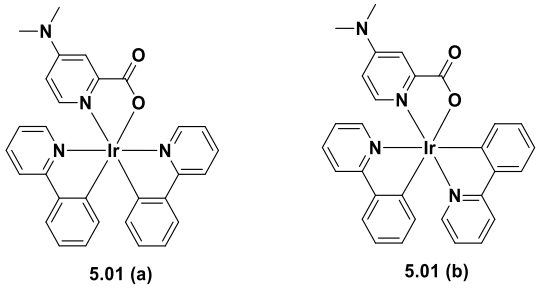

Figure 239. Isomers of **5.01.**[61]

The change in the binding orientation of the phenylpyridine ligand gives rise to diverging absorption wavelengths, quantum yields of phosphorescence and excited state lifetetime.[61] The b isomer displays shorter absorption wavelengths and a reduction in both lifetime and emission quantum yields. The maximum absorption wavelength is shifted by 30 nm, while the quantum yield of luminescence is reduced by 5 % and the lifetime by 0.07 μs. While these changes may not seem significant in and of themselves, they are very

notable considering that the structural differences between the isomers are vanishingly small. The emission wavelength for both isomers is the same (520 nm) suggesting that the LUMO is not markedly affected.[61]

This was confirmed by DFT calculations, which indicated that the HOMO for both isomers is localised on the phenyl ring of one of the phenylpyridine spectator ligands. Depending on the isomer, this phenyl ring is either *trans* or *cis* to the picolinate ligand, which has a significant effect on the HOMO energies of the complex. The presence of isomers was found to adversely affect the efficiency of light-emitting devices, with films containing mixtures of isomers performing poorly compared to films with isomerically pure complexes.

The authors note that the generation of these isomers is a natural consequence of the production of vacuum processed OLED devices and cannot be avoided using this technique.[61] This has important consequences for the manufacture of OLED devices containing iridium picolinate complexes.[61]

The effect of the picolinate on the symmetry of the resulting iridium complex has been noted by other groups as well.[161] Matt and co-workers designed a synthetic pathway to an iridium (III) polyoxometalate conjugate (**5.03**, **Figure 240**) for photonic applications.[161]

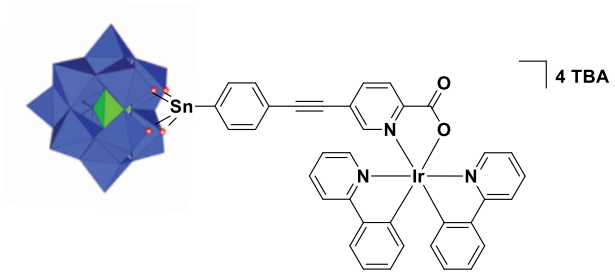

5.03

Figure 240. Iridium (III) complex using ethynylpicolinate as a tether to a tin polyoxometalate unit.[161]

In previous work, the authors had established the importance of enhancing the conjugation between a metal centre and a polyoxometalate unit to ensure the desired charge separation in the excited state.[162] Therefore, they decided to include an alkyne unit to act as a 'molecular wire', similarly, to design principles applied in this thesis. Interestingly, the authors utilise both on- and off-complex Sonogashira couplings to generate the final compound (**5.03**), demonstrating that picolinate complexes possesses a high degree of synthetic versatility and adaptability.[161] The synthetic accessibility of picolinate iridium complexes is an important part of their allure as OLED components.[153,160]

As a feature in their characterisation of **5.03**, the authors reported on the NMR spectrum of iridium complexes prior to coupling to the polyoxometalate unit.[161] In these spectra, they demonstrate that the asymmetry of the picolinate ligand cause a split in the spectator ligand proton signals, with each pyridine and phenyl ring appearing as a discrete set of signals. As with more symmetrical iridium polypyridyl complexes, the pyridine signals manifest at higher chemical shifts, while the phenyl signals were further upfield. Using

2D NMR spectroscopy, Izzet and co-workers confirmed that the phenyl ring *trans* to the coordinating oxygen of the picolinate ring was at lower ppm than the phenyl ring *trans* to the nitrogen.[161]

These publications confirm that the introduction of the picolinate ligand leads to a disruption of electronic and geometric symmetry within the overall iridium complex. This loss of symmetry will only increase when the picolinate is substituted with electron withdrawing or donating groups to influence the photophysical properties.

The effect of substituting electron-donating and withdrawing groups around the picolinate pyridine ring was investigated by Zhang and co-workers.[163] They generated the family of iridium (III) picolinate complexes displayed in **Figure 241**.

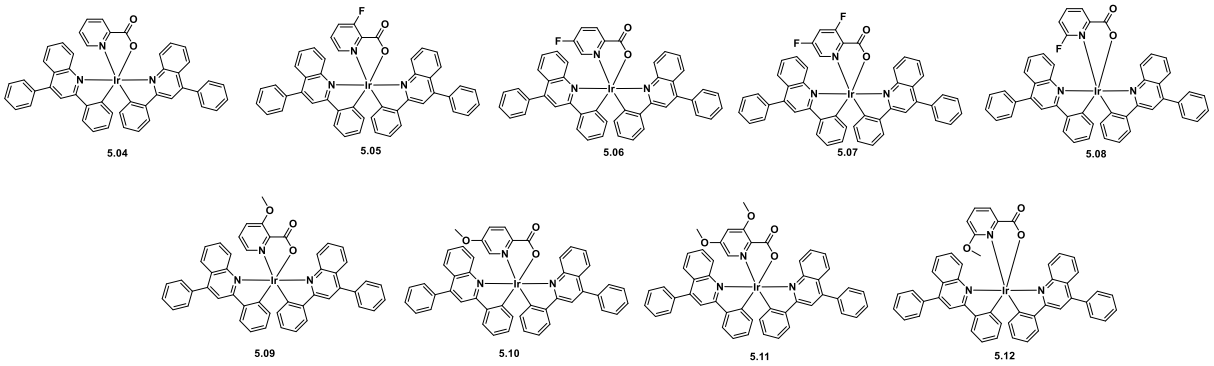

Figure 241. Iridium (III) picolinate complexes bearing fluorine and methoxy substituents.[163]

The authors found the substitution to have little effect on the absorption of the complexes, with changes in the ^{3}MLCT absorption bands limited to 6 nm. The emission of the complexes is universally broad and featureless, with emission wavelengths varying from 575 to 616 nm in MeCN. The largest difference in emission wavelength is recorded for complexes **5.07** and **5.11**, indicating the effect of two substituents to be greater than that of a single fluorine or methoxy unit. The emission lifetime of the complexes ranges between 0.5 and 1.5 μs, with quantum yields of luminescence in MeCN reaching 86.3 % for **5.11**. This could be the result of trends observed by Minaev *et al.*, who showed that adding electron donating units to the picolinate ring shifted the LUMO to the spectator ligands, increasing the LC character of the excited state and enhancing quantum yields of emission.[159] The long emission lifetime suggests the excited state to be triplet in nature, although no sensitivity of the emission to oxygen was reported.[163]

Interestingly, the authors noted that substitution at the *ortho* position relative to the nitrogen as in complexes **5.08** and **5.12**, leads to destabilisation of the complex. Additionally, the quantum yields of emission and emission lifetime are significantly reduced for these two complexes relative to the others in the group, falling to under 20% and 0.5 μs respectively. This is likely due to the steric strain imposed on the N-Ir bond by the close proximity of the donor/acceptor groups, which destabilises the complex.

Davidson *et al.* reported similar work to that undertaken by Zhang and co-workers, but incorporated alkyne linkers into the picolinate complexes, as shown in **Figure 242.**[152]

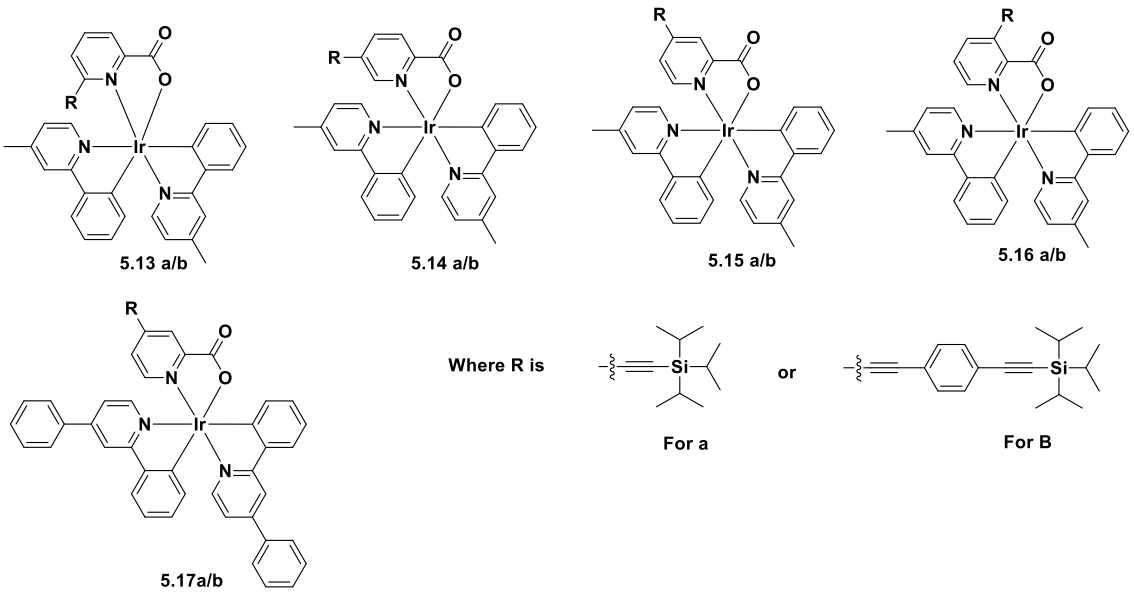

Figure 242. Picolinate complexes including alkyne linkers.[152]

The authors initially attempted to synthesis the ligands off-complex but were not able to fully purify the resulting reaction mixture. Consequently, the bromopicolinate precursor was complexed to the prerequisite iridium dimer prior to Sonogashira coupling reactions.[152]

When the photophysical properties of the complexes were investigated, and they all display absorption typical of iridium picolinate complexes, with high energy bands arising due to $\pi - \pi^*$ and $n - \pi^*$ transitions and both singlet and triplet MLCT bands at lower energies.[152]

The emission of the complexes is universally broad and featureless, suggesting a CT excited state with emission lifetimes in the low double digit ns range. Interestingly, the quantum yields of luminescence are below 20 % for all but one complex. This suggests that the excited state is either not localised on the phenylpyridine spectator ligands as with other previously discussed substituted picolinates, or it has access to a new nonradiative decay pathway. The complex with the highest quantum yield of luminescence is complex **5.13a**. Substitution at this position has been shown by others to weaken the picolinate-metal bond, potentially lowering the influence of the ligand on any resulting excited state.[152]

DFT studies indicated that the HOMO for all alkyne-substituted iridium complexes is localised on the phenylpyridine spectator ligands, with no involvement from the picolinate. The LUMO of the ethynyl-TIPS substituted complexes is extended along the alkyne bridge, with the introduction of the phenyl spacer group increasing the extent of delocalisation.[152]

The trends observed in the absorption and emission wavelengths in this family of complexes suggest that the positions *para* to the nitrogen and the carboxylic acid group have some of the strongest effects on the photophysical properties of the complexes, and therefore the highest degree of electronic involvement.[152]

The work done by Davidson *et al.* and Zhang *et al.* shows substitutions on the picolinate to not necessarily result in immediate transfer of the excited state to the phenylpyridine spectator ligand.[152,163]

Beeby and co-workers also investigated how rotationally restricting the substituents on the picolinate would impact its photophysical properties. They generated a series of iridium complexes bearing progressively more sterically hindered picolinate ligands, as displayed in **Figure 243.**[73]

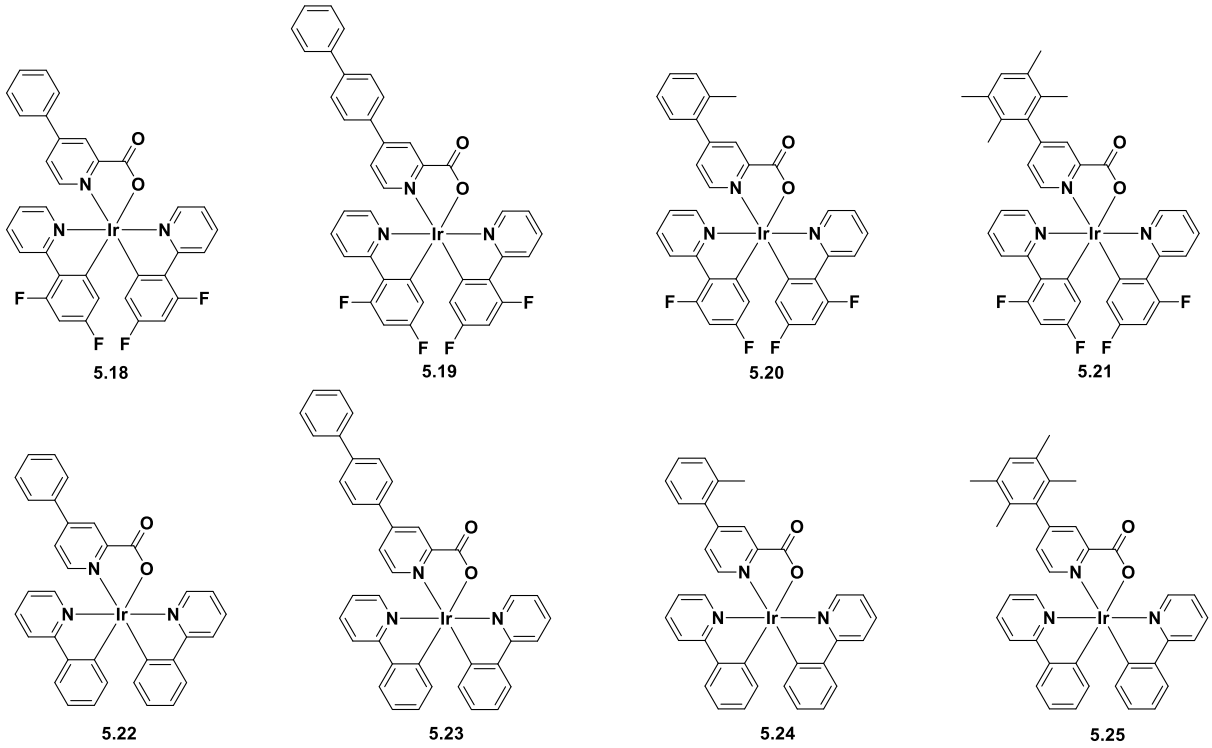

Figure 243. Iridium complexes bearing picolinate ligands with rotationally restricted functional groups.[73]

The authors found the excited state to be heavily influenced by the degree of torsional twisting between the picolinate pyridine ring and the adjacent phenyl ring(s). The emission profiles are very heavily affected, with the more rotationally restricted toluene and tetramethylbenzene complexes indicating signs of LC and MLCT mixing, while the less restricted phenyl and biphenyl complexes show predominantly MLCT character.[73] Introduction of the fluorinated phenylpyridine ligands leads to a more pronounced LC character than observed in their non-fluorinated counterparts, suggesting that the electron-withdrawing effect of the halogens results in a lowering of the phenylpyridine LC state, allowing a greater degree of contribution to the excited state.[73]

In addition to the emission wavelength and profile, the quantum yields of emission also change significantly depending on the degree of torsional twisting. Increasing the twist results in higher quantum yields of luminescence. The quantum yield of luminescence also increases with the introduction of fluorine atoms to the phenylpyridine rings. This again indicates that localising the excited state on the phenylpyridine ligands increases the quantum yield of emission. Low temperature emission spectra confirmed the nature of the excited states.[73]

The above work shows that the relative energies of the MLCT and LC state within picolinate iridium complexes are very close, and that small structural modifications can affect the localisation of the LUMO.

However, modification of the picolinate ligand does not always lead to significant changes in the excited state. This is exemplified by the work of Wong and co-workers, who reported the synthesis of novel picolinate-containing arylboron iridium complexes (**Figure 244**).[164]

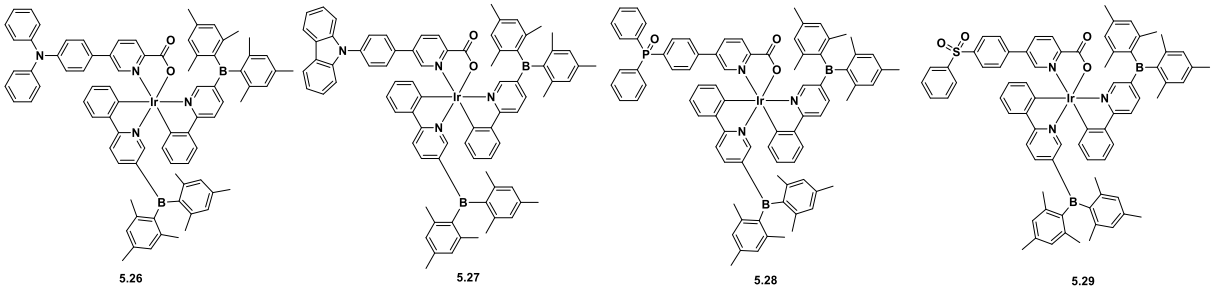

Figure 244. Iridium complexes prepared by Liu *et al.*[164]

These ligands were prepared off-complex, followed by complexation with the iridium dimer. The complexes exhibit complex absorption spectra, owing to the large number of chromophores in the structure, including small charge-transfer transitions past 500 nm. The emission spectra all manifest broad and featureless profiles, indicative of a charge-transfer excited state. The quantum yields of emission are high, above 95 % for all reported complexes.[164]

Solvatochromic emission studies show that the emission shifts to longer wavelengths in more polar solvents, offering confirmation of CT excited state behaviour. Interestingly, the difference in emission wavelengths between CH_2Cl_2 and toluene solution and the polymethylmethacrylate (PMMA) film are negligible, despite differences in polarity. The emission wavelengths for all complexes are largely similar, suggesting that the substituent on the picolinate ligand had little to no influence over the excited state.[164]

TD-DFT calculations indicate that the contribution of the picolinate ligands to the emissive excited state is negligible, with the LUMO largely located on the $B(Mes)_2$ phenylpyridine ligands.[164] These results demonstrate that modifications of the picolinate ligands do not inevitably lead to significant changes to the photophysical properties of the entire complex.

In summary, picolinate iridium complexes often exhibit nearly isoelectronic MLCT and LC excited states which can be preferentially populated by making small structural changes. Interestingly, very few of the above studies show any form of emissive solvatochromic analysis, bar the work done by Wang and co-workers.[164] Considering the ability of solvents to influence excited state behaviour demonstrated in previous chapters of this thesis, this could be regarded as a significant gap in the literature. This echoes an opinion presented by Baranoff and Curchod, who argued that investigations of **FIrpic** had been limited to 'snapshots' of photophysical behaviour in very specific electronic environments.[153] Given that the final application for many iridium picolinate complexes are organic films, determining the level of sensitivity their electronic energy levels exhibit to their local environment is of great importance.

5.2 Aims

Generate a family of substituted picolinate iridium complexes bearing both donor and acceptor groups linked to the picolinate core via acetylene bridges. Investigate their photophysical properties, with specific emphasis on the sensitivity of the excited state to solvent.

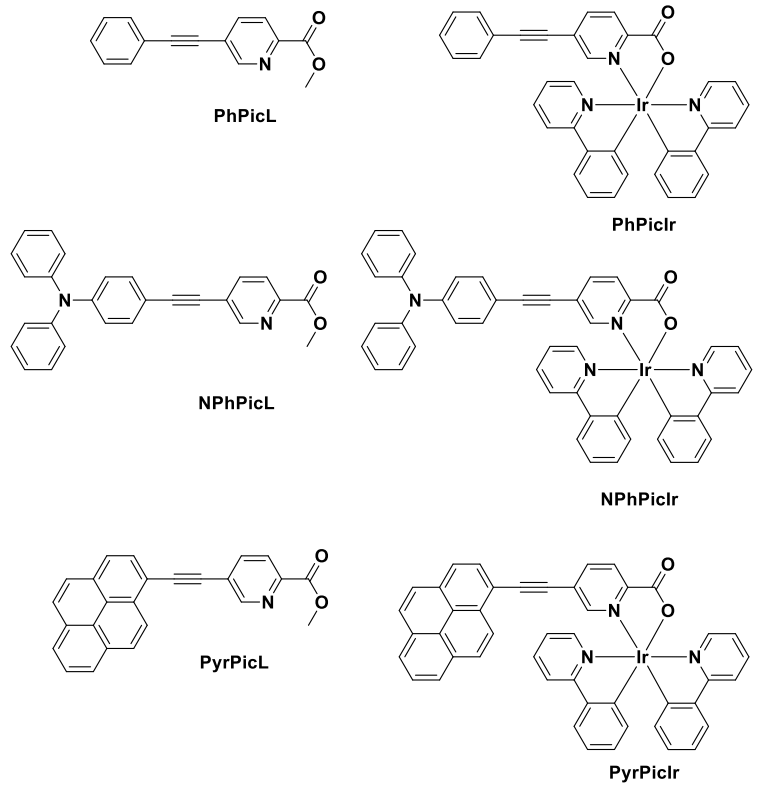

Figure 245. Structure of the target ligands and iridium complexes.

5.3 Synthesis and Characterisation

The picolinate ligands were synthesised off-complex, despite the difficulties reported for this synthetic approach.[73,152] Off-complex synthesis enables spectroscopic characterisation of the ligands and facilitates comparisons between the free ligands and the complexes to determine the extent of photophysical changes induced by the introduction of a metal centre. Off-complex picolinate synthesis has been reported by Romero and co-workers, who used the resulting compounds as components in metal-organic frameworks (MOFs).[165] **Scheme 28** illustrates their synthetic approach.

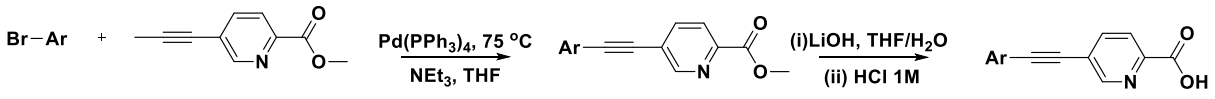

Scheme 28. Synthesis of ethynyl picolinates.[165]

It differs from the approach of Jornet-Mollá *et al.* in two significant ways. Firstly, the reaction temperatures are kept below 80 ˚C, indicating that ethynyl picolinates become unstable at higher temperatures.[152,165] The second difference is the use of the methyl-protected picolinate precursor instead of the ethyl-protected version, suggesting a difference in the relative stabilities of the ester.

5.3.1 Synthesis and Characterisation of PhPicL, NPhPicL, DeprotPic and PyrPicL

Taking advantage of these existent synthetic protocols, **PhPicL** was synthesised utilising the conditions shown in **Scheme 29.**

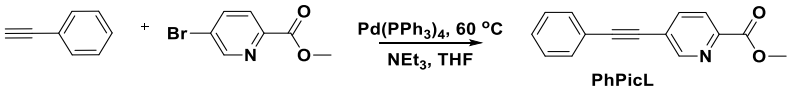

Scheme 29. Synthesis of **PhPicL.**

The reaction proceeded at low temperatures, with the reagents initially suspended in the THF and slowly dissolving into solution as the reaction vessel was heated. After cooling, the THF was removed via rotary evaporator, the crude product dissolved in CH_2Cl_2 and washed with water. Purification via silica column chromatography using a 20:80 ethyl acetate:petroleum ether resulted in recovery of the final product **PhPicL** in 42 % yield.

The ^{1}H NMR of **PhPicL** with spin systems assigned is shown in **Figure 246**. The spectrum consists of five distinct signals in the aromatic region originating from the phenyl and pyridine ring, and one signal at lower ppm from the methyl group of the ester.

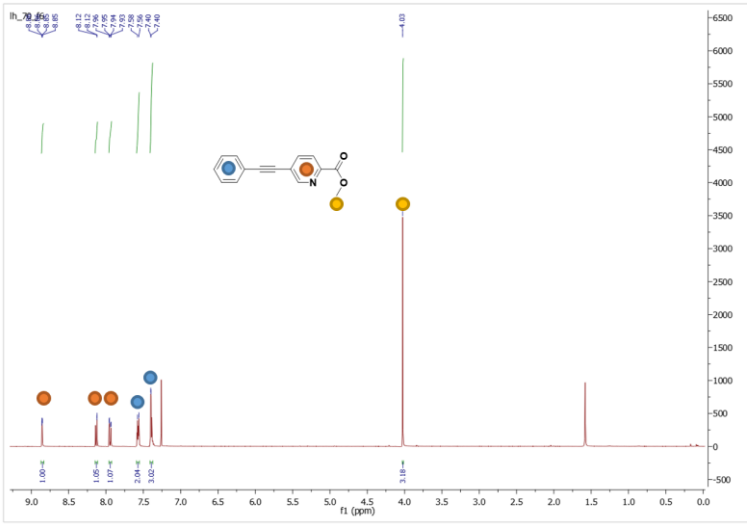

Figure 246. ^{1}H NMR of **PhPicL** with spin systems assigned ($CDCl_3$, 400 MHz, 298 K).

The three most downfield signals integrate to one proton each, the next two signals to 2 and 3 respectively and the most upfield signal to 3 protons. The TOCSY spectrum (**Figure 247)** indicates the correlation between the different signals of the individual spin systems. From this spectrum, we can deduce that the

three most downfield signals arise from the three protons on the pyridine ring, who are more deshielded than the rest of the protons in the compound. This is due to the electronegativity of the nitrogen atom in addition to the induced magnetic field of the ring current. The next two signals in the spectrum arise from the phenyl ring, with the more upfield of the two resulting from an overlap of two signals, including the single proton - *para* to the ethynyl bond.

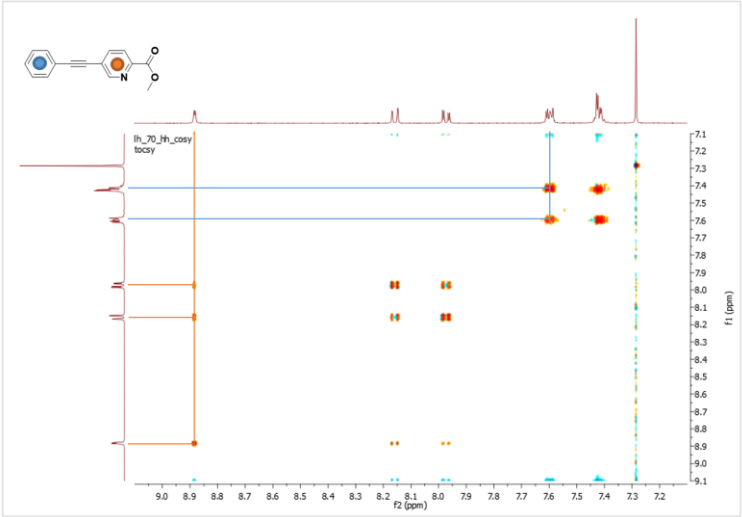

Figure 247. TOCSY NMR spectrum of **PhPicL** showing the correlation of protons in the individual spins systems ($CDCl_3$, 400 MHz, 298 K).

The ^{13}C spectrum of **PhPicL** is displayed in **Figure 248.** It exhibits the by-now familiar cluster of peaks in the aromatic region, as well as two peaks between 80 and 100 ppm arising from the ethynyl bond. Unlike the other ligands investigated in this thesis, a single peak appears further upfield, at around 53 ppm. This is the methyl carbon of the ester group.

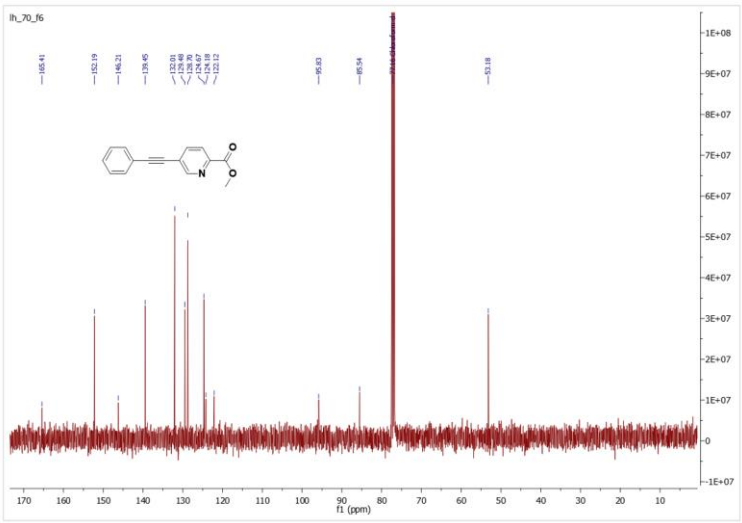

Figure 248. ^{13}C NMR spectrum of **PhPicL** ($CDCl_3$, 101 MHz, 298 K).

For a full assignment of the NMR of **PhPicL** please see the experimental section.

The synthesis of **NPhPicL** was performed using the same methodology as **PhPicL**, shown in **Scheme 30.**

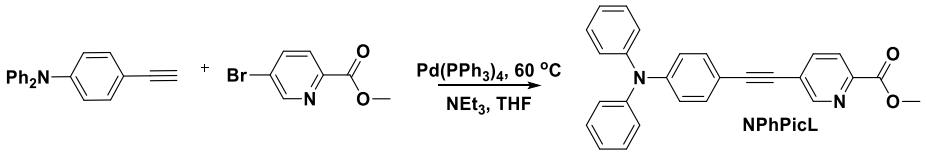

Scheme 30. Synthesis of **NPhPicL.**

NPhPicL was purified applying the same techniques as **PhPicL**, with a yield of 34 %. The ^{1}H NMR spectrum of **NPhPicL** is displayed in **Figure 249**. It consists of a higher number of peaks than **PhPicL**, as expected due to the larger number of protons in the structure. All but one peak are found in the aromatic region, with the single peak at 4.05 ppm integrating to 3 and representing the methyl ester protons.

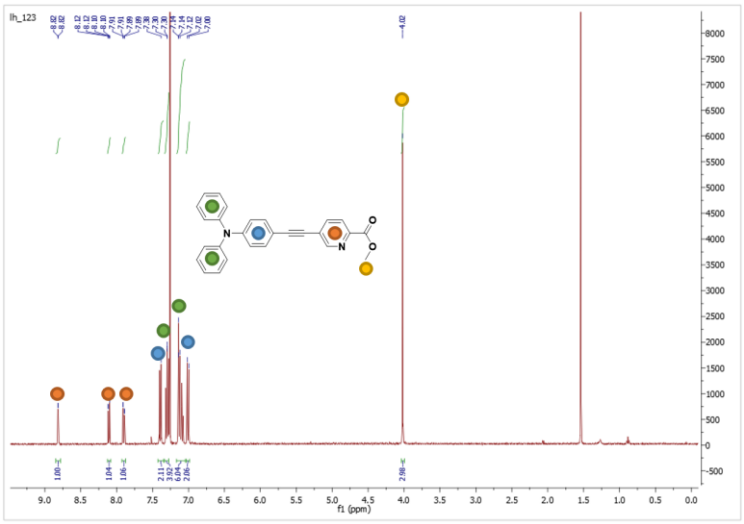

Figure 249. ^{1}H NMR spectrum of **NPhPicL** showing assigned spin systems ($CDCl_3$, 400 MHz, 298 K).

The three most upfield signals all integrate to a single proton, and likely represent the pyridine protons similarly to the spectrum of **PhPicL**. The remaining signals are clustered between 7 and 7.5 ppm, representing the protons on the single proximal and two distal rings of the triphenylamine moiety. Using the TOCSY spectrum displayed in **Figure 250**, we can confirm the two signals bracketing the cluster arise from the proximal phenyl ring, while the two central signal clusters represent the protons of the distal rings.

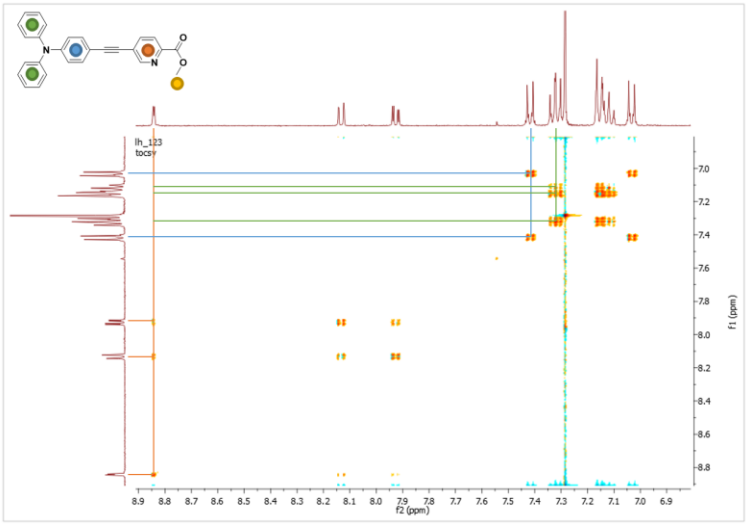

Figure 250. TOCSY NMR spectrum of **NPhPicL**, showing the correlation between protons in the individual spin systems ($CDCl_3$, 400 MHz, 298 K).

The ^{13}C spectrum for **NPhPicL** is shown in **Figure 251**, and is similar to that of **PhPicL**, with most of the signals appearing in the aromatic region of the spectrum.

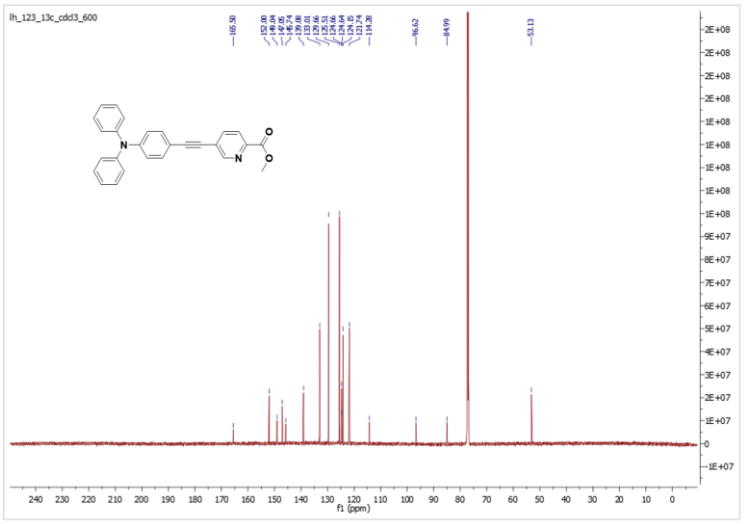

Figure 251. ^{13}C NMR spectrum of **NPhPicL** ($CDCl_3$, 151 MHz, 298 K).

There are now three peaks between 85 and 115 ppm instead of the two observed in **PhPicL**. Using 2D HMBC spectroscopy (**Figure 252**), we can confirm that the most upfield signal is correlated to one of the protons on the pyridine ring, suggesting that it represents the proximal carbon of the acetylene bond. The other two carbon peaks are correlated to signals arising from the proximal triphenylamine ring, indicating that they arise from the acetylene bond and the carbon bonded to the nitrogen atom. Additionally, we observe correlation between the methyl proton peak and the highest downfield carbon signal, suggesting that this is the carbonyl carbon.

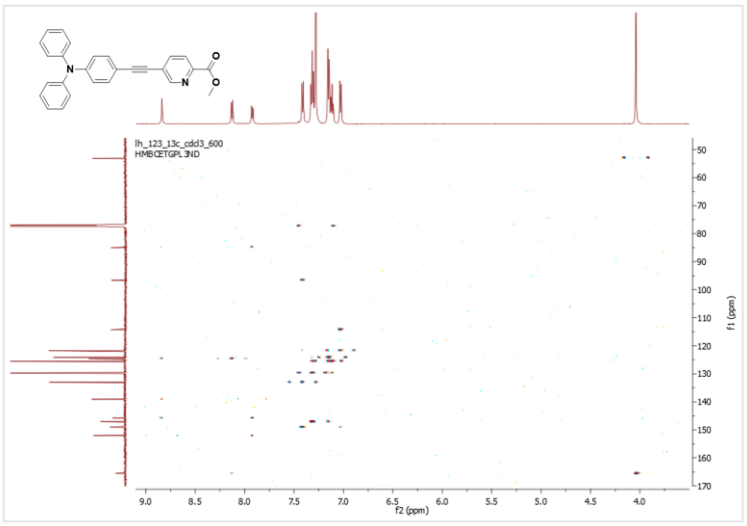

Figure 252. HMBC NMR spectrum of **NPhPicL,** showing the correlation of proton and carbon atoms over multiple bonds ($CDCl_3$, 600 MHz, 298 K).

For a full assignment of the proton spectrum see the experimental section.

To determine whether there are any significant differences between the methyl ester and carboxylic acid versions of the picolinate ligands, **DeprotPic** was generated according to the conditions shown in **Scheme 31**.

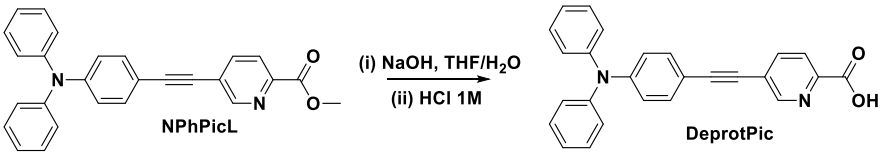

Scheme 31. Synthesis of **DeprotPic** from **NPhPicL.**

The synthesis was performed in line with slightly altered conditions found in the work by Romero and co-workers, with sodium hydroxide used to remove the methyl protecting group followed by acidification with HCl to generate **DeprotPic**.[165] The THF was removed by rotary evaporator and the product extracted using CH_2Cl_2. The obtained yield of 48 % suggests at least partial solubility of **DeprotPic** in aqueous media, likely due to the carboxylic acid moiety. Consequently, no further deprotection reactions were performed for the other ligands to prevent loss of material.

The ^{1}H NMR spectrum for **DeprotPic** is shown in **Figure 253**, and resembles that of **NPhPicL** very closely. The only major observable difference is the loss of the methyl proton peak at 4 ppm, indicating full conversion to the deprotected product. The proton of the carboxylic acid group cannot be detected, and likely forms part of the baseline.

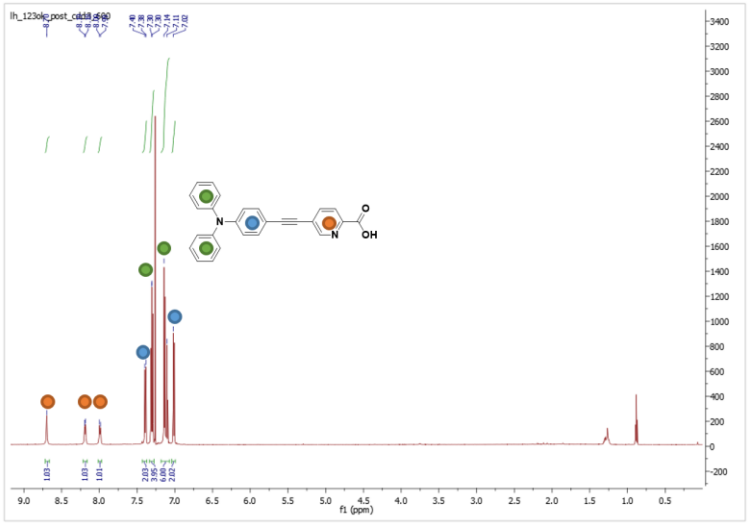

Figure 253. ^{1}H NMR spectrum of **DeprotPic** showing the assigned spin systems ($CDCl_3$, 600 MHz, 298 K).

The TOCSY spectrum for **DeprotPic** is displayed in **Figure 254**. It indicates no change in the order in which the proton signals appear in the spectrum when compared to **NPhPicL**.

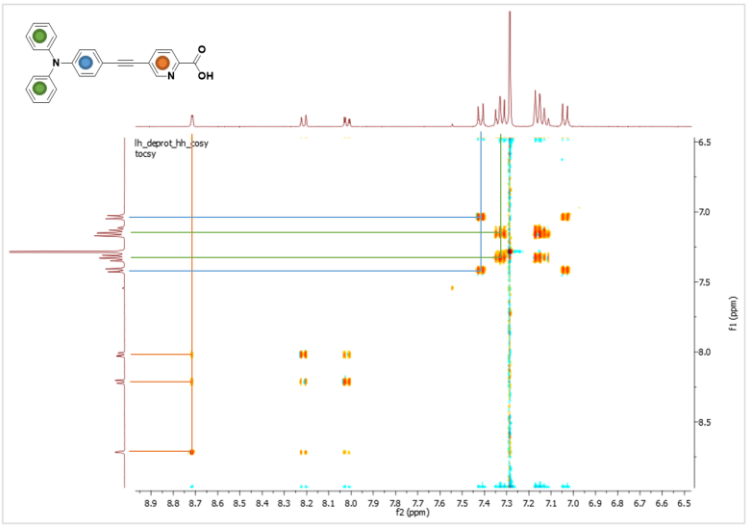

Figure 254. TOCSY NMR spectrum of **DeprotPic**, showing the correlation between the protons in the different spin systems ($CDCl_3$, 400 MHz, 298 K).

Finally, the ^{13}C spectrum of **DeprotPic** is displayed in **Figure 255**. Again, the greatest difference between this spectrum and the one for **NPhPicL** is the loss of the methyl carbon signal appearing at 53 ppm in the latter. The aliphatic signals under 35 ppm arise due to residual hexanes used to dry the product following filtration.

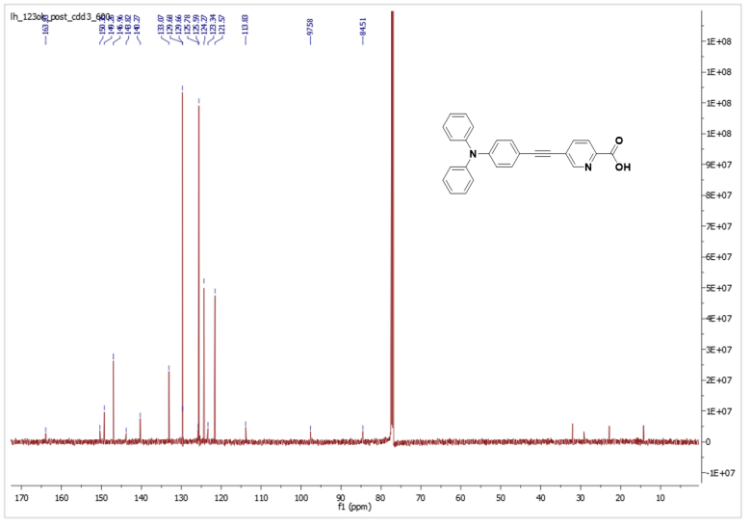

Figure 255. ^{13}C NMR spectrum of **DeprotPic** ($CDCl_3$, 151 MHz, 298 K).

An overlay of the ^{1}H NMR spectra of **DeprotPic** and **NPhPicL** is exhibited in **Figure 256**. At lower ppm, the loss of the methyl ester group is clearly visible. The signals of the triphenylamine signals are identical between the two carbons, suggesting no change in the electronic environment upon conversion from the ester to carboxylic acid for those protons. The signals in the pyridine rings are more significantly affected, with the most downfield proton signal shifting to lower ppm following conversion to the carboxylic acid. Conversely, the remaining two pyridine signals are shifted to higher ppm, indicating that the loss of the methyl group has a significant impact on the electronic environment of the pyridine ring.

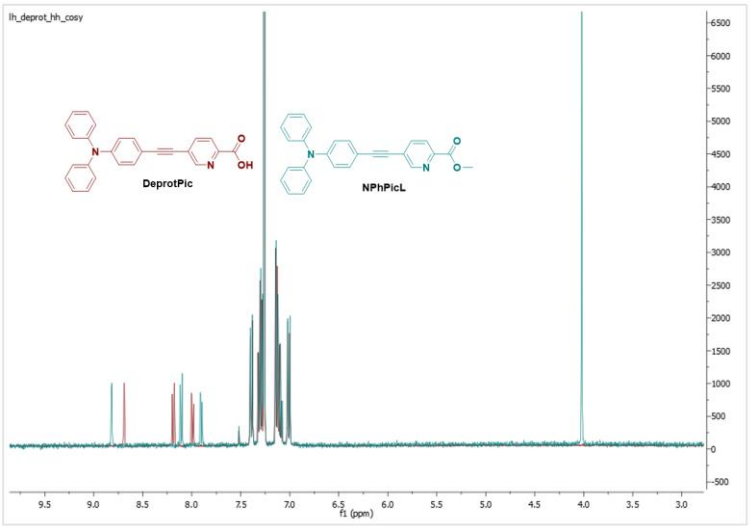

Figure 256. Overlay of the ^{1}H NMR spectra of **DeprotPic** (maroon) and **NPhPicL** (aquamarine) ($CDCl_3$, 400 MHz, 298 K).

These differences suggests a potential change in the spectroscopic properties between the two compounds, which will be further discussed later in this chapter.

Finally, **PyrPicL** was synthesised according to the procedures illustrated in **Scheme 32**.

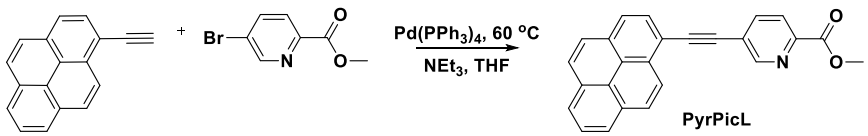

Scheme 32. Synthesis of **PyrPicL**.

The purification was accomplished following the same procedures established for the other picolinate ligands, and the final product was recovered with a yield of 20 %. The low yield reflects the difficulties of working with pyrene.

The ^{1}H NMR spectrum of **PyrPicL** with assigned spin systems is shown in **Figure 257.**

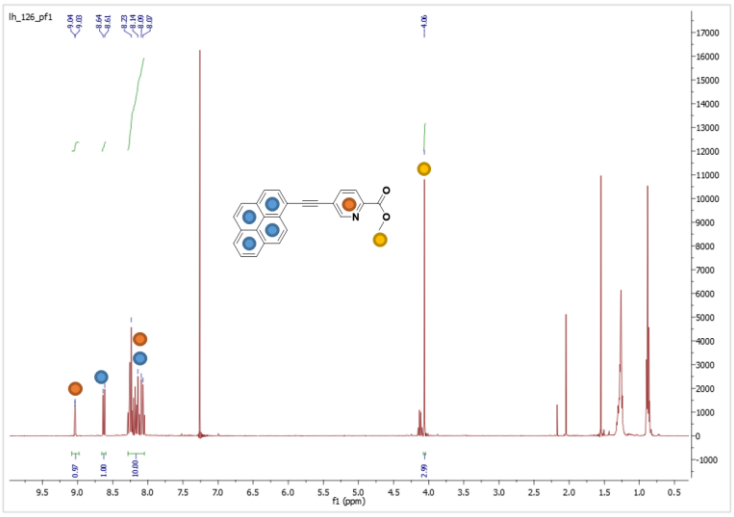

Figure 257. ^{1}H NMR spectrum of **PyrPicL** with the spin systems assigned ($CDCl_3$, 400 MHz, 298 K).

The spectrum exhibits two signals at higher shifts in the aromatic region integrating to one proton each, as well as a complex cluster of peaks integrating to 10 protons. The methoxy signal is found at 4.06 ppm. There are a large number of residual hexane signals in the aliphatic region, remnants of the solvent used to wash the precipitate during purification.

The TOCSY NMR spectrum for **PyrPicL** (**Figure 258**) indicates the correlation between the protons in the compound. From it, we can determine that two of the pyridine ring signals form part of the complex multiplets between 8 and 8.5 ppm, with the remaining eight protons originating from the pyrene moiety. The close clustering of these signals makes individual assignment of the pyrene protons very difficult.

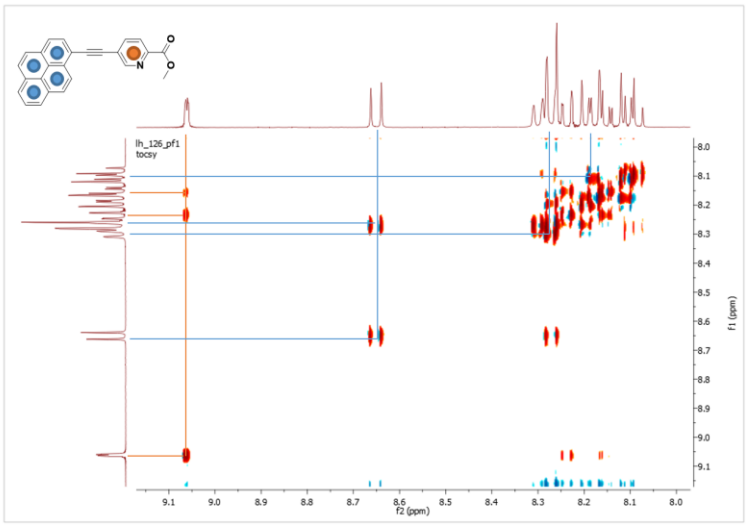

Figure 258. TOCSY NMR spectrum of **PyrPicL** showing the correlation of different protons in the spin systems of the compound ($CDCl_3$, 400 MHz, 298 K).

The ^{13}C NMR spectrum for **PyrPicL** is displayed in **Figure 259**. It includes a large cluster of peaks in the aromatic region of the spectrum. Additionally, the expected acetylene peaks appear between 90 and 100 ppm, with the methyl carbon showing at 53 ppm. Residual solvent peaks can be found in the aliphatic region of the spectrum.

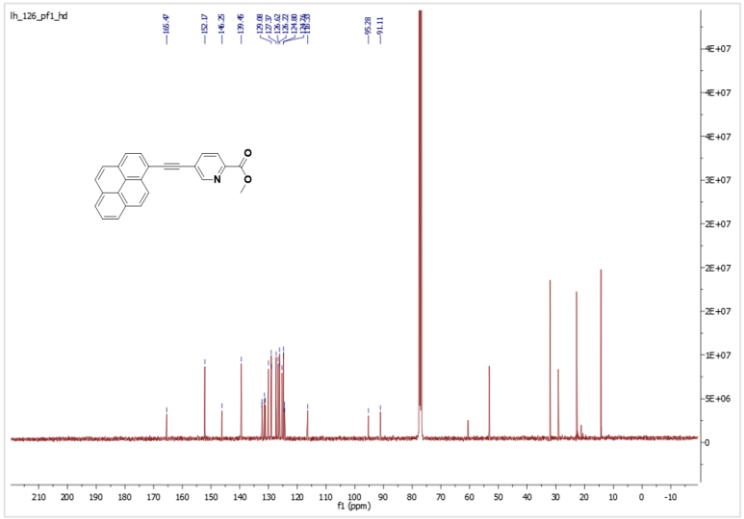

Figure 259. ^{13}C NMR spectrum of **PyrPicL** ($CDCl_3$, 400 MHz, 298 K).

5.3.2 Synthesis and Characterisation of PhPicIr, NPhPicIr and PyrPicIr

The synthesis of the iridium picolinate complexes differed slightly from that of iridium bipyridine complexes, as shown in **Scheme 33** below.

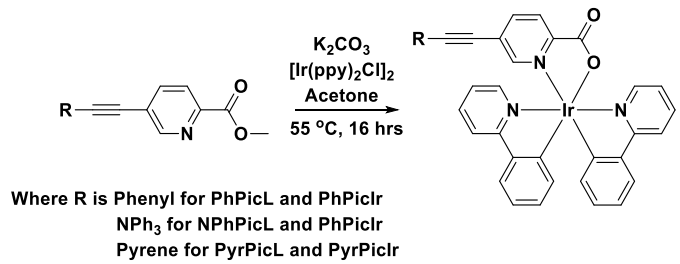

Scheme 33. Synthesis of **PhPicIr**, **NPhPicIr** and **PyrPicIr.**

The purification procedures varied significantly to work shown in previous chapters. The solvent was removed by rotary evaporator, the crude solid dissolved in CH_2Cl_2, followed by a water wash. The complex was then purified via silica column chromatography using an acetone : Petroleum Ether mobile phase gradient, rising from 1 : 4 to neat acetone, with the product eluting as an orange/yellow band. The yields for the reactions were 70 %, 50 % and 35 % for **PhPicIr**, **NPhPicIr** and **PyrPicIr** respectively.

The ^{1}H NMR spectrum for **PhPicIr** is shown below in **Figure 260**, displaying a large number of peaks in the aromatic region. As discussed in the introduction to this chapter, the picolinate ligand introduces a high degree of asymmetry to the complex, leading to a splitting of the spectator ligand signals.[161]

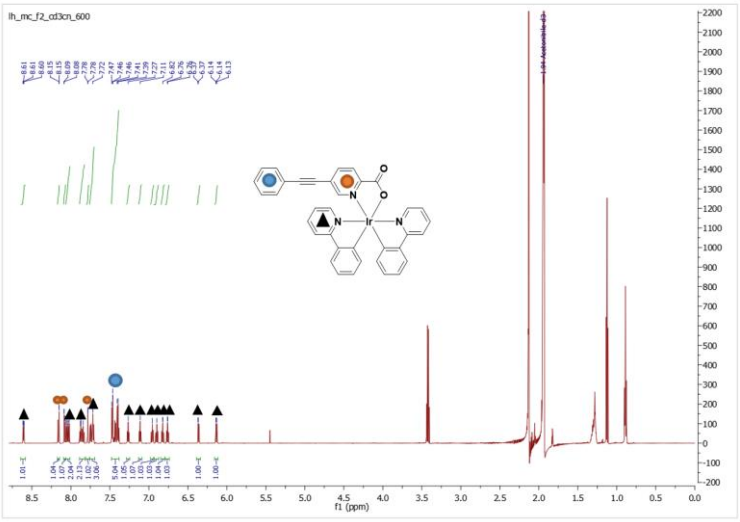

Figure 260. ^{1}H NMR spectrum of **PhPicIr** showing the spin systems assigned (MeCN-d_3, 600 MHz, 298 K).

This splitting can be easily observed in the TOCSY spectrum for **PhPicIr**, displayed in **Figure 261**. This spectrum exhibits the high number of non-equivalent spin systems in the complex, with two on the picolinate and four on the spectator ligands adding up to a total of six. Most downfield signals arise from one of the spectator ligand pyridine rings, the second most from the pyridine signals of the picolinate ligand. A mix of phenyl and pyridine ring systems of the phenylpyridine ligands are next, with the signals of the picolinate signal ring appearing as a cluster of signals around 7.5 ppm. A full assignment of the proton signals can be found in the experimental section.

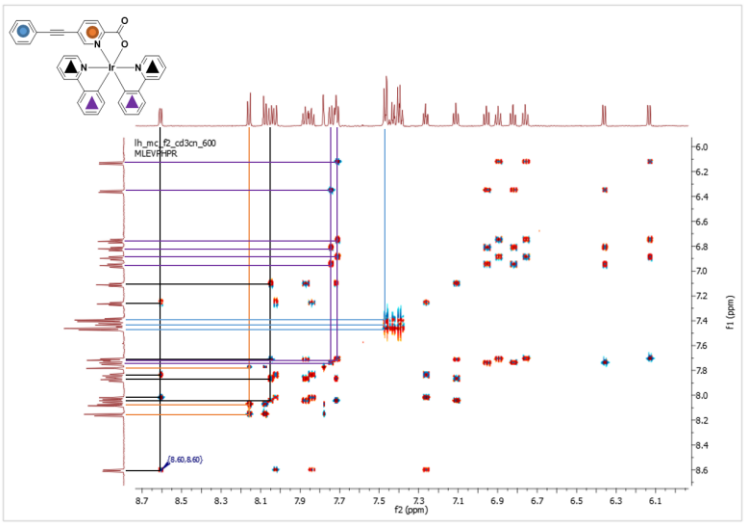

Figure 261. TOCSY NMR spectrum for **PhPicIr** showing the correlation of protons in the distinct spin systems (MeCN-d_3, 600 MHz, 298 K).

The ^{13}C NMR spectrum for **PhPicIr** displays the same high number of peaks observed in the proton spectrum, as reported in **Figure 262**.

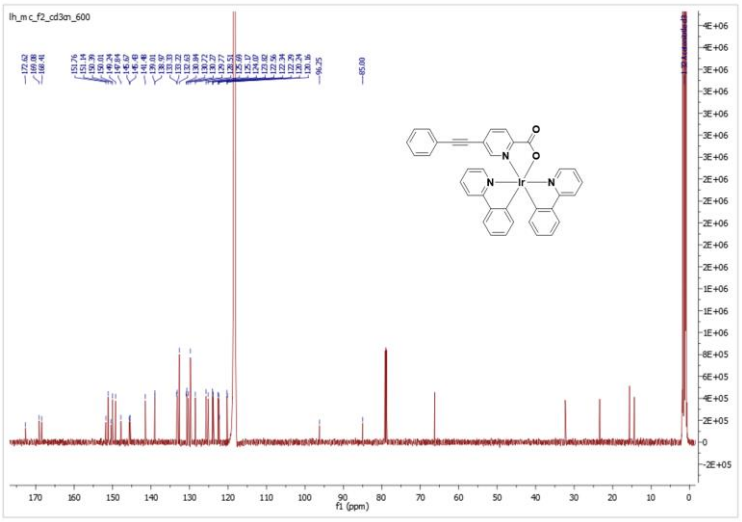

Figure 262. ^{13}C NMR spectrum for **PhPicIr** (MeCN-d_3, 600 MHz, 298 K).

The acetylene signals appear between 80 and 100 ppm, with the remaining complex signals manifesting in the aromatic region. The aliphatic signals again arise from residual solvent used in the purification process.

The ^{1}H NMR spectrum for **NPhPicIr** is displayed below in **Figure 263**, and resembles that of **PhPicIr**. It exhibits a higher degree of signal overlap compared to the previous complex, resulting in a smaller number of peaks integrating to more protons.

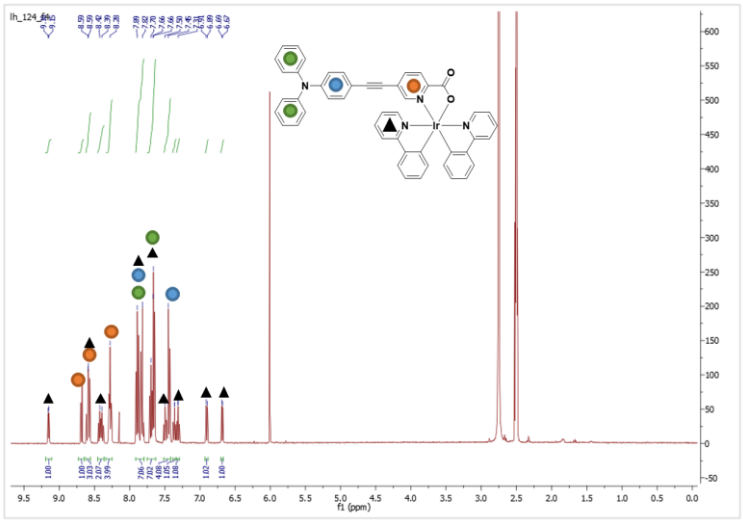

Figure 263. ^{1}H NMR spectrum of **NPhPicIr** showing the assigned spin systems (MeCN-d_3, 600 MHz, 298 K).

The TOCSY NMR spectrum for **NPhPicIr** is displayed in **Figure 264**. The furthest downfield signals arise from the pyridine rings of the spectator ligands, followed by the pyridine ring of the picolinate ligand. The signals of the phenyl systems on the spectator ligands tend to appear the furthest upfield, with the triphenylamine rings manifesting between 6.8 and 7.5 ppm.

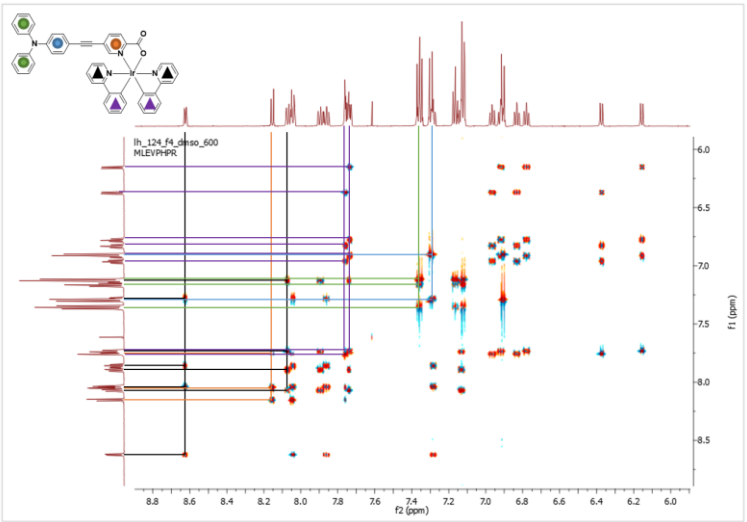

Figure 264. TOCSY NMR spectrum of **NPhPicIr** showing the proton correlations in the various spin systems (MeCN-d_3, 600 MHz, 298 K).

The ^{13}C NMR spectrum for **NPhIrPic** is displayed below in **Figure 265**. There are a high number of peaks in the aromatic region of the carbon spectrum, with some exhibiting much higher intensities than others. These most likely represent the carbon atoms in the triphenylamine rings, as they have a higher degree of equivalency than other carbons in the complex. The set of three signals at lower ppm representing the two acetylene and one nitrogen-bonded carbon of the proximal phenyl ring are also clearly visible.

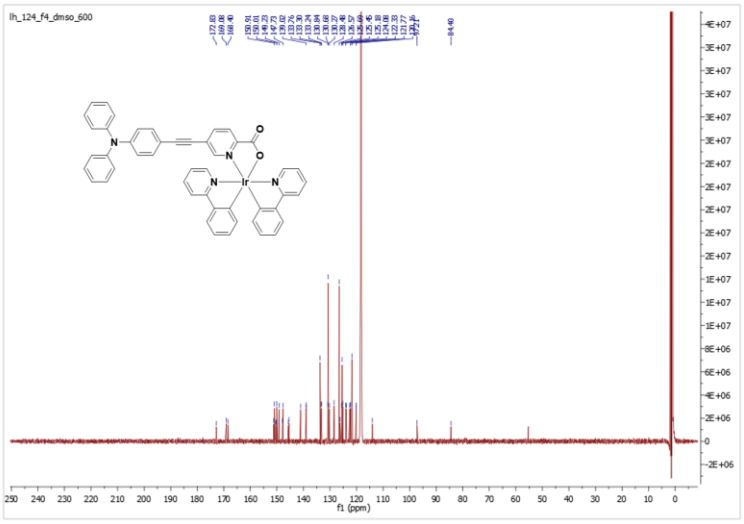

Figure 265. ^{13}C NMR spectrum of **NPhPicIr** (MeCN-d_3, 600 MHz, 298 K).

The ^{1}H NMR spectrum of the final complex, **PyrPicIr**, is depicted below in **Figure 266**. It displays the same grouping of pyrene signals as the precursor ligand, indicating the high degree of similarity in the electronic environment the pyrene protons are found in. The remaining signals in the spectrum represent the protons of the spectator ligand systems, which are again split due to the asymmetry introduced by the picolinate.

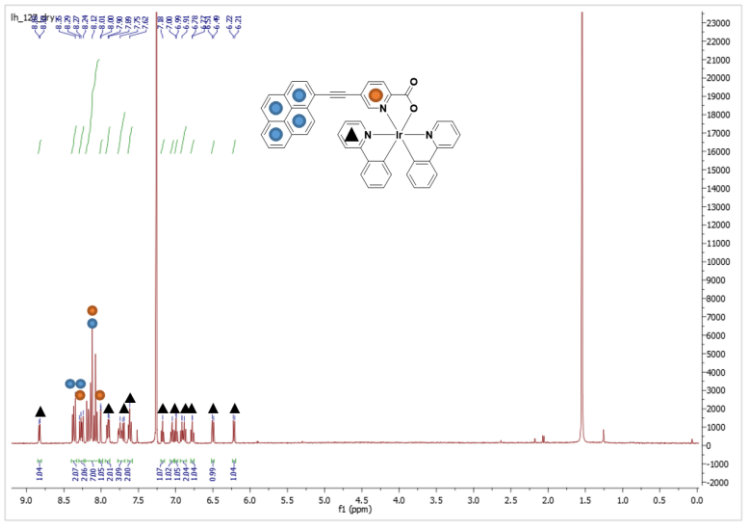

Figure 266. ^{1}H NMR spectrum of **PyrPicIr** with the spins systems assigned ($CDCl_3$, 600 MHz, 298 K).

The TOCSY NMR spectrum for the complex (**Figure 267**) shows the same trends observed in the other two iridium complexes

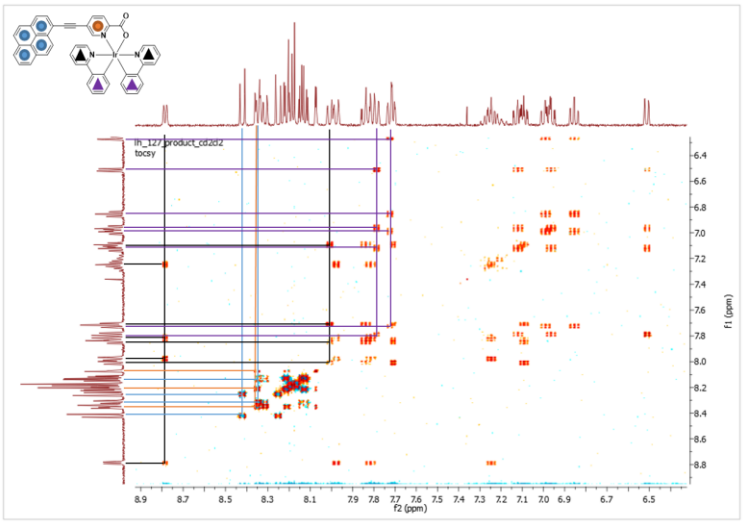

Figure 267. TOCSY NMR spectrum of **PyrPicIr** showing the correlation of protons in the separate spin systems ($CDCl_3$, 600 MHz, 298 K).

Finally, the ^{13}C NMR spectrum of **PyrPicIr** is displayed below in **Figure 268**. The signals are of a low intensity as the sample submitted for analysis was dilute. However, it is still possible to recognise the high number of nearly equivalent carbon signals between 120 and 150 ppm, arising from the pyrene moiety.

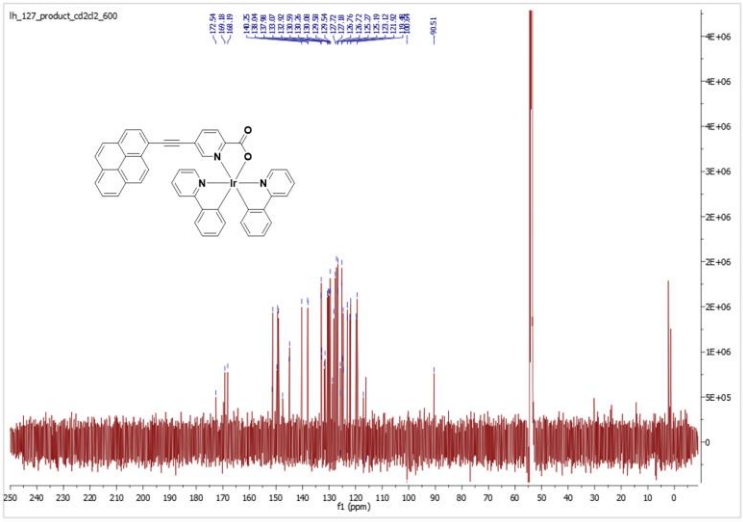

Figure 268. ^{13}C NMR spectrum of **PyrPicIr** (CD_2Cl_2, 400 MHz, 298 K).

5.3.3 Attempted Synthesis of CF_3PicL and PicRu Complexes

As pyrene acts as a functionally independent chromophore in many photophysical processes, it was attempted to generate a picolinate ligand bearing a more conventional electron-withdrawing group. Trifluorotoluene was selected based on previous experience working with the precursor materials, where it demonstrated a promising influence on the photophysical properties of other complexes investigated in this thesis.

The synthetic conditions chosen for the Sonogashira coupling reaction were identical to those already discussed in this section, as shown in **Scheme 34.**

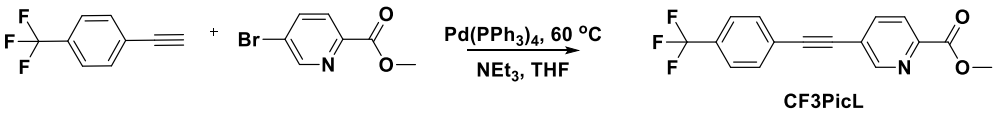

Scheme 34. Synthetic approach to generate **CF_3PicL.**

However, the resulting crude reaction mixture contained two fractions with almost identical R_f values in all trialled solvent systems. As both fractions where white solids, it proved impossible to isolate them using both traditional silica column chromatography and automated low pressure liquid chromatography (LPLC) systems. The NMR spectrum in **Figure 269** clearly indicates the presence of a secondary picolinate species, including a secondary methyl ester signal at around 4 ppm. The signal at 8.15 is characteristic of the trifluorotoluene moiety and has been observed in previous complexes containing this functional group, suggesting that synthesis of the final product was successful.

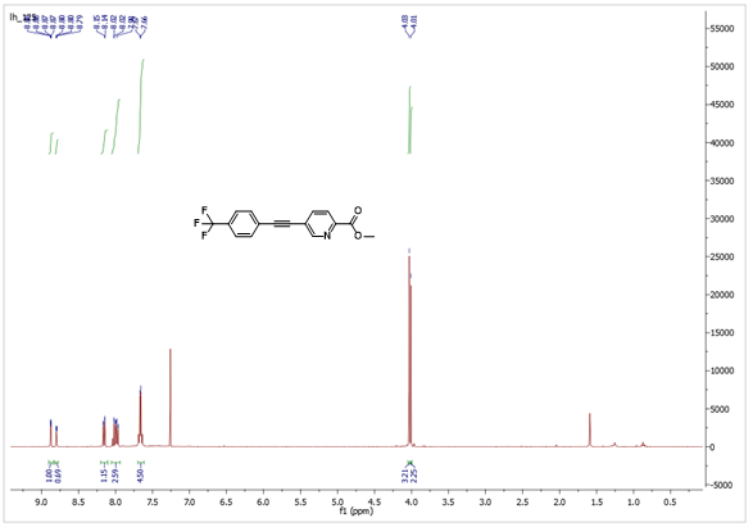

Figure 269. ^{1}H NMR of **CF_3PicL** fraction containing impurities ($CDCl_3$, 400 MHz, 298 K).

It is likely that the starting material, the brominated picolinate, has R_f value and affinity for silica very similar to the target compound. Given the inability to distinguish them by colour, separation proved impossible.

Additionally, attempts to generate the ruthenium complexes for the picolinate complexes were unsuccessful (**Scheme 35**).

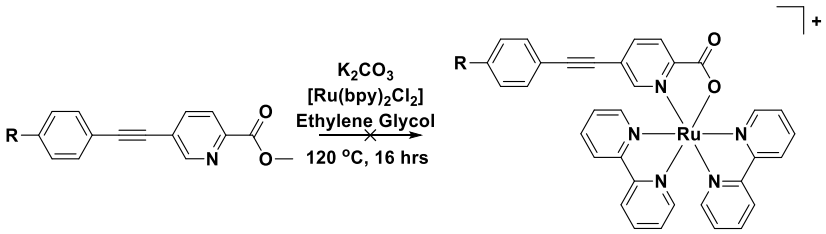

Scheme 35. Unsuccessful synthesis of ruthenium picolinate complexes.

The higher temperatures required for complexation of the ligands to the ruthenium metal centre led to decay of the picolinate, as reported by other groups.[73,152] Therefore, only the iridium complexes could be spectroscopically analysed.

Samples of all generated compounds were submitted for analysis by mass spectrometry. Signals corresponding to the mass of **PhPicL**, **NPhPicL**, **PyrPicL** and **PhPicIr** were found in their respective samples. Despite repeated submissions, no signals corresponding to the masses for **NPhPicIr**, **PyrPicIr** and **DeprotPic** could be identified. However, analysis of the mass spectrometry spectra for **NPhPicIr** and **PyrPicIr** resulted in the discovery of a signal corresponding to the mass of the iridium complex without the picolinate (**Figure 270**). This suggests that the bonds between the picolinate and the iridium are weaker than the bonds between the iridium and the phenylpyridine spectator ligands.

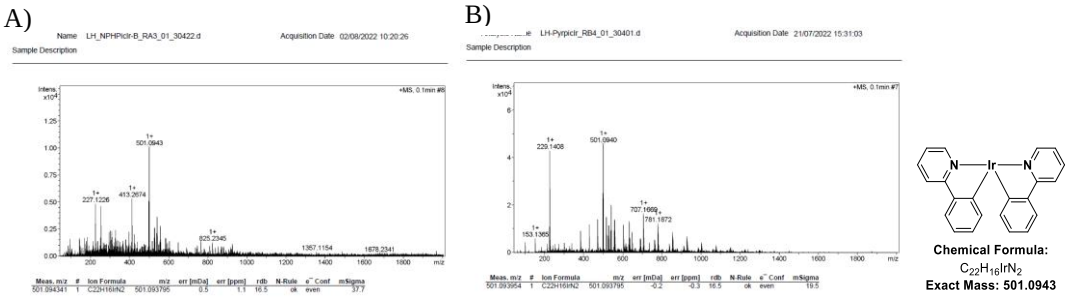

Figure 270. Mass spectrometry results for **NPhPicIr** (A) and **PyrPicIr** (B) with the exact mass and structure of the iridium fragment shown on the right.

5.3.4 Crystallographic Analysis

5.3.4.1 PhPicL

A sample of **PhPicL** was recovered from the complexation attempt with $[Ir(ppy)_2Cl]_2$ to generate **PhPicIr**. The recovered sample crystallised and was found suitable for single crystal x-ray diffraction studies. Data collection and refinement was conducted by Dr. Brendan Twamley in Trinity College Dublin

A specimen of $C_{14}H_{11}NO_3$, approximate dimensions 0.010 mm x 0.120 mm x 0.320 mm, was used for the X-ray crystallographic analysis. The X-ray intensity data were measured (λ = 1.54178 Å) on a Bruker Apex Kappa Duo with an Oxford Cobra Cryosystem low temperature device using a MiTeGen micromount. Using the OLEX2 Software Package, the structure was solved with the SHELXT structure solution program using Intrinsic Phasing and refined with the SHELXL refinement package with Least Squares minimisation, using the space group P21/c, with Z = 8 for the formula unit, $C_{14}H_{11}NO_3$. The final anisotropic full-matrix least-

squares refinement on F2 with 349 variables converged at R1 = 6.09%, for the observed data and wR2 = 18.64% for all data. The goodness-of-fit was 0.957.

The compound in the recovered sample had undergone conversion from the methyl ester to the carboxylic acid, as displayed in **Figure 271**. This resulted in extensive hydrogen bonding, particularly since the sample contained water. The carboxylic acid proton of one molecule bonds with the oxygen atom of a water molecule, and the proton of that water molecule bonds to the oxygen and pyridyl nitrogen of second picolinate compound.

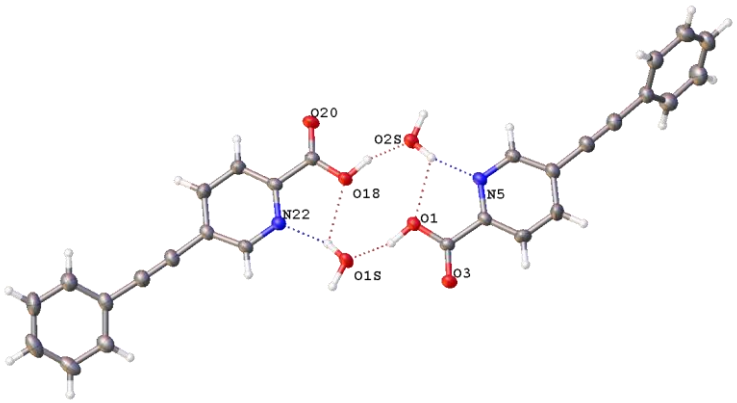

Figure 271. Molecular structure of **PhPicL**, showing H_2O assisted hydrogen-bonded assembly of two independent molecules in the asymmetric unit. Atomic displacement shown at 50% probability and heteroatoms labelled only.

This results in a repeating pattern of hydrogen bonding, with water molecules and picolinate ligands alternating with each other (**Figure 272**). The method of binding of the oxygen atom and the nitrogen of the pyridine ring is reminiscent of binding to a metal centre. The distance between the nitrogen and the proton is shorter than that the distance between the oxygen and the proton.

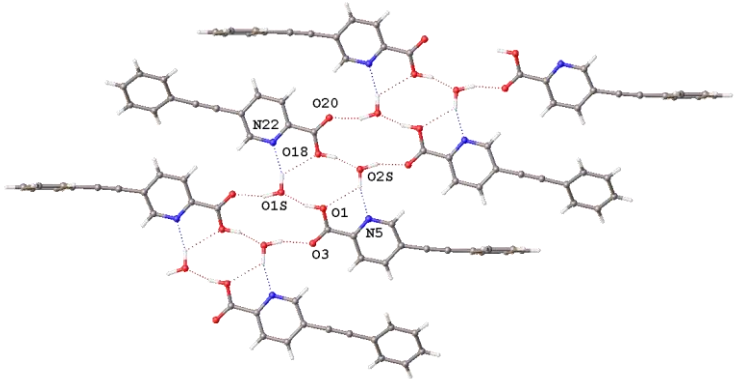

Figure 272. Schematic hydrogen bonding assembly in **PhPicL** viewed normal to the (111) direction.

Figure 272 also indicates significant flexing in the phenylacetylene groups of some picolinate molecules. Every second row of picolinate complexes in the image have their phenyl rings at a right angle to the pyridine ring, making the bend in the acetylene particularly noticeable.

This becomes even clearer in **Figure 273**, which exhibits the packing structure of the sample. The flex in the acetylene linker allows partial stacking of the phenyl rings, potentially lowering the overall energy of the conformation despite the significant strain on the acetylene bond.

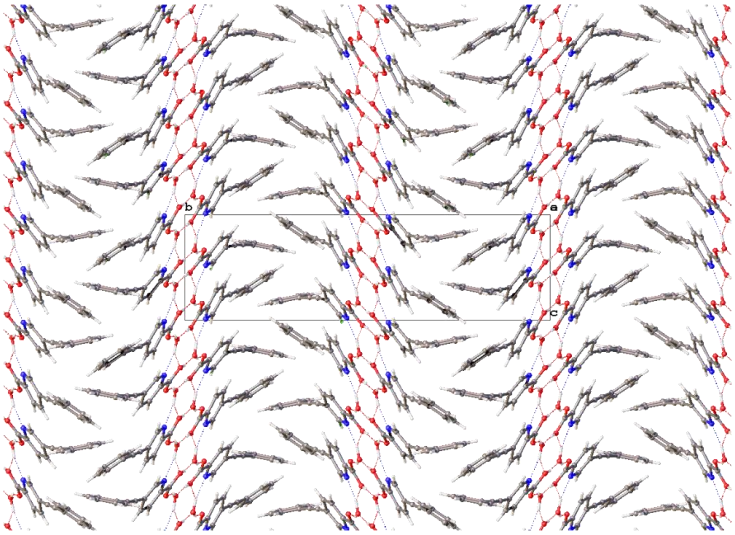

Figure 273. Schematic packing diagram of **PhPicL** viewed normal to the a-axis showing the extended hydrogen bonding assembly forming a ribbon motif.

5.3.4.2 NPhPicL

A sample of **NPhPicL** suitable for single crystal x-ray diffraction studies was obtained by the slow evaporation of CH_2Cl_2. The specimen of $C_{27}H_{20}N_2O_2$, approximate dimensions 0.027 mm x 0.065 mm x 0.123 mm, was used for the X-ray crystallographic analysis. The X-ray intensity data were measured (λ = 1.54178 Å) on a Bruker Apex Kappa Duo with an Oxford Cobra Cryosystem low temperature device using a MiTeGen micromount. Using the OLEX2 Software Package, the structure was solved with the SHELXT structure solution program using Intrinsic Phasing and refined with the SHELXL refinement package with Least Squares minimisation, using the space group $P\bar{1}$, with Z = 2 for the formula unit, $C_{27}H_{20}N_2O_2$. The final anisotropic full-matrix least-squares refinement on F^2 with 422 variables converged at R1 = 7.22%, for the observed data and wR2 = 22.22% for all data. The goodness-of-fit was 1.042. There was disorder in the crystal, resulting in two major conformations as shown in **Figure 274**.

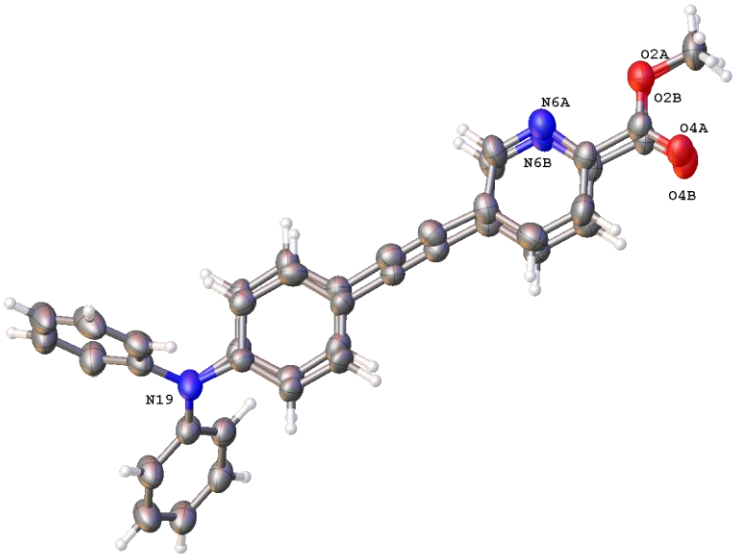

Figure 274. Disordered molecular structure of **NPhPicL**, showing the two disordered locations of the methyl (ethynylphenyl) picolinate. Atomic displacement shown at 50% probability and heteroatoms labelled only.

Interestingly, the disorder does not affect the distal triphenylamine rings, suggesting that they adopt their preferred orientations in both conformations. The ratio between the two conformations is nearly equal, as displayed in **Figure 275.**

A)

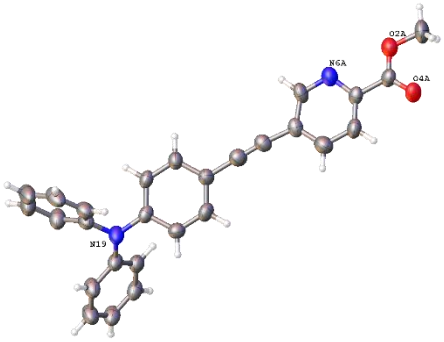

B)

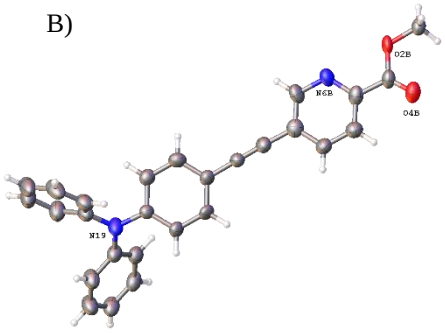

Figure 275. Individual images of each disordered moiety in **NPhPicL** with (A) 58% occupied and (B) 42|% occupied. Atomic displacement shown at 50% probability and heteroatoms labelled only.

The crystal packing structure is depicted in **Figure 276**, and highlights the close interactions between the picolinate molecules. They appear to pair up, with weak hydrogen bonds between the nitrogen of the pyridine ring and oxygen of the ester group bonding to the protons of the proximal phenyl group of the triphenylamine moiety of the neighbouring picolinate molecule.

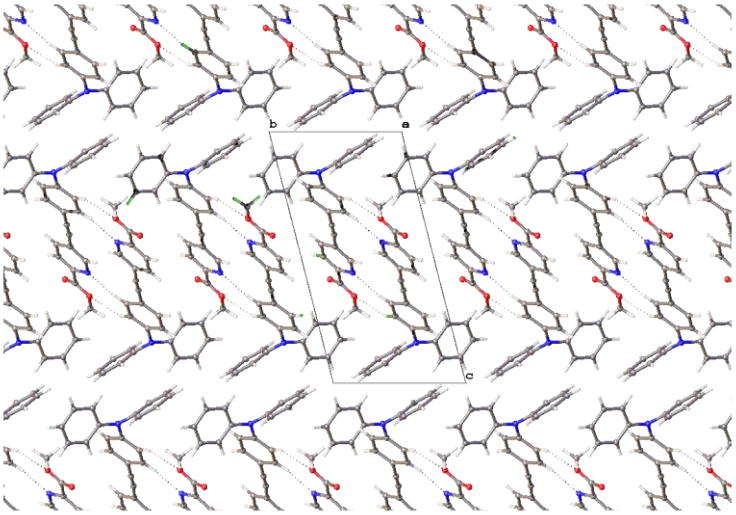

Figure 276. Schematic packing diagram of **NPhPicL** viewed normal to the a-axis, with weak hydrogen bonding shown as dotted lines.

5.3.3.3 PhPicIr

A crystal of **PhPicIr** suitable for single crystal x-ray diffraction studies was grown by the slow evaporation of toluene. The specimen of $C_{41.25}H_{30}IrN_3O_2$, approximate dimensions 0.088 mm x 0.190 mm x 0.225 mm, was used for the X-ray crystallographic analysis. The X-ray intensity data were measured (λ = 0.71073 Å) on a Bruker Apex Kappa Duo with an Oxford Cobra Cryosystem low temperature device using a MiTeGen micromount.

Using the OLEX2 Software Package, the structure was solved with the SHELXT structure solution program using Intrinsic Phasing and refined with the SHELXL refinement package with Least Squares minimisation, using the space group $P\bar{1}$, with Z = 2 for the formula unit, $C_{41.25}H_{30}IrN_3O_2$. The final anisotropic full-matrix least-squares refinement on F^2 with 479 variables converged at R1 = 2.75%, for the observed data and wR2 = 6.09% for all data. The goodness-of-fit was 1.074. The crystal structure of **PhPicIr** is shown in **Figure 277** along with a disordered toluene remaining from the crystallisation process. The complex adopts a distorted octahedral structure, with the oxygen and nitrogen of the picolinate ligand *trans* to the cyclometallating carbon atoms of the phenylpyridine spectator ligands. The nitrogen of the picolinate ligand forms a 172.13° angle to the opposing carbon, while the oxygen forms a 173.21° angle to the opposing carbon. The bond lengths of between the coordinating atoms on the picolinate and the metal centre are 2.142 Å (Ir-N) and 2.155 Å (Ir-O). These are longer than the bond lengths between the metal centre and the coordinating ligands of the spectator ligands (2.043, 2.030 Å for Ir-N, 2.009 and 1.999 Å for Ir-C). The acetylene linker shows marginal distortion (3.81° from straight), with the phenyl and pyridine ring of the picolinate ligand sharing a plane.

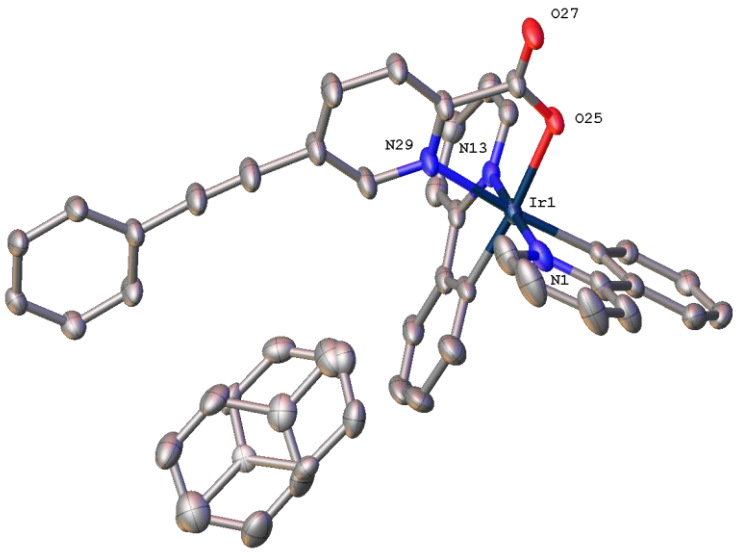

Figure 277. Molecular structure of **PhPicIr**, showing the disordered toluene solvent molecule. Atomic displacement shown at 50% probability, heteroatoms labelled only and hydrogen atoms omitted for clarity.

The crystal packing of the **PhPicIr** sample is exhibited in **Figure 278.**

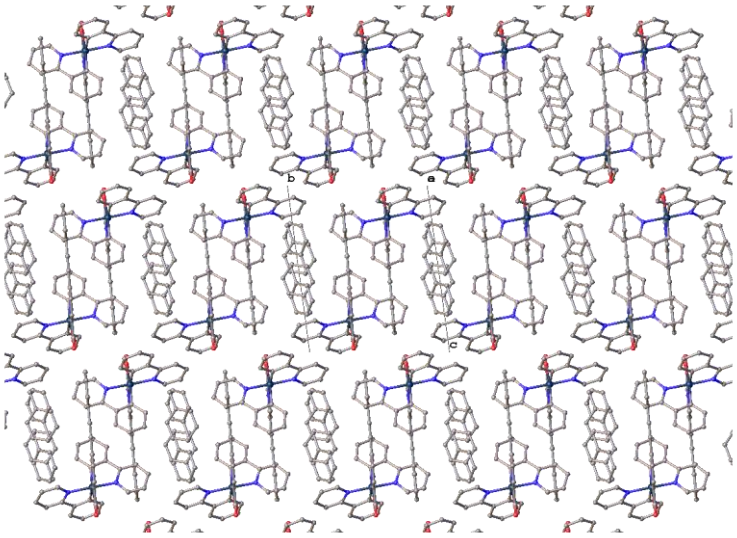

Figure 278. Schematic packing diagram of **PhPicIr** viewed normal to the a-axis with hydrogen atoms omitted.

The packing shows the complexes forming head-to-tail pairs, with the phenyl and pyridine ring of one picolinate ligand positioned across from the pyridine and phenyl ring of its neighbour. The solvent molecules occupy the spaces between the complex pairs.

5.3.4.4 PyrPicIr

A crystal of **PyrPicIr** suitable for single crystal x-ray diffraction studies was grown from the slow evaporation of CH_2Cl_2 and toluene. The specimen of $C_{49.50}H_{32}IrN_3O_2$, approximate dimensions 0.029 mm x

0.047 mm x 0.203 mm, was used for the X-ray crystallographic analysis. The X-ray intensity data were measured (λ = 1.54178 Å) on a Bruker Apex Kappa Duo with an Oxford Cobra Cryosystem low temperature device using a MiTeGen micromount. Using the OLEX2 Software Package, the structure was solved with the SHELXT structure solution program using Intrinsic Phasing and refined with the SHELXL refinement package with Least Squares minimisation, using the space group $P2_1/n$, with Z = 4 for the formula unit, $C_{49.50}H_{32}IrN_3O_2$. The final anisotropic full-matrix least-squares refinement on F^2 with 518 variables converged at R1 = 8.68%, for the observed data and wR2 = 24.95% for all data. The goodness-of-fit was 1.067.

The crystal structure of **PyrPicIr** is shown in **Figure 279**, adopting a distorted octahedral structure with residual toluene incorporated into the final crystal structure. The oxygen and nitrogen atoms of the picolinate ring are *trans* to the cyclometallating carbon atoms of the phenylpyridine rings, The nitrogen of the picolinate ligand forms a 174.21° angle to the opposing carbon, while the oxygen forms a 167.96° angle to the opposing carbon. This results in a greater distortion of the octahedron than in **PhPicIr**. The bond lengths of between the coordinating atoms on the picolinate and the metal centre are 2.159 Å (Ir-N) and 2.176 Å (Ir-O), while the bond lengths between the metal centre and the coordinating ligands of the spectator ligands were 2.091, 2.072 Å for Ir-N, 2.048 and 2.020 Å for Ir-C. These bond lengths are greater than in **PhPicIr**, suggesting that the bonds in **PyrPicIr** are weaker. This could explain the loss of the picolinate ligand from the complex during the mass spectrometry experiments. The acetylene linker appears to flex slightly, distorting from the anticipated 180° by 10°.

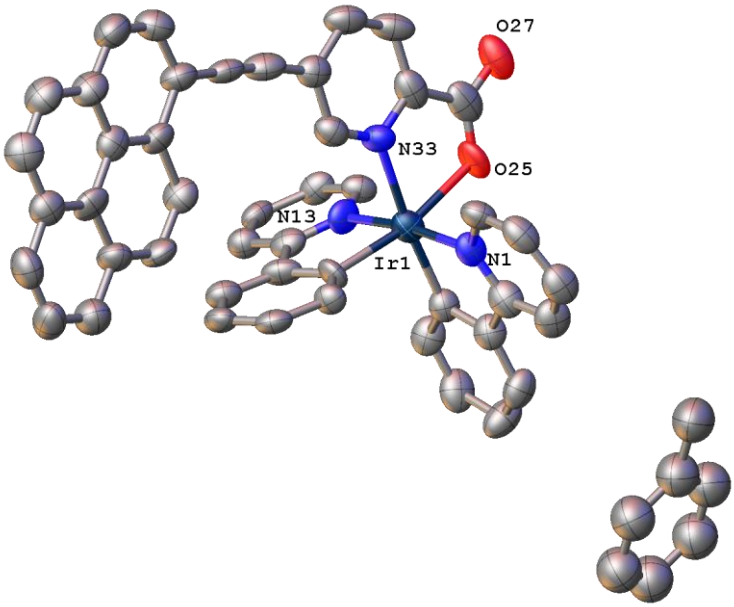

Figure 279. Molecular structure of **PyrPicIr**, showing the half-occupied toluene solvent molecule. Atomic displacement shown at 50% probability and heteroatoms labelled only.

The packing structure of the **PyrPicIr** sample is shown in **Figure 280**. It resembles the structure of **PyrIr** quite closely. In both samples, the pyrene groups adopt a 'face-to-face' configuration, with the iridium complex playing a secondary role in determining the packing arrangement.

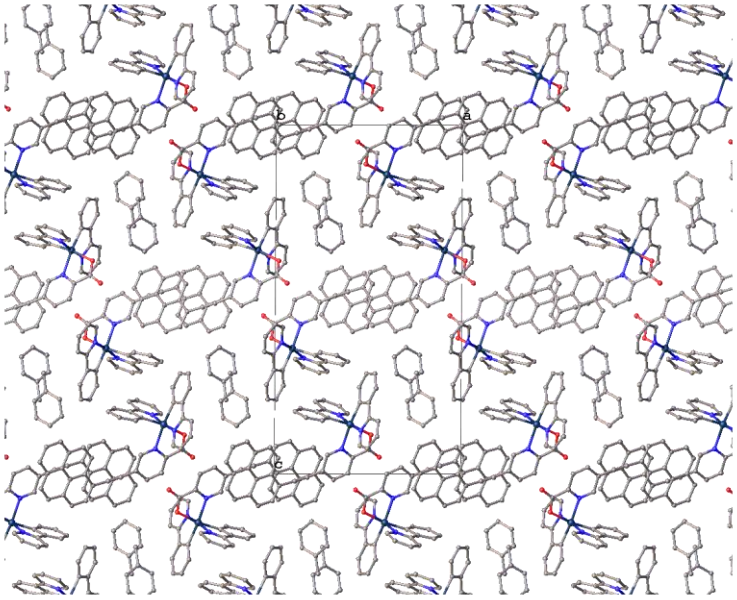

Figure 280. Schematic packing diagram of **PyrPicIr** viewed normal to the b-axis with hydrogen atoms omitted.

The spectator phenylpyridine ligands do appear to engage in a stacking behaviour with neighbouring molecules similar to that of the pyrenes, but over much longer atomic distances.

In summary, these crystal structures show large differences based on the ability of the picolinate groups to form intermolecular hydrogen bonds. For **PhPicL**, the lack of a methoxy protecting group leads to both oxygen and the nitrogen atoms of the system becoming heavily involved in hydrogen bonding, resulting in a very ordered repeating lattice based around water molecules as bridging units between picolinate molecules. For **NPhPicL**, the presence of the methyl protecting group reduces the overall ability of the molecule to form hydrogen bonds, although some intermolecular interactions are still visible.

For both complexes, hydrogen bonds no longer play any role in the formation of the crystal lattice. Instead, it is the rings of the picolinate ligands which dominate the intermolecular interactions, with face-to-face stacking being readily apparent in both **PhPicIr** and **PyrPicIr**.

Additionally, the bond lengths between the picolinate ligand and the iridium centre are greater in **PhPicIr** than in **PyrPicIr**, suggesting weaker metal-ligand bond strength in the latter. This could influence the photophysical properties, as electronic communication between the ligand and the metal govern the excited state properties of transition metal complexes.

5.4 Photophysical Analysis

5.4.1 Spectroscopic Analysis of PhPicL, NPhPicL and PyrPicL

5.4.1.1 Solvatochromic Absorption and Emission

The photophysical properties of the three picolinate ligands were evaluated in a wide range of solvents. The absorption and emission properties of **PhPicL** are shown in **Figure 281.**

The absorption is very low intensity compared to the other ligands investigated in this work, such as **PhL**. The relatively smaller size of **PhPicL** reduces the total number of transitions available to each molecule, with the picolinate ligand comprised of merely half the total number of conjugated rings of its bipyridyl cousin. The methyl ester functional group is not expected to contribute significantly to the absorption. The absorption bands are at short wavelengths, indicating the presence of high energy $\pi - \pi^*$ and $n - \pi^*$ transitions. In as simple a molecule as **PhPicL**, no charge-transfer processes are expected due to the lack of significant donor moieties such as OMe or NPh_2. Neither the intensity of the absorption nor its wavelengths change in different solvents, suggesting that the ground state is not sensitive to them.

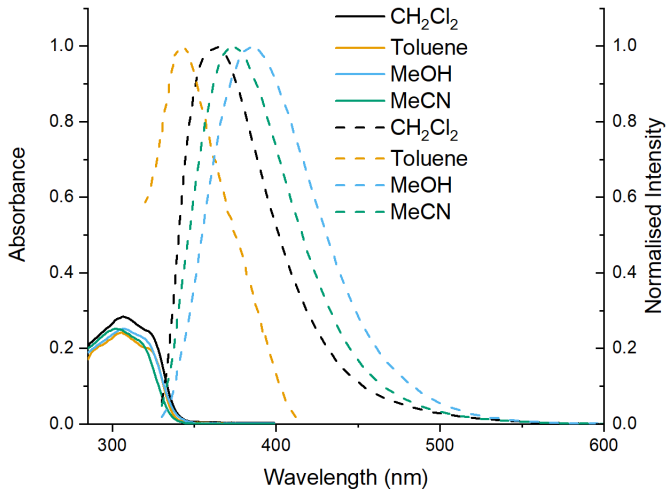

Figure 281. Absorption and normalised emission spectra of **PhPicL**; UV-vis spectra shown with solid lines and emission spectra shown with dotted lines (λ_{ex} = 310 nm), [10^{-5} M], 298 K.

The emission spectrum is broad and featureless, indicating solvatochromic behaviour with emission in more polar solvents at lower energies. This is indicative of at least a partial charge-transfer excited state, with emission in toluene peaking at 345 nm while emission in MeOH peaks at 385 nm. Due to the low Stokes shift in toluene, the excitation wavelength was decreased in order to capture the peak of the emission band.

The same studies were performed on **NPhPicL**, with the results shown below in **Figure 282**. **NPhPicL** displays higher levels of absorbance in the UV region than **PhPicL**, likely due to the increased number of phenyl rings present in the structure. Additionally, a new absorption band at 380 nm has emerged, representing the charge-transfer (CT) transition from the triphenylamine donor into the picolinate acceptor.

The absorption wavelength is similar to that observed in **NPhL**, suggesting high degrees of pyridine ring involvement in both transitions. Neither the absorption wavelength nor the absorbance change significantly depending on solvent, indicating that the ground state is not sensitive to the local electronic environment.

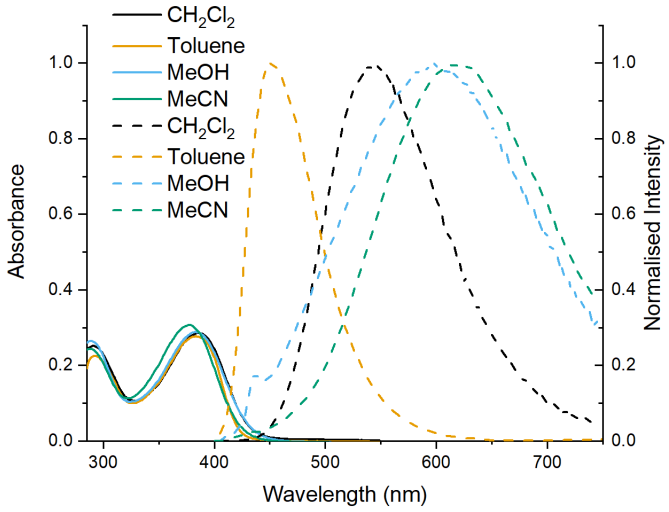

Figure 282. Absorption and normalised emission spectra of **NPhPicL**; UV-vis spectra shown with solid lines and emission spectra shown with dotted lines (λ_{ex} = 310 nm), [10^{-5} M], 298 K.

The emission is broad and featureless, displaying considerably stronger solvatochromic behaviour than **PhPicL**. This suggests a greater dipole in the excited state, which can be more readily stabilised by polar solvents. In toluene, the emission peaks at 450 nm while in MeCN it peaks at 620 nm.

The photophysics of **DeprotPic** were also investigated, with the results displayed in **Figure 283.** It has the same number of absorption bands as **NPhPicL**, but the one at lower energies exhibits a much higher degree of sensitivity to solvent. The carboxylic acid is substantially more sensitive to the local electronic environment than the methyl ester, as was suggested in the crystallographic analysis of **PhPicL** and **NPhPicL**. This sensitivity leads the charge-transfer transition of **DeprotPic** to occur at varying energies depending on the solvent, ranging from 365 in MeOH to 395 in CH_2Cl_2 and toluene. In this specific scenario, the polarity of the solvents may not play the most pivotal role, but instead the ability to form hydrogen bonds. MeOH shows a greater ability to participate in this type of interaction than toluene and CH_2Cl_2, increasing the energy gap of the charge-transfer.

The emission is broad and featureless, with strong sensitivity to solvent suggesting a CT excited state. Interestingly, the emission of **DeprotPic** in MeOH occurs at higher energies than in CH_2Cl_2, (525 nm vs 575 nm).

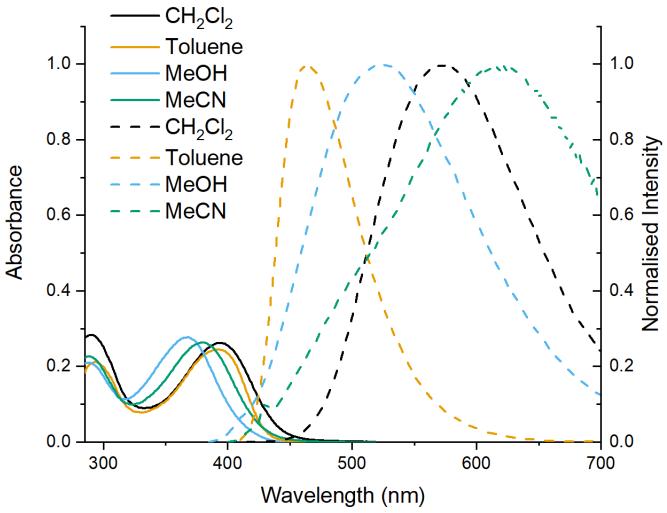

Figure 283. Absorption and normalised emission spectra of **DeprotPic**; UV-vis spectra shown with solid lines and emission spectra shown with dotted lines (λ_{ex} = 310 nm), [10^{-5} M], 298 K.

The solvent behaviour of **DeprotPic** indicates that it is strongly interacting with the solvent, beyond the expected solvatochromic stabilisation. MeOH in particular greatly affects the spectroscopic properties of **DeprotPic**, while **NPhPicL** exhibits no such change. This suggests that the observed differences arise from the loss of the methyl protecting group, as this is the only structural difference between the two compounds.

The final solvatochromic absorption and emission experiments performed on **PyrPicL** are displayed in **Figure 284**. They show the same high energy, low absorbance peaks in the UV region as the other picolinate ligands, originating from π – π* and n – π* transitions in the pyridine and pyrene moieties respectively, with some small contribution from the carbonyl. At lower energies, the same absorption patterns as in **PyrIr** are observed, with a set of absorption bands exhibiting hyperfine splitting originating from π – π* transitions in the pyrene chromophore. The absorption is not sensitive to solvent.

The emission spectra change significantly depending on solvent. In toluene, an emission peak around 425 nm manifests a distinct shoulder at 445 nm and is very narrow, suggesting π* - π emission. In CH_2Cl_2, MeOH and MeCN the absorption is shifted to lower energies, with the band becoming broad and featureless, indicative of CT excited states.

This demonstrates that similarly to some other picolinate systems found in literature, the π – π* and charge-transfer excited states are very close in energy.[73,153] In more polar solvents, the charge-transfer excited state is stabilised and drops to lower energies than the π* - π excited states. In less polar solvents, the π* - π excited state is lower in energy, leading to emission from it as opposed to the CT observed in more polar solvents.

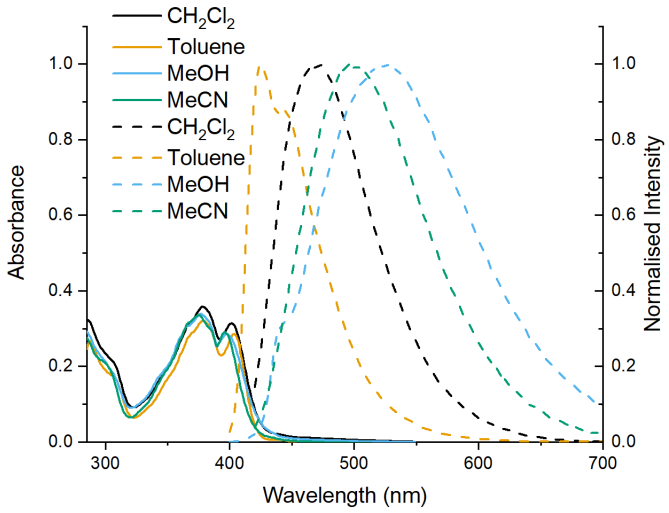

Figure 284. Absorption and normalised emission spectra of **PyrPicL**; UV-vis spectra shown with solid lines and emission spectra shown with dotted lines (λ_{ex} = 310 nm), [10^{-5} M], 298 K.

The molar extinction coefficients at the greatest absorption wavelength for all picolinate ligands are reported in **Table 19**

Table 19. Molar extinction coefficients for **PhPicL**, **PyrPicL**, **NPhPicL** and **DeprotPic** (CH_2Cl_2, 10^{-5} M, 298 K).

Compound	Wavelength (nm)	ε (L mol^{-1} cm^{-1})
PhPicL	320	24700
PyrPicL	400	31400
NPhPicL	390	28400
DeprotPic	395	26200

5.4.1.2 Excitation Studies of **PhPicL**, **NPhPicL**, **DeprotPic** and **PyrPicL**

Excitation studies were performed on the four organic compounds to determine the observed emission originated from the recorded absorption bands. They confirm that the observed photophysical properties stem from the synthesised target compounds, not from any remaining impurities. The four excitation spectra are exhibited in **Figure 285.**

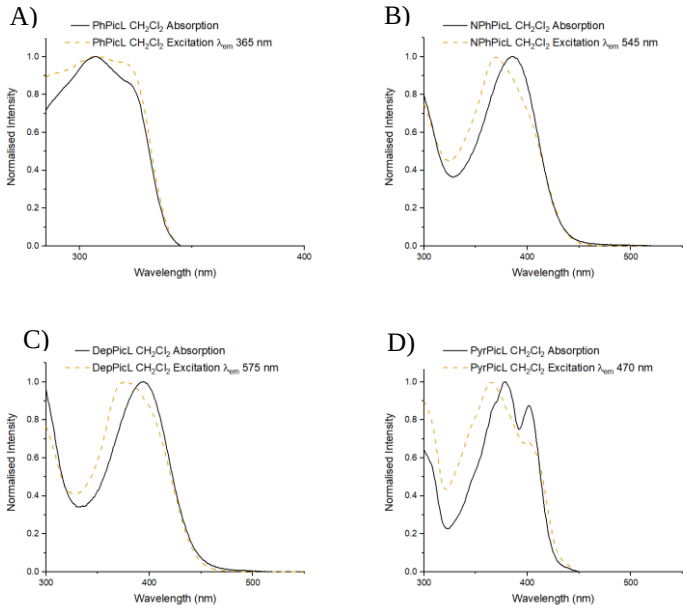

Figure 285. Normalised excitation studies in CH_2Cl_2 (dashed lines), compared to normalised absorption profiles in CH_2Cl_2 (solid lines) of **PhPicL** (A), **NPhPicL** (B) **DeprotPic** (C) and **PyrPicL (D)** [10-5 M], 298 K.

The excitation studies show all recorded emission originating from the absorption of the four complexes.

5.4.1.3 Low Temperature Emission Studies of PhPicL, NPhPicL, DeprotPic and PyrPicL

Low temperature emission studies of the four compounds were performed at 77 K in a 4:1 Ethanol : Methanol solution. The low temperature spectra can then be compared to the emission spectra obtained at room temperature. Shifts to higher energies at low temperatures are indicative of charge-transfer excited states, as the excited state is no longer able to be stabilised by solvent rearrangement when frozen in a glass matrix. The emission studies are shown in **Figure 286**.

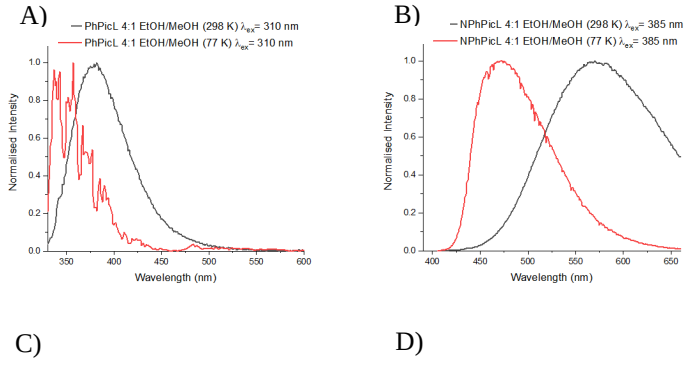

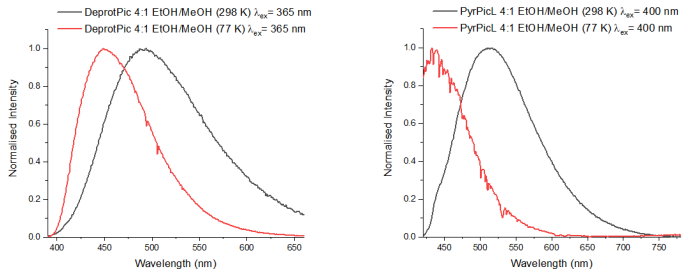

Figure 286. Low temperature emission studies of **PhPicL** (A), N**PhPicL** (B) **DeprotPic** (C) and **PyrPicL (D)**. Recorded in a MeOH/EtOH 4:1 solution at 298 K (black line) and in a frozen glass at 77 K (red line). [10^{-5} M].

For **PhPicL** (A), the low temperature emission spectrum shows a high number of emission bands with significant hyperfine splitting, with a modest shift to higher energies. This suggests that the excited state has shared charge transfer and π^* - π character, with the hyperfine splitting blending into the broad band observed at higher temperatures.

For **NPhPicL** (B) the low temperature spectrum exhibits a shift to shorter wavelengths of 100 nm compared to room temperature emission, confirming a largely charge-transfer excited state.

For **DeprotPic** (C), the shift is only 50 nm, indicating that the excited state is less stabilised by solvent interactions than **NPhPicL**. The interactions of **DeprotPic** with MeOH observed in section 5.4.1.1 could play a role in this, as the emission in MeOH was already at higher energies at room temperature compared to the emission of **NPhPicL** in the same solvent.

The emission of **DeprotPicL** and **NPhPicL** at low temperatures differed by 20 nm, with **DeprotPicL** emitting at 450 nm and **NPhPicL** at 470 nm. This compares to a difference of 80 nm at room temperature.

For **PyrPicL** (D) the low temperature emission is shifted to higher energies than the emission at room temperature, but no hyperfine splitting can be observed. Consequently, the excited state is largely charge-transfer in nature.

5.4.1.4 Emission Lifetime and Quantum Yields of Fluorescence of PhPicL, NPhPicL, DeprotPic and PyrPicL

The emission lifetime and quantum yields of fluorescence were obtained for the four prepared compounds and are shown in **Table 20**. The emission lifetime for **PhPicL** could not be recorded as it was not sufficiently emissive. The emission lifetime for the other three compounds was recorded between 2 and 4 ns, confirming the singlet character of the excited state.

The quantum yield of emission varied widely over the series of prepared compounds. For **PhPicL**, it was calculated at 1.57 % using the single-point method with fluorescein as a reference.[108]

For **NPhPicL**, it was recorded at 91.86 %, reaffirming the high photon-harvesting efficiency the triphenylamine moiety is known to possess.[60]

For **DeprotPic**, the quantum yield drops to 56.18 %, suggesting that the increase in solvent interactions observed during previous spectroscopic investigations is lowering the efficiency of the compound compared

to **NPhPicL**. This is an example of how small structural changes can have significant impact on the efficiency of optical processes.

Finally, **PyrPicL** possesses a quantum yield of fluorescence of 95.13 %, the highest in the series. The strong emission of the ligand makes it a promising candidate for complexation to a metal centre, assuming the same efficiency can be maintained when transitioning from a singlet to a triplet excited state.

Table 20. (a) Emission lifetime of **PhPicL**, **NPhPicL**, **DeprotPic** and **PyrPicL** in CH_2Cl_2, [10^{-5}M], 298 K (b) Fluorescence quantum yield with Fluorescein as a standard (Φ_f = 79 % in 0.1 M aq. NaOH).[108]

Compound	Lifetime (ns)[a]	Quantum Yield of Fluorescence (%) [b]
PhPicL	-	1.57
NPhPicL	3.63	91.86
DeprotPic	2.77	56.18
PyrPicL	2.03	95.13

In summary, the picolinate ligands display interesting spectroscopic properties, with small structural differences having significant effect on the solvent interactions, quantum yields of fluorescence and nature of the excited states of the prepared compounds.

Subsequent investigations into the spectroscopic properties of the iridium complexes will shed more light on the behaviour of this underexplored class of material.

5.4.2 Spectroscopic Analysis of PhPicIr, NPhPicIr and PyrPicIr

5.4.2.1 Solvatochromic Absorption and Emission of **PhPicIr**, **NPhPicIr** and **PyrPicIr**

Similarly, to the fully organic systems, the photophysical properties of the iridium complexes were analysed, starting with their absorption and emission in different solvents.

The absorption and emission spectra of **PhPicIr** in a range of solvents are shown below in **Figure 287**, and closely mirrors the properties of the ligand. The absorbance values overall are lower compared to those of previously prepared iridium complexes, potentially due to the smaller size of the photoactive ligand under investigation.

The absorption intensities are greatest at higher energies, from 285 to 330 nm, composed of a mixture of π – π^* and n – π^* transitions in the various ligands forming the complex. At lower energies, the intensities of the absorption bands drop significantly, slowly tailing out to 500 nm. These are likely composed of a series of MLCT transitions, as there are different ligands which would have separate MLCT transition energies. At the

lowest absorption wavelengths, between 450 and 500 nm, ^{3}MLCT transitions occur due to the high spin-orbit coupling coefficient of iridium.[43]

Since the solvent has no effect on the shape or intensity of the absorption spectra, the ground state is not sensitive to the local electronic environment.

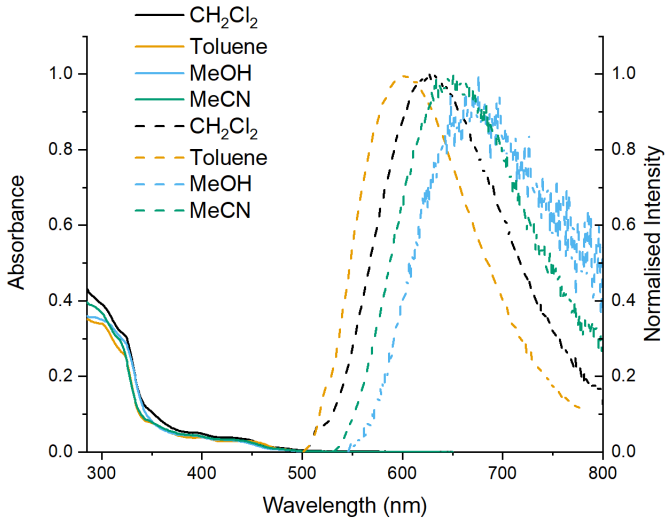

Figure 287 Absorption and normalised emission spectra of **PhPicIr**; UV-vis spectra shown with solid lines and emission spectra shown with dotted lines (λ_{ex} = 450 nm), [10^{-5} M], 298 K.

The emission bands in all solvents are broad and featureless, with the emission wavelength decreasing with increasing solvent polarity. These two findings combined suggest a charge-transfer based excited states. The intensity of the emission decreases with solvent polarity, indicated by the increase in the signal-to-noise ratio. In MeOH and MeCN the emission is functionally quenched. A large Stokes shift between the absorption and emission wavelengths suggests that the emissive excited state is triplet, although degassing and emission lifetime experiments will be necessary to confirm this.

The absorption and emission spectra of **NPhPicIr** are shown below in **Figure 288**. The spectra differ significantly from those of **PhPicIr**. The absorption displays the same CT band at 400 nm as **DeprotPic** and **NPhPicL** did, with higher energies transitions arising due to a mixture of $\pi - \pi^*$ and $n - \pi^*$ transitions. The absorption wavelengths and intensities of the CT band vary slightly depending on the solvent, suggesting a moderate influence of the local electronic environment on the ground state energy levels. The ^{3}MLCT absorption can be seen as a very weak shoulder absorbing up to 500 nm.

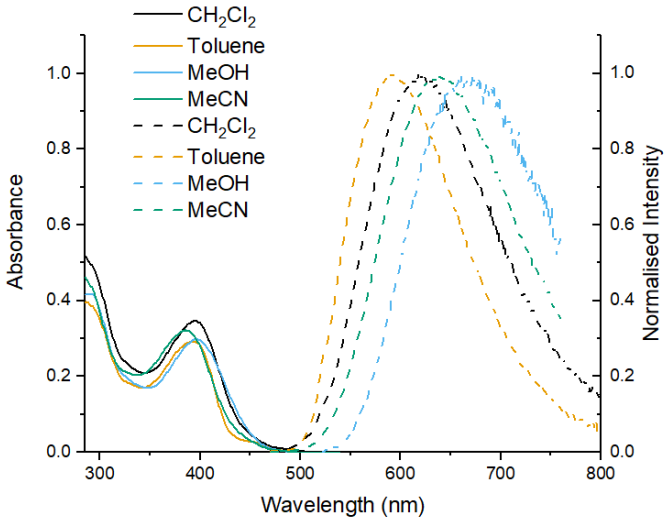

Figure 288. Absorption and normalised emission spectra of **NPhPicIr**; UV-vis spectra shown with solid lines and emission spectra shown with dotted lines (λ_{ex} = 450 nm), [10^{-5} M], 298 K.

The emission wavelength of the complex shifts to longer wavelengths in higher polarity solvents, indicating a charge-transfer excited state. The emission in Toluene is 590 nm and 675 nm in MeOH.

The absorption spectrum of **PyrPicIr** in a range of solvents is shown in **Figure 289**. The absorption spectra are very similar to those of the **PyrPicL** ligand, with the pyrene π – π* transitions dominating at lower energies while the phenyl and pyridyl π - π * and n – π* transitions occur at higher energies. The ^{3}MLCT absorption can be seen as a long tale absorbing to 500 nm.

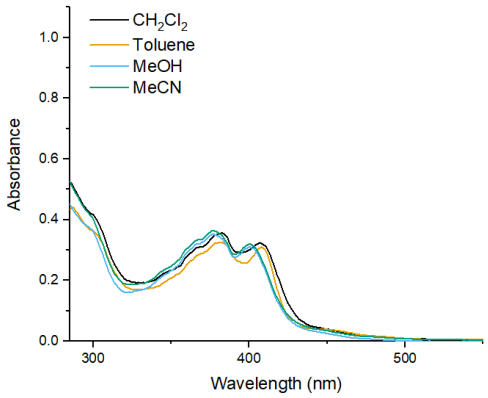

Figure 289. Absorption spectrum of **PhPicIr** in a range of solvents; (λ_{ex} = 450 nm), [10^{-5} M], 298 K.

No emission for **PyrPicIr** was found at room temperature in air, regardless of excitation wavelength.

The molar absorption coefficients for all complexes in MeCN are reported below in **Table 21**.

Table 21. Molar extinction coefficients for **PhPicIr**, **PyrPicIr** and **NPhPicIr** (MeCN, 10^{-5} M, 298 K)

Compound	Wavelength (nm)	ε (L mol^{-1} cm^{-1})
PhPicIr	400	4860
PyrPicIr	405	32200
NPhPicIr	380	32000

The low absorption of **PhPicIr** is due to the lack of chromophores absorbing at long wavelengths.

5.4.2.2 Excitation Studies of **PhPicIr**, **NPhPicIr** and **PyrPicIr**

Excitation studies of **PhPicIr** and **PyrPicIr** are displayed below in **Figure 290.**

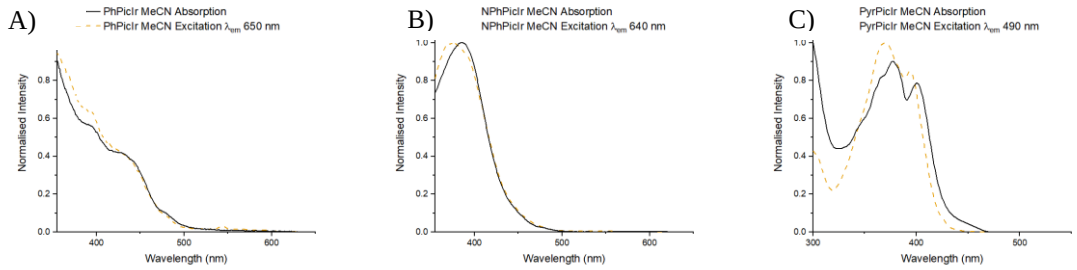

Figure 290. Normalised excitation studies in MeCN (dashed lines), compared to normalised absorption profiles in MeCN (solid lines) of **PhPicIr** (A), **NPhPicIr** (B) **PyrPicIr** (C), obtained under an argon atmosphere) [10-5 M], 298 K.

The excitation spectra for **PhPicIr** and **NPhPicIr** manifest as expected, with all absorption processes contributing to the observed emission. In the case of **PyrPicIr**, the results are slightly more complex – since the emission wavelength is the same as in ^{3}MLCT absorption, the contribution of that absorption process is reduced relative to the rest of the transitions in the complex. This suggests the emissive state has low ^{3}MLCT character.

5.4.2.3 Degassing Studies of **PhPicIr**, **NPhPicIr** and **PyrPicIr**

Degassing studies were performed on the three complexes to determine whether they have the ability to sensitise molecular oxygen to singlet oxygen. The results of these studies are displayed in **Figure 291**. All three of the prepared complexes show an oxygen response, indicating a triplet excited state. However, the ability of **PhPicIr** and **NPhPicIr** to sensitise singlet oxygen is poor, as neither of the spectra exhibit a greater than 20% increase in emission in argon compared to air.

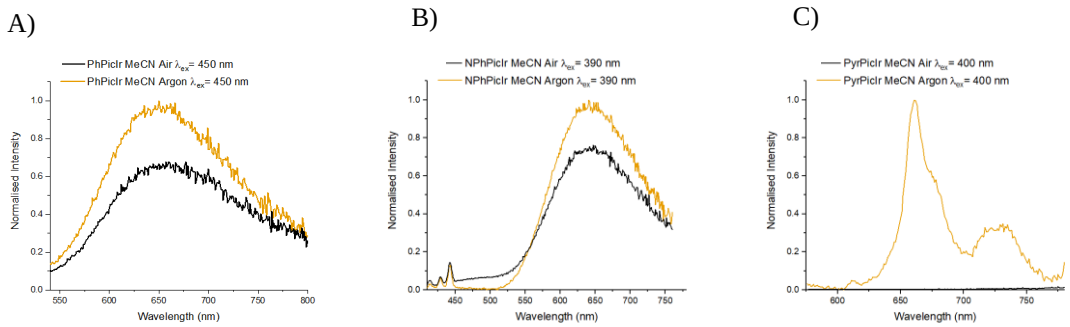

Figure 291. Emission spectra of **PhPicIr** (A), **NPhPicIr** (B) and **PyrPicIr** (C) in MeCN under either air (black line) or argon (yellow line) atmospheres [10-5 M], 298 K.

PyrPicIr does show an emission under an argon atmosphere, with a fine-structured emission band reminiscent of **PyrIr** and indicative of a ^{3}IL excited state. The high signal-to-noise ratio of the complexes again reinforces the low emission intensity.

5.4.2.5 Low Temperature Emission Studies of **PhPicIr**, **NPhPicIr** and **PyrPicIr**

Low temperature emission studies of the three iridium complexes were performed in a 4:1 Ethanol : Methanol glass and compared to the room temperature emission spectra in the same solvent. No room-temperature emission spectrum could be recorded for **PhPicIr** due low levels of emission.

The low temperature emission spectrum for **NPhPicIr** (B) shows the same behaviour observed in other iridium complexes in this thesis. The emission at 77 K is shifted to higher energies and manifests a greater number of peaks, suggesting the presence of several different excited states with very similar energies.

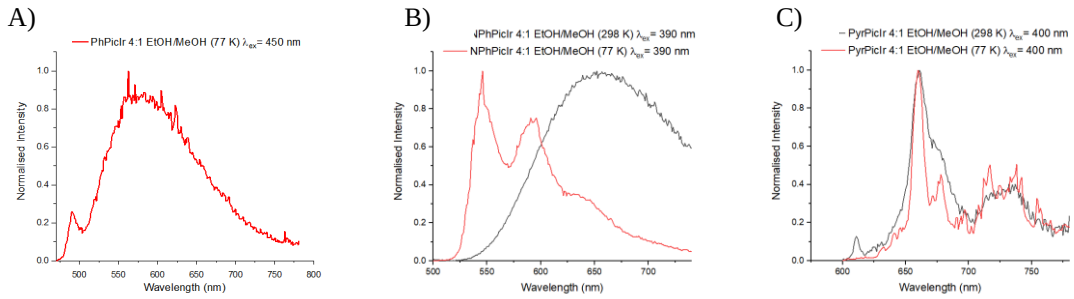

Figure 292. Low temperature emission studies of **PhPicIr** (A), **NPhPicIr** (B) and **PyrPicL** (C). Recorded in a MeOH/EtOH 4:1 solution at 298 K (black line) and in a frozen glass at 77 K (red line). [10^{-5} M].

The low temperature spectra for **PyrPicIr** (C) match the room temperature spectra closely, aside from showing a larger degree of fine structure. This represents the characteristic peaks of the pyrene ^{3}IL excited state, with low sensitivity to solvent or temperature as there is no charge-transfer dipole formed.

5.4.2.6 Emission Lifetime and Quantum Yields of Emission for PhPicIr, NPhPicIr and PyrPicIr

The quantum yields of emission in MeCN and the emission lifetime in MeCN and toluene were recorded for the three complexes and are reported in **Table 22**. There are several observations worth discussing. The emission lifetime for **PhPicIr** is remarkably short, in the range of 10 ns. While not unheard of for picolinate

iridium complexes, this lifetime differs significantly from that of compounds **NPhPicIr** and **PyrPicIr**.[73,152] These results indicate that modifications of the picolinate ligand can significantly extend emission lifetime.

Table 22. [(a)] Emission lifetime of **PhPicIr**, **NPhPicIr**, and **PyrPicIr** in MeCN, [10^{-5}M], 298 K [(b)] Phosphorescence quantum yield with $[Ru(bpy)_3Cl_2]$ as a standard (Φ_f = 9.7 % in MeCN).[40]

Compound	Lifetime (ns)[a] MeCN	Quantum Yield of Emission (%) [b]
PhPicIr	10.90	0.64
NPhPicIr	771.27	0.54
PyrPicIr	1336.3	0.1104

The quantum yields of emission for all three complexes are below 1 % in MeCN. This suggests the presence of nonradiative decay processes in every complex.

5.4.2.7 Spectroscopic Analysis of NPhPicIr Film

A crystallisation attempt of **NPhPicIr** involving the slow evaporation of cyclohexane resulted in the growth of a film along the sides of a sample tube, shown in **Figure 293**.

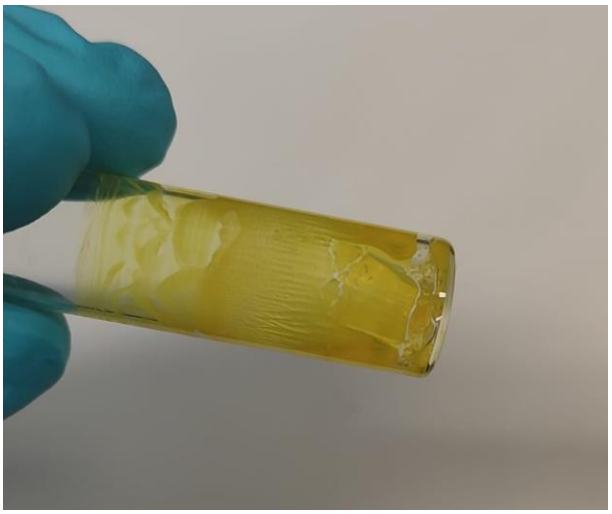

Figure 293. NPhPicIr film grown from the slow evaporation of cyclohexane.

Using handheld UV lamps, it was discovered that the solid-state film exhibited emissive properties. As the sample tube fit into both the UV-Vis spectrophotometer and the fluorimeter it was decided to perform a brief qualitative analysis of these properties.

The normalised absorption and emission properties of the film are reported below in **Figure 294**. The absorption spectrum shows significant error because the sample tube is made of glass and not of quartz, but the broad CT absorption band at 400 nm observed in solution can be readily identified in the solid state.

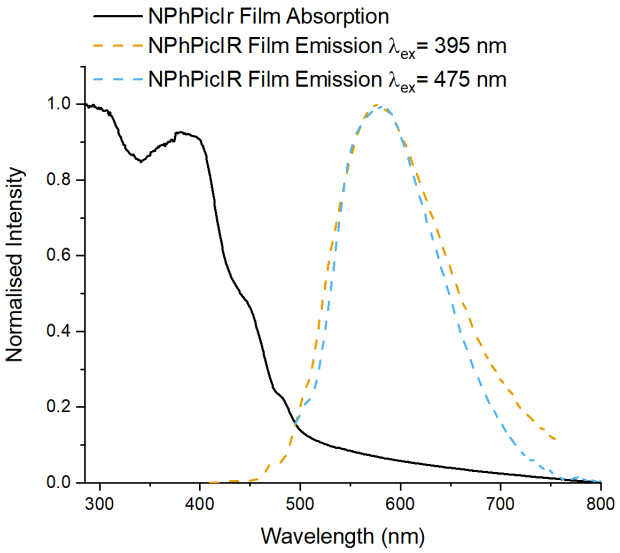

Figure 294. Normalised absorption and emission spectra of the **NPhPicIr** film; UV-vis spectra shown with solid line and emission spectra shown with dotted lines.

There are shoulders in the absorption spectrum at 430 and 480 nm, potentially indicating that the ^{3}MLCT absorption occurs at greater intensities in solid state than in solution.

The emission peaks at 590 nm regardless of excitation wavelength, as well as excitation and degassing studies for the **NPhPicIr** film are exhibited in **Figure 295**. A generally good agreement with the peak positions of the absorption is apparent, but the relative intensities are very different. The shoulder peaks at 430 and 480 nm contribute significantly more to the emission than the peak at 380 nm.

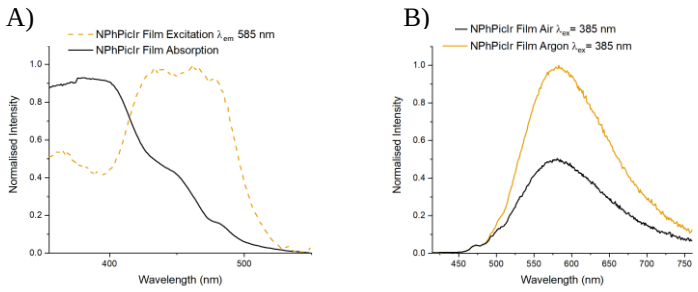

Figure 295. (A) Normalised excitation studies (dashed lines), compared to normalised absorption profiles (solid lines) of the **NPhPicIr** film, 298 K (B) Emission spectra of **NPhPicIr** film under either air (black line) or argon (yellow line) atmospheres [10-5 M], 298 K.

The degassing studies were performed by blowing argon into the sample tube and then sealing it from air. The results indicate a significant increase in emission intensity, confirming the triplet nature of the emissive excited state.

5.4.2.8 Summary of Photophysical Properties

There are numerous examples in the literature demonstrating small changes in the structure of picolinate complexes have significant impacts on the nature of the emission and the excited state, notably swapping

from ^{3}LC to ^{3}MLCT states.[73,152,153] This was not observed in the complexes investigated in the course of this work. Instead, all complexes exhibited behaviour commonly associated with charge-transfer excited states, including solvatochromic emission and higher energy emission at low temperatures. The potential of these complexes as OLED emitters is weak, as they all show very low quantum yields of luminescence. However, the work proves that modifications to the picolinate ligand can result in significant changes in the excited state properties of the resulting iridium complexes, informing future studies in this field.

5.5 Future Work

In view of the fact that that off-complex synthetic protocols for the synthesis of substituted picolinate ligands have now been established, future work can incorporate alternative light-harvesting chromophores such as Nile red (**Figure 296**).

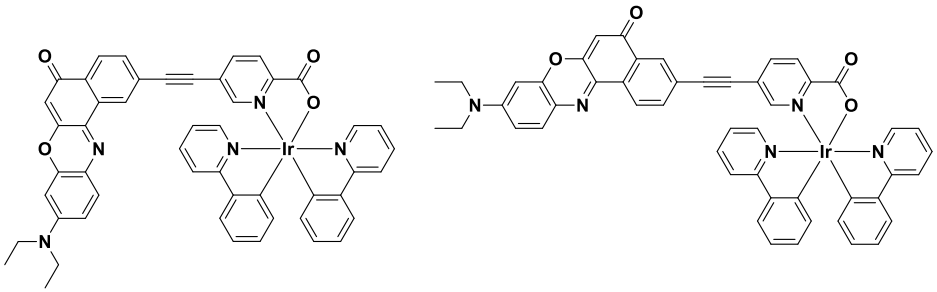

Figure 296. Nile-red containing picolinate iridium complexes.

Nile-red containing transition metal complexes have recently been found to possess interesting photophysical properties, including a non-emissive 'dark state' which sensitises molecular oxygen with high efficiency.[40]

Attempts to synthesise the ruthenium picolinate complexes should be expanded upon, in order to investigate the effects of changing the metal centre on the picolinate energy levels. Additionally, the residual charge on the ruthenium complexes would allow them to cross cell membranes more easily than the neutral iridium picolinates, widening the scope of potential applications to include photodynamic therapy.

Finally, the highly asymmetric nature of picolinate ligands would conceivably facilitate the straightforward generation of bimetallic species bearing 'bridging' chromophores, as shown in **Figure 297**.

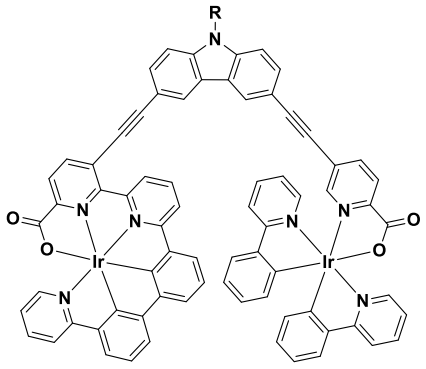

Figure 297. Bimetallic iridium picolinate complex.

Considering that the number of substituted picolinate complexes reported in literature is lower than the number of polypyridyl complexes, significant scope for expansion remains. Future investigations into the structure-property relationships governing the photophysical behaviour of picolinate complexes will undoubtedly lead to the discovery of new potential applications.

6 Experimental Section

6.01 Technical Information

General Experimental Methods

All reactions were performed under an argon or nitrogen atmosphere, unless otherwise stated. Flash chromatography was performed using silica gel (Fluka 60) particle size 0.04-0.063 mm as the stationary phase, with all runs carried out in air. All chemicals and solvents were purchased from Sigma-Aldrich or Fluorochem and used without further purification.

A CEM Discover 300 W multimode reactor was used to carry out microwave reactions using specialised 'snap-cap' vials.

^{1}H NMR, ^{13}C{^{1}H} NMR, ^{31}P NMR, and ^{19}F NMR spectra were recorded using a Bruker Advance DPX-400 MHz, Bruker AV-400 MHz, or Bruker AV-600 MHz spectrometer in $CDCl_3$ or CD_3CN with tetramethylsilane as the internal standard. Electrospray ionization (ESI) mass spectra were recorded on a micromass LCT electrospray mass spectrometer, or a Bruker MicrOTOF-Q-III mass spectrometer. Atmospheric Pressure Chemical Ionization (APCI) mass spectra were recorded on a Bruker MicrOTOF-Q-III mass spectrometer. Accurate MS were referenced against leucine enkephalin (555.6 g mol-1) or [Glu1]-Fibrinopeptide B (1570.6 g mol-1) and were reported within 5 ppm. MALDI-TOF mass spectra were recorded on a Waters MALDI-QTOF Premier spectrometer using an α-cyano-4-hydroxy cinnamic acid matrix.

X-ray Crystallography

all crystallography experiments were carried out by Dr. Brendan Twamley in Trinity College with a Bruker SMART APEX CCD diffractometer and a Rigaku Saturn-724 diffractometer using graphite-monochromated Mo-Kα radiation (λ = 0.71073 Å) source. Data were corrected for absorption effects using the Multi-Scan method (SADABS). Using the OLEX2 Software Package, the structure was solved with the SHELXT structure solution program using Intrinsic Phasing and refined with the SHELXL refinement package with Least Squares minimisation,

Photophysical Analysis

UV-vis absorption spectra were recorded on a Shimadzu UV-2450 spectrophotometer. Emission and excitation spectra, emission quantum yields, and low temperature emission spectra were recorded on a Horiba FluoroMax-4 spectrofluorometer.

Emission quantum yields of solutions were measured using the single-point relative method, using Fluorescein in 0.1 M aq. NaOH (for organic ligands, unless stated otherwise) or $[Ru(bpy)_3](PF_6)$ in MeCN (for ruthenium and iridium complexes) as the reference, at 298 K. $[Ru(bpy)_3](PF_6)_2$ was purchased from TCI Europe n.v. and used without purification. Fluorescein was purchased from Fluka and used without purification. Emission lifetime measurements were performed on a Horiba-Jobin-Yvon FluoroLog FL-3-11 spectrofluorometer with a TBX-04-D picosecond photodetection module using a NanoLED pulsed diode laser excitation sources (λ_{ex} = 320, 370 or 460 nm depending on absorption wavelength).

6.1 Chapter 1

PhL

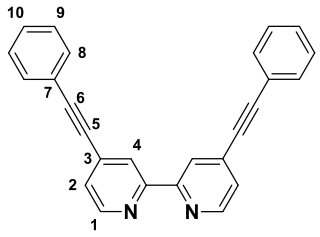

4,4'-dibromo-2,2'-bipyridine (0.1 g, 0.3 mmol, 1 eq.) and phenylacetylene (2 mL, 18.21 mmol, 50.9 eq.) were added to a specialised 'snap cap' vial together with $Pd(PPh_3)_4$ (50 mg, 0.04 mmol) and triethylamine (4 mL). Argon was bubbled through the solution before the vial was sealed and heated to 130 °C for 3 hours at 150 W in a CEM Discover S-Class Single Mode Microwave reactor. The volatiles were removed using a rotary evaporator and the crude solid dissolved in CH_2Cl_2 before being washed with 3 x 50 mL H_2O and subsequently dried over Mg_2SO_4. The solution was concentrated and the sample purified using silica column chromatography (99.95:0.05 $CHCl_3$:MeOH → 99.5:0.5 $CHCl_3$:MeOH) to give PhL as a white solid.

^{1}H NMR (400 MHz, $CDCl_3$) δ 8.69 (s, 2H, **1**), 8.56 (s, 2H **4**), 7.58 (m, 4H, **8/9**), 7.43 (d, ^3J = 4.2 Hz, 2H, **2**), 7.39 (m, 6H, **8/9 and 10**)

^{13}C NMR (101 MHz, $CDCl_3$) δ 155.18 (C_q), 149.01 (CH), 132.97 (C_q), 131.99 (CH), 129.26 (CH), 128.52 (CH), 125.70 (CH), 123.51 (CH), 122.17 (C_q), 94.53 (C_q), 86.91 (C_q)

HRMS (m/z APCI$^+$, CH_2Cl_2): [M+Na] ($C_{26}H_{16}N_2Na$) Calc. 379.1206, Found 379.1206

CF_3L

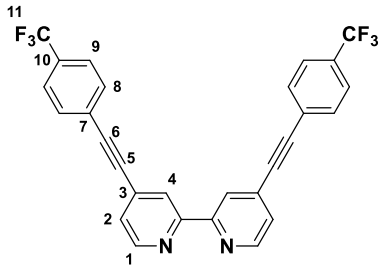

4,4'-dibromo-2,2'-bipyridine (0.1 g, 0.31 mmol, 1 eq.) and 4-ethynyltrifluorotoluene (0.15 mL, 8.8 mmol, 28.4 eq.) were added to an RBF and placed under inert atmosphere together with $Pd(PPh_3)_4$ (90 mg, 0.072 mmol). A solution of Toluene (3 mL) and triethylamine (3 mL) was degassed separately and added to the RBF via syringe. The reaction was heated to 80 °C for 16 hours. The volatiles were removed using a rotary evaporator and the crude solid dissolved in CH_2Cl_2 before being washed with 3 x 50 mL H_2O and subsequently dried over Mg_2SO_4. The solution was concentrated and the sample purified using silica column chromatography (99.95:0.05 $CHCl_3$:MeOH → 99.5:0.5 $CHCl_3$:MeOH) to give CF_3L as a white solid.

^{1}H NMR (400 MHz, $CDCl_3$) δ 8.71 (d, J = 5.0 Hz, 2H, **1**), 8.57 (s, 2H, **4**), 7.70 – 7.63 (m, 8H, **8/9**), 7.44 (dd, J = 5.0, 1.5 Hz, 2H, **3**)

^{13}C NMR (101 MHz, $CDCl_3$) δ 155.73 (C_q), 149.48 (CH), 132.32 (CH), 132.06 (C_q), 131.18 (C_q), 126.11 (C_q), 125.79 (CH), 125.60 (CH), 125.29 (C_q), 123.52 (CH), 92.51 (C_q), 89.12 (C_q)

^{19}F NMR (377 MHz, $CDCl_3$) δ -62.92.

HRMS (m/z APCI$^+$, CH_2Cl_2): [M+H] ($C_{28}H_{15}F_6N_2$) calc. 493.1134 Found 493.1122

OMeL

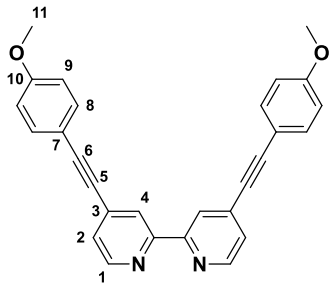

4,4'-dibromo-2,2'-bipyridine (0.1 g, 0.31 mmol, 1 eq.) and 4-ethynylanisole (0.2 mL, 15.1 mmol, 48.7 eq.) were added to a snap cap vial together with $Pd(PPh_3)_4$ (90 mg, 0.072 mmol) and a solution of toluene (3 mL) and trimethylamine (3 mL). Argon was bubbled through the solution before the vial was sealed and heated to 130 ^{o}C for 2 hours at 150 W in a CEM Discover S-Class Single Mode Microwave reactor. The volatiles were removed using a rotary evaporator and the crude solid dissolved in CH_2Cl_2 before being washed with 3 x 50 mL H_2O and subsequently dried over Mg_2SO_4. The solution was concentrated and the sample purified using silica column chromatography ($CHCl_3$ → 99.5:0.5 $CHCl_3$:MeOH) to give OMeL as a pale yellow solid.

^{1}H NMR (400 MHz, $CDCl_3$) δ 8.67 (s, 2H, **1**), 8.52 (s, 2H, **4**), 7.55 – 7.49 (m, 4H, **8/9**), 7.40 (d, *J* = 4.5 Hz, 2H, **2**), 6.93 – 6.88 (m, 4H, **8/9**), 3.85 (s, 6H, **11**).

^{13}C NMR (101 MHz, $CDCl_3$) δ 160.53, 149.16 (CH), 133.72 (CH), 125.57 (CH), 123.39 (CH), 114.34 (CH), 94.86, 86.13, 55.51 (CH).

HRMS (m/z APCI$^+$, CH_2Cl_2): [M+H] $C_{28}H_{21}N_2O_2$ calc. 417.1598 Found 417.1600

PhRu

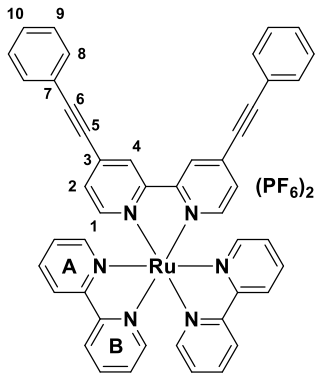

[Ru(2,2'-bipyridine)$_2$Cl$_2$] (0.02 g, 0.04 mmol) and 4,4'-bis(phenylethynyl)-2,2'-bipyridine (0.017 mg, 0.047 mmol) were combined in ethylene glycol (6 mL) in a specialised sealed snap-cap vial. The vial was placed in a CEM Discover S-Class Single Mode Microwave reactor and heated to 160 ^{o}C for 1 hour (150 W) under pressure. Upon cooling, the ethylene glycol solution was added to a saturated aqueous KPF_6 solution and the resulting precipitate washed with H_2O. The crude was purified by column chromatography (silica) using CH_3CN:H_2O:sat. KNO_3 (90:9:1). The first red fraction was collected, reduced and the product precipitated out of solution using saturated KPF_6 solution to give PhRu as a black solid.

^{1}H NMR (600 MHz, CD_3CN) δ 8.64 (d, *J* = 1.3 Hz, 2H **4**), 8.51 (s, 2H, **A**), 8.50 (s, 2H, **B**), 8.08 (m, 4H, **A/B**), 7.79 (d, *J* = 5.3 Hz, 2H, **A**), 7.72 (m, 4H, **1** and **B**), 7.65 – 7.63 (m, 4H, **8**), 7.54 – 7.39 (m, 12H, **A**, **B**, **2**, **9** and **10**).

^{13}C NMR (151 MHz, CD_3CN) δ 157.85 (C_q), 157.82 (C_q), 157.80 (C_q), 152.82 (CH), 152.69 (CH), 152.59 (CH), 139.00 (CH), 138.98 (CH), 133.38 (C_q), 132.98 (CH), 131.31 (CH), 129.95 (CH), 129.72 (CH), 128.63, (CH) 127.11 (CH), 125.28 (CH), 121.99 (C_q), 98.72 (C_q), 86.26 (C_q).

HRMS (m/z APCI$^+$, MeCN): [M – PF_6] ($C_{46}H_{32}N_6F_6PRu$) calc. 915.1374, Found 915.1390

<u>CF_3Ru</u>

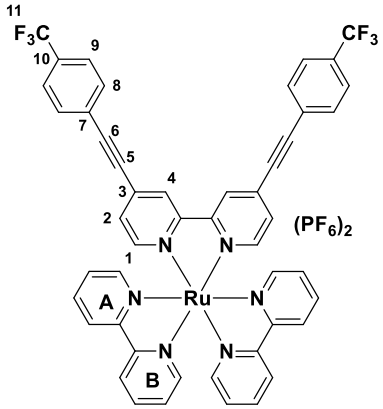

[Ru(2,2'-bipyridine)$_2$Cl$_2$] (0.077 g, 0.16 mmol) and 4,4'-bis((4-(trifluoromethyl)phenyl)ethynyl)-2,2'-bipyridine (0.05 mg, 0.101 mmol, 0.63 eq.) were combined in ethylene glycol (6 mL) in a specialised sealed snap-cap vial. The vial was placed in a CEM Discover S-Class Single Mode Microwave reactor and heated to 160 ^{o}C for 1 hour (150 W) under pressure. Upon cooling, the ethylene glycol solution was added to a saturated aqueous KPF_6 solution and the resulting precipitate washed with H_2O. The crude was purified by column chromatography (silica) using CH_3CN:H_2O:sat. KNO_3 (90:9:1). The first red fraction was collected, reduced and the product precipitated out of solution using saturated KPF_6 solution to give CF_3Ru as a red solid.

^{1}H NMR (600 MHz, CD_3CN) δ 8.68 (d, *J* = 1.4 Hz, 2H, **4**), 8.52 (s, 2H, **A**), 8.50 (s, 2H, **B**), 8.11 – 8.06 (m, 4H, **A** and **B**), 7.85 – 7.75 (m, 12H, **8, 9, A,** and **1**), 7.73 – 7.70 (m, 2H, **B**), 7.49 (dd, *J* = 5.9, 1.7 Hz, 2H, **2**), 7.42 (ddd, *J* = 8.2, 5.7, 1.2 Hz, 4H, **A** and **B**).

^{13}C NMR (151 MHz, CD_3CN) δ 157.91(C_q), 157.80 (C_q), 157.75 (C_q), 152.88 (CH), 152.83 (CH), 152.59 (CH), 139.08 (CH), 139.06 (CH), 133.58 (CH), 132.61 (C_q), 131.93 ($C_{q\text{-}F}$), 129.90 (CH), 128.66 (CH), 127.28 (CH), 126.76 (CH-F), 126.14 (C_q), 125.30 (CH), 118.26 (C_q), 96.59 (C_q), 88.13 (C_q).

HRMS (m/z APCI$^+$, MeCN): [M – PF_6] ($C_{48}H_{30}F_6N_6Ru$) calc. 453.0740, Found 453.074

OMeRu

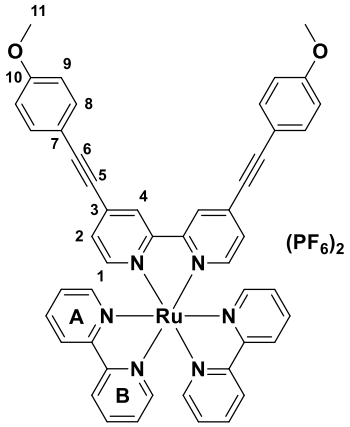

Ru(2,2'-bipyridine)$_2$Cl$_2$] (0.02 g, 0.04 mmol) and 4,4'-bis((4-methoxyphenyl)ethynyl)-2,2'-bipyridine) (0.017 mg, 0.04 mmol) were combined in ethylene glycol (6 mL) in a specialised sealed snap-cap vial. The vial was placed in a CEM Discover S-Class Single Mode Microwave reactor and heated to 160 ^{o}C for 1 hour (150 W) under pressure. Upon cooling, the ethylene glycol solution was added to a saturated aqueous KPF_6 solution and the resulting precipitate washed with H_2O. The crude was purified by column chromatography (silica) using CH_3CN:H_2O:sat. KNO_3 (90:9:1). The first red fraction was collected, reduced and the product precipitated out of solution using saturated KPF_6 solution to give OMeRu as a red solid.

^{1}H NMR (600 MHz, CD_3CN) δ 8.59 (d, *J* = 1.5 Hz, 2H, **4**), 8.51 (s, 2H, **A**), 8.49 (s, 2H, **B**), 8.11 – 8.04 (m, 4H, **A** and **B**), 7.81 – 7.77 (m, 2H, **A**), 7.72 – 7.70 (m, 2H, **B**), 7.68 (d, J = 6 Hz, 2H, **1**), 7.59 – 7.55 (m, 4H, **8**), 7.47 – 7.38 (m, 6H, **2**, **A** and **B**), 7.06 – 6.99 (m, 4H, **9**), 3.85 (s, 6H, **11**).

^{13}C NMR (151 MHz, CD_3CN) δ 162.36, 157.88, 157.82, 152.84 (CH), 152.64 (CH), 152.57 (CH), 138.99 (CH), 138.97 (CH), 134.87 (CH), 133.90, 129.44 (CH), 128.66 , 126.83 (CH), 125.30 (CH), 115.64 (CH), 113.85 , 99.58, 85.59, 56.30 (CH).

HRMS (m/z APCI$^+$, MeCN): [(M – $(PF_6)_2$)/2] ($C_{48}H_{36}N_6O_2Ru$) calc. 415.0973 Found 415.0975

PhIr

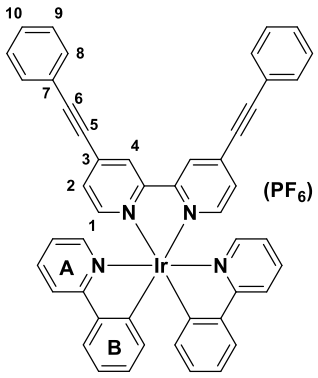

$[Ir(ppy)_2Cl_2]_2$ (0.020g, 0.018mmol) and 4,4'-bis(phenylethynyl)-2,2'-bipyridine (0.014 g, 0.04 mmol) were added to $CHCl_3$ (4mL). The solution was refluxed overnight. Once cooled, the solution was washed with deionised water, dried over $MgSO_4$ and filtered. The resulting solid was dissolved in CH_2Cl_2 and subjected to column chromatography (silica) using CH_2Cl_2/MeOH (98:2). The first orange band was collected and the liquid removed on a rotary evaporator. The resulting solid was redissolved in MeOH and precipitated using sat. aqueous KPF_6. The suspension was filtered to give **PhIr** as an orange solid.

^{1}H NMR (600 MHz, acetone) δ 9.07 (d, *J* = 1.2 Hz, 2H **4**), 8.26 (d, *J* = 8.1 Hz, 2H **A**), 8.15 – 8.11 (m, 2H, **1**), 8.02 – 7.98 (m, 2H, **A**), 7.97 – 7.94 (m, 2H, **A**), 7.92 (dd, *J* = 7.9, 1.0 Hz, 2H, **B**), 7.81 – 7.79 (m, 2H, **2**), 7.68 – 7.63 (m, 4H, **8**/**9**), 7.56 – 7.47 (m, 6H, **8**/**9** and **10**), 7.20 (ddd, *J* = 7.3, 5.9, 1.4 Hz, 2H, **A**), 7.05 (tt, *J* = 3.6, 1.8 Hz, 2H **B**), 6.94 (td, *J* = 7.4, 1.3 Hz, 2H, **B**), 6.35 (dd, *J* = 7.5, 0.8 Hz, 2H, **B**).

^{13}C NMR (151 MHz, acetone) δ 168.56 (C_q), 156.92 (C_q), 151.56 (CH), 150.96 (C_q), 150.38 (CH), 144.94 (C_q), 139.68 (CH), 135.24 (C_q), 132.91 (CH), 132.49 (CH), 131.33 (CH), 131.26 (CH), 130.95 (CH), 129.86 (CH), 127.80 (CH), 125.88 (CH), 124.61 (CH), 123.55 (CH), 121.99 (C_q), 120.88 (CH), 98.94 (C_q), 86.40 (C_q).

HRMS (m/z APCI$^+$, MeCN): [M – (PF_6)] ($C_{48}H_{32}N_4Ir$) calc. 857.2254 Found 857.2259

CF_3Ir

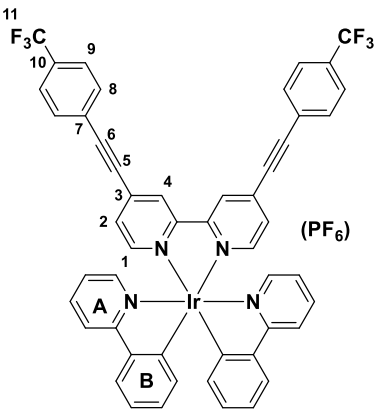

$[Ir(ppy)_2Cl_2]_2$ (0.056 g, 0.052 mmol) and 4,4'-bis((4-(trifluoromethyl)phenyl)ethynyl)-2,2'-bipyridine (0.05 g, 0.102 mmol) were added to $CHCl_3$ (4mL). The solution was refluxed overnight. Once cooled, the solution was washed with deionised water, dried over $MgSO_4$ and filtered. The resulting solid was dissolved in CH_2Cl_2 and subjected to column chromatography (silica) using CH_2Cl_2/MeOH (98:2). The first orange band was collected and the liquid removed on a rotary evaporator. The resulting solid was redissolved in MeOH and precipitated using sat. aqueous KPF_6. The suspension was filtered to give **CF_3Ir** as an orange solid.

^{1}H NMR (600 MHz, CD_3CN) δ 8.71 (d, *J* = 1.0 Hz, 2H **4**), 8.08 (d, *J* = 8.1 Hz, 2H, **A**), 8.02 – 7.98 (m, 2H, **1**), 7.87 (ddd, *J* = 8.2, 5.7, 1.5 Hz, 2H, **A**), 7.81 (m, 10H, **B**, **8** and **9**), 7.67 – 7.66 (m, 2H, **A**), 7.60 (dd, *J* = 5.7, 1.6 Hz, 2H, **2**), 7.09 – 7.05 (m, 4H, **A** and **B**), 6.94 (td, *J* = 7.5, 1.3 Hz, 2H, **B**), 6.28 (dd, *J* = 7.6, 0.8 Hz, 2H, **B**).

^{13}C NMR (151 MHz, CD_3CN) δ 168.31, 156.74, 151.83, 150.76, 150.43, 145.04, 139.71 (CH), 134.41, 133.70 (CH), 132.50 (CH), 131.46 (CH), 131.07 (CH), 127.93 (CH), 126.81 (CH), 125.94 (CH), 124.60 (CH), 123.77 (CH), 120.97, 96.80, 88.13.

HRMS (m/z APCI$^+$, MeCN): [M – (PF_6)] ($C_{50}H_{30}F_6N_4Ir$) calc. 993.2002 Found 993.2002

OMeIr

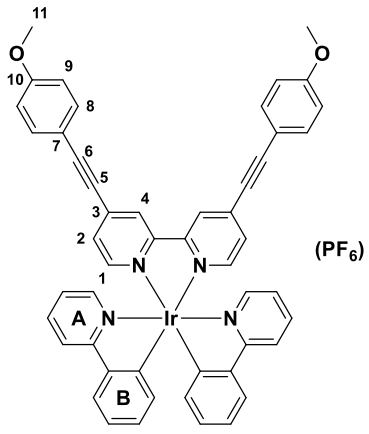

$Ir(ppy)_2Cl_2]_2$ (0.020g, 0.018mmol) and 4,4'-bis((4-methoxyphenyl)ethynyl)-2,2'-bipyridine (0.014 g, 0.038 mmol) were added to $CHCl_3$ (4mL). The solution was refluxed overnight. Once cooled, the solution was washed with deionised water, dried over $MgSO_4$ and filtered. The resulting solid was dissolved in CH_2Cl_2 and subjected to column chromatography (silica) using CH_2Cl_2/MeOH (98:2). The first orange band was collected and the liquid removed on a rotary evaporator. The resulting solid was redissolved in MeOH and precipitated using sat. aqueous KPF_6. The suspension was filtered to give **OMeIr** as an orange solid

^{1}H NMR (400 MHz, CD_3CN) δ 8.62 (s, 2H, **4**), 8.07 (d, *J* = 8.2 Hz, 2H, **A**), 7.93 (d, *J* = 5.7 Hz, 2H, **1**), 7.90 – 7.83 (m, 2H, **A**), 7.81 (d, *J* = 7.5 Hz, 2H, **B**), 7.67 (d, *J* = 5.6 Hz, 2H, **A**), 7.61 – 7.56 (m, 4H, **8**), 7.50 (dd, *J* = 5.7, 1.4 Hz, 2H, **2**), 7.09 – 7.00 (m, 8H, **A**, **B** and **9**), 6.93 (dd, *J* = 7.4, 6.5 Hz, 2H, **B**), 6.27 (d, *J* = 7.3 Hz, 2H, **B**), 3.85 (s, 6H, **11**).

^{13}C NMR (151 MHz, CD_3CN) δ 168.35, 162.42, 156.66, 151.50 (CH), 151.05, 150.37 (CH), 145.06, 139.62 (CH), 135.54, 134.96 (CH), 132.51 (CH), 131.41 (CH), 130.39 (CH), 127.37 (CH), 125.90 (CH), 124.56 (CH), 123.66 (CH), 120.91 (CH), 115.64 (CH), 113.77, 99.79, 85.62, 56.30 (CH_3).

HRMS (m/z, APCI$^+$, MeCN): [M – (PF_6)] ($C_{50}H_{36}N_4O_2Ir$) calc. 917.2466 Found 917.2465

6.2 Chapter 2

NPhL

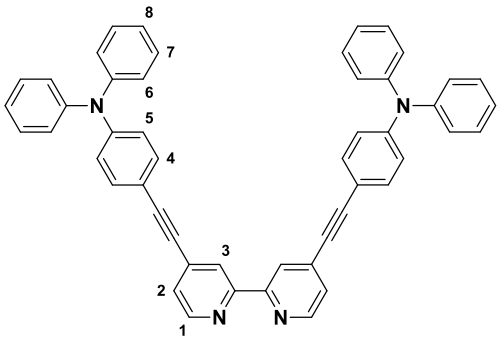

4,4'-dibromo-2,2'-bipyridine (0.1 g, 0.3 mmol, 1 eq.) and 4-ethynyl-N,N-diphenylaniline (0.202 mg, 0.75 mmol, 2.5 eq.) were added to a specialised 'snap cap' vial together with $Pd(PPh_3)_4$ (50 mg, 0.04 mmol), and triethylamine (4 mL). Argon was bubbled through the solution before the vial was sealed and heated to 130 ºC for 3 hours at 150 W in a CEM Discover S-Class Single Mode Microwave reactor. The volatiles were removed using a rotary evaporator and the crude solid dissolved in CH_2Cl_2 before being washed with 3 x 50 mL H_2O and subsequently dried over Mg_2SO_4. The solution was concentrated and the sample purified using silica column chromatography (99.95:0.05 $CHCl_3$:MeOH → 99.5:0.5 $CHCl_3$:MeOH) to give **NPhL** as a yellow solid

^{1}H NMR (600 MHz, $CDCl_3$) δ 8.68 (d, *J* = 4.3 Hz, 2H, **1**), 8.55 (s, 2H, **3**), 7.41 (m, 6H, **5** and **2**), 7.30 (t, *J* = 7.6 Hz, 8H, **6**/**7**), 7.13 (dd, *J* = 7.7, 0.8 Hz, 8H, **6**/**7**), 7.09 (td, *J* = 7.5, 0.9 Hz, 4H, **8**), 7.01 (d, *J* = 8.2 Hz, 4H, **4**).

^{13}C NMR (151 MHz, $CDCl_3$) δ 149.12 (C_q), 148.67 (CH), 147.03 (CH), 133.24 (CH), 129.65 (CH), 125.72 (CH), 125.53 (CH), 124.15 (CH), 123.65 (CH), 121.67 (CH), 114.28 (C_q), 86.46 (C_q).

HRMS (m/z): $C_{50}H_{34}N_4$ Calc.: 691.2856, Found: 691.2869 [M+H]

PyrL

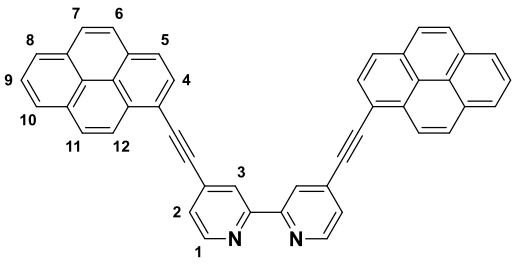

4,4'-dibromo-2,2'-bipyridine (0.1 g, 0.3 mmol, 1 eq.) and 1-ethynylpyrene (0.170 mg, 0.75 mmol, 2.5 eq.) were added to a specialised 'snap cap' vial together with $Pd(PPh_3)_4$ (50 mg, 0.04 mmol), and triethylamine (4 mL). Argon was bubbled through the solution before the vial

was sealed and heated to 130 °C for 3 hours at 150 W in a CEM Discover S-Class Single Mode Microwave reactor. The volatiles were removed using a rotary evaporator and the crude solid dissolved in CH_2Cl_2 before being washed with 3 x 50 mL H_2O and subsequently dried over Mg_2SO_4. The solid was used without any further purification due to its insolubility.

BrRu

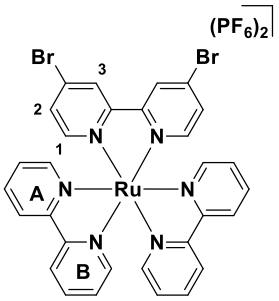

[Ru(2,2'-bipyridine)$_2$Cl$_2$] (0.02 g, 0.04 mmol) and 4,4'-dibromo-2,2'-bipyridine (0.02 g, 0.1 mmol, 2.5 eq.) were combined in ethylene glycol (6 mL) in a specialised sealed snap-cap vial. The vial was placed in a CEM Discover S-Class Single Mode Microwave reactor and heated to 160 °C for 1 hour (150 W) under pressure. Upon cooling, the ethylene glycol solution was added to a saturated aqueous KPF_6 solution and the resulting precipitate washed with H_2O. The crude was purified by column chromatography (silica) using CH_3CN:H_2O:sat. KNO_3 (90:9:1). The first red fraction was collected, reduced and the product precipitated out of solution using saturated KPF_6 solution to give **BrRu** as a black solid

^{1}H NMR (600 MHz, CD_3CN) δ 8.74 (d, *J* = 2.0 Hz, 2H, **3**), 8.49 (dd, *J* = 8.1, 4.5 Hz, 4H, **A** and **B**), 8.06 (dtd, *J* = 9.3, 8.0, 1.4 Hz, 4H, **A** and **B**), 7.77 – 7.74 (m, 2H, **A**), 7.69 – 7.65 (m, 2H, **B**), 7.59 (dd, *J* = 6.1, 2.0 Hz, 2H, **1**), 7.55 (d, *J* = 6.1 Hz, 2H, **2**), 7.45 – 7.35 (m, 4H, **A** and **B**).

^{13}C NMR (151 MHz, CD_3CN) δ 157.97 (C_q), 157.83 (C_q), 157.79 (C_q), 153.31 (CH), 152.86 (CH), 152.64 (CH), 139.00 (CH), 138.98 (CH), 134.81, 131.94 (CH), 129.19 (CH), 128.60 (CH), 128.59 (CH), 125.27 (C_q).

HRMS (m/z): ($C_{30}H_{22}Br_2N_6Ru$) Calc. 362.9652, Found: 362.9647 [M/2, -2PF_6]

NPhRu

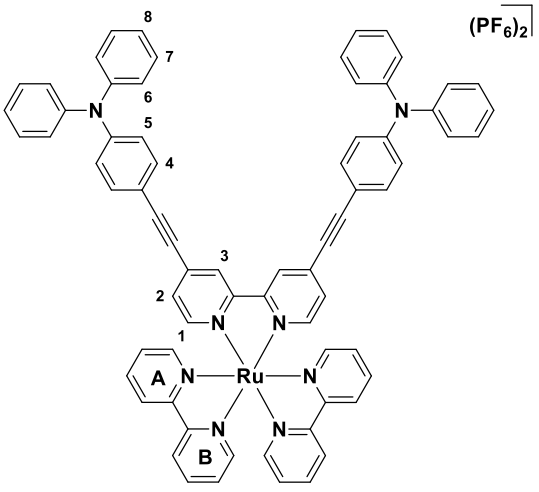

[Ru(2,2'-bipyridine)$_2$Cl$_2$] (0.02 g, 0.04 mmol) and 4,4'-bis(acetyltriphenylamine)-2,2'-bipyridine (0.071 g, 0.1 mmol, 2.5 eq.) were combined in ethylene glycol (6 mL) in a specialised sealed snap-cap vial. The vial was placed in a CEM Discover S-Class Single Mode Microwave reactor and heated to 160 °C for 1 hour (150 W) under pressure. Upon cooling, the ethylene glycol solution was added to a saturated aqueous KPF_6 solution and the resulting precipitate washed with H_2O. The crude was purified by column chromatography (silica) using CH_3CN:H_2O:sat. KNO_3 (90:9:1). The first red fraction was collected, reduced and the product precipitated out of solution using saturated KPF_6 solution to give **NPhRu** as a black solid

^{1}H NMR (400 MHz, CD_3CN) δ 8.59 (d, *J* = 1.4 Hz, 2H, **3**), 8.52 (d, *J* = 8.1 Hz, 4H, **A** and **B**), 8.09 (dt, *J* = 7.6, 3.8 Hz, 4H **A** and **B**), 7.82 (d, *J* = 4.9 Hz, 2H, **B**), 7.73 (d, *J* = 4.9 Hz, 2H, **A**), 7.69 (d, *J* = 5.9 Hz, 2H, **1**), 7.49 – 7.34 (m, 18H, **A, B, 2, 4** and **6/7**), 7.26 – 7.13 (m, 12H, **6/7 and 8**), 7.03 – 6.93 (m, 4H, **5**).

^{13}C NMR (151 MHz, CD_3CN) δ 157.88 (C_q), 157.87 (C_q), 157.78 (C_q), 152.82 (CH), 152.63 (CH), 152.47 (CH), 150.84 (C_q), 147.55 (C_q), 138.97 (CH), 138.94 (CH), 134.27 (CH), 133.94 (C_q), 130.77 (CH), 129.29 (CH), 128.66 (CH), 128.64 (CH), 126.84 (CH), 126.72 (CH), 125.78 (CH), 125.29 (CH), 121.40 (CH), 113.35 (C_q), 100.21 (C_q), 86.08 (C_q).

HRMS (m/z): ($C_{70}H_{50}F_{12}N_8P_2Ru$) Calc. 552.1604, Found: 552.1609 [M/2, -2PF_6]

NPhIr

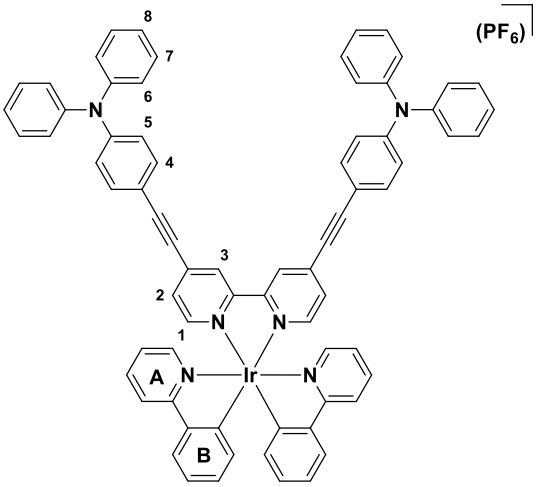

$[Ir(ppy)_2Cl_2]_2$ (0.020g, 0.018mmol) and 4,4'-bis(acetyltriphenylamine)-2,2'-bipyridine (0.032 g, 0.04 mmol, 2.5 eq.) were added to $CHCl_3$ (4mL). The solution was refluxed overnight. Once cooled, the solution was washed with deionised water, dried over $MgSO_4$ and filtered. The resulting solid was dissolved in CH_2Cl_2 and subjected to column chromatography (silica) using CH_2Cl_2/MeOH (98:2). The first orange band was collected and the liquid removed on a rotary evaporator. The resulting solid was redissolved in MeOH and precipitated using sat. aqueous KPF_6. The suspension was filtered to give **NPhIr** as an orange solid.

^{1}H NMR (400 MHz, CD_3CN) δ 8.57 (s, 2H, **3**), 8.06 (d, *J* = 8.1 Hz, 2H **A**), 7.91 – 7.77 (m, 6H, **1, A** and **B**), 7.66 (d, *J* = 5.7 Hz, 2H, **A**), 7.44 (dd, *J* = 12.7, 5.0 Hz, 6H, **4** and **2**), 7.36 (t, *J* = 7.9 Hz, 8H, **6/7**), 7.21 – 7.10 (m, 12H, **6/7** and **8**), 7.04 (dd, *J* = 9.9, 5.4 Hz, 4H, **A** and **B**), 6.92 (dd, *J* = 10.4, 8.1 Hz, 6H, **B** and **5**), 6.27 (d, *J* = 7.4 Hz, 2H, **B**).

^{13}C NMR (151 MHz, CD_3CN) δ 168.35 (C_q), 156.60 (C_q), 151.38 (CH), 151.09 (C_q), 150.88 (C_q), 150.33 (CH), 147.52 (C_q), 145.04 (C_q), 139.61 (CH), 135.57 (C_q), 134.35 (CH), 132.50 (CH), 131.40 (CH), 130.76 (CH), 130.21 (CH), 127.23 (CH), 126.85 (CH), 125.89 (CH), 125.77 (CH), 124.55 (CH), 123.64 (CH), 121.34 (CH), 120.90 (CH), 113.25 (C_q), 100.46 (C_q), 86.13 (C_q).

HRMS (m/z): ($C_{72}H_{50}F_6N_6PIr$) Calc.:1191.3727, Found: 1191.3739 [M-PF_6]

PyrIr

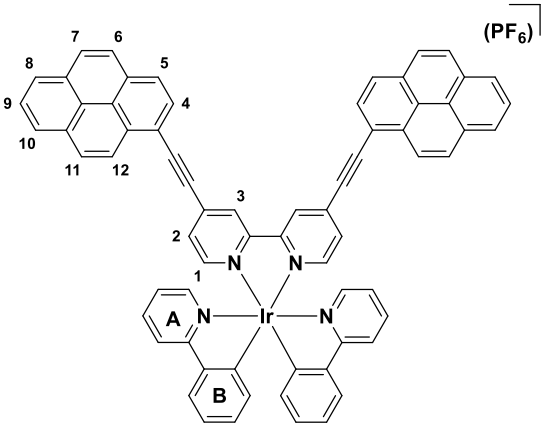

$[Ir(ppy)_2Cl_2]_2$ (0.020g, 0.018mmol) and 4,4'-bis(acetylpyrene)-2,2'-bipyridine (0.024 g, 0.04 mmol, 2.5 eq.) were added to $CHCl_3$ (4mL). The solution was refluxed overnight. Once cooled, the solution was washed with deionised water, dried over $MgSO_4$ and

filtered. The resulting solid was dissolved in CH_2Cl_2 and subjected to column chromatography (silica) using CH_2Cl_2/MeOH (98:2). The first orange band was collected and the liquid removed on a rotary evaporator. The resulting solid was redissolved in MeOH and precipitated using sat. aqueous KPF_6. The suspension was filtered to give **PyrIr** as an orange solid.

^{1}H NMR (600 MHz, CD_3CN) δ 8.93 (s, 2H, **3**), 8.75 (d, *J* = 9.0 Hz, 4H, **HPyr**), 8.42 – 8.38 (m, 4H, **HPyr**), 8.34 (d, *J* = 7.5 Hz, 2H, **HPyr**), 8.31 (s, 4H, **HPyr**), 8.25 (d, *J* = 8.9 Hz, 2H, **HPyr**), 8.19 (d, *J* = 8.9 Hz, 2H **HPyr**), 8.14 (m, 4H, **A** and **HPyr**), 8.07 (d, *J* = 5.6 Hz, 2H, **1**), 7.95 – 7.91 (m, 2H, **A**), 7.90 (dd, *J* = 8.0, 0.9 Hz, 2H, **B**), 7.82 – 7.79 (m, 2H, **A**), 7.72 (dd, *J* = 5.6, 1.5 Hz, 2H, **3**), 7.18 – 7.10 (m, 4H, **A** and **B**), 7.01 (td, *J* = 7.5, 1.3 Hz, 2H, **B**), 6.40 – 6.34 (m, 2H, **B**).

^{13}C NMR (151 MHz, CD_3CN) δ 168.45 (C_q), 156.82 (C_q), 151.66 (CH), 151.05 (C_q), 150.43 (CH), 145.11 (C_q), 139.75 (CH), 135.22 (C_q), 133.81 (C_q), 133.55 (C_q), 132.57 (CH), 132.15 (C_q), 131.89 (C_q), 131.51 (CH), 131.42 (CH), 130.70 (CH), 130.48 (CH), 130.42 (CH), 128.22 (CH), 127.94 (CH), 127.77 (C_q), 127.55 (CH), 127.52 (CH), 126.00 (CH), 125.97 (CH), 125.83 (CH), 125.12 (C_q), 124.75 (C_q), 124.67 (CH), 123.78 (CH), 121.02 (CH), 115.99 (C_q), 98.34 (C_q), 92.22 (C_q).

HRMS (m/z): ($C_{68}H_{40}N_4Ir$) Calc. 1105.2882, Found: 1105.2886 [M-2PF_6]

6.3 Chapter 3

Ligands Prepared by Dr. Alexandra Horan of UCD.

N,*N*-Diphenyl-4-(4,4,5,5-tetramethyl-1,3,2-dioxaborolan-2-yl)aniline and 4-(*N*,*N*-diphenylamino)phenylacetylene were prepared according to literature procedures.[166] [167]

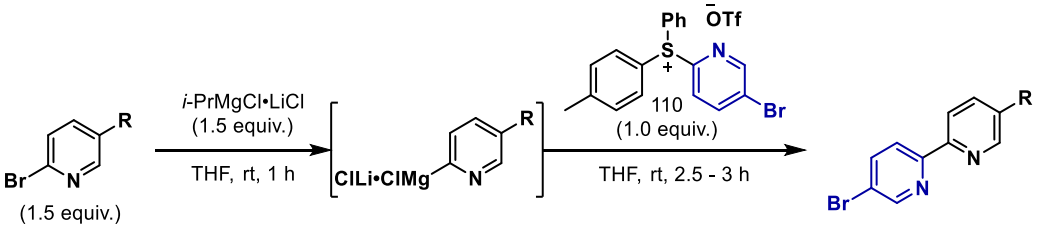

Scheme S1. Synthesis of bis-heteroaryls using Grignard reagents and sulfonium salts

Bromopyridine (1.5 equiv.) was added to an oven-dried crimp top vial which was sealed, evacuated and purged with N_2 three times. Bromopyridine was dissolved in dry THF (0.3 M) at rt. *i*-PrMgCl•LiCl (1.5 equiv., 1.2 M in THF) was added dropwise to the stirring solution over 2 min. The reaction was allowed to stir at rt for 1 h. Sulfonium salt (1.0 equiv.) was added to a separate oven-dried crimp top vial which was sealed, evacuated and purged with N_2 three times. Sulfonium salt was dissolved in dry THF (0.3 M) and added dropwise down the side of the vial to the Grignard reagent solution over 2 min. The reaction was allowed to stir at rt for the time stated. Saturated aq. NH_4Cl (5 mL) was added slowly to quench any excess Grignard reagent. The product was extracted with EtOAc (3 x 10 mL), the combined organic layers were washed with H_2O (20 mL) and brine (20 mL) and dried over anhydrous Na_2SO_4. Following concentration *in vacuo*, the desired product was isolated by FCC.

2-Bromo-5-(4-(trifluoromethyl)phenyl)pyridine (P1)

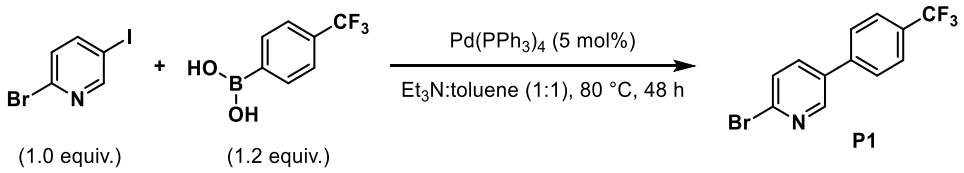

2-Bromo-5-iodopyridine (1.14 g, 4.00 mmol), 4-(trifluoromethyl)phenylboronic acid (0.91 g, 4.8 mmol) and $Pd(PPh_3)_4$ (0.145 g, 0.200 mmol) were added to an oven-dried crimp top vial, which was evacuated and purged with N_2 three times. Dry Et_3N (4 mL) and dry toluene (4 mL) were added to the vial and the reaction mixture was heated to 80 °C for 48 h, then concentrated *in vacuo*. Purification by FCC (5% Et_2O in pentane) gave product P1 as a white solid (0.478 g, 39%).

^{1}H NMR (500 MHz, Chloroform-*d*) δ 8.60 (d, *J* = 2.5 Hz, 1H,), 7.77 – 7.72 (m, 3H,), 7.66 (d, *J* = 8.2 Hz, 2H), 7.59 (d, *J* = 8.3 Hz, 1H).

^{13}C NMR (126 MHz, Chloroform-*d*) δ 148.7 (CH), 142.1 (CBr), 140.2 (C_q), 137.1 (CH), 134.8 (C_q), 130.8 (q, *J* = 32.8 Hz, C_q), 128.4 (CH), 127.5 (CH), 126.4 (q, *J* = 3.8 Hz, CH), 124.1 (q, *J* = 272.2 Hz, CF_3).

^{19}F NMR (470 MHz, Chloroform-*d*) δ -62.7 (CF_3).

HRMS (ESI-TOF) *m/z*: $[M+H]^+$ Calc'd for: $C_{12}H_7BrF_3N$ 301.9787, 303.9767; found: 301.9788, 303.9768.

5-Bromo-5'-(4-(trifluoromethyl)phenyl)-2,2'-bipyridine (

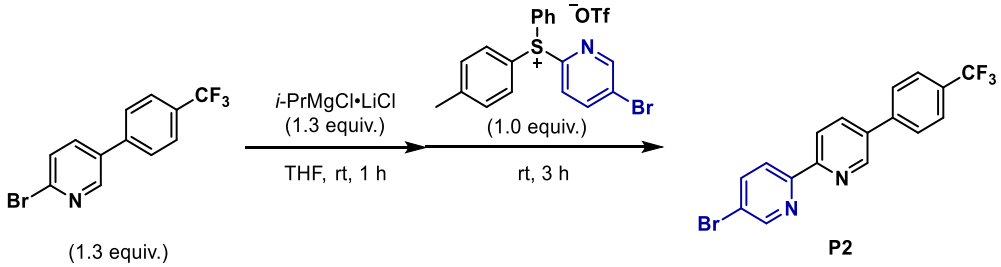

Product P2 was synthesised *via* general procedure A using P1 (0.30 g, 0.99 mmol) and a bromopyridyl sulfonium salt (0.385 g, 0.760 mmol). The Grignard reagent was formed at rt for 1 h and the ligand coupling reaction was stirred at rt for 3 h. Purification by FCC (10% Et_2O in pentane) gave bipyridine P2 as a white solid (114.1 mg, 40%).

TLC R_f = 0.36 (10% Et_2O in pentane).

^{1}H NMR (400 MHz, Chloroform-*d*) δ 8.90 (d, *J* = 2.3 Hz, 1H), 8.74 (d, *J* = 2.3 Hz, 1H), 8.48 (d, *J* = 8.2 Hz, 1H), 8.36 (d, *J* = 8.4 Hz, 1H), 8.02 (dd, *J* = 8.2, 2.3 Hz, 1H), 7.96 (dd, *J* = 8.4, 2.3 Hz, 1H), 7.75 (s, 4H).

^{13}C NMR (101 MHz, Chloroform-*d*) δ 155.0 (C_q), 154.2 (C_q), 150.5 (C_q), 147.9 (C_q), 141.2 (C_q), 139.7 (CH), 135.6 (CH), 135.5 (C_q), 130.5 (q, *J* = 32.5 Hz, C_q), 127.5 (CH), 126.3 (q, *J* = 3.8 Hz, CH), 124.2 (q, *J* = 272.2 Hz, CF_3), 122.5 (CH), 121.5 (CBr), 121.2 (CH).

^{19}F NMR (376 MHz, Chloroform-*d*) δ -62.6 (CF_3).

HRMS (ESI-TOF) *m/z*: $[M+H]^+$ Calc'd for: $C_{17}H_{11}BrF_3N_2$ 379.0052, 381.0033; found: 379.0053, 381.0033.

L1

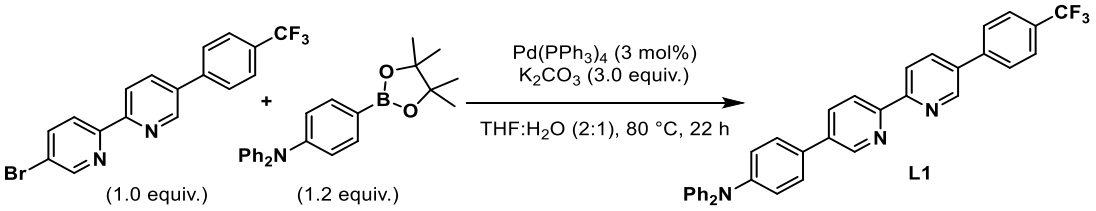

Bipyridine P2 (69 mg, 0.18 mmol), *N*,*N*-diphenyl-4-(4,4,5,5-tetramethyl-1,3,2-dioxaborolan-2-yl)aniline (82 mg, 0.22 mmol), K_2CO_3 (75 mg, 0.54 mmol) and $Pd(PPh_3)_4$ (5.8 mg, 0.0033 mmol) were added to an oven-dried crimp top vial, which was evacuated and purged with N_2 three times. THF (0.6 mL) and H_2O (0.3 mL) were added to the vial and the reaction mixture was heated to 80 °C for 22 h. The reaction mixture was then cooled to rt, diluted with H_2O (20 mL) and extracted with CH_2C**L2** (3 x 20 mL). The combined organic layers were dried over anhydrous Na_2SO_4. Purification by FCC (20% Et_2O in pentane) gave product **L1** as a yellow solid (86.5 mg, 88%).

TLC $\boldsymbol{R_f}$ = 0.14 (20% Et_2O in pentane).

^{1}H NMR (500 MHz, Chloroform-*d*) δ 8.96 – 8.91 (m, 2H), 8.54 (d, *J* = 8.3 Hz, 1H), 8.50 (d, *J* = 8.2 Hz, 1H), 8.05 (dd, *J* = 8.3, 2.4 Hz, 1H), 8.02 (dd, *J* = 8.2, 2.4 Hz, 1H), 7.77 (s, 4H), 7.55 (d, *J* = 8.7 Hz, 2H), 7.33 – 7.27 (m, 4H), 7.20 – 7.14 (m, 6H), 7.10 – 7.05 (m, 2H).

^{13}C NMR (126 MHz, Chloroform-*d*) δ 155.8 (C_q), 153.9 (C_q), 148.4 (C_q), 147.9 (CH), 147.5 (C_q), 147.4 (CH), 141.4 (C_q), 136.4 (C), 135.5 (CH), 135.0 (C_q), 134.7 (CH), 130.9 (C_q), 130.4 (q, *J* = 32.5 Hz, C_q), 129.5 (CH), 127.8 (CH), 127.5 (CH), 126.2 (q, *J* = 3.7 Hz C_q), 125.0 (CH), 124.3 (q, *J* = 271.9 Hz, CF_3), 123.60 (CH), 123.56 (CH), 121.2 (CH), 121.1 (CH).

^{19}F NMR (470 MHz, Chloroform-*d*) δ -62.6 (CF_3).

HRMS (ESI-TOF) *m/z*: $[M+H]^+$ Calc'd for: $C_{35}H_{25}F_3N_3$ 544.1995; found: 544.1995.

L2

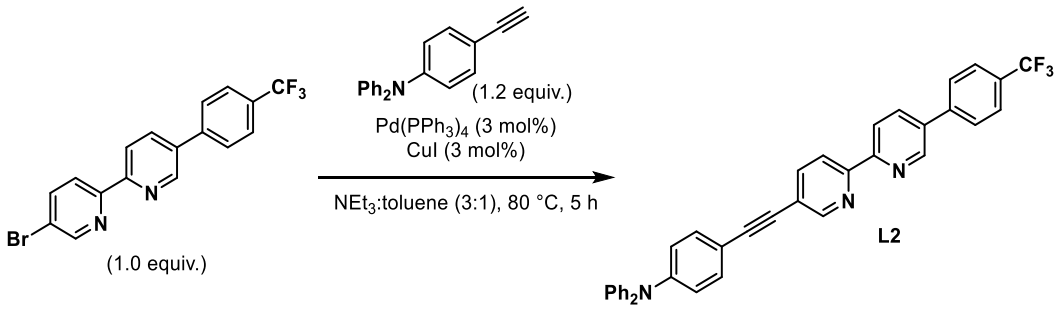

Bipyridine P2 (45 mg, 0.12 mmol), 4-(*N*,*N*-diphenylamino)phenylacetylene (38 mg, 0.14 mmol), $Pd(PPh_3)_4$ (4.2 mg, 0.0036 mmol) and CuI (0.7 mg, 0.0036 mmol) were added to an oven-dried crimp top vial, which was evacuated and purged with N_2 three times. Dry Et_3N (0.48 mL) and toluene (0.24 mL) were added to the vial and the reaction mixture was heated to 80 °C for 5 h. The reaction mixture was then cooled to rt, diluted with saturated aq. NH_4Cl (20 mL) and extracted with CH_2C**L2** (3 x 20 mL). The combined organic layers were dried over anhydrous Na_2SO_4. Purification by FCC (20% Et_2O in pentane) gave product **L2** as a yellow solid (45.9 mg, 67%).

TLC $\boldsymbol{R_f}$ = 0.30 (20% Et_2O in pentane).

^{1}H NMR (400 MHz, Chloroform-*d*) δ 8.93 (d, *J* = 2.4 Hz, 1H), 8.81 (d, *J* = 2.1 Hz, 1H), 8.53 (d, *J* = 8.2 Hz, 1H), 8.44 (d, *J* = 8.3 Hz, 1H), 8.04 (dd, *J* = 8.2, 2.4 Hz, 1H), 7.93 (dd, *J* = 8.3, 2.1 Hz, 1H), 7.76 (s, 4H), 7.41 (d, *J* = 8.6 Hz, 2H), 7.33 – 7.27 (m, 4H), 7.16 – 7.12 (m, 4H), 7.12 – 7.06 (m, 2H), 7.03 (d, *J* = 8.6 Hz, 2H).

^{13}C NMR (101 MHz, Chloroform-*d*) δ 155.4 (C_q), 153.9 (C_q), 151.7 (CH), 148.6 (C_q), 147.9 (CH), 147.2 (C_q), 141.3 (C_q), 139.3 (CH), 135.5 (CH), 135.2 (C_q), 132.8 (CH), 130.4 (q, *J* = 32.4 Hz, C_q), 129.6 (CH), 127.5 (CH), 126.2 (q, *J* = 3.5 Hz, CH), 125.3 (CH), 124.2 (q, *J* = 272.3 Hz, CF_3), 124.0 (CH), 122.1 (CH), 121.4 (CH), 121.2 (C_q), 120.6 (CH), 115.1 (C_q), 94.5 (C_q), 85.8 (C_q).

^{19}F NMR (376 MHz, Chloroform-*d*) δ -62.6 (CF_3).

HRMS (ESI-TOF) *m/z*: $[M+H]^+$ Calc'd for: $C_{37}H_{25}F_3N_3$ 568.1995; found: 568.1995.

2-Bromo-5-((4-(trifluoromethyl)phenyl)ethynyl)pyridine (P3)

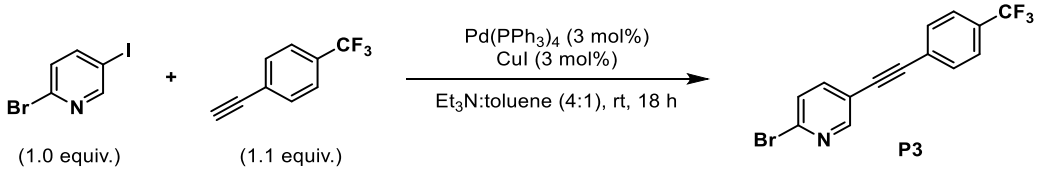

2-Bromo-5-iodopyridine (0.568 g, 2.00 mmol), $Pd(PPh_3)_4$ (69 mg, 0.06 mmol) and CuI (11 mg, 0.06 mmol) were added to an oven-dried crimp top vial, which was evacuated and purged with N_2 three times. 4-(Trifluoromethyl)phenylacetylene (0.36 mL, 2.2 mmol), dry Et_3N (4 mL) and dry toluene (1 mL) were added to the vial and the reaction mixture was stirred at rt for 18 h, then concentrated *in vacuo*. Purification by FCC (5% Et_2O in pentane) gave product P3 as a white solid (0.465 g, 71%).

TLC $\boldsymbol{R_f}$ = 0.47 (5% Et_2O in pentane).

^{1}H NMR (500 MHz, Chloroform-*d*) δ 8.53 (d, *J* = 2.4 Hz, 1H), 7.66 (dd, *J* = 8.3, 2.4 Hz, 1H), 7.63 (s, 4H), 7.50 (d, *J* = 8.3 Hz, 1H).

^{13}C NMR (126 MHz, Chloroform-*d*) δ 152.6 (CH), 141.8 (C_q), 140.7 (CH), 132.1 (CH), 130.8 (q, *J* = 32.6 Hz, C), 127.9 (CH), 126.1 (C_q), 125.6 (q, *J* = 3.7 Hz, CH), 123.9 (q, *J* = 271.9 Hz, CF_3), 119.2 (CBr), 92.5 (C_q), 87.1 (C_q).

^{19}F NMR (376 MHz, Chloroform-*d*) δ -62.9 (CF_3).

HRMS (ESI-TOF) *m/z*: $[M+H]^+$ Calc'd for: $C_{14}H_7BrF_3N$ 325.9787, 327.9767; found: 325.9786, 327.9765.

5-Bromo-5'-((4-(trifluoromethyl)phenyl)ethynyl)-2,2'-bipyridine (P4)

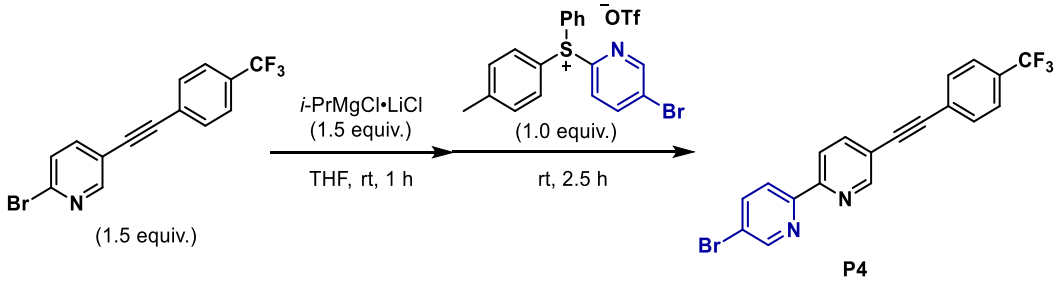

Product P4 was synthesised *via* general procedure A using P3 (0.23 g, 0.69 mmol) and a bromopyridyl sulfonium salt (0.233 g, 0.460 mmol). The Grignard reagent was formed at rt for 1 h and the ligand coupling reaction was stirred at rt for 2.5 h. Purification by FCC (5% Et_2O in pentane) gave bipyridine P4 as a white solid (89.2 mg, 48%).

TLC R_f = 0.38 (5% Et_2O in pentane).

^{1}H NMR (400 MHz, Chloroform-*d*) δ 8.81 (d, *J* = 2.0 Hz, 1H), 8.73 (d, *J* = 2.3 Hz, 1H), 8.41 (d, *J* = 8.2 Hz, 1H), 8.35 (d, *J* = 8.5 Hz, 1H), 7.97 – 7.95 (m, 1H), 7.95 – 7.93 (m, 1H), 7.72 – 7.61 (m, 4H).

^{13}C NMR (126 MHz, Chloroform-*d*) δ 154.5 (C_q), 153.9 (C_q), 151.9 (CH), 150.5 (CH), 139.7 (CH), 132.1 (CH), 130.7 (q, *J* = 32.8 Hz, C_q), 126.5 (C_q), 125.6 (q, *J* = 3.7 Hz, CH), 124.0 (q, *J* = 272.0 Hz, CF_3), 122.8 (CH), 121.7 (CBr), 120.4 (CH,), 120.0 (C_q), 92.3 (C_q), 88.7 (C_q).

^{19}F NMR (376 MHz, Chloroform-*d*) δ -62.9 (CF_3).

HRMS (ESI-TOF) *m/z*: $[M+H]^+$ Calc'd for: $C_{19}H_{11}BrF_3N_2$ 403.0052, 405.0034; found: 403.0050, 405.0031.

L3

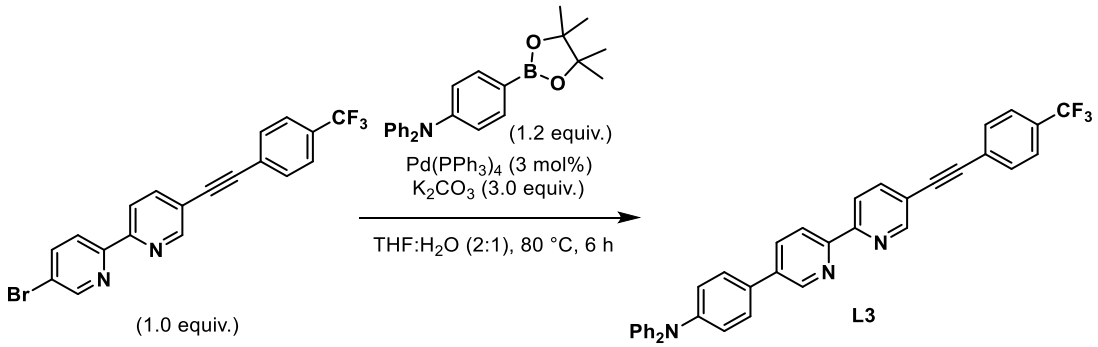

Bipyridine **P4** (46 mg, 0.11 mmol), *N*,*N*-diphenyl-4-(4,4,5,5-tetramethyl-1,3,2-dioxaborolan-2-yl)aniline (52 mg, 0.14 mmol), K_2CO_3 (46 mg, 0.33 mmol) and $Pd(PPh_3)_4$ (3.8 mg, 0.0033 mmol) were added to an oven-dried crimp top vial, which was evacuated and purged with N_2 three times. THF (0.36 mL) and H_2O (0.18 mL) were added to the vial and the reaction mixture was heated to 80 °C for 6 h. The reaction mixture was then cooled to rt, diluted with H_2O (20 mL) and extracted with CH_2Cl_2 (3 x 20 mL). The combined organic layers were dried over anhydrous Na_2SO_4. Purification by FCC (10% Et_2O in pentane) gave product **L3** as a yellow solid (42.9 mg, 69%).

TLC R_f = 0.12 (10% Et_2O in pentane).

^{1}H NMR (400 MHz, Chloroform-*d*) δ 8.92 (d, *J* = 2.4 Hz, 1H), 8.84 (d, *J* = 2.1 Hz, 1H), 8.47 (d, *J* = 8.3 Hz, 1H), 8.46 (d, *J* = 8.3 Hz, 1H), 8.00 (dd, *J* = 8.3, 2.4 Hz, 1H), 7.96 (dd, *J* = 8.3, 2.1 Hz, 1H), 7.70 – 7.62 (m, 4H), 7.54 (d, *J* = 8.6 Hz, 2H), 7.33 – 7.27 (m, 4H), 7.22 – 7.12 (m, 6H), 7.11 – 7.04 (m, 2H).

^{13}C NMR (101 MHz, Chloroform-*d*) δ 155.3 (C_q), 153.6 (C_q), 151.9 (CH), 148.4 (C_q), 147.5 (C_q), 147.4 (CH), 139.6 (CH), 136.5 (C_q), 134.6 (CH), 132.1 (CH), 130.8 (C_q), 130.6 (q, *J* = 33.1 Hz, C_q), 129.6 (CH), 127.9 (CH), 126.6 (C_q), 125.6 (q, *J* = 3.5 Hz, CH), 125.0 (CH), 124.0 (q, *J* = 272.3 Hz, CF_3), 123.58 (CH), 123.56 (CH), 121.5 (CH), 120.4 (CH), 119.5 (C_q), 92.1 (C_q), 88.9 (C_q).

^{19}F NMR (376 MHz, Chloroform-*d*) δ -62.8 (CF_3).

HRMS (ESI-TOF) *m/z*: $[M+H]^+$ Calc'd for: $C_{37}H_{25}F_3N_3$ 568.1995; found: 568.1995.

<u>Ru1</u>

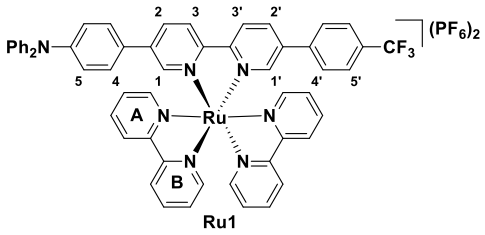

Ru(bpy)$_2$C**L2** (30 mg, 0.06 mmol) , and **L1** (34 mg, 0.06 mmol)were dissolved in ethylene glycol and the reaction mixture heated to 140 ^{o}C for 16 h under Argon. After cooling, saturated aqueous KPF_6 was added and the resulting precipitate isolated by filtration. The crude product was purified using column chromatography (silica, MeCN, H_2O, sat. KNO_3, 90:9:1 v/v) followed by treatment with KPF_6 and recrystallised from MeOH and Et_2O to yield **Ru1** (50 mg, 65 % yield)

^{1}H NMR (600 MHz, CD_3CN) δ 8.57 (d, *J* = 8.5 Hz, 1H, **2/2'**), 8.53 (d, *J* = 8.6 Hz, 1H, **2/2'**), 8.51-8.44 (m, 4H, **A** and **B**), 8.32 (dd, *J* = 8.5, 2.1 Hz, 1H, **3/3'**), 8.26 (dd, *J* = 8.6, 2.1 Hz, 1H, **3/3'**), 8.12-8.01 (m, 4H, **A**

and **B**), 7.88 (m, 2H, **A** and **B**), 7.82-7.72 (m, 6H, **5', A** and **B, 1/1'**), 7.58 (d, *J* = 8.2 Hz, 2H, **4'**), 7.46-7.38 (m, 4H, **A** and **B**), 7.38-7.31 (m, 4H, **NPh$_2$**), 7.29 – 7.23 (m, 2H, **4/5**), 7.20-7.12 (m, 2H, **NPh$_2$**), 7.12-7.03 (m, 4H, **NPh$_2$**), 6.98- 6.92 (m, 2H, **4/5**)

^{13}C NMR (151 MHz, CD_3CN) δ, 158.08 (C_q), 158.06 (C_q), 157.93 (C_q), 157.86 (C_q), 157.28 (C_q), 155.03 (C_q), 153.03 (CH), 152.98 (C_q), 152.89 (CH), 152.81 (CH) 150.55 (CH), 150.30 (C_q), 148.97 (CH), 147.75 (C_q), 140.33 (C_q), 139.85 (C_q), 139.10 (C_q), 138.90 (CH), 138.82 (C_q), 138.76 (CH), 138.74 (C_q), 137.06 (CH), 135.35 (CH), 131.42 (C_q), 130.67 (CH), 128.89 (CH), 128.69 (CH), 128.56 (C_q), 128.52 (CH), 128.49 (C_q), 127.54 (C_q), 127.06 (CH), 126.48 (CH), 125.46 (CH), 125.43 (CH), 125.39 (CH), 125.36 (CH), 125.26 (CH), 125.22 (CH), 124.93 (CH), 122.38 (CH).

^{19}F NMR (377 MHz, acetone) δ -63.33 (s), -71.65 (s), -73.52 (s).

^{31}P NMR (162 MHz, acetone) δ -144.26 (m).

HRMS (m/z, APCI$^+$, MeOH) $[M-(PF_6)_2]^{2+}$, $(C_{55}H_{40}F_3N_7Ru)^{2+}$, Calculated mass: 478.617229; Found: 478.618508.

<u>Ru2</u>

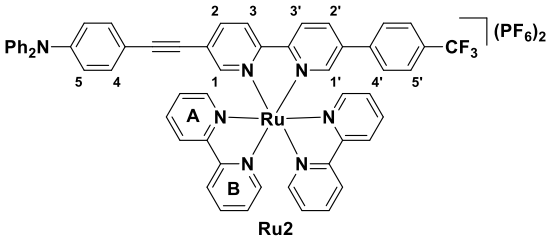

Ru2

Ru(bpy)$_2$C**L2** (28 mg, 0.05 mmol) , and **L2** (30 mg, 0.05 mmol)were dissolved in ethylene glycol and the reaction mixture heated to 140 ^{o}C for 16 h under Argon. After cooling, saturated aqueous KPF_6 was added and the resulting precipitate isolated by filtration. The crude product was purified using column chromatography (silica, MeCN, H_2O, sat. KNO_3, 90:9:1 v/v) followed by treatment with KPF_6 and recrystallised from MeOH and Et_2O to yield **Ru2** (25 mg, 38 % yield)

^{1}H NMR (600 MHz, CD_3CN) δ 8.56 (d, J = 8.6 Hz, 1H, **2**), 8.53-8.45 (m, 5H, **2'**, **A** and **B**), 8.32 (dd, J = 8.5, 2.0 Hz, 1H, **3**), 8.11 (dd, J = 8.5, 1.8 Hz, 1H, **3'**), 8.10-8.02 (m, 4H, **A** and **B**), 7.84 (dd, J = 9.0, 5.7 Hz, 2H, **A** and **B**), 7.80 (dd, J = 7.4, 1.8 Hz, 2H, **1** and **1'**), 7.77-7.69 (m, 4H, **A** and **B, 5'**), 7.57 (d, J = 8.3 Hz, 2H, **4'**), 7.46-7.38 (m, 4H, **A** and **B**), 7.38-7.32 (m, 4H, **NPh$_2$**), 7.32-7.28 (m, 2H, **4/5**), 7.16 (dd, J = 11.6, 4.2 Hz, 2H, **NPh$_2$**), 7.14-7.09 (m, 4H, **NPh$_2$**), 6.93 – 6.89 (m, 2H, **4/5**).

^{13}C NMR (151 MHz, CD_3CN) δ 158.02 (C_q), 157.98 (C_q), 157.96 (C_q), 156.98 (C_q), 155.91 (C_q), 154.00 (CH), 153.15 (CH), 153.01 (CH), 152.84 (CH), 152.76 (CH), 150.55 (CH), 150.47 (C_q), 147.63 (CH), 140.24 (CH), 138.99 (CH), 138.96 (CH), 138.93 (CH), 137.13 (CH), 133.83 (CH), 130.74 (CH), 128.98 (CH), 128.66 (CH), 128.62 (C_q), 128.52 (C_q), 127.12 (C_q), 126.69 (CH), 125.63 (CH), 125.51 (CH), 125.49 (C_q), 125.40 (CH), 125.33 (CH), 125.14 (CH), 121.59 (CH), 118.31 (C_q), 98.67 (C_q), 84.51 (C_q).

^{19}F NMR (377 MHz, acetone) δ -63.35 (s), -71.65 (s), -73.53 (s).

^{31}P NMR (162 MHz, acetone) δ -144.26

HRMS (m/z, APCI$^+$, MeOH) $[M-(PF_6)_2]^{2+}$ $(C_{57}H_{40}F_3N_7Ru)^{2+}$, Calculated mass: 490.617527; Found: 490.618130.

Ru3

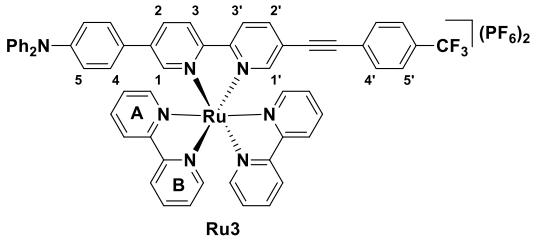

Ru3

Ru(bpy)$_2$C**L2** (28 mg, 0.05 mmol) , and **L3** (30 mg, 0.05 mmol)were dissolved in ethylene glycol and the reaction mixture heated to 140 ^{o}C for 16 h under Argon. After cooling, saturated aqueous KPF_6 was added and the resulting precipitate isolated by filtration. The crude product was purified using column chromatography (silica, MeCN, H_2O, sat. KNO_3, 90:9:1 v/v) followed by treatment with KPF_6 and recrystallised from MeOH and Et_2O to yield **Ru3** (10 mg, 15 % yield)

^{1}H NMR (600 MHz, CD_3CN) δ 8.50 (m, 6H, **A** and **B**, **2** and **2'**), 8.25 (dd, J = 8.6, 2.1 Hz, 1H, **3'**), 8.17 (dd, J = 8.5, 1.8 Hz, 1H, **3**), 8.10-8.02 (m, 4H, **A** and **B**), 7.88 (d, J = 1.6 Hz, 1H, **1'**), 7.84 (dd, J = 15.4, 5.2 Hz, 2H **A** and **B**), 7.76-7.71 (m, 5H, **A** and **B**, **1, 5'**), 7.65 (m, J = 8.2 Hz, 2H, **4'**), 7.45-7.37 (m, 4H, **A** and **B**), 7.37-7.33 (m, 4H, **NPh$_2$**), 7.27-7.22 (m, 2H, **4/5**), 7.18 – 7.14 (m, 2H, **NPh$_2$**), 7.08 (dd, J = 8.5, 1.0 Hz, 4H, **NPh$_2$**), 6.95-6.92 (m, 2H, **4/5**).

^{13}C NMR (151 MHz, CD_3CN) δ 157.05 (C_q), 156.99 (C_q), 156.89 (C_q), 156.35 (C_q), 153.82 (CH), 153.42 (CH), 152.12 (CH), 152.00 (CH), 151.81 (CH), 151.79 (CH), 149.66 (C_q), 148.13 (CH), 146.76 (C_q), 139.84 (CH), 139.49 (C_q), 138.04 (CH), 137.94 (CH), 134.34 (CH), 132.24 (CH), 130.59 (C_q), 129.73 (CH), 127.75 (CH), 127.66 (CH), 127.61 (CH), 127.56 (CH), 126.46 (C_q), 125.73 (CH), 125.57 (CH), 124.79 (CH), 124.52 (CH), 124.46 (CH), 124.41 (CH), 124.38 (CH), 124.29 (CH), 123.60 (CH), 122.68 (C_q), 121.35 (CH), 94.21 (C_q), 86.14 (C_q).

^{19}F NMR (377 MHz, acetone) δ -63.36 (s), -71.70 (s), -73.58 (s).

^{31}P NMR (162 MHz, acetone) δ -139.89.

HRMS (m/z, APCI$^+$, MeOH) $[M-(PF_6)_2]^{2+}$, $(C_{57}H_{40}F_3N_7Ru)^{2+}$, Calculated mass: 490.617527; Found: 490.618130.

6.4 Chapter 4

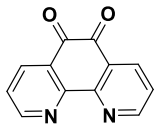

1,10-Phenanthroline (2.3 g, 12.76 mmol) and KBr (2.3 g, 19.32 mmol) were combined in a round bottom flask and cooled to 0 ^{o}C. Concentrated H_2SO_4 (35 mL) and HNO_3 (30 mL) were cooled in a separate flask and added dropwise to the solids. The reaction mixture was heated to 130 ^{o}C and stirred vigorously for 6 hours. The solution was cooled to room temperature and neutralized with NaOH. The resulting yellow precipitate was collected by filtration and washed with cold MeOH to give **L3** as a yellow crystalline powder (1.88 g, 70 % yield).

^{1}H NMR (400 MHz, $CDCL_3$) δ 9.14-9.12 (dd, 2H), 8.53-8.50 (dd, 2H), 7.61-7.63 (dd, 2H)

(ESI): m/z calcd. for $C_{12}H_6N_2O_2$[M+H]: 211.0502 found 211.0507

Intermediate 1

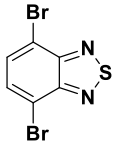

2,1,3-Benzthothiadiazole (0.5 g, 3.6 mmol) was placed under inert atmosphere and dissolved in HBr (10 mL, 36% aqueous sol.). Br_2 (0.5 mL, 9.71 mmol) in HBr (15 mL, 36% aqueous sol.) was added dropwise and the mixture refluxed at 130 ^oC for 6 hours. $NaHSO_3$ was added to neutralize the solution and quench remaining Br_2. The solution was filtered and the collected solid washed with deionized H_2O and minimum cold Et_2O. The solid was dissolved in CH_2Cl_2 and purified using silica column chromatography (CH_2Cl_2) to give **Intermediate 1** as an off-white solid (0.725 g, 67 % yield).

^{1}H NMR (400 MHz, $CDCL_3$) δ 7.73 (s, 2H)

(ESI): m/z calcd. for $C_6H_2Br_2N_2S$ [M+]: 291.8311 found 291.8319

Intermediate 2

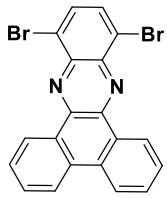

4,7-dibromobenzothiadiazole (**Intermediate 1**, 0.200 g, 0.68 mmol) and $NaBH_4$ (0.125 g, 3.3 mmol, 5 eq.) were combined in a 3 necked RBF and placed under inert atmosphere. 20 mL EtOH was added dropwise and the reaction refluxed for 3 hours. The solution was cooled, quenched with deionised water and acidified with conc. HCl. 1,10-Phenanthrenequinone (0.160 g, 0.79 mmol, 1.15 eq.) was dissolved in 10 mL EtOH and added to the solution, which was then stirred at reflux for 12 hours. The resulting yellow precipitate was isolated by filtration, washed with Et_2O and minimum CH_2Cl_2 to give **Intermediate 2** as a yellow solid (0.150 g, 50.3 % yield).

^{1}H NMR (400 MHz, $CDCl_3$) δ 9.48-9.47 (d, 2H) 8.58-8.56 (d, 2H), 8.03 (s, 2H), 7.85 (t, 2H), 7.78 (t, 2H)

HRMS (ESI): m/z calcd. for $C_{18}H_{11}Br_2N_2$ [M+]: 436.9283, found 436.9286

Intermediate 3

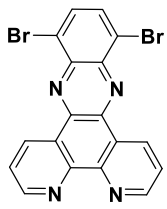

4,7-dibromobenzothiadiazole (**Intermediate 1**, 0.06 g, 0.2 mmol) and $NaBH_4$ (0.150 g, 4 mmol, 20 eq.) were combined in a 3 necked RBF and placed under inert atmosphere. 20 mL EtOH was added dropwise and the reaction refluxed for 30 hours. The solution was cooled, quenched with deionised water and acidified with conc. HCl. 1,10-phenanthroline-5,6-dione (0.042 g, 0.2 mmol, 1 eq.) was dissolved in 10 mL EtOH and added to the solution, which was then stirred at reflux for 12 hours. The resulting brown precipitate was isolated by filtration, washed with Et_2O and minimum CH_2Cl_2 to give **Intermediate 3** as a brown solid (0.073 g, 82 % yield).

^{1}H NMR (400 MHz, $CDCl_3$) δ 9.73-9.71 (dd, 2H), 9.33-9.32 (dd, 2H), 8.11 (s, 2H), 7.87-7.84 (dd, 2H)

(ESI): m/z calcd. for $C_{18}H_8Br_2N_4$ [M+H]: 438.9188 found 438.9192

NPhC

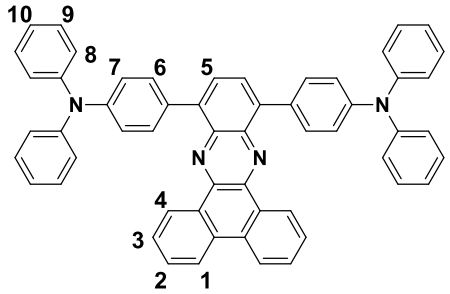

10,13-dibromodibenzophenazine (**Intermediate 2**, 0.150 g, 0.34 mmol), 4-(diphenylamino)phenylboronic acid (0.320 g, 1.1 mmol, 3.2 eq.) and $Pd(PPh_3)_4$ (0.060 g, 0.005 mmol) were combined in a RBF and placed under inert atmosphere. 4 mL of degassed Toluene:EtOH 1:1 were added along with 2 mL of an aqueous 2M Na_2CO_3 solution. The reaction was refluxed for 36 hours. Once cooled, the mixture was dissolved in CH_2Cl_2, washed with H_2O and saturated NaCl solution before being dried over $MgSO_4$. The crude fraction was purified via dry loading column chromatography (silica) CH_2Cl_2/MeOH (95:5) to give **NPhC** as a yellow crystalline solid (0.010 g, 4% yield).

^{1}H NMR (600 MHz, $CDCl_3$) δ 9.18 (d, 3J = 7.9 Hz, 2H, **1**), 8.57 (d, ^{3}J = 8.1 Hz, 2H, **4**), 8.00 (s, 2H, **5**), 7.92 (d, ^{3}J = 8.5 Hz, 4H, **7**) 7.78 (m, 2H, **2**) 7.70 (m, 2H, **3**) 7.34 (m, 12H**, 6** and **9**), 7.28 (m, 8H, **8**) 7.08 (t, J = 7.2 Hz, 4 H, **10**)

^{13}C NMR (151 MHz, $CDCl_3$) δ 148.0 (C_q), 147.6 (C_q), 141.3 (C_q), 140.4 (C_q), 139.1 (C_q), 132.8 (C_q), 132.4 (C_q), 132.2 (CH, **6**), 130.8 (Cq), 130.3 (CH, **2**), 129.5 (CH, **9**), 129.4 (CH, **5**), 128.2, (CH, **3**), 126.7 (CH, **1**), 124.8 (CH, **8**), 123.0 (CH, **10**), 122.9 (CH, **7**), 122.9 (CH,**4**) ppm.

(MALDI): m/z calcd. for $C_{56}H_{38}N_4$ [M+]:766.3096, found 766.3105

NPhNL

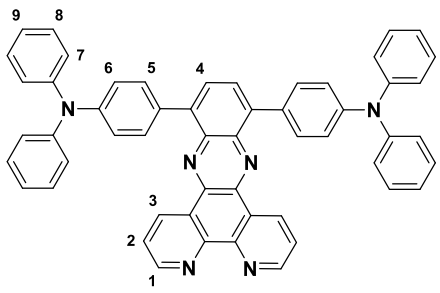

10,13-dibromodipyridophenazine (**Intermediate 3**, 0.150 g, 0.34 mmol), 4-(diphenylamino)phenylboronic acid (0.280 g, 0.96 mmol, 3 eq.) and $Pd(PPh_3)_4$ (0.060 g, 0.005 mmol) were combined in a RBF and placed under inert atmosphere. 4 mL of degassed Toluene:EtOH 1:1 were added along with a 2 mL of an aqueous 2M Na_2CO_3 solution. The reaction was refluxed for 36 hours. Once cooled, the mixture was dissolved in CH_2Cl_2, washed with water and brine before being dried over $MgSO_4$. The fraction was reduced and Et_2O was added. The resulting precipitate was isolated by filtration and washed with H_2O and Et_2O before being dissolved in CH_2Cl_2. The crude fraction was purified via dry loading column chromatography (silica) using CH_2Cl_2/MeOH (95:5) to give **NPhNL** as a red crystalline solid (0.120 g, 46 % yield).

^{1}H NMR (600 MHz, $CDCl_3$) δ 9.52 (d, J = 7.8 Hz, 2H, **1**), 9.42 (d, J = 7.8 Hz, 2H, **3**), 8.11 (s, 2H, **4**), 7.90 (d, J = 7.7 Hz, 2H, **2**), 7.86 (d, J = 8.6 Hz, 4H, **5**), 7.34 (m, **8 and 6**, 12H) 7.28 (m, 8H, **7**), 7.11 (t, J = 7.2 Hz, 4H, **9**)

^{13}C NMR (151 MHz, $CDCl_3$) 147.9, (C_q), 147.6 (C_q), 140.8 (C_q), 139.2 (C_q), 131.9 (CH **5**), 131.6 (C_q), 130.8 (CH, **4**), 129.4 (CH, **8**), 124.9 (CH, **7**), 123.4 (CH, **9**), 122.5 (CH, **6**)

(MALDI): m/z calcd. for $C_{54}H_{36}N_6$ [M+]:768.3001, found 768.3019

CzC

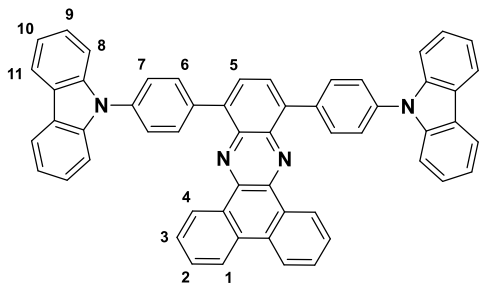

10,13-dibromodibenzophenazine (**Intermediate 2**, 0.200 g, 0.26 mmol), 4-(9H-Carbazol-9-yl)benzeneboronic acid (0.350 g, 1.22 mmol 4.69 eq.) and $Pd(PPh_3)_4$ (0.080 g, 0.007 mmol) were combined in a RBF and placed under inert atmosphere. 4 mL of degassed Toluene:EtOH 1:1 were added along with 2 mL of an aqueous 2M Na_2CO_3 solution. The reaction was refluxed for 36 hours. Once cooled, the mixture was dissolved in CH_2Cl_2, washed with H_2O and saturated NaCl solution before being dried over $MgSO_4$. The fraction was reduced and Et_2O was added. The resulting precipitate was isolated by filtration and washed with H_2O and Et_2O before being dissolved in CH_2Cl_2. The crude fraction was purified via dry loading column chromatography (silica) starting with EtOAc and swapping to CH_2Cl_2/MeOH (95:5) to give **CzC** as an orange/red crystalline solid (0.110 g, 56 % yield).

^{1}H NMR (600 MHz, $CDCl_3$) δ 9.24 (d, J = 7.9 Hz, 2H, **1**,), 8.60 (d, J = 8.0 Hz, 2H, **4**), 8.29 (d, J = 7.9 Hz, 4H, **6**), 8.22 (m, 6H, **5 and 11**), 7.88 (d, J = 7.9 Hz, 4H, **7**), 7.81 (m, 2H, **2**), 7.73 (m, 2H, **3**), 7.69 (d, J = 8.2 Hz, 4H, **8**), 7.52 (m, 4H, **9**), 7.36 (m, 4H, **10**)

^{13}C NMR (151 MHz, $CDCl_3$) δ 141,9 (C_q), 141.1 (C_q), 140.3 (C_q), 139.6 (C_q), 137.8 (C_q), 137.4 (C_q), 132.8 (CH, **6**), 132.5 (C_q), 130.7 (CH, **2**), 130.6 (C_q), 123.0 (CH, **5**), 128.3 (CH, **3**), 126.7 (CH, **1**), 126.6 (CH, **7**), 126.2 (CH, **9**), 123.7 (C_q), 123.2 (CH, **4**), 120.6 (CH, **11**), 120.2 (CH, **10**), 110.2 (CH, **8**)

(MALDI): m/z calcd. for $C_{56}H_{34}N_4$ [M+]:762.2783, found 762.2808

CzNL

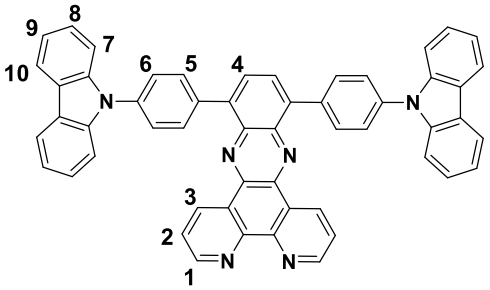

10,13-dibromodipyridophenazine (**Intermediate 3**, 0.200 g, 0.26 mmol), 4-(9H-Carbazol-9-yl)benzeneboronic acid (0.326 g, 1.14 mmol, 4.45 eq.) and $Pd(PPh_3)_4$ (80 mg, 0.007 mmol) were combined in a RBF and placed under inert atmosphere. 4 mL of degassed Toluene:EtOH 1:1 were added along with 2 mL of an aqueous 2M Na_2CO_3 solution. The reaction was refluxed for 36 hours. Once cooled, the mixture was dissolved in CH_2Cl_2, washed with H_2O and saturated NaCl solution before being dried over $MgSO_4$. The solution was reduced and Et_2O was added. The resulting precipitate was isolated by filtration and washed with H_2O and Et_2O before being redissolved in CH_2Cl_2. The crude fraction was purified via dry loading column chromatography (silica) starting with EtOAc and swapping to CH_2Cl_2/MeOH (95:5) to give **CzNL** as an orange/red crystalline solid (100 mg, 50 % yield).

^{1}H NMR (600 MHz, $CDCl_3$) δ 9.46 (d, J = 7.9 Hz, 2H, **1**), 9.29 (s, 2H, **3**), 8.25 (m, 10H, **4, 10** and **6**), 7.90 (d, J = 8.0 Hz, 4H, **5**), 7.79 (dd, J = 7.8, 4.4 Hz, 2H, **2**), 7.68 (d, J = 8.2Hz, 4H, **7**), 7.62 (m, 4H, **8**), 7.37 (m, 4H, **9**)

^{13}C NMR (151 MHz, $CDCl_3$) δ 152.91 (CH, **3**), 141.0 (C_q), 140.7 (C_q), 140.6 (C_q), 139.8 (C_q), 137.8 (C_q), 137.4 (C_q), 134.3 (CH, **1**), 132.8 (C_q), 132.7 (CH, **5**), 130.9 (CH, **4**), 127.9 (C_q), 126.7 (CH, **6**), 126.2 (CH, **8**), 124.6 (CH, **2**), 123.8 (C_q), 120.6 (CH, **10**), 120.4 (CH, **9**), 110.1 (CH, **7**)

(MALDI): m/z calcd. for $C_{54}H_{32}N_6$ [M+H]:765.2767, found 765.2767

NPhNRu

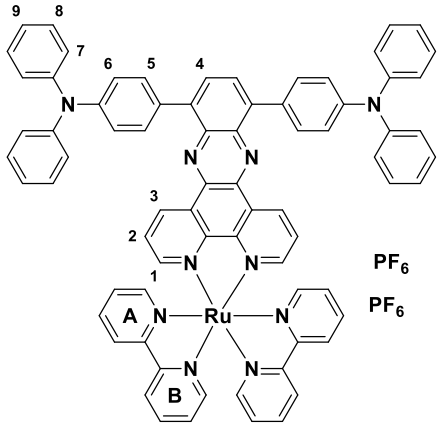

[Ru(2,2'-bipyridine)$_2$Cl$_2$] (0.012 g, 0.025 mmol) and 4,4'-(dipyridophenazine-10,13-diyl)bis(N,N-diphenylaniline) (0.020 mg, 0.026 mmol) were combined in ethylene glycol (6 mL) in a specialised sealed snap-cap vial. The vial was placed in a CEM Discover S-Class Single Mode Microwave reactor and heated to 160 °C for 1 hour (150 W) under pressure. Upon cooling, the ethylene glycol solution was added to a saturated aqueous KPF_6 solution and the resulting precipitate washed with H_2O. The crude was purified by column chromatography (silica) using CH_3CN:H_2O:sat. KNO_3 (90:9:1). The first red fraction was collected, reduced and the product precipitated out of solution using saturated KPF_6 solution to give **NPhNRu** as a black solid (0.015 mg, 40 % yield)

^{1}H NMR (600 MHz,CD_3CN) δ 9.37 (dd, J = 8.1, 1.0 Hz, 2H, **3**), 8.57 (d, J = 8.2 Hz, 2H, **A**), 8.53 (d, J = 8.0 Hz, 2H, **B**), 8.21 (s, 2H, **4**), 8.15 (dd, J = 5.2, 1 Hz, 2H, **1**) 8.12 (m, 2H, **A**), 8.01 (dd, J = 11.4, 4.4 Hz, 2H, **B**), 7.90 (d, J = 8.7 Hz, 2H, **5**), 7.85 (m, 4H, **A** and **2**), 7.72 (d, J = 5.0 Hz, 2H, **B**), 7.46 (m, 2H, **A**), 7.37(m, 8H, **8**), 7.25 (m, 6H, **6** and **B**), 7.22 (m, 8H, **7**) 7.16-7.10 (m, 4 H, **9**)

^{13}C NMR (151 MHz, CD_3CN) δ 158.1 (C_q), 158.0 (C_q), 154.5 (CH, **1**), 153.0 (CH, **B**), 153.0 (CH, **A**), 151.5 (C_q), 148.9 (C_q), 141.9 (C_q), 140.1 (C_q), 139.8 (C_q), 139.0 (CH, **A**), 138.9 (CH, **B**), 134.6 (CH, **3**), 132.9 (CH, **5**), 132.5 (CH, **4**), 132.4 (C_q), 132.0 (C_q), 130.6 (CH, **8**), 128.6 (CH, **A**), 128.5 (CH, **2**), 128.4 (CH, **B**), 125.8 (CH, **7**), 125.3 (CH, **A**), 125.3 (CH, **B**), 124.6 (CH, **9**), 123.2 (CH, **6**).

HRMS (MALDI): m/z calcd. for $C_{74}H_{52}N_{10}F_6PRu$ [M+]:1327.3062, found 1327.3068

CzNRu

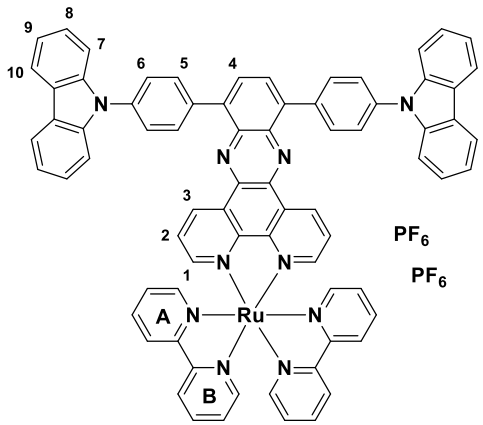

[Ru(2,2'-bipyridine)$_2$Cl$_2$] (0.024 g, 0.05 mmol) and 4,4'-(dipyridophenazine-10,13-diyl)bis(9-H carbazole) (0.040 mg, 0.052 mmol) were combined in ethylene glycol (6 mL) in a specialised sealed snap-cap vial. The vial was placed in a CEM Discover S-Class Single Mode Microwave reactor and heated to 160 °C for 1 hour (150 W) under pressure. Upon cooling, the ethylene glycol solution was added to a saturated aqueous KPF_6 solution and the resulting precipitate washed with H_2O. The crude was purified by column chromatography (silica) using CH_3CN:H_2O:sat. KNO_3 (90:9:1). The first red

fraction was collected, reduced and the product precipitated out of solution using saturated KPF_6 solution to give **CzNRu** as an orange solid (0.028 mg, 75 % yield).

^{1}H NMR (600 MHz,CD_3CN) δ 9.47(dd, J = 8.2, 1.2 Hz, 2H, **3**), 8.54 (d, J = 8.3 Hz, 2H, **A**), 8.51 (d, J = 8.2 Hz, 2H, **B**), 8.48 (s, 2H, **4**), 8.32 (d, J = 8.3 Hz, 4H, **5**), 8.26 (d J= 7.8, 4H, **10**), 8.16 (dd, J = 5.3, 1.2 Hz, 2H, **1**), 8.11 (td, J = 8.0, 1.4 Hz, 2H, **A**), 8.01 (td, J =8.0, 1.4 Hz, 2H, **B**), 7.95 (d, J = 8.3 Hz, 4H, **6**), 7.87 (m, 4H, **2** and **A**), 7.74 (d, J = 5.3 Hz, 2H, **B**), 7.67 (d, J = 8.3 Hz, 4H, **7**), 7.53 (dd, J = 10.9, 3.8 Hz, 4H, **8**), 7.45 (dd, J = 9.6, 3.7 Hz, 2H, **A**), 7.36 (dd, J = 10.9, 3.8 Hz, 4H **9**), 7.26 (dd, J = 9.8, 3.6 Hz, 2H, **B**)

^{13}C NMR (151 MHz, CD_3CN) δ 158.2 (C_q,), 158.0 (C_q), 154.7 (CH, **1**), 153.1 (CH, **B**), 153.0 (CH, **A**), 151.7 (C_q), 141.8 (C_q), 141.7 (C_q), 140.5 (C_q), 140.2 (C_q), 139.0 (CH, **A**), 138.9 (CH**, B**), 138.4 (C_q), 137.8 (C_q), 134.8 (**3**), 133.7 (Ch, **5**), 133.3 (CH, **4**), 128.6 (CH, **2** and **A**), 128.5 (CH, **B**), 127.6 (CH, **6**), 127.3 (CH, **8**), 125.3 (CH, **A**), 125.3 (CH, **B**), 124.4 (C_q), 121.4 (CH, **10**), 121.3 (CH, **9**), 110.9 (CH, **7**).

HRMS (MALDI): m/z calcd. for $C_{74}H_{48}N_{10}F_6PRu$ [M+]:1323.2749, found 1323.2771

NPhNIr

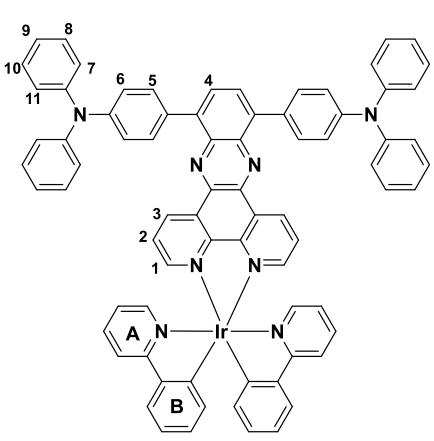

$[Ir(ppy)_2Cl_2]_2$ (0.020g, 0.018mmol) and 10,13-triphenylaminedipyridophenazine (0.0286g, 0.0371mmol) were added to $CHCl_3$ (4mL). The solution was refluxed overnight. Once cooled, the solution was washed with deionised water, dried over $MgSO_4$ and filtered. The resulting solid was dissolved in CH_2Cl_2 and subjected to column chromatography (silica) using CH_2Cl_2/MeOH (98:2) to give a purple crystalline solid (0.022g, 47% yield)

^{1}H NMR (600MHz, DMSO) δ 9.41 (dd, J=1.4, 1.5Hz, 2H; **3**), 8.29-8.27 (m, 6H; **1, 4** and **A**), 8.21 (dd, J=5.4, 5.2Hz 2H; **2**), 7.97 (d, J= 7.7Hz, 2H; **B**), 7.93 (d, J=8.7Hz, 4H; **5**), 7.90 (m, 2H; **A**), 7.64 (d, J= 5.3Hz, 2H; **A**), 7.38 (m, 8H; **8,10**), 7.22 (d, J-8.7Hz, 4H; **6**), 7.18 (dd, J= 8.8, 8.4Hz, 8H, **7,11**), 7.13 (t, J= 7.7Hz, 4H; **9**), 7.08 (t, J= 7.5Hz, 2H, **B**), 7.02 (t, 7.3Hz, 2H, **A**), 6.97 (t, 7.5Hz, 2H, **B**) 6.30 (d, J=7.2Hz, 2H; **B**) ppm.

^{13}C NMR (151MHz, DMSO) δ 167.25 (C_Q), 152.07 (CH, **1**), 150.06 (C_Q), 149.92 (CH, **A**), 147.72 (C_Q), 147.48 (C_Q), 144.47 (C_Q), 140.45 (C_Q), 139.29 (CH, **A**) 139.18 (C_Q), 138.76 (C_Q), 135.50 (CH, **3**), 132.41 (CH, **5**), 131.80 (CH, **4**), 131.67 (CH **B**), 131.55 (C_Q), 131.33 (C_Q), 130.78 (CH **B**), 130.18 (CH, **7/11**), 129.18 (CH **2**), 125.61 (CH **B**), 125.02 (CH, **10/8**), 124.28 (CH **A**), 124.03 (CH, **9**), 122.98 (CH **B**), 122.47 (CH, **6**), 120.50 (CH, **A)** ppm.

HRMS (m/z) Calculated [M] $(C_{76}H_{52}N_8Ir)^+$ Calc.: 1269.39, found: 1269.388

CzNIr

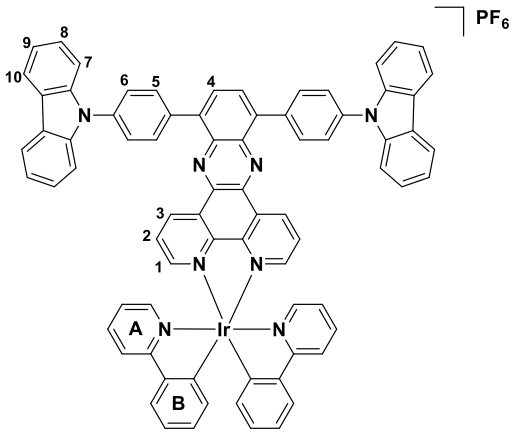

$[Ir(ppy)_2Cl_2]_2$ (0.020g, 0.018mmol) and 10,13-dicarbazoledipyridophenazine (0.0285g, 0.0372mmol) were added to $CHCl_3$ (4mL). The solution was refluxed overnight. Once cooled, the solution was washed with deionised water, dried over $MgSO_4$ and filtered. The resulting liquid was evaporated. This was then dissolved in methanol and aqueous solution of KPF_6. This was then washed again and dried over $MgSO_4$, filtered and evaporated using rotavap. The resulting solid was dissolved in CH_2Cl_2 and subjected to column chromatography (silica) using CH_2Cl_2/MeOH (98:2) to give deep orange crystalline solid (0.015g, 32% yield)

^{1}H NMR (400MHz, C_2D_6CO) δ 9.75 (d, J=8.2 Hz, 2H; **3**), 8.59 (s, 2H; **4**), 8.54 (d, J=3.8 Hz, 2H,**1**), 8.44 (d. J=8.4Hz, 4H; **5)**, 8.29 (m, 6H **A** and **10**), 8.21 (dd, J=8.2, 5.2 Hz, 2H, **2**), 8.06-7.92 (m, 8H, **A**/**B**/**6**), 7.89 (d, J=5.9 Hz, 2H, **A**), 7.67 (d, J=8.2 Hz, 4H, **7**), 7.51 (t, J=7.6 Hz, 4H, **8**), 7.36 (t, J=7.5 Hz, 4H, **9**), 7.11 (t, J=7.3 Hz, 2H, **B**), 7.05 (t, J=6.5 Hz, 2H, **A**), 7.00 (t, J=7.6 Hz, 2H, **B**), 6.47 (d, J=7.6 Hz, 2H, **B**)

^{13}C NMR (151MHz, C_2D_6CO) δ 167.80, 152.57 (CH, **1**), 150.17, 149.56 (CH **A**), 144.23, 140.80, 140.66, 139.63, 139.29, 138.73 (CH **A/B**), 137.55, 135.69 (CH **3**), 132.77 (CH **5**), 132.26 (CH **4**), 131.75 (CH **B**), 131.30, 130.45 (CH **B**), 128.64 (CH **2**), 126.45 (CH **6**), 126.21 (CH **8**), 125.01 (CH **A/B**), 123.58, 123.52 (CH **A**), 122.73 (CH **B**), 120.44 (CH **10**), 120.30 (CH **9**), 119.95 (CH **A**), 109.84 (CH **7**)

HRMS (m/z) Calculated [M] ($C_{76}H_{48}N_8Ir$) Calc.: 1265.36, found: 1265.36.

6.5 Chapter 5

PhPicL

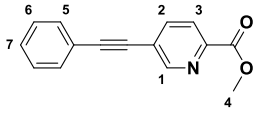

Methyl-5-bromopicolinate (0.216 g, 1 mmol) and phenylacetylene (1 g, 0.95 mL, 9.8 mmol, 10 eq.) were suspended in tetrahydrofuran (5 mL) with triethylamine

(0.3 mL) and $Pd(PPh_3)_4$ (0.040 g, 0.035 mmol) and heated to 60 °C for 16 hours. After cooling, the solvent was removed by rotary evaporator, with the resulting solid dissolved in CH_2Cl_2 and washed with 3 x 50 mL water. The organic fraction was dried over Mg_2SO_4 and concentrated. The product was isolated by silica column chromatography using a 20:80 Ethyl Acetate : Petroleum Ether mobile phase. The product eluted as a colourless, blue fluorescing band, and was precipitated using hexanes. The product was dried by filtration (100 mg, 42 % yield).

^{1}H NMR (400 MHz, $CDCl_3$) δ 8.86 (dd, *J* = 2.1, 0.7 Hz, 1H, **1**), 8.13 (dd, *J* = 8.1, 0.8 Hz, 1H, **3**), 7.95 (dd, *J* = 8.1, 2.1 Hz, 1H, **2**), 7.61 – 7.53 (m, 2H, **5**), 7.45 – 7.34 (m, 3H, **6** and **7**), 4.03 (s, 3H, **4**).

^{13}C NMR (101 MHz, $CDCl_3$) δ 165.41 ($C_{c=o}$), 152.19 (CH), 146.22 (C_q), 139.44 (CH), 132.00 (CH), 129.47 (CH), 128.69 (CH), 124.66 (CH), 124.17 (C_q), 122.12 (C_q), 95.82 (C_q), 85.55 (C_q), 53.17 (CH_3).

HRMS (m/z APCI$^+$, CH_2Cl_2): [M + Na] ($C_{15}H_{11}NNaO_2$) Calc. 260.0682 Found 260.0688

NPhPicL

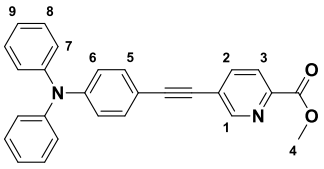

Methyl-5-bromopicolinate (0.216 g, 1 mmol) and 4-ethynyl-diphenylaniline (0.280 g, 1.04 mmol, 1 eq.) were suspended in tetrahydrofuran (5 mL) with triethylamine (0.3 mL) and $Pd(PPh_3)_4$ (0.040 g, 0.035 mmol) and heated to 60 °C for 16 hours. After cooling, the solvent was removed by rotary evaporator, with the resulting solid dissolved in CH_2Cl_2 and washed with 3 x 50 mL water. The organic fraction was dried over Mg_2SO_4 and concentrated. The product was isolated by silica column chromatography using a 20:80 Ethyl Acetate : Heptane mobile phase. The product eluted as a light yellow, blue fluorescing band, and was precipitated using hexanes. The product was dried by filtration (0.140 g, 34 % yield).

^{1}H NMR (400 MHz, $CDCl_3$) δ 8.82 (d, *J* = 1.7 Hz, 1H, **1**), 8.11 (d, *J* = 8.1 Hz, 1H, **3**), 7.90 (dd, *J* = 8.1, 2.1 Hz, 1H, **2**), 7.39 (d, *J* = 8.7 Hz, 2H, **5**), 7.33 – 7.27 (m, 4H, **7/8**), 7.11 (dd, *J* = 18.0, 7.5 Hz, 6H, **7/8** and **9**), 7.01 (d, *J* = 8.8 Hz, 2H, **6,**), 4.02 (s, 3H, **4)**

^{13}C NMR (151 MHz, $CDCl_3$) δ 165.50 ($C_{c=o}$), 152.00 (CH), 149.04 (C_q), 147.05 (C_q), 145.74 (C_q), 139.08 (CH), 133.01 (CH), 129.66 (CH), 125.51 (CH), 124.66 (CH), 124.64 (C_q), 124.15 (CH), 121.74 (CH), 114.28 (C_q), 96.62 (C_q), 84.99 (C_q), 53.13 (CH_3).

HRMS (m/z APCI$^+$, CH_2Cl_2): [M + Na] ($C_{27}H_{20}N_2NaO_2$) Calc. 427.1417 Found 427.1422

DeprotPic

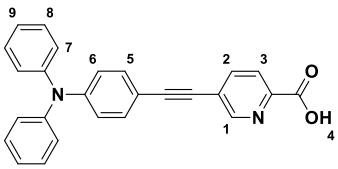

Methyl 5-((4-(diphenylamino)phenyl)ethynyl)picolinate (**NPhPicL**, 0.800 g, 0.25 mmol) and NaOH (1 g, 25 mmol) were suspended in THF and stirred at room temperature for 16 hours. The THF was removed by rotary evaporator and the resulting solids suspended in CH_2Cl_2, followed by a 3 x 150 mL water wash. The organic phase was dried over Mg_2SO_4 and concentrated, after which the product was precipitated with hexanes and isolated by filtration as a white powder (0.037 g, 48 % yield).

^{1}H NMR (600 MHz, $CDCl_3$) δ 8.72 (s, 1H, **1**), 8.21 (d, *J* = 7.9 Hz, 1H, **3**), 8.01 (d, *J* = 7.8 Hz, 1H, **2**), 7.41 (d, *J* = 8.7 Hz, 2H, **6**), 7.34 – 7.30 (m, 3H, **7/8**), 7.16 (dd, *J* = 8.5, 0.9 Hz, 3H, **7/8**), 7.12 (dt, *J* = 8.3, 1.0 Hz, 2H, **9**), 7.03 (d, *J* = 8.7 Hz, 2H, **5**).

^{13}C NMR (151 MHz, $CDCl_3$) δ 163.93 (C_q), 150.35 (CH), 149.26 (C_q), 146.96 (C_q), 143.82 (C_q), 140.27 (CH), 133.07 (C_q), 129.68 (CH), 125.78 (C_q), 125.59 (CH), 124.27 (CH), 123.34 (CH), 121.57 (CH), 113.83 (C_q), 97.58 (C_q), 84.51 (C_q).

PyrPicL

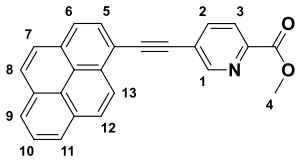

Methyl-5-bromopicolinate (0.216 g, 1 mmol) and 1-ethynylpyrene (0.226 g, 1.04 mmol, 1 eq.) were suspended in tetrahydrofuran (5 mL) with triethylamine (0.3 mL) and $Pd(PPh_3)_4$ (0.040 g, 0.035 mmol) and heated to 60 ^{o}C for 16 hours. After cooling, the solvent was removed by rotary evaporator, with the resulting solid dissolved in CH_2Cl_2 and washed with 3 x 50 mL water. The organic fraction was dried over Mg_2SO_4 and concentrated. The product was isolated by silica column chromatography using a 20:80 Ethyl Acetate : Heptane mobile phase. The product eluted as a light yellow, blue fluorescing band, and was precipitated using hexanes. The product was dried by filtration (0.072 g, 20 % yield).

^{1}H NMR (400 MHz, $CDCl_3$) δ 9.04 – 9.01 (m, 1H, **1**), 8.63 (d, *J* = 9.1 Hz, 1H, **HPyr**), 8.32 – 8.03 (m, 10H, **HPyr**, **2** and **3**), 4.06 (s, 3H, **4**).

^{13}C NMR (101 MHz, $CDCl_3$) δ 165.47 (C_q), 152.17 (CH), 146.25 (C_q), 139.45 (CH), 132.37 (C_q), 132.22 (C_q), 131.36 (C_q), 131.13 (C_q), 130.07 (CH), 129.08 (CH), 128.98 (CH), 127.37 (CH), 126.62 (CH), 126.22 (C_q), 126.18 (CH), 125.27 (CH), 124.80 (C_q), 124.76 (CH), 124.61 (C_q), 124.44 (C_q), 124.38 (C_q), 116.33 (C_q), 95.28 (C_q), 91.11 (C_q).

HRMS (m/z APCI^{+}, CH_2Cl_2): [M + Na] ($C_{25}H_{15}NNaO_2$) Calc. 384.0995 Found 384.1004

PhPicIr

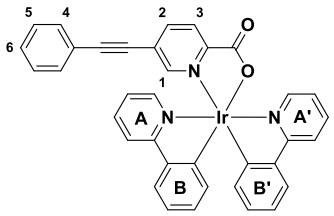

Methyl 5-(phenylethynyl)picolinate (**PhPicL**, 0.030 g, 0.125 mmol), K_2CO_3 (0.040 g, 0.29 mmol), $[Ir(ppy)_2Cl]_2$ (0.070 g, 0.065 mmol) were suspended in acetone (5 mL) and heated at 55 ^{o}C for 16 hours under an argon atmosphere. After cooling, the solvent was removed by rotary evaporator, with the resulting solid dissolved in CH_2Cl_2 and washed with 3 x 50 mL water. The organic fraction was dried over Mg_2SO_4 and concentrated. The product was isolated by silica column chromatography using a acetone : Petroleum Ether mobile phase gradient, increasing the acetone fraction from 1 : 4 to neat, with the product eluting in the latter solvent system. The product eluted as a yellow/orange band, and was precipitated using hexanes (0.032 g, 70 % yield).

^{1}H NMR (600 MHz, CD3CN) δ 8.63 – 8.58 (m, 1H, **A**), 8.16 (dt, J = 3.9, 2.0 Hz, 1H, **3**), 8.06 (m, 3H, **A**, **A'** and **2**), 7.91 – 7.82 (m, 2H, **A'** and **A**), 7.78 (d, J = 1.3 Hz, 1H, **1**), 7.73 (ddd, J = 10.6, 7.7, 3.7 Hz, 3H, **A'**, **B** and **B'**), 7.49 – 7.37 (m, 5H, **4**, **5** and **6**), 7.27 (ddd, J = 7.3, 5.8, 1.3 Hz, 1H, **A**), 7.11 (ddd, J = 7.3, 5.8, 1.4 Hz, 1H, **A'**), 6.99 – 6.92 (m, 1H, **B**), 6.90 (dd, J = 11.4, 4.8 Hz, 1H **B'**), 6.82 (td, J = 7.4, 1.3 Hz, 1H, **B**), 6.76 (td, J = 7.4, 1.3 Hz, 1H, **B'**), 6.36 (dd, J = 7.6, 0.8 Hz, 1H, **B**), 6.17 – 6.12 (m, 1H, **B'**).

^{13}C NMR (151 MHz, CD_3CN) δ 172.62 ($C_{c=o}$), 169.08 (C_q), 168.41 (C_q), 151.76 (CH), 151.14 (C_q), 150.39 (C_q), 150.01 (CH), 149.24 (CH), 147.84 (C_q), 145.67 (C_q), 145.43 (C_q), 141.48 (CH), 139.01 (CH), 138.97 (CH), 133.33 (CH), 133.22 (CH), 132.63 (CH), 130.84 (CH), 130.72 (CH), 130.27 (CH), 129.77 (CH), 128.51 (CH), 125.69 (CH), 125.17 (CH), 124.07 (CH), 123.82 (CH), 122.56 (CH), 122.34 (CH), 122.29 (C_q), 120.24 (CH), 120.16(CH), 96.25 (C_q), 85.00 (C_q).

HRMS (m/z APCI$^+$, CH_2Cl_2): [M + Na] ($C_{36}H_{24}N_3IrNaO_2$) Calc. 746.1392 Found 746.1412

NPhPicIr

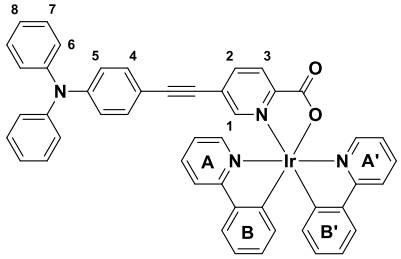

Methyl 5-((4-(diphenylamino)phenyl)ethynyl)picolinate (**NPhPicL**, 0.050 g, 0.125 mmol), K_2CO_3 (0.040 g, 0.29 mmol), $[Ir(ppy)_2Cl]_2$ (0.070 g, 0.065 mmol) were suspended in acetone (5 mL) and heated at 55 °C for 16 hours under an argon atmosphere. After cooling, the solvent was removed by rotary evaporator, with the resulting solid dissolved in CH_2Cl_2 and washed with 3 x 50 mL water. The organic fraction was dried over Mg_2SO_4 and concentrated. The product was isolated by silica column chromatography using a acetone : Petroleum Ether mobile phase gradient, increasing the acetone fraction from 1 : 4 to neat, with the product eluting in the latter solvent system. The product eluted as a yellow/orange band, and was precipitated using hexanes (0.029 g, 50 % yield).

^{1}H NMR (600 MHz, CD_3CN) δ 8.60 – 8.59 (m, 1H **A**), 8.14 – 8.12 (m, 1H, **3**), 8.02 (m, 3H, **A**, **A'** and **2**), 7.88 – 7.85 (m, 1H **A'**), 7.85 – 7.81 (m, 1H, **A**), 7.72 (m, 4H, **1**, **A'**, **B** and **B'**), 7.36 – 7.31 (m, 4H, **6**/**7**), 7.29 – 7.24 (m, 3H, **4** and **A**), 7.16 – 7.08 (m, 7H, **6**/**7**, **8** and **A'**), 6.96 – 6.92 (m, 1H, **B**), 6.92 – 6.86 (m, 3H, **5** and **B'**), 6.83 – 6.77 (m, 1H, **B**), 6.75 (td, *J* = 7.5, 1.3 Hz, 1H, **B'**), 6.35 (dd, *J* = 7.7, 1.0 Hz, 1H, **B**), 6.13 (dd, *J* = 7.6, 1.0 Hz, 1H, **B'**).

^{13}C NMR (151 MHz, CD_3CN) δ 172.83 ($C_{c=o}$), 169.08 (C_q), 168.40 (C_q), 151.19 (C_q), 150.91 (CH), 150.43 (C_q), 150.23 (C_q), 150.01 (CH), 149.23 (CH), 147.86 (C_q), 147.73 (C_q), 145.68 (C_q), 145.42 (C_q), 141.10 (CH), 139.02 (CH), 138.97 (CH), 133.76 (CH), 133.30 (CH), 133.24 (CH), 130.84 (CH), 130.68 (CH), 130.27 (CH), 128.48 (CH), 126.57 (CH), 126.23 (C_q), 125.69 (CH), 125.45 (CH), 125.18 (CH), 124.08 (CH), 123.82 (CH), 122.56 (CH), 122.33 (CH), 121.77 (CH), 120.24 (CH), 120.16 (CH), 114.04 (C_q), 97.21 (C_q), 84.40 (C_q).

PyrPicIr

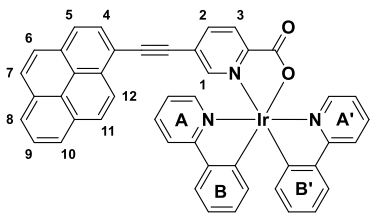

Methyl 5-(pyren-1-ylethynyl)picolinate (**PyrPicL**, 0.045 g, 0.125 mmol), K_2CO_3 (0.040 g, 0.29 mmol), $[Ir(ppy)_2Cl]_2$ (0.070 g, 0.065

mmol) were suspended in acetone (5 mL) and heated at 55 ºC for 16 hours under an argon atmosphere. After cooling, the solvent was removed by rotary evaporator, with the resulting solid dissolved in CH_2Cl_2 and washed with 3 x 50 mL water. The organic fraction was dried over Mg_2SO_4 and concentrated. The product was isolated by silica column chromatography using a acetone : Petroleum Ether mobile phase gradient, increasing the acetone fraction from 1 : 4 to neat, with the product eluting in the latter solvent system. The product eluted as a yellow/orange band, and was precipitated using hexanes (0.019 g, 35 % yield).

^{1}H NMR (400 MHz, $CDCl_3$) δ 8.85 (d, *J* = 5.0 Hz, 1H **A**), 8.39 (dd, *J* = 8.3, 6.6 Hz, 2H, **HPyr**), 8.29 (dd, *J* = 11.6, 7.6 Hz, 2H, **3** and **HPyr**), 8.24 – 8.06 (m, 7H, **2** and **HPyr**), 8.03 (d, *J* = 1.4 Hz, 1H, **1**), 7.97 – 7.90 (m, 2H, **A** and **A'**), 7.82 – 7.70 (m, 3H, **A**, **A'** and **B**), 7.64 (t, *J* = 7.1 Hz, 2H, **A'** and **B'**), 7.23 – 7.15 (m, 1H, **A**), 7.07 (t, *J* = 7.0 Hz, 1H **A'**), 7.04 – 6.98 (m, 1H **B**), 6.97 – 6.88 (m, 2H **B** and **B'**), 6.80 (dd, *J* = 7.4, 6.2 Hz, 1H, **B'**), 6.52 (d, *J* = 6.8 Hz, 1H **B**), 6.24 (d, *J* = 6.8 Hz, 1H **B'**).

^{13}C NMR (101 MHz, $CDCl_3$) δ 172.66 (C_q), 169.34 (C_q), 167.91 (C_q), 150.72 (CH), 149.18 (CH), 148.84 (C_q), 148.35 (CH), 147.08 (C_q), 144.30 (C_q), 144.23 (C_q), 139.66 (CH), 137.40 (CH), 132.82 (CH), 132.59 (CH), 132.46 (C_q), 132.41 (C_q), 131.32 (C_q), 131.02 (C_q), 130.34 (CH), 129.87 (CH), 129.80 (CH), 129.18 (CH), 128.00 (CH), 127.33 (CH), 126.71 (CH), 126.32 (CH), 125.44 (C_q), 124.92 (CH), 124.72 (CH), 124.56 (C_q), 124.28 (CH), 122.42 (CH), 122.25 (CH), 121.83 (CH), 121.44 (CH), 119.26 (CH), 118.85 (CH), 115.61 (C_q), 95.94 (C_q), 90.04 (C_q).

7 References

1 D. J. Kennett and B. Winterhalder, *Behavioral ecology and the transition to agriculture*, University of California Press, Berkeley, California, 2006.

2 S. S. Tasnim, M. M. Rahman, M. M. Hasan, M. Shammi and S. M. Tareq, *Heliyon*, 2022, **8**.

3 R. Wengenmayr and T. Bührke, *Renewable Energy: Sustainable Concepts for the Energy Change: Second Edition*, Wiley-VCH, Germany 2013.

4 M. Victoria, N. Haegel, I. M. Peters, R. Sinton, A. Jäger-Waldau, C. del Cañizo, C. Breyer, M. Stocks, A. Blakers, I. Kaizuka, K. Komoto and A. Smets, *Joule*, 2021, **5**, 1041–1056.

5 J. Zhao, W. Wu, J. Sun and S. Guo, *Chem. Soc. Rev.*, 2013, **42**, 5323–5351.

6 S. Chu, W. Li, Y. Yan, T. Hamann, I. Shih, D. Wang and Z. Mi, *Nano Futures*, 2017, **1**.

7 B. Matt, J. Fize, J. Moussa, H. Amouri, A. Pereira, V. Artero, G. Izzet and A. Proust, *Energy Environ. Sci.*, 2013, **6**, 1504–1508.

8 K. K. W. Lo, A. W. T. Choi and W. H. T. Law, *Dalton Trans.*, 2012, **41**, 6021–6047.

9 Y. Huang, K. Li, J. Zhou, J. Guan, F. Zhu, K. Wang, M. Liu, W. Chen and N. Li, *Chem. Eng. J.*, 2022, **439**, 135744.

10 *WCRF International*, 2022.

11 L. Barazzuol, R. P. Coppes and P. van Luijk, *Mol. Oncol.*, 2020, **14**, 1538–1554.

12 B. P. Cabral, M. da G. D. Fonseca and F. B. Mota, *Oncotarget*, 2018, **9**, 30474–30484.

13 S. Chakraborty and T. Rahman, *Ecancermedicalscience*, 2012, **6**, ed16.

14 R. Oun, Y. E. Moussa and N. J. Wheate, *Dalton Trans.*, 2018, **47**, 6645–6653.

15 M. G. Vander Heiden, *Nat. Rev. Drug Discov.*, 2011, **10**, 671–684.

16 C. Yewale, D. Baradia, I. Vhora, S. Patil and A. Misra, *Biomaterials*, 2013, **34**, 8690–8707.

17 Q. Pan, Q. Li, S. Liu, N. Ning, X. Zhang, Y. Xu, A. E. Chang and M. S. Wicha, *Stem Cells*, 2015, **33**, 2085–2092.

18 Z.-B. Xu, F.-Q. Yu, F. Wu, H. Zhang, K. Wang and X.-L. Zhang, *J. Porphyr. Phthalocyanines*, 2015, **19**, 1046–1052.

19 H. Huang, B. Yu, P. Zhang, J. Huang, Y. Chen, G. Gasser, L. Ji and H. Chao, *Angew. Chemie - Int. Ed. Engl.*, 2015, **54**, 14049–14052.

20 J. Liu, Y. Chen, G. Li, P. Zhang, C. Jin, L. Zeng, L. Ji and H. Chao, *Biomaterials*, 2015, **56**, 140–153.

21 J. S. McCaughan, *Drugs Aging*, 1999, **15**, 49–68.

22 F. Bolze, S. Jenni, A. Sour and V. Heitz, *Chem. Comm.*, 2017, **53**, 12857–12877.

23 W.-F. Cheong, S. A. Prahl and A. J. Welch, *A Review of the Optical Properties of Biological Tissues*, 1990, vol. 26.

24 F. Heinemann, J. Karges and G. Gasser, *Acc. Chem. Res.*, 2017, **50**, 2727–2736.

25 X. Liu, G. Li, M. Xie, S. Guo, W. Zhao, F. Li, S. Liu and Q. Zhao, *Dalton Trans.*, 2020, **49**, 11192–11200.

26 A. K. Gupta and T. F. Anderson, *J. Am. Acad. Dermatol.*, 1987, **17**, 703–734.

27 C. Varano, *Micros. Today*, 2020, **28**, 60–60.

28 S. Abbas, I. ud D. Din, A. Raheel and A. Tameez ud Din, *Appl. Organomet. Chem.*, 2020, **34**, 1–16.

29 S. J. Remington, *Protein Sci.*, 2011, **20**, 1509–1519.

30 H. S. Tran Cao, S. Kaushal, C. Lee, C. S. Snyder, K. J. Thompson, S. Horgan, M. A. Talamini, R. M. Hoffman and M. Bouvet, *Asian J. Endosc. Surg.*., 2011, **25**, 48–54.

31 J. C. Delong, R. M. Hoffman and M. Bouvet, *Expert Rev. Anticancer Ther.*, 2016, **16**, 71–81.

32 K. Teegardin, J. I. Day, J. Chan and J. Weaver, *Org. Process Res. Dev.*, 2016, **20**, 1156–1163.

33 S. S. Tan, L. Zou and E. Hu, *Catal. Today*, 2006, **115**, 269–273.

34 N. Serpone, A. V. Emeline, S. Horikoshi, V. N. Kuznetsov and V. K. Ryabchuk, *Photochem. Photobiol. Sci.*, 2012, **11**, 1121–1150.

35 A. Fujishima and K. Honda, *Nature*, 1972, **238**, 37–38.

36 K. A. Adegoke and N. W. Maxakato, *Mater. Today Chem.*, 2022, **23**, 100605.

37 K. Michael, *Discuss. Faraday Soc.*, 1950, **9**, 14–19.

38 S. M. Draper, D. J. Gregg, E. R. Schofield, W. R. Browne, M. Duati, J. G. Vos and P. Passaniti, *J. Am. Chem. Soc.*, 2004, **126**, 8694–8701.

39 V. Gopi, S. Subbiahraj, K. Chemmanghattu and P. C. Ramamurthy, *Dye. Pigm.*, 2020, **173**, 1–12.

40 C. Condon, R. Conway-Kenny, X. Cui, L. J. Hallen, B. Twamley, J. Zhao, G. W. Watson and S. M. Draper, *J. Mater. Chem. C*, 2021, **9**, 14573–14577.

41 S. Verma, P. Kar, A. Das and H. N. Ghosh, *Dalton Trans.*, 2011, **40**, 9765–9773.

42 D. Wei, F. Ni, Z. Zhu, Y. Zou and C. Yang, *J. Mater. Chem. C*, 2017, **5**, 12674–12677.

43 L. Flamigni, A. Barbieri, C. Sabatini, B. Ventura and F. Barigelletti, *Top. Curr. Chem.*, 2007, **281**, 143–203.

44 A. J. Howarth, M. B. Majewski and M. O. Wolf, *Coord. Chem. Rev.*, 2015, **282**–**283**, 139–149.

45 K. W. Lee, J. D. Slinker, A. A. Gorodetsky, S. Flores-Torres, H. D. Abruña, P. L. Houston and G. G. Malliaras, *Phys. Chem. Chem. Phys.*, 2003, **5**, 2706–2709.

46 L. B. Josefsen and R. W. Boyle, *Met. Based. Drugs*, 2008, **2008**.

47 J. Lu, Y. Zheng and J. Zhang, *Phys. Chem. Chem. Phys.*, 2015, **17**, 20014–20020.

48 H. Abrahamse and M. R. Hamblin, *Biochem. J.*, 2016, **473**, 347–364.

49 J. J. Sutton, D. Preston, P. Traber, J. Steinmetzer, X. Wu, S. Kayal, X. Z. Sun, J. D. Crowley, M. W. George, S. Kupfer and K. C. Gordon, *J. Am. Chem. Soc.*, 2021, **143**, 9082–9093.

50 Y. Lu, N. McGoldrick, F. Murphy, B. Twamley, X. Cui, C. Delaney, G. M. Ó. Máille, J. Wang, J. Zhao and S. M. Draper, *Chem. Eur. J.*2016, **22**, 11349–11356.

51 P. Zhang, L. Pei, Y. Chen, W. Xu, Q. Lin, J. Wang, J. Wu, Y. Shen, L. Ji and H. Chao, *Chem. Eur. J.*, 2013, **19**, 15494–15503.

52 H. J. Bolink, E. Coronado, S. Garcia Santamaria, M. Sessolo, N. Evans, C. Klein, E. Baranoff, K. Kalyanasundaram, M. Graetzel and M. K. Nazeeruddin, *Chem. Comm.*, 2007, 3276–3278.

53 F. Heinemann, J. Karges and G. Gasser, *Acc. Chem. Res.*, 2017, **50**, 2727–2736.

54 J. J. Sutton, D. Preston, P. Traber, J. Steinmetzer, X. Wu, S. Kayal, X. Sun, J. D. Crowley, M. W.

George, S. Kupfer and K. C. Gordon *J. Am. Chem. Soc*, 2021, **3** 9082-9093.

55 Y. Kuramochi and O. Ishitani, *Front. Chem.*, 2019, **7**, 1–9.

56 S. Campagna, F. Puntoriero, F. Nastasi, G. Bergamini and V. Balzani, *Top. Curr. Chem.*, 2007, **280**, 117–214.

57 C. Wu, Q. Li, X. Zhang, C. Shi, G. Li, M. Wang, K. Li and A. Yuan, *Chemistryopen*, 2019, **8**, 339–343.

58 H. Ishida, S. Tobita, Y. Hasegawa, R. Katoh and K. Nozaki, *Coord. Chem. Rev.*, 2010, **254**, 2449–2458.

59 S. Tschierlei, A. Neubauer, N. Rockstroh, M. Karnahl, P. Schwarzbach, H. Junge, M. Beller and S. Lochbrunner, *Phys. Chem. Chem. Phys.*, 2016, **18**, 10682–10687.

60 Z. Zhao, X. Yin, T. Peng, N. Wang and S. Wang, *Inorg. Chem.*, 2020, **59**, 7426–7434.

61 E. Baranoff, H. J. Bolink, F. De Angelis, S. Fantacci, D. Di Censo, K. Djellab, M. Grätzel and M. K. Nazeeruddin, *Dalton Trans.*, 2010, **39**, 8914–8918.

62 A. Frei, R. Rubbiani, S. Tubafard, O. Blacque, P. Anstaett, A. Felgenträger, T. Maisch, L. Spiccia and G. Gasser, *J. Med. Chem.*, 2014, **57**, 7280–7292.

63 A. P. Castano, T. N. Demidova and M. R. Hamblin, *Photodiagnosis Photodyn. Ther.*, 2004, 1, 279–293.

64 C. Schweitzer and R. Schmidt, *Chem. Rev.*, 2003, **103**, 1685–1757.

65 C. S. Allardyce and P. J. Dyson, *Platinum Metals Rev.*, 2001,**45**, 62.

66 L. Zeng, P. Gupta, Y. Chen, E. Wang, L. Ji, H. Chao and Z. S. Chen, *Chem. Soc. Rev.*, 2017, **46**, 5771–5804.

67 J. Liu, Y. Chen, G. Li, P. Zhang, C. Jin, L. Zeng, L. Ji and H. Chao, *Biomaterials*, 2015, **56**, 140–153.

68 M. Göppert-Mayer, *Ann. Phys.*, 1931, **401**, 273–294.

69 T. Terai and T. Nagano, *Pflug. Arch. Eur. 2013 4653*, 2013, **465**, 347–359.

70 C. Vonesch, F. Aguet, J. L. Vonesch and M. Unser, *IEEE Signal Process. Mag.*, 2006, **23**, 20–31.

71 Y. Lu, J. Wang, N. McGoldrick, X. Cui, J. Zhao, C. Caverly, B. Twamley, G. M. Ó Máille, B. Irwin, R. Conway-Kenny and S. M. Draper, *Angew. Chemie Int. Ed. Engl*, 2016, **55**, 14688–14692.

72 L. Murphy, A. Congreve, L. O. Pålsson and J. A. G. Williams, *Chem. Comm.*, 2010, **46**, 8743–8745.

73 R. J. Davidson, Y. T. Hsu, D. Yufit and A. Beeby, *Organometallics*, 2018, **37**, 2003–2006.

74 E. C. Constable, M. Neuburger, P. Rösel, G. E. Schneider, J. A. Zampese, C. E. Housecroft, F.

Monti, N. Armaroli, R. D. Costa and E. Ortí, *Inorg. Chem.*, 2013, **52**, 885–897.

75 A. E. Friedman, J. C. Chambron, J. P. Sauvage, N. J. Turro and J. K. Barton, *J. Am. Chem. Soc.*, 1990, **112**, 4960–4962.

76 J. Wang, J. Xue, Z. Yan, S. Zhang, J. Qiao and X. Zhang, *Angew. Chemie - Int. Ed. Engl.*, 2017, **56**, 14928–14932.

77 M. Patra and G. Gasser, *Chembiochem* , 2012, **13**, 1232–1252.

78 A. Martin, A. Byrne, C. Dolan, R. J. Forster and T. E. Keyes, *Chem. Comm.*, 2015, **51**, 15839–15841.

79 E. C. Glazer, D. Magde and Y. Tor, *J. Am. Chem. Soc.*, 2007, **129**, 8544–8551.

80 D. Magde, M. D. Magde and E. C. Glazer, *Coord. Chem. Rev.*, 2016, **306**, 447–467.

81 J. Wang, Y. Lu, N. McGoldrick, C. Zhang, W. Yang, J. Zhao and S. M. Draper, *J. Mater. Chem. C*, 2016, **4**, 6131–6139.

82 Y. Wang, S. Liu, M. R. Pinto, D. M. Dattelbaum, J. R. Schoonover and K. S. Schanze, *J. Phys. Chem. A*, 2001, **105**, 11118–11127.

83 E. C. Glazer, D. Magde and Y. Tor, *J. Am. Chem. Soc.*, 2007, **129**, 8544–8551.

84 D. Magde, M. D. Magde and E. C. Glazer, *Coord. Chem. Rev.*, 2016, **306**, 447–467.

85 E. C. Glazer, D. Magde and Y. Tor, *J. Am. Chem. Soc.*, 2005, **127**, 4190–4192.

86 R. Chinchilla and C. Nájera, *Chem. Soc. Rev.*, 2011, **40**, 5084–5121.

87 P. V. James, K. Yoosaf, J. Kumar, K. G. Thomas, A. Listorti, G. Accorsi and N. Armaroli, *Photochem. Photobiol. Sci.*, 2009, **8**, 1432–1440.

88 G. K. M. So, G. Cheng, J. Wang, X. Chang, C. C. Kwok, H. Zhang and C. M. Che, *Asian J. Chem.*2017, **12**, 1490–1498.

89 K. Nakamaru, *Bull. Chem. Soc. Jpn.*, 1982, **55**, 1639–1640.

90 L. Q. Song, J. Feng, X. S. Wang, J. H. Yu, Y. J. Hou, P. H. Xie, B. W. Zhang, J. F. Xiang, X. C. Ai and J. P. Zhang, *Inorg. Chem.*, 2003, **42**, 3393–3395.

91 S. Medina-Rodríguez, S. A. Denisov, Y. Cudré, L. Male, M. Marín-Suárez, A. Fernández-Gutiérrez, J. F. Fernández-Sánchez, A. Tron, G. Jonusauskas, N. D. McClenaghan and E. Baranoff, *Analyst*, 2016, **141**, 3090–3097.

92 S. K. Seth and P. Purkayastha, *Eur. J. Inorg. Chem.*, 2020, **2020**, 2990–2997.

93 I. E. Pomestchenko, C. R. Luman, M. Hissler, R. Ziessel and F. N. Castellano, *Inorg. Chem.*, 2003, **42**, 1394–1396.

94 Z. Hao, K. Zhang, P. Wang, X. Lu, Z. Lu, W. Zhu and Y. Liu, *Inorg. Chem.*, 2020, **59**, 332–342.

95 M. Vonlanthen, A. Cevallos-Vallejo, E. Aguilar-Ortíz, A. Ruiu, P. Porcu and E. Rivera, *Polymer J.* ., 2016, **99**, 13–20.

96 N. Pragti, B. K. Kundu, S. N. Upadhyay, N. Sinha, R. Ganguly, I. Grabchev, S. Pakhira and S. Mukhopadhyay, *Dalton Trans.*, 2022, **51**, 3937–3953.

97 H. Chen, J. Wang, F. Zhao, Y. Wang, H. He and H. Xia, *Inorganica Chim. Acta*, 2019, **498**, 119155.

98 W. J. Xu, S. J. Liu, X. Zhao, N. Zhao, Z. Q. Liu, H. Xu, H. Liang, Q. Zhao, X. Q. Yu and W. Huang, *Eur. J. Chem.*, 2013, **19**, 621–629.

99 R. Bodapati, M. Sarma, A. Kanakati and S. K. Das, *J. Org. Chem.*, 2015, **80**, 12482–12491.

100 R. Bodapati, C. Sahoo, M. Gudem and S. K. Das, *Inorg. Chem.*, 2019, **58**, 11470–11479.

101 K. R. Benson, J. Stash, K. L. Moffa, R. H. Schmehl, T. J. Dudley and J. J. Paul, *Polyhedron*, 2021, **205**, 115300.

102 D. S. Tyson, C. R. Luman, X. Zhou and F. N. Castellano, *Inorg. Chem.*, 2001, **40**, 4063–4071.

103 M. Chandrasekharam, C. P. Kumar, S. P. Singh, V. Anusha, K. Bhanuprakash, A. Islam and L. Han, *RSC Adv.*, 2013, **3**, 26035–26046.

104 M. Sarma, T. Chatterjee, S. Ghanta and S. K. Das, *J. Org. Chem.*, 2012, **77**, 432–444.

105 V. Balzani, G. Bergamini, S. Campagna and F. Puntoriero, eds. V. Balzani and S. Campagna, Springer Berlin Heidelberg, Berlin, Heidelberg, 2007, pp. 1–36.106 A. M. Horan, V. K. Duong and E. M. McGarrigle, *Org. Lett.*, 2021, **23**, 9089–9093.

107 V. K. Duong, A. M. Horan and E. M. McGarrigle, *Org. Lett.*, 2020, **22**, 8451–8457.

108 Z. C. Yang, M. Wang, A. M. Yong, S. Y. Wong, X. H. Zhang, H. Tan, A. Y. Chang, X. Li and J. Wang, *Chem. Comm.*, 2011, **47**, 11615–11617.

109 W. G. Fisher, W. P. Partridge, C. Dees and E. A. Wachter, *Photochem. Photobiol.*, 1997, **66**, 141–155.

110 B. Balázs, Z. Tóth, I. Kacsir, A. Sipos, P. Buglyó, L. Somsák, E. Bokor, G. Kardos and P. Bai, *Front. Chem.*, 2022, **10**, 1–9.

111 M. Ankathatti, A. Manalac, M. Weersink, S. A. Mcfarland and L. Lilge, *Coord. Chem. Rev.*, 2022, **470**, 214712.

112 W. Kaiser and C. G. B. Garrett, *Phys. Rev. Lett.*, 1961, **7**, 229–231.

112a A. Jechow, *Photonics*, 2022, **9,** 52.

113 M. Pawlicki, H. A. Collins, R. G. Denning and H. L. Anderson, *Angew. Chemie Int. Ed. Engl.*, 2009,

48, 3244–3266.

114 M. A. Albota, C. Xu and W. W. Webb, *Appl. Opt.*, 1998, **37**, 7352–7356.

115 M. Albota, D. Beljonne, J. L. Brédas, J. E. Ehrlich, J. Y. Fu, A. A. Heikal, S. E. Hess, T. Kogej, M. D. Levin, S. R. Marder, D. McCord-Maughon, J. W. Perry, H. Röckel, M. Rumi, G. Subramaniam, W. W. Webb, X. L. Wu and C. Xu, *Science*, 1998, **281**, 1653–1656.

116 Z. Zheng, Q. Zhang, Z. Yu, M. Yang, H. Zhou, J. Wu and Y. Tian, *J. Mater. Chem. C*, 2013, **1**, 822–830.

117 K. D. Bonin and T. J. McIlrath, *J. Opt. Soc. Am. B*, 1984, **1**, 52.

118 N. S. Makarov, M. Drobizhev and A. Rebane, *Opt. Express*, 2008, **16**, 4029.

119 D. P. Prabhakaran, Direct Laser Writing, 2020. (accessed September 2022)

120 J.-H. Li, J.-T. Wang, P. Hu, L.-Y. Zhang, Z.-N. Chen, Z.-W. Mao and L.-N. Ji, *Polyhedron*, 2008, **27**, 1898–1904.

121 O. Mongin, M. Four, S. Chevreux, M. Blanchard-Desce and G. Lemercier, *Chimia* 2015, **69**, 666–669.

122 S. C. Boca, M. Four, A. Bonne, B. van der Sanden, S. Astilean, P. L. Baldeck and G. Lemercier, *Chem. Comm.*, 2009, **30** 4590–4592.

123 J. Karges, S. Kuang, F. Maschietto, O. Blacque, I. Ciofini, H. Chao and G. Gasser, *Nat. Commun.*, 2020, **11**, 1–13.

124 N. Durand, R. Mhanna, P. Savel, H. Akdas-Kiliç, J. P. Malval, O. Soppera and J. L. Fillaut, *Chem. Comm.*, 2020, **56**, 12801–12804.

125 N. Durand, A. Amar, R. Mhanna, H. Akdas-kiliç, O. Soppera, J. Malval, A. Boucekkine and J. Fillaut, *Molecules*, 2022, **27**, 1493.

126 J. Geng, Y. Dai, X. X. Wang, M. Y. Hu, T. Tao and W. Huang, *Tetrahedron*, 2015, **71**, 654–662.

127 J. Oelerich and G. Roelfes, *Chem. Sci.*, 2013, **4**, 2013–2017.

128 N. J. Lundin, P. J. Walsh, S. L. Howell, J. J. McGarvey, A. G. Blackman and K. C. Gordon, *Inorg. Chem.*, 2005, **44**, 3551–3560.

129 J. Yang, Y. Gao, T. Jiang, W. Liu, C. Liu, N. Lu, B. Li, J. Mei, Q. Peng and J. Hua, *Chem. Front*, 2017, **1**, 1396.

130 F. Bellina, A. Carpita and R. Rossi, *Synthesis (Stuttg).*, 2004, **2004**, 2419–2440.

131 J. Bariwal and E. Van Der Eycken, *Chem. Soc. Rev.*, 2013, **42**, 9283–9303.

132 N. T. S. Phan, M. Van Der Sluys and C. W. Jones, *Adv. Synth. Catal.*, 2006, **348**, 609–679.

133 A. M. ROUHI, *Chem. Eng. News.*, 2004, **82**, 49–58.

134 T. E. Jacks, D. T. Belmont, C. A. Briggs, N. M. Horne, G. D. Kanter, G. L. Karrick, J. J. Krikke, R. J. McCabe, J. G. Mustakis, T. N. Nanninga, G. S. Risedorph, R. E. Seamans, R. Skeean, D. D. Winkle and T. M. Zennie, *Org. Process Res. Dev.*, 2004, **8**, 201–212.

135 M. Yamada, Y. Tanaka, Y. Yoshimoto, S. Kuroda and I. Shimao, *Bull. Chem. Soc. Jpn.*, 1992, **65**, 1006–1011.

136 X.-X. Wang, T. Tao, J. Geng, B.-B. Ma, Y.-X. Peng and W. Huang, *Chem. Asian J.*2014, **9**, 514–525.

137 B. A. DaSilveira Neto, A. S. Lopes, M. Wüst, V. E. U. Costa, G. Ebeling and J. Dupont, *Tetrahedron Lett.*, 2005, **46**, 6843–6846.

138 W. Z. Yuan, Y. Gong, S. Chen, X. Y. Shen, J. W. Y. Lam, P. Lu, Y. Lu, Z. Wang, R. Hu, N. Xie, H. S. Kwok, Y. Zhang, J. Z. Sun and B. Z. Tang, *Chem. Mater.*, 2012, **24**, 1518–1528.

139 M. P. Sk and A. Chattopadhyay, *RSC Adv.*, 2014, **4**, 31994–31999.

140 M. Torimura, S. Kurata, K. Yamada, T. Yokomaku, Y. Kamagata, T. Kanagawa and R. Kurane, *Anal. Sci.*, 2001, **17**, 155–160.

141 K. A. Opperman, S. L. Mecklenburg and T. J. Meyer, *Inorg. Chem.*, 1994, **33**, 5295–5301.

142 S. Doose, H. Neuweiler and M. Sauer, *Chemphyschem*, 2009, **10**, 1389–1398.

143 V. Balzani, G. Bergamini, S. Campagna and F. Puntoriero, eds. V. Balzani and S. Campagna, Springer Berlin Heidelberg, Berlin, Heidelberg, 2007, pp. 143-204.

144 P. L. Santos, J. S. Ward, P. Data, A. S. Batsanov, M. R. Bryce, F. B. Dias and A. P. Monkman, *J. Mater. Chem. C*, 2016, **4**, 3815–3824.

145 D. Jung, B. Thirupathaiah, E. Lee, G. Kwon, C. Kim and S. Y. Seo, *J. Nanosci. Nanotechnol.*, 2016, **16**, 924–929.

146 L. Ventelon, S. Charier, L. Moreaux, J. Mertz and M. Blanchard-Desce, *Angew. Chemie*, 2001, **113**, 2156–2159.

147 G. Tang, A. A. Sukhanov, J. Zhao, W. Yang, Z. Wang, Q. Liu, V. K. Voronkova, M. Di Donato, D. Escudero and D. Jacquemin, *J. Phys. Chem. C*, 2019, **123**, 30171–30186.

148 S. S. Reddy, V. G. Sree, K. Gunasekar, W. Cho, Y. S. Gal, M. Song, J. W. Kang and S. H. Jin, *Adv. Opt. Mater.*, 2016, **4**, 1236–1246.

149 F. Ni, Z. Wu, Z. Zhu, T. Chen, K. Wu, C. Zhong, K. An, D. Wei, D. Ma and C. Yang, *J. Mater. Chem. C*, 2017, **5**, 1363–1368.

150 T. Norrby, A. Börje, B. Åkermark, L. Hammarström, J. Alsins, K. Lashgari, R. Norrestam, J.

Mårtensson and G. Stenhagen, *Inorg. Chem.*, 1997, **36**, 5850–5858.

151 A. Florence Tikum, Y. J. Jeon, J. H. Lee, M. H. Park, I. Y. Bae, S. H. Kim, H. J. Lee and J. Kim, *J. Inorg. Biochem.*, 2018, **180**, 204–210.

152 R. Davidson, Y.-T. Hsu, C. Bhagani, D. Yufit and A. Beeby, *Organometallics*, 2017, **36**, 2727–2735.

153 E. Baranoff and B. F. E. Curchod, *Dalton. Trans.*, 2015, **44**, 8318–8329.

154 D. Song, Y. Yu, L. Yue, D. Zhong, Y. Zhang, X. Yang, Y. Sun, G. Zhou and Z. Wu, *J. Mater. Chem. C*, 2019, **7**, 11953–11963.

155 H. W. Bae, G. W. Kim, R. Lampande, J. H. Park, I. J. Ko, H. J. Yu, C. Y. Lee and J. H. Kwon, *Org. Electron.*, 2019, **70**, 1–6.

156 J. Xiao, M. Zhao, Y. Wang and X. Zhang, *Nanophotonics*, 2017, **6**, 1309–1328.

157 J. Bauri, R. B. Choudhary and G. Mandal, *J. Mater. Sci. 2021 5634*, 2021, **56**, 18837–18866.

158 F. K. Yam and Z. Hassan, *Microelectronics J.*, 2005, **36**, 129–137.

159 B. Minaev, V. Minaeva and H. Ågren, *J. Phys. Chem. A*, 2009, **113**, 726–735.

160 S. Lee and W. S. Han, *Inorg. Chem. Front.*, 2020, **7**, 2396–2422.

161 B. Matt, J. Moussa, L. M. Chamoreau, C. Afonso, A. Proust, H. Amouri and G. Izzet, *Organometallics*, 2012, **31**, 35–38.

162 B. Matt, C. Coudret, C. Viala, D. Jouvenot, F. Loiseau, G. Izzet and A. Proust, *Inorg. Chem.*, 2011, **50**, 7761–7768.

163 M. Zhang, Y. Y. Hu, M. Pan, B. H. Tong, S. Wang, H. D. Zhou, P. Shi and Q. F. Zhang, *Dye. Pigment.*, 2019, **165**, 11–17.

164 B. Liu, F. Dang, Z. Feng, Z. Tian, J. Zhao, Y. Wu, X. Yang, G. Zhou, Z. Wu and W. Y. Wong, *J. Mater. Chem. C*, 2017, **5**, 7871–7883.

165 V. Jornet-Mollá and F. M. Romero, *Tetrahedron Lett.*, 2015, **56**, 6120–6122.

166 C. Wu, B. Wang, Y. Wang, J. Hu, J. Jiang, D. Ma and Q. Wang, *J. Mater. Chem. C*, 2019, **7**, 558–566.

167 J. Nociarová, P. Osuský, E. Rakovský, D. Georgiou, I. Polyzos, M. Fakis and P. Hrobárik, *Org. Lett.*, 2021, **23**, 3460–3465.